UCL-University College London
Institute of Ophthalmology
Faculty of Brain Sciences

Roles of the small leucine-rich repeat proteoglycans OMD and PRELP in development and cancer

By

Vasiliki Papadaki

Thesis submitted to University College London for the degree of Doctor of Philosophy

2014

Declaration

I, Vasiliki Papadaki confirm that the work presented in this thesis is my own. Where information has been derived from other sources, I confirm that this has been indicated in the thesis. Also, the current thesis does not exceed the maximum limit of 100,000 words.

Abstract

Osteomodulin (OMD) and Proline/arginine-rich and Leucine-rich Repeat protein (PRELP) belong to the small leucine-rich repeat proteoglycan (SLRP) family and as extracellular matrix components have the ability to influence various cellular functions, including cell growth, migration and proliferation, while their mutation or aberrant expression can cause developmental disorders and cancer. This thesis extends previous work in further understanding the roles of OMD and PRELP in cancer and also during mouse development.

In the current project *OMD* and *PRELP* are overexpressed in a bladder cancer cell line where they are found to alter cell morphology, reduce cell invasion and anchorage-independent growth, while they also inhibit tumour growth in xenograft mouse models. Additionally, we show that OMD and PRELP mediate their effects by cross-regulating different signalling pathways and also by affecting tight junction formation.

Furthermore, novel knock-out mouse models of OMD and PRELP were generated, where a Lac-Z cassette has been inserted in the coding regions of the two genes, allowing us to follow their expression under X-gal staining. Therefore a detailed analysis of expression patterns was initially conducted. OMD and PRELP were both expressed in skeletal elements during mouse development, while in adult mice they were differentially expressed in neurons and epithelia of the brain and the eye, and in the urothelium of the bladder. Finally, the novel knock-out mice were used to assess any cancer-related aberrant phenotypes arising from OMD and PRELP deficiency. The bladders of the knock-out mice presented with early stages of urothelial papillary formations, where the junctional complexes were also disrupted, suggesting that lack of OMD and/or PRELP is permissive for cancer initiation.

Overall, with our current findings we hope to improve the understanding of SLRP biology in carcinogenesis, and we would like to propose OMD and PRELP as potential targets for the development of cancer therapies.

Publications

Part of the work outlined in this thesis is associated with the following publications and presentations:

Papadaki V*, Hamamoto R*, Tamura T*, Watson J*, Dellett M, Sasai N, Nik-Zainal S, Longbottom R, Nakakido M, Saloura V, Veerakumarasivam A, Neal D, Murphy G, Ponder B, Tsumoto K, Nakamura Y, Kelly J, Ohnuma S, "Osteomodulin and PRELP are novel redundant tumor-suppressor genes involved in bladder cancer initiation", Currently ready for submission to *Cell*

Papadaki V*, Dellett M*, Hu W*, Ohnuma S: ″Small leucine rich proteoglycan family regulates multiple signalling pathways in neural development and maintenance″, Review, *Dev Growth Differ*. 2012 Apr;54(3):327-40

Poster presentation: ″Roles of SLRP proteins in neural development and function″, **Vasiliki Papadaki** (presenting author), Margaret Dellett, Shin-ichi Ohnuma. Society for Neuroscience-SFN 2013 Annual Meeting (November 9-13, 2013), San Diego, California

*These authors made an equal contribution to this paper

Acknowledgments

Firstly, I would like to thank my supervisor, Prof. Shin-ichi Ohnuma, for providing me with the opportunity to undertake my PhD in his lab and also for his support and guidance.

I would also like to thank all the members of the Ohnuma laboratory. I am extremely grateful to Dr. Margaret Dellett who stood both like a supervisor and a friend to me. Her advice and help was crucial (especially with all the mouse techniques) and she managed to always lift my confidence and motivation when needed. A big thank you goes to Kristin Lühders as well, who was always supporting me through my difficulties and for being the best person to travel with. Our first conference trip together to San Diego couldn't have been better. My gratitude also goes to Dr. Toshiya Tamura, whose experience and scientific knowledge were vital for the continuation of my project, and also for his help with my initial experiments.

Further thanks go to the other lab members Nasrin, Michelle, Wanzhou and Steve for being always kind and helpful. An extra thank you goes to Steve for all his help with the mice. I would like to also mention the girls from the 4th floor, Laura, Ewa, Asma, Lucy and also Su, with whom the lunchtime discussions were always a welcome distraction. I am also grateful to Peter Munro and Mark Hayes for their help with the confocal and EM. Thank you to UCL and especially Takeda Pharmaceutical Company for providing the funding for this research and also the knock-out mice.

Finally, thank you to all my friends outside of the lab Michalis, Ioanna, Kostas, Anastasis, Justyna for being so supportive and understanding over the past three years. Also, many thanks go to my neighbour and friend Vanessa, our evening walks with Sally often helped me to clear my mind during writing. Special thanks to my flatmate Constantinos and also my best friend Lia for her massive support throughout the last year. Last but not least, a huge thank you to my parents and brother for their love and encouragement in every decision of my life.

Table of Contents

List of Figures

Chapter 1 General Introduction

Chapter 3 OMD and PRELP suppress bladder tumour growth *in vitro* and *in vivo*

Chapter 4 Expression patterns of the *OMD* gene in mouse

Chapter 5 Expression patterns of the *PRELP* gene in mouse

Chapter 6 Phenotyping of OMD and PRELP knock-out mice

Appendix A

List of Tables

Abbreviations

Aq	Aqueduct
BBB	Blood-brain barrier
β-gal	β-galactosidase
BMC	Bone mineral content
BMD	Bone mineral density
BMPs	Bone morphogenetic proteins
CB	Ciliary body
Cdc42	Cell division control protein 42 homolog
CP	Choroid plexus
CS	Chondroitin sulphate
CSF	Cerebrospinal fluid
D3V	Dorsal 3rd ventricle
DAPI	4',6-diamidino-2-phenylindole
DMEM	Dulbecco's Modified Eagle's Medium
dpc	days post coitum
DS	Dermatan sulphate
E	Embryonic day
ECM	Extra-cellular matrix
EGF	Epidermal growth factor
EGFR	Epidermal growth factor receptor
EMT	Epithelial to mesenchymal transition
ERKs	Extracellular-signal-regulated kinases
ETS	E26 transformation-specific
FBS	Fetal bovine serum
FGF	Fibroblast growth factor
FGFR	Fibroblast growth factor receptor
GAG	Glycosaminoglycan
GFP	Green fluorescent protein
GrDG	Granule dentate gyrus
HGF	Hepatocyte growth factor
ICH	Immunocytochemistry
IF	Immunofluorescence
IGF	Insulin growth factor

IGFR	Insulin growth factor receptor
Ihh	Indian hedgehog homolog
IOP	Intra-ocular pressure
KO	Knock-out
KS	Keratan sulphate
LRR	Leucine rich repeat
LOH	Loss of heterozygosity
LV	Lateral ventricle
MAC	Membrane attack complex
MAPK	Mitogen-activated protein kinase
MMP	Matrix metalloproteinase
MoDG	Molecular dentate gyrus
NVU	Neuro-vascular unit
OMD	Osteomodulin/osteoadherin
PBS	Phosphate buffer saline
PFA	Paraformaldehyde
PG	Proteoglycan
PoDG	Polymorph dentate gyrus
PRELP	proline/arginine-rich and leucine-rich repeat protein
PTHrP	Parathyroid hormone-related protein
RGC	Retinal ganglion cells
RPE	Retinal pigment epithelium
SLRP	Small leucine-rich repeat protein
TGF-β	Transforming growth factor beta
TLR	Toll-like receptor
TSG	Tumour-supressor gene
TSK	Tsukushi
VNO	Vomeronasal organ
VSMCs	Vascular smooth muscle cells
WB	Western blot
WT	Wild type
X-gal	5-bromo-4-chloro-3-indolyl-β-D-galactopyranoside

Chapter 1

General Introduction

1.1 Preface to the Introduction

The current project interrogates the novel proposition that two small leucine-rich repeat proteoglycan (SLRP) family members, osteomodulin/osteoadherin (OMD) and proline/arginine-rich and leucine-rich repeat protein (PRELP) are involved in cancer. So far, there are no published literature reports associating these two molecules to cancer, but there are many studies of other SLRP members showing their relation to tumour formation and their potential as anti-cancer agents. In addition, the spatio-temporal expression of the two proteins is studied using novel knock-out mice models, providing important information. Following a brief description of the cancer disease, the SLRP protein family and the project aims are extensively presented below.

1.2 Cancer

Cancer can be defined as a large group of diseases, medically known as malignant neoplasms, where cells divide and grow uncontrollably forming malignant tumours, and thus disrupting the normal functions of the affected organ. In some cases, tumour cancer cells acquire the ability to penetrate and infiltrate adjacent normal tissues, where a new tumour can be formed, a processed named as local metastasis. In other cases, cancer cells can penetrate the blood vessels, becoming circulating tumour cells, whereby they can metastasize to more distant organs or tissues of the body.

Approximately 14.1 million cancer cases and 8.2 million cancer deaths are estimated to have occurred in 2012 worldwide (Globocan 2012, IARC-International Agency for Research on Cancer). Cancer accounts for around 13% of all deaths annually, with lung cancer being the most common type followed by liver, stomach, colorectal and then breast cancer (World Health Organisation, 2014). Today, cancer constitutes the leading cause of death among adults aged between 40 and 80 years old, followed by heart disease (Siegel et al., 2014). The majority of cancer cases are attributed to environmental factors (e.g. smoking, nutrition, infections, radiation), while a small percentage, around 5-10% of cancers, are caused by genetic factors (Anand et al., 2008). In the genetic context, development and progression of human tumours involves the accumulation of multiple alterations, such as activation of

oncogenes and inactivation of tumour-suppressor genes (TSG), which often can rise through the aforementioned environmental factors. An exception constitutes the group of hereditary cancers, which are caused by an inherited genetic defect, accounting for less than 10% of the total cancers (Roukos, 2009). The most striking examples are mutations in the *BRCA1* and *BRCA2* genes leading to a very high risk of breast and ovarian cancer and the hereditary non-polyposis colorectal cancer (HNPCC) syndrome, which is present in about 3% of people with colorectal cancer (Cunningham et al., 2010).

1.2.1 Molecular basis of cancer – Oncogenes and tumour-suppressor genes

Already by the mid-1980s two main types of cancer-causing genes were identified, i.e. oncogenes and tumour-suppressor genes, emerging from various genomic alterations, including nucleotide mutations, chromosomal aberrations, DNA rearrangements, gene amplifications, etc. (Macconaill and Garraway, 2010). Today the basic principle in cancer research is that tumour development is a multistage process extending over decades, and which is driven by progressive accumulation of mutations, as well as epigenetic abnormalities, in genes that have variable and multiple functions (Stratton et al., 2009; Weinstein, 2002; Weinstein and Joe, 2006). In other words, a single genetic change is rarely sufficient for the development of a malignant tumour and the knowledge gathered so far points to a process of multiple steps with sequential alterations in several, often many, oncogenes, TSGs, or microRNA genes (Croce, 2008). In addition, mutations involved in cancer progression can be classified as drivers, conferring growth advantage on the cells carrying them and therefore being positively selected during the evolution of cancer, and as passengers, which do participate in cancer development (Stratton et al., 2009). Usually, driver mutations are activating in dominant genes, i.e. mutation in only one allele is sufficient to contribute to tumour development (oncogenes), and account for almost 90% of the cancer-related genes, whereas the remaining 10% include tumour-suppressor genes which act in a recessive manner and mutations in both alleles are needed to nullify the protein function (Stratton et al., 2009). Therefore, identification of the driver mutations and the genes that encompass them, and further distinction from other passenger events that simply accumulate during cell growth, is important for the advancement of more efficient therapies.

I.B. Weinstein firstly used the term "oncogene addiction" to describe the phenomenon where some cancers are dependent on one or few genes in order to maintain their malignant phenotype (Weinstein, 2000).

1.2.1.1 Oncogenes

Proto-oncogenes are genes coding for proteins that control cell proliferation, differentiation and apoptosis, and upon activation they become tumour-inducing agents (oncogenes) (Todd and Wong, 1999). There are three ways of oncogene activation including mutations, chromosomal translocation, e.g. by juxtaposition close to enhancer elements, and amplification/duplication, and their products can be classified in six broad groups: chromatin remodelers, growth factors, growth factor receptors, transcription factors, signal transducers and apoptosis regulators (Croce, 2008).

In some tumours, for example, the Fos and Jun proteins form the AP1 transcription factor, which regulates cell proliferation and survival (Shaulian and Karin, 2001). In prostate carcinomas the *TMPR552* gene fuses with and activates *ERG1* or *ETV1*, genes which belong to the ETS family of transcription regulators, and leads to increased proliferation and inhibited apoptosis of prostate gland cells (Tomlins et al., 2005). In addition, the WNT family of proteins inhibits phosphorylation of β-catenin resulting in cell proliferation and invasion (Giles et al., 2003). Mutations occurring in protein kinases, like the epidermal growth factor receptor (EGFR) or the fibroblast growth factor receptor (FGFR) families, including genes such as *EGFR*, *ERBB2/ERBB3/ERBB4*, *FGFR1/FGFR2/FGFR3* deregulate signalling in many pathways and often are found in lung and breast cancer and gastrointestinal tumours (Johnson and Lapadat, 2002; Paez et al., 2004; Stephens et al., 2004). One of the most common oncogene in human cancer is the *RAS* set of genes (including *KRAS*, *HRAS* and *NRAS*), which encode for small GTPases involved in cellular signal transduction. *RAS* mutations result in permanently activated protein products, which in turn continuously transduce signals that induce unceasing cell growth and proliferation (Goodsell, 1999). Another well-known oncogene often found mutated in many cancers is the *MYC* gene, which as a transcription factor is again capable of regulating cell growth and proliferation (through binding on Enhancer Box sequences (E-boxes) and recruiting histone

acetyltransferases) (Oster et al., 2002). Apart from the oncogenes explained briefly here, there are many more genes involved in cancer initiation and progression.

1.2.1.2 Tumour-suppressor genes

Tumour-suppressor genes code for proteins that usually have a repressive effect on the regulation of the cell cycle, preventing unrestrained cellular growth, while they promote DNA repair and cell cycle checkpoint activation. Because their cancer-preventative effects usually require the presence of only one single functional allele, tumour-suppressor genes are considered recessive following the "two-hit" hypothesis, as it was proposed by A.G. Knudson for retinoblastoma cases (Knudson, 1971).

The first "classic" tumour suppressor gene identified is the retinoblastoma tumour susceptibility gene (*RB1*). Loss of pRB function has been implicated in the development of numerous cancers, while pRB-deficient cells have altered regulation of G1 checkpoints, changes in the control of cell cycle exit (differentiation, senescence, quiescence), and altered levels of autophagy, apoptosis, angiogenesis, and metastatic potential (Burkhart and Sage, 2008). The RB family proteins physically interact with transcription factors, best characterized of which are the E2Fs (Sherr, 2004). Another important tumour suppressor is the p53 suppressor protein encoded by the *TP53* gene, which is recognized as the most frequently inactivated gene in human cancers (Kandoth et al., 2013). The INK4 family of Cdk inhibitors, and especially the founding member $p16^{INK4a}$ as well as $p14^{ARF}$ interfere with RB and p53 respectively, forming part of a signalling network that monitors cell cycle and restrains aberrant growth-promoting signals (Sharpless and DePinho, 1999; Sherr, 2001). Other well-studied TSGs are for example the *APC* gene, involved in the WNT and β-catenin signalling cascade, being responsible for familial adenomatous polyposis and some colorectal cancers (Morin et al., 1997; Rubinfeld et al., 1993), the *PTEN* gene, which participates in phosphoinositide metabolism inhibiting the AKT signalling pathway, and is often mutated in glioblastoma, endometrial and advanced prostate cancers (Sulis and Parsons, 2003); the *MSH2* and *MLH1* DNA mismatch repair genes; the *BRCA1* and *BRCA2* genes associated with familial breast and ovarian cancer, and many other genes that are not mentioned here.

1.2.2 Extracellular matrix and tumour microenvironment

The extracellular matrix (ECM) constitutes a three-dimensional structure that surrounds the cells and defines the cellular microenvironment (Aumailley and Gayraud, 1998). The main ECM components are different types of collagens, elastins, laminins, fibronectins (fibrous components) and proteoglycans (including hyaluronic acid and chondroitin/heparan/keratan sulphate) (Frantz et al., 2010). Although in the beginning ECM was considered to have a purely supporting role for cells within the tissue, now it is recognized as an important regulator of cell and tissue behaviour via transmembrane signalling, thereby contributing to differentiation, proliferation, survival, polarity and migration of cells (Hynes, 2009; Radisky and Bissell, 2004).

During tumour formation, the malignant cells have been found to create their own tumour microenvironment, which in turn essentially affects the malignant cells themselves but also the other surrounding cells of the ECM (Fang and Declerck, 2013; Lu et al., 2012). The tumour microenvironment is composed of endothelial cells (ECs), pericytes, invading inflammatory cells and leucocytes, fibroblasts and multiple ECM components, forming the so-called tumour stroma (Hanahan and Weinberg, 2011; Hanna et al., 2009).

The importance of the tumour stroma in cancer growth, invasion and metastasis has been amplified the last years, as many recent studies have demonstrated that the tumour stroma does not have a passive support structure, but rather plays an active role in cancer progression (Bissell and Hines, 2011; Blavier et al., 2006; Derynck et al., 2001; Gilkes et al., 2014; Radisky and Bissell, 2004; Sainio, 2014; Shekhar et al., 2001). The architecture of tumour-associated ECM is fundamentally different from normal tissue stroma and these morphological changes can promote cell transformation, tumour growth, motility and invasion, enable metastatic dissemination and facilitate establishment of secondary tumours at distant sites (Clarijs et al., 2003; Ruiter et al., 2002). Important mediators in these procedures are the matrix metalloproteinases (MMPs), which represent the most prominent family of proteinases associated with tumorigenesis.

MMPs have multiple roles, regulating the extracellular matrix turnover and cancer cell migration, while they can also affect signalling pathways that control cell growth, inflammation, or angiogenesis (Kessenbrock et al., 2010). For example, MMP-1 derived from tumour-infiltrating fibroblasts has been shown to play a critical role in the cleavage of PAR-1 (proteinase activated receptor-1), which appears to drive cancer cell migration and invasive behaviour of the tumour (Boire et al., 2005), highlighting the important roles of stroma-derived proteinases in the progression of tumorigenesis. Additionally, a number of ECM degrading proteolytic enzymes, such as MMP-2, -13, and -14 have been implicated in ECM remodelling, while MMP-14 (MT1-MMP) may be critical and rate limiting in collagen turnover, potently patterning the tissue to facilitate single-cell and finally collective-cell migration and invasion (Friedl and Wolf, 2008; Itoh and Seiki, 2006; Sabeh et al., 2009; Sabeh et al., 2004; Zarrabi et al., 2011). In a different context, MMP-9 appears to be critical for the formation of the metastatic niche, which is most likely linked with its ability to liberate VEGF and thereby support angiogenesis (Bergers et al., 2000; Kaplan et al., 2005).

Thus, it is becoming obvious that the tumour ECM is a dynamical structure surrounding the malignant cancer cells, which can fundamentally affect tumour growth and metastasis. Therefore, combination therapies that target components of the tumour microenvironment may be a key strategy to overcome compensatory mechanisms that tumours usually rely on to survive and also achieve more permanent and efficient therapies (Blansfield et al., 2008; Mangiameli et al., 2007).

1.3 Small leucine rich repeat proteoglycans

1.3.1 Structural biology

The small leucine-rich repeat proteoglycans (SLRPs) are a group of proteins sharing various structural and functional similarities that have multiple roles in the organization of the extracellular matrix and on cell behaviour (Hocking et al., 1998). Being part of the leucine-rich repeat (LRR) superfamily of proteins, SLRPs are characterized by a central LRR domain flanked by conserved cysteine motifs on their N- and C- terminal sides (McEwan et al., 2006). Today, the SLRP family is composed of 17 members, which are sub-divided into five classes based on their

homology, chromosomal organization and the spacing between their N-terminal Cys-rich clusters (Fig. 1.1) (Dellett et al., 2012; Schaefer and Iozzo, 2008), while two recent studies have included one extra member in the first class (Nastase et al., 2014; Ni et al., 2014).

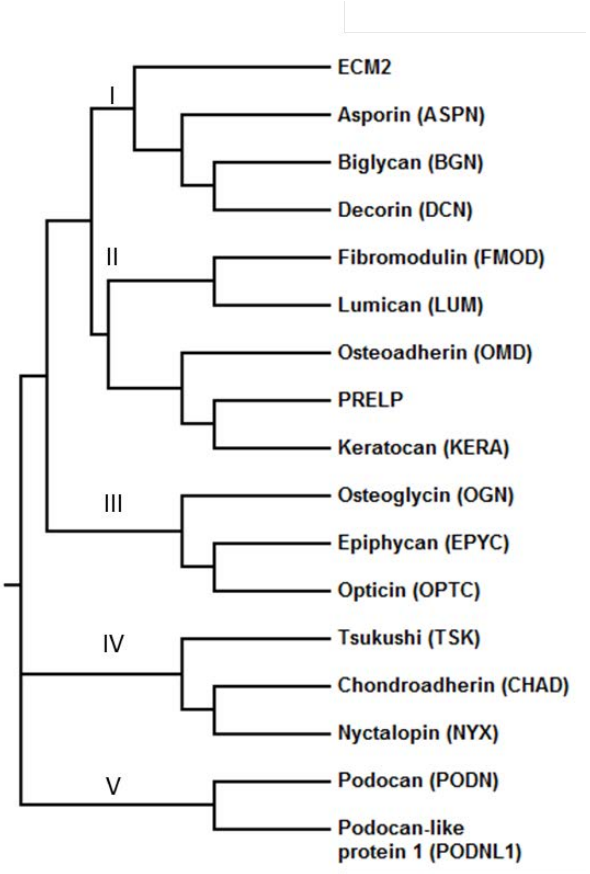

Figure 1.1: Phylogenetic analysis of the SLRP family and structural organization. Dendrogram displaying the phylogeny and the five distinct classes of the growing SLRP protein family. Generated by multiple sequence alignment using ClustalW2 from the European Bioinformatics Institute (http://www.ebi.ac.uk/Tools/msa/clustalw2/).

Structural analysis has shown that SLRPs consist of 2 main structural components, a conserved protein core which has a role in protein-protein interactions, and several different types and numbers of glycosaminoglycan (GAG) side chains, which form chondroitin (CS), keratan (KS) or dermatan sulphate (DS) (Hocking et al., 1998; Iozzo, 1997; Iozzo, 1998). More specifically, the core proteins contain a number of leucine-rich repeats (LRRs), which contain a consensus sequence LXXLXLXXNXL, where X is any amino-acid, L is leucine, isoleucine or valine, N is asparagine, cysteine or threonine. The total number of LRRs varies between the different members, with typical LRRs expanding from 20 to 29 residues,

while the most common length is 24 amino acids (McEwan et al., 2006). However, as mentioned before, all SLRPs contain additional N- and C-terminal domains.

The N-terminal cluster usually contains four cysteines, with their internal spacing varying between the five classes (exceptions are ECM2 with 2 cysteines, Tsukushi with 5 and Podocan with 6). In class I the cysteines are spaced in a Cx_3CxCx_6C configuration, where C = cysteine and x = any other amino acid. In class II, they are arranged as Cx_3CxCx_9C, in class III as Cx_2CxCx_6C, in class IV as $C_{X3}C_XC_{X6\text{-}17}C$ and in class V as $C_{X3\text{-}4}C_XC_{X9}C$ (see Table 1.1) (Schaefer and Iozzo, 2008). Taking into account the structure of decorin, the most well characterized member, it can be speculated that this N-terminal cluster is probably a capping motif common to all SLRPs, irrelative of the spacing and number of cysteines (McEwan et al., 2006; Scott et al., 2004). Furthermore, these four N-terminal cysteines form a disulphide knot between the first LRR (LRR-I) and a β-hairpin, while the variation in the number of residues between cysteines provides variety in the length of the β-hairpin (McEwan et al., 2006). Such cysteine N-terminal capping motifs are also found in other LRRs besides the SLRPs, like the Nogo receptor ectodomain and the glycoprotein GPIba (He et al., 2003; Huizinga et al., 2002; Uff et al., 2002).

McEwan *et al*. also determined the relatively new C-terminal motif specific to SLRPs, which basically consists of the penultimate LRR, usually being the longest repeat of the protein, named as “ear repeat” (McEwan et al., 2006). Ear repeats can vary in length and sequence between different SLRP members, with classes I and III having 30 residues, while class II members range from 31 residues (fibromodulin, osteomodulin and lumican) to notably “long ears” of keratocan and PRELP, with 38 and 39 residues respectively (Fig. 1.2) (McEwan et al., 2006). So far no such motifs have been identified in classes IV and V.

Instead, proteins such as chondroadherin and nyctalopic seem to adopt a different kind of C-terminal cap including four C-terminal cysteines linked to form two disulphide bonds, a motif often found in other eukaryotic LRR proteins (like GPIba and Nogo), whilst on the other hand, podocan has 12 C-terminal glutamate residues (Ross et al., 2003; McEwan et al., 2006).

Table 1.1: Structure of SLRP family members

SLRP member		Number of LRR	N-terminal Cys-rich cluster	Ear repeat	GAG type/Member	Reference
Biglycan Decorin Asporin† ECM2	Class I	12*	$C_{X3}C_XC_{X6}C$	Yes	CS/DS (DKN, BGN)	(Iozzo, 1999; Matsushima et al., 2000) (Dammer et al., 1995; Schaefer and Schaefer, 2010)
Fibromodulin Lumican PRELP† Keratocan Osteomodulin	Class II	12	$C_{X3}C_XC_{X9}C$	Yes	KS	(Sommarin et al., 1998) (Vogel, 1994) (Blochberger et al., 1992; Corpuz et al., 1996) (Plaas and Wong-Palms, 1993) (Bengtsson et al., 1995)
Epiphycan Opticin† Osteoglycin	Class III	8	$C_{X2}C_XC_{X6}C$	Yes	DS (EPYC) KS (OGN) *O*-linked oligosaccharides (OPTC/EPYC)	(Reardon et al., 2000) (Funderburgh et al., 1997; Johnson et al., 1997)
Chondroadherin Nyctalopin Tsukushi	Class IV	12	$C_{X3}C_XC_{X6\text{-}17}C$	No	Potential sites for glycosylation	(Ohta et al., 2004) (Neame et al., 1994)
Podocan Podocan-like 1 protein	Class V	20*	$C_{X3\text{-}4}C_XC_{X9}C$	No	Potential sites for glycosylation	(Ross et al., 2003) (Mochida et al., 2011)

*ECM2 has 15 LRRs, Podocan-like protein 1 has 21 LLRs; †Asporin, PRELP and Opticin have no GAG chains, but have potential sites for substitution by N or *O*-linked oligosaccharides (Grover and Roughley, 2001; Iozzo, 1999). C=cysteine, X=any other residue, CS=Chondroitin sulfate, DS=Dermatan sulfate, KS=Keratan sulfate.

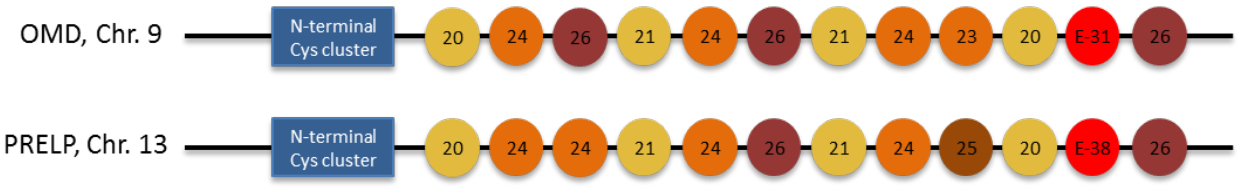

Figure 1.2: Structural organization of OMD and PRELP. Each circle represents a LLR with the number of residues written inside it, while the circles are shaded according to their length. The red LRR named E is the extended Ear repeat having 30 residues in OMD and 38 in PRELP (by V.Papadaki).

Most SLRPs are synthesized as proteoglycans containing CS, DS or KS sulphate side chains, while some appear as glycoproteins containing *N*-linked oligosaccharides (see Table 1.1). Class I proteins decorin and biglycan bind chondroitin and dermatan sulphate side chains, whilst asporin instead of a GAG chain contains a stretch of aspartic acid residues in its N-terminus (Iozzo 1997; Henry et al., 2001; Lorenzo et al., 2001). Class II fibromodulin, lumican, keratocan and OMD all bind keratan sulphate side chains, whereas PRELP often exists as a glycoprotein lacking a GAG attachment, but has four potential N-linked glycosylation sites (Blochberger et al., 1992; Plaas & Wong-Palms, 1993; Vogel, 1994; Bengtsson et al., 1995; Corpuz et al., 1996; Sommarin et al., 1998). In addition, PRELP can bind heparin and heparan sulphate through its 22 amino-acid N-terminal region, which contains two threonine residues to which they may attach, whereas the presence of KS in bovine PRELP has also been suggested, due to a shift in the electrophoretic mobility following keratanase digestion (Bengtsson et al., 2000; Bengtsson et al., 1995). Class III epiphycan and osteoglycin contain DS and KS respectively, while opticin has potential sites for substitution by *O*-linked oligosaccharides (Johnson et al., 1997; Funderburgh et al., 1997; Reardon et al., 2000). Class IV and V proteins have not been found to bear any GAG side chains but have many potential sites for glycosylation (Neame et al., 1994; Ross et al., 2003; Ohta et al., 2004; Mochida et al., 2011).

1.3.2 SLRPs expression, functions and signalling pathways

Due to their proteoglycan structure, SLRPs tend to localize in the extracellular matrix (ECM) and after secretion can interact with a variety of many other ECM proteins. Initially SLRPs were thought to act exclusively as structural components modulating synthesis, assembly and degradation of collagen fibrils, but today are also recognised as important regulators of cell-matrix crosstalk, influencing a variety of biological processes such as cell proliferation, differentiation, survival, adhesion, inflammation, angiogenesis and tumorigenesis (Merline et al., 2009). Thus, SLRPs are justifiably defined as matricellular proteins. In addition, although they have similar structure and some common functions, their expression is dynamic and varies, presenting different spatio-temporal patterns during development and adult life. Since one of the main subjects examined in this project is the murine expression

patterns of OMD and PRELP, the differential expression of SLRPs will be described in detail at the introductions of the relative chapters (Chapters 4&5). Alternatively, SLRP cellular functions and affected signalling pathways will be presented below.

1.3.2.1 Structure and adhesion

As mentioned before, SLRPs are active components of the ECM and through their multipotent binding abilities can regulate matrix and more specifically collagen fibril assembly. Most of the SLRPs that modulate fibrillogenesis belong to class I and class II. Firstly, decorin, which is the archetypal and best-characterized SLRP, was named after its ability to "decorate" collagen fibrils (Pogany and Vogel, 1992). It binds to collagen type I, II, III, V, VI, XII and XIV (Bidanset et al., 1992; Douglas et al., 2006; Ehnis et al., 1997; Font et al., 1996; Whinna et al., 1993) while it participates in collagen fibril growth and regulation of fibril diameter *in vitro* (Fig. 1.3) (Danielson et al., 1997). Furthermore, Elefteriou *et al*. demonstrated that the GAG chain of decorin binds to tenascin-X mediating its interaction with collagen fibrils and thus contributing to extracellular matrix integrity (Elefteriou et al., 2001). The *in vivo* function of decorin in regulating collagen fibrillogenesis was established by the use of knock-out mice, which showed abnormal skin fragility due to loosely packed networks of collagen fibres and increased fibril diameter (Danielson et al., 1997; Reed and Iozzo, 2002).

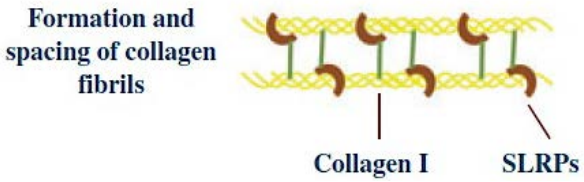

Figure 1.3: SLRPs and collagen assembly. SLRPs have a curved shape and bind to collagen fibrils through their core protein, thereby participating in the formation and spacing of the fibrils (by Theocharis et al., 2010)

Biglycan follows as the second most-studied SLRP and was found to bind to collagen type I, II, III and IV *in vitro*, though without influencing fibril diameter or fibrillar kinetics (Douglas et al., 2006; Schonherr et al., 1995; Wiberg et al., 2002). Biglycan null mice show an osteoporosis-like phenotype with thin dermis and reduced bone mass due to larger, irregular fibrils (Corsi et al., 2002; Xu et al., 1998). Fibromodulin, a class II KS SLRP, binds to collagen type I and II and also regulates

fibrillogenesis, especially in the peripheral cornea, where the sclera and corneal stromas are integrated during development (Chen et al., 2010), while fibromodulin-deficient animals have an abnormal tendon phenotype with impaired collagen fibrils (Kalamajski and Oldberg, 2009; Svensson et al., 1999; Viola et al., 2007). Similarly, lumican binds to collagen type I and participates in fibrillar assembly in tendons and cornea, which is further supported by the fact that lumican knock-out mice demonstrated increased skin fragility and also bilateral corneal opacity (Chakravarti et al., 1998; Chakravarti et al., 2000; Ezura et al., 2000).

PRELP binds collagen type I and II (Bengtsson et al., 2002), while OMD binds the non-collagenous domain 4 of collagen type IX and $\alpha_v\beta_3$ integrin (Lucchini et al., 2004; Tillgren et al., 2009). The core protein of PRELP has been demonstrated to interact with collagen fibrils and thus it was suggested that it may play a role in linking basement membranes or cells to the adjacent extracellular matrix, something that could be further supported by the fact that PRELP also binds perlecan through its 22 amino acid N-terminal region and in that way can function as a basement membrane anchor (Bengtsson et al., 2000; Bengtsson et al., 2002). So far there are no studies about OMD or PRELP null mice. However, considering their structural similarities with the other SLRP members mentioned above we can speculate that they may have additional roles in cell-cell/cell-matrix adhesion processes and in extracellular matrix organization.

In addition, it was demonstrated that decorin and biglycan together can co-ordinate in regulating collagen fibril assembly in tendons (Zhang et al., 2006) and in the cornea (Zhang et al., 2009). Finally, it was shown that in tendon, lumican was increased in the absence of fibromodulin, suggesting that they can co-operate and maybe function as a pair like decorin and biglycan (Svensson et al., 1999; Chakravarti et al., 2003).

1.3.2.2 Signalling pathways and other biological functions

Apart from the roles SLRPs have in ECM structure they participate in many important cellular processes through interactions with multiple signalling pathways, as described extensively in reviews by Dellett *et al*., Merline *et al*. and Schaefer & Schaefer (Dellett et al., 2012; Merline et al., 2009; Schaefer and Schaefer, 2010),

while the most studied pathways and relative SLRP members will be briefly described here. To start with, decorin binds to and sequesters transforming growth factor beta, TGF-β, inhibiting the TGF signalling pathway, modulating in that way cell proliferation (Li et al., 2008; Yamaguchi et al., 1990). In addition, decorin can act as modulator of programmed cell death, due to its interaction with the insulin-like growth factor receptor by binding to the IGF-IR and signalling via the PI3K/Akt pathway, thus having an anti-apoptotic effect of tubular epithelial and endothelial cells, affecting fibrosis and angiogenesis (Nastase et al., 2014; Schaefer et al., 2007; Schonherr et al., 2005; Schonherr et al., 2004). Furthermore, decorin interacts with ErbB receptors (Csordas et al., 2000; Iozzo et al., 1999b), epidermal growth factor receptor EGFR (Santra et al., 2000), lipoprotein-receptor related protein LRP-1 (Brandan et al., 2006; Cabello-Verrugio and Brandan, 2007) and the Met receptor (Goldoni et al., 2009), thus acting through many signalling pathways (further details on some of these pathways which are involved in cancer will be discussed in the next section).

Biglycan has been shown to decrease caspace-3 activity in mesangial cell protecting them from apoptosis (Schaefer et al., 2003), while on the contrary, lumican mediates Fas and FasL-related apoptosis by inducing Fas in mouse embryonic fibroblasts (Vij et al., 2005). Biglycan and decorin interact with WISP-1 in fibroblasts and osteogenic cells (Desnoyers et al., 2001; Inkson et al., 2009), while both proteins can also bind TNFα, thus having roles in inflammation (Tufvesson and Westergren-Thorsson, 2002). In addition, soluble biglycan can act as endogenous ligand of TLR4 and TLR2 in macrophages, further affecting downstream signalling via p38, p42/44 and NFκB (Schaefer et al., 2005). Additional multifunctional inflammatory signalling properties of decorin and biglycan are described in a recent review by Moreth *et al*. (Moreth et al., 2012).

Tsukushi (TSK) can regulate embryonic development in the *Xenopus* embryo by modulating several growth factors. For example, TSK binds to Vg1, and potentiates its activity in promoting axis formation (Ohta et al., 2006), functions as a Wnt signalling inhibitor regulating peripheral eye formation (Ohta et al., 2011), while it also binds to bone morphogenetic protein 4 (BMP4) ablating its activity in inhibiting axis formation (Ohta et al., 2004). Moreover, in the *Xenopus* embryo TSK regulates

endoderm formation by binding and activating Xenopus nodal-related protein-2 (Xnr2) and by binding and inhibiting FGF8b (Morris et al., 2007). In the same context, biglycan promotes axis formation by binding to and inhibiting BMP4 (Moreno et al., 2005), while in osteoblasts it is essential for BMP-4 and Wnt signal transduction in the stimulation of cellular differentiation (Berendsen et al., 2011; Chen et al., 2004). Also, study by Tillgren *et al*. showed that osteomodulin binds and fibromodulin binds bFGF in cell-free systems, but did not explore the functional significance of these interactions (Tillgren et al., 2009). Additionally, lumican-mediated induction of corneal epithelial cell migration has been shown to be dependent on ERK1/2 signalling (Seomun and Joo, 2008). Finally, expression of OMD is down-regulated by TGF-β1 and up-regulated by BMP-2 during bone development (Rehn et al., 2006), while the protein can bind osteoblasts via $\alpha_v\beta_3$ integrin, an interaction mentioned previously (Lucchini et al., 2004).

At present, it has also been established that various SLRPs actively participate in bone development and homeostasis, and are further involved in cell proliferation, matrix and mineral deposition, and bone remodelling (Nikitovic et al., 2012). More details on the roles of SLRPs in bone pathophysiology will be presented in Chapter 6, where the effects of OMD and PRELP on bone development are examined.

1.3.3 SLRPs in Cancer

During the process of carcinogenesis many growth factors are secreted from the malignant cells that further stimulate cell growth but also enhance the surrounding stromal cells to secrete more molecules that in turn increase permissiveness in tumour growth. The extracellular matrix integrity is crucial to maintain normal homeostasis and prevent invasion and metastasis of cancer cells, and both tumour and stromal cells are involved in the re-organisation of the ECM to promote tumour growth, invasion and migration. In that context, as SLRPs are important regulators of the extracellular matrix structure, their expression is markedly altered in the tumour microenvironment. Modified expression of SLRPs, and more generally of matrix-accumulated proteoglycans, in stromal cell membranes can affect survival, signalling, growth, adhesion and migration of cancer cells. No less than 8 SLRPs have been found to be implicated in cancer so far and again the most well studied members will be discussed below.

1.3.3.1 Expression patterns and clinical significance

The expression levels of SLRPs do not show a stable pattern but fluctuate between different cancer types. To start with, decorin is found overexpressed in pancreatic cancer (Crnogorac-Jurcevic et al., 2001; Koninger et al., 2004), in breast cancer (Leygue et al., 2000), in leukaemia (Campo et al., 2006), in chondrosarcoma (Soderstrom et al., 2002), and in squamous cell laryngeal carcinoma (Stylianou et al., 2008). On the contrary, decorin expression was found downregulated in 2 types of non-small cell lung cancer, adenocarcinoma and squamous cell carcinoma (McDoniels-Silvers et al., 2002), in colorectal cancer (Mlakar et al., 2009), in thyroid tumours (Arnaldi et al., 2005), in ovarian tumours (Nash et al., 2002) and in a variety of cancer cell lines (Santra et al., 1997). Of note is the fact that, while in normal tissues the ratio of CS and DS decorin side chains is balanced, in tumour tissue, and specifically in pancreatic cancer (Skandalis et al., 2006), colorectal cancer (Theocharis, 2002), ovarian cancer (Nash et al., 2002) and gastric cancer (Skandalis et al., 2005), the chondroitin sulphate chains become predominant. Due to the fact that DS is chemically more complex than CS and requires additional enzymes to be synthesized, it was proposed that synthesis of a chemically simpler CS is favoured in tumour tissue (Goldoni and Iozzo, 2008; Theocharis et al., 2010). In line with this concept, CS side chains have been proposed to be more permissive to cell migration favouring tumour aggressiveness (Merle et al., 1999).

There are not many studies analysing the prognostic significance of decorin expression levels in terms of patience survival. However, high expression of decorin in patients with advance ovarian cancer was associated with poor response to treatment and a greater incidence of relapse for the patients that initially responded (Newton et al., 2006). In addition, decreased amounts of decorin were associated with poor prognosis in node-negative invasive breast cancer (Troup et al., 2003) and some types of soft tissue tumours (Matsumine et al., 2007).

The other two class I SLRPs, biglycan and asporin, were overexpressed in various types of cancer. For example, asporin was overexpressed in breast cancer (Turashvili et al., 2007), while biglycan was overexpressed in salivary gland carcinoma (Leivo et al., 2005), in colorectal cancer (Galamb et al., 2009), in intrahepatic cholangiocellular carcinoma (Nishino et al., 2008), in pancreatic cancer

(Weber et al., 2001) and pancreatic cancer cell lines (Chen et al., 2002), and in the stroma of basal cell carcinoma (Hunzelmann et al., 1995).

Lumican, a class II SLRP, was found overexpressed in breast cancer (Leygue et al., 1998) and in melanomas (Sifaki et al., 2006), whilst there was altered expression in various types of human malignancies like osteosarcomas (Nikitovic et al., 2008) and pulmonary (Matsuda et al., 2008), pancreatic (Ishiwata et al., 2007) and colon carcinomas (Lu et al., 2002). Similarly to decorin, there are not constant reports regarding the role of lumican as prognostic indicator or patience survival, but lumican overexpression was associated with poor prognosis in advanced colorectal and pancreatic cancers (Ishiwata et al., 2007), as well as in lung adenocarcinomas and squamous cell carcinomas (Matsuda et al., 2008). Also, low lumican expression in breast tumours was correlated with large tumour size, increased host inflammatory response, slower time to progression and poorer survival (Troup et al., 2003), while rectal tumours expressing higher levels of lumican were more sensitive to pre-operative radiotherapy (Watanabe et al., 2006). Another class II SLRP, fibromodulin, was found overexpressed in leiomyoma (Levens et al., 2005), B-cell chronic lymphocytic leukaemia and mantle cell lymphoma (Mayr et al., 2005; Mikaelsson et al., 2005).

Finally, one of our two proteins of interest, PRELP, was described as one of four genes comprising a genetic signature that allows discrimination of two types of brain tumour, glioblastoma multiforme and meningothelial meningioma (Castells et al., 2009). However, this study did not explore the functional significance that PRELP could have in the diagnostic procedure.

1.3.3.2 Knockout mice and functions related to cancer

Among the several SLRP knockouts that have been established only decorin deficient mice show susceptibility to cancer. Around 30% of decorin null mice develop spontaneous intestinal tumours (Bi et al., 2008), while double-knockout mice of decorin and the tumour suppressor p53 together showed a faster rate of tumour emergence which leads to earlier mortality (mice succumbed very early with a mean survival of ≈ 4 months versus 6 months for the p53 null mice alone) (Iozzo et al., 1999). Collectively, these studies could represent genetic evidence that lack of

decorin is “permissive” for tumour development (Goldoni and Iozzo, 2008; Iozzo and Sanderson, 2011).

Several functional studies have demonstrated that some SLRPs can regulate hallmark activities, like proliferation and migration, of cancer cells. In this context, ectopic decorin suppressed the proliferation of colorectal, ovarian, gastrointestinal, genital, skeletal, cutaneous, and bone marrow cancer cell lines (Goldoni and Iozzo, 2008). Following the evidence that decorin has a potency to act as an inhibitor of tumour cell proliferation *in vitro*, many of the recent studies have focused on the antitumor therapeutic effect decorin may have *in vivo*. Adenoviral-mediated delivery of decorin inhibits the in vivo tumorigenicity of lung, squamous and colon carcinoma tumour xenografts in immunocompromised mice (Reed et al., 2002; Tralhao et al., 2003), arrests mammary adenocarcinoma growth and prevents metastatic spreading to the lungs (by reducing ErbB2 receptor levels) (Reed et al., 2005; Theocharis, 2002). In addition, ectopic decorin expression in a rat glioma model prolongs the animal’s lifespan, whilst the size of the tumour is directly proportional to the concentration and time point that decorin is expressed (Biglari et al., 2004). On the contrary, in a mouse osteosarcoma model decorin expression did not affect the primary tumour volumes, but inhibited metastasis to the lung (Shintani et al., 2008).

Seidler *et al*. were the first group to demonstrate that decorin can be administered as a therapeutic agent against cancer. Specifically, these researchers used the A431 squamous carcinoma model, where they showed that systemic injection of decorin protein core localises within the tumour, antagonizes EGFR activity and induces apoptosis of the tumour cells (Seidler et al., 2006). Another report from the same group proved that again systemic injection of decorin can reduce breast tumour growth and metabolism and halt metastatic spread to the lungs (Goldoni et al., 2008). In addition, ectopic decorin expression can revert the malignant phenotype in several cell lines of various histogenetic origins (Santra et al., 1997; Santra et al., 1995).

Lumican is another SLRP what was implicated in cancer in several studies. To start with, stable expression of lumican in B16F1 mouse melanoma cells reduced anchorage-independent growth and xenograft tumour formation, increased apoptosis and suppressed migration (Vuillermoz et al., 2004). In addition, other studies showed

that lumican regulates vertical growth and binds to β1-containing integrin receptors on melanoma cells, thereby inhibiting their migration by disrupting focal adhesion complexes (Brezillon et al., 2009; Brezillon et al., 2007; D'Onofrio et al., 2008). Furthermore, Zelts *et al*. identified that this inhibitory ability was mediated through the lumican protein core, and specifically the 9th LRR named as lumcorin (Zeltz et al., 2009), while knockdown of lumican in HEK293 cells increased cellular proliferation (Ishiwata et al., 2004). Finally, another SLRP, osteoglycin, inhibited migration of hepatocellular carcinoma cells *in vitro*, and also suppressed their ability to metastasize, when xenografted into mice (Cui et al., 2008).

Collectively, all these findings about SLRP's involvement in cancer progression and the fact that decorin and lumican can indeed antagonize primary tumour growth and metastases *in vivo* further show the potential that these molecules have in clinical application as anti-cancer agents.

1.3.3.3 Mechanisms of action

So far the mechanisms of SLRP activity in cancer are poorly characterised and most of the published studies are focused only on few representative members of the gene family, such as decorin, biglycan and lumican, with research on other SLRPs lagging far behind. However, there has been some significant progress in understanding the way extracellular matrix proteoglycans work against tumorigenesis and the most important findings will be described below.

Initially, decorin was found to supress tumour cell growth by directly binding the epidermal growth factor receptor (Iozzo et al., 1999b; Moscatello et al., 1998). The EGFR region that decorin binds to is partially overlapping but distinct from the EGF (natural ligand of EGFR) binding domain and this interaction between the SLRP and the receptor leads to autophosphorylation, and a sustained downregulation of EGFR, as well as other EGFR-like receptors, such as ErbB4 and ErbB2 (Csordas et al., 2000; Santra et al., 2000; Santra et al., 2002). This in turn triggers prolonged activation of the mitogen-activated protein kinase (MAPK) pathway – activation of ERK1/2, Ca2+ influx, induction of the cyclin-dependent kinase (CDK) $p21^{WAF1/CIP1}$ and growth arrest (as shown in the same studies), while decorin-bound EGFR is further internalised and degraded leading to consequent reduction of receptor number

(Fig. 1.4) (Zhu et al., 2005). In addition, in glioma cells exposed to oxygen and glucose deprivation, ectopic decorin protects cells from apoptosis by inducing expression of $p21^{WAF1/CIP1}$, $p27^{Kip1}$, PI3K and Ras (Santra et al., 2006), whilst in prostate cancer cells decorin binds androgen receptors as well as EGFR, with a downstream suppression of the PI3K pathway (Hu et al., 2009).

Apart from EGFR and ErbB4/ErbB2 decorin appears to interact with other RTKs as well. A more recent study by Goldoni *et al*., demonstrated that exogenous decorin binds to Met, the hepatocyte growth factor (HGF), leading to receptor downregulation and thus attenuating the Met signalling pathway (Goldoni et al., 2009). Notably, several biological activities mediated by the Met signalling cascade, like cell scatter, evasion and migration, were blocked by decorin through a downregulation of non-canonical β-catenin levels (Fig. 1.4) (Iozzo et al., 2011). Additionally, Myc, which is a downstream target of Wnt or RTK pathways (EGFR or Met), was markedly downregulated by decorin accompanied by an induction of phosphorylation at Thr58, further leading to proteasomal degradation of Myc and suppression of cell motility, migration and tumour growth both *in vitro* and *in vivo* (Buraschi et al., 2010). In the same study by Buraschi *et al*., it was also shown that systemic delivery of decorin in three tumour xenograft models caused downregulation of Met and a concurrent suppression of β-catenin and Myc levels. Overall, by antagonistically binding to multiple tyrosine kinase receptors, decorin participates in reduction of primary tumour growth and metastatic spreading.

In addition, in a recent study by Neill *et al*., decorin inhibited pro-angiogenic factors such as HIF-1α and VEGFA via the Met receptor (Neill et al., 2012), while in an alternative mechanism decorin directly interacted with VEGFR2 leading to rapid phosphorylation of AMPK and increased levels of the paternally expressed gene 3 (Peg3) and other Peg3-dependent autophagy-related genes, thereby leading to autophagy and angiostasis (Buraschi et al., 2013; Goyal et al., 2014). Moreover, another mechanism was proposed linking inflammation and cancer growth, where decorin binds to TLR2/4 thereby activating MAPKs and NF-κB, inducing the transcription of *TNF*, interleukin 12B and 10 (*IL-12B*, *IL10*), and the programmed cell death protein 4-*PDCD4*-gene (Merline et al., 2011). This decorin-induced expression of PDCD4 further leads to translational repression of IL-10, which is an

anti-inflammatory cytokine, and therefore an enhanced inflammatory response is mediated. At the same time, when decorin was overexpressed in tumor xenografts an induced pro-inflammatory immune response through inhibition of TGF-β1, subsequent downregulation of the oncogenic microRNA-21 (miR-21) and an increased PDCD4 abundance was noted (Merline et al., 2011). The latter findings were also independently confirmed in a different study by Soria-Valles *et al*., thereby emphasizing the relation of decorin with TGF-β1 and miR-21 (Soria-Valles et al., 2013). Finally, decorin is also able to bind to the insulin growth factor receptor and its ligand, IGF-IR and IGF-I respectively, and thus attenuate the IGF-I-induced Akt and ERK1/2 pathways, further leading to inhibition of downstream ribosomal s6 kinases and resulting in decreased migration and invasion of bladder cancer cells (Iozzo et al., 2011). All the above mechanisms are also shown in Figure 1.4, summarizing all the possible ways that have been discovered so far, through which decorin acts against tumorigenesis (Nastase et al., 2014).

The other two SLRPs that have been studied in detail so far are biglycan and lumican, and their cancer-related signaling pathways will be shortly described here. Briefly, in pancreatic tumour cells biglycan overexpression caused inhibition of cell proliferation by G1 arrest, an effect associated with upregulation of the p27 CDK inhibitor and downregulation of cyclin A and proliferating cell nuclear antigen (PCNA), as well as with attenuated activation of Ras and Erk (Weber et al., 2001). In addition, biglycan inhibited oncogenic properties of HER-2/neu-transformed fibroblasts and this effect was dependent on protein kinase C (PKC) and the cAMP response element binding protein (CREB) (Recktenwald et al., 2012), while another study showed that biglycan can act as a pro-angiogenic factor in murine tumour endothelial cells, via interactions with the TLR2/4 receptors, and thus influence their migration and morphology (Yamamoto et al., 2012).

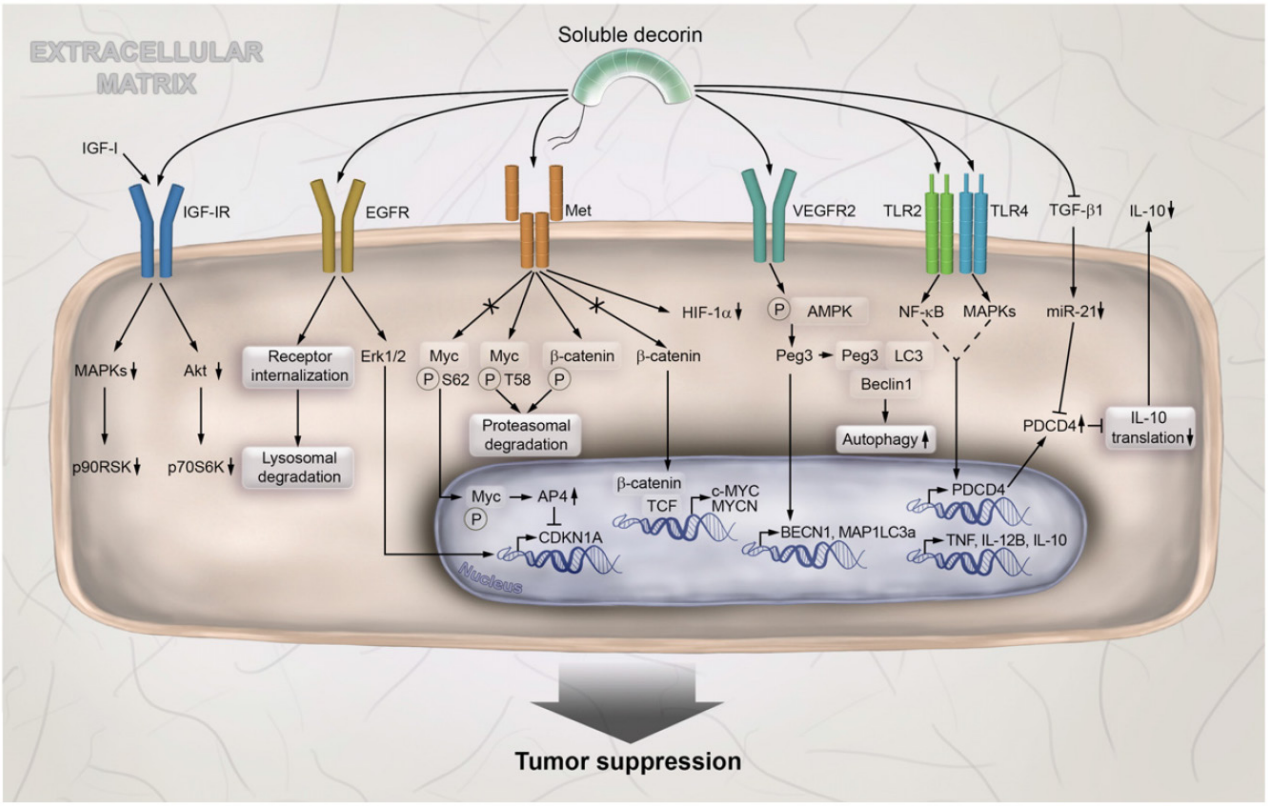

Figure 1.4: Decorin signalling in cancer. Decorin binds to IGF-IR and also its ligand IGF-I at different binding sites and decreases both IGF-I-induced MAPK and Akt activation leading to lower levels of ribosomal s6 kinases. Through binding to EGFR, decorin leads to receptor internalization and its lysosomal degradation, while after EGFR phosphorylation Erk1/2 are activated, leading to the transcription of the CDKN1A gene corresponding to cyclin-dependent kinase inhibitor 1, p21WAF1. When decorin activates Met, the HGF receptor, phosphorylation at Threonine 58 follows, which causes Myc and β-catenin to be phosphorylated for proteasomal degradation, thereby inhibiting translocation of these two molecules in the nucleus, negatively affecting cell evasion and migration. In addition, through Met, decorin inhibits pro-angiogenic factors such as HIF-1α. Alternatively, decorin interacts with VEGFR2 thereby leading to rapid phosphorylation of AMPK and increased levels of Peg3, causing autophagy and angiostasis. Moreover, decorin binds to TLR2/4 thereby activating MAPKs and NF-κB, linking inflammation and cancer growth. By inhibiting TGF-β signalling, decorin decreases the abundance of oncogenicmicroRNA-21 (miR-21) and prevents the miR-21-dependent translational repression of PDCD4 and thus reduces the levels of IL-10 protein. For more information see the main text. Abbreviations: AMPK, 5′ adenosine monophosphate-activated protein kinase; AP4, activating enhancer-binding protein; BECN1, Beclin1; CDKN1A, cyclin-dependent kinase inhibitor 1; EGFR, epidermal growth factor receptor; Erk, extracellular-signal-regulated kinase; HGF, hepatocyte growth factor; HIF-1α, hypoxia inducible factor-1α; IGF-I, insulin growth factor type I; IGF-IR, insulin-like growth factor type I receptor; IL, interleukin; MAP1LC3a,microtubule-associated protein 1 light chain 3 alpha; MAPK,mitogen-activated protein kinase; NF-κB, nuclear factor kappa-light-chain-enhancer of activated B cells; PDCD4, programmed cell death 4; Peg3, paternally expressed gene 3; TCF/LEF, lymphoid enhancer-binding factor/T-cell-specific factor; TNF-α, tumour necrosis factor; TGF-β, transforming growth factor-β; VEGFR2, vascular endothelial growth factor receptor. Adopted by Nastase *et al.*, 2014.

In analogy to decorin, lumican inhibits colony formation in soft agar (a hallmark of malignant transformation) of a variety of cell types including fibrosarcoma, carcinoma and normal embryonic cells, and this effect is mediated through increased expression of the cyclin-dependent kinase inhibitor $p21^{WAF1}$ (Li et al., 2004). However, it appears that the underlying mechanism is different compared to decorin, as in lumican expressing cells upregulation of p21 happens in a p53-dependent manner with a subsequent decrease in cyclins A, D1 and E (Vij et al., 2004). Furthermore, lumican reduces anchorage-independent growth and *in vivo* tumorigenicity in immunocompromised mice of cells transformed by the v-K-*ras* and v-*src* oncogenes, which suggests that lumican might be selectively inhibiting transformation caused by these 2 viral oncogenes and thus play a role in the development of some human cancers (Iozzo and Sanderson, 2011; Yoshioka et al., 2000).

Finally, there have been some studies linking the activity of SLRP's with matrix metalloproteinases, demonstrating how ECM and proteoglycan degradation can play a major role in the control of tumour progression. More specifically, it was shown that membrane-type matrix metalloproteinase-1 (MT1-MMP or MMP-14) can cleave lumican, leading to abrogation of its activity to supress tumour cell colony formation in soft agar (Li et al., 2004), while it can also cleave decorin inhibiting its anti-vascularisation effect in the cornea (Mimura et al., 2011). In contrast, another two studies showed that lumican regulates bone marrow mesenchymal stem cell (MSC) functions and migration via mechanisms that involve a decrease of MMP-14 expression and activity, while via the same mechanism lumican also inhibits angiogenesis in *in vivo* Matrigel plug assays (Malinowski et al., 2012; Niewiarowska et al., 2011).

In conclusion, the roles of SLRPs in cancer initiation and progression are quite complex and additional research is required to support their potential as valid therapeutic agents against cancer. However, as studies on SLRPs are constantly increasing, there is a novel emerging concept that this cancer-repressive activity functions wholly within the extracellular matrix and therefore a "basically inert" matrix component can turn into a tumour suppressor or pro-inflammatory agent (Schaefer and Iozzo, 2012), offering novel perspectives in the fight against cancer.

1.3.4 OMD and PRELP in cancer

So far there are no published studies involving osteomodulin in any cancer-related field, while PRELP has only been linked to cancer once, as one of four genes comprising a genetic signature for diagnosis of a brain tumour type (Castells et al., 2009). In collaboration with Dr. R. Hamamoto and Dr. T. Tamura, we previously discovered by microarray analysis that expression of *OMD* and *PRELP* is reduced in a number of cancers. The largest differences in expression were seen with bladder cancer, so downregulation of *OMD* and *PRELP* in urological cancers was reconfirmed by RT-PCR. A significant reduction in OMD and PRELP expression was seen in urothelial cell carcinoma and renal cell carcinoma (Fig. 1.5). More reductions in expression were seen in high stage and grade bladder tumours, and in bladder tumours that metastasized.

Further study of the effect of OMD and PRELP overexpression in a bladder cancer cell line was conducted by a previous lab member, Dr. Julie Watson, who found that both genes affected cell cycle progression, increased susceptibility of cells to mitomycin C-mediated apoptosis, abolished anchorage-independent growth of cancer cells and affected their morphology and migration capability. In search of signalling pathways involved, she found several signalling molecules to be differentially phosphorylated or expressed in OMD- and/or PRELP-transfectants, including EGFR, p38 MAPK, c-Jun, Akt, β-catenin and Smad2, suggesting that OMD and PRELP regulate networks of genes centred on the kinases, ERK, JNK, PI3K and p38 MAPK, and affect gene transcription through the HNF transcription factors. Collectively, from data generated previously in our lab and from collaborators, we have identified OMD and PRELP as candidate regulators of carcinogenesis, which may have the potential to alter the activities of cancer cells and/or affect cancer progression or initiation through a variety of mechanisms. More details on the previous data collected so far are presented in Chapter 3 and in the Appendix at the end of this thesis.

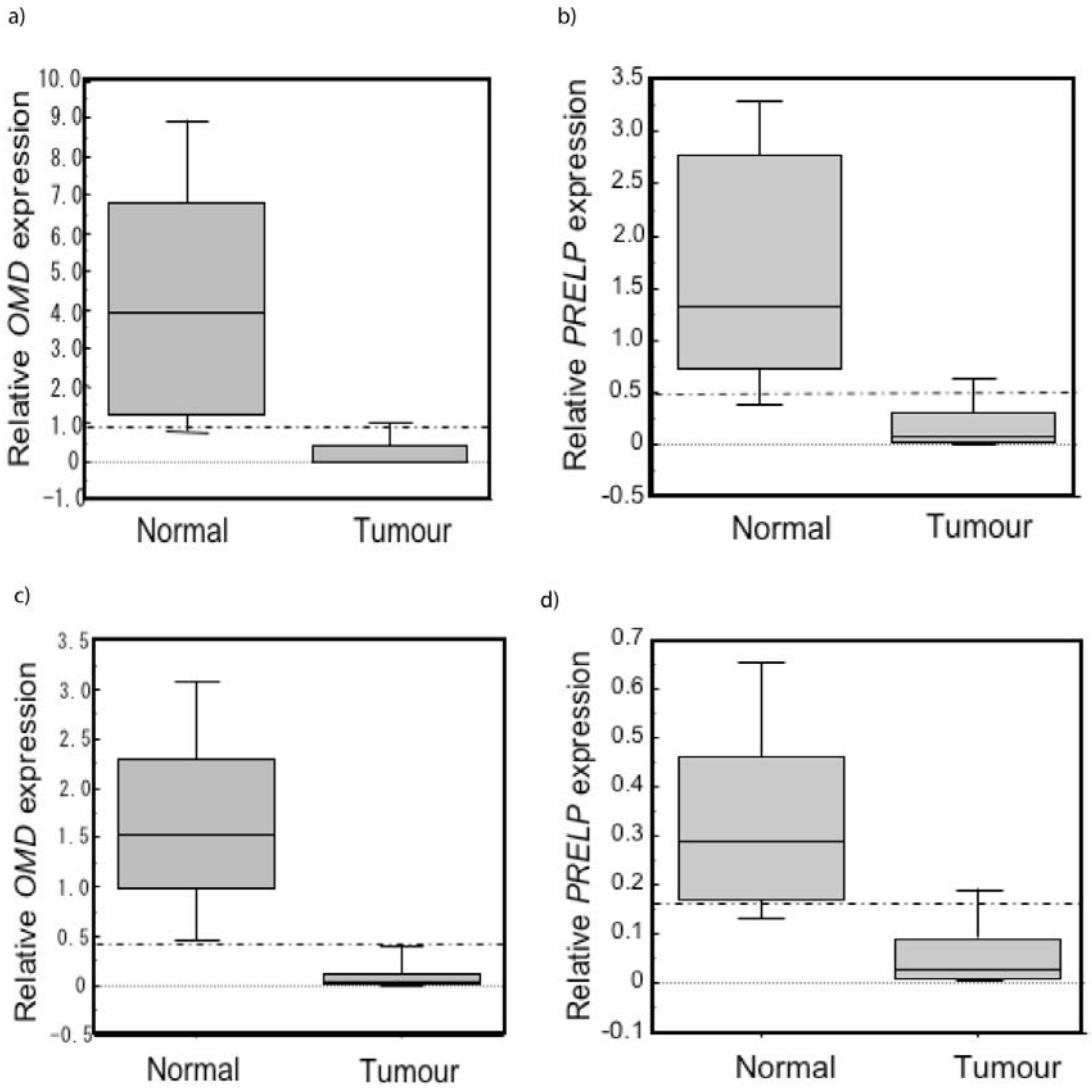

Figure 1.5: Expression of *OMD* and *PRELP* in urothelial cell carcinoma and renal cell carcinoma. Quantitative RT-PCR of a cohort of tumours and normal samples. Tissue was snap-frozen and sectioned. Epithelial cells were isolated by laser-capture microdissection, and RT-PCR was carried out. Data was normalized to *GAPDH* expression. 126 bladder tumours and 31 normal bladder samples were examined for expression of (a) *OMD* and (b) *PRELP*. 78 renal cell carcinomas and 15 normal kidney samples were examined for expression of (c) *OMD* and (d) *PRELP*. Graphs and data are kindly provided by Dr. Hamamoto and Dr. Watson.

1.4 Project hypothesis and aims

The small leucine-rich proteoglycans are important extracellular regulators of matrix architecture and of signalling into the cell. Disruption of the normal expression, or mutation, of various family members leads to a spectrum of musculoskeletal and optical disorders, while an emerging body of evidence suggests that SLRPs are also involved in carcinogenesis. While OMD and PRELP still remain two-little studied members of the SLRP family, our lab (with additional help from

our collaborators) has managed to collect a respectable amount of data demonstrating the involvement of *OMD* and *PRELP* genes in cancer. Initially, the fact that these two genes were found significantly downregulated in urothelial cell carcinoma and renal cell carcinoma, while their expression was also correlated with disease progression in urothelial cell carcinoma, was our starting point. In addition, overexpression of OMD and PRELP in the EJ28 bladder cancer cell line lead to inhibition of cell cycle progression and proliferation, and to enhancement of apoptosis and drug susceptibility (unpublished data, acquired by Dr. Watson), further supporting the involvement of the two genes in cancer. Hence, we began this project under the hypothesis that *OMD* and *PRELP* act as tumour-suppressor genes and can regulate functions involved in carcinogenesis.

The test our hypothesis the present study has the following aims:

- To determine the roles of OMD and PRELP in cellular functions involved in carcinogenesis and specifically in bladder cancer, and elucidate their mechanisms of action.
- To establish the spatial-temporal pattern of OMD and PRELP expression in the mouse.
- To characterise the phenotypes of neonatal and adult *OMD* and *PRELP* knock-out mice.

Chapter 2

Materials and Methods

2.1 Materials

2.1.1 Standard Solutions

Table 2.1: Standard solutions used throughout this project

Solution	Composition/Methods
Ampicillin stock solution 50μg/ml	Mix 1.10g Ampicillin Sodium Salt (Sigma, UK) + 22ml dH_2O (1100mg / 50(mg/ml)), filter with 0.22 μm syringe filter (Anachem, UK), 1ml aliquots, store at -20°C
Phosphate Buffer Saline (PBS)	Add 137mM NaCl, 2.7mM KCl, 100mM Na_2HPO_4, 20mM KH_2PO_4 in 800ml dH_2O, stir to dissolve, top up water to 1L, autoclave
50X TAE buffer	Provided ready in 1L bottles
1X TAE buffer for gel electrophoresis	For 1L: use 20ml of 50X TAE into 980ml dH_2O
Luria-Bertani (LB) Broth	25g LB Broth powder (Fisher Scientific, UK) in 1L dH_2O, autoclave
LB-agar	40g LB-agar powder (Fisher Scientific, UK) in 1L dH_2O, autoclave
Agarose (for soft agar assay)	Seaplaque Agarose (Lonza,UK). Make 1.4%, 1.2%, 0.7% and 0.6% in 50ml dH_2O, autoclave
Blocking Buffer (ICH/IF)	PBS with 10% goat serum (Sigma, UK) + 0.3% Triton-X 100 (Sigma, UK) + 0.1% sodium azide (Sigma, UK), filter sterilize, store at 4°C for 1 month
Transfer Buffer (WB)	Tobwin transfer buffer: Dissolve 3.03g Tris-base (Sigma, UK), 14.4g Glycine (Sigma, UK) in 600ml PBS, add 200ml Methanol (Sigma, UK), stir and top up with PBS to 1L
Blocking Buffer (WB)	PBS with 5% non-fat milk + 0.1% Triton-X 100
Wash buffer (WB)	1L PBS with 0.1% Triton-X 100
Paraformaldehyde (PFA) 4%	Freshly prepared using 32% PFA (Electronic Microscopy Sciences, USA). Mix 7 parts dH_2O and 1 part of 32% PFA
1x Trypsin	100ml bottles of 1X Tripsin-EDTA (PAA, UK) kept at 4°C
Doxycycline stock solution	Dissolve 0.1g Doxycycline hyclate (Sigma, UK) in 10ml dH_2O (final concentration of 10mg/ml), filter with 0.22 μm syringe filter, 1ml aliquots, store at -20°C
Crystal violet	For 100% stock solution, add 5mg crystal violet powder (Sigma, UK) to 5ml dH_2O, store at room temperature
Stripping buffer (WB)	Use Restore Plus Western blot Stripping buffer (Thermo Scientific, UK, Prod #46430)
X-gal (stock solution)	Dissolve 0.1g of X-gal (Melford, UK) in 5 ml dimethylformamide-DMF (Sigma, UK), store in the dark, -20°C
X-gal staining solution	Dissolve 5.35mM $K_3Fe(CN)_6$, 5.35mM $K_4Fe(CN)_6 3H_2O$, 1.2mM $MgCl_2$, 0.01% Sodium deoxycolate, 0.02% NP40, in 100ml PBS (all chemicals are from Sigma, UK), store in the dark, at RT

Ammonium Persulfate (APS 10%)	Freshly prepared, dissolve 0.2g APS (Sigma, UK) in 2ml dH_2O
100% (w/v) Trichloroacetic acid (TCA)	Dissolve 500g TCA (as shipped) into 350 ml dH2O, store at RT
0.03% Alcian blue	Dissolve 0.015g of alcian blue (Sigma, UK) in 10ml 100% ethanol and 10ml acetic acid, store at RT
0.1% Alizarin red	Dissolve 100mg alizarin red (Sigma, UK) in 100ml dH_2O, add 1% KOH
Methylene Blue solution	Dissolve 0.3g of methlylene blue (Sigma, UK) in 30ml ethanol/100ml dH_2O, 0.1% KOH
Basic fuchsin solution	Dissolve 1g of basic fuchsin (Sigma, UK) in 100ml 50% ETOH in dH_2O
Citrate buffer pH 6.0 for antigen retrieval	Dissolve 10mM citric acid (Sigma, UK), 0.05% Tween (Sigma, UK), pH 6.0, store at RT for 3 months
Tris-EDTA buffer pH 9.0 for antigen retrieval	Dissolve 10mM Tris (Fisher Scientific, UK), 1mM EDTA, .05% Tween (Sigma, UK), pH 9.0, store at RT for 3 months

2.1.2 Cell lines and media

Table 2.2: Cell lines and media used throughout this project

Cell lines/Media	Origin/Composition
EJ28 cell line	Epithelial bladder, urinary carcinoma cell line, grown in complete DMEM, CLS #300172
HEK 293T cells	Epithelial human kidney cells that constitutively express the simian virus 40 (SV40) large T antigen, cultured in complete DMEM, CRL#11268
Complete DMEM medium	Dulbecco's Modified Eagle Media (Gibco, Invitrogen, UK,#31885-049) + 10% FBS (Fetal Bovine Serum)(Biosera, UK) + 100 U/ml Penicillin/Streptomycin (Sigma, UK)
2X DMEM	Dissolve 3.35g powder DMEM (Gibco, #31600), 0.92g $NaHCO_3$ and 0.44g HEPES in 100ml dH_2O, pH to 7.4, filter-sterilize, add 25ml FBS and 2.5ml P/S

2.2 Methods

2.2.1 DNA/RNA Methods

2.2.1.1 Vectors

All the vectors (plasmids as well as viral vectors) that were used throughout the project are described below:

a) pIRES2-EGFP-OMD/mtOMD: plasmid coding for the human OMD cDNA or the myc-tagged OMD cDNA and the GFP protein. Original vector from Clontech. OMD/mtOMD cDNA was cloned into the vector by Dr. Watson

b) pIRES2-EGFP-PRELP/mtPRELP: plasmid coding for the human PRELP or the myc-tagged PRELP cDNA and the GFP protein. Original vector from Clontech. PRELP/mtPRELP cDNA was cloned into the vector by Dr. Watson

c) pLenti.TRE/CMVmin-KGF.IRES-eGFP.hPGK-rtTA2S-M2: Lentiviral "all-in-one" expression vector utilizing the Tet on system, coding for the KGF gene under an inducible GFP promoter, followed by the IRES-eGFP element and the hPGK promoter coding for the transactivator protein rtTA2S-M2. Kindly provided by Prof. Sam Janes (UCL)

d) pLenti.TRE/CMVmin.IRES-eGFP.hPGK-rtTA2S-M2: Lentiviral expression "all-in-one" vector utilizing the Tet on system, with no gene under the inducible TRE/CMVmin promoter, acting as a control for the previous vector. Kindly provided by Prof. Sam Janes (UCL)

Vectors a-b were used for creation of stable cell lines overexpressing OMD and PRELP, and also served as template to amplify OMD/mtOMD and PRELP/mtPRELP cDNAs for cloning into the lentivector; vectors c & d were used to create an inducible system for OMD/PRELP.

2.2.1.2 Plasmids transformation and selection

Prior to transformation water bath was balanced to exactly 42°C and a vial of SOC media (Invitrogen, UK) was prewarmed to 37°C. Plasmids (lab stocks stored at -20°C) mentioned above as well as vials of competent E.coli cells (DH5a-100μl)

where thawed on ice. 100µl of DH5a cells were used for each transformation. 1µl of each plasmid DNA was added into each vial of competent cells and these were mixed by tapping the tube gently. The tubes were subsequently incubated on ice for 30 minutes and then heat-shocked for exactly 45 seconds in the 42°C waterbath. After that the tubes were put again on ice and 900µl of SOC medium was added under sterile conditions. This mixture was incubated at 37°C for 1 hour in a shaking incubator at 250 rpm. 10-200µl of the transformed cells were then spread on pre-warmed LB agar + ampicillin (50µg/mL) 10cm plates. The plates were then inverted and incubated overnight at 37°C.

After 12-16 hours bacterial colonies had formed on the LB-agar plates which contained plasmids conferring ampicillin resistance. In order to have a starter culture of the bacteria carrying our plasmids of interest, from plates where well-separated colonies had developed a single colony of transformed bacteria was picked and transferred into 5ml LB containing 50µg/mL ampicillin. This starter culture was then incubated at 37°C in a shaking incubator at 250 rpm, in order to proceed with the next step which was plasmid DNA extraction from the bacteria.

2.2.1.3 DNA purification – Mini preps – Maxi preps

Mini-preps and maxi-preps were performed to extract the plasmid DNA from the bacterial cells using the corresponding Endofree plasmid purification kit (Qiagen, UK) continuing from our starter cultures (as mentioned above) exactly as described in the Qiagen kit handbooks. Determination of DNA concentration and purity was done using the Nanodrop ND-1000 spectrophotometer.

2.2.1.4 Gel electrophoresis

For all the procedures involving gel electrophoresis 1% and 2% agarose gels were used. 1g or 2g of agarose powder (Fisher Scientific, UK) were dissolved in 100ml 1x TAE buffer (table 2.1) by microwaving with hand stirring every 30 seconds. After the mix was completely dissolved, agarose was slightly cooled under cold tap running water, and 10µl of SYBR Safe DNA gel stain (Life technologies, UK) was added. The agarose was mixed by swirling and poured into a gel former with the appropriate size comb and was left to set. Once the gel was ready it was transferred (along with the former) to the suitable size gel tank and was submerged

into 1x TAE buffer. The combs where removed just before the samples were loaded. A final volume of 20µl (with loading dye) of each sample was loaded into each well along with a ladder marker. Gels were run at 80V until the dye front was almost at ~85% of the distance down the gel and gel images were captured using a UVP transilluminator.

2.2.1.5 Restriction enzyme digestion

Restriction enzyme digestion was performed either to confirm the propagated plasmid's identities or to prepare vectors and inserts for ligation (will be explained in detail in the next section) during cloning procedures. Unless stated otherwise, all single digests were carried out with 2µl DNA (in a concentration of ~400ng of DNA), 2µl of buffer (NEB, UK), 2µl BSA 10X (NEB, UK 10µg/ml), 13.5µl of water and lastly 0.5µl restriction enzyme into a 1.5ml Eppendorf tube. For the double digest the quantity of the water was readjusted to have a final volume of 20µl. Reactions were incubated in 37°C for 1.5 hours (time and temperature always depending on the restriction enzyme). After the incubation 4µl of loading dye (NEB, 6x concentration) was added to each tube and the samples were analysed by gel electrophoresis. Undigested DNA (control samples) was always run alongside the digested ones, while a DNA 1kb Ladder (Roche/Invitrogen, UK) was used. The restriction enzymes used as well as the conditions of the reactions are listed beneath:

Table 2.3: Restriction digestion enzymes used in this project

Restriction enzyme	Buffer	BSA needed	T/Incubation time	Manufacturer
EcoRV-HF	NEB Buff. 3 (B7003S)	Yes	37°C / 1.5h	NEB, R3195L
MluI	NEB Buff. 2 (B7002S)	Yes	37°C / 1.5h	NEB, R0198L
NheI	NEB Buffer 2	Yes	37°C / 1.5h	NEB, R0131L

2.2.1.6 Ligation

Inserts and vector were prepared by PCR/gel purification and restriction enzyme digestion, followed by phosphatase treatment of the vector to avoid self-ligation

(Calf intestinal alkaline phosphatase-CIAP, Promega, UK). Around 40µl of vector (up to 10pmol of 5'-ends), 5µl CIAP 10x reaction buffer and diluted CIAP (0.01u/µl) were mixed and incubated at 37°C for 30 minutes. Another aliquot of diluted CIAP (of the same quantity as before) was added to the mixture and another incubation for 30 minutes at 37°C followed. Next, DNA purification was performed (Macherey-Nagel kit, UK) and the vector was ready for ligation. For the ligation, insert(s) and vector were mixed in an eppendorf tube in a ratio of 3:1 (insert:vector). To calculate this ratio 2µl of each insert and vector were run on an agarose gel and according to the band intensities and the length of each fragment the values for the ligation were calculated using the following formula:

$$Li = 3 * Lv * \frac{Si}{Sv} * \frac{lv}{li} * \frac{Vi}{Vv}$$

,where v=vector and i=insert, so Sv is size of vector, Si is size of insert, lv and li are the relative intensities of the bands on the gel (the weaker band is given the value of 1), Vv and Vi are the volumes loaded on the gel (usually are equal), and the volume of the vector that will be used for the ligation is Lv. According to that formula the volume of the insert to be used for the ligation, Li, is calculated. 5µl of 10X ligation buffer (NEB) and 1µl of T4 DNA ligase (NEB) were included to the mix and water was added to a final volume of 20µl. The reaction mix was left at 16ºC overnight. 5µl of the ligation was then used for subsequent transformation and plating of E.coli competent cells (DH5a). DNA from the derived colonies was mini-prepped and screened for the insert with restriction enzyme digestions. Successful clones were sent for sequencing to confirm the result.

2.2.1.7 Quantitative RT-PCR

RNA was collected using the RNeasy Purification Kit (Qiagen, UK). Three biological replicates of each sample were collected. Concentration of RNA was checked on a Nanodrop spectrophotometer. Reverse transcription was carried out on 2µg of each sample in a volume of 20µl, using 5x First strand buffer, 0.1M DTT, 500ng random primers (Promega), 2.5mM each of dNTPs (Promega) and 200 units Superscript reverse transcriptase II (Invitrogen). A negative water control was always included, as were reactions for every sample but without the addition of reverse transcriptase, to act as negative control for the reaction and to make sure that

during PCR amplification was only due to the cDNA and not due to genomic DNA. Tubes were then incubated at 25ºC for 10 minutes, at 42ºC for 50 minutes, at 70ºC for 15 minutes and then cooled on ice. Also treatment with RNaseH (Invitrogen) followed at 37 ºC for 30 minutes (for more detailed protocol, check the online manual for Superscript Reverse Transcriptase II, Invitrogen). 20ng of cDNA was then loaded into each well of a 96-well dish. Triplicate samples of each cDNA were included for each primer set. Primers against OMD and/or PRELP and GAPDH were used. 200nM of each forward and reverse primers, and 1x Fast SYBR-green master mix (Applied Biosystems) were then added to each sample, to make a final volume of 20µl in each well. Plates were then loaded onto 7900HT Real-time PCR machine (Applied Biosystems) and run on the standard programme. Ct data was linearized, normalized to GAPDH. Means of each set of three technical replicates were taken, and then means and standard deviations of each set of three biological replicates were calculated, while analysis was conducted using the Pfaffle method (Pfaffle M.W., 2001). This method entails the relative quantification of a target gene transcript in comparison to a reference gene transcript. The relative expression ratio is calculated from the real-time PCR efficiencies and the crossing point deviation of an unknown sample versus a control. Sequences of primers were as follows:

OMD Forward: 5'-TCTTCCCAACATTGTAGAACTCAG-3'
OMD Reverse: 5'-ATTGTTTGACCATTAGTGCTTCGT-3'
PRELP Forward: 5'-CTGTCCCACAACAGGATCAGCAG-3'
PRELP Reverse: 5'-CAGGTCCGAGGAGAAGTCATGG-3'
GAPDH Forward: 5'-CCCCACCACACTGAATCTCC-3'
GAPDH Reverse: 5'-GGTACTTTATTGATGGTACATGACAAG-3'

Additionally, qPCR using the Taqman method was done for PRELP expression. 50ng of cDNA in 2µl volume were used and 10µl of TaqMan Gene Expression Master Mix 2X (Applied Biosystems), 1µl of TaqMan Gene Expression for PRELP (Applied Biosystems, #Hs00160431_m1) or TaqMan Gene Expression for GAPDH (Applied Biosystems, #Hs99999905_m1) were added topped up with water to a final volume of 20 µl. Plates were again loaded onto 7900HT Real-time PCR machine and run on the standard programme indicated for the Taqman assay, and data were analysed in the same way.

2.2.2 Cell culture Methods

2.2.2.1 Cell culture

The EJ28 cell line was cultured in complete DMEM medium (see table 2.2 for complete medium compositions) in T75cm^2 flasks (PAA, UK). Cell passaging was always done under sterile conditions inside a hood (Microflow II Biological cabinet) using the same type of flasks usually every 2-3 days, after the cells had reached 80-90% confluency, to avoid cell death. The procedure involves splitting the cells and re-plating them into new flasks. Firstly, the medium was removed from each flask, followed by rinsing with 5ml 1X PBS (PAA, UK). PBS was removed and 2ml of 1X trypsin (PAA, UK), promoting disruption of the cells adhesion, (prewarmed in 37°C waterbath) was added per flask. After 2-3 minutes when cells were completely detached, 10.5ml fresh medium (prewarmed in 37°C waterbath) was added to stop the reaction and the resulting mix was transferred to a 50ml Falcon tube. From that, usually 1 or 2ml (depending on the time we wanted to re-split the cells) were plated into new T75 flasks and fresh complete medium was added to a final volume of 20ml per flask. In cases where we needed to count the cells in order to use a specific amount, cells were diluted in Trypan Blue 0.4% solution (Sigma, UK) and the hematocytometer was used. Flasks were always kept in a 37°C incubator with 5% CO_2 supply (Sanyo, MCO-18AIC, Japan).

When needed, cell freezing was done in early passages to keep a stock of the cells. Approximately one million cells in a volume of 1ml of complete medium plus 5% DMSO (Sigma, UK) was aliquoted in each cryo-tube (PAA, UK), and cells were frozen overnight in a Nalgene Mr. Frosty Cryo 1°C Freezing container. The next day tubes were transferred in a liquid nitrogen tank, to be kept for long-term storage.

2.2.2.2 Lentiviral transfections/transductions

Cells were seeded in a 48-well plate one day prior to transfection, in a cell density of 2x10^4 cells/well in 500μl medium. After 24 hours, when cells were around 70% confluent, their medium was removed, and the appropriate amount of lentivirus to give an MOI of 5 was mixed with 300μl fresh complete cell medium (in the presence of 8μg/ml Hexadimethrine bromide, Sigma, UK), which was then added to the cells, followed by a swirling of the plate. Cells were incubated in a 37°C

incubator with 5% CO_2 supply for 24 hours. Then, the virus-containing medium was removed and fresh medium was added. After another 24 hours the medium was changed again and cells were cultured normally from this point onwards. All the experiments involving lentiviruses were conducted in a category II safety hood and room.

2.2.2.3 Anchorage independent growth assay (or soft agar assay)

Autoclaved, sterile solutions of 1.2% Seaplaque agarose were microwaved until liquidified, and then cooled to 40ºC in a water bath. 2x DMEM was made up and filtered-sterilised. Twice the usual amount of serum and antibiotics was added to these solutions. The media were then mixed with the 1.2% agarose solution to yield a final solution of 1x growth medium + 0.6% agarose solution. The solution was quickly poured into 6-well plates, before hardening. 1ml of solution was added per well. Plates were then incubated at 4ºC overnight to allow the agarose to set thoroughly (bottom gel). For the top gel, sterile solution of 0.6% Seaplaque agarose was microwaved and cooled to 40ºC in a water bath. This solution was then mixed with the aforementioned 2x growth medium to yield 1x growth medium + 0.3% agarose. A suspension of 5000 cells in 200µl 1x growth medium was then added to a 2ml aliquot of the 1x growth medium + 0.3% agarose solution, and the resultant mixture was plated out on the top of the bottom gel. Once the top layer had cooled and hardened, 1ml of growth medium was added on top of the agarose, to keep it moist. Triplicate samples of each cell line were prepared in this way. Then, plates were incubated for 3 to 4 weeks in a 37°C incubator with 5% CO_2 supply, until visible colonies appeared. Colonies were then stained with 1% Crystal Violet (Sigma, UK) and the whole well was imaged with a stereoscope. Pictures of all the wells were imported into a computer and colonies were counted using the Image J software (open source, developed by National Institutes of Health, USA).

2.2.2.4 3D Matrigel morphogenesis assay

For 3D morphogenesis, EJ28 and EJ28-OMD/PRELP transfected cells were plated on top of a layer of growth factor–reduced Matrigel (BD Bioscience, #356231). In brief, 8-well multi chamber coverslips were covered with 100 µl Matrigel and left to gel for 45 min at 37°C. 10,000 cells in 200 µl of Matrigel were

then plated and cultured in complete DMEM. The medium was replaced with fresh medium twice a week. After 7 days, 3D morphogenesis was assessed by light microscopy.

2.2.2.5 Matrigel invasion assay

Assay insert plates (BD Bioscience, #354480) were prepared by rehydrating the Matrigel™ coating with PBS for 2 hours at 37°. The rehydration solution was carefully removed, 0.75 ml DMEM containing 10% fetal bovine serum was added to the plate well as a chemoattractant, and 0.5 ml of cell suspension (2.5x10^4 cells) in DMEM containing 0.1% FBS was added to each insert well. The assay insert plates were incubated for 48 hours at 37°C. Following incubation, the medium was removed from the upper chamber and the insert membrane was stained with hematoxylin using Hemacolor® (MERCH, HX093929). After staining, cells attached to the top of membrane were wiped off and the dye staining cells under the membrane was eluted with 0.1M citric acid (unbuffered) and absorbance was read at 630 nm.

2.2.2.6 Cdc42 activation assay

Cells were seeded at 1 x 10^5 cells/well in 10% FBS containing DMEM in 24 well plate and after 24 h, cells were harvested and analysed for levels of active Cdc42 using the G-LISA assay kits (Cytoskeleton; #BK127).

2.2.2.7 Transwell co-culture assay

1x10^5 cells/well of EJ28 cells were seeded on the bottom of 6-well plates, while 5x10^4 cells of each EJ28/ EJ28-OMD/mtOMD/PRELP/mtPRELP were seeded on transwells with 0.4μm pores (VWR, UK #29442-104). Both the lower compartment and the transwell were filled with complete DMEM. Cells were co-cultured like this for 72 hours, after which brightfield images of both the cell layer on the transwell and the bottom of the wells were captured. Living cells were counted after thrypsinisation and trypan blue staining.

2.2.2.8 Xenograft

EJ28 and EJ28-OMD/PRELP transfected cells were used for the xenograft experiments. Xenografts were initiated by subcutaneous implantation of 5×10^6 cells, suspended in 100µl of MATRIGEL (Becton Dickinson, USA) solution, into the right flank of nude mice in accordance with UK Home Office regulations and allowed to develop to measurable size. Two weeks after inoculation, tumour measurements were started. Tumour volume was assessed using digital callipers. The volume was calculated using the following formula: tumour volume (mm^3) = (a) x $(b)^2$ / 2, where (a) is longer diameter, (b) is shorter diameter.

2.2.2.9 Lentiviral production

Viral production was conducted by a 3-plasmid co-transfection of HEK 293T cells and the JetPEI (Polyplus transfection, USA) system. For a full viral preparation $16\text{-}18x10^6$ cells were seeded in 9 T175 flasks in complete DMEM. The next day the transfection mixture was performed for each flask, where: 20µg of the mtOMD or GFP expressing lentivector (vectors c and d from section 2.2.1.1), 7µg pMD.G2 and 13µg pCMV-dR8.74 plasmids were added to 1ml 150Mm NaCl, mixed by hand and passed through a 0.22µl filter. 80µl of JetPEI were added to 1ml 150Mm NaCl and the mixture was vortexed for 10 seconds. Then the NaCl/PEI solution was added to the NaCl/DNA solution, was mixed by hand, and was left to incubate at room temperature for 30 minutes. After the incubation the NaCl/PEI/DNA solution was added to 13ml of complete DMEM. The old medium was removed from each flask of 293T cells and the medium with the transfection mix was added (a total of 15ml/flask), and cells were left for 4hours at 37ºC, after which the medium was replaced with fresh complete DMEM. The next day the medium was replaced again with fresh DMEM. The fourth day, the virus-containing medium was removed from the flasks and was centrifuged at 300g for 10 minutes at 4 ºC. In the meantime fresh medium was added to the flasks, which were put back to the incubator until the following day. The supernatant from the centrifugation was filtered through 0.45µm filters and was transferred into clean, dry Beckman centrifuge tubes, which were in turn ultracentrifuged at 17,000 rpm for 2hours at 4ºC. After the centrifuge the supernatant was discarded and the tubes with the virus pellet were covered in parafilm and left to incubate on ice for 30 minutes. Afterwards, the pellet was

thoroughly resuspended with the few drops of medium that were left on the walls of the tubes, using a P10 pipette. The virus was aliquoted into 20μl aliquots and stored at -80ºC until use. The following day the same procedure was performed with the medium that was now present in the flasks, after which the cells were discarded. All the work involving viral preparation was performed in a class II safety hood. All the above procedures were conducted in the UCL-Ryan Building, in Professor Sam Jane's laboratory.

2.2.2.10 Lentiviral titration

For viral titration HEK 293T cells were seeded in a 12-well plate with a density of 50,000/well in 1.5ml complete DMEM. The next day the medium was exchanged with 1.5ml fresh DMEM containing 1.5μl polybrene (4μg/ml) (Sigma, UK) per well, and was left at room temperature for 5 minutes. Next, the medium was exchanged again for a mix of media/polybrene/virus with a final volume of 1.5ml/well. A serial dilution of the mixture was performed, where 20μl of the virus (day 4 or 5) were added in 2ml of DMEM/polybrene (first well) and then 500μl of this mix were added to the next well containing 1.5ml DMEM/polybrene, was mixed again, and again 500μl were removed to be added to the next well, and so on. Four serial dilutions were performed in this way. One well served as negative control with no virus. The next day the medium was exchanged with fresh DMEM containing 10μg/ml doxycycline (Sigma, UK), to allow for expression of the genes under the inducible promoter, and the cells were incubated for another 48hours. The fifth day the cells were harvested by trypsinisation, and after centrifugation at 3000 rpm for 3 minutes were resuspended in 0.5ml PBS. This solution was then passed through a FACS analyser (BD Biosciences, USA), operated by Grazyna Galatowicz, where the percentage of the GFP positive cells was calculated. The viral titer was calculated by the formula: Viral titer = (proportion of GFP positive cells x number of seeded cells)/Volume of virus (in ml), where the volume of the virus that results in no more that 20% of positive cells is used. This method gives the number of viral transduction units (TU) per ml. All the experiments involving lentiviruses were conducted in a category II safety hood and room.

2.2.3 Protein methods

2.2.3.1 SDS/PAGE electrophoresis

Cell lysates were obtained using RIPA protein extraction buffer (50mM Tris-HCl, pH 8.0, 150mM NaCl, 1% NP-40, 0.5% Sodium deoxycholate, 0.1% SDS, Sigma, UK), supplemented with "Complete EDTA-free" protease inhibitors (Roche) and phophatase inhibitors (Roche). The amount of protein in each sample was determined using a BCA assay kit (Thermo scientific). Laemmli sample buffer (62.5mM Tris, pH 6.8, 20% glycerol, 2% SDS, 0.01% bromophenol blue, Biorad, UK) was added to samples, which were heated to 95ºC for 5min in a heatblock for the purpose of protein denaturation. SDS-PAGE gels were poured, with a concentration of 10% acrylamide. 30µg of each protein sample was run out on the gel, alongside a molecular weight marker (All Blue Marker, Biorad, UK). Electrophoresis was performed with the Mini-Protean III system (Biorad), at 70V for the stacking gel and 100V for the running gel, in 1X running buffer. Proteins were transferred onto nitrocellulose membranes (GE healthcare), using the BioRad wet transfer system at 25V for 20 min. Protein integrity was checked using Ponceau stain (Sigma, UK). Membranes were then blocked in PBS/0.1% Triton-X + 5% non-fat milk for 30 minutes at room temperature, and incubated overnight with the primary antibody according to the manufacturer's instructions. Membranes were then washed thrice in PBS/0.1% Triton-X for ten minutes per wash, and incubated in a 1:2000 dilution of secondary HRP-conjugated antibody in the same buffer that the primary antibody was diluted in, for 1h at room temperature. Membranes were washed thrice in PBS/0.1% Triton-X, for 10 minutes per wash. ECL reagents (GE Healthcare) were applied for 5 minutes in dark conditions. Membranes were then wrapped in cling film and exposed to autoradiography film (Kodak, UK).

When needed, membranes were stripped in stripping buffer (Biorad, UK) for 15 minutes, and were subsequently washed thrice in PBS/0.1% Triton-X for 10 minutes per wash. This was particular useful to detect levels of the protein of interest in relation to a loading control. All the antibodies used in the western blots are summarised in the table below:

Table 2.4: List of antibodies used in Western blotting

Antibody	Manufacturer	Host species	Dilution
Anti-OMD	Abgent, #AP7474b	Rabbit polyclonal	1:250
Anti-OMD	Abnova, #H00004958-M01	Mouse monoclonal	1:250
Anti-PRELP	Abnova, #H00005549-B01P	Mouse polyclonal	1:250
Anti-PRELP	Abgent, #AP6665b	Rabbit polyclonal	1:250
Anti-β actin	Cell Signaling, #3700	Mouse monoclonal	1:1000
Anti-GFP	Invitrogen, #A-11122	Rabbit polyclonal	1:1000
Anti-myc	Cell Signaling, #2276	Mouse monoclonal	1:1000
Anti-p-Akt	Cell Signaling, #4060	Rabbit polyclonal	1:2000
Anti-p-ERK1/2	Cell Signaling, #4370	Rabbit polyclonal	1:2000
Anti-pEGFR	Cell Signaling, #3777	Rabbit polyclonal	1:1000
Anti-EGFR	Cell Signaling, #4267	Rabbit polyclonal	1:1000
Anti-p-IGF-1R	Cell Signaling, #3918	Rabbit polyclonal	1:1000
Anti-IGF-1R	Cell Signaling, #9750	Rabbit polyclonal	1:1000
Mouse IgG HRP-conjugated	GE Healthcare, #NXA931	Sheep	1:2000
Rabbit IgG HRP-conjugated	GE Healthcare, # NA934	Donkey	1:2000

When needed, protein concentration was performed before running the sample through the SDS/PAGE gel. Briefly, 1 volume of 100% TCA stock solution was added to 4 volumes of protein sample and the mixture was incubated at 4°C for 10 minutes. Centrifugation at 14K rpm for 15 minutes followed, after which the supernatant was removed leaving the protein pellet intact. The pellet was washed with 200μl of cold acetone and was centrifuged again under the same conditions. The last steps were repeated two more times and finally the protein pellet was dried by placing the tubes in 95°C heat block for 5-10 min to drive off the acetone. For SDS-PAGE, add sample buffer (with or without β-ME) was added and after boiling the samples for 5 minutes at 95°C they were ready to load onto the polyacrylamide gel. Alternatively, Millipore amicon ultra-centrifugal filter units were occasional used (Millipore, #UFC503024), following the manufacturer's' instructions.

When needed commercially available recombinant human EGF ligand (R&D Systems, UK, #236-EG), IGF ligand (R&D Systems, UK, #291-G1) and TGF-β ligand (Sigma, UK, #T7039) were used.

2.2.3.2 Co-immunoprecipitation

Co-immunoprecipitation was performed using the commercially available kit ProFound c-Myc Tag IP/Co-IP Kit (Thermo Scientific, UK, #23620) according to the manufacturer's instructions.

2.2.3.3 Immunocytochemistry (ICH)

Cells were seeded at the desired density in 8-well slide-chambers (Tissue culture Lab Tek II, Thermo Scientific Nunc, UK) in 400μl medium. When cells had reached the confluency we wanted, they were washed twice with PBS and then fixed with the addition of 100μl 4% PFA (see table 2.1) or ice-cold methanol for 10 minutes at 37°C or at -20°C respectively. The immunofluorescence procedure started with addition of 100μl per well of blocking buffer (table 2.1) for 15 minutes (200μl/well). Then, the primary antibody was diluted (at desired concentration) in blocking buffer and was added to the wells (200μl/well), incubating for 24 hours at 4°C, after which the wells were washed 3 times x 10 minutes with PBS. Secondary antibodies (fluorescent) were also diluted in blocking buffer and were added to the cells, which were then left to incubate for 1 hour in the dark at room temperature. The 8-well chamber slide was then washed 3x10 minutes with PBS and finally, after the plastic compartment forming the chambers was removed, a drop of mounting medium Prolong Gold anti-fade with DAPI (Invitrogen, UK) was added to all the cells, covered-up by a cover slip. All slides were stored at 4°C after mounting. Images were captured using a 3-filter fluorescent microscope (Carl Zeiss Axioskop 2 Plus) with the QICAM 12-bit Color Fast 1394 (Qimaging) and the Openlab 5.5.0 (Improvision) software. Softwares used for imaging process were Adobe Photoshop CS6 (Adobe Systems Incorporated, Eastern Europe) and Image J.

2.2.3.4 Immunofluorescence (IF)

Frozen sections were thawed at room temperature and were post-fixed for 10 minutes in 4% PFA. Following 3 times, 5 minutes rinses in 1X PBS the slides were

incubated for 1 hour in blocking buffer (see Table 2.1) and were subsequently incubated with primary antibody in blocking buffer in the appropriate dilution overnight at 4°C. The next day slides were washed with 1x PBS 5 times for 8 minutes each and were incubated with the secondary fluorescent antibody diluted in blocking buffer for 1h in the dark. Slides were washed again afterwards with 1x PBS 5 times for 8 minutes each, and were mounted using Prolong Gold anti-fade with DAPI. All slides were stored at 4°C after mounting. Images were captured using a 3-filter fluorescent microscope (Carl Zeiss Axioskop 2 Plus) with the QICAM 12-bit Color Fast 1394 (Qimaging) and the Openlab software or a confocal Zeiss LSM 710 microscope and the LSM software. Softwares used for imaging process were Adobe Photoshop CS6 (Adobe Systems Incorporated, Eastern Europe) and Image J.

Regarding paraffin sections, antigen retrieval was performed before staining. Sections were de-waxed with Histoclear (Fisher Scientific, UK) for 10 minutes, rehydrated in decreasing concentrations of ethanols (100%, 75%, 50%, 25% ethanol in ddH_2O and ddH_2O) for 2 minutes each. Slides were subjected to antigen retrieval using 10 mM citrate buffer (pH 6.0) or Tris-EDTA buffer (pH 9.0) (see Table 2.1) for 10 minutes in a microwave. Slides were allowed to cool for 40 minutes afterwards and were rinsed two times with PBS, after which they were immersed in blocking buffer for 1h, continuing the immunofluorescence protocol from here onwards. A list of all the antibodies used is presented below in Table 2.5.

Table 2.5: List of antibodies used in ICH/IF throughout this project

Antibody	Manufacturer	Host species	Dilution	Antigen retrieval
AP2α	DSHB, #3B5-s3	Mouse	1:10	-
Pax6	Millipore, #AB2237	Rabbit	1:1000	Tris-EDTA, pH 9.0
Islet-1	DSHB, #40.3A4-s	Mouse	1:500	-
Occludin	Invitrogen, #33-1500	Mouse	1:100	-
ZO-1	Kindly provided by Prof. Karl Matter	Rabbit	1:100	Tris-EDTA, pH 9.0
ZO-2	Kindly provided by Prof. Karl Matter	Rabbit	1:100	Tris-EDTA, pH 9.0
ZO-3	Kindly provided by Prof. Karl Matter	Rabbit	1:100	Tris-EDTA, pH 9.0
Cingulin	Kindly provided by Prof. Karl Matter	Rabbit	1:100	-

β-catenin	Cell Signaling, #8480	Rabbit	1:100	Citrate, pH 6.0
E-cadherin	Cell Signaling, #3195	Mouse	1:400	Citrate, pH 6.0
Vimentin	Cell Signaling, #5741	Rabbit	1:100	Citrate, pH 6.0
Myc	Cell Signaling, #2276	Mouse	1:1000	-
GFP	Invitrogen, #A-11122	Rabbit	1:100	-
Uroplakin-III	Fitzgerald, #10R-U103a	Mouse	1:100	Tris-EDTA, pH 9.0
CK18	Abcam, #ab668	Mouse	1:25	-
Laminin	Abcam, #ab11575	Rabbit	1:200	Tris-EDTA, pH 9.0
CK5	Abcam, #ab75869	Rabbit	1:25	-
HuC/HuD	Molecular probes, #A-16A11	Mouse	1:200	-
NeuN	Millipore, #MAB377	Mouse	1:100	-
β-III Tubulin, neuronal	Abcam, #ab18207	Rabbit	1:500	-
GFAP	Millipore, #AB5804	Mouse	1:100	-
Calbindin	Sigma, #C2724	Rabbit	1:1500	-
NG2	Millipore, #AB5320	Rabbit	1:100	-
PECAM-1	Santa Cruz, #sc-1506	Rabbit	1:100	-
α-SMA	Sigma, #C6198	Mouse	1:200	-
Fibrinogen	Abcam, #ab34269	Rabbit	1:100	Tris-EDTA, pH 9.0
Ki-67	Abcam, #ab16667	Rabbit	1:100	Citrate, pH 6.0
Mouse Alexa-488	Molecular Probes, #A-11001	Goat	1:500	-
Mouse Alexa-546	Molecular Probes, #A-11030	Goat	1:500	-
Rabbit Alexa-488	Molecular Probes, #A-11008	Goat	1:500	-
Rabbit Alexa-546	Molecular Probes, #A-11035	Goat	1:500	-

2.2.3.5 Preparation of samples for electron microscopy

Cells or segments of bladders were fixed in 3%glutaraldehyde/1% paraformaldehyde in 0.08M sodium cacodylate-HCl buffer(pH7.4) and after washing with PBS were immersed in 1% aqueous osmium tetroxide solution for 2h at RT. Samples were washed again and dehydrated by single 15 min. incubations in 50%,

70%, 90% and 100% ethanol (3x), 2 x 20 minute changes of propylene oxide and left overnight in a 1:1 mixture of propylene oxide:araldite for the solution to infiltrate. Afterwards, samples were transferred to araldite resin, rotating for 6 hours to remove any traces of propylene oxide prior to embedding. Finally, they were embedded in fresh resin for 24h at 60°C. Semithin sections were cut using a Leica ultracut S microtome with diamond knife, were stained with a mixture of 1% borax and 1% toluidine blue in 50% ethanol at 60°C, and after drying were mounted in DPX. Ultrathin sections were cut at 60 or 100nm, stained with lead citrate and viewed in a JEOL 101 TEM operating at 100kV. Preparation of the samples (cells or tissues) was performed by Dr. Peter Munro, while I examined the samples using the TEM.

2.2.4 Mice

All animal procedures were performed in accordance to the Animals (Scientific procedures) Act 1986 of the UK Government. All mice were housed in compliance with the Home Office Code of Practice. Mice were kept in individually ventilated cages (IVCs), in a 12 hour light:dark cycle and were fed a complete pelleted mouse diet and with constant access to water. Mice on the C57BL/6J background were used in this study.

2.2.4.1 Generation of Knock-out mice

OMD and PRELP knock-out mice were generated by Takeda Pharmaceutical Company and wild type and heterozygote founders were imported to our animal facility. Briefly, *OMD* or *PRELP* flox ES cells were generated from C57BL/6J ES cells by homologous recombination with the targeting vectors which were constructed by insertion of the first LoxP sequence in upstream of exon 2, which contains the initiation codon on the OMD or PRELP locus, and insertion of the neomycin resistant unit, second LoxP sequence and LacZ unit in downstream of exon 3. Cre expression plasmid was electroporated into the recombinant flox ES cells to generate ES cells harboring KO allele. The resulting KO ES cells were injected into ICR tetraploid blastocysts to generate chimeric male mice, and the chimeric mice were backcrossed to C57BL/6J females. Single knockout mice ($OMD^{LacZ/LacZ}$ and $PRELP^{LacZ/LacZ}$) and their double knock-out ($OMD^{LacZ/LacZ}PRELP^{LacZ/LacZ}$) were generated by cross breeding within the colony.

2.2.4.2 Collection of embryos, p0 new-borns and adult organs

Embryonic litters were generated through timed matings, which involved the pairing of male and female mice overnight. The next morning, females were checked for vaginal plugs and the presence of a plug was designated as 0.5 dpc. If plugs were not seen the pair was left together one more night. Pregnant females were euthanised in a CO_2 chamber at the relevant time point and embryos were dissected from the uterus and place in ice-cold PBS. Afterwards embryos were separated from the Reichert's membrane and visceral yolk sac using fine forceps and were fixed either in 4% PFA or in 95% ethanol for β-galactosidase staining or skeletal preparation respectively.

P0 new-borns were collected the day of birth after closely monitoring pregnant females. They were euthanized with an overdose of by intra-peritoneal (IP) injection of pentobarbitone. Afterwards heads and bodies were separated for better penetration of the solutions and were fixed for 3h in 4% PFA at 4°C. Organs were isolated from adult mice and were directly put in 4% PFA.

2.2.4.3 Genotyping

Genotyping of mice for the *OMD* and *PRELP* genes was performed by utilising gDNA isolated from ear punches as soon as mice were weaned at 3 weeks of age, with the help of Steven Bolsover. For embryos, tail snips (<0.5 cm) were used. Briefly, ear punches or tail snips were digested overnight at 55^{o}C in 200 µl of the commercially available DirectPCR® reagent (Viagen Biotech, LA, USA) containing 0.01% Proteinase K (Invitrogen, UK). The following morning samples were incubated at 85^{o}C for 15 minutes to deactivate proteinase K. The supernatant was collected from the digest mix after centrifugation for 1 min at 13 000 rpm at room temperature and was ready to be used as DNA template for the following PCR.

For *PRELP* genotyping each PCR was prepared with a master mix of 12.5µl 2X Multiplex PCR master mix (Qiagen, UK), 5µl 5X Q solution (Qiagen, UK), 2µM primer mix (PRELP-A, PRELP-B, LacZ-A), 3µl of ultra-pure dH_2O and 2.5µl of DNA template. PCR conditions used were as follows: 9 min denaturation at 95°C followed by 40 cycles of 94°C denaturation for 30 sec, 63°C annealing for 120 sec, 72°C extension for 90 sec, and completed by 10 min final extension at 72°C. For

OMD genotyping two separate master mixes were used with two different primer sets. Each PCR reaction contained 2.5µl 10X PCR buffer, 0.5µl of 10mM DNTP mixture, 0.75µl of 50mM $MgCl_2$, 0.05µl of Taq polymerase, 1.25µl of 1% W (all the above are from Invitrogen, UK), 12.45 µl of ultra-pure dH_2O, 2 µM of primer mix (one primer mix contained OMD-A & OMD-B, while other mix contained OMD-B & LacZ-5756F), and 5µl of DNA template. PCR conditions used were as follows: 180 sec denaturation at 95°C followed by 35 cycles of 94°C denaturation for 30 sec, 61°C annealing for 90 sec, 72°C extension for 90 sec, and completed by 10 min final extension at 72°C. PCR was carried out in a C1000 Thermocycler (Biorad, UK).

The following primers were used for *OMD* and *PRELP* genotyping:

OMD-A: 5' GGGAATGCTTTGACTTTCTGAGTTA 3'

OMD-B2: 5' TGGACCTTAAGTCTTACATCACAGG 3'

LacZ-5756F: 5' CATTGTCAGACATGTATACCCCGTA 3'

PRELP-A: 5' CACTGCAGGAAGAGTCATCTTTTCT 3'

PRELP-B: 5' TACACTTTCTCCCAGCTTCTATTCC 3'

LacZ-A: 5' CATTGTCAGACATGTATAGCCCGTA 3'

2.2.4.4 Tissue cryopreservation and sectioning

For preparation of fresh-frozen sections, embryos or tissues from adult mice were fixed in 4% PFA for different amount of time depending on the size. Generally, embryos were fixed for 1h, p0 new-borns were fixed for 3h, eyes for 30 minutes, bladders for 1h and brains for 3h. After fixation tissues were washed in PBS, transferred to 30% sucrose (Sigma, UK) solution and were kept there until they sunk. Afterwards, they were embedded in optimal cutting temperature (OCT) compound (Tissue Tek, Sakura Finetek) and were snap frozen in a dry ice / isopentane bath. Frozen tissues were stored at -80°C until use. Usually, 10-18 micron serial sections were cut with a Leica CM3050 cryostat, mounted onto Superfrost Plus® glass slides (Fisher Scientific, UK) and stored at -80°C until use.

2.2.4.5 Paraffin embedding of tissues and sectioning

Embryos and tissues for paraffin sectioning (stored at 4% PFA) were processed in the Institute's Pathology department using an automated machine (Leica ASP 300S) and were then embedded in plastic moulds with warm wax, left on a cold plate to set. 5 μm sections were cut using a sledge microtome in the Pathology department. Wax sections were transferred in a 40°C water bath and then were mounted onto superfrost slides. Slides were dried off of the excess water and they were put on a hot plate (around 60°C) for 30 minutes, allowing the wax to flatten. Slides were then stored at room temperature until required for further analysis.

2.2.4.6 X-gal staining of embryos and tissues

X-gal staining was performed in whole embryos or tissues (for brain and bone), or using single cryo-sections of embryos and the other organs, including brain, bladder and eye. The procedure was the same in both cases, where after fixation the samples were washed with PBS containing 2mM $MgCl_2$ two times for 20 minutes each, and were then incubated overnight in the X-gal staining solution (containing 1x X-gal, diluted from the stock solution) at 37°C in the dark. The following day samples were washed with dH_2O and were either counterstained with eosin and mounted, or were directly mounted with DPX. Images were captured using bright field microscopy (Carl Zeiss Axioskop 2 Plus) with the QICAM 12-bit Color Fast 1394 (Qimaging) and the Openlab 5.5.0 (Improvision) software. Whole-mount stained embryos and organs were observed and photographed using a Leica M80 stereoscope and an attached Leica PFC 420C camera. For expression analysis using cryo-sections, immunofluorescence was performed on top of the X-gal staining, where after washing the X-gal solution slides were directly immerged in the appropriate blocking buffer and the immunofluorescence protocol was then followed. Regarding bone analysis, the knee joints were whole-mount X-gal stained, as described above, and were then post-fixed for another 24h with 4% PFA. Next, they were immersed in 11% formic acid solution in water for 24h in order to decalcify them. After decalcification, they were washed extensively with dH_2O and were prepared for paraffin sectioning, as described in the previous method.

Clearing of the X-gal stained embryos was performed in a series or gradual glycerol/KOH solutions. Briefly, after washing the X-gal solution embryos were post-fixed in 4% PFA for 24hours, after which they were transferred in 70% ethanol and stored. Clearing was later performed with a series of 20%, 50%, 80% and 100% (v/v) glycerol solutions containing 1% KOH (w/v). Each incubation step lasted 4-5 days, during which time embryos were kept at 30°C. At the final step embryos were observed and photographed using a Leica stereoscope.

2.2.4.7 Hematoxylin and eosin staining & special stains

H+E staining was performed in an automated system in the Pathology department. Briefly, paraffin sections were de-waxed in xylene and passed through 2 changes of absolute alcohol, 2 changes of 90% alcohol, 1 change of distilled water and were stained in Harris hematoxylin for 5 changes. Then, they were washed in running tap water for 1 change, differentiated in 1% acid alcohol for 1 change, washed again in tap water for 1 change, passed through 2 changes of 90% alcohol, counterstained with eosin for 3 changes, dehydrated in 95% alcohol for 2 changes and cleared with xylene. Finally they were mounted using DPX. Every change lasts around 10 seconds. Special stains, including von Kossa, alcian blue, congo red and MSB, were also performed in the Pathology department following department's specific protocol for each stain. Methylene blue and basic fuchsin staining was performed on semi-thin sections of xenografted tumours, where drops of methylene blue (Table 2.1) covering the sections were left on the slide for 1 minute at 67°C, followed by wash with dH_2O. Then slides were covered with basic fuchsin solution (Table 2.1) for 2 minutes at room temperature. Finally, they were rinsed with dH_2O and mounted with DPX.

2.2.4.8 Mouse urine testing

Mouse urine was tested for blood and protein using Fisherbrand™ Urine Reagent Strips (Fisher Scientific, #23-111-262). Drops of urine were loaded onto the appropriate pads on the strips and measurements were calculated within one minute, depending on the colouration of each pad.

2.2.4.9 Gait ink test

The gait test was performed using the standard ink method (Girirajan et al, 2008). The front and hind paws of the mice were dipped in black non-toxic stain and the mice were then left to walk through a long corridor on a piece of white paper, leaving a trail of the walking pattern. Every mouse was tested thrice. The papers were then scanned to a computer and the different parameters were quantified using Image J.

2.2.4.10 Skeletal staining

Skeletal staining was performed on E15.5 and E17.5 embryos. In both cases embryos were collected as described and were fixed in 95% ethanol for four days. After fixation all the visceral organs were removed and each embryo was placed in a glass vial. Afterwards they were stained with the alcian blue solution (see Table 2.1) rotating for 3 days at room temperature, followed by consecutive washes of 70%, 50%,25% ethanol and lastly water (around 4 hours each), over a period of two days. They were then stained with the alizarin red staining solution (see Table 2.1) for another 3 days rotating at room temperature, and were washed in dH_2O+1% KOH two times, for 3 hours each. Next, they were passed through a gradient of glycerol and 1% KOH (20%, 50%, 80% glycerol solutions containing 1% KOH) leading to clearing of the embryos. Each incubation step lasted 2-3 days, during which time embryos were kept at room temperature, rotating. Finally they were transferred to 100% glycerol, photographed using a Leica stereoscope, and were stored in this solution.

2.2.4.11 Piximus and micro-CT measurements

Both Piximus and micro-CT experiments were performed in the UCL-Anatomy Building, in Professor Tim Arnet's laboratory. The Lunar PIXImus Densitometer (GE Medical Systems) was used according to manufacturer's instructions. For the micro-CT the SkyScan1172 (Bruker, Belgium) X-ray scanner was used, again according to manufacturer's instructions. Embryos were fixed in 70% ethanol prior to scanning. The NRecon v1.6 software (Bruker) was used for image reconstruction, the CTan v1.9 (Bruker) was used for data analysis and the μCTVol v2.0 (Bruker) for

3D model visualisation. The scanner was set at voltage of 90kVp and a current of 112μA, while the scanning resolution was set at 8.6 μm.

2.2.5 Statistical analysis

Statistical analysis and graph compilation was performed using the GraphPad Prism5 software (GraphPad Software, Inc, USA). Significance of differences was determined by unpaired two-tailed Student's *t*-test unless specified otherwise. *P* values less than 0.05 were considered significant.

Chapter 3

OMD and PRELP suppress bladder tumour growth *in vitro* and *in vivo*

3.1 Introduction

Bladder cancer is the ninth most common malignant cancer diagnosed worldwide (Lu et al., 2012). About 90% of the diagnosed cases are urothelial cell carcinomas that arise from bladder epithelial cells, while the remaining are squamous cells carcinomas and adenocarcinomas. At diagnosis, 80% of the patients present with low-grade non-muscle invasive papillary carcinoma, which rarely invades and metastasizes (classified as superficial Ta/T1 lesions), while 20% have muscle-invasive tumours (classified as T2 or higher T3/T4 lesions) (El Behi et al., 2013). Of note is the marked difference in survival rates between the two cancer types, suggesting two distinct underlying genetic profiles. Non-invasive papillomas are mainly characterised by alterations in the *FGFR3* gene and chromosome 9, accompanied by low frequency of *TP53* alterations, whilst muscle-invasive tumours are marked by high frequency alterations in genes involved in the p53 and Rb pathways (Luis et al., 2007).

As described extensively in the main introduction, SLRPs, as components of the ECM and the tumour microenvironment, can modulate cell survival, proliferation and migration, and are thereby involved in the biology of various types of cancer. Although there are not many findings regarding SLRPs and bladder cancer, there have been some studies linking so far only decorin and biglycan with urothelial malignancies. More specifically, decorin mRNA levels were found to be markedly decreased in primary bladder cancers compared to normal counterparts in two independent microarray datasets (Dyrskjot et al., 2004; Morrione et al., 2013; Sanchez-Carbayo et al., 2006), while decorin was also shown to negatively regulate IGF-IR signalling in urothelial carcinoma-derived cells, inhibiting their migration and invasion (Iozzo et al., 2011). In addition, Niedworok *et al*. recently showed that overexpression of biglycan resulted in inhibition of bladder tumour growth both *in vitro* and *in vivo*, whilst high biglycan expression in human tumour biopsies was associated with favourable prognosis (Niedworok et al., 2013).

Referring again to the genetic backgrounds of bladder cancer, one important thing that needs to be mentioned here, in relation to the current project, is the finding that loss of heterozygosity (LOH) on chromosome 9 is the most frequent genetic alteration identified in bladder tumours, with around 60-70% of the tumours showing

LOH of at least one locus on either arm of the chromosome (Keen and Knowles, 1994; Simoneau et al., 1996; Stadler et al., 1994). In addition, Hirao *et al*. showed that allelic loss at specifically the 9q arm was detected in 74.5% of newly diagnosed bladder cancer cases and that this allele loss was associated with invasive forms of the disease, thereby suggesting the existence of a tumour suppressor gene at this loci, which adding up to p53 alterations, may be important in the development of a more aggressive form of the disease (Hirao et al., 2005). While several LOH studies managed to localize some candidate tumour suppressor loci on the 9p arm, including the *MTS1*/*MTS2* genes, the location of putative TSGs on the q arm is less certain with most deletions being between 9q13-21.1 and 9q33-34.1 (Cairns et al., 1994; Czerniak et al., 1999; Habuchi et al., 1995; Linnenbach et al., 1993). However, because there is considerable variation in the specific regions of loss between different patients, it was suggested that even if 9q harbours a bladder cancer gatekeeper gene, it is unlikely that the gene will be identified through LOH analysis alone (van Tilborg et al., 2002). Of note is that Simoneau *et al*. identified another region, at 9q22.3, that was deleted in 35% of informative cases and was the unique LOH in some of the tumours screened (Simoneau et al., 1999). Our gene of interest, *OMD*, is located as well in the 9q22.3 region and the finding that this region might contain potent tumour suppressor genes further enhances our hypothesis that osteomodulin is involved in cancer acting as a TSG.

3.1.1 Current findings about OMD and PRELP

Concerning OMD and PRELP, our collaborators Dr. Hamamoto and Dr. Tamura analysed microarray data comparing gene expression in tumours and normal tissue for many different types of cancer, and found that *OMD* and *PRELP* expression were both reduced in bladder cancer to less than a tenth of their normal level. Further confirmation of the downregulation was confirmed by RT-PCR using human urological tumour biopsies, while further reductions in expression were seen in high stage and grade bladder tumours, and in bladder tumours that metastasized. Briefly, 126 bladder tumours and 31 normal bladder samples were studied, and on average *OMD* and *PRELP* expression were reduced by 90% (Fig.1.5). More information and detailed results of this analysis can be found in Appendix A. Thus, we obtained very strong indications that OMD and PRELP are indeed involved in cancer initiation and

progression, and that they may represent potential tumour-suppressor genes, functioning in a similar way to other SLRPs that were discussed previously.

The initial analysis to prove the above hypothesis was conducted by previous lab member Dr. Julie Watson, who used the EJ28 human bladder cancer line as a model of study. This cell line was chosen as it was one of the cell lines that Dr. Hamamoto had found expressed OMD and PRELP at a very low level and it also gave the highest transfection efficiency. Therefore, it was decided to perform a gain-of-function analysis by creating stable transfected EJ28 cells to overexpress OMD or PRELP and test whether this would revert the cancer cells to a more normal, untransformed phenotype. Indeed, Dr. Watson found that OMD and PRELP overexpression inhibited cell cycle progression and proliferation, while it enhanced apoptosis and drug-mediated apoptosis. Also, cellular morphology was affected in OMD overexpressing cells showing unique round shapes with many pin-like extensions, which are significantly different from the flattened fibroblast-like shape of control EJ28 cells, while PRELP overexpression resulted in elongated cells with stress fibre like filamentous extensions protruding along the substrate. Furthermore, Dr. Watson conducted a series of western blotting experiments to determine how expression of proximal cell cycle regulators and signalling molecules, that were known to be involved in bladder carcinogenesis and/or SLRP activity, are affected in OMD and PRELP transfected cells (presented in detail in Section 3.2.6.2). Finally, Dr. Hamamoto performed mRNA expression profiling using microarrays after overexpression or suppression of OMD/PRELP and with a subsequent pathway analysis identified the main pathways affected, which included the p53, tight junction, adherens junction and Wnt signalling pathways (Appendix A).

Having all these initial data, I took over this project from this point and further wanted to assess some more *in vitro* cancer hallmark properties of the transfected cells, like anchorage-independent growth and migration. In addition, together with Dr. Tamura Toshiya, a collaborator from Takeda Pharmaceutical Company, we wanted to assess the effect of OMD and PRELP *in vivo* using the xenograft mouse model and also further analyse the mechanisms of actions involved. Moreover, a different system of overexpression was also explored.

3.2 Results

The initial experiments were performed with the cell lines that Dr. Watson had constructed via antibiotic selection of stable transfectants and single clonal growth by limiting dilution. Also, she used tagged versions of the OMD and PRELP cDNAs, where 6 myc tags and a unique sequence between the 5^{th} and 6^{th} tag were placed at the C-terminus of the open reading frames for each cDNA. The addition of the tag provided an easier way for protein detection through western blotting, as so far no working antibodies against the OMD or PRELP proteins have been identified. So, for the experiments presented in this chapter, 6 different cell types were used that included:

- EJ28-OMD, EJ28 cells transfected to overexpress the human OMD cDNA and an eGFP marker gene
- EJ28-PRELP, EJ28 cells transfected to overexpress the human PRELP cDNA and an eGFP marker gene
- EJ28-mtOMD, EJ28 cells transfected to overexpress a myc-tagged version of the human OMD cDNA and an eGFP marker gene
- EJ28-mtPRELP, EJ28 cells transfected to overexpress a myc-tagged version of the human PRELP cDNA and an eGFP marker gene
- EJ28-vector, EJ28 cells transfected with the vector expressing only the marker eGFP gene, serving as control
- EJ28-WT, wild type non-transfected EJ28 cells

We should mention here that Dr. Watson had isolated and tested two different clones of all the above transfected cell lines, in order to confirm that the obtained results were due to OMD/PRELP overexpression and not because of any functional cell changes arising from the insertion site of the plasmids. Indeed, the results she acquired in her *in vitro* assays were very similar between the two different clones of each OMD/PRELP/mtOMD/mtPRELP- and vector-transfectants, thereby confirming the validity of these results. In most of the *in vitro* assays presented here we also used both clones of the transfected cell lines, which always gave comparable outcomes, while occasionally only one clone was used due to time and material limitations. For presentation purposes (and since the different clones resulted in the same outcome) our results are displayed here as one transfected cell line named as EJ28-OMD, EJ28-PRELP etc.

The overexpression of OMD and PRELP in the EJ28 stable transfectants was confirmed by RT-PCR at RNA level and by western blotting at protein level for the myc-tagged constructs, by Dr. Watson. I also reconfirmed the overexpression in the above cell lines by RT-PCR, where the expression difference was variable amongst the different cell lines from 5 to almost 15 times higher than the EJ28-WT cells (Fig. 3.1). The same result was obtained when comparing the different transfectants with the EJ28-vector control cells.

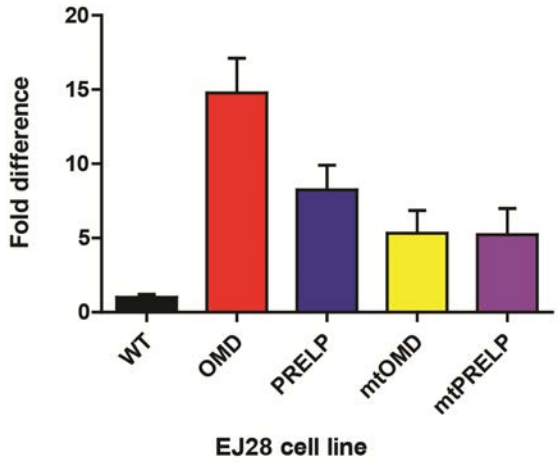

Figure 3.1: Confirmation of overexpression of untagged and myc-tagged OMD and PRELP in EJ28 cells. For each cell line, all of which were seeded in 6-well plates, RNA was collected from 3 different wells. Technical triplicates of each biological sample were tested in qRT-PCR. Analysis was performed using the Pfaffle method and values were normalised to endogenous GAPDH expression levels. Results are presented as fold-difference compared to EJ28-WT cells which is set to 1. Error bars indicate standard deviation (SD).

3.2.1 OMD and PRELP overexpression inhibit anchorage-independent growth

The anchorage-independent growth assay, also called the soft agar assay, is the gold standard *in vitro* method to assay tumor–forming ability. It assesses the ability of cells to grow suspended in soft agar, without attachment to a substrate or to other cells. It has long been known that transformed cells are typically capable of anchorage-independent growth, whilst normal cells are not (Stoker et al., 1968).

To test whether OMD or PRELP overexpression affected anchorage-independent growth, 5.000 cells of each stably transfected EJ28-OMD/PRELP/mtOMD/mtPRELP/vector control and EJ28 WT cell lines were seeded in triplicates into a mixture of growth medium and semi-solid agar in 6-well plates, and after 3 to 4 weeks formation of colonies was assessed. As shown in Figure 3.2 A&B colonies formed from the WT and vector-only cells with a mean number of 783 ± 46.19 and 814 ± 35.48 colonies per 962mm^2 surface area respectively. In contrast, anchorage independent growth was completely abolished in the OMD transfected cell line (mean number of colonies was 1.12 ± 0.74), while there was a significant reduction in the colony number of the other transfected lines, i.e. 461.0 ± 24.58 for PRELP, 309.5 ± 26.51 for mtOMD and 426.0 ± 33.96 for mtPRELP (p<0.05 for all transfected cell lines against WT or vector control). These data are collected from three individual experiments, demonstrating complete and consistent inhibition of colony formation from the OMD overexpressing cells, and to a lesser extent from the other lines tested (which could be attributed to the different levels of cDNA expression, i.e. OMD cells had a 15-fold increased expression compared the WT versus the mtOMD cells that showed only a 5-fold difference), indicating an anti-tumour effect of our genes.

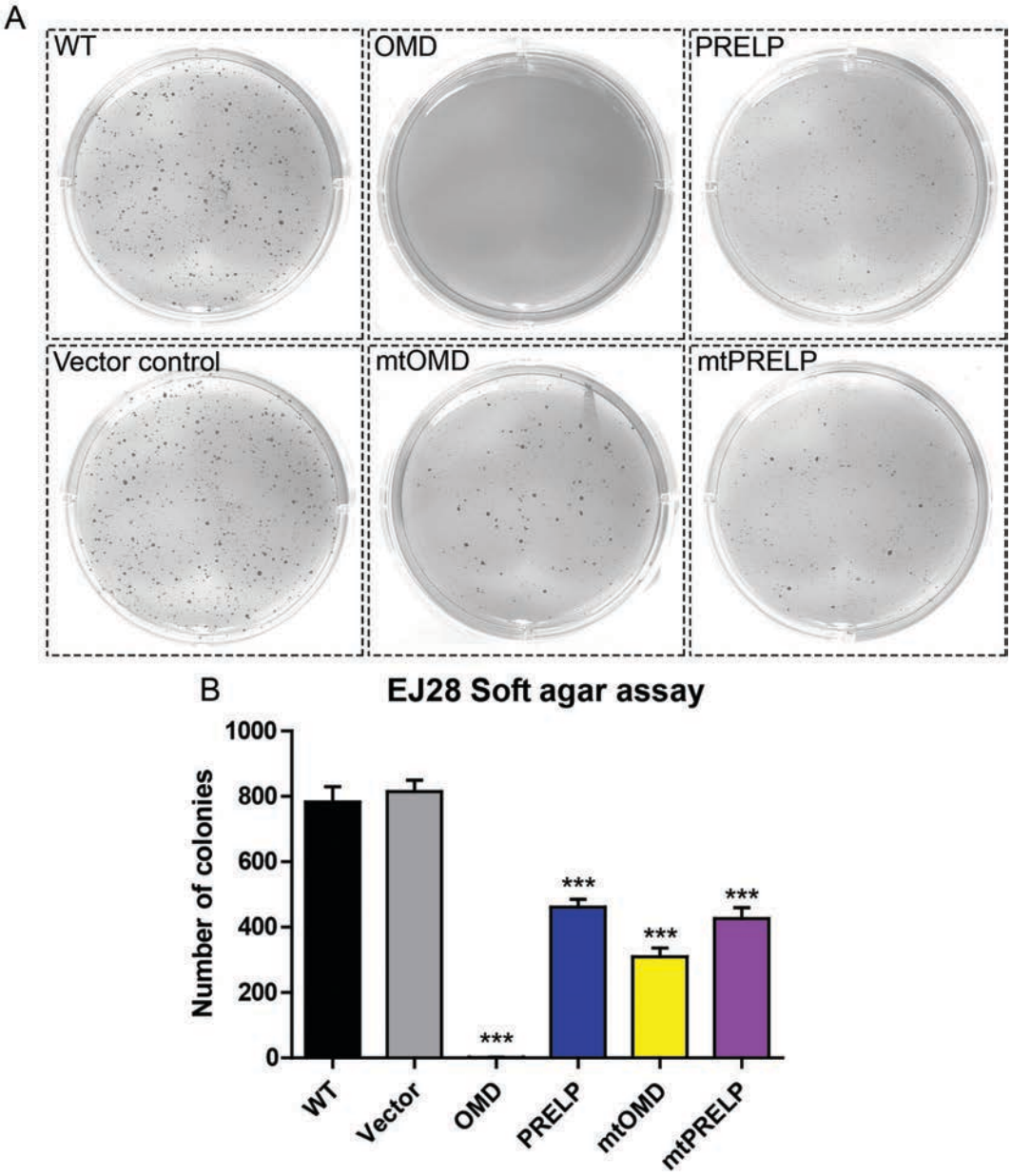

Figure 3.2: Anchorage independent growth assay of EJ28 cells. (A) Representative images of colonies that grew in soft agar. OMD completely abolished, while PRELP, mtOMD and mtPRELP strongly inhibited formation of colonies. The experiment was performed thrice and each cell line was seeded in triplicate wells. (B) Quantification of formed colonies. Multiple t-tests were carried out comparing means from every transfected cell line to the WT or vector-only control, *** equals $p<0.0001$, against WT or Vector control. Error bars indicate standard error of the mean (SEM).

3.2.2 OMD and PRELP overexpression alters the 3D morphology of EJ28 cells cultured in an ECM-mimicking microenvironment

Apart from providing structural support, the extracellular matrix can regulate the dynamic behaviour of cells by affecting cell-cell communication, cell-cell or cell-

matrix adhesion and also cell differentiation, therefore being a major component of normal homeostasis. Thus, *in vitro* 3D cultures of cells in an ECM-mimicking microenvironment can allow phenotypic discrimination between malignant and non-malignant cells, where the former form proliferative and expanding colonies while the latter remain as circular, partly-grown colonies. This experiment was performed with the help of Dr. Tamura, and we used Matrigel as a biologically active basement membrane matrix, where EJ28-WT, vector-only, OMD and PRELP-transfected cells were allowed to grow for seven days. On the last day 3D morphogenesis was assessed by observation under light microscopy. The experiment was performed thrice (in duplicates), and a representative image of each cell type is presented in Figure 3.3, demonstrating expanding colonies with spike-like formations in the wild type and vector-only transfected cells, whereas OMD and PRELP overexpressing cells had smaller and rounded colonies, indicating that the two genes can reduce the invasive phenotype of the EJ28 cells and can alter the morphology of the cells in 3D Matrigel culture.

3.2.3 OMD overexpression inhibits invasiveness of the EJ28 cell line

Migration and invasion of cancer cells into the basement membrane and the adjacent ECM is a key step in cancer metastasis, and examining the invading potential of cells *in vitro* is of major interest in cancer studies. The invasiveness of the EJ28 cell line was assessed by the Matrigel invasion assay, where cells are plated on a Matrigel-coated porous membrane and invasion through the matrix to the opposite site of the pores (towards a chemoattractant) is determined by cell staining and subsequent quantification (as described in Section 2.2.2.5). This experiment was also performed with the help of Dr. Tamura. Since the OMD transfected cells had consistently a stronger phenotype in all the assays tested compared to the other cell lines, and due to time and material limitations only the EJ28-WT and EJ28-OMD overexpressing cells were included in this experiment. Presented in Figure 3.4A, are representative images of the bottom side of the porous membrane, where cells, stained with Hemacolor hematoxylin, were cultured in 0.1% FBS, and it is visible that only few cells invade through the matrix and the pores (left panels). Addition of chemoattracant-containing medium (10% FBS) resulted in invasion of the cells through the pores. Comparison between the WT and OMD overexpressing cells

reveals a much higher invading cell population in the control sample, indicating a decrease in the invasiveness potential due to the *OMD* gene overexpression. Quantification of the invaded cells was performed by solubilising the hematoxylin dye and measuring the absorbance index, which was subsequently converted to relative invasiveness measured as percentage of the control (0.1% FBS) (Fig. 3.4B). OMD overexpressing cells had a significantly lower invasion ratio compared to EJ28 WT cells (p=0.0007), suggesting that OMD has the ability to inhibit matrix cell invasion, further confirming its potential as a tumour-supressing gene.

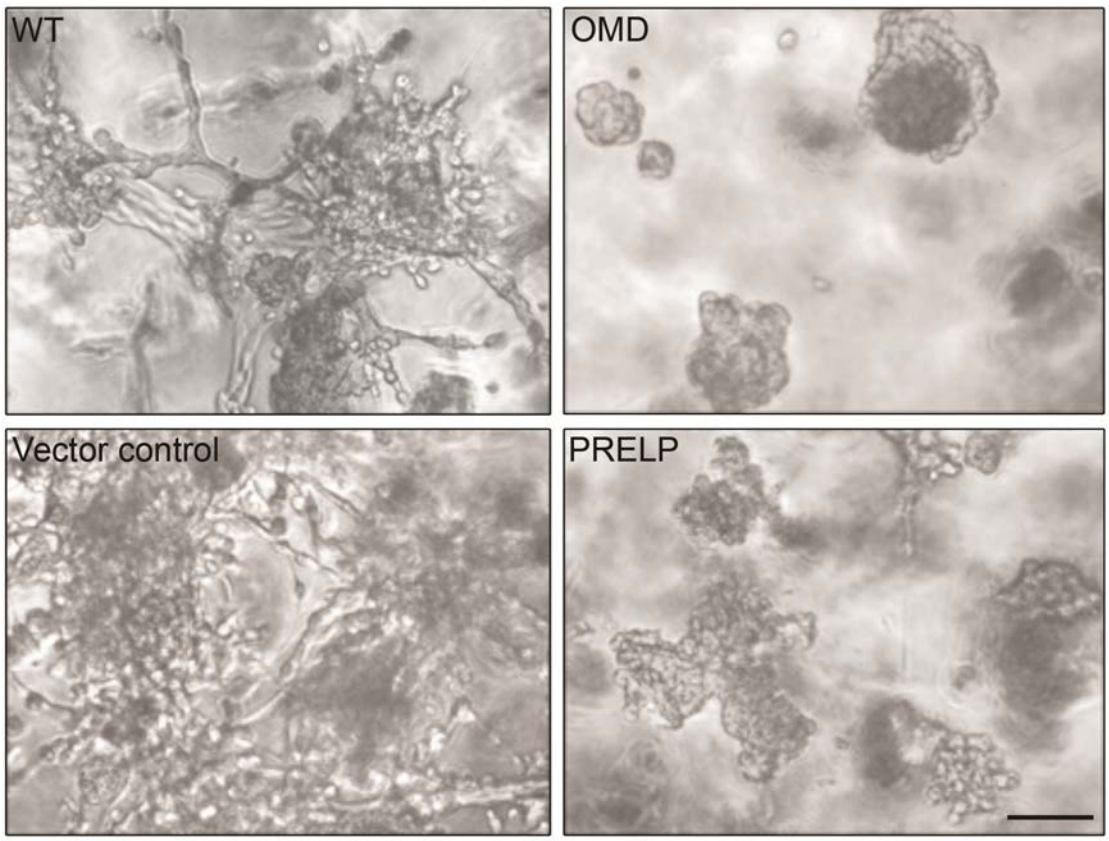

Figure 3.3: 3D morphogenesis of EJ28 cells in Matrigel. 10000 cells were mixed with matrigel and medium containing 10% FBS and were seeded onto 8-well multi chambers pre-coated with matrigel. After 7 days, 3D morphogenesis was assessed by light microscopy. The experiment was performed thrice in duplicates, with the help of Dr. Tamura. EJ28-WT and vector-only transfected cells show expanding colonies with spike-like formations, demonstrating good ability of the cells to proliferate and migrate in an ECM-mimicking microenvironment. In contrast, OMD and PRELP overexpression resulted in smaller and rounded colonies, therefore inhibiting the invasive phenotype of cancer cells. Scale bar represents 100μm for all images.

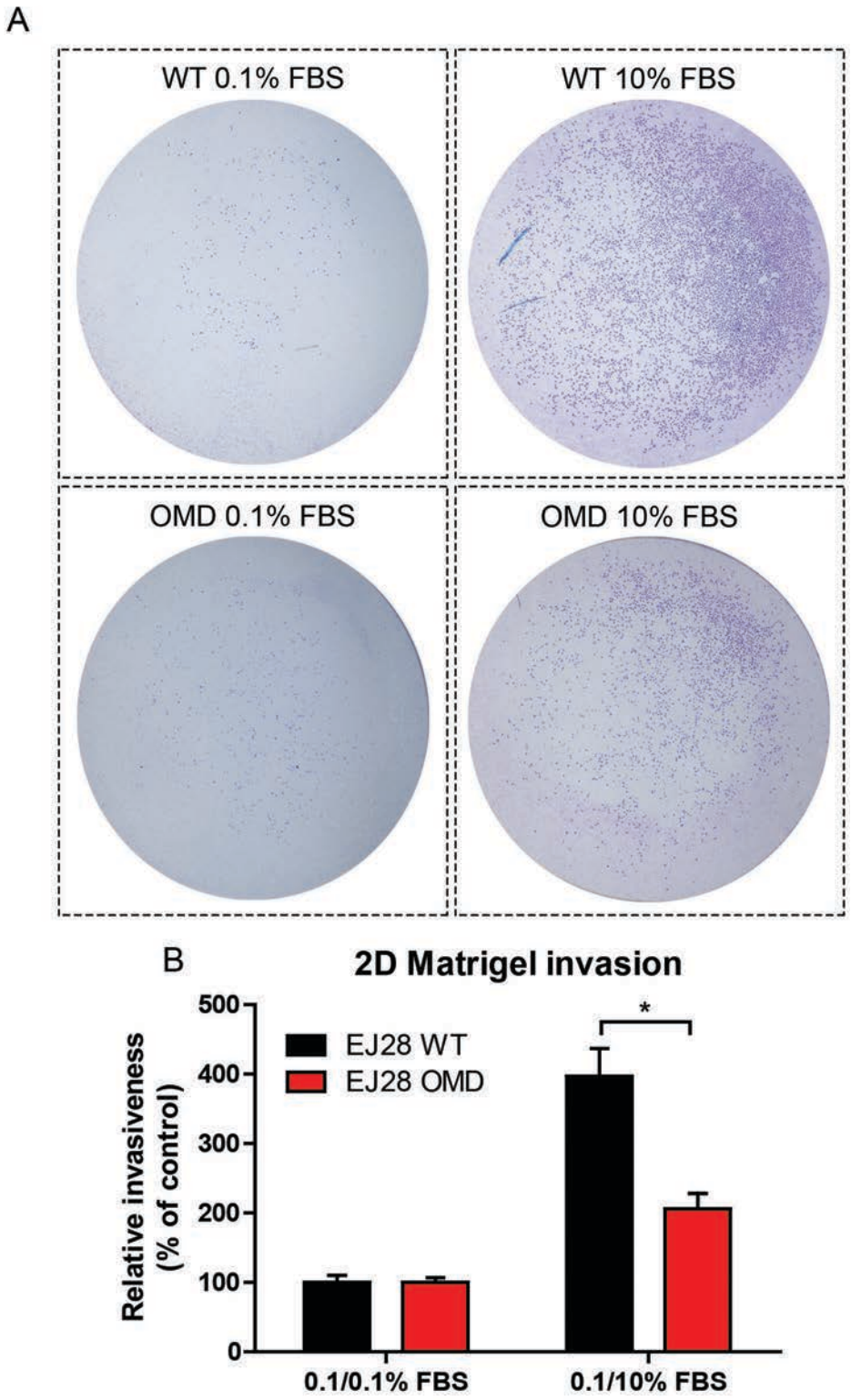

Figure 3.4: 2D Matrigel invasion assay of EJ28 cells. Cells were seeded on matrigel-coated porous membranes and invasion through the pores was assessed after the addition of 10% FBS as chemoattracant. Cells were visualised with Hemacolor hematoxylin. The experiment was performed once in triplicates, again with the help of Dr. Tamura (A) Images of the bottom side of the membrane in 0.1% FBS (left panel) and 10% FBS (right panel), showing decreased invasion ability of the OMD transfected cells through the matrigel covered pores. (B) Quantification of the invaded cells was calculated through hematoxylin absorbance and is presented as relative invasiveness, measured as percentage of the control (0.1% FBS). Student's t-test was performed, * equals $p<0.05$. Error bars refer to SD.

3.2.4 Secretion of OMD and PRELP inhibits normal cell growth under co-culture conditions

As extracellular matrix proteins, OMD and PRELP are expected to be secreted from the expressing cells into the culture medium. Therefore, together with Dr. Tamura we performed a modified transwell assay to assess the effect of the secreted proteins on neighbouring cells. In this assay wild type EJ28 cells are seeded on the bottom of 6-well plates and are cultured together with a transwell insert, on the surface of which, EJ28-WT or OMD/PRELP/mtOMD/mtPRELP transfected cells are seeded. The pores of the membrane are 0.4 μm allowing diffusion of soluble particles in the lower compartment while preventing cell migration or cell-cell contact. A schematic illustration of the co-culture assay is shown in Figure 3.5B, where Cell B always represents EJ28 wild type cells, and Cell A varies between WT and the four different transfected cell lines. In Figure 3.5A representative pictures of Cell B (EJ28-WT cells) are shown for each different condition (co-culture with the various transfected lines). An empty transwell insert served as a negative control, and as shown in panel A, EJ28 cells co-cultured with either no-cells or EJ28-WT had good survival index and were confluent after 72h in this experimental setup. On the contrary, wells that had transwell inserts with either OMD or mtOMD cells were characterized by increased detachment and cell death of the EJ28 WT cells. The same effect was observed when mtPRELP cells were seeded in the transwell, while the PRELP overexpressing line had a moderate impact on the wild type cells (Fig. 3.5A). Cell viability of the bottom EJ28-WT cells (Cell B) per condition was evaluated with trypan-blue staining and subsequent counting of the living cells after 72h of co-culture, while Cell A remained confluent until the end of the experiment in all conditions. Co-culture with OMD or mtOMD cell lines caused a significant reduction on the EJ28-WT cell viability of around 80% compared to the control conditions (p=0.0033 and p=0.0057 respectively), data that were consistent between two different repeats. The experiment was performed only once for the PRELP and mtPRELP cell lines and thus, although presented here, these data are considered inconclusive. Overall, even though these are preliminary results, this experimental setup demonstrates that secreted OMD (and maybe PRELP) protein, has the ability to suppress, and additionally reduce, the viability of EJ28 cancer cells.

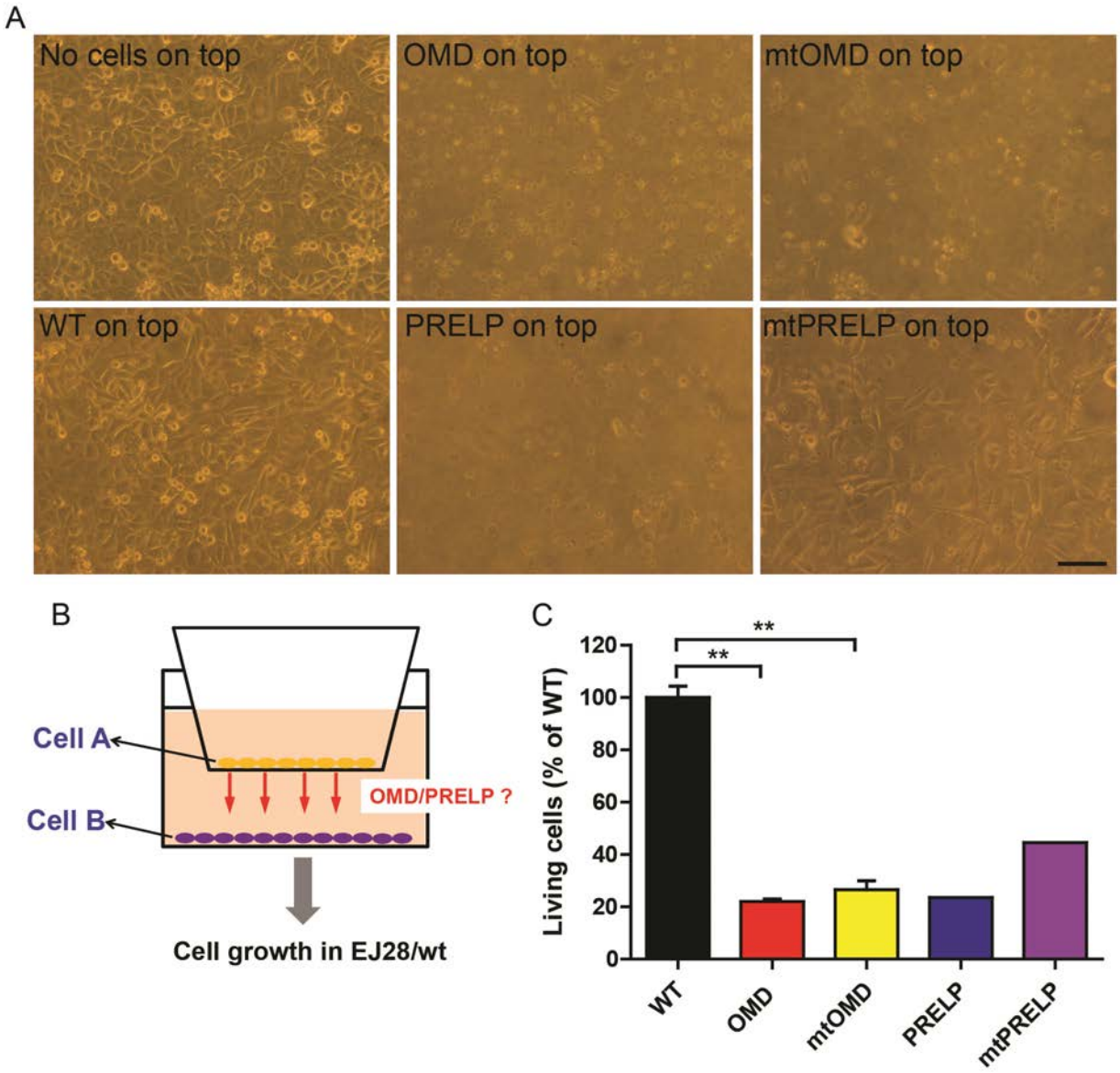

Figure 3.5: Transwell co-culture assay of EJ28 cells. The effect of secreted OMD/mtOMD/PRELP/mtPRELP proteins on the viability of EJ28-WT cells is assessed, where WT cells are seeded in the bottom of 6-well plates and the different transfectants are seeded in a porous insert and placed on top of the wells. Diffusion of soluble particles is allowed through the pores but not cell migration. A schematic illustration of the assay is presented in (B), while in (A) brightfield images of the bottom EJ28-WT cells after 72hours of co-culture with the different transfected cells are shown, demonstrating a strong reduction in cell viability in the presence of OMD, mtOMD, PRELP and mtPRELP overexpressing cells. Scale bar represents 50μm for all images. (C) Quantification of the bottom EJ28-WT cell viability under the four different transfectants, presented as percentage of the viable cells co-cultured with WT cells on the transwell insert. Student's t-test was performed. ** equals $p<0.01$. Error bars refer to SD. Co-culture with PRELP and mtPRELP transfectants was conducted only once and therefore no statistical analysis was carried out for these samples.

3.2.5 OMD and PRELP overexpression inhibits tumour development in the mouse xenograft model

Numerous murine models have been developed to study human cancer with the most widely used model being the human tumor xenograft. In this model, human tumour cells are transplanted, either under the skin or into the organ type in which the tumour originated, into immunocompromised or immunodeficient mice (e.g. the xenograft will be readily accepted by athymic nude mice or severely compromised immunodeficient-SCID mice) (Morton and Houghton, 2007). Depending upon the number of cells injected, or the size of the tumour transplanted, the tumour will develop over 1–8 weeks (or in some instances 1–4 months, or longer), and the response to candidate therapeutic agents can be studied *in vivo*.

In order to assess the effect of OMD and PRELP in *in vivo* tumour progression, mouse xenografts were performed using the EJ28 OMD/PRELP transfected cell lines. During this experiment 6 mice were used. Every mouse was injected subcutaneously in the flank with wild type cells in the left side, while 3 mice were injected with OMD-overexpressing cells and the other 3 mice with the PRELP-overexpressing cells in the right side, to compare tumour progression for a period of 42 days.

In Figure 3.6 A and B the tumour volumes as well as the relative tumour growth of the three different cell types are presented over the 42-day period. Wild type EJ28 cells grew tumours of around 1300 mm^3, whereas EJ28-OMD cells completely failed to support tumour growth, with volumes of around 100mm^3 from the first up to 200mm^3 till the last measurement (Fig. 3.21A, Day 42, p=0.0006, Day35 p<0.0001, Day 26 p=0.0003, Day 21 p=0.0209). PRELP overexpressing cells did not show such dramatic reduction in tumour growth, but did cause a slower increase of the tumour volume in the last two time points. The effect is more pronounced if we compare the relative tumour growth, as demonstrated in Figure 4.6B, where EJ28-PRELP cells grew statistically slower compared to the wild type cell lines during the last 10 days of the experiment (Day 42, p=0.0265, Day35 p<0.0338).

Overall, the *in vitro* anti-tumor effects of OMD (and to a lesser extent of PRELP) on cancer progression were confirmed as well in *in vivo* xenograft

experiments, demonstrating the potential of the two molecules as anti-cancer effectors.

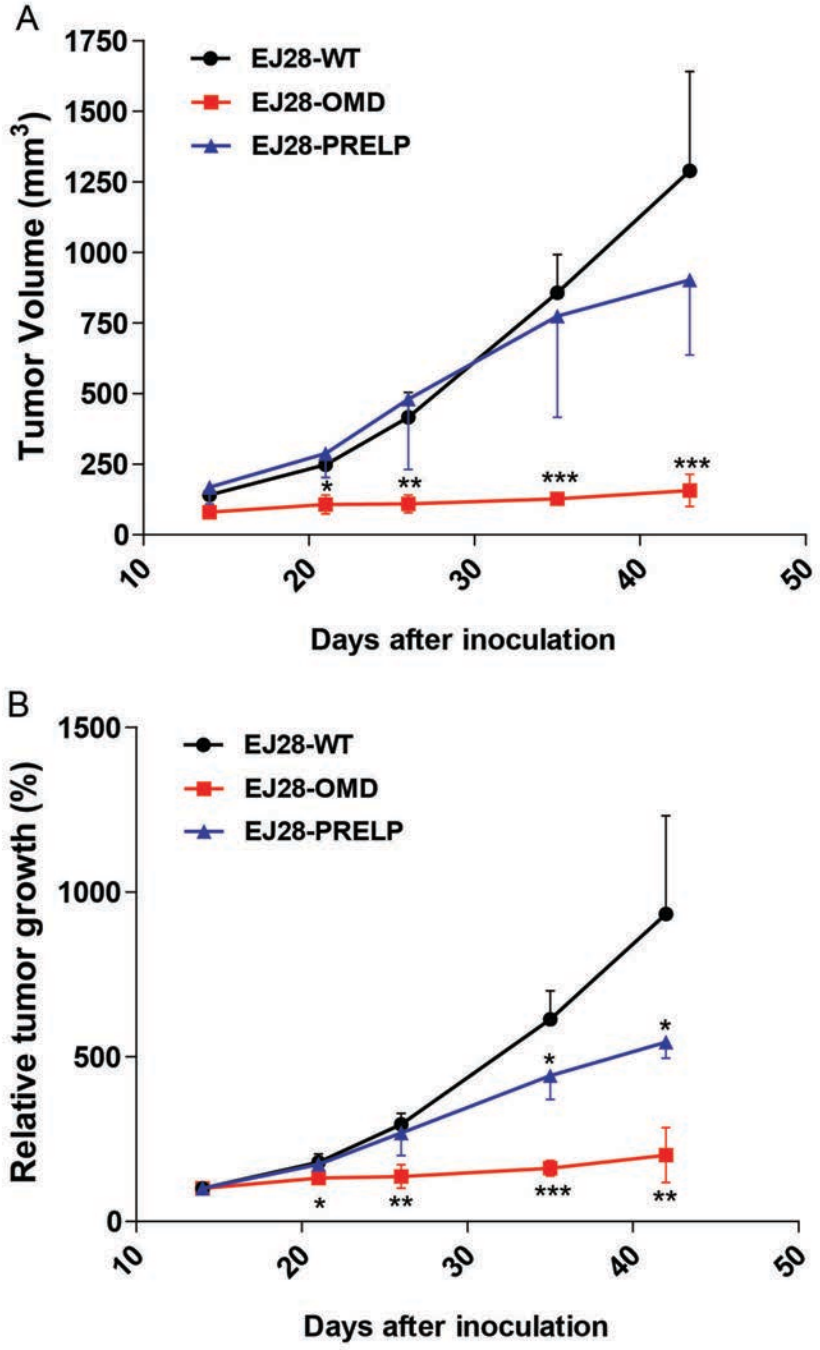

Figure 3.6: OMD inhibits tumour formation and PRELP supresses tumour growth in the mouse EJ28 xenograft model. 5×10^6 cells of each EJ28-WT/OMD/PRELP cell line were injected in the right and left flanks of nude mice. Two weeks after inoculation measurement of the forming tumours started. (A) Graph representing the average tumour volume over a period of 42 days, including 6 tumours for the WT cells and three tumours for the OMD/PRELP overexpressing cells. (B) Relative tumour growth presented as percentage of the first measurement. Student's t-test was carried out at each time point. * equals $p<0.05$, ** $p<0.01$, *** $p< 0.001$, versus WT. Error bars refer to SD. Injections of the EJ28 cells in the mice were performed with the help of Dr. Tamura.

3.2.6 Mechanisms of action of OMD and PRELP

Having already established some of the anti-tumor properties of the OMD and PRELP, we wanted to further examine the mechanisms through which these two genes/proteins operate. As explained in the introduction of this chapter, initial microarray analysis was performed on cell lines over-expressing or under-expressing the *OMD* and *PRELP* genes, and through KEGG pathway analysis the affected signalling cascades were identified. One of these is the tight junction (TJ) pathway (*p* values of 0.0146 and 0.0412 for OMD and PRELP respectively, data provided by Dr. Hamamoto), while others include the p53, the adherens junction and the Wnt signalling pathways (see Appendix A). Also, Dr. Margaret Dellett, a previous post-doc in the Ohnuma lab, analysed the microarray data using the Ingenuity Pathway Analysis (IPA) software, and generated illustrations of the affected pathways showing which molecules are negatively or positively regulated from alterations in the *OMD* or *PRELP* gene expressions. The tight junction pathway under *OMD* overexpression is displayed in Figure 3.7, showing that some TJ components such as ZO-1 and Nectin are transcriptionally activated by *OMD* overexpression, suggesting that OMD or PRELP have the ability to positively regulate these junctions. Hence, tight junction formation was further assessed in the stably transfected EJ28 cell lines. In addition, since Wnt is also another one of the affected pathways, together with Dr. Tamura we analysed some of the pathway's components in order to establish possible mechanisms of action.

3.2.6.1 OMD and PRELP increase tight junction formation

Tight junction formation was assessed in the OMD and PRELP over-expressing cell lines through immunofluorescence using several different antibodies against TJ components. Firstly, occludin staining was performed, and we observed a substantial increase of the cell surface, cell-cell contact staining in the OMD and PRELP cells compared to the controls (either WT or vector transfected). This was also accompanied by a decrease in the nuclear/cytosolic signal, as in the OMD/PRELP expressing cells the cytosol and nucleus often appeared dark, in contrast to the uniform staining seen in the control cells. More specifically, only around 40% of total cell-cell contact surface was positive for occludin in the EJ28 vector-control cells, while this figure increased to almost 90% for the OMD cells and 60% for

PRELP (p<0.0001 for both) (Fig. 3.8). Continuing, we conducted staining using antibodies against ZO-1 and cingulin, both major participants in the TJ protein complex, where we noticed the same outcome (Fig. 3.9 & 3.10). For both markers, the cell membrane signal (indicative of TJ formation between cells) was significantly increased in the OMD overexpressing cells (~90% of total cell-cell surface), and to a lesser extent in the PRELP ones (60-65%), against the control samples (30-40%, p<0.0001 for all comparisons), indicating that OMD and PRELP have the ability to increase tight junction formation.

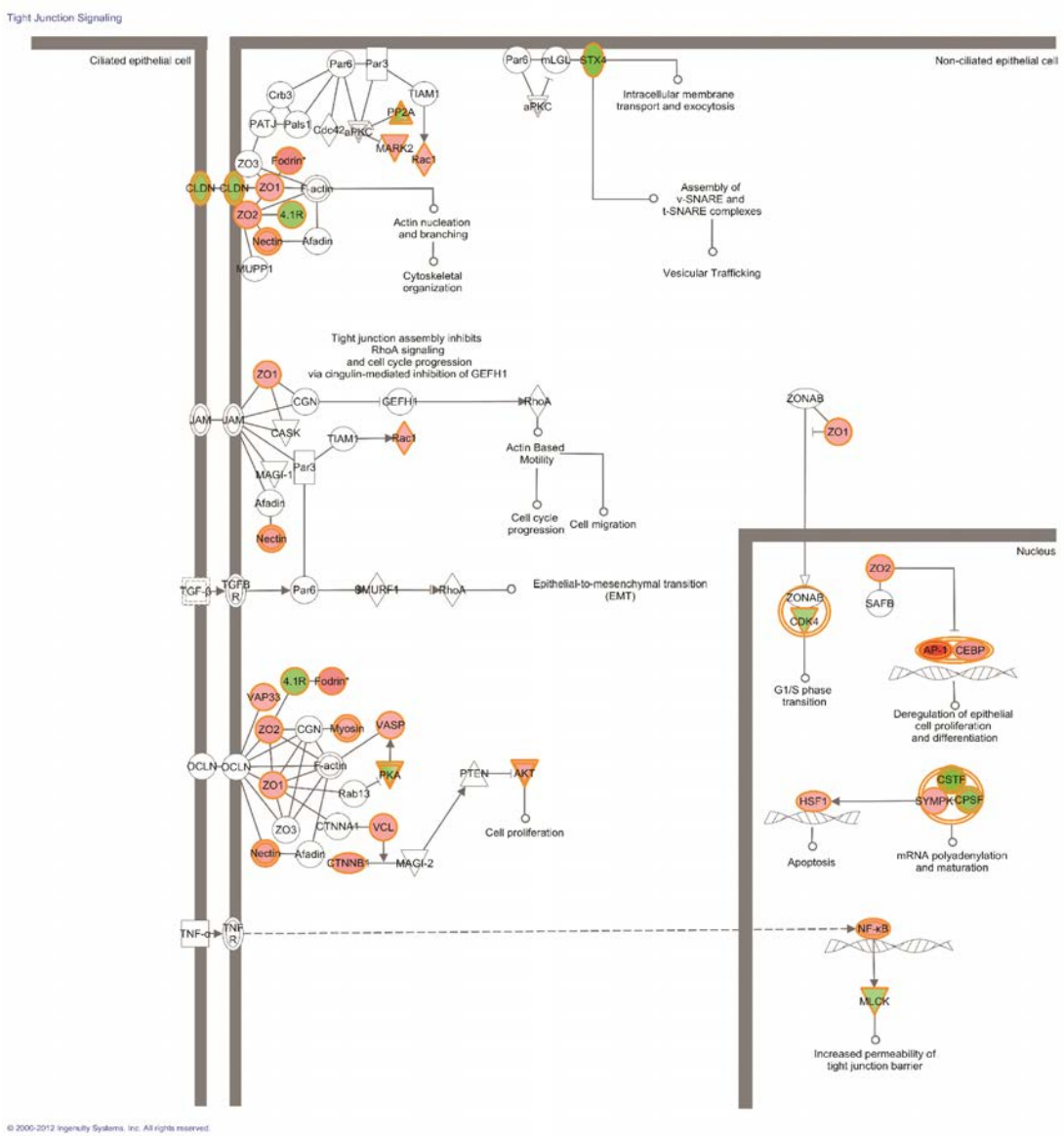

Figure 3.7: Tight junction pathway regulated by *OMD* overexpression. The schematic illustration of the pathway was generated using the Ingenuity Pathway Analysis (IPA) software. Red colour indicates transcription upregulation, while green colour indicates downregulation of the component. Image was kindly provided by Dr. Margaret Dellett.

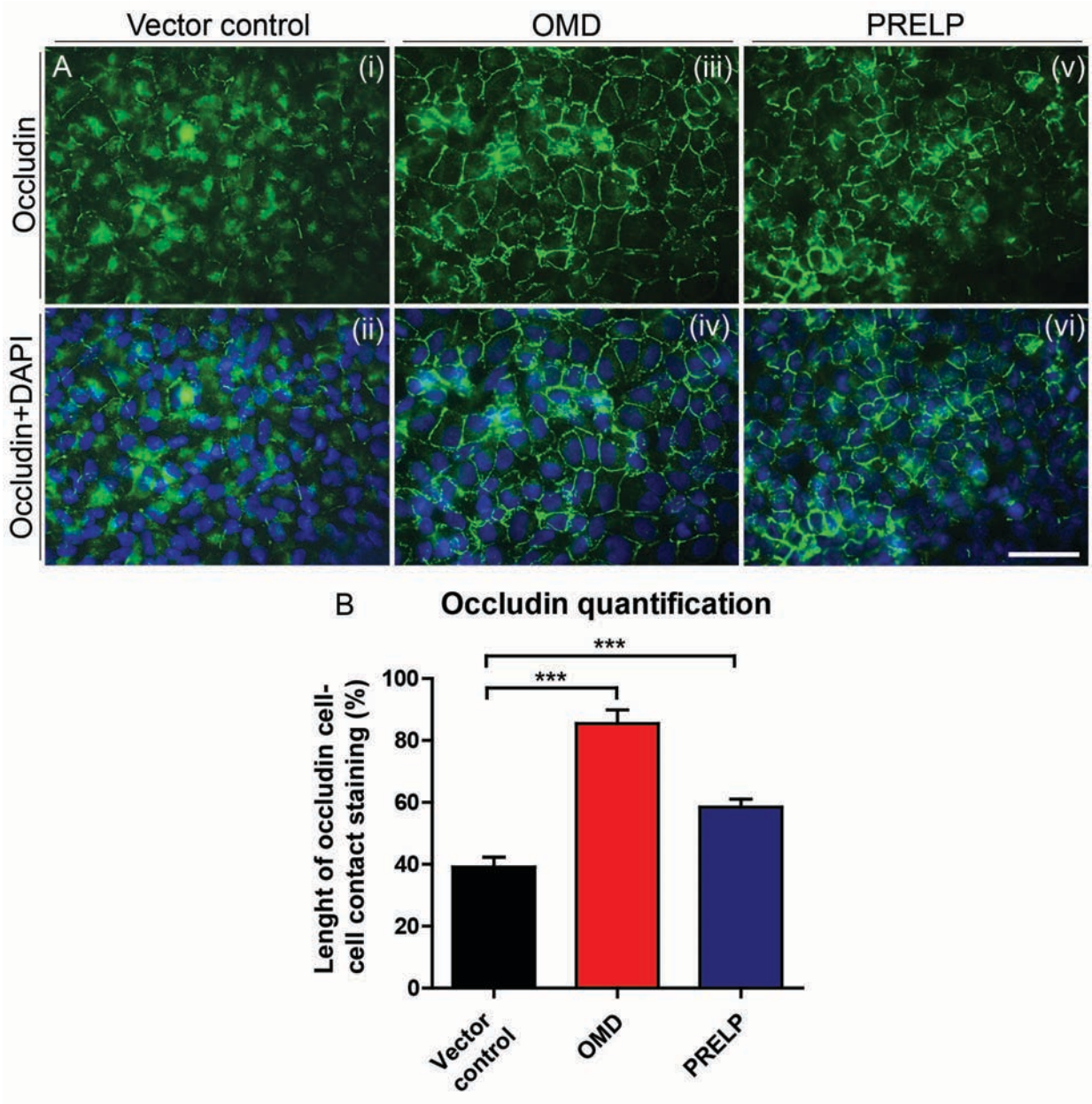

Figure 3.8: Occludin staining of EJ28 cells. OMD and PRELP overexpression results in increased cell-cell contact staining. Cells were cultured in 8-well multi chamber glass slides (in duplicates) and after reaching 100% confluency they were cultured for another 7 days to allow for junctions to be formed. On the 7th day they were fixed with ice-cold methanol and stained. Experiment was performed twice. In panel (A) images of vector-only, OMD and PRELP transfected EJ28 cells are shown, where (i), (iii) & (v) represent staining with an occludin primary antibody, visualised with an alexa-488 (green) secondary antibody. (ii), (iv) & (vi) are the same images with the addition of 4',6-diamidino-2-phenylindole (DAPI)-blue to visualize the nuclei. Scale bar represents 100µm for all images. (B) Percentage of occludin cell surface staining in each cell line tested. Quantification was performed in three random areas under 20x magnification, using the Image J software, where the length of occludin-positive cell–cell contacts was measured by drawing lines following the staining pattern. Staining inside the cells or unclear staining between neighbouring cells was ignored. Data are presented as mean ± SEM. Student's t-test was carried out. *** equals $p<0.001$ versus vector-control.

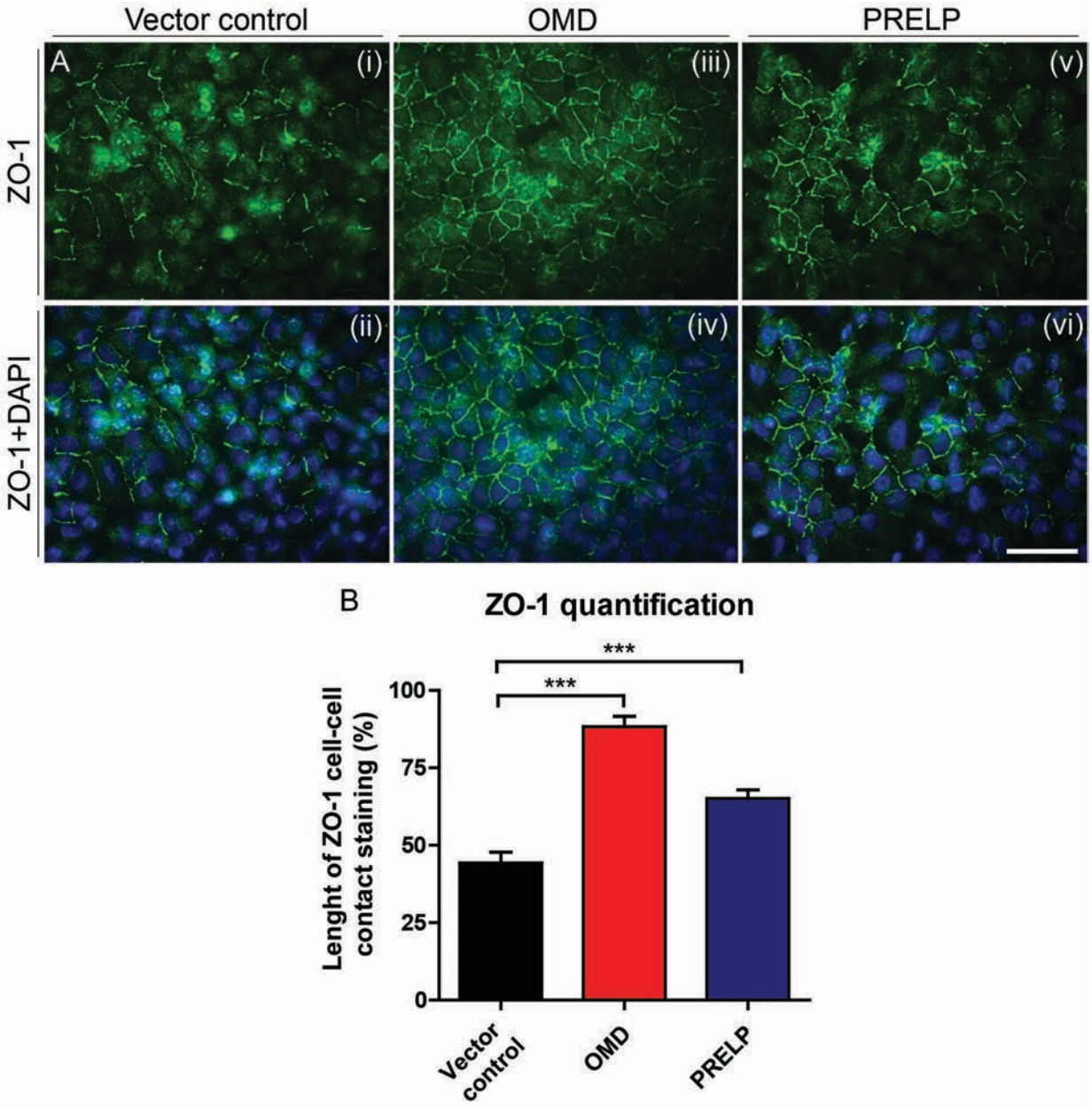

Figure 3.9: ZO-1 staining of EJ28 cells. OMD and PRELP overexpression results in increased cell-cell contact staining. Cells were cultured in 8-well multi chambers on a glass slide (duplicates) and after reaching 100% confluency they were cultured for another 7 days to allow for efficient tight junction formation. On the 7th day they were fixed with ice-cold methanol and stained. The experiment was performed twice. In panel (A) images of vector-only, OMD and PRELP transfected EJ28 cells are shown, where (i), (iii) & (v) represent staining with a rabbit ZO-1 primary antibody, visualised with an anti-rabbit alexa-488 (green) secondary antibody. Increased staining in cell-cell surfaces can be observed in the OMD and PRELP overexpressing cells. (ii), (iv) & (vi) are the same images with the addition of DAPI (blue) to visualize the nuclei. Scale bar represents 100μm for all images. (B) Percentage of ZO-1 staining per cell surface in each cell line tested. Quantification was performed in three random areas under 20x magnification, using the Image J software, where similarly to before, the length of ZO-1-positive cell–cell contacts was measured by drawing lines following the staining pattern. Staining inside the cells or unclear staining between neighbouring cells was ignored. Data are presented as mean ± SEM. Student's t-test was carried out. *** equals p<0.001 versus vector-control.

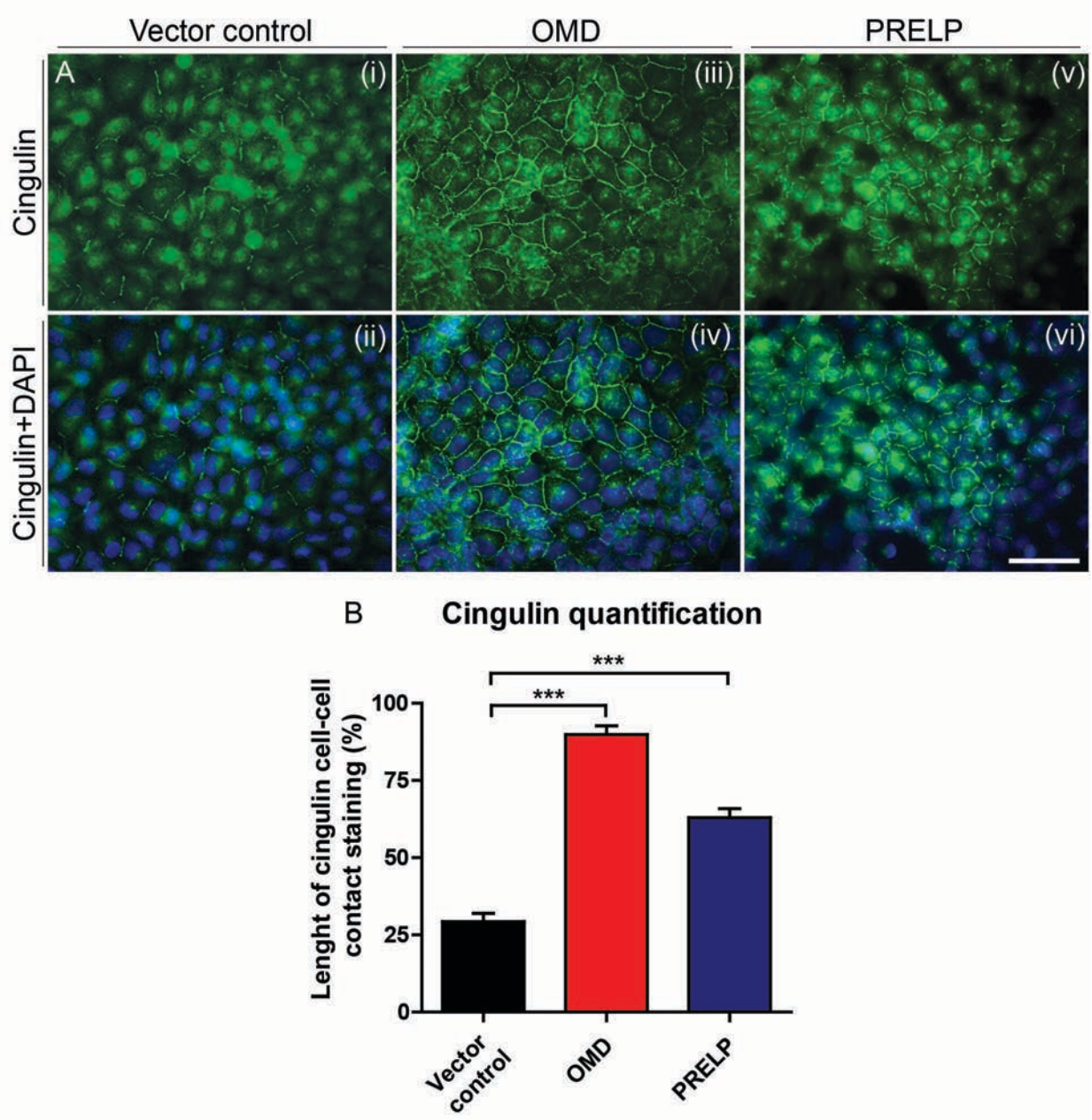

Figure 3.10: Cingulin staining of EJ28 cells. OMD and PRELP overexpression results in increased cell-cell contact staining. Cells were cultured in 8-well multi chambers on a glass slide (in duplicates) and after reaching 100% confluency they were cultured for another 7 days to allow tight junction formation. On the 7th day they were fixed with ice-cold methanol and stained. Experiment was performed twice. In panel (A) images of vector-only, OMD and PRELP transfected EJ28 cells are shown, where (i), (iii) & (v) represent staining with a rabbit primary antibody against cingulin, visualised with an anti-rabbit alexa-488 (green) secondary antibody. In OMD and PRELP transfected cells a very strong increase of cingulin staining localised in cell-cell membranes can be observed. (ii), (iv) & (vi) are the same images with the addition of DAPI (blue) to visualize the nuclei. Scale bar represents 100μm for all images. (B) Percentage of cingulin staining per cell surface in each cell line tested. Quantification was performed in three random areas under 20x magnification, using the Image J software, where, as previously, the length of cingulin-positive cell–cell contacts was measured by drawing lines following the staining pattern. Staining inside the cells or unclear staining between neighbouring cells was ignored. Data are presented as mean ± SEM. Student's t-test was carried out. *** equals $p<0.001$ versus vector-control.

In order to further confirm the formation of tight junctions, the OMD overexpressing cells (having the strongest effect) and control EJ28 wild type cells were examined by electron microscopy. Shown in Figure 3.11 are representative EM images of both samples, demonstrating tight junctions between neighbouring cells in the OMD overexpressing cell line (arrows). On the other hand, similar TJ complexes were not seen that often in the WT cells even though adjacent cells were in close proximity. However, in order to have a more conclusive result regarding functional tight junction formation in these cells, a more careful analysis needs to be conducted including more samples, quantification of the observed tight junctions and maybe gold-labelled staining of TJ components.

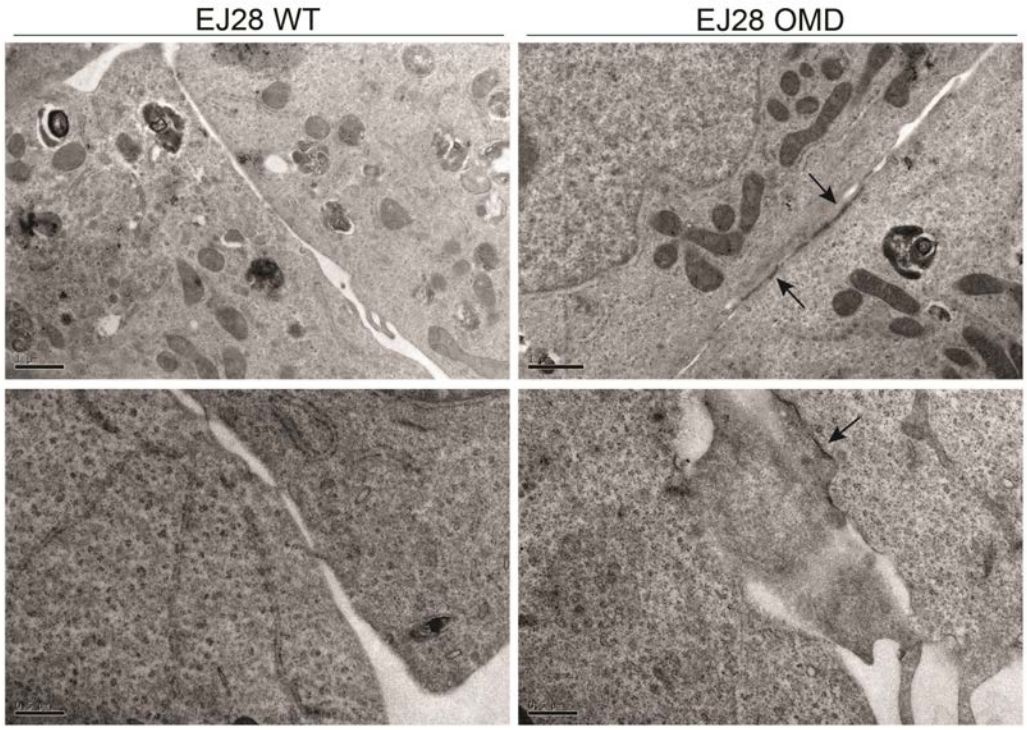

Figure 3.11: Electron microscopy analysis of EJ28-WT and EJ28-OMD cells. Cells from both lines were seeded in 6-well plates and after reaching confluency were cultured for one more week to allow formation of junctions. Left panel represents EJ28 wild type cells and right panel EJ28-OMD transfected cells, where arrows denote tight junctions seen between neighbouring cells, which were scarcely observed in the WT samples. Scale bars in the top images equal to 1μm, in the bottom images to 0.5μm.

Next, together with Dr. Tamura, we examined the expression of β-catenin, E-cadherin and vimentin, which provide information related to adherens junction, the canonical Wnt pathway, and epithelial to mesenchymal transition (EMT). Figure 3.12A demonstrates an increase of β-catenin staining intensity in the OMD/PRELP

transfectants compared to the vector-transfected control, accompanied by enhanced localization of the signal in the plasma membrane of the cells. This might suggest an activation of adherens junction and potential inhibition of the canonical Wnt pathway. However, E-cadherin expression was not increased in any of the transfected samples and we could not observe specific localization around the cell membranes (Fig. 3.12B), which might be due to incomplete adherens junction formation or insufficient staining conditions. Furthermore, alternation of adherens junction often is linked with EMT. Thus, staining with vimentin, which can be used as a marker of EMT, was performed, where the staining pattern between the control and OMD/PRELP transfected cells appeared quite similar (Fig. 3.12C), indicating no apparent cell status transition under these conditions.

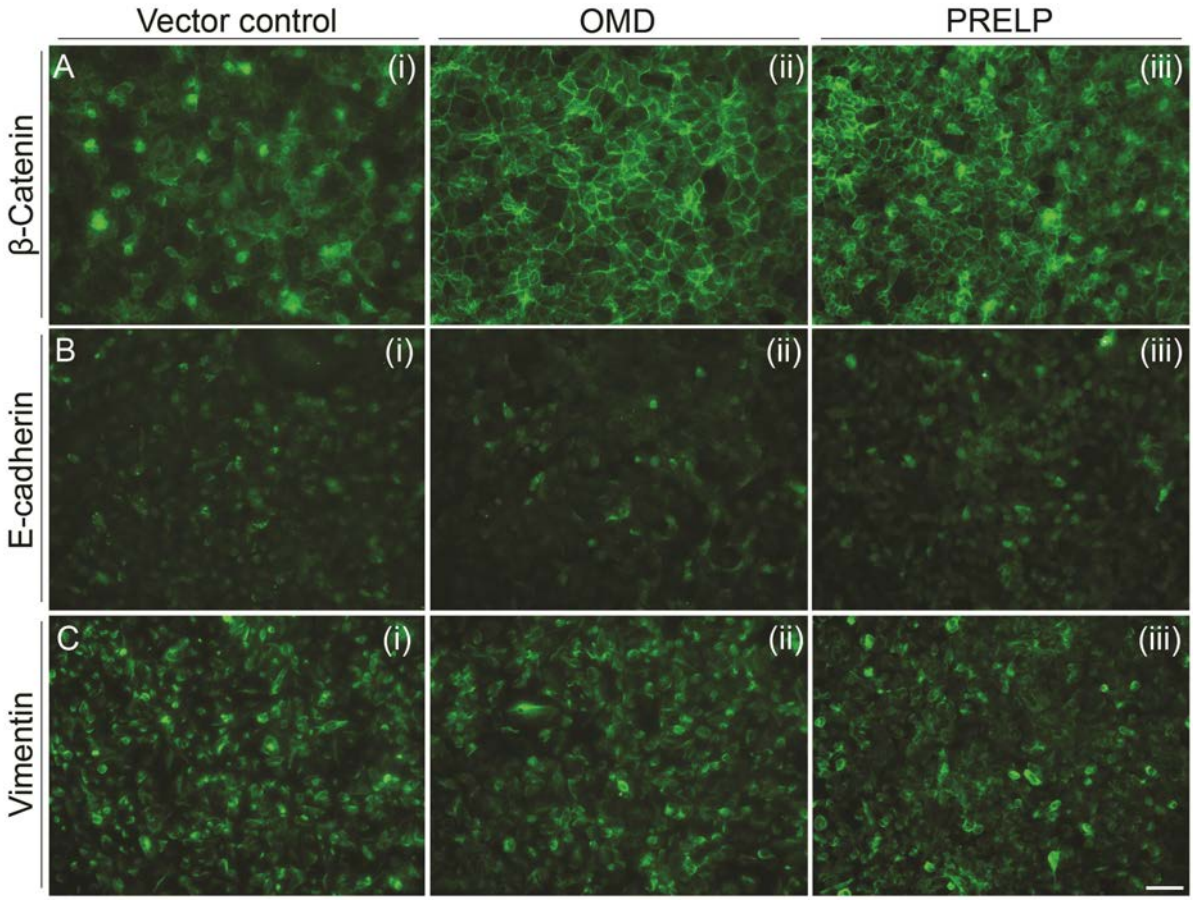

Figure 3.12: β-Catenin, E-Cadherin and vimentin staining of EJ28 cells. EJ28-vector only, OMD and PRELP transfected cells were seeded in 8-well multi chamber glass slides (in duplicates) and after reaching confluency were cultured another 7 days, followed by fixation and staining. For all three markers, secondary alexa-488 (green) antibodies were used. (A) β-catenin staining intensity is increased in OMD/PRELP transfectants compared to vector-control cells and enhanced localisation in the plasma membrane can be observed. (B) E-cadherin and (C) vimentin staining did not show differences in the staining pattern between the different cell lines. Scale bar represents 100μm for all images.

3.2.6.2 Signalling pathways affected by OMD and PRELP

The initial analysis involving components of the affected signalling pathways in the OMD and PRELP transfected cell lines was performed by Dr. Watson, where through western blotting she examined expression of several signalling molecules including AKT/p-AKT, ERK1/2 and p-ERK1/2, c-Jun/p-c-Jun, p38 and p-p38, Smad2 and p-Smad2, β-catenin and lastly EGFR. Some of these molecules remained unaffected by OMD and PRELP over-expression, while others were affected positively or negatively in the various transfectants. The most prominent changes included inhibition of phospho-Akt, EGFR and phospho-Smad2, while β-catenin expression was increased, as we also demonstrated with immunofluorence staining in Fig. 3.12. For reference, Dr. Watson's findings are summarized below, in Table 3.1.

Table 3.1: Expression of signalling mediators in stably transfected cell lines compared to controls. - means no change in expression, one arrow indicates small difference, two arrows indicate significant difference.

	OMD	mtOMD	PRELP	mtPRELP
ERK1/2	-	-	-	-
p-ERK1/2	-	-	-	-
Akt	-	-	-	-
p-Akt	↓↓	↓↓	↓↓	↓↓
c-Jun	↑	↑	-	-
p-c-Jun	-	↓	-	↓
p38	-	-	↑	-
p-p38	↑↑	↑↑	↑	↑
EGFR	↓↓	↓↓	↓	↓
b-Catenin	↑↑	↑↑	↑↑	-
Smad2	-	-	-	-
p-Smad2	↓↓	↓↓	↓↓	↓↓

Since our purpose was not to replicate all the previous findings, but at the same time wanted to establish a more conclusive mechanism of action, we chose to further complement only few of the involved pathways using the EJ28 OMD over-expressing cell line. Therefore the EGF pathway was examined, and in addition the IGF pathway was chosen as well, since both molecules are involved in the downstream signalling of other SLRP family members (Iozzo et al., 2011; Santra et al., 2002).

More specifically, together with Dr. Tamura, we performed ligand-induced activation of EGFR and IGF1R and examined their downstream targets p-Akt and p-ERK1/2. As shown in Figure 3.13A, addition of EGF (ligand) resulted in phosphorylation of the receptor (EGFR) in both the WT and OMD over-expressing cells. However, this phosphorylation was reduced in the OMD samples, indicating that somehow OMD inhibits normal activation of the receptor. Moreover, while p-Akt levels are generally decreased in the OMD cells under normal conditions (as Dr. Watson also established), under EGF ligand induction, although increased, p-Akt still remains inhibited compared to the control. In addition, phosphorylation of ERK1/2, which is downstream of the Ras component of the pathway, was strongly activated by EGF. This phosphorylation was slightly suppressed by OMD, in both absence and presence of exogenous EGF ligand. Following that, an immunoprecipitation assay was performed by Dr. Tamura in order to investigate any possible physical interaction between the OMD protein and the EGF receptor. Since we did not have a good antibody against OMD, for this experiment the mtOMD cell line was used, as through the myc-tag the OMD protein could be strongly bound by anti-myc binding beads and subsequently detected in western blotting. Shown in Figure 3.13B is the blot from the co-IP, demonstrating that indeed OMD interacts with the EGFR. Given that the EGFR total protein level is also reduced in the OMD transfectants (around 2/3 reduction compared to the WT, unpublished data by Dr. Watson), we can conclude that OMD acts through direct inhibition of the EFG pathway, affecting both the receptor as well some of the downstream components.

The same experimental approach was also employed for the IGF-1 pathway, where addition of the IGF-1 (the ligand) phosphorylated the receptor (IGF-1R), as expected (Fig. 3.13C). However, this time IGF-1 mediated phosphorylation of the IGF-1R was not inhibited by OMD overexpression. In addition, IGF-1 application strongly activated downstream phosphorylation of Akt, which again was not further inhibited by OMD. Also, p-ERK1/2 levels increased only slightly upon ligand activation of the receptor and they did not differ between OMD transfectants and WT control samples. Lastly, co-IP did not reveal any interactions between mtOMD protein and the IGF-1 receptor, suggesting that there is no profound or direct effect of the OMD protein with this signalling cascade (Fig. 3.13D).

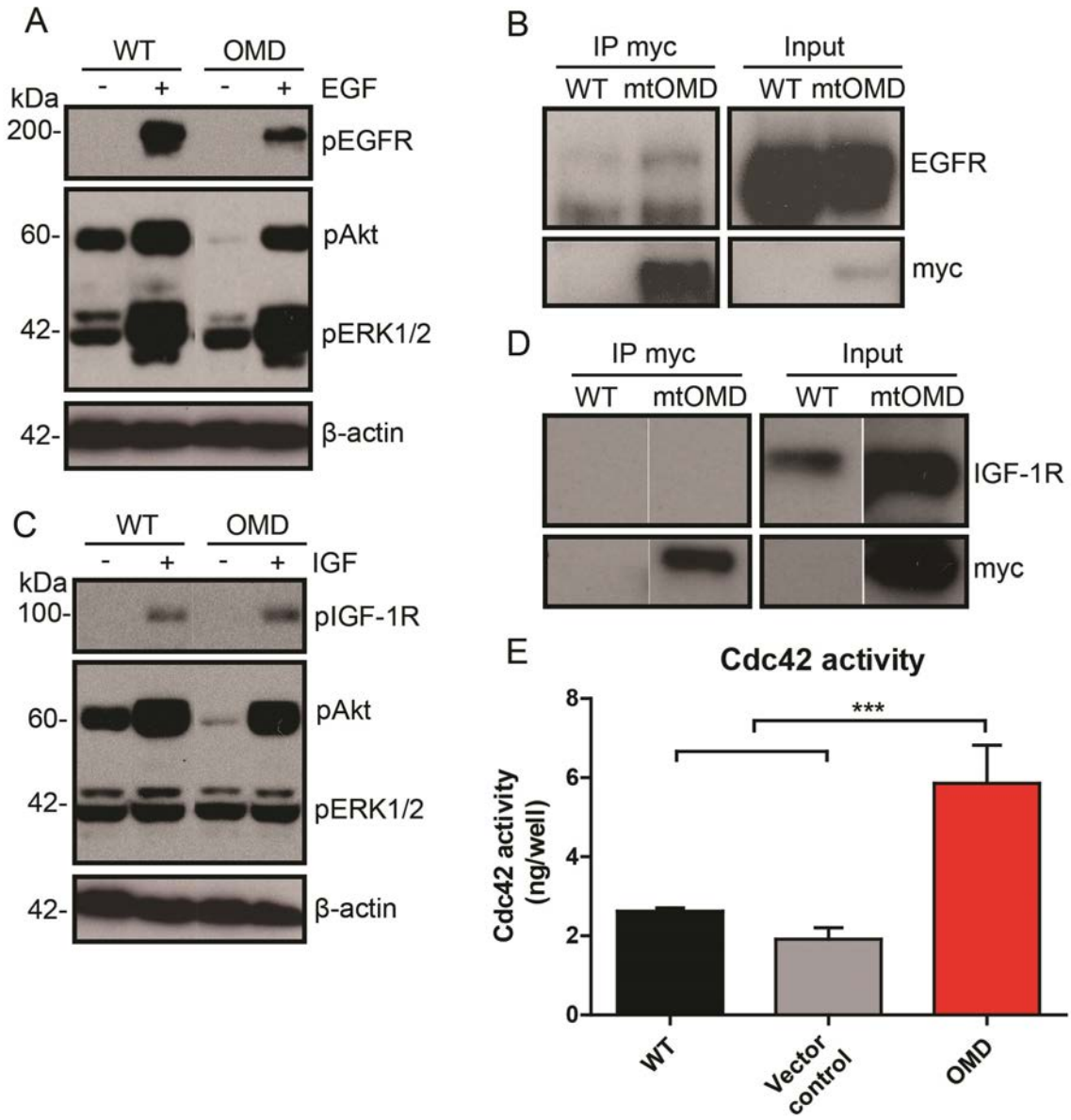

Figure 3.13: EGF and IGF signalling analysis of EJ28 OMD overexpressing cells. (A) Activation of the EGF pathway via addition of EGF ligand (10ng/ml). EGF-mediated phosphorylation of tyrosin-1068 of EGF receptor (EGFR) was strongly suppressed by OMD expression. Downstream phosphorylation of Akt and ERK1/2 is lower in OMD overexpressing samples compared to WT controls. (B) Protein binding assay showing interaction of mtOMD with EGFR. (C) Activation of IGF pathway via addition of IGF ligand (10ng/ml). Phosphorylation of the IGF receptor (IGF-1R) is not affected by OMD overexpression. (D) Co-IP showing no interaction between mtOMD and the IGF receptor. Experiments were performed with three different biological samples (lysates). Blots from (B) and (D) are kindly provided by Dr. Tamura, who performed the co-ip experiments. (E) Effect of OMD on Cdc42 activity. EJ28 WT/Vector control and OMD-transfected cells were seeded in triplicates in a density of 1 x 10^5 cells/well after 24h cells were analysed for levels of active Cdc42 using a G-LISA assay kit. Data are presented as means ± SD, ***p<0.001. These data are also kindly provided by Dr. Tamura, who performed the Cdc42 activation assay.

All SLRP family members previously tested are known to directly interact with TGF-β family members and to regulate transcription of downstream targets mainly via phosphorylation of Smad2. Indeed, Smad2 phosphorylation is suppressed by OMD over-expression (Table 3.1, data acquired by Dr. Watson). In addition, β-catenin, which is a major component of the Wnt pathway, is also affected (its expression is increased, Table 3.1), and, as also shown in the previous section, localization of β-catenin to the plasma membrane is strongly activated in OMD and PRELP transfected cell lines. Furthermore, Cdc42 is known to be regulated by EGF and Wnt pathways and is also involved in the regulation of tight junction formation. Hence, it was decided to examine Cdc42 expression in the OMD transfected cells, and discovered that Cdc42 activity was strongly activated by OMD overexpression (Figure 3.13E), indicating a further connection of OMD activity with the Wnt/EGF pathways and tight junction regulation.

Finally, having established an apparent connection between OMD and the EGF, and TGF-β pathways, probably in a context dependent manner, together with Dr. Tamure we decided to examine the roles of those components in relation to tight junctions. To this end, EGF (10 ng/ml), TGF-β1 (10 ng/ml) and also IGF-1 (100 ng/ml) ligands were applied to OMD over-expressing EJ28 cells, and the effects on tight junction formation were analysed through occludin staining. Figure 3.14 demonstrates that EGF and TGF-β strongly inhibited OMD-induced tight junction formation, while IGF-1 did not affect the tight junction status, indicating that OMD-mediated modulation of EGF and TGF-β pathways is important for the sequential regulation of tight junction formation.

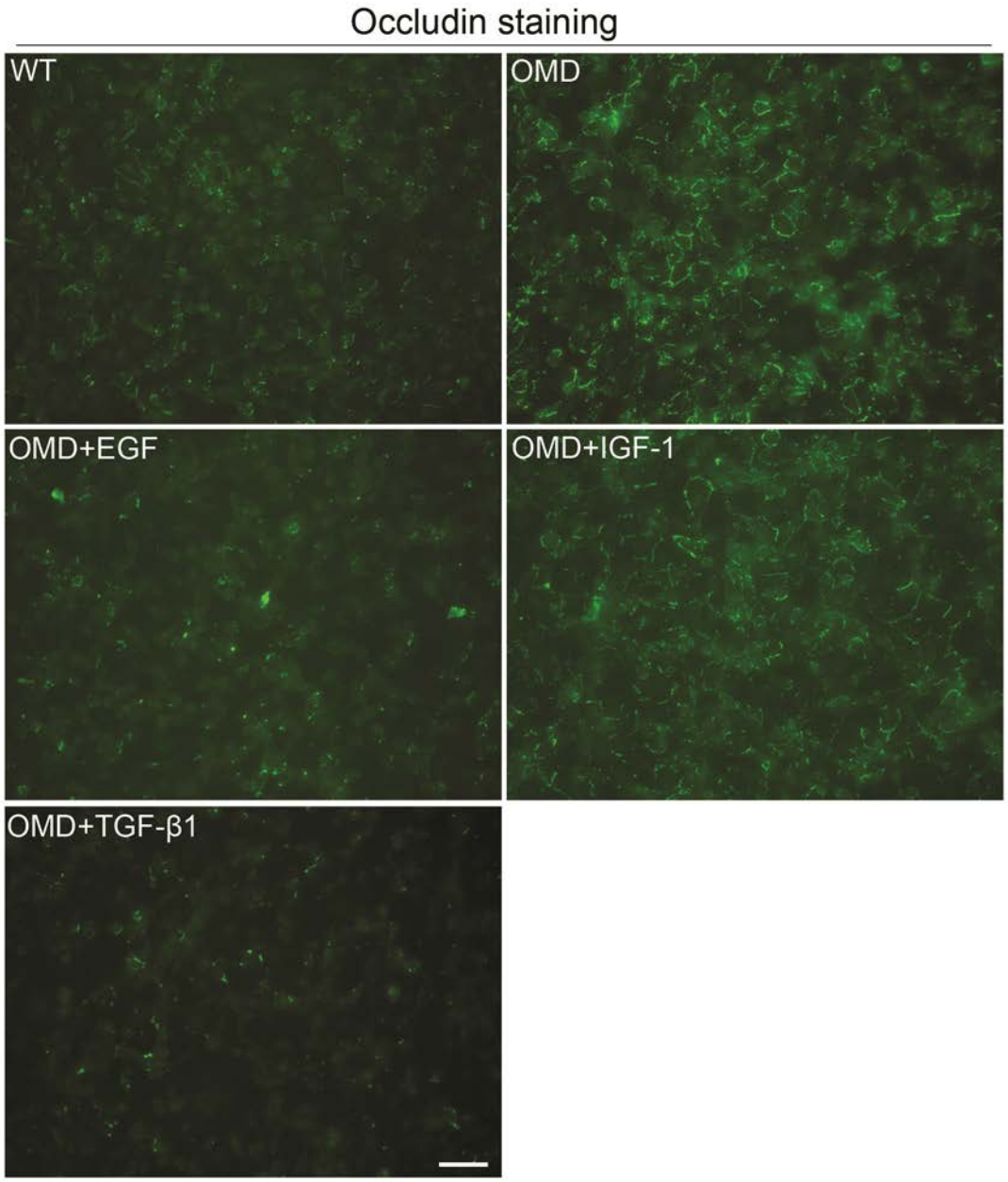

Figure 3.14: Occludin staining of EJ28 cells after addition of EGF, IGF-1 and TGF-β1 ligands. Cells were seeded on 8-well multi chamber glass slides (in duplicates) and after reaching confluency were cultured for another seven days to allow tight junction formation. Ligands were applied every other day after reaching confluency. The last day cells were fixed in ice-cold methanol and stained with a primary antibody against occludin, visualized by a secondary alexa-488 (green). OMD-induced tight junction formation was inhibited by the addition of EGF and TGF-β1. Scale bar represents 100μm for all images.

3.2.6.3 Analysis of xenograft tumours

Further analysis was performed on the xenografted tumours, where H+E staining revealed slightly different cellular contents between the wild type and OMD samples (Fig. 3.15A). Quantification of the nuclei number was conducted in 8 random areas in the centre of the tumour mass, demonstrating less nucleuses in the EJ28-OMD overexpressing tumours compared to the wild types (Fig. 3.15B, p=0.0002). In addition, the nuclear to cytoplasmic ratio was increased in the OMD samples, with a value of 36.60 ± 0.7945 versus 26.43 ± 1.535 for the WT (p<0.0001), suggesting a more organised distribution and an increased cytosolic content in the OMD cell masses (Fig. 3.15C).

Another set of the xenografted tumours was prepared for electron microcopy imaging and semi-thin sections were stained with methylene blue and basic fuchsin, thereby coloring the cells blue and the extracellular matrix pink. As presented in Figure 3.15 D&E the OMD sample has a lot more matrix between the cells in the main tumor mass compared with the wild type, suggesting a possible role of OMD in matrix deposition or maintenance in the tumor microenvironment.

Finally, the samples were examined under electron microscopy where indeed more extracellular matrix between the cells was observed in the EJ28-OMD tumour, but also more tight junctions between neighboring cells could be seen compared to the control. Two representative images are shown in Figure 3.16 A&B, where no tight junctions are present in three adjacent EJ28 wild type cells, whereas TJ have formed in the OMD over-expressing cells (arrows), further supporting our previous *in vitro* analysis. Immunofluorescence using an antibody against occludin was also attempted on snap-frozen tumors, where, although clear tight junctions between cells could not be seen, an overall higher intensity of the staining was observed in the OMD samples compared to the WT controls (Fig. 3.16 C&D).

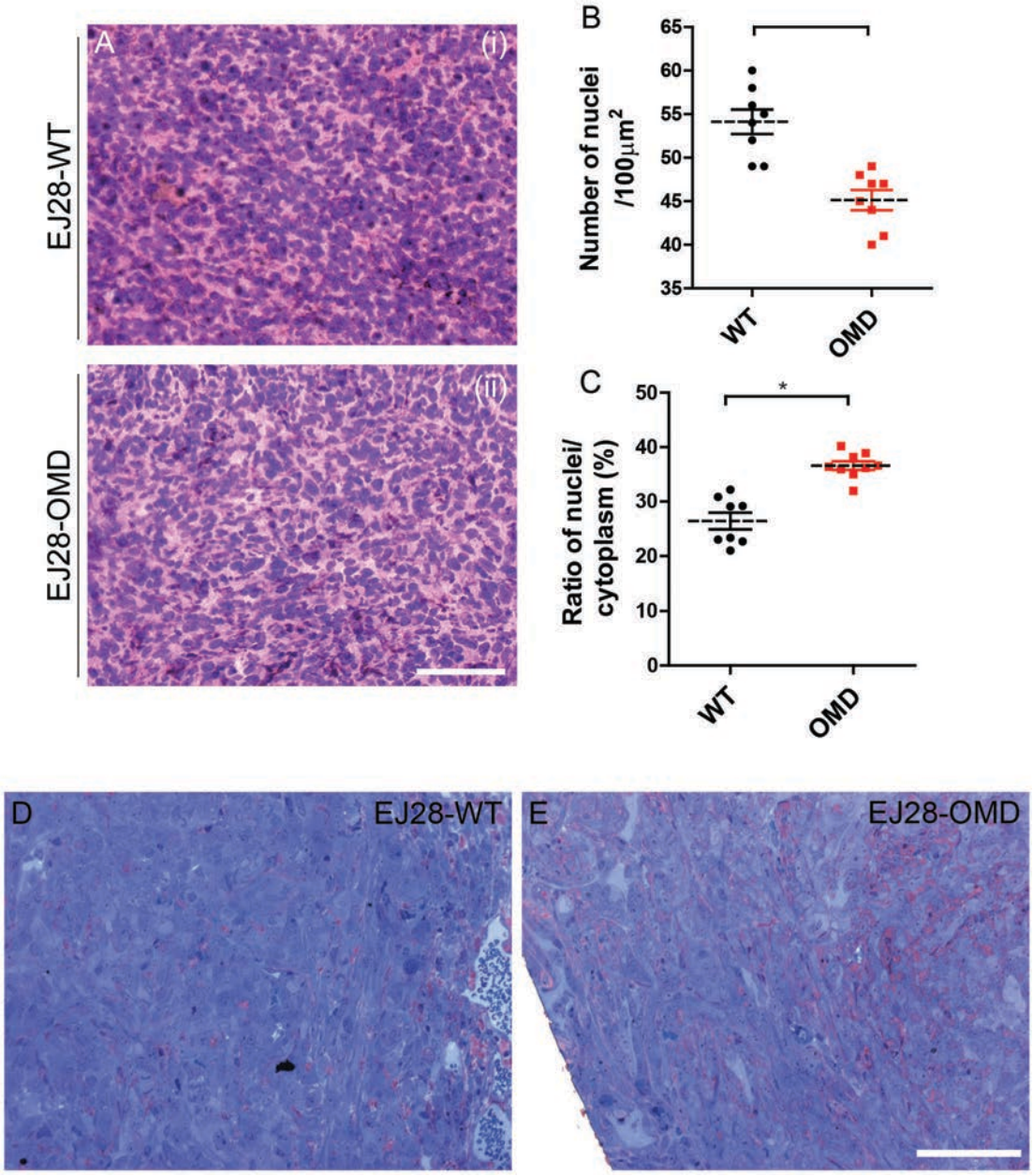

Figure 3.15: Analysis of the EJ28-WT and EJ28-OMD xenografted tumours. OMD overexpression alters the tumour cellularity. (A) H+E staining of tumour sections. (B) Quantification of the nuclei in 8 random100µm^2 areas in WT and OMD EJ28 tumour sections and (C) ratio of the nuclei/cytoplasm in the same areas. Measurements were calculated using the Image J software. Student's t-test was carried out, * equals $p<0.05$, data are presented as mean ± SEM. (D) and (E) are images of tumour semi-thin sections stained for methylene blue and basic fuchsin, staining the cells blue and the intermediate stroma pink, demonstrating more extracellular matrix in the OMD tumour compared to the wild type. Scale bars represent 100 µm in all images.

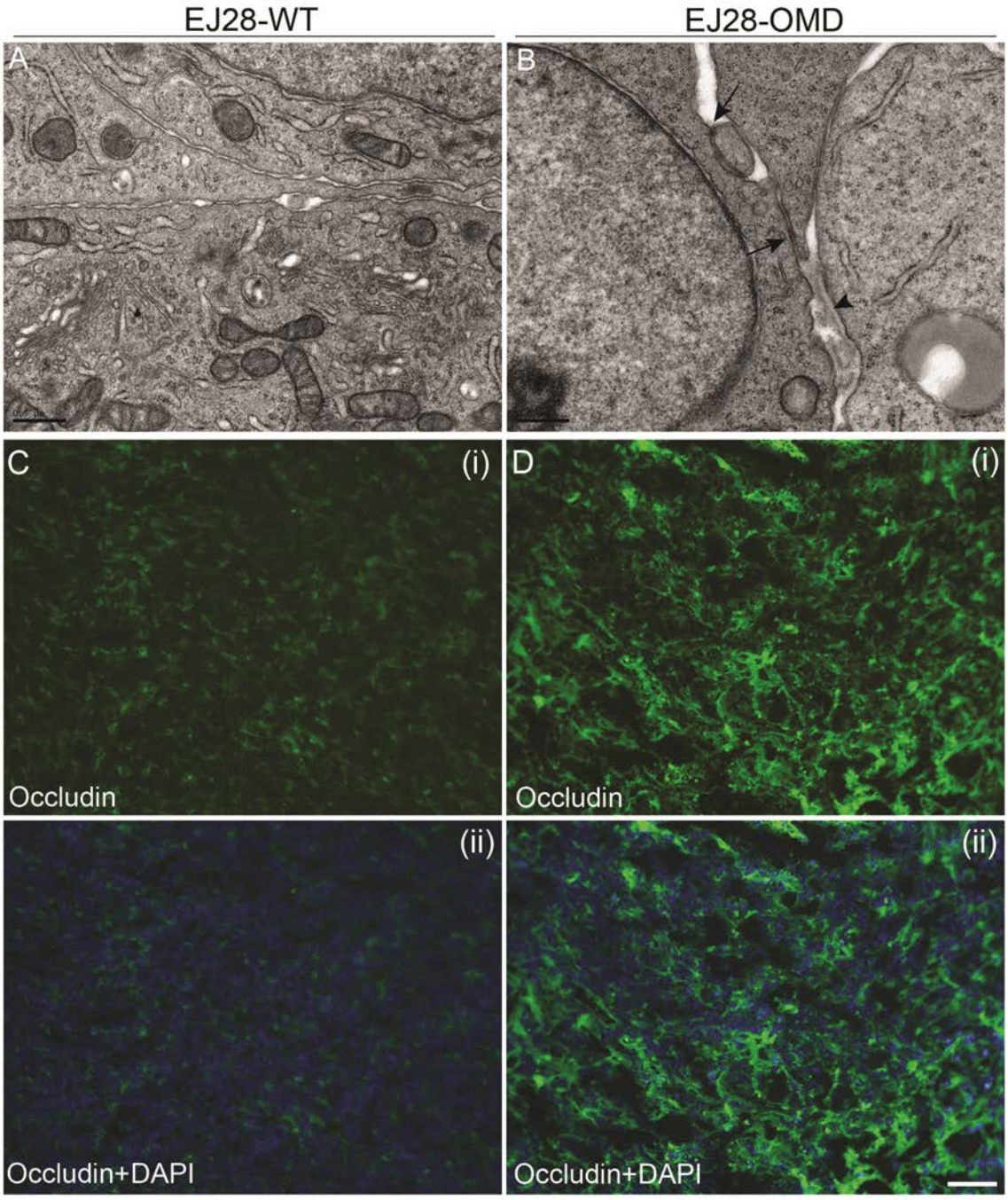

Figure 3.16: Increased occludin staining in the xenografted EJ28-OMD tumours compared to the WT. (A) & (B) Electron microscopy analysis of the xenografted tumours showing tight junction formation (arrows) in the OMD samples but not in the WT. Also more extracellular matrix can be seen between the OMD-overexpressing cells (arrowhead). (C) & (D) EJ28-WT and OMD tumours were snap-frozen and after sectioning were stained using an occludin antibody and an alexa-488 (green) secondary. Panel D(i): OMD sample demonstrates a higher staining intensity when compared to the WT tumour-panel C(i), indicating increased TJ components expression in the OMD-overexpressing cells. Scale bars represent 0.5μm in panels (A) & (B), and 100μm in panels (C) & (D).

3.2.7 Overexpression of OMD with an inducible lentivector

3.2.7.1 Choosing the right vector

As mentioned earlier, Dr. Julie Watson who worked previously on this project, showed that overexpression of OMD and PRELP in the EJ28 bladder cancer cell line inhibited cell cycle progression and proliferation, while it enhanced apoptosis. As a result, study of the overexpression effects was difficult because transfected cells had a tendency to die and/or gradually lose the plasmid expression after several passages. Indeed, all the *in vitro* assays described earlier in this chapter were performed using early passages of Dr. Watson's transfected cells lines, as in later passages expression of the two genes became undetectable. Hence, it was decided to overexpress the 2 genes with a different expression system.

We ideally wanted to have controllable expression under an inducible promoter, and thus chose the doxycycline Tet-on system, where transcription can be activated in the presence of tetracycline or doxycycline (dox) and is often preferred to the Tet-off system, as maintenance in the off state does not require chronic drug administration (Figure 3.17A). The vector we decided to use is a lentiviral gene transfer vector, as lentiviruses have now emerged as the most efficient and versatile system for permanent *in vitro*, as well as *in vivo*, gene transfer. More specifically, this vector can be characterised as an "all-in-one" vector, because it contains all the elements needed for the tet-on system, where a TRE/CMVmin promoter, composed of the tetracycline responsive element (TRE) and the minimal CMV promoter, is used for the transcription of our genes of interest. In parallel, the tetracycline transactivator protein, rtTA2S-M2, is transcribed under a human PGK promoter, while we also have the expression of the GFP marker protein under the IRES (Internal ribosome entry site) element (Fig. 3.17B). In that way, one single transfection of either our cell lines or animal model is enough for a controllable expression system, and the need for an extra transfection to provide the rtTA protein becomes abolished, which is quite important and useful for *in vivo* studies. This vector was originally engineered by Olivier Danos's group (Barde et al., 2005), and was kindly provided to us by Professor Sam Janes (UCL).

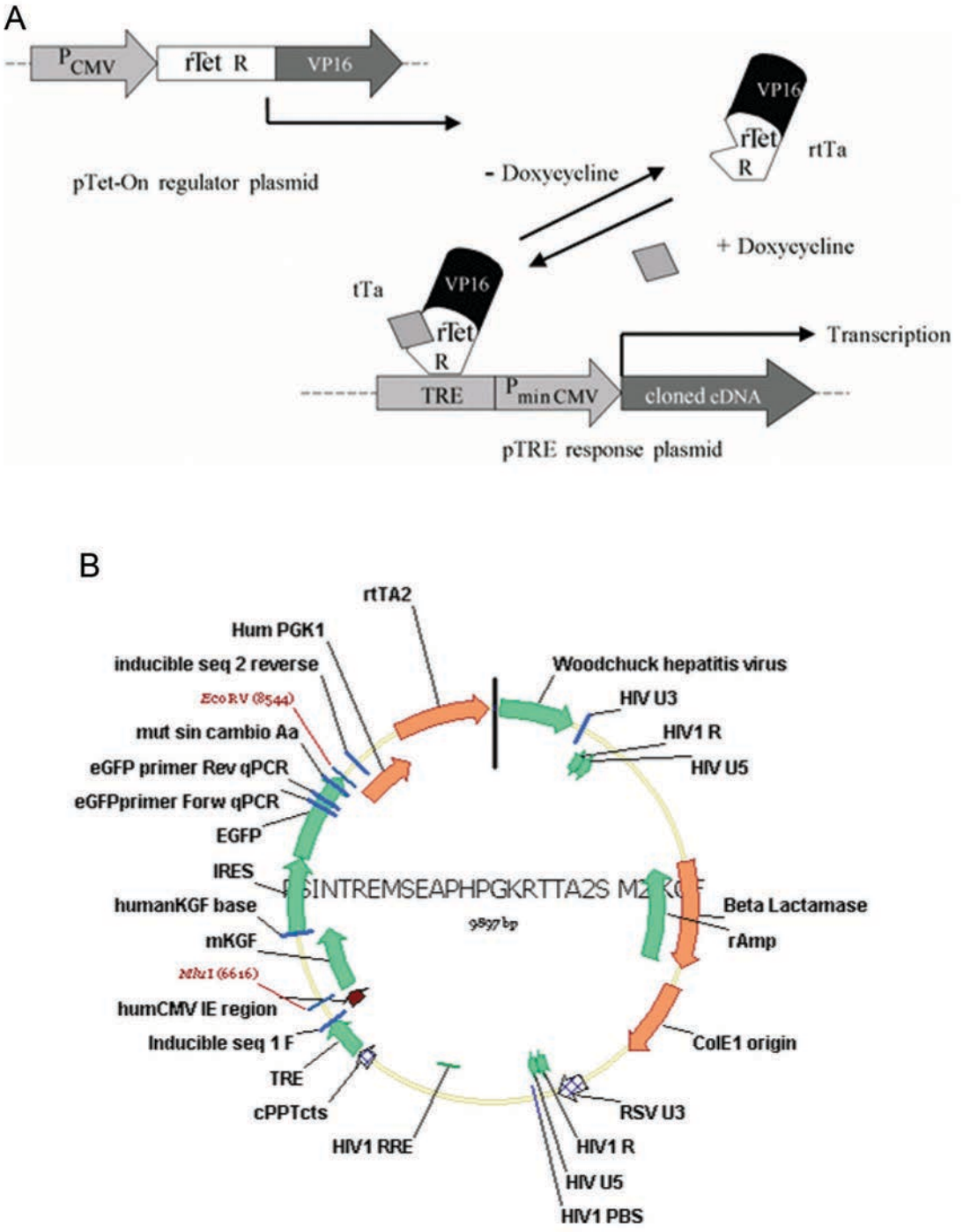

Figure 3.17: Schematic presentation of the Tet-On expression system and plasmid map of the lentivector used for overexpression of OMD and PRELP. (A) The reverse tetracycline-controlled transactivator (rtTa) is a fusion of a mutant TetR with the VP16 activator. In the absence of tetracycline, rtTa is free and transcription does not occur. When doxycycline is added to the system, it binds to rtTa which in turn binds tetracycline response elements (TRE), activating transcription of the cDNA. PminCMV = Minimum cytomegalovirus promoter. (B) Plasmid map of the inducible-promoter lentivector provided by from Prof. Sam Janes (UCL). In this case, the KGF gene (mKGF) is under the TRE (TRE/CMVmin) promoter, followed by the IRES element transcribing for the GFP (EGFP) gene. The transactivator rtTA2 is under the human PGK promoter (Hum PGK1), while some of the viral sequences are visible, like the Woodchuck Hepatitis Virus (WHP), the posttranscriptional Regulatory Element (WPRE), and also the ampicillin resistance gene (rAMP) among others. Two of the restriction sites used for cloning by Prof. James's group, utilizing the MluI and EcoRV restriction enzymes (which we will use as well), are also visible.

3.2.7.2 Cloning of OMD, mtOMD, PRELP and mtPRELP into the vector

I wanted to clone the human OMD, mtOMD, PRELP and mtPRELP cDNAs under the TRE promoter and for this purpose a triple ligation consisting of: (a) the cDNAs, (b) the IRES-EGFP fragment and (c) the vector, was conducted. Specific primers were designed to amplify the four cDNAs and the IRES-EGFP fragment so that the desired restriction sites were inserted in their 5′ and 3′ prime ends, as presented in the following table (Table 3.2). A schematic representation of the cloning strategy is also displayed in Figure 3.18A.

Table 3.2: Triple ligation fragments and restriction sites

Prime end	OMD + mtOMD cDNA	PRELP + mtPRELP cDNA	IRES-EGFP	Vector
5′	MluI	MluI	NheI	MluI
3′	NheI	NheI	EcoRV	EcoRV

PCR was successful for the 5 inserts, and after gel extraction and double restriction digestion with the appropriate enzymes (as mentioned in table 3.2), the fragments were ready for the ligation. In parallel, after restriction digestion of the lentivector with the MluI and EcoRV enzymes, the vector was separated from the KGF-IRES-EGFP sequence with gel extraction, and following treatment with alkaline phosphatase was ready for the ligation. The four triple ligations (consisting of OMD or mtOMD cDNA-IRES.EGFP-vector and PRELP or mtPRELP cDNA-IRES.EGFP-vector) were set up and left to ligate overnight, and after transformation, colony retrieval, and DNA extraction, restriction enzyme digestions were set up to confirm successful ligated clones. A representative image of a positive clone for each of OMD and PRELP inserts is shown in Figure 3.18B, demonstrating the expected band sizes (as explained in Table 3.3), while similar results were obtained also for the myc-tagged cDNAs of the two genes. After validating the insertion of our cDNAs into the lentivector, in the correct position, the samples were sent for sequencing and all sequences were confirmed to be as expected.

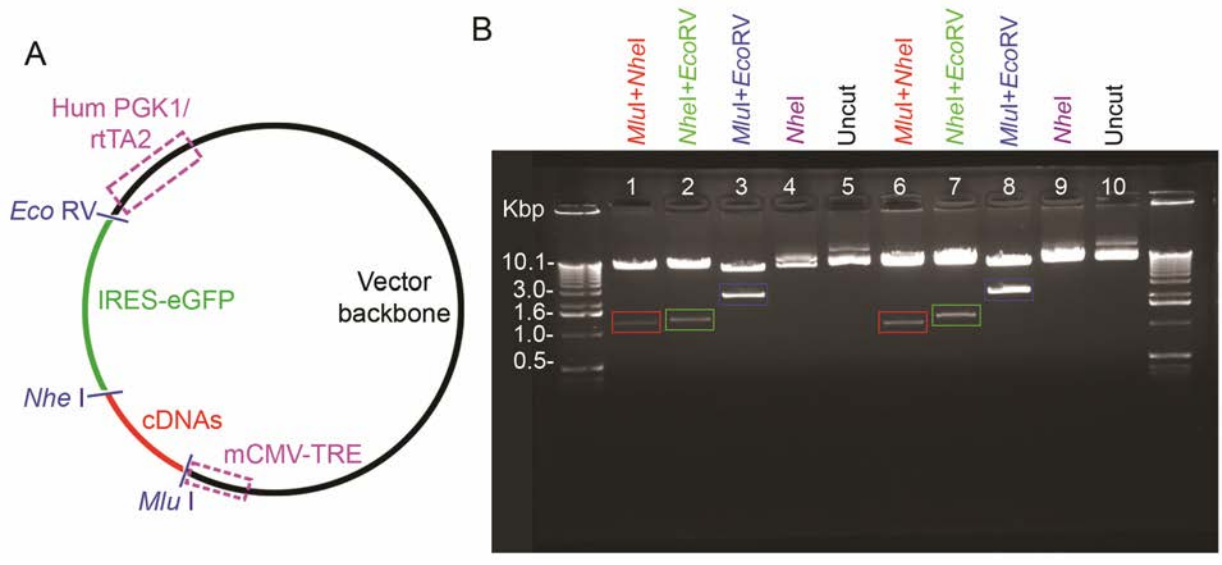

Figure 3.18: Cloning strategy for insertion of the OMD, mtOMD, PRELP and mtPRELP cDNAs into the inducible lentivector. (A) Schematic presentation of the triple ligation fragments consisting of the four different cDNAs, the IRES-eGFP fragment and the vector backbone. The position of the different cDNAs is marked with red colour, while the IRES-EGFP fragment is marked green. The restriction enzymes used for the insertion of the fragments are also visible, together with the mCMV-TRE promoter and the human PGK promoter transcribing for the tetracycline transactivator protein (HumPGK1/rtTA2). (B) Agarose gel after restriction enzyme digestion of the ligated vectors, showing successful cloning of the cDNAs into the vector, with expected insert sizes. Lanes 1-5 are for OMD-IRES.EGFP-vector ligation, and lanes 6-10 are for PRELP-IRES.EGFP-vector. Inserts are color-coded as in (A). The sizes of the expected bands and the sizes of the obtained bands are demonstrated in detail in Table 3.3

Table 3.3: Expected and obtained band sizes from restriction enzyme digestion of OMD and PRELP clones, as shown in Figure 3.18B

Restriction Enzymes	Expected bands (bp)		Obtained bands (Kbp)	
	OMD	PRELP	OMD	PRELP
MluI+NheI	1266	1149	~1.3	~1.2
NheI+EcoRV	1330	1330	~1.4	~1.4
MluI+EcoRV	2596	2479	~2.8	~2.7
NheI	10590	10473	~10.1	~10.1
Undigested	10590	10473	~10.1	~10.1

3.2.7.3 Lentiviral production and titration

Production of the lentiviruses was performed in co-operation with Prof. Sam Jane's lab, at the Rayne Building at UCL, as our lab did not have the necessary safety-level equipment for this kind of experiments. 293T cells were used as the producer cells and the standard protocol of 3-plasmid co-transfection was performed (for details see Section 2.2.2.9). Two batches of viruses were collected at day 4 and 5 of production and after ultra-centrifugation, were transferred back to our building and stored at -80°C until use. Unfortunately, due to health and safety management issues at the Rayne building, the one-week production protocol was conducted only once, and we managed to produce only two instead the five viruses we wanted. The produced lentiviruses included the control eGFP-only (TRE.minCMV-IRES.eGFP days 4&5), and the mtOMD-coding (TRE.minCMV-mtOMD-IRES.eGFP days 4&5) viruses.

In the meantime, even though only the above two viruses were produced, it was decided to use them for some *in vitro* and *in vivo* preliminary experiments, in order to confirm some of our previous results and also acquire some more information on the OMD protein. Before conducting any work on the EJ28 cell line, titration of the viruses was necessary, as it ensures viral viability and provides a measure of what fraction of target cells can be transduced, i.e. how infectious the virus is. Titration was performed by lentiviral transfection of 293T cells in several different viral dilutions and subsequent FACS analysis of the transfected cells through the reporter GFP marker, resulting in the biological titre being measured in transducing units per ml (TU/ml). An example of the cells after 3 days of transduction (2 days of doxycycline treatment) is shown in Figure 3.19, where strong expression of the GFP marker protein can be seen, demonstrating high transduction efficiency of the viruses. Also, declining GFP expression according to the different viral volumes can be observed (as expected), while slightly stronger signal can be seen in the control GFP-only transduced cells compared to the mtOMD (Fig. 3.19 A vs. B). Finally, after FACS analysis of the transduced cells viral titres were calculated, ranging from 4.45×10^6 TU/ml to 8.5×10^6 TU/ml, as shown in detail in Table 3.4. This range of biological titre is considered low for direct *in vivo* applications, but is sufficient for *in vitro* cell line transductions, which comprises my primary aim.

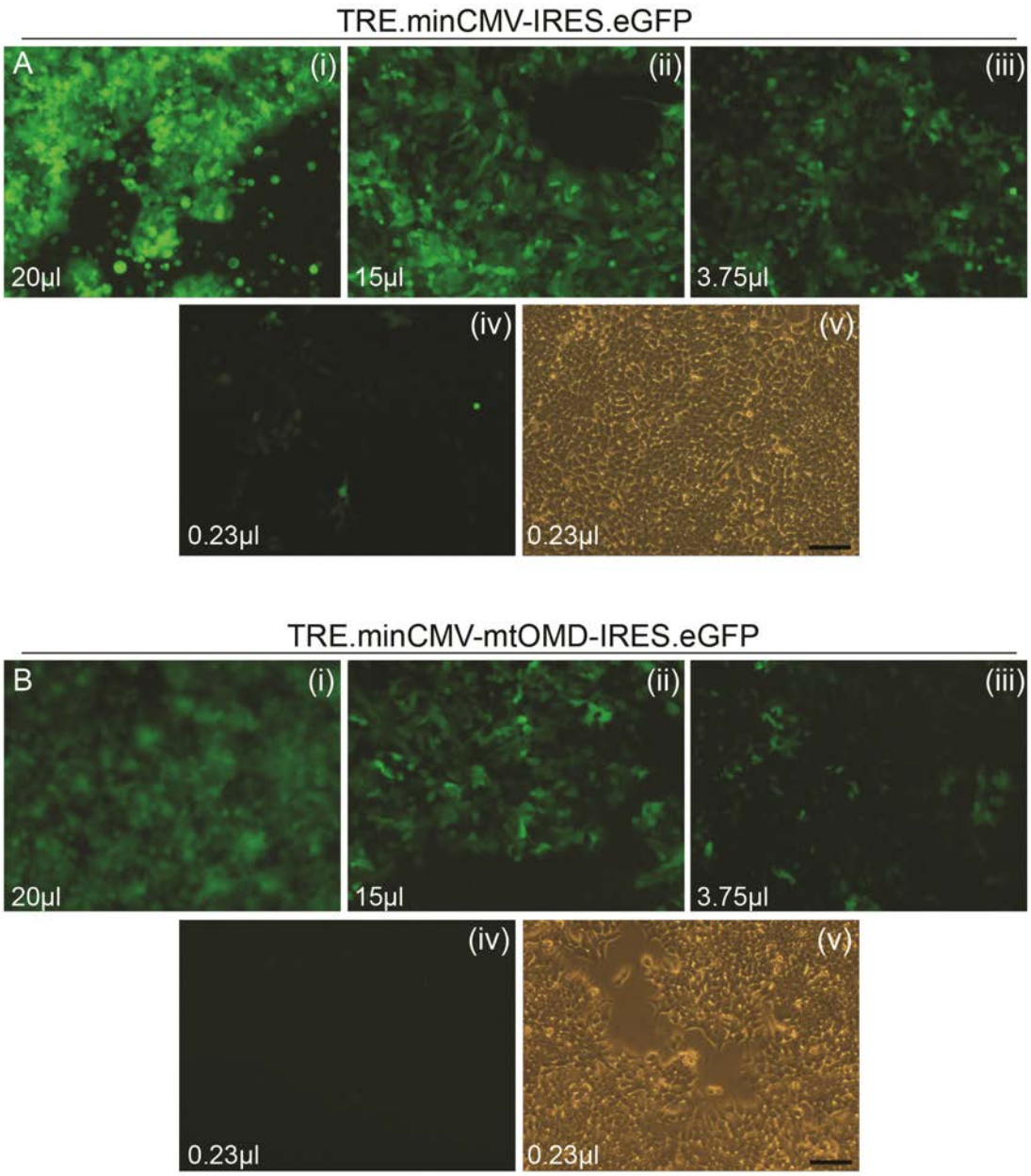

Figure 3.19: Viral titration of the control-GFP and mtOMD lentiviruses, through transduction of HEK293T cells. HEK293T cells were infected with several different dilutions of lentiviruses and after two days of doxycycline induction strong GFP fluorescence can be seen, indicating successful viral transduction. (A) (i)-(iv) Fluorescent images of 293T cells transduced with the TRE.minCMV-IRES.eGFP virus showing declining GFP intensity according to the different viral volumes that were used, i.e. 20µl, 15µl, 3.75µl, and 0.23 µl, while (v) shows a bright field image of panel (iv). (B), the same as (A) but for the TRE.minCMV-mtOMD-IRES.eGFP virus. Scale bars represent 50µl for all images.

Table 3.4: Viral titres of the two lentiviruses after HEK293T cell transduction

Viral preparations	Titer (TU/ml)
TRE.minCMV-IRES.eGFP day 4	5.1×10^6
TRE.minCMV-IRES.eGFP day 5	8.5×10^6
TRE.minCMV-mtOMD-IRES.eGFP day 4	4.45×10^6
TRE.minCMV-mtOMD-IRES.eGFP day 5	5.2×10^6

3.2.7.4 Lentiviral transfection of the EJ28 cell line

After lentiviral production and titration, EJ28 cells were transfected with the 2 viruses (collected at day 4) at an MOI of 5, and after doxycycline treatment GFP-positive cells were isolated by FACS sorting. Initially, real-time PCR was performed to confirm overexpression of the OMD cDNA in the TRE.minCMV-mtOMD-IRES.eGFP transfected cells (written onwards as TRE-mtOMD), against EJ28 wild type cells and TRE.minCMV-IRES.eGFP control cells (written as TRE-GFP). In both cases OMD mRNA transcripts of TRE-mtOMD cells after doxycycline treatment (+dox) were considerably higher than the control, with the fold difference reaching around 30-40 thousand, confirming strong overexpression (Fig. 3.20A). However, increased OMD mRNA expression was also seen in the transfected but not induced (-dox) samples, of about 5000-fold difference, indicating quite high background transcription under the TRE-minCMV promoter.

Confirmation of the OMD overexpression was also performed through protein detection using a primary antibody against the myc-tag, which usually provides strong and specific signal. Cell lysates were taken at 3h, 6h and 24h post doxycycline addition and representative western blots from all three different time points can be seen in Figure 3.20B, demonstrating strong induction of the mtOMD transcript even at 3h, with the signal getting stronger in the following hours. The same results were obtained even after 48 or 72 hour post transduction, replicated through different biological samples. In addition, four bands are always observed, with the strongest at 75kDa, the middle around 55kDa and two smaller bands around 45kDa, with the latter probably representing the core OMD protein and the rest different post-translational modifications. These bands are not present in the TRE-GFP or WT

control samples, suggesting that they are specific for the mtOMD protein. Furthermore, faint bands at 75kDa are also visible at the TRE-OMD (-dox) samples, representing background transcription without doxycycline induction, confirming the real-time PCR data (arrowheads). Detection of the GFP protein in TRE-GFP both +dox and –dox samples also implies background transcription without induction. Overall, expression of the mtOMD protein through the lentiviral transfections is quite high under induction of the inducible promoter, accompanied by medium background expression indicating a degree of leakage in this inducible system.

Given the fact that OMD is an extracellular-matrix protein, we also wanted to test the cell medium for secreted levels of OMD since detection of the myc-tagged protein in cell lysates under the inducible system is very strong. Plain media without any FBS was collected after 72h of doxycycline induction from TRE-mtOMD, TRE-GFP and WT cell culture wells. The different media were additionally concentrated with TCA treatment or through protein-specific filter centrifugations and were afterwards applied to SDS-PAGE electrophoresis. Presented in Figure 3.21 is a representative blot, showing strong expression of the myc-tagged protein in the media of the TRE-mtOMD samples indicating high levels of OMD secretion, with or without the addition of doxycycline. Although, there is a small size difference in the bands between these two conditions, this is due to the concentration of the samples and the accumulation of high levels of protein in very small volumes, which do not run equally through the acrylamide gel. For instance, looking at the TCA-concentrated bands, very strong expression can be seen in the dox treated sample-media, with the lower edges of the band being at 75kDa, which is the same size as the –dox sample and also the bigger band seen at the TRE-mtOMD lysates (which are included in the blot, acting as positive control). More importantly, only one band is observed in the cell medium as opposed to the 4 bands of the cell lysates, suggesting that the 75kDa variant of the protein is the one with the final post-translational modifications and is subsequently secreted outside the cell. Finally, these results were replicated with three different biological samples and concentration of the medium with TCA was more effective, always producing stronger bands than the filter-processed samples. The positive signal seen in the non-induced samples can be attributed to the background expression of the vector, as explained earlier.

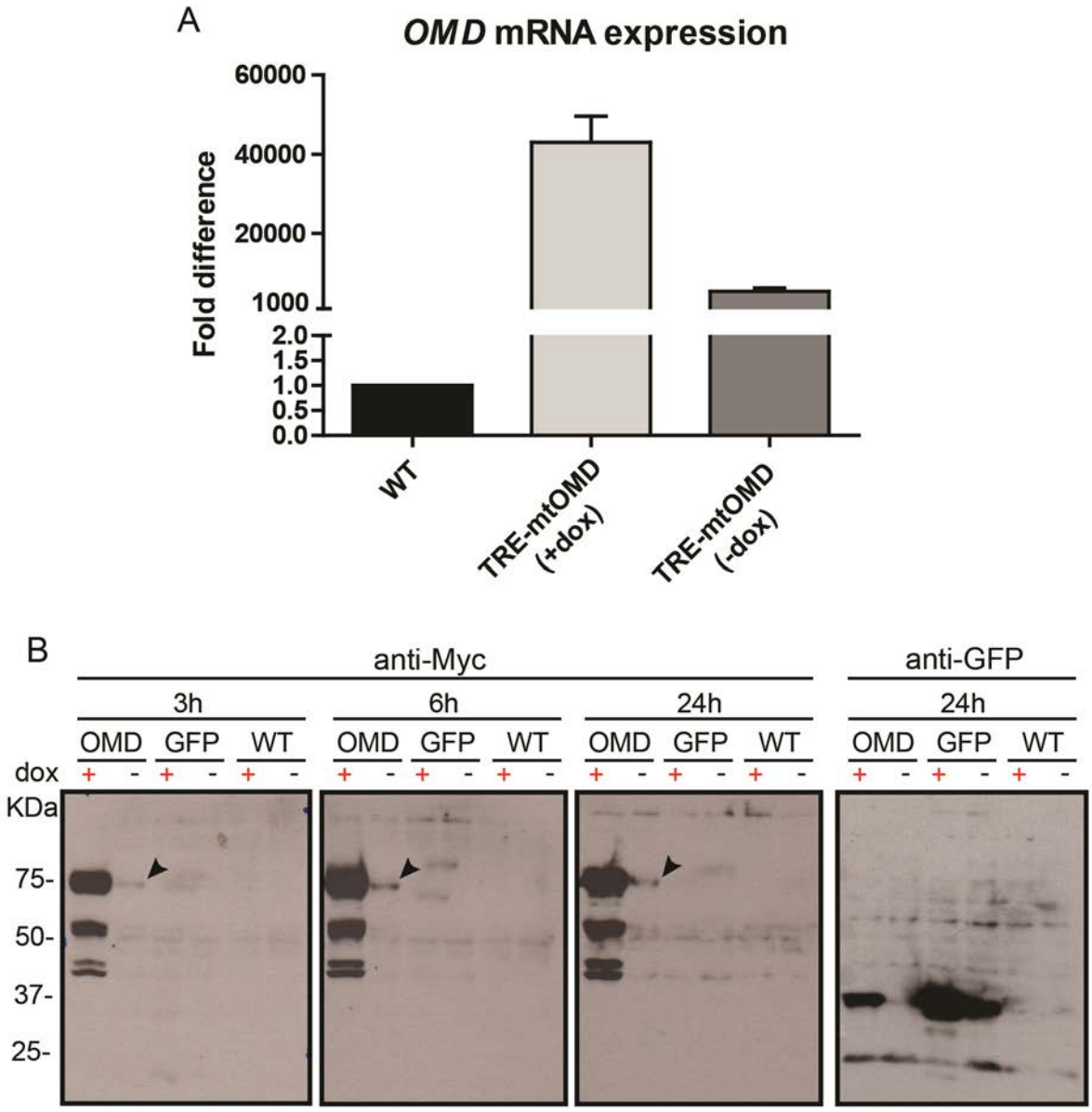

Figure 3.20: Confirmation of mtOMD overexpression in TRE-mtOMD EJ28 cells after induction with doxycycline. (A) qRT-PCR of EJ28-WT and TRE-mtOMD transfected cells showing successful overexpression of mtOMD. Increased quantity of mtOMD transcripts is also seen in the non-induced (-dox) transfected samples, displaying high background expression. Analysis was performed using the Pfaffle method and values were normalised to endogenous GAPDH expression levels. Results are presented as fold-difference compared to EJ28-WT cells which is set to 1, while the same results are obtained when compared with the control TRE-GFP transfected cells. Error bars refer to standard deviation (SD). (B) Western blot of EJ28-WT/TRE-mtOMD/TRE-GFP cell lysates demonstrating expression of the mtOMD protein at 3h, 6h and 24h after doxycycline induction. In the right panel GFP expression can be also seen after induction. Arrowheads indicate background expression in the absence of dox. The bands around 40kDa probably represent the core protein, while the other bands correspond to post-translational modifications. Experiments were performed thrice with different biological samples (RNA or lysates).

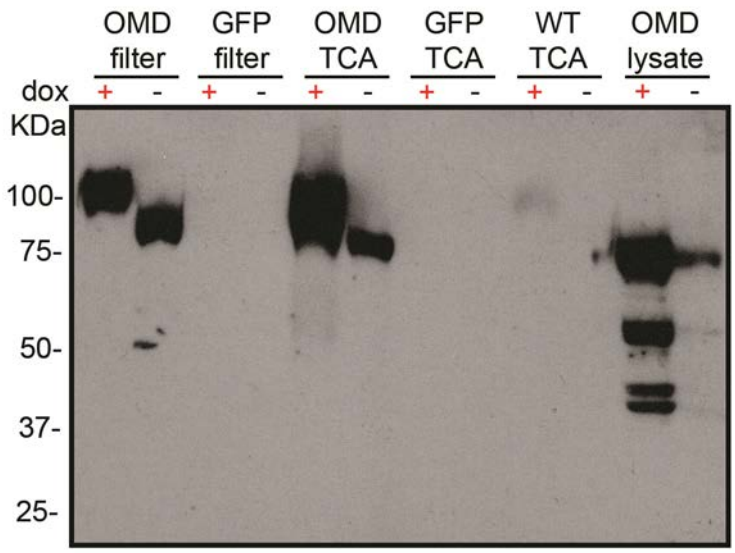

Figure 3.21: Secretion of the mtOMD protein in the extracellular space. Western blot of concentrated media collected from EJ28-WT/TRE-mtOMD/TRE-GFP cell cultures after 48h of doxycycline induction, using anti anti-myc primary antibody. Concentration was performed with TCA and protein-specific filter centrifugations. The last two lanes on the left represent TRE-mtOMD cell lysates (after 6h of dox induction), acting as a positive control for the myc signal.

3.2.7.5 Detection of mtOMD through IF

Immunofluorescence staining was performed using antibodies against the myc-tag and the GFP, in order to visualise the mtOMD protein in the EJ28 transfected cells. TRE-mtOMD, TRE-GFP and WT cells were fixed and stained after 42h of doxycycline induction and representative images are shown in Figure 3.22 & 3.23. In detail, strong myc staining was always visible outside and around the cell nuclei, often in "spotty" formations. Looking closer to high magnification images (Fig. 3.22 B&C), it can be speculated that mtOMD signal may be localised in the endoplasmic reticulum, and especially the rough ER, whose membranes are continuous with the outer membrane of the nuclear envelope, indicating OMD protein synthesis. In addition, signal might be also localised in the Golgi apparatus and in vesicles either travelling between the ER and Golgi, or in preparation for secretion outside the cell. Since the Golgi system plays a key role in the production of GAG chains forming the final form of proteoglycans, it can be hypothesized that the myc signal observed in these cells represents different forms of the OMD protein relative to the degree of post-translational modifications that have occurred. These may also correspond to the four different bands seen at western blots of lysates from the same cells.

In contrast to the western blot data, no myc positive signal was seen in the TRE-mtOMD non-induced cells, while moderate background GFP signal was observed in the TRE-GFP (-dox) samples (Fig. 3.22 D and 3.23 B). In addition, no staining against myc was seen in the WT or TRE-GFP induced samples, confirming the specificity of the antibody staining. Finally, even though transfected cells were FACS-sorted through GFP expression, we can observe that even after dox induction not all present cells are GFP positive, suggesting a possible mixture of successfully transfected and not-transfected cells in the culture.

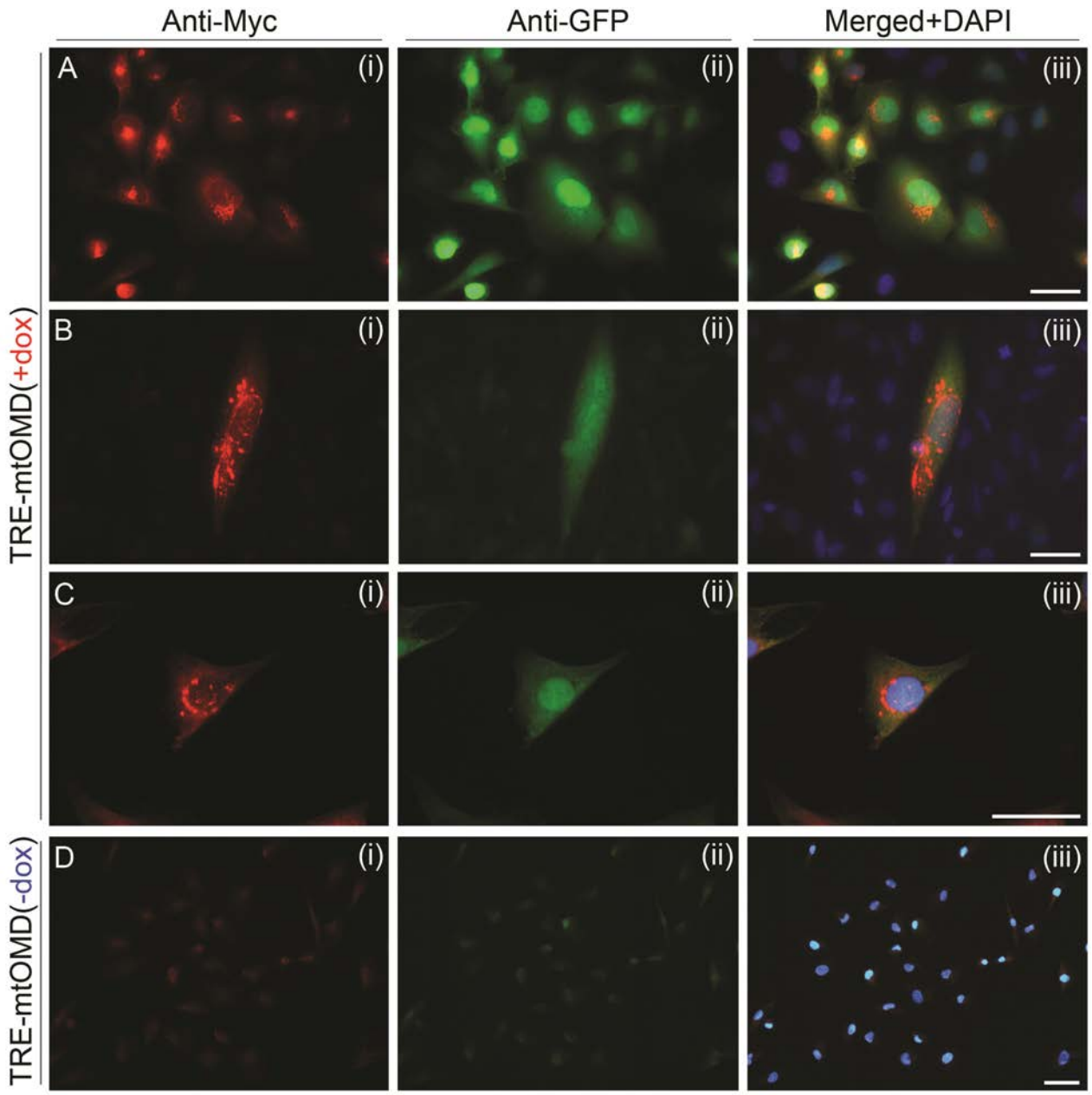

Figure 3.22: Expression and localisation of mtOMD in EJ28 cells (part one). EJ28 TRE-mtOMD cells were seeded on cover-slips in 6-well plates and after 48hours of doxycycline induction were fixed and stained with anti-myc and anti-GFP primary antibodies. Secondary alexa-546 (red) was used to visualise the myc signal-panels (i) and alexa-488 (green) was used for GFP-panels (ii), while panels (iii) show the merged images with the addition of DAPI as nuclear staining. Images (A), (B) & (C) represent dox-induced samples showing strong staining for both myc and GFP, where mtOMD signal is always seen outside and around the cell nuclei. Panel (D) shows non-induced transfected cells, demonstrating minor background staining. Scale bars represent 50μm.

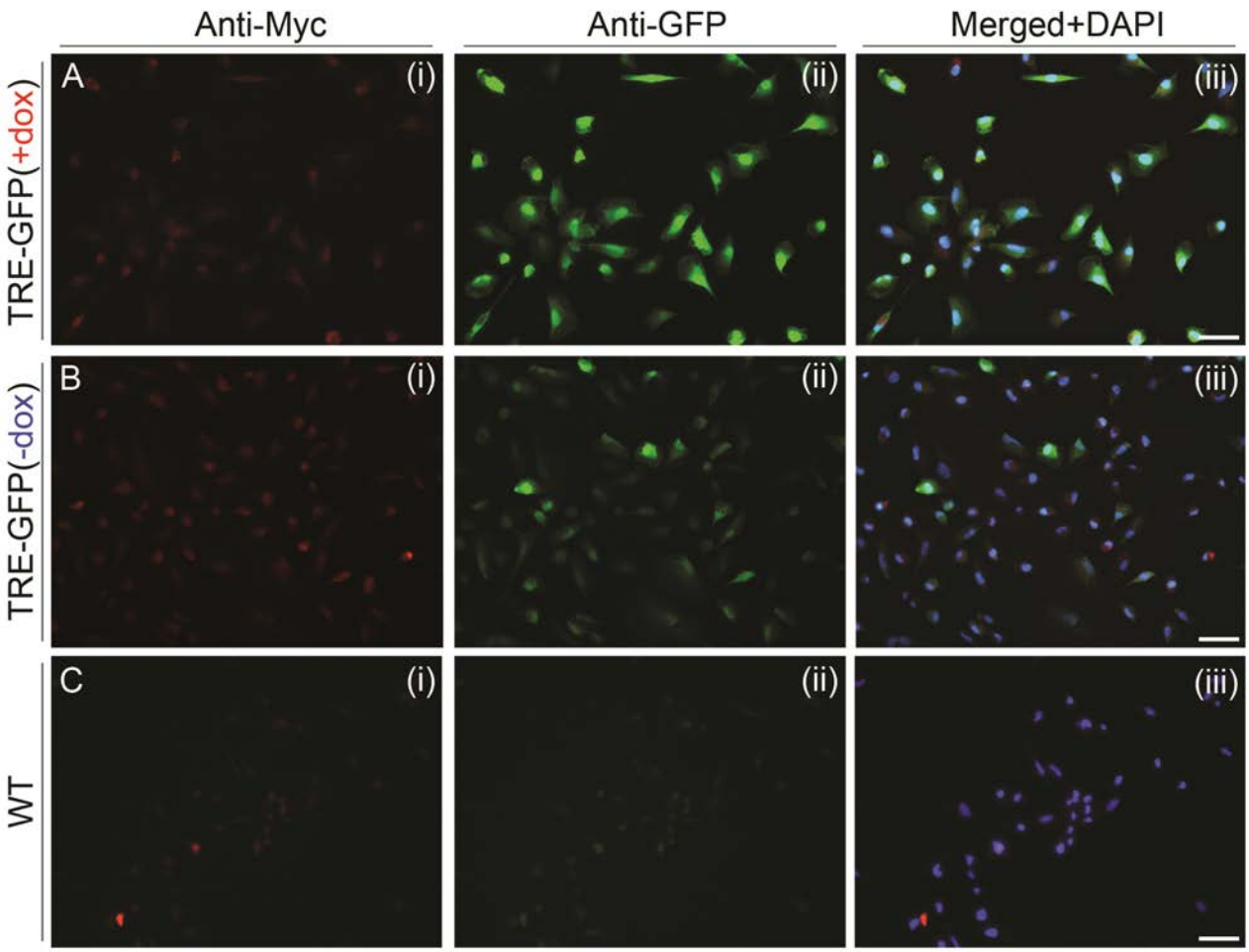

Figure 3.23: Expression and localisation of mtOMD in EJ28 cells (part two). Continuing from Figure 3.22, the control EJ28 TRE-GFP and WT samples are presented here. Only minor background myc signal is seen in both control cell lines, showing the specificity of the staining in the induced TRE-mtOMD samples. All TRE-GFP cells are positive for GFP after dox induction, while moderate GFP signal can be also seen in the (-dox) non-induced samples-panel B(ii), demonstrating background expression under the TRE promoter. Scale bars represent 50μm.

3.2.7.6 EJ28 anchorage-independent growth under doxycycline induction

The soft agar assay was performed again, as previously described, including now EJ28-WT, TRE-mtOMD and TRE-GFP transfected cells, which were also FACS-sorted in order to have a more uniform population of positively transfected cells. Doxycycline was added to the medium of both the bottom and top gel layers, as well as in the media covering the gels, which was replaced twice a week. The experiment was performed twice, in triplicates for each different cell group and as presented in Figure 3.24 the results were variable. Initially, our control TRE-GFP transfected cells did not behave similarly to the wild type cells, forming less than half the colonies observed in the WT samples. More specifically, TRE-GFP (-dox) had 377.7 ± 82.53 vs. 769.8 ± 73.78 for the WT, indicating a possible functional problem with the transfected cells. Addition of doxycycline further inhibited colony formation, even though induction of GFP alone should not have this kind of effect. Therefore, we concluded that lentiviral transfection, conducted at least under the current circumstances, must have had additional unexpected effects on the cells.

Low number of colonies was observed as well in the TRE-mtOMD ±dox samples, but due to the control irregularities we cannot know if this results from the OMD protein overexpression. If indeed, inhibition of colony formation was due to the mtOMD protein (over-expression of the protein was doubly-confirmed), then the same effect seen in the –dox samples can be attributed to the background expression without induction (as seen in the western blot analysis).

Furthermore, in this assay non-sorted transfected cells were included as well (named ns.TRE-mtOMD), in order to discriminate the potential anti-tumour effects between a mixture of non/over-expressing cells and a pure population expressing the mtOMD protein. We did notice a small reduction in the colony number in the ns.TRE-mtOMD induced cells versus the non-induced, which could be due to the further increased over-expression of the protein under doxycycline treatment. However, more prominent was the difference between the sorted and non-sorted samples, suggesting that having pure populations of expressing cells is important for the anti-cancerous effect mediated by the mtOMD protein.

Because of the control problems mentioned above, the data arising from this assay were not considered conclusive, and hence no statistical comparisons were made. Moreover, since we had already confirmed the effects of OMD/PRELP overexpression using Dr. Watson's stably transfected cell lines and due to time limitations, no more *in vitro* assays were performed using the inducible EJ28 cells.

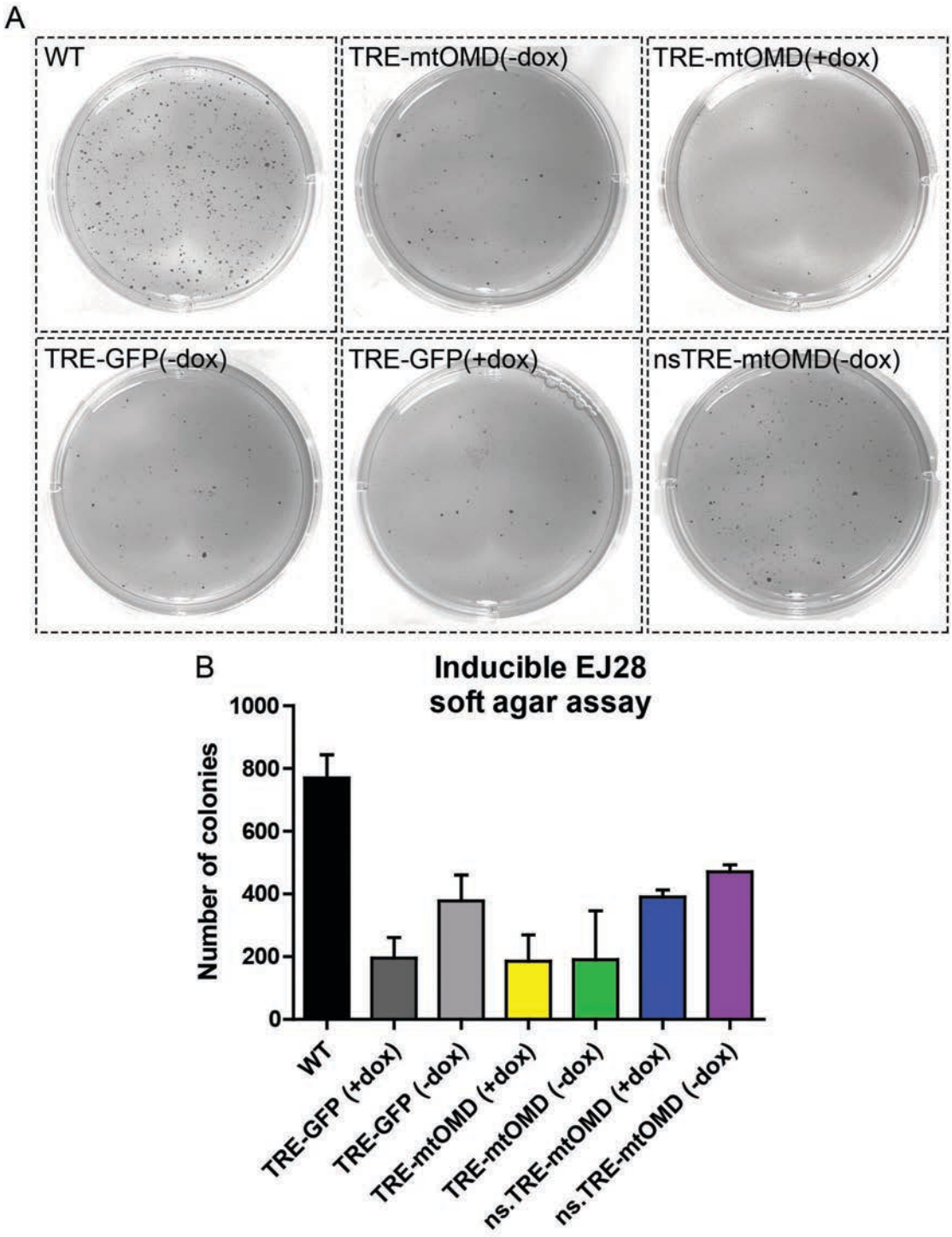

Figure 3.24: Anchorage independent growth assay of the lentiviral transfected EJ28 cells. (A) Representative images of colonies that grew in soft agar. Although TRE-mtOMD cells inhibited the formation of colonies, the control TRE-GFP transfected cells did not respond similarly to the WT cells, having much fewer colonies. However, the non-sorted TRE-mtOMD cells (ns.TRE-mtOMD) did present with more colonies than the sorted cell lines, indicating the importance of having a pure population overexpressing OMD. (B) Quantification of formed colonies per well (962mm^2). Data are presented as mean ± SD. No statistical analysis was conducted due to the control TRE-GFP abnormal cell behaviour.

3.3 Discussion

The small leucine-rich proteoglycans (SLRPs) are emerging as important regulators of extracellular matrix structure and of several signalling pathways, and their mutation or aberrant expression can cause developmental disorders and diseases, including cancer. Already, there is an emerging body of evidence suggesting that SLRPs are involved in carcinogenesis, including altered expression patterns in resected tumours compared to normal tissue, utility of decorin and lumican as predictive biomarkers in breast cancer, enhanced susceptibility of the decorin knockout mouse to cancer and several lines of functional evidence from *in vitro* and *in vivo* models.

Previous lab members, including Dr. R. Hamamoto, Dr, T. Toshiya and Dr. J. Watson had found, by RT-PCR, that expression of two SLRPs, *OMD* and *PRELP*, is greatly reduced in urothelial cell carcinoma and renal cell carcinoma compared to normal tissue. Based on these initial findings, Dr. Watson studied these two proteins in the EJ28 bladder cancer cell line, where she found that overexpression of OMD and PRELP leads to inhibition of cell cycle progression/proliferation, while at the same time it enhances apoptosis and drug susceptibility. These conclusions lead us to hypothesize that *OMD* and *PRELP* act as tumour suppressor genes and are able to affect tumour development and progression.

Indeed, together with Dr. Toshiya Tamura, we managed to show that OMD and PRELP exert certain anti-tumour effects on cells derived from human bladder cancer, and can also inhibit tumour growth *in vivo*. Furthermore, we carried out functional analysis and discovered that one of the ways OMD and PRELP act is through regulation of tight junction formation. In addition, we demonstrated that OMD interacts with the endothelial growth factor receptor (EGFR), therefore affecting downstream components of the pathway and further modulating cell behaviour.

Anti-cancer effects of OMD and PRELP on the EJ28 bladder cancer cell line and in *in vivo* mouse xenografts

The *in vitro* experimental analysis that was conducted during this project demonstrated that OMD and PRELP regulate cell functions that are essentially related to the "hallmark" characteristics of cancer cells, as specified by Hanahan and

Weinberg (Hanahan and Weinberg, 2011). More specifically, overexpression of OMD and PRELP in EJ28 cells inhibited anchorage independent growth (Fig. 3.2), led to altered 3D cell morphology when cultured in a matrix medium (Fig. 3.3) and OMD additionally inhibited cell invasiveness through a matrix-coated porous membrane (Fig. 3.4). Inhibition of anchorage-independent growth has previously been reported with other SLRPs, like lumican and decorin. For instance, stable expression of lumican induced a 6-fold reduction in anchorage-independent growth of melanoma and breast cancer cells, and also reduced the invasive potential of these cells (Li et al., 2004; Vuillermoz et al., 2004). The same effect was seen when decorin was overexpressed in colon cancer cells, whereas addition of decorin protein in mammary carcinoma cells also inhibited colony formation in soft agar (Goldoni et al., 2008; Santra et al., 1995). Moreover, we demonstrated that secreted OMD and PRELP proteins decrease EJ28 cell viability (Fig. 3.5). In the same context, addition of biglycan inhibited proliferation of J82 bladder cancer cells (Niedworok et al., 2013), while overexpression of decorin reduced the proliferation index of RT4 and T24 human bladder cancer cell lines (Sainio et al., 2013). Therefore, there is very strong evidence that SLRP molecules, now including OMD and PRELP, can act as tumour suppressors.

One thing we should mention here is the clonal nature of the different cell lines we used for this part of the project. As mentioned in the results section, Dr. Watson had isolated two different clones of each OMD, mtOMD, PRELP, mtPRELP and control vector-EGFP overexpressing cells through limiting dilution and after antibiotic selection. When creating stable transfected cell lines it is preferable to select more than one clones and test if the effects of overexpression (in our case) are reproducible between the different clones, and also if the levels of expression are comparable. In this way, we can be sure that the results we obtain are valid and are indeed due to OMD/PRELP overexpression and not due to an adverse insertion site that could alter the general properties of the cells.

Dr. Watson indeed obtained comparable results between the different clones she generated, demonstrating the true effects of OMD/PRELP overexpression. In agreement with this, we also got similar results in the experiments where both clones of each overexpressing cDNA were used. Additionally, the observed effects were

also usually similar between the tagged and non-tagged versions of the overexpressed proteins, further enhancing the validity of our results. Occasionally, small differences were seen in some of the *in vitro* experiments, such as the formed colonies between the OMD and mtOMD cells in the soft agar assay (Fig. 3.2), implying that the tag might have a small impact in the overexpression effects, under certain circumstances. However, we did not see any other differences in the assays we performed that included both tagged and non-tagged versions of the proteins. Therefore, we can confirm that OMD and PRELP can truly enhance and promote anti-tumor properties of the EJ28 cells.

Previous studies have shown that overexpression of decorin or injection of recombinant decorin protein into mouse xenograft models slows the growth of lung, squamous, mammary and colon carcinoma cells and also in some cases can prevent metastasis of the primary tumour (Buraschi et al., 2010; Goldoni et al., 2008; Reed et al., 2002; Reed et al., 2005; Tralhao et al., 2003). In addition, overexpression of lumican blocked melanoma invasion and metastasis, and also induced tumour cell apoptosis (Brezillon et al., 2009). In this project we show for the first time that OMD and PRELP can have similar anti-cancer effects in mouse xenograft models. The *in vitro* anti-tumour effects of OMD and PRELP were replicated in *in vivo* mouse xenografts of the EJ28 cell line (Fig. 3.6), thereby strongly confirming that OMD, and PRELP to a lesser extent, have the ability to inhibit *in vivo* tumour growth.

OMD and PRELP are regulators of tight junction formation and cancer-related signalling pathways

Microarray expression profiling analysis after overexpression or depletion of the *OMD* and *PRELP* genes was conducted by our collaborator Dr. Hamamoto, who identified many of the affected targets and the involved signalling pathways. Among those, tight junction and adherens junction pathways appear to play particularly important roles (Fig. 3.7, KEGG pathway analysis, Appendix A). Indeed, OMD and PRELP overexpression increased tight junction formation, as demonstrated by increased cell-cell membrane staining of the TJ components occludin, ZO-1 and cingulin, and also by electron microscopy of EJ28-OMD transfected cells (Fig. 3.8, 3.9, 3.10 & 3.11, the same was also observed in xenografted tumours-Fig. 3.16). A similar effect was seen regarding the adherens junctions, where increased β-catenin

expression and translocation to the membrane, due to OMD and PRELP overexpression (Fig. 3.12A), may be indicative of activation of the adherens junction pathway. However, E-cadherin signal could not be observed in cell-cell membranes in either the WT or the transfected cells (Fig. 3.13B). This could be due to faulty adherens junction formation, as a general characteristic of the EJ28 cell line, or could be attributed to defective staining procedure. Overall, it can be observed that OMD and PRELP reorganize cellular architecture (changes in cell morphology were seen by Dr. Watson) and cell-cell adhesion towards the epithelial cell type, which is characterised by well-developed junctions and an apical-baseolateral polarization.

The epithelial to mesenchymal transition (EMT) is an important feature of embryonic development and its importance in the pathogenesis of cancer and other human diseases is increasingly being recognised (Polyak and Weinberg, 2009). During EMT epithelial cells lose their junctions and polarity, and reorganize their cytoskeleton acquiring instead mesenchymal features like increased motility, invasiveness and resistance to apoptosis. This reorganization is accompanied by changes in gene expression of junctional proteins, i.e. downregulation of claudins, occludin, ZO-1 and E-cadherin, and activation of N-cadherin and vimentin (Lamouille et al., 2014). Overexpression of OMD and PRELP did not cause any changes in vimentin expression (Fig. 3.12C), therefore indicating no apparent EMT transition. On the contrary, localization of β-catenin to the cell membranes and increased expression of occludin, ZO-1 and cingulin in apical tight junctions could suggest a mesenchymal to epithelial transition (MET), the reverse process of EMT, where cells acquire a more epithelial character and are more "immune" towards a cancer phenotype.

Moreover, apart from EMT, altered expression of many TJ components has been related with cancer cells transformation and metastasis (Runkle and Mu, 2013). For example, loss of the tumour suppressor von Hipperl-Lindau (VHL) causes down-regulation of occludin and claudin-1, independent of E-cadherin, in early lesions of renal cell carcinomas (Harten et al., 2009), while decreased occludin expression is often seen in other tumour types (Tsukita et al., 2008). Therefore, regulation of tight junction is a critical step in both early tumourigenesis and in later stages during EMT

and metastasis. Regulation of TJ components by *OMD* and *PRELP* indicates their anti-tumour potential and emphasizes their roles as tumour suppressor genes.

In addition, we have managed to identify some of the critical signalling mediators that are affected by OMD and PRELP overexpression. Dr. Hamamoto's expression profiling analysis showed that mRNA levels of Akt, a key intracellular regulator in multiple signalling pathways, were significantly affected by both OMD and PRELP, and also Dr. Watson had previously shown that phosphorylation of Akt is reduced under OMD/PRELP overexpression (Table 3.1). Together with Dr. Tamura we confirmed that in non-stimulated EJ28 cells OMD overexpression reduced phosphorylation of both Akt and the critical cell proliferation mediators ERK1/2 (Fig. 3.13A). Since Akt phosphorylation is regulated by EGF and IGF pathways (Pollak, 2012; Takeuchi and Ito, 2010), we tested the effects of EGF and IGF-1 ligands on EJ28-WT and -OMD cells, and discovered that phosphorylation of the EGF receptor was reduced in the OMD cells, while no effects were seen in the IGF pathway (Fig. 3.13 A&C). Performing a co-IP assay revealed that OMD binds to the EGF, but not the IGF, receptor (Fig. 3.13 B&D).

Previously, decorin was found to directly bind the EGFR (Iozzo et al., 1999; Moscatello et al., 1998), leading to autophosphorylation, and a sustained downregulation of the receptor, as well as other EGFR-like receptors, such as ErbB4 and ErbB2 (Csordas et al., 2000; Santra et al., 2000; Santra et al., 2002). Decorin was also able to bind the IGF-IR and its ligand, thus attenuating the IGF-I-induced Akt and ERK1/2 pathways, resulting in decreased migration and invasion of bladder cancer cells (Iozzo et al., 2011). Furthermore, the TGF-β/Smad2 pathway is a common signaling target of SLRPs (Morris et al., 2007; Nikitovic et al., 2011) and significantly contributes to the inhibition of epithelial properties and activation of the epithelial-mesenchymal transition (Lui et al., 2003). Therefore, the EFG, IGF, TGF-β/Smad2 pathways and also other molecules like β-catenin, which is involved in the Wnt signaling cascade, are all targets of SLRPs in cancer signaling (presented in detail in Chapter 1).

In addition, the role of Cdc42 in epithelial cells has been of particular interest as one of its targets is the Par6–aPKC complex, a major regulator of cell polarity and TJ assembly (Iden and Collard, 2008; Lin et al., 2000; Matter and Balda, 2003).

Increased Cdc42 activity by OMD overexpression could therefore be related to its ability to regulate tight junction formation. Finally, application of EGF and TGF-β strongly inhibited OMD-induced tight junction formation (Fig. 3.14), indicating that OMD-mediated modulation of EGF and TGF-β pathways is also important for the regulation of tight junction formation.

In this context, it has already been shown that TGF-β can modulate epithelial polarity by regulation of the polarity protein Par6. More specifically, the TGF-β type I receptor (TβRI) was found to be co-localised with occludin and Par6 at tight junctions, while cell stimulation with TGF-β induced redistribution of the TGF-β type II receptor (TβRII) to the tight junctions (instead of its normal localization in puncta distributed over the cell surface) and subsequent interaction with the TβRI/Par6 complex (Barrios-Rodiles et al., 2005; Ozdamar et al., 2005). Through this interaction TβRII phosphorylates Par6 on serine 345, an event which in turn recruits the E3 ubiquitin ligase Smurf1 resulting in RhoA ubiquitination and localised degradation (Ozdamar et al., 2005). RhoA is a small GTPase protein which is responsible for stress fiber formation and for the maintenance of apico-basal polarity and junctional stability (Perez-Moreno et al., 2003), and hence, its degradation at TJs leads to the dissolution of these junctions and promotes an EMT state. Overall, these studies have shown that this Smad-independent TGF-β-induced mechanism facilitates the disassembly of tight junctions during TGF-β-mediated EMT. Another study by Kojima et al., showed that TGF-β-mediated TJ disassembly and EMT was alternatively induced by down-regulation of claudin-1 expression and the fence function (Kojima et al., 2007).

Finaly, regarding EGF, a previous study has shown that EGF-induced EGFR activation in MDCK II cells significantly inhibited claudin-2 expression while simultaneously inducing cellular redistribution and increased expression of claudin-1, -3, and -4 (Singh and Harris, 2004). Therefore, we see that EFG and especially TGF-β have multiple roles in TJ disassembly and function and any possible association of OMD with these pathways could indirectly regulate tight junction formation/function. Definitely, a more thorough investigation of the tight junction components and TJ-related signaling pathways is necessary in order to discover how OMD and PRELP can regulate TJs.

EJ28-OMD xenografted tumours have different cellularity and increased extra-cellular matrix

The strong anti-tumour effect of OMD and PRELP was observed also in *in vivo* xenograft models of the EJ28 bladder cancer cells. A preliminary analysis of the xenografted tumours revealed different cellularity in the OMD and WT tumours, where the wild type samples had more nucleuses and less cytoplasm compared to the OMD-transfected derived tumours (Fig. 3.15 A-C). Differences in tumour cellularity are observed in different stages of breast tumours, where often smaller pathological lesions present with reduced cancer-cellularity (Rajan et al., 2004). Hence, cell consistency of OMD-overexpressing samples might indicate a less proliferative and aggressive tumorigenic potential.

Finally, OMD-derived tumours had more extra-cellular stroma within the tumour mass (Fig. 3.15 D&E). This could be attributed to the mechanical properties of the OMD protein, which as an SLRP and ECM component, participates in ECM architectural organization and assembly of collagen fibrils (Lucchini et al., 2004; Tillgren et al., 2009). The architecture of tumour-associated ECM is fundamentally different from the normal tissue stroma (Clarijs et al., 2003), and OMD overexpression could be driving the on-going ECM assembly during tumorigenesis towards the latter direction. In addition, it is possible that overexpression of OMD protein can reorganize the tumour stroma in a way that makes it less sensitive to matrix metalloproteinases (MMPs) degradation. MMPs are involved in cancer progression by cleavage of the ECM, therefore releasing matrix molecules that can in turn inhibit apoptosis and enable cell invasion (Sternlicht and Werb, 2001). In tumours the tight regulation of MMPs expression and activity is lost and usually overexpression of some members, such as MMP-2 and MMP-9, correlates with poor survival and increased disseminating capability of cancer cells (Littlepage et al., 2010; Strongin, 2006). In a recent study it was shown that integrin $\alpha_v\beta_3$ expression induced up-regulation of MMP-2, resulting in prostate cancer metastasis (Dutta et al., 2014). Knowing that OMD binds $\alpha_v\beta_3$ integrin (Lucchini et al., 2004), it may be possible that osteomodulin can indirectly affect MMP expression or vice versa. Another SLRP, lumican, was shown to affect cell migration and angiogenesis via mechanisms that involve a decrease of MMP-14 expression and activity (Malinowski

et al., 2012; Niewiarowska et al., 2011). Therefore, it is highly likely that SLRPs can also affect tumour development or metastasis through modulation of MMPs. Due to time limitations, MMP status of EJ28-WT and -OMD tumours was not investigated in the current project, but it is of primary interest to explore the possible interplay between OMD/PRELP and MMPs.

Overexpression of OMD using an inducible system – findings and technical difficulties

As it was mentioned earlier in this chapter, study of the overexpression effects was not always easy because transfected cells had a tendency to die and/or gradually lose the plasmid expression after several passages. It was therefore desirable to overexpress OMD and PRELP under an inducible promoter. The doxycycline tet-on system was employed and OMD, PRELP and myc-tagged versions of the two cDNAs were successfully cloned into a lentivector, coding at the same time for an eGFP marker protein and also for the tetracycline transactivator protein, rtTA2S-M2, which is necessary for activation of the TRE promoter (Fig. 3.17, 3.18). Unfortunately, due to technical problems during the lentiviral production only the control GFP- and the mtOMD- coding viruses were produced. Nevertheless, transfection of EJ28 cells with the above viruses was conducted and expression levels of OMD transcripts were very high (Fig. 3.20). At that point, it became noticeable that the non-induced samples also showed high levels of OMD expression, indicating a moderate degree of leakage in this inducible system. This system was firstly used in CHO cells, where it was satisfying in terms of basal activity, inducibility and dox responsiveness (Barde et al., 2006). Transduction of the EJ28 cells was indeed efficient and expression of mtOMD protein was very strong after doxycycline treatment, but was always accompanied by expression in the non-induced samples (Fig. 3.20).

Even though this system did not appear to be totally controllable (not in the degree we had expected), useful information was gathered regarding the OMD protein expression. Firstly, it was confirmed that OMD can be found within the cells but also in the extracellular space, demonstrating secretion of the protein (Fig. 3.21). Also, different band sizes from cell lysates indicate presence of the core protein (~40kDa) and the modified proteoglycan after addition of the GAG side chains,

~50kDa and 75kDa, the latter of which was also the secreted form of the protein (Fig. 3.20 & 3.21). Furthermore, intracellular localization of the protein was always seen outside and around the cell nuclei, often in "spotty" formations (Fig. 3.22). During cell staining no background myc-tag or GFP signal was seen in the non-induced mtOMD cells, whereas GFP signal could be observed in the non-dox GFP-transduced control cells (Fig. 3.23), suggesting strong activation even at the tet-off state.

Lastly, anchorage independent growth of the lentiviral transduced cells was assessed, where the control-GFP cells did not correspond similarly to the wild type EJ28 cells, indicating possible functional transformation of the cells due to the lentiviral transfection. Addition of doxycycline resulted unexpectedly in even lower number of colonies, suggesting that very high GFP expression somehow could become toxic for the cells (Fig. 3.24). However, during culturing of the cells, with or without addition of dox, no cell death or phenotypic changes were seen under microscopic observation. Given the fact the control transfected cells behaved strangely in the soft agar assay, no more experiments were conducted with these cell lines. Transduction of EJ28-cells with lower multiplicities of infection would be the next step, in order to optimize the inducible system so that background expression can be minimum and at the same time viral infection cannot transform the cells and change their properties.

Chapter 4

Expression patterns of the *OMD* gene in mouse

4.1 Introduction

Osteoadherin or osteomodulin (OMD) is a leucine- and aspartic acid-rich keratan sulfate proteoglycan belonging to class II of the SLRP family. OMD was firstly isolated from the mineralized matrix of bovine bone, where it was shown that the protein is rather acidic and binds to hydroxyapatite, which was used to purify the protein (Sommarin et al., 1998; Wendel et al., 1998). Expression of OMD mRNA was detected in mature osteoblasts located in trabecular bovine bone, while northern blot analysis from various bovine tissues also confirmed expression only in bone, suggesting that OMD may be involved in mineral deposition (Sommarin et al., 1998). The same pattern was also seen in rat tissues, where OMD mRNA was detected in osteoblasts of the trabeculae, and was especially strong in the area between cartilage and bone (Shen et al., 1999). In addition, OMD was located to the mineralized bone matrix, with highest concentration again at the border between bone and cartilage, a pattern similar to that of bone sialoprotein (Ramstad et al., 2003).

A later study by Buchaille *et al*., showed for the first time expression of OMD mRNA in human odontoblasts and also in mature rat molars, specifically in odontoblasts, ameloblasts and in cells of the alveolar bone surrounding the teeth (Buchaille et al., 2000). Expression of OMD in rat and mouse developing teeth was also described in another two studies, while ultrastructural analysis demonstrated localization of OMD close to collagen fibers, indicating its role in ECM organisation (Couble et al., 2004; Petersson et al., 2003). A recent paper demonstrated that osteoadherin starts to be expressed within the alveolar bone of mouse embryos at E17 stage of development and it is later specifically localised in the growing teeth, in the predentin/dentin interface and the mineralization front, in new-born mice (Nikdin et al., 2012). In the same study, expression of OMD was examined in rat dental pulp *in vitro* cultures, where the levels of OMD expression peaked when ECM maturation and mineralization had initiated, suggesting that osteoadherin can be considered a marker for mineralizing cells such as mature odontoblasts and osteoblasts (Nikdin et al., 2012).

Thus, OMD is so far mainly linked with bone ECM, and it has been shown that OMD expression is regulated by the transcription factor Runx2, Smads and the

cytokines TGF-β1 and BMP2, all important factors for hard tissue development (Rehn et al., 2006; Tasheva et al., 2004). Moreover, overexpression of OMD in the MC3T3E1 mouse calvariae osteoblast cell line led in increased osteoblast differentiation features, while it also reduced proliferation and migration probably through affecting the EGF receptor activity (Rehn et al., 2008).

Among other members of the SLRP family, decorin, biglycan, fibromodulin and lumican have been reported to be expressed in bone and dentin, thereby regulating osteoid ECM deposition and organization (Cam et al., 1997; Gori et al., 2001; Raouf et al., 2002; Scholzen et al., 1994; Wegrowski et al., 1995). In addition, asporin, another SLRP, is involved in the regulation of chondrocyte activity mediated by TGF-β (Kizawa et al., 2005). Apart from skeletal tissues, SLRPs are differentially expressed in other organs as well. For example, lumican is expressed in mouse cornea stroma, heart, lung and kidney (Ying et al., 1997); keratocan is expressed in mouse/chick cornea and in the chick brain (Conrad and Conrad, 2003); fibromodulin has been found in the mouse adult retina (Ali et al., 2011); opticin has been found in the human and mouse eye, and specifically in the vitreous and the non-pigmented ciliary body (Ramesh et al., 2004; Takanosu et al., 2001); and lastly decorin has been also found to be expressed in the developing postnatal rat brain (Kappler et al., 1998).

There have been several engineered models of SLPR-deficient mice, involving mostly biglycan, decorin, lumican, fibromodulin and some double knock-outs (KO) of the aforementioned proteins. Most of these models exhibit phenotypes of reduced bone mass, skin fragility and abnormal collagen fibrillogenesis, while decorin-deficient mice present also with intestinal tumour formation (all SLRP-KO models are presented in detail in section 6.1). To date, no knock-out models for OMD have been established. Also, most of the studies presented earlier used *in situ* hybridization for the identification of OMD mRNA expression or custom-made antibodies against osteoadherin in order to explore protein expression patterns, focusing mainly on dental or skeletal tissues, while there has been no detailed examination of *OMD* expression during mouse development or in any adult soft tissues. A more straightforward and sensitive method for establishing *OMD*

expression, and a more extensive analysis that expands from early embryonic life to adult tissues, are therefore required.

In collaboration with Takeda Pharmaceutical Company, we have established the first OMD KO mouse model, where the coding sequence of the *OMD* gene has been replaced with a Lac-Z reporter gene so that transcription under the OMD promoter/enhancer leads to β-galactosidase expression instead of OMD. Apart from studying the effects of OMD depletion, this system provides an excellent model for analysis of expression patterns with just X-gal staining of heterozygote animals. The aim of this part of the project was therefore to examine the temporal and spatial expression of OMD during mouse embryonic development and in adult organs, before assessing any phenotypic effects due to OMD absence.

4.2 Results

OMD knock-out mice were constructed in Takeda Pharmaceutical Company. Briefly exons 2 and 3 (where the transcription domain is located) were replaced with a Lac-Z reporter gene. A detailed description of the knock-out strategy is described in section 2.2.4.1, while a simple graphic showing the *OMD* gene locus and the Lac-Z insertion site is shown in Figure 4.1A. Transgenic mice founders were received and our mouse colony was established through heterozygote-pair breeding as $OMD^{+/LacZ}$ animals were fertile and produced litters containing all three genotypes. Heterozygote and knock-out animals grew normally into adulthood and had a life-span comparable to the wild type mice, while no apparent phenotypic differences could be seen during expansion of the colony. A typical example of a genotyping set is shown in Figure 4.1B, demonstrating the different DNA bands corresponding to the three genotypes.

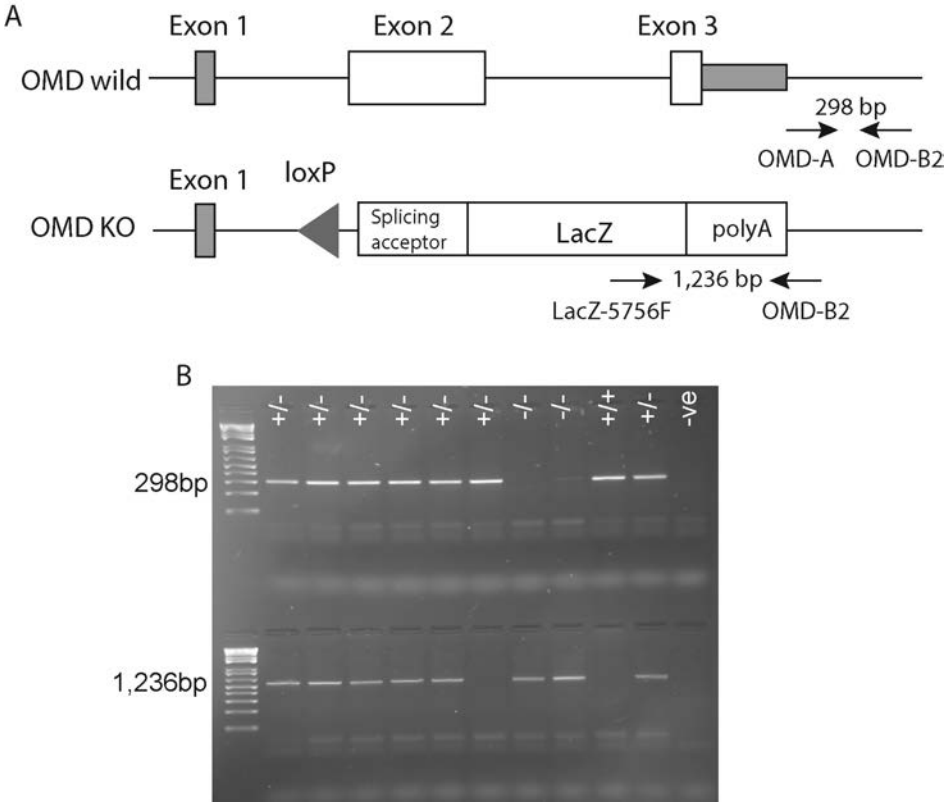

Figure 4.1: Knock-out strategy and genotyping of OMD mice. (A) Schematic drawing of the *OMD* gene locus and the Lac-Z insertion site together with the primer pairs used for genotyping. (B) An exemplar agarose gel from a genotyping set demonstrating the bands corresponding to the different genotypes.

As mentioned in the introduction of this chapter, before analyzing the effects of *OMD* depletion, the expression pattern of the gene/protein through Lac-Z detection was first studied in heterozygote animals. More specifically, *OMD* gene expression was examined in embryonic life through X-gal staining of mouse embryos at 3 developmental stages (12.5dpc, 15.5dpc and 17.5dpc) and at day of birth (P0), where it was most predominantly expressed in craniofacial and skeletal tissues. In addition, this expression pattern appeared to be expanding during adulthood, including internal organs as well, where specific areas of the brain, bladder and eye were positive for β-gal signal. Detailed analyses of the gene expression in every developmental stage and in several organs will be presented and discussed below.

4.2.1 OMD expression in E12.5 embryos

Embryos were collected at 12.5dpc after arranged time-matings and entire litters were whole-mount stained for β-galactosidase. $OMD^{+/+}$ embryos had no staining at all, while $OMD^{+/LacZ}$ and $OMD^{LacZlLacZ}$ embryos showed staining around the mouth area, and more specifically in the developing mandible and maxilla (Fig 4.2). In knock-out litter-mates staining was more intense than heterozygotes, where long-bone cartilage primordia of the forelimb and the developing somites were additionally stained for β-gal (Fig. 4.2 arrows). Also, faint staining could be seen around the brain, in the developing frontal bone.

Upon sectioning of $OMD^{+/LacZ}$ embryos β-galactosidase positive cells appeared to be confined to the mesenchyme of the developing mandible, while there was no visible staining in other areas, such as the somites, the forelimb and the developing cranium (Fig 4.3).

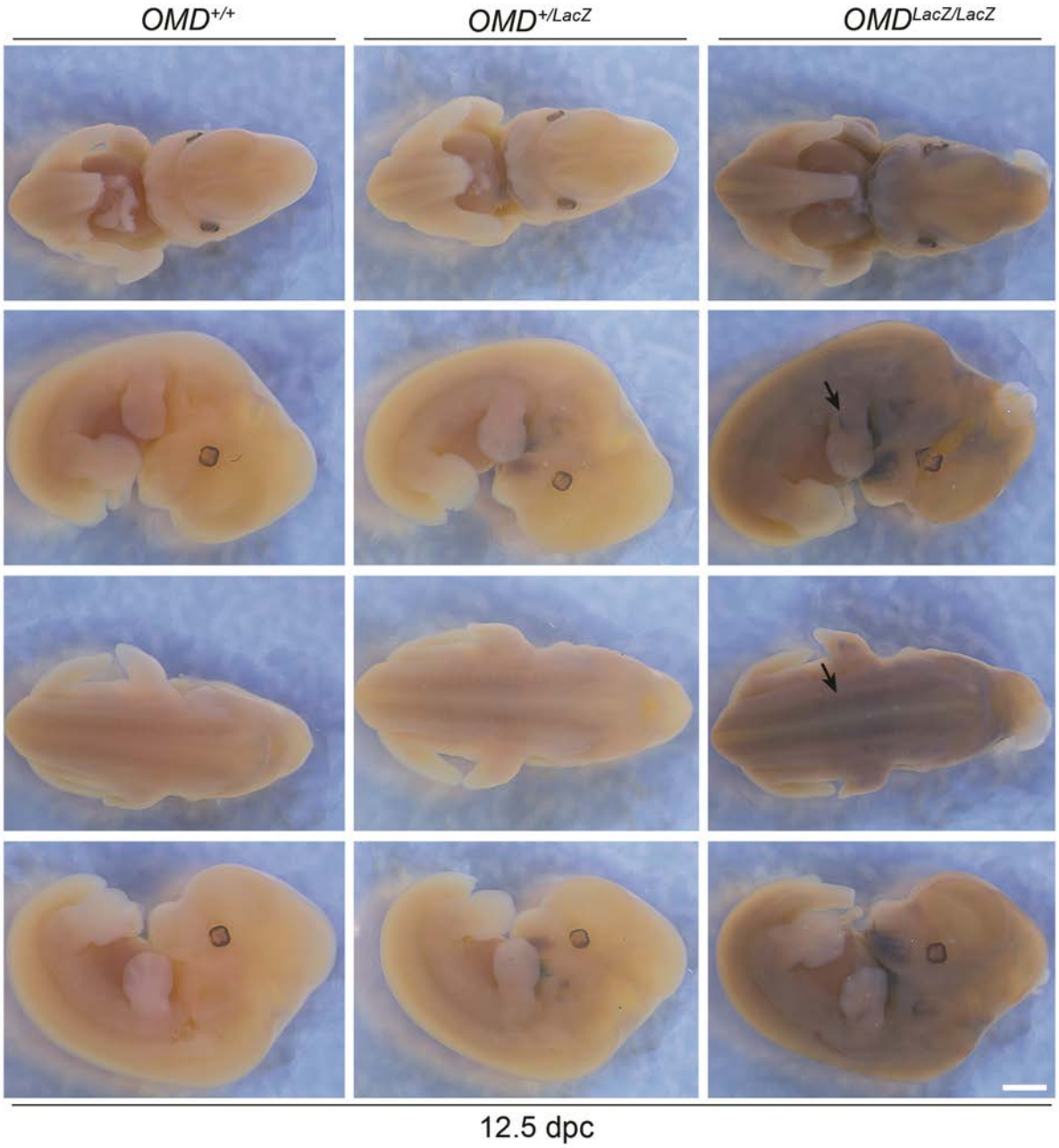

Figure 4.2: OMD expression in E12.5 transgenic embryos. X-gal signal is seen mostly in the developing mouth and maxilla, while arrows indicate expression in the developing somites and cartilage primordia of the front limbs. Scale bar, 1mm for all images.

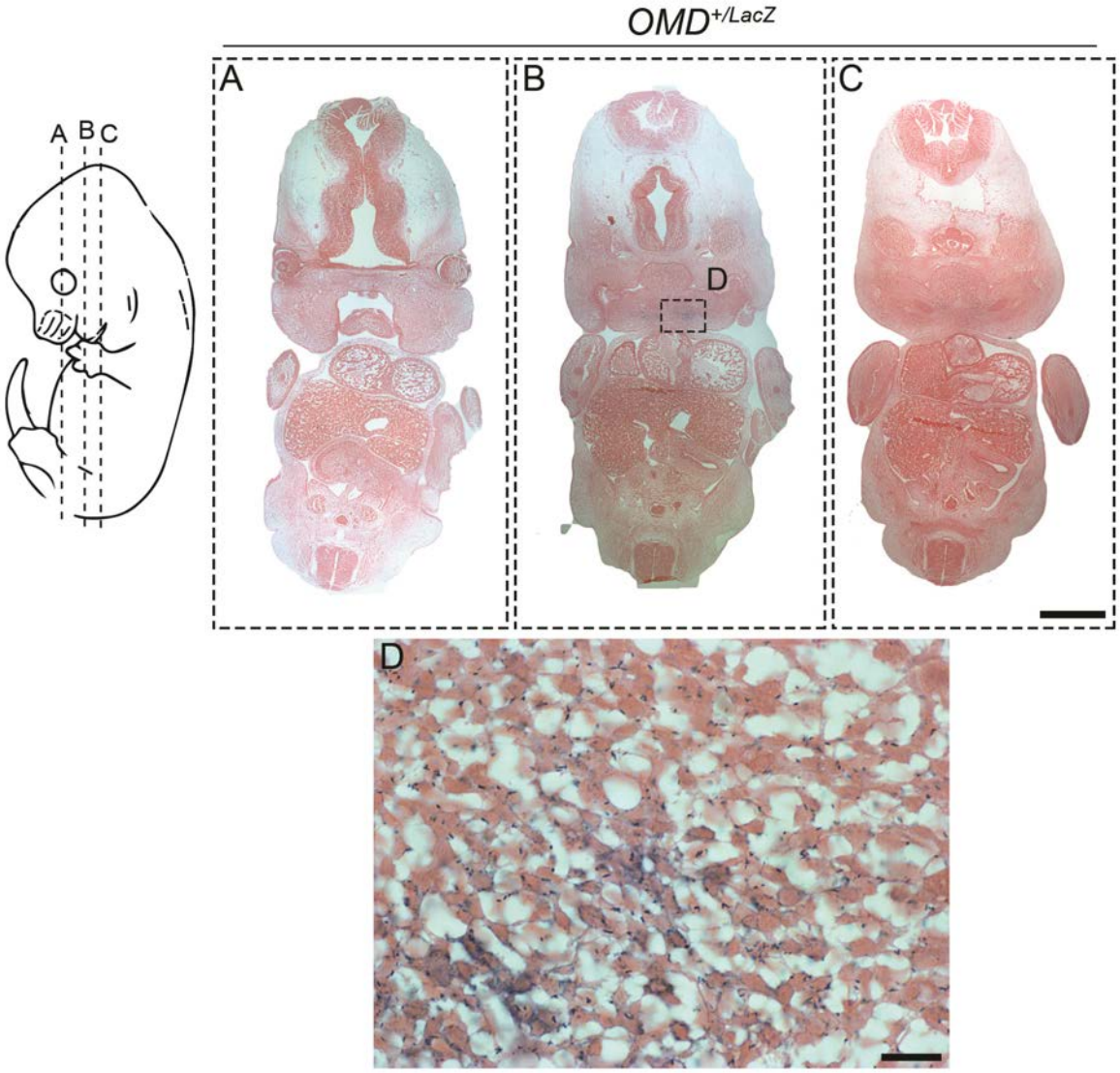

Figure 4.3: OMD expression in sections of an X-gal stained *OMD*$^{+/LacZ}$ E12.5 embryo. (A), (B) and (C) denote three different section planes, while in picture (D) X-gal expression can be seen in the developing mandible mesenchyme. Scale bar for (A), (B), (C) is 1mm, for (D) 50µm.

4.2.2 OMD expression in E15.5 embryos

Embryos were again collected at 15.5dpc after time-matings and the whole litter was stained for β-galactosidase overnight. Wild type embryos had no staining, while heterozygotes and homozygous knock-outs showed intense staining, mostly in the developing skeleton (Fig. 4.4). As shown in Figures 4.4 & 4.5A, Lac-Z activity can be seen at the digit tips, the metatarsals (hindlimb), metacarpus (frontlimb) and in phalanges, the ribs, the developing long bones of hands and legs, the vertebrae, the maxillary region, the developing jaw, the nasal septum, the intramembranous bones of the head (frontal and parietal cranial bones), the zygomatic as well as the endochondral occipital bone. After clearing the stained embryos, all the areas described above can be seen in greater detail (Fig. 4.5B), while in Fig. 4.5C & 4.5D it is visible that Lac-Z activity in the long bones is localized in the osteogenic perichondrium surrounding the developing ossifying centers. Also, the intensity of the staining in the $OMD^{LacZ/LacZ}$ embryos was usually stronger compared to the $OMD^{+/LacZ}$ heterozygotes.

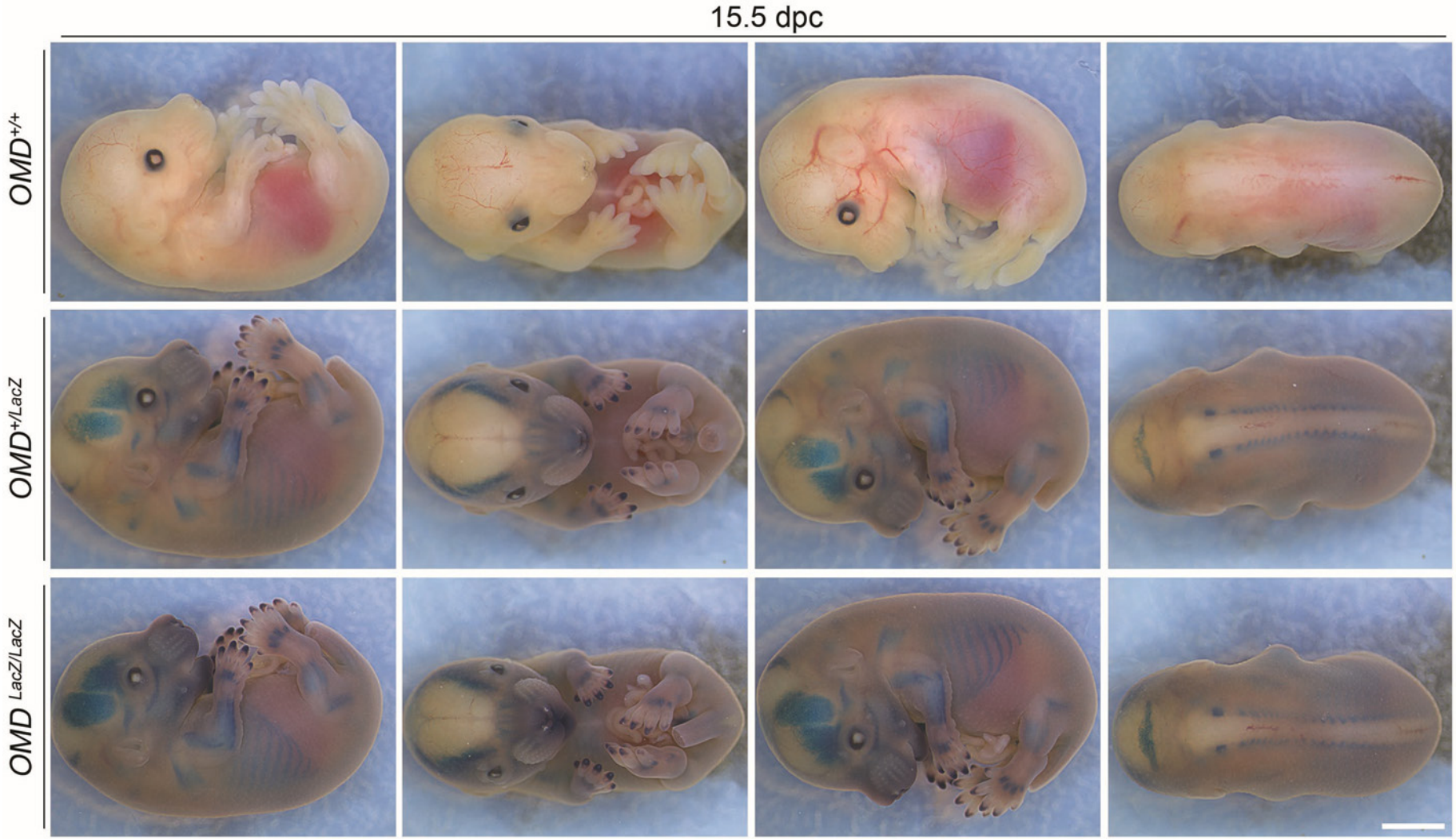

Figure 4.4: OMD expression in E15.5 embryos. Whole mount X-gal staining of wild type, heterozygous and homozygous knock-out embryos demonstrating Lac-Z activity in the developing skeleton. Signal is seen in the long bones of hands and legs, the ribs, the metatarsals and metacarpals, the digit tips, the vertebral bodies, the snout and the bones of the head, i.e. frontal, parietal, zygomatic and occipital bones. No background signal is seen in the wild type embryos. Scale bar, 2mm for all images.

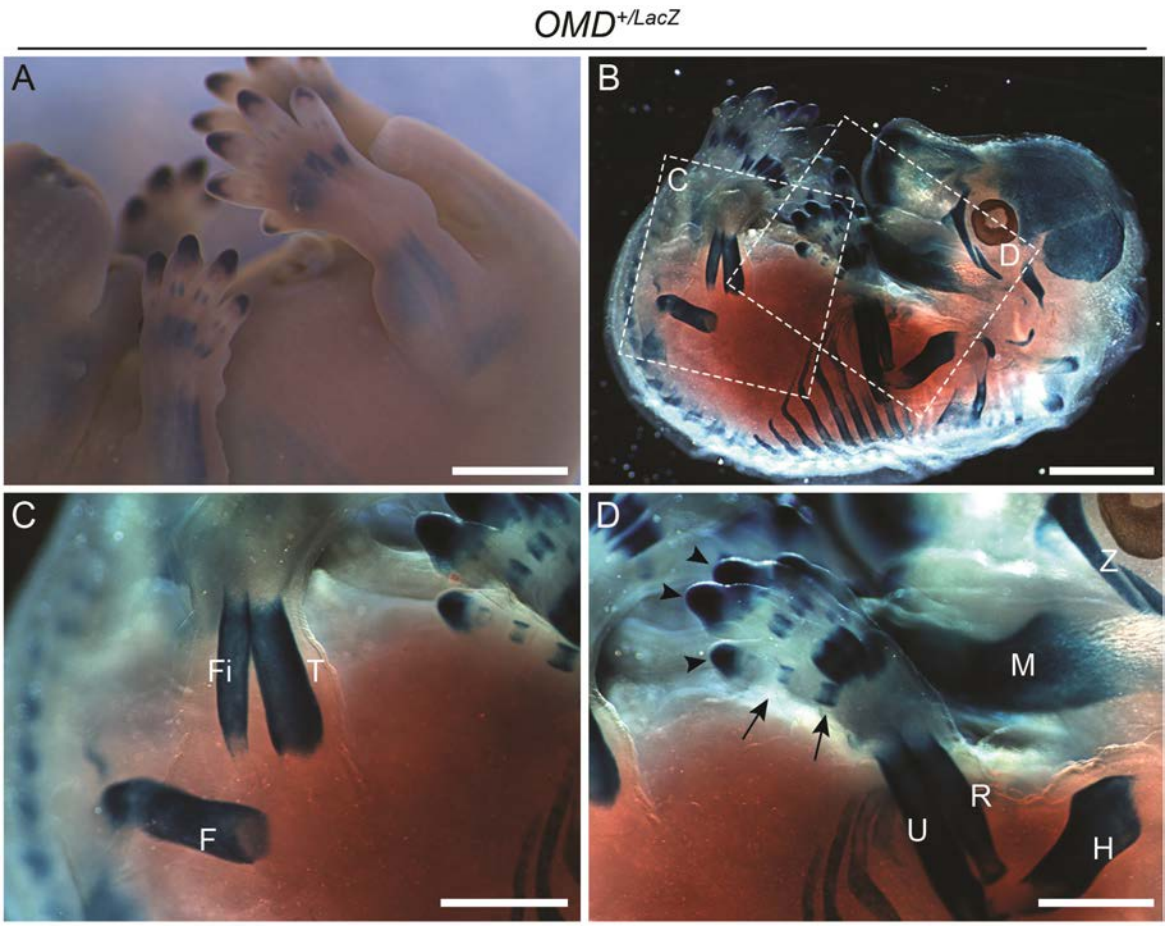

Figure 4.5: Cleared *OMD*$^{+/LacZ}$ embryos after X-gal staining. (A) A closer image of the limbs showing Lac-Z activity in the digit tips, the metatarsals and metacarpals, and the long bones of the hand and leg. (B) A whole-mount X-gal stained and cleared embryo, where all the β-gal positive areas can be seen in greater detail. (C) Magnified view of (B) demonstrating β-gal signal in the periosteum of tibia, fibula and femur. (D) Another close-up view of (B) showing OMD expression in the osteogenic perichondrium of radius, ulna, humerus, metacarpals (arrows), digit tips (arrowheads) and also the lower jaw (mandible) and zygomatic bone around the eye. Scale bars, 2mm. F, femur; Fi, fibula; T, tibia; H, humerus; M, mandible; R, radius; U, ulna; Z, zygomatic bone.

As most of the signal observed was related to skeletal tissues, the bone formation process will be briefly described here in order to understand in detail the areas where OMD is expressed. Osteogenesis can be divided into two major modes, both of which involve the transformation of pre-existing mesenchymal tissue into bone tissue. The bones of the skull are formed by the process known as intramembranous ossification, where mesenchymal tissue is directly converted into bone, whereas the axial skeleton and the long bones of the limbs are formed by the other pathway, called endochondral ossification. In the later process mesenchymal cells aggregate to form cartilage tissue which is subsequently replaced by bone (Horton, 1990). Endochondral ossification can be divided into five stages, starting with the commitment of mesenchymal cells to become cartilage cells (induced by the transcription factors Pax1 and Scleraxis). Secondly, these mesenchymal cells condense and differentiate into *chondrocytes* (cartilage cells), which then rapidly proliferate to form a spatial model for the future bone, secreting at the same time a cartilage-specific ECM. At this stage the cartilage model is surrounded by the perichondrium. In the next stage the perichondrium around the diaphysis (the central area where calcification occurs) becomes *periosteum* (containing a layer of undifferentiated-osteoprogenitor cells) and a bone collar is produced. Internally, the chondrocytes stop dividing and increase their volume becoming *hypertrophic chondrocytes*, also enhancing their secreted matrix with collagen X and fibronectin so it can now be mineralised by calcium carbonate. Finally, while blood vessels invade this cartilage model, hypertrophic chondrocytes die by apoptosis and the space that is created becomes the bone marrow. At the same time, cells of the periosteum differentiate into *osteoblasts*, which also begin forming matrix in the partially degraded cartilage, and eventually most of the cartilage is replaced by the newly-forming bone. A schematic representation of osteogenesis, together with an example of X-gal stained E15.5 frontlimbs from OMD wild type and heterozygote embryos, is shown in Figure 4.6.

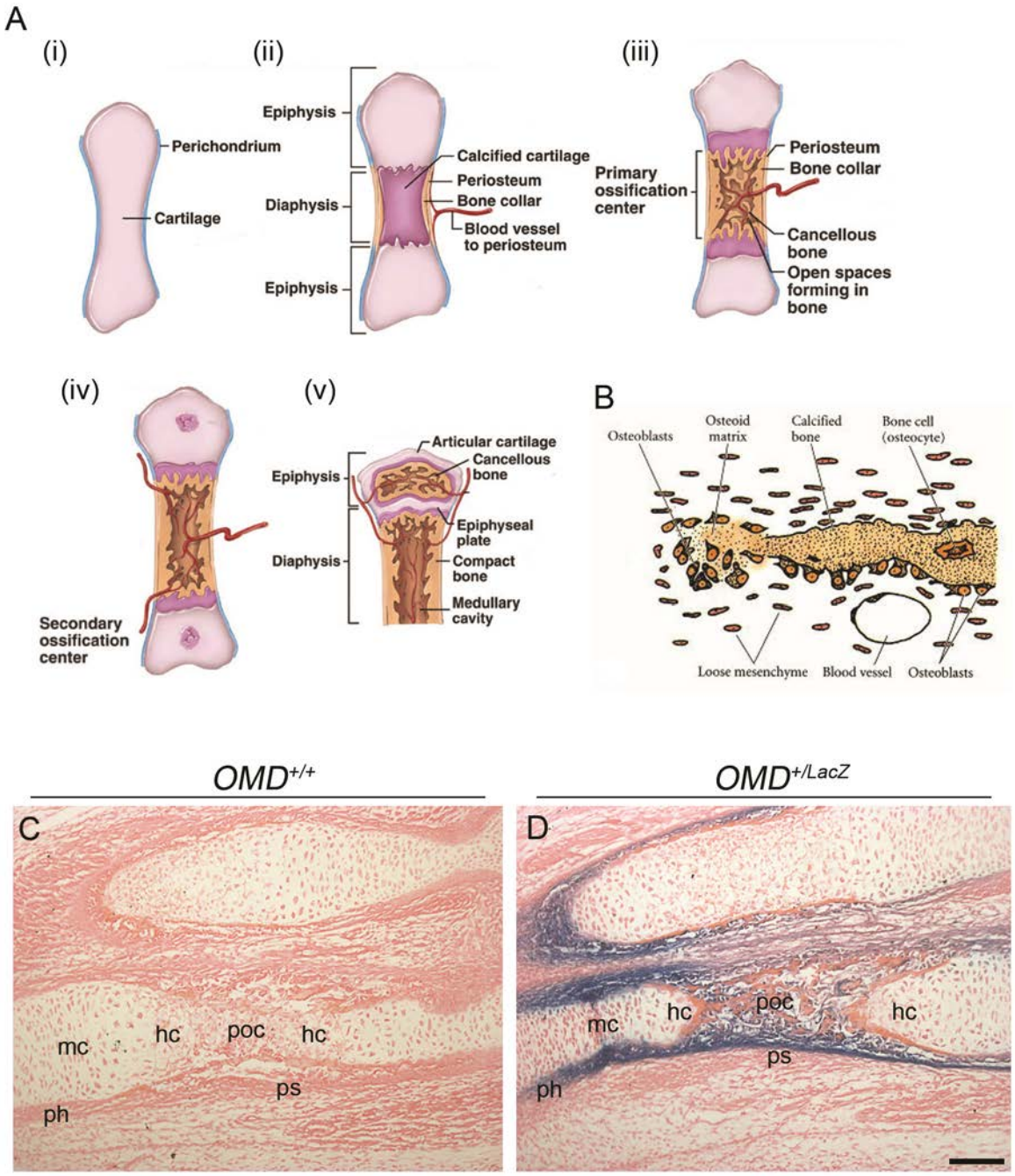

Figure 4.6: A brief description of osteogenesis. (A) The five basic steps of endochondral ossification. Detailed explanation is described in the text. Adopted by McGraw-Hill. (B) Schematic diagram of intramembranous ossification. Mesenchymal cells condense and differentiate into osteoblasts, which deposit osteoid matrix. These osteoblasts are arrayed along the calcified region of the matrix and become osteocytes once they are trapped within the bone matrix. Adopted by Gilbert SF, 2006. (C) & (D) X-gal stained sagittal sections of E15.5 *OMD*$^{+/+}$ and *OMD*$^{+/LacZ}$ frontlimbs demonstrating Lac-Z activity in the perichondrium/periosteum and the primary ossification groove of the heterozygote ulna (lower bone). Scale bar, 100μm for both images. mc, mature chondrocytes; hc, hypertrophic chondrocytes; poc, primary ossification center; ph, perichondrium; ps, periosteum.

The long bones of many mammals (including mice and humans) continue to grow after birth and this is possible due to the remaining cartilaginous tissue surrounding the ossified matrix. During bone formation, endochondral ossification grows outward in both directions from the center of the bone, but when the ossification front approaches the ends of the cartilage model the chondrocytes located close to the ossification front proliferate before they undergo hypertrophy so that they push the cartilaginous ends of the bone to extend. These areas at the two ends of the long bones are called epiphyseal growth plates and are essentially composed of three distinct chondrocyte regions, comprising of small proliferating chondrocytes, mature chondrocytes and hypertrophic chondrocytes. Thus, the bone can continue to grow for as long as the epiphyseal growth plate can produce chondrocytes.

Following the whole-mount Lac-Z staining, embryos were embedded in paraffin, sectioned and counterstained with eosin in order to further analyze the β-gal expression in detail. In coronal sections of heterozygote 15.5 dpc embryonic heads we can see more clearly some of the areas described earlier. For example, β-gal signal can be seen in chondrocytes of the developing nasal septum (those located mostly around the edges), the mesenchyme in the distal tongue and the regions of the head undergoing ossification including the developing maxilla and the intramembranous frontal/parietal bones (Fig. 4.7). In contrast, the fatal brain and eye showed no signs of β-gal and therefore *OMD* expression. On sagittal sections of $OMD^{+/LacZ}$ embryos Lac-Z activity was detected in the perichondrium and mostly in the periosteum of long bones, i.e. humerus, scapula, radius, ulna, femur and tibia, as well as around the ribs and in chondrocytes of the vertebral bodies (Fig. 4.8). More specifically, cells in the primary spongiosa and the ossification grooves of the various bones in the developing appendicular and axial skeleton were always positive for β-gal, suggesting OMD expression in osteoblasts. In addition, X-gal staining was also observed in the ossified regions of the parietal and frontal cranial bones, as well as in the ossified mandible, pre-maxilla, the nasal septum and the mesenchyme forming the tip of the tongue (Fig. 4.8 B, C&E), as shown already in the coronal sections of the head. Finally, in Figure 4.8 G&H and 4.8 I sections of the two femurs from a heterozygous embryo are shown, where it is clearly visible that OMD is expressed in the perichondrium/periosteum and in the forming ossification groove of

the diaphysis, where the primary ossification center is located. There is no staining in mature or proliferating chondrocytes, whereas occasionally in some of the long bones a lower level of staining can be seen in the apoptotic hypertrophic chondrocytes (Fig. 4.8H).

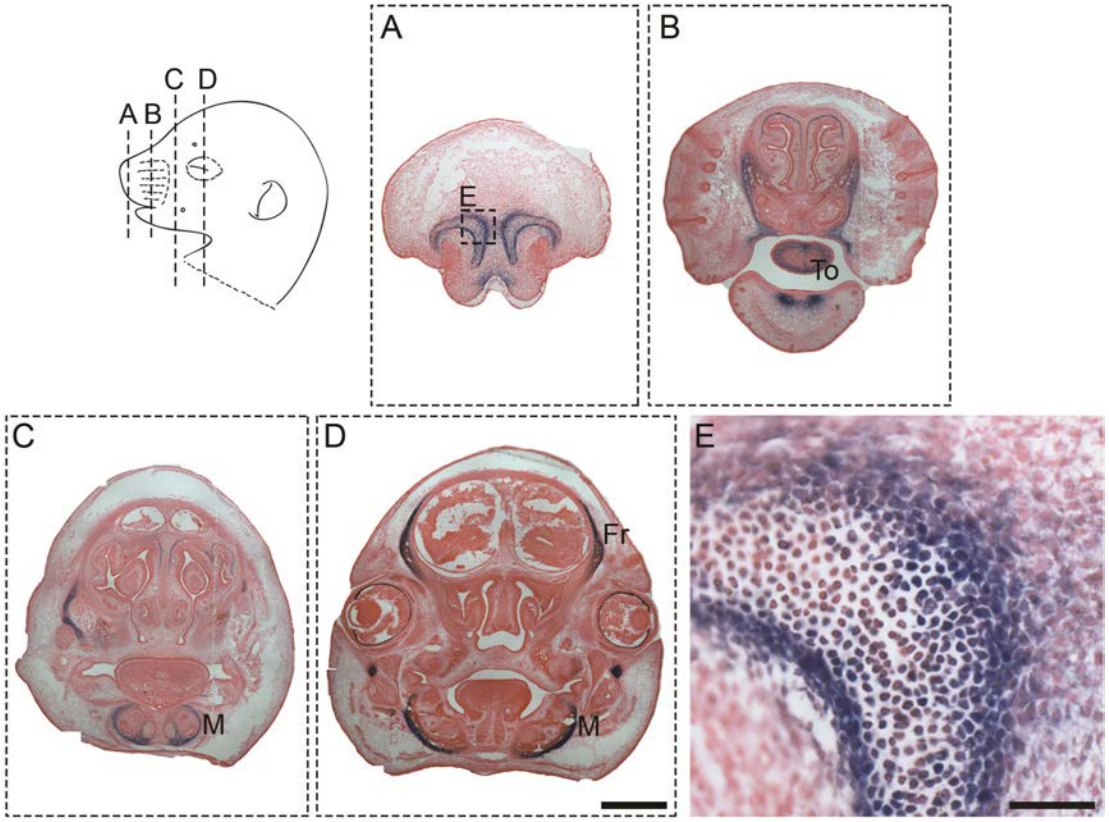

Figure 4.7: OMD expression in the E15.5 embryonic head. (A)-(D) Four different coronal sections of an *OMD*$^{+/LacZ}$ head demonstrating Lac-Z activity in the nasal septum, the ossifying maxilla and mandible, part of the tongue and the ossified frontal bone. (E) A magnified view of (A) showing β-gal signal in chondrocytes and in mesenchymal condensations around the edges of the cartilaginous nasal septum. Scale bars, 2mm for (A), (B), (C) & (D), 100μm for (E). M, mandible; Fr, frontal bone; To, tongue.

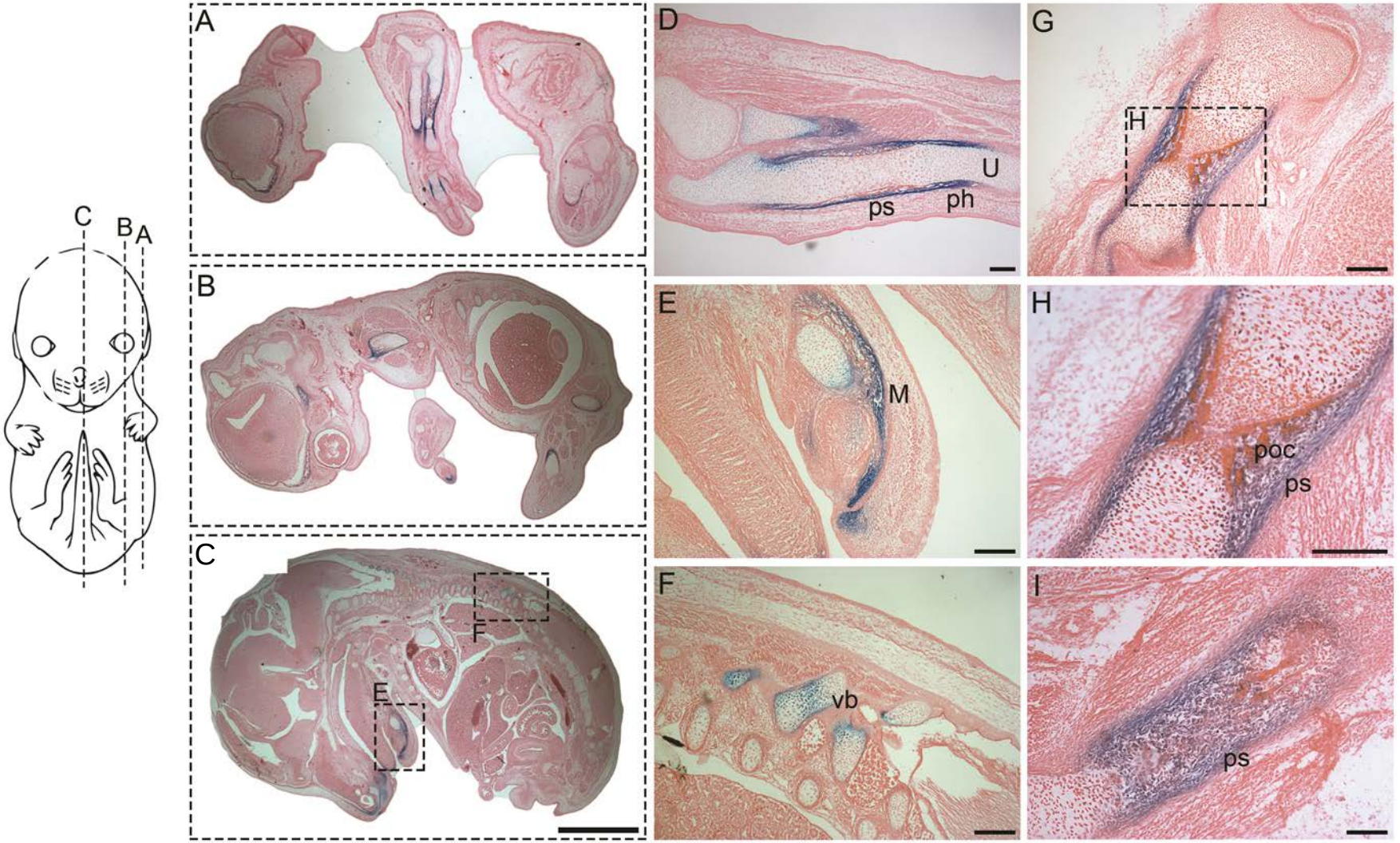

Figure 4.8: OMD expression in sagittal sections of X-gal stained *OMD*$^{+/LacZ}$ E15.5 embryos. (A)-(C) Three different sagittal planes of a stained heterozygote 15.5dpc embryo, demonstrating OMD expression in the long bones, the cranial bones, the nasal septum and the vertebrae. (D) View of a forelimb showing Lac-Z activity in the periosteum (ps) and perichondrium (ph) of ulna (U). (E) Magnified view of the lower jaw, where expression can be seen in the ossified mandible (M). (F) X-gal staining in chondrocytes of the vertebral bodies (vb). (G)-(I) Femurs exhibiting OMD expression in the periosteum and the primary ossification centre (poc). Scale bars, 2mm for (A)-(C), 140μm for (D), 100μm for (E)-(I).

4.2.3 OMD expression in E17.5 embryos

Embryos at stage E17.5 were collected and whole mount-stained for X-gal overnight. Although the staining procedure worked, due to the big size and complete skin development of these embryos, penetration of the staining solutions in all internal tissues was unequal, resulting in variable coloration of the β-gal substrate, even between the same genotypes within a litter. Thus, it was decided to freeze down E17.5 embryos and subsequently stain single cryo-sections for β-gal expression. In addition, head and body were separated in all embryos (for better penetration of fixative and cryopreservation solutions) and were sectioned individually.

Similar to E15.5 embryos, most of the β-gal signal can be seen in developing skeletal elements. After X-gal staining and clearing of E17.5 embryos, β-gal signal can be seen in the developing long bones and ribs of the axial skeleton, as well as in the cranial bones, the jaw and the tip of the tongue, as shown in Figure 4.9A. Sectioning and subsequent staining of $OMD^{+/LacZ}$ embryos revealed OMD expression in the periosteum and probably perichondrium all around the calcified long bones (Fig. 4.9). In addition, OMD expression is occasionally seen in proliferating or pre-hypertrophic chondrocytes away from the ossification centres, for example in the ribs and the upper limb joints (Fig. 4.9B). Furthermore, expression of OMD in the vertebral column is located in the chondrocytes but also around the ossified regions of the vertebrae, as shown in Figures 4.9 D&E. More specifically, OMD appears to be expressed in the proliferating/resting chondrocytes of the vertebral discs but not in the hypertrophic/apoptotic chondrocytes (ossifying vertebral bodies) with only few cells of the inner annulus fibrosus (af) positive, while the collar bone around the ossified areas is again OMD-positive (Fig. 4.10 D&E). Faint β-gal signal can also be seen in the spinal cord (Fig. 4.9E). Moreover, in a longitudinal section of the femur β-gal positive signal can be seen in the primary spongiosa (psp), while less signal is seen now in the bone collar probably due to the fact that ossification has advanced and many more osteoblasts are now found in the forming bone matrix (Fig. 4.9 F&G). Finally, very strong signal is observed in the digit tips of forelimb and hindlimb, and as shown in X-gal stained cryo-sections of the forelimb in Fig. 4.9H, mesenchymal cells between the outer skin and the chondrocytes of the digits are OMD positive along with the periosteum/perichondrium of the phalanges.

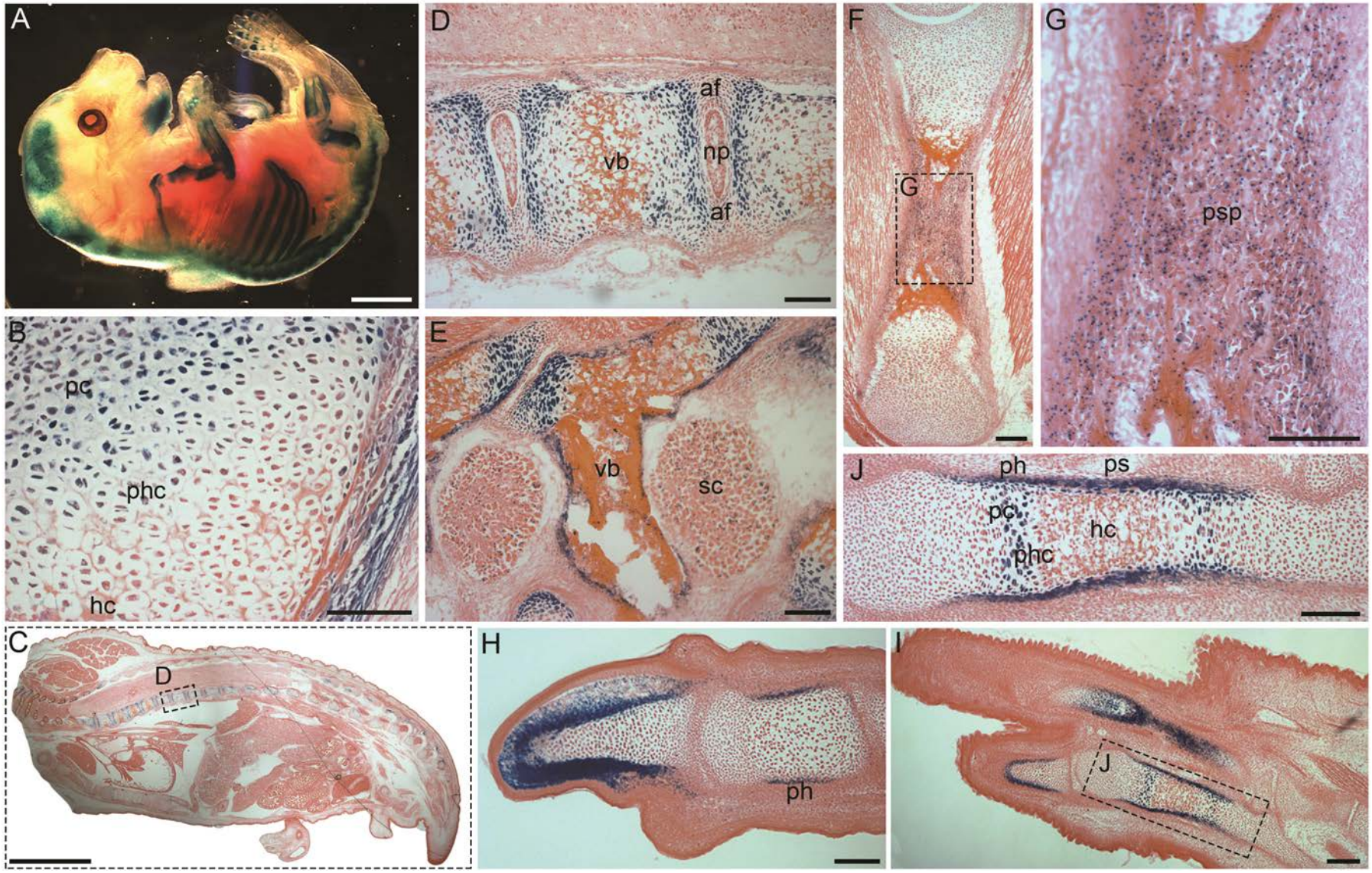

Figure 4.9: OMD expression in sagittal sections of X-gal stained *OMD*$^{+/LacZ}$ E17.5 embryos. (A) Whole-mount stained and cleared E17.5 heterozygote embryo demonstrating X-gal staining in all the skeletal elements. (B) Part of the ulna showing β-gal signal in mature/proliferating and occasionally pre-hypertrophic, but not in hypertrophic chondrocytes. (C) Sagittal section of the whole embryo body. (D)-(E) Lac-Z activity in the vertebral discs and bodies can be seen in resting/proliferating chondrocytes and around the ossified matrix, while some signal is seen in the chondrocytes of the annulus fibrosus and the spinal cord. X-gal staining is observed all around the primary spongiosa in the femur (F)-(G), in the mesenchyme between the skin and the chondrocytes and also in the perichondrium of the digit tips (H), and in the perichondrium/periosteum and chondrocytes of the phalanges (I)-(J). Scale bars, 3mm for (A), (C), 140μm for (F), (I), 100μm for all the rest. af, annulus fibrosus; np, nucleus pulposus; ph, proliferating chondrocytes; phc, pre-hypertrophic chondrocytes; hc, hypertrophic chondrocytes; ph, perichondrium; ps, periosteum; psp, primary spongiosa.

A wider view of the forelimb including phalanges and metacarpals is shown in Fig. 4.9I, while in Fig. 4.9J a magnified view of the distal phalanx is demonstrated showing Lac-Z (and thus OMD) expression in the periosteum/perichondrium and the proliferating and pre-hypertrophic chondrocytes around the primary ossification center.

In order to further analyse the expression of OMD in the embryonic E17.5 mouse eye, brain and the rest of the head structures, frozen $OMD^{+/LacZ}$ heads were sectioned coronally from front to back and subsequently stained with X-gal. In Fig. 4.10 four representative sections are presented. As shown in sections A and E, chondrocytes of the cartilaginous nasal capsule are positive for β-gal. Further inwards the signal is decreased but maintained in the nasal septum chondrocytes closer to the epithelium (at the perichondrium), while there is no staining in the olfactory epithelium or the developing teeth (currently at the bell stage). In addition, cells around the ossifying regions of the maxilla and the mandible are also positive (resembling the expression found in the periosteum/perichondrium during endochondral ossification of the long bones) (Fig. 4.10 C, F, G). Although staining was seen in the parietal and frontal bones of the head in the whole-stained and other paraffin-embedded sagittaly-sectioned embryos, when cryosectioning the head coronally we could not see the same strong signal possibly due to the small thickness of the sections. At the very back of the head signal was seen again around the periosteum/perichondrium of all the forming bones and in resting chondrocytes flanking the already ossified regions. Finally, no staining was observed either in the eye or the developing brain.

Overall, during this developmental stage OMD is expressed mainly in skeletal elements, including mostly the perichondrium and periosteum of the long bones together with a population of resting chondrocytes, as well as in the cartilaginous nasal capsule, the mandible and maxillae, and the ossifying regions of the cranial bones.

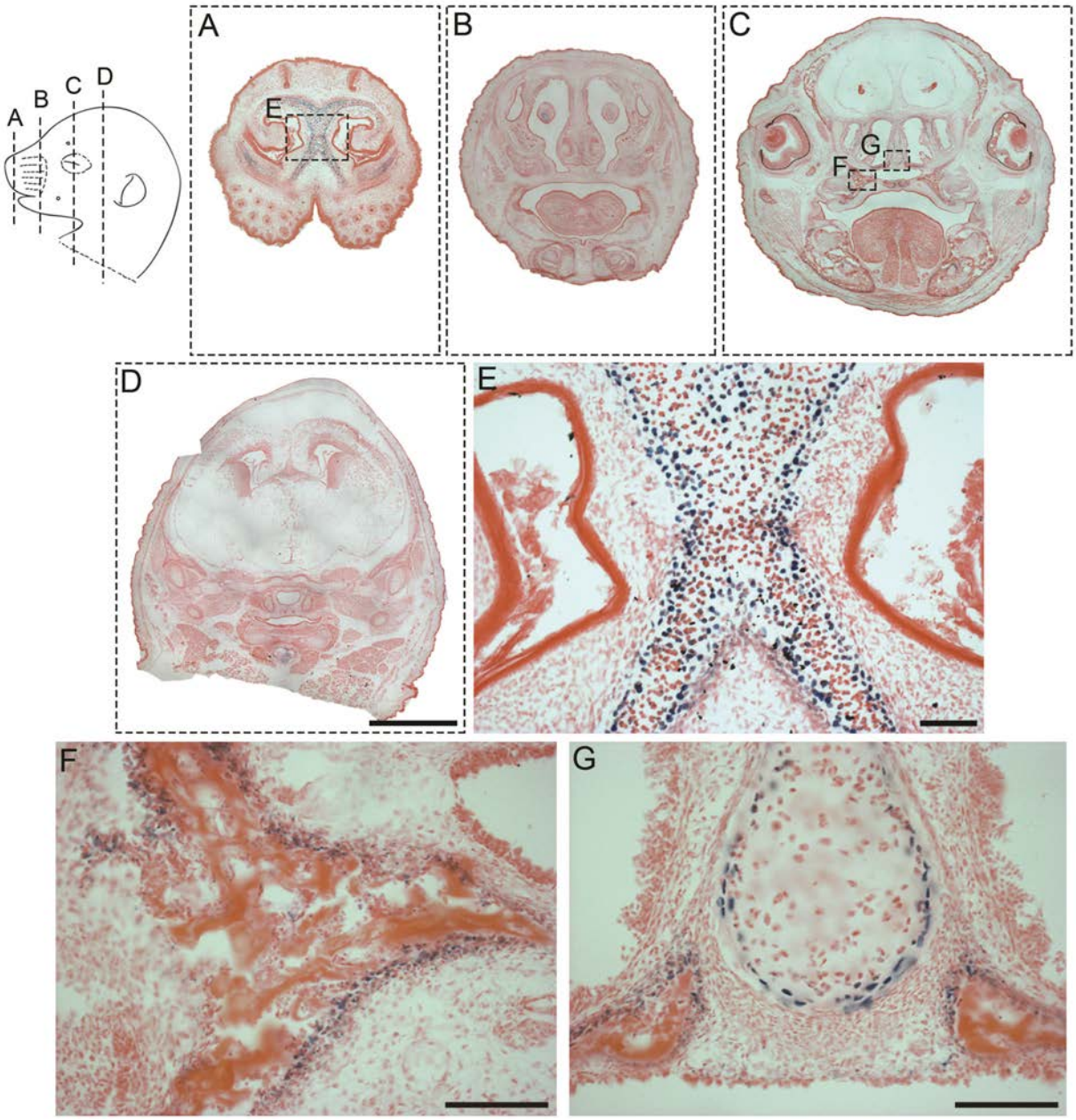

Figure 4.10: OMD expression in coronal sections of X-gal stained *OMD*$^{+/LacZ}$ E17.5 heads. (A)-(D) Four different coronal planes showing Lac-Z activity in the nasal capsule and the ossified regions of the cranial bones. (E) Chondrocytes of the nasal septum positive for β-gal and therefore OMD. (F) β-gal signal in the periosteum of the alveolar bone, where osteoblasts are usually localized. (G) Deeper nasal septum demonstrating X-gal staining in chondrocytes located at the edges of the septum and around the ossified matrix of the maxilla. Scale bars, 3mm for (A)-(D), 100μm for (F) and (G).

4.2.4 OMD expression in new-born (P0) mice

New-born (P0) neonates were collected within 16 hours of their birth time from $OMD^{+/LacZ}$ ♂ x $OMD^{+/LacZ}$ ♀ crossings, so all the 3 genotypes would occur within the same litter. Size of the litters varied between 8-11 pups and the ratio of genotypes followed Mendelian inheritance, while no differences were observed in the size or gross anatomy between individual new-borns. Similarly to E17.5 embryos, after euthanization heads and bodies were separated and processed for freezing, followed by subsequent sectioning and staining with X-gal. Again, no staining was observed in any $OMD^{+/+}$ sections, while β-gal signal was very strong in all the skeletal elements in $OMD^{+/LacZ}$ sections.

More specifically, in coronal sections of the head X-gal staining was seen initially in the chondrocytes of the cartilaginous snout and in some mesenchymal cells around the infranasal depression (Fig. 4.11A). In sections further into the head, staining was restricted to the perichondrium all around the cartilaginous nasal septum and in some of the chondrocytes forming the main part of the septum/nasal capsule. B-gal signal was observed in a few cells of the prospective olfactory epithelium, whereas in the vomeronasal organ (VNO) signal was only present in the vomeronasal cartilage and not in the epithelium (Fig. 4.11 B-D). B-gal was also observed in all the ossified regions of both the maxilla and mandible, with the signal being very strong in the periosteum and less intense within the osteoid matrix, while the areas around the palatal shelf fusions were also stained blue (Fig. 4.11 & 4.12). Furthermore, substantial staining was observed in all the developing teeth, including the maxillary and mandibular incisors and molars, where most of the dental papilla was β-gal positive together with a proportion of the pre-odontoblasts/odontoblasts (Fig 4.11B & 4.12 A-B). Signal was also seen in mesenchymal cells of the tongue, initially located mostly between central muscle groups and under the dorsal epithelium, while further in the tongue positive cells were mostly confined under the epithelium, possibly in the lamina propria.

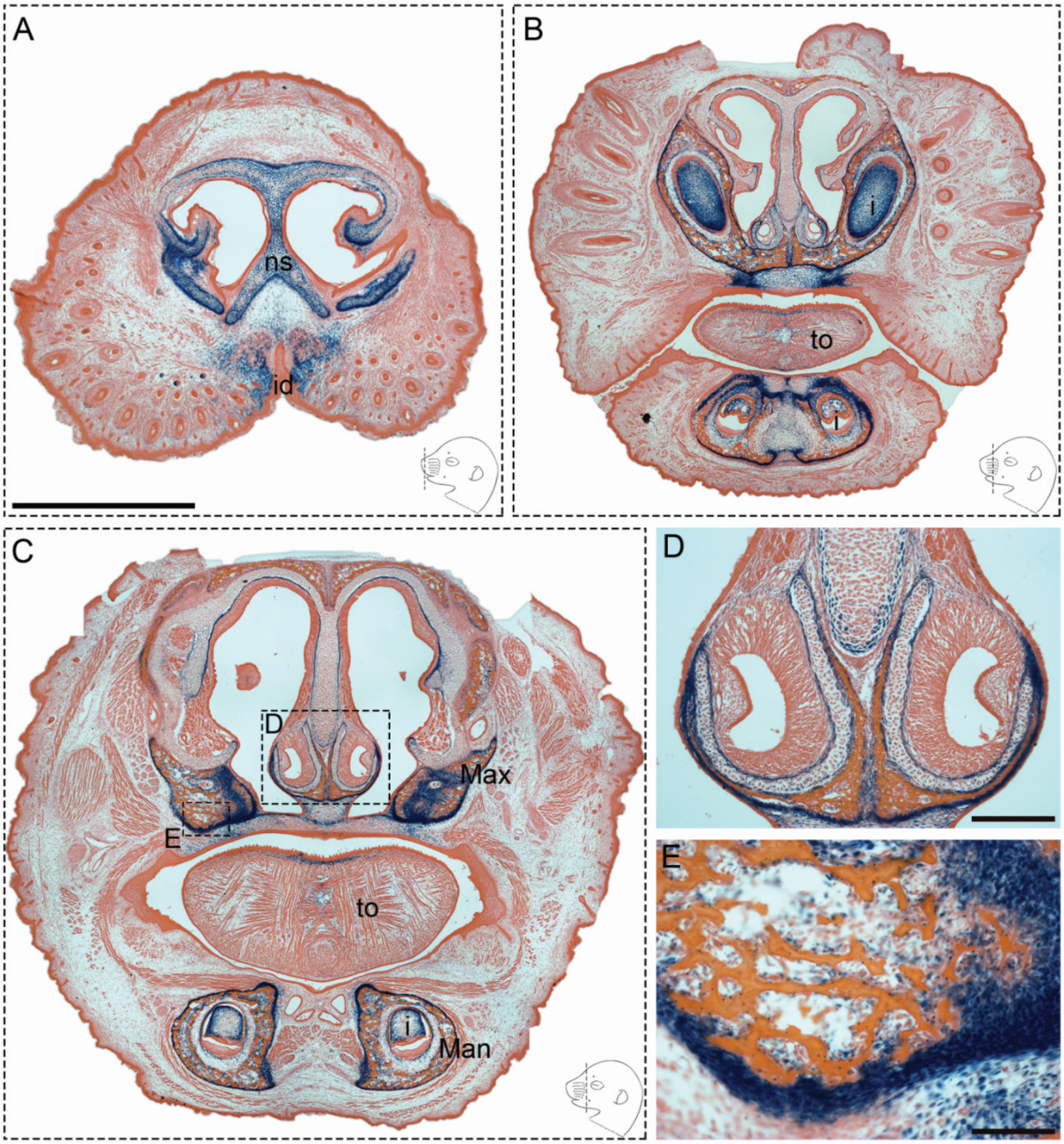

Figure 4.11: OMD expression in coronal sections of X-gal stained *OMD*$^{+/LacZ}$ P0 heads. Lac-Z activity can be seen in chondrocytes of the nasal septum and around the infranasal depression, in (A). The signal is expanded to the incisors and the ossified regions of the maxilla and mandible, in (B) and (C). (D) B-gal signal can be seen in the edges of the cartilaginous vomeronasal organ (VNO), in chondrocytes of the nasal septum and in the surrounding ossified matrix. (E) Magnified view of ossified maxilla demonstrating β-gal signal, and thus OMD expression, in the periosteum and within the matrix of the bone, probably in osteoblasts. Scale bars, 3mm for (A)-(C), 150μm for (D), 50μm for (E). id, infranasal depression; ns, nasal septum; i, incisors, Max, maxilla; Man, mandible; to, tongue.

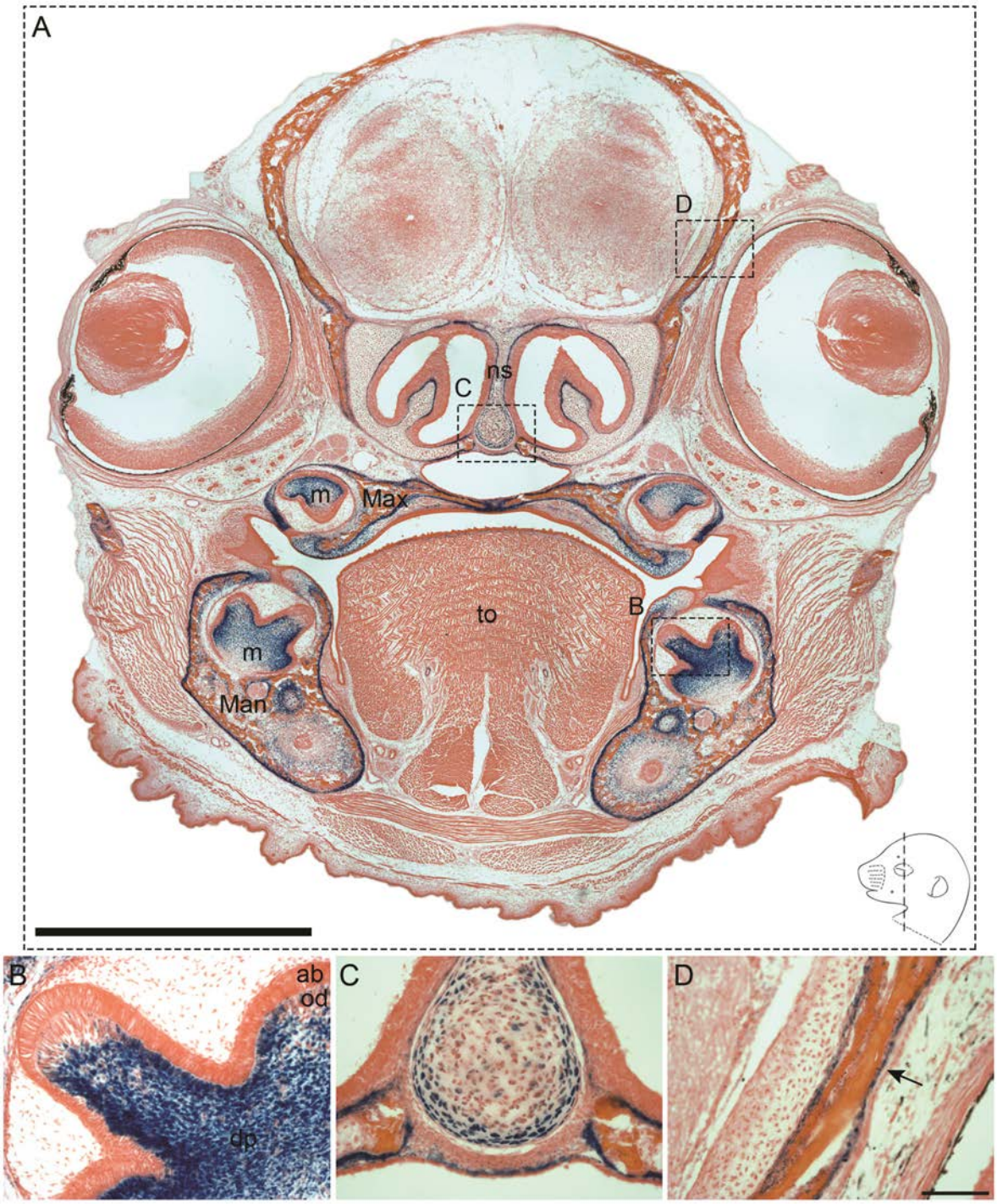

Figure 4.12: OMD expression in coronal sections of X-gal stained *OMD*$^{+/LacZ}$ P0 heads (continued). (A) Lac-Z activity is observed in the cartilaginous nasal septum, the ossified alveolar bones of the mandible and maxilla, the ossified frontal bones and in the developing mandibular and maxillary molars. (B) Magnified view of the mandibular molar demonstrating strong β-gal signal in the dental papilla and in a proportion of the odontoblasts, but not in the ameloblasts. (C) Lac-Z expression is seen in the marginal chondrocytes of the nasal septum and in the periosteum of the neighbouring bones. (D) β-gal signal in the periosteum (arrow) and within the matrix of the frontal bone. Scale bars, 3mm for (A), 100μm for (B)-(D). m, molar; Max, Maxilla; Man, mandible; ns, nasal septum; to, tongue; dp, dental papilla; od, odontoblasts; am, ameloblasts.

As mentioned earlier, all the ossified regions of the head are positive for OMD, including the calvaria bones, i.e. the frontal and parietal, as well as the zygomatic and occipital bones. In the posterior half of the head positive for b-gal are also the hyoid and basisphenoid bone/canals, the exoccipital bones and the ossified atlas (again the signal is stronger in the periosteum/perichondrium), as seen in Figure 4.13 A&B. Unlike the calvaria and the rest of the mouse skull bones that develop by intramembranous ossification, these last bones belong to the cranial base and develop by endochondral ossification. Thus, cranial base bones harbor all the different zones of the maturing chondrocytes flanking the ossification centers, similar to developing long bones. In Figure 4.13C and 4.13D the ossified center of the basisphenoid bone and the chondrocytes flanking the center of the hyoid bone are shown respectively, where OMD expression is strongly localised to the periosteum (and maybe a small area of the perichondrium) and to the zone of proliferative chondroblasts. Weaker signal can be seen within the osteoid matrix, indicating that OMD is either secreted from or expressed in the osteoblasts trapped in the forming osteoid, as well as in some of the resting chondrocytes, probably the ones that are committed to divide later or will be part of the perichondrium. The same expression pattern can be seen in the ossified exoccipital bones and atlas (Fig. 4.13B and in detail Fig.4.13E). Finally, weak, "spotty" OMD expression can be seen in the developing choroid plexus and other thalamic areas of the brain, as well as in areas of the spinal cord (Fig. 4.13F).

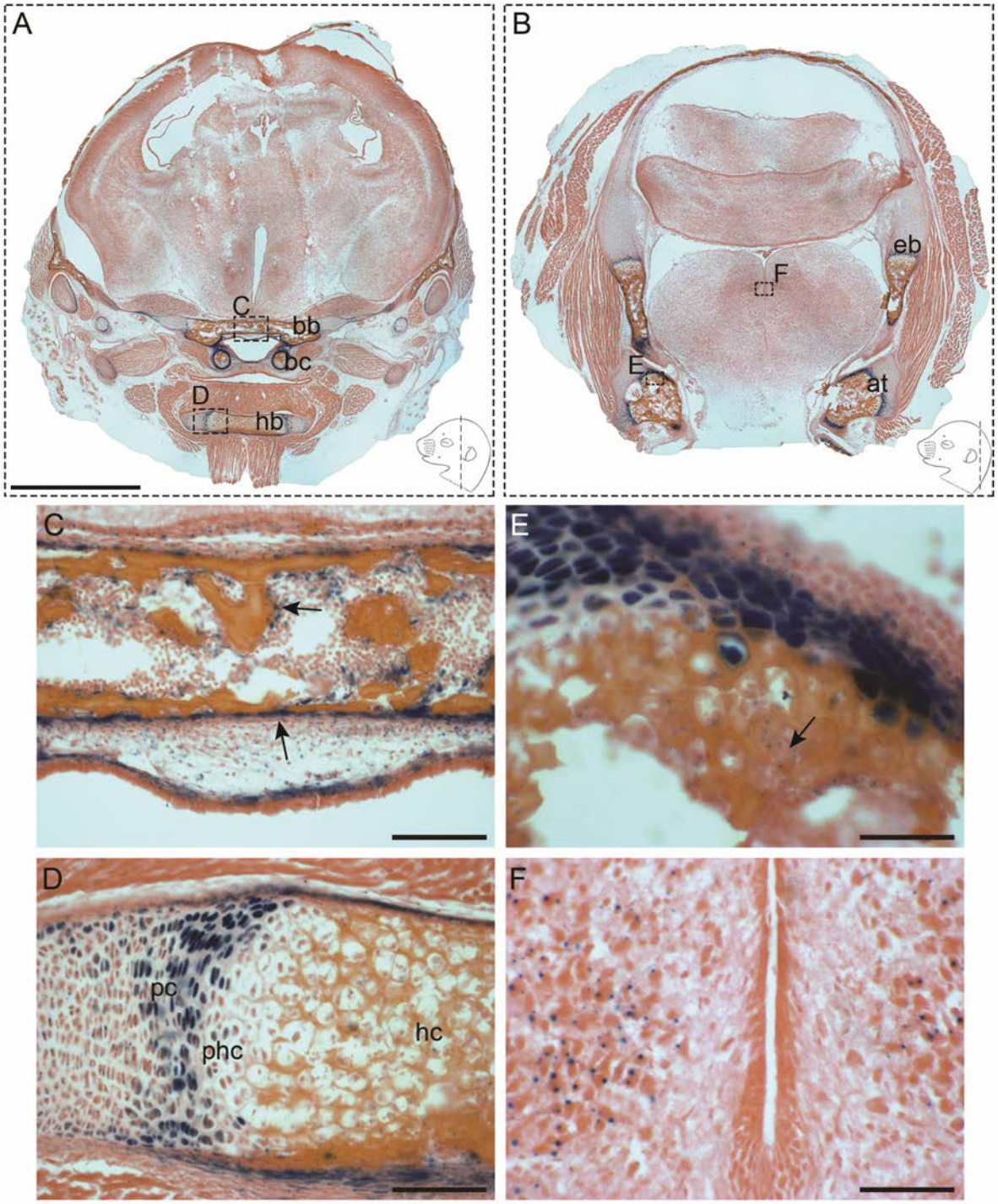

Figure 4.13: OMD expression in coronal sections of X-gal stained *OMD*$^{+/LacZ}$ P0 heads (last). In the posterior part of the head Lac-Z activity is observed in the hyoid and basisphenoid bones & canals, as well as in the exoccipital bones and the atlas, in (A) & (B). (C) Magnified view of the basisphenoid bone demonstrating β-gal signal in the periosteum and inside the osteoid matrix (arrows). (D) Magnified view of the hyoid bone, which develops by endochondral ossification and therefore harbours all the different chondrocytic populations around the ossification centre. X-gal staining is visible in the periosteum as well as in the proliferating chondrocytes and in part of the pre-hypertrophic chondrocytes, but not in the hypertrophic ones, reminding the expression pattern seen in the long bones. (E) Similar expression can be observed in the growing atlas, where columnar chondrocytes but also the forming osteoid matrix (arrow) is positive for β-gal. (F) Lac-Z activity is observed for the first time in the spinal cord. Scale bars, 3mm for (A)-(B), 100μm for (C)-(D), 50μm for (E)-(F). bb, basisphenoid bone; bc, basisphenoid canals; hb, hyoid bone; eb, exoccipital bone; at, atlas; pc, proliferating chondrocytes; phc, pre-hypertrophic chondrocytes; hc, hypertrophic chondrocytes.

Regarding OMD expression in the body of newborn *OMD*$^{+/LacZ}$ mice, sagittal sections from a heterozygote mouse are displayed in Figure 4.14, where it is visible that OMD is mostly expressed in the periosteum and within the osteoid matrix of all the skeletal elements. This is very noticeable when looking at the long bones of the forelimb, i.e. radius and ulna at Figure 4.14C and humerus at Fig. 4.14D. Strong b-gal signal is very specific around the forming cortical bone, as well as in the trabecular osteoid matrix found in the bone marrow cavity, indicating probable expression of OMD by osteoblasts (Fig. 4.14E). Also, some proliferating or probably resting chondrocytes at the edges of the growing bone are positive for X-gal, as well as chondrocytes found at the ribs (Fig. 4.14 A and D, arrows). In addition, signal can be observed in and around the ossified vertebrae, while resting and/or proliferating, but not hypertrophic, chondrocytes are also positive (Fig. 1.14 F&H). Similarly to E17.5 embryos, faint signal is also seen in the spinal cord (Fig. 4.14F). Finally, in a magnified cross-section of the clavicle bone, we can observe clear OMD expression around the bone cavity, where cortical bone is being synthetized (Fig. 4.14G).

Overall, OMD expression is quite strong in p0 mice and is confined around all the ossified bone structures in both axial and appendicular skeletal elements, while at this stage expression can be also observed in the growing teeth, as well as in areas of the brain.

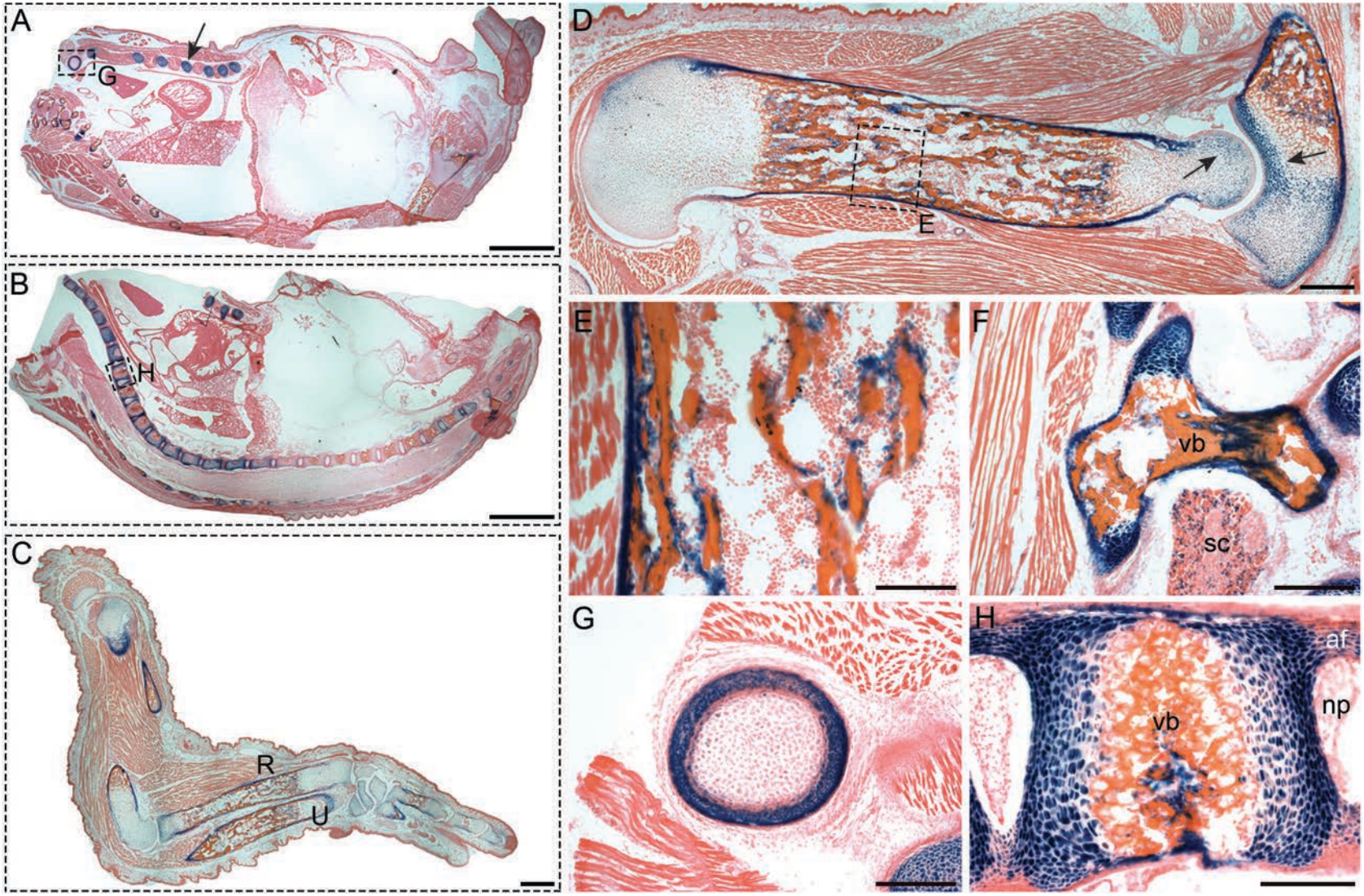

Figure 4.14: OMD expression in sagittal sections of X-gal stained *OMD*$^{+/LacZ}$ P0 bodies. Lac-Z activity can be seen in the ribs and the vertebral bodies in sagittal whole-body sections in (A) and (B), while signal is also seen in the periosteum and within the bone matrix in the upper limb (i.e. radius and ulna) in (C). (D) B-gal signal in the humerus bone is localised in the periosteum and within the osteoid matrix, but also in proliferating or resting chondrocytes (arrows). (E) Magnified view of the humerus demonstrating expression in the developing cortical (periosteum) but also trabecular bone (within the forming osteoid matrix), indicating OMD expression by osteoblasts. (F) & (H) X-gal staining in the vertebral bodies is observed in the ossified matrix and in chondrocytes surrounding the ossification centres and in the annulus fibrosus. No signal is seen in the nucleus pulposus of the vertebral discs. (G) Cross-section of the clavicle showing Lac-Z activity in the cortical bone. Scale bars 3mm in (A)-(B),140μm in (C)-(D), 100μm in (F), (G), (H) and 50μm in (E).

R, radius; U, ulna; vb, vertebral bodies; np, nucleus pulposus; af, annulus fibrosus, sc, spinal cord.

4.2.5 OMD expression in adult mice

Heterozygous and homozygous transgenic mice grew into adulthood, were fertile and had a normal life span without any apparent abnormalities and with normal reproductive rate. In order to examine *OMD* expression during adult life various internal organs were isolated from $OMD^{+/LacZ}$ adult mice and subsequently stained for β-galactosidase. The organs that were analysed are brain, eye, bladder, and bone, and all will be presented and discussed below, each in a separate sub-section. Due to the nature of the speciments, X-gal activity in the bone, and specifically in the knee joint, covering part of femur and part of tibia, was assessed by whole-mount staining, followed by decalcification and subsequent cryo-sectioning, while all the other organs where fixed, sectioned and afterwards stained for X-gal. Unfortunately, X-gal staining was inadequate to confirm specific OMD expression in other organs, such as kidney and spleen, due to endogenous b-galactosidase activity in the control $OMD^{+/+}$ sections. In such cases *in situ* hybridization was performed to explore the expression of mRNA *OMD* gene transcripts using wild type $OMD^{+/+}$ samples. However, this approach failed twice and therefore focus was given on the other organs. In addition, after confirming the expression patterns of OMD in each organ, immunofluorescence staining was performed to identify the specific cell types that were positive for β-gal, and thus OMD.

4.2.5.1 OMD expression in the adult mouse bladder

In order to investigate if *OMD* is expressed in the mouse bladder, whole bladders were isolated from adult $OMD^{+/LacZ}$ and $OMD^{+/+}$ littermates and after processing and sectioning were subsequently stained for hematoxylin and eosin (H+E) and X-gal. As shown in figure 4.15A, the mouse bladder, similarly to humans, is composed of two distinct parts, the epithelium that coats the urogenital tract from the renal pelvis to the urethra called the urothelium, and the surrounding muscle layer, which includes the internal and external layers. The mouse urothelium consists of 3 different cell layers: the basal cells (which form a single layer resting on the basal membrane of the epithelium), the intermediate cells and the most superficial “umbrella” cells (which are parallel to the basal membrane and “cover” the intermediate cells, Fig. 4.15B arrows). X-gal staining of $OMD^{+/LacZ}$ bladders

revealed β-gal expression only at the urothelium and specifically in or around the umbrella cell layer (Fig. 4.15 C-D), while *OMD*$^{+/+}$ samples didn't have any β-gal positive staining.

Further staining with several markers against the three different layers of the bladder urothelium confirmed β-gal, and thus OMD, expression in the superficial umbrella cell layer. More specifically, antibodies against uroplakin-3 (umbrella cells), laminin (basement membrane of the epithelium), CK5 (cytokeratin 5-intermediate/basal cells), and CK18 (cytokeratin 18-umbrella cells) were used. In *OMD*$^{+/LacZ}$ bladders β-gal positive cells were always co-localised with uroplakin-3 and CK18, but not with laminin or CK5, and thus we can conclude that OMD is expressed in a subpopulation of the umbrella epithelial cells (Fig. 4.16).

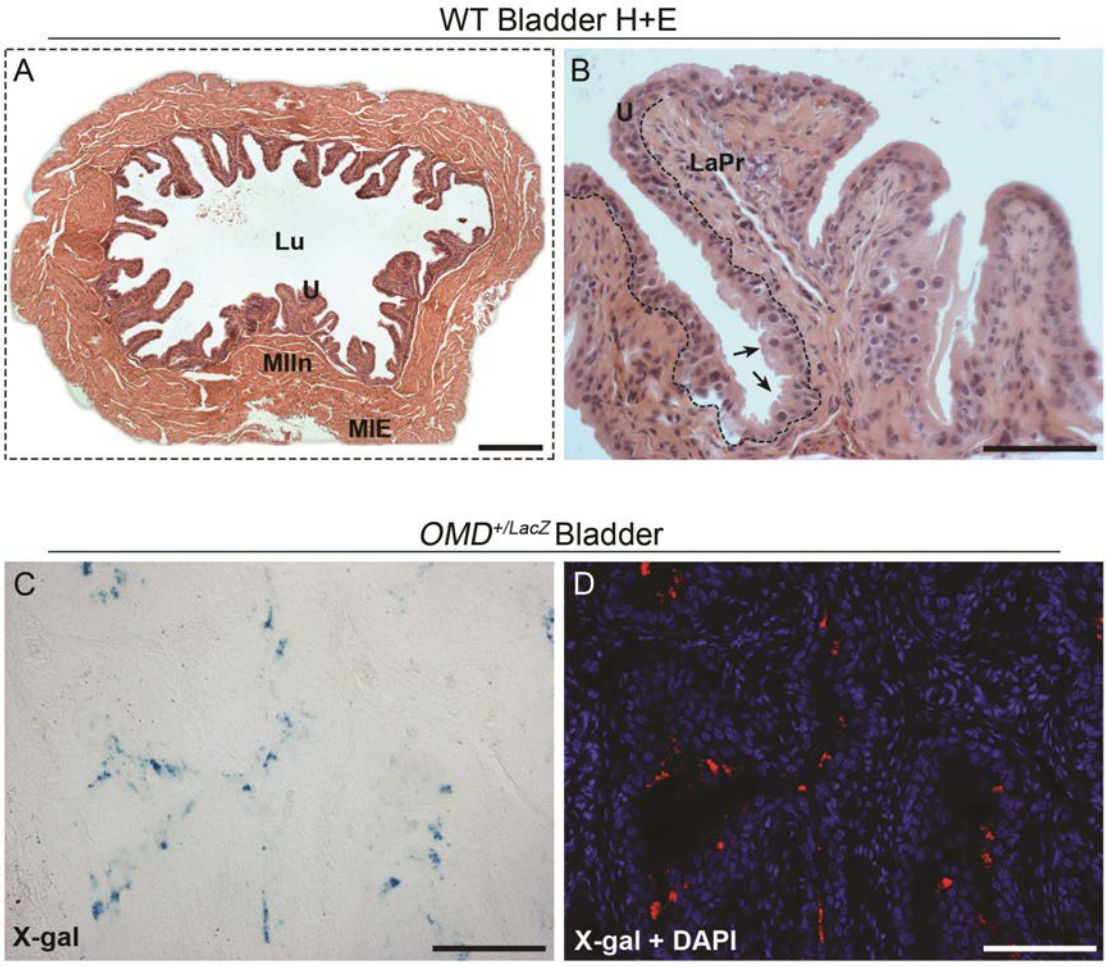

Figure 4.15: Mouse bladder morphology and OMD expression in X-gal stained *OMD*$^{+/LacZ}$ bladders. (A) H+E stained *OMD*$^{+/+}$ bladder where the different parts, i.e. lumen (Lu), urothelium (U) and muscle (MlIn, musclaris internal; MlE, muscularis external) are visible. (B) Magnified view of the urothelium (U) and underlying lamina propria (LaPr). Outer umbrella cells are marked with arrows. (C)-(D) X-gal staining in OMD heterozygote bladders is observed in the outer urothelial layer, probably in umbrella cells. In (D) the X-gal signal is coloured red and DAPI is used to stain cell nuclei. Scale bars, 500μm for (A), 100μm for (B)-(D).

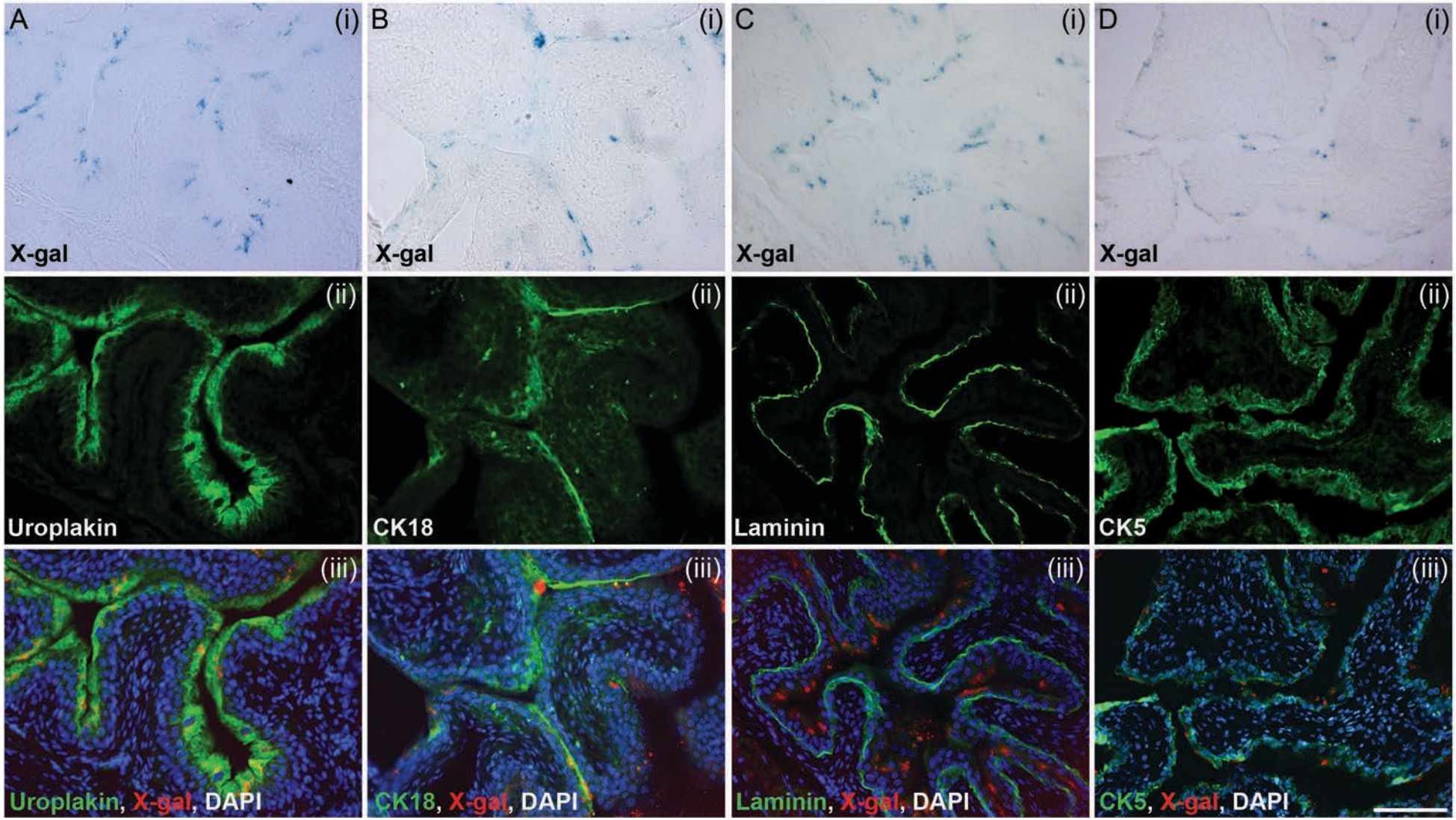

Figure 4.16: OMD expression in the adult mouse bladder is localised in the umbrella cell layer. Panels (i) represent X-gal staining, (ii) are specific antibody staining using alexa-488 (green) as secondary, while in panels (iii) are the merged images with the X-gal signal coloured red and DAPI used as a cell nuclei stain. B-gal signal is co-localised with uroplakin (A-iii) and CK18 (B-iii), but not with laminin (C-iii) or CK5 (D-iii), indicating OMD expression in the umbrella cell layer. Scale bar, 100μm for all images.

4.2.5.2 OMD expression in the adult mouse eye

Whole eyes from *OMD*$^{+/LacZ}$ and *OMD*$^{+/+}$ littermates were isolated, cryopreserved and sectioned sagittaly after freezing. Initially, H+E staining was performed in sections from a wild type control sample in order to identify and familiarise with all the separate areas of the mouse eye. As shown in figure 4.17A, the major components are the lens, which occupies most of the space and is surrounded by the vitreous, the cornea and sclera, the ciliary body (CB), the retinal pigment epithelium (RPE) and the multi-layered retina with the optic nerve connecting to the brain. Figure 4.17B shows all the retinal cell layers in detail, while in Figure 4.17C a higher magnification of the CB is shown, where the inner pigmented cell layer can be distinguished from the outer non-pigmented epithelial cell layer. The trabecular meshwork can also be recognised just below the CB and above the sclera.

Performing X-gal staining in *OMD*$^{+/LacZ}$ eye sections revealed OMD expression in the retinal ganglion cell layer and part of the inner nuclear layer (Fig. 4.17D). In addition, positive β-gal signal was seen in the ciliary body, and more specifically at the non-pigmented epithelium of the CB (Fig. 4.17E). In order to identify the specific cell types where OMD is expressed, immunofluorescence staining against various mouse retinal markers was performed after the X-gal reaction. Initially, OMD was co-localised with Pax6 (a marker for retinal ganglion cells-RGCs, amacrine, displaced amacrines and retinal stem cells of the CB) in a sub-population of cells both in the retinal ganglion cell layer and the inner nuclear layer. In addition, a number of cells of the non-pigmented epithelium of the CB were also positive for Pax6 and β-gal (Fig. 4.18). Moreover, all the cells exhibiting b-gal signal were also positively stained with HuC/HuD, a marker for new-born neurons (which essentially stain all RGCs), horizontals and amacrine cells, thereby confirming that OMD is expressed in the retinal ganglion cell layer and in the amacrines of the inner nuclear layer, but not in horizontal cells (Fig. 4.19A). In addition, using AP2-alpha which marks only the displaced amacrines at the RGC and the amacrines at the INL, shows that a small sub-population of the cells expressing OMD at the RGC are displaced amacrines (Fig. 4.19B). Looking closer at the INL, we can see that OMD is

expressed in the space between the amacrine cells but does not overlap with the cell bodies (Fig. 4.19B).

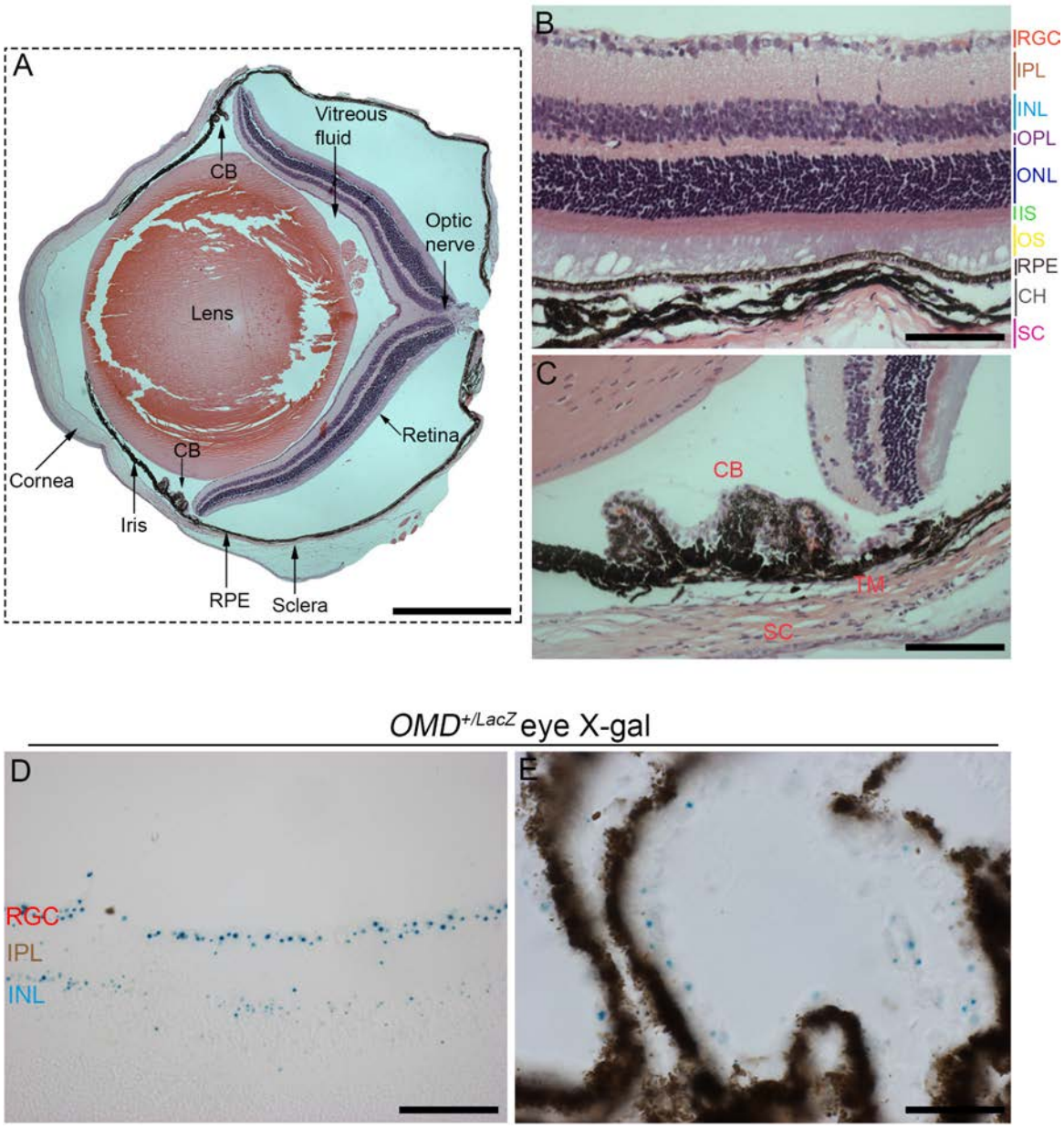

Figure 4.17: Mouse eye morphology and OMD expression in X-gal stained *OMD*$^{+/LacZ}$ eyes. (A) Section of a wild type sample stained with H+E demonstrating the major parts that form the mouse eye. (B) H+E stained mouse retina with all the different retinal cell layers labelled. RGC, retinal ganglion cells; IPL, inner plexiform layer; INL, inner nuclear layer; OPL, outer plexifrom layer; ONL, outer nuclear layer; IS, inner segments; OS, outer segments; RPE, retinal pigment epithelium; CH, choroid; SC, sclera. (C) Ciliary body (CB) of the eye stained with H+E. TM, trabecular meshwork; SC, sclera. (D) Lac-Z activity in the OMD heterozygous retina can be seen in the ganglion cell layer and in part of the INL. (E) In the ciliary body Lac-Z activity is observed in the non-pigmented epithelial cells. Scale bars, 1mm for (A), 100μm for (B)-(D), 50μm for (E).

Moreover, Islet-1, a marker for horizontals, bipolar and RGCs, was co-localised with the x-gal signal only in few cells in the retinal ganglion cell layer, whereas there was no X-gal activity in bipolar or horizontal cells (Fig. 4.19C). In conclusion, OMD was found to be expressed in the retinal ganglion cells, but also in a sub-population of amacrines and displaced amacrines. As expected, no β-gal signal was seen in the wild type samples.

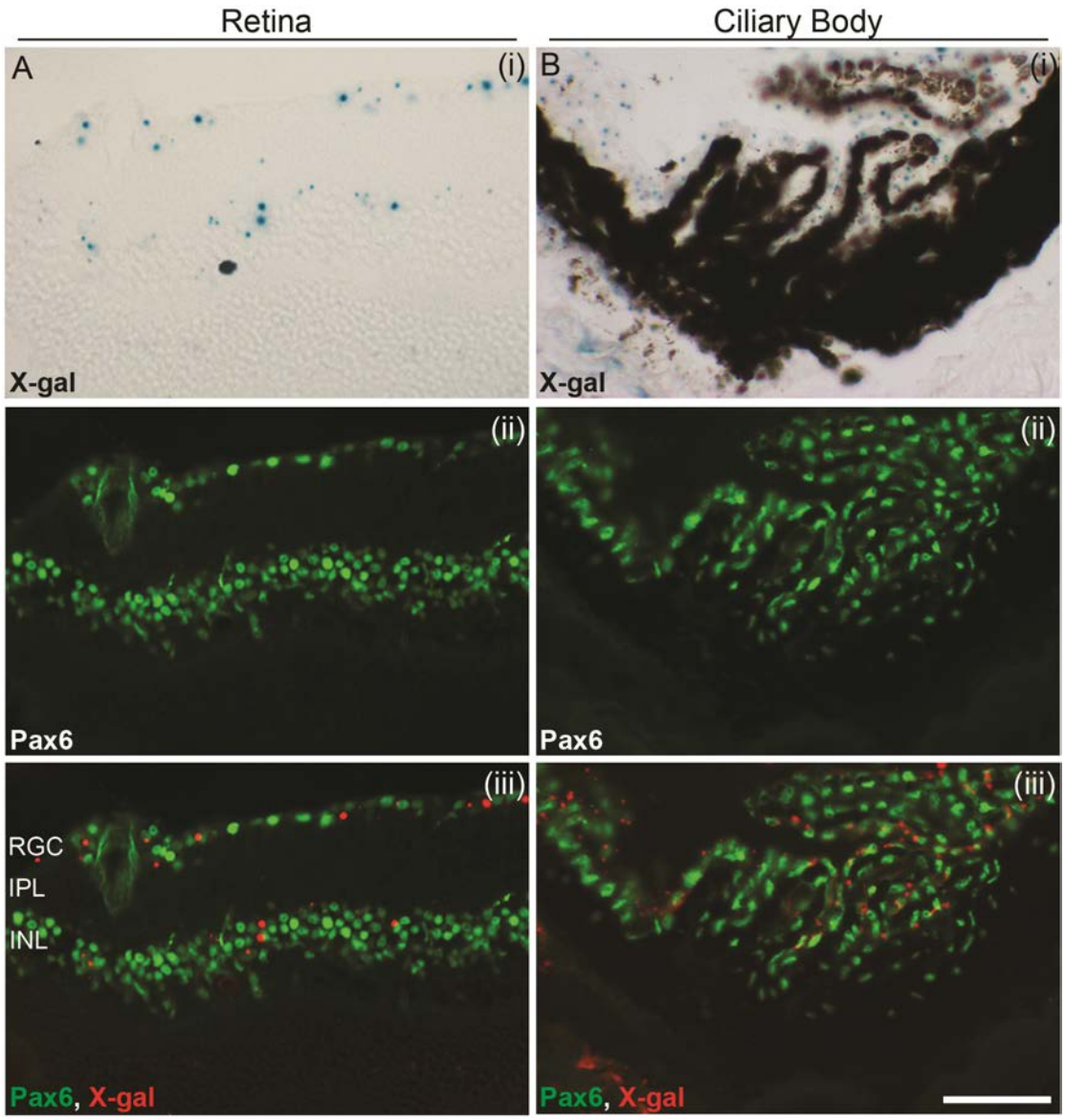

Figure 4.18: OMD expression in the adult mouse retina and CB is co-localised with Pax6-positive cells. Panels (i) represent X-gal staining, (ii) are Pax6 antibody staining using alexa-488 (green) as secondary, while in panels (iii) are the merged images with the X-gal signal coloured red. B-gal signal in the retina can be observed in a sub-population of Pax6 positive cells in the RGC and INL layers, while in the ciliary body the signal is always around Pax6-positive epithelial cells. Scale bar, 50μm for all images. RGC, retinal ganglion cells; IPL, inner plexiform layer; INL, inner nuclear layer.

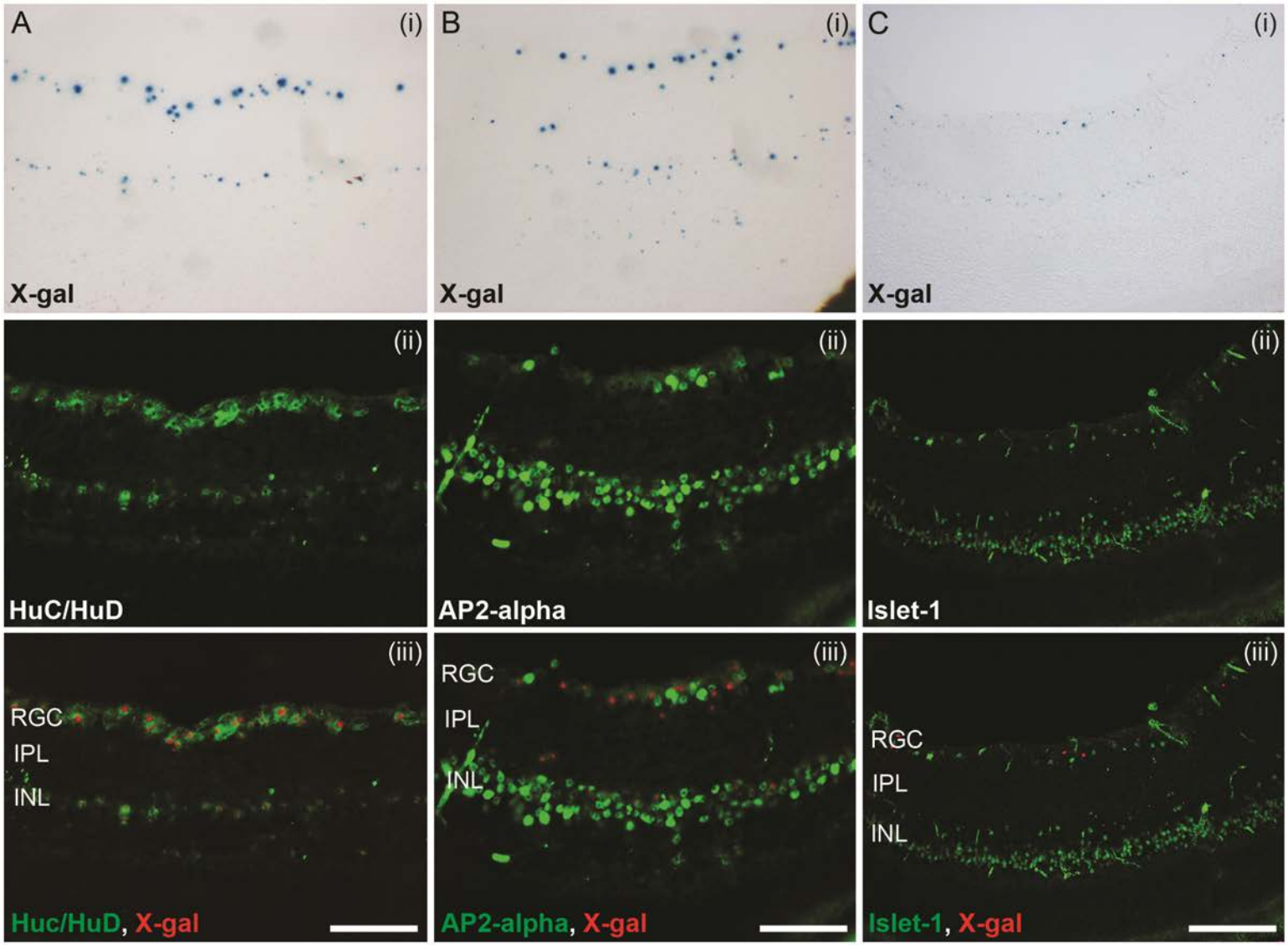

Figure 4.19: OMD is expressed in retinal ganglion cells, amacrines and displaced amacrines. Panels (i) represent X-gal staining, (ii) are specific antibody stainings using alexa-488 (green) as secondary, while in panels (iii) are the merged images with the X-gal signal coloured red. B-gal signal is co-localised with HuC/HuD-positive cells, indicating OMD expression in RGCs and amacrines (A). X-gal staining is also co-localised with AP2-α-positive cells indicating OMD expression in displaced amacrine cells in the RGC layer and in a sub-population of amacrine cells in the INL (B), while no signal is present in horizontal cells, marked with Islet-1 (C). Scale bars, 50μm for (A)-(B), 100μm for (C). RGC, retinal ganglion cells; IPL, inner plexiform layer; INL, inner nuclear layer.

4.2.5.3 OMD expression in the adult mouse brain

As described before, whole brains were isolated from adult *OMD*$^{+/LacZ}$ and *OMD*$^{+/+}$ littermates and were either whole-mount stained for X-gal, or processed for cryo-sectioning and subsequently stained. In the latter case, X-gal staining was performed in serial sections covering the whole brain from the olfactory lobes to the end of the cerebellum.

Starting with the whole-mount stained heterozygote sample, intense X-gal signal was observed in the whole cerebrum area, but not in the olfactory lobes, the cerebellum, the optic nerves (arrows) or the optic chiasm (arrowhead) (Fig. 4.20 A&B). Sagittaly cutting the brain in the middle of the left hemisphere revealed that all the areas of the cortex, the accessory olfactory bulb, the caudate putamen (striatum), the hippocampus and the hypothalamic areas were strongly stained, while less signal is present in the midbrain, the thalamic areas and the pons/medulla (Fig. 4.20C). No staining at all was seen the corpus callosum or the anterior commissure. Magnified views of the striatum and the hippocampus are shown in Figure 4.20 E and F respectively, demonstrating blue "spotty" staining all around the fibres of the internal capsule, whereas all the pyramidal neuronal areas together with the dentate gyrus were also positive for β-gal, and thus OMD. In addition, faint staining was observed around the main blood vessels (Fig. 4.20G) as well as in specific cells lining the cortex of the cerebellum (Fig. 4.20H). No background staining was seen in the wild type brain (Fig. 4.20D), indicating the specificity of the β-gal signal in the heterozygote animals.

All these areas were studied in more detail using cryo-sectioned *OMD*$^{+/LacZ}$ brains, and as expected blue "spotty" staining was seen in all the aforementioned areas. Firstly, β-galactosidase activity was observed in all the parts of the anterior olfactory area (dorsal, medial, lateral and ventral), the frontal association cortex, all the parts of the orbital cortex (dorsolateral, lateral, ventral and medial) and at the prelimbic cortex. Moving closer to the bregma, the positive staining continued throughout most of the regions of the brain, including the caudate putamen and all the areas of the cortex, but not the corpus callosum, the anterior commissure or the optic nerves (Fig. 4.21 A&E). In addition, β-gal signal was occasionally seen around the capillaries (Fig. 4.21, arrowheads). Moving further along the posterior axis and

after passing the bregma, β-gal activity, and thus OMD expression, is continued throughout the cerebral cortex, the striatum and the globus pallidus, around all the thalamic regions and also at the hippocampal region, as already shown. More specifically, all three fields of CA1, CA2 and CA3 pyramidal cell populations of the hippocampus as well as the dentate gyrus are expressing OMD (Fig. 4.21 B&D), while very modest signal can be observed in the choroid plexus (Fig. 4.21G). Lastly, in the cerebellum area there is distinct β-gal staining between the cerebellar commissure and the ansiform lobules, somewhere between the granular and the molecular layer, probably where the Purkinje cells reside (Fig 4.21 C&F).

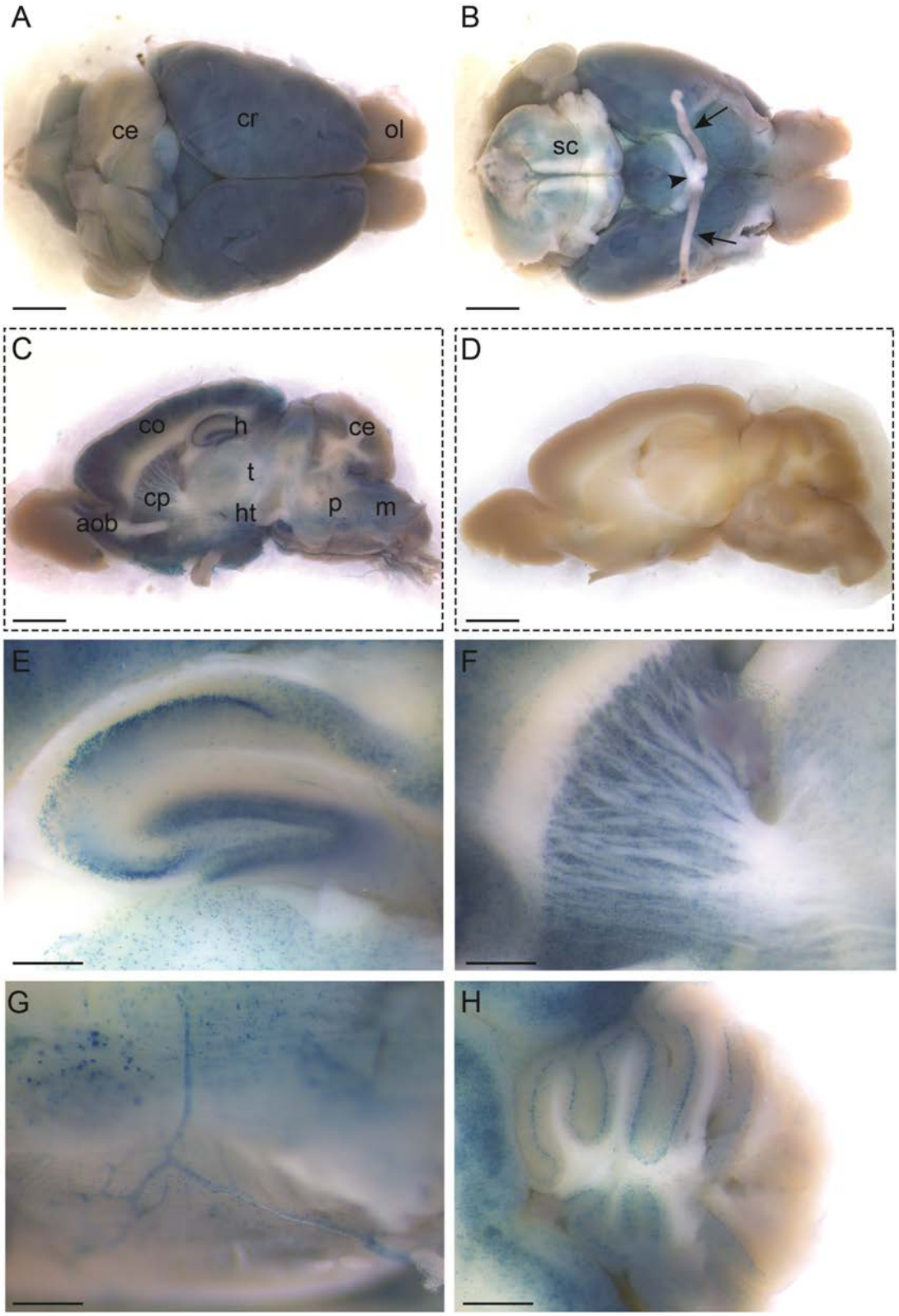

Figure 4.20: OMD expression in the adult mouse brain. Brains were isolated from *OMD*$^{+/+}$ and *OMD*$^{+/LacZ}$ animals and were whole-mount stained for X-gal. (A)-(B) Dorsal and ventral sides of the brain demonstrating Lac-Z activity in the whole cerebrum but not the optic verves (arrows) or the optic chiasm (arrowhead). Cutting the brain sagittaly revealed β-gal signal in all the internal areas, including the cortex, the hippocampus, the striatum and the thalamic areas (C), while no background staining is observed in the wild type sample (D). (E) & (F) Magnified views of the hippocampus and the striatum respectively. Faint β-gal signal can be seen occasionally in the ventricles (G), while in (H) X-gal staining in specific cells of the cerebellum is visible. Scale bars, 2mm for (A)-(D), 250μm for (E), 200μm for (F), 150μm for (G), 1mm for (H). cr, cerebrum; ce, cerebellum; ol, olfactory lobes; sc, spinal cord; co, cortex; cp, caudate putamen (striatum); aob, accessory olfactory bulb; h, hippocampus; t, thalamus; ht, hypothalamus; p, pons; m, medulla.

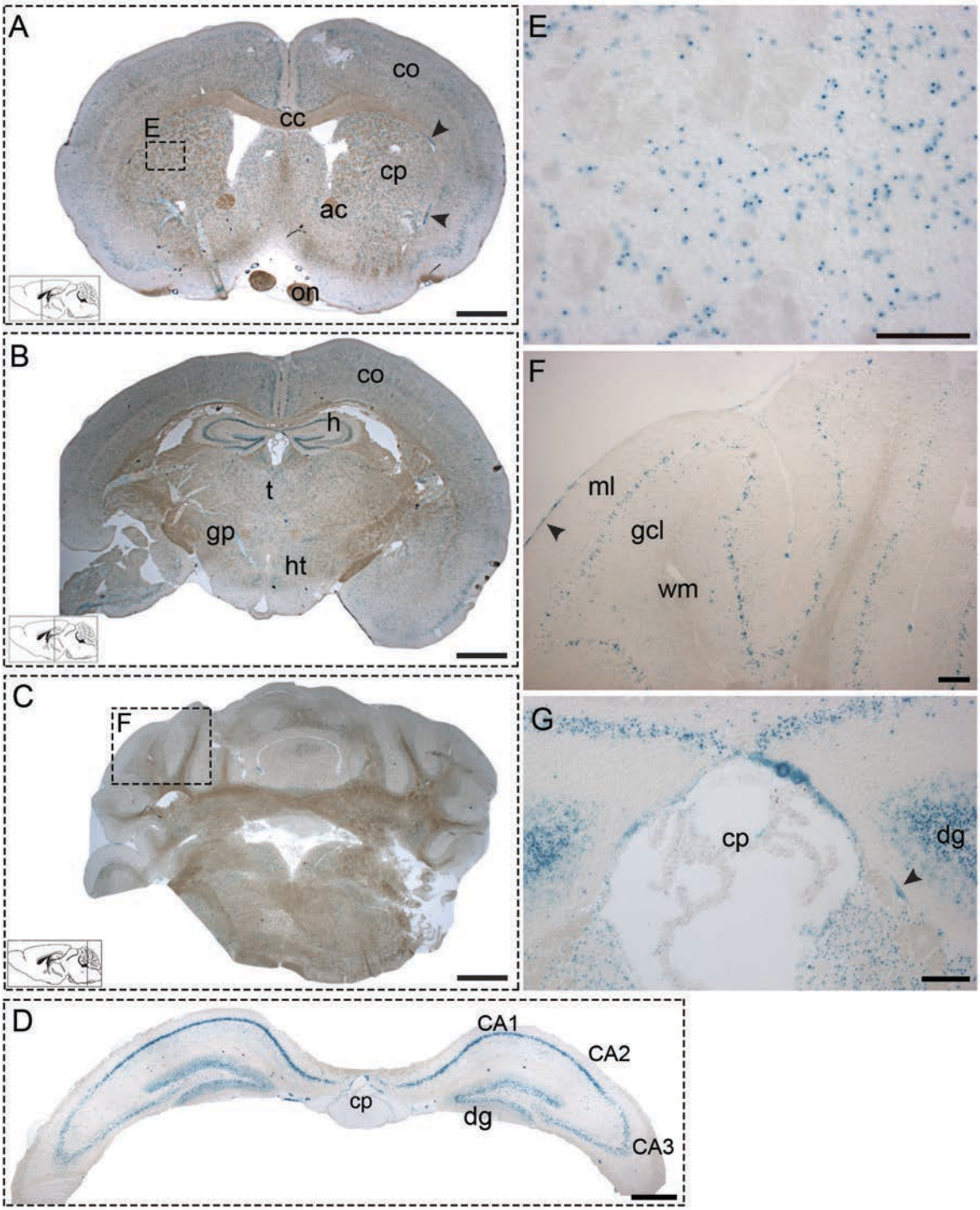

Figure 4.21: OMD expression in sections of the adult mouse brain. Brains from OMD heterozygous mice were cryo-sectioned and subsequently stained with X-gal. (A)-(C) Three different coronal planes demonstrating Lac-Z activity, and thus OMD expression, all around the cortex, striatum, hippocampus, thalamic areas and in the cerebellum. (D) Magnified view of the hippocampus showing Lac-Z activity in all the pyramidal cell populations and the dentate gyrus. B-gal signal as seen in the striatum area (E), in the cerebellum between the molecular and granular cell layer, where Purkinje cells are located (F), whereas faint staining is occasionally seen in the choroid plexus (G). Scale bars, 1mm for (A)-(C), 140μm for (D) and (F), 100μm for (E) and (G). co, cortex; cp, caudated putamen (striatum); cc, corpus callosum; ac, anterior commissure; on, optic nerve; h, hippocampus; t, thalamus; ht, hypothalamus; gp, globus pallidus; ml, molecular layer; gcl, granular cell layer; wm, white matter; cp, choroid plexus; dg, dentate gyrus; CA1/2/3, pyramidal cell populations of the CA1/2/3 fields.

As explained before, in order to identify the specific cell types where OMD is expressed, immunofluorescence against various mouse neural markers, following X-gal staining, was performed on *OMD*$^{+/LacZ}$ samples. The antibodies that were used included NeuN (a neuron-specific protein which is present in most CNS and PNS neuronal cell types), β-III Tubulin-neuronal (an antibody against beta III tubulin specific for neuronal cell types of the CNS/PNS), GFAP (Glial Fibrillary Acidic Protein-a marker for astrocytes) and calbindin (a marker for Purkinje cells). In Figure 4.22 co-localisation of OMD with NeuN-positive neurons is demonstrated in two different areas of the brain, i.e. the cortex and part of the hippocampus in panels A and B respectively. As also indicated by arrowheads, the spotty X-gal signal is always found within or in the periphery of NeuN positive cells, suggesting that OMD is largely expressed by neurons. Moreover, using the neuronal specific anti-β-III tubulin marker, we observe that, although the majority of OMD expressing cells are not positive for the marker, in certain areas (including parts of the hippocampus and the cortex) β-III tubulin neurons do express OMD (Fig. 4.23 panel A, hippocampus). In addition, as demonstrated in a higher magnification image (Fig. 4.23 panel B), β-signal appears to be systematically localised in the cytoplasm or around the nucleus of the expressing cell (arrowheads). Furthermore, regarding astrocytic populations, only few GFAP-positive cells co-expressed β-gal. However, as the X-gal staining is mostly found around the nuclei and not within neuronal dendrites or axons, it was quite difficult to identify the localisation of the signal in cells with neuronal processes, like astrocytes. An example is given in Figure 4.24A, where OMD expression is seen around a cell nucleus, which in this case probably belongs to the neighbouring GFAP positive astrocyte (arrowhead). Finally, in the cerebellum, OMD expression was confirmed in the Purkinje cell layer using the calbindin marker, whereas signal was also seen in the molecular layer, where it is either localised in Purkinje axons or is additionally expressed in nearby basket cells (Fig. 4.24B).

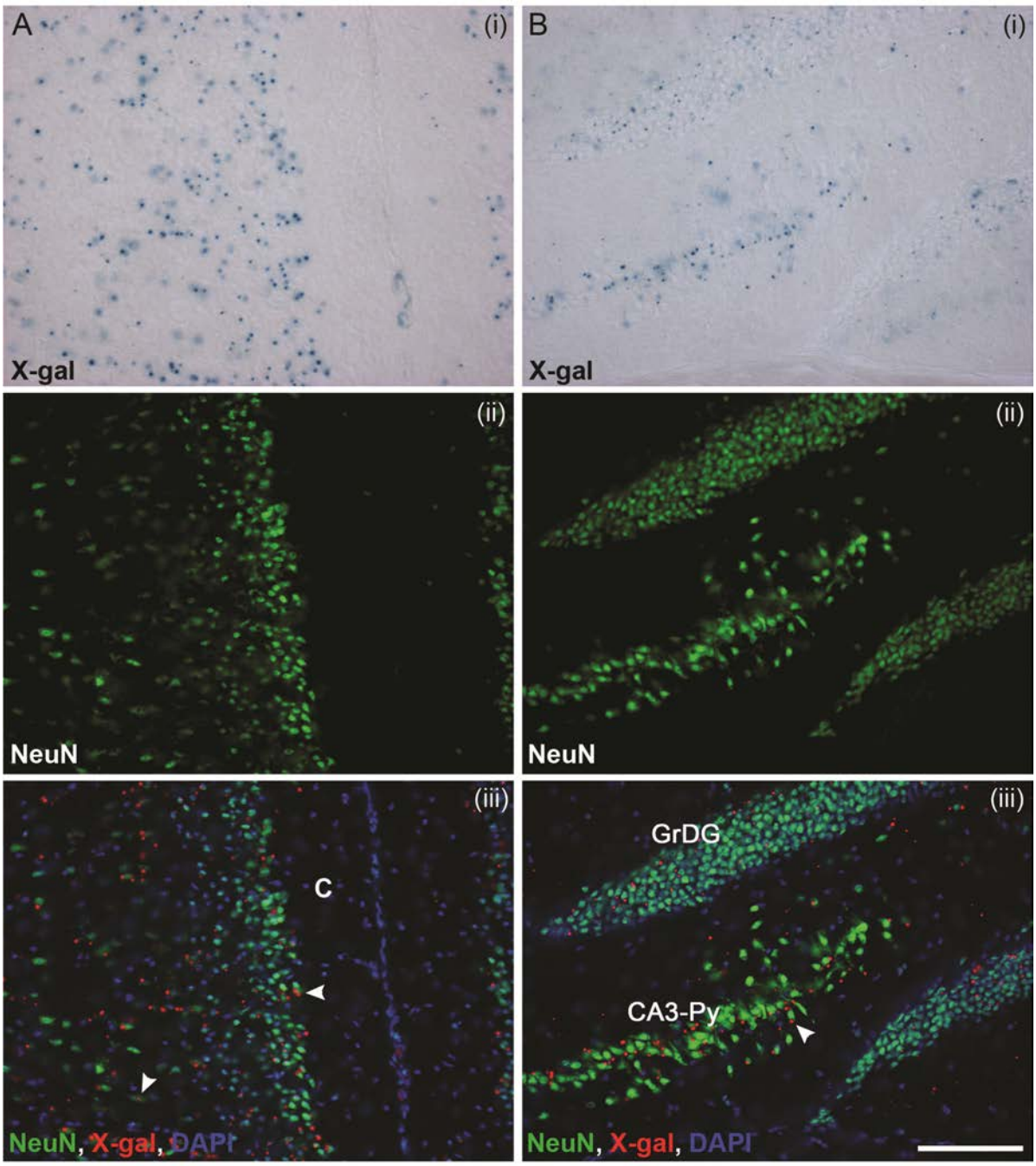

Figure 4.22: OMD is expressed in adult neurons. Panels (i) represent X-gal staining, (ii) are NeuN antibody staining using alexa-488 (green) as secondary, while in panels (iii) are the merged images with the X-gal signal coloured red and DAPI (blue) used as a nuclei stain. B-gal signal is co-localised with NeuN-positive neurons in the cortex (A) and in pyramidal cells of the hippocampus (B), as also noted with arrowheads. Scale bar, 100μm for all images. C, cortex; GrDG, granule dentate gyrus; CA3-Py, pyramidal cells of CA3 field.

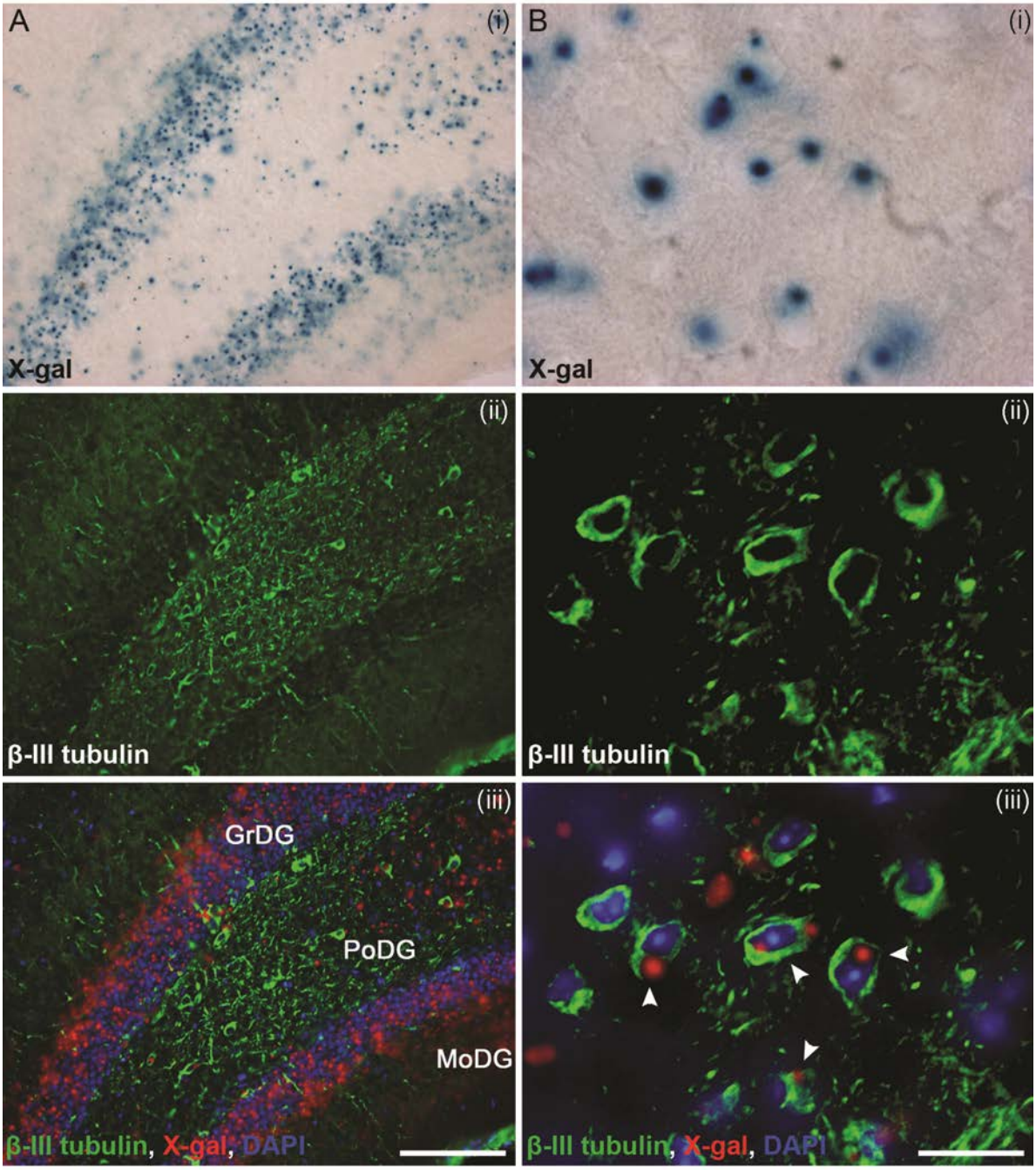

Figure 4.23: OMD is expressed in adult neurons (continued). Similarly to before, panels (i) represent X-gal staining, (ii) are β-III neuronal tubulin staining using alexa-488 (green) as secondary antibody, while in panels (iii) are the merged images with the X-gal signal coloured red and DAPI (blue) used as a nuclei stain. In (A) strong Lac-Z activity can be seen in the granule dentate gyrus (GrDG), where not many cells are positive for β-III tubulin. B-gal signal is also seen in polymorph cells (PoDG), where it is co-localised with β-III positive neurons, while more diffuse X-gal staining can be seen in the molecular layer (MoDG). (B) A magnified view of cells in the PoDG demonstrates X-gal staining (and therefore OMD expression) in β-III tubulin positive neurons, and specifically in the cytoplasm adjacent to the cell nuclei (arrows). Scale bars, 100μm for (A), 50μm for (B). GrDG, granule dentate gyrus; PoDG, polymorph dentate gyrus; MoDG, molecular dentate gyrus.

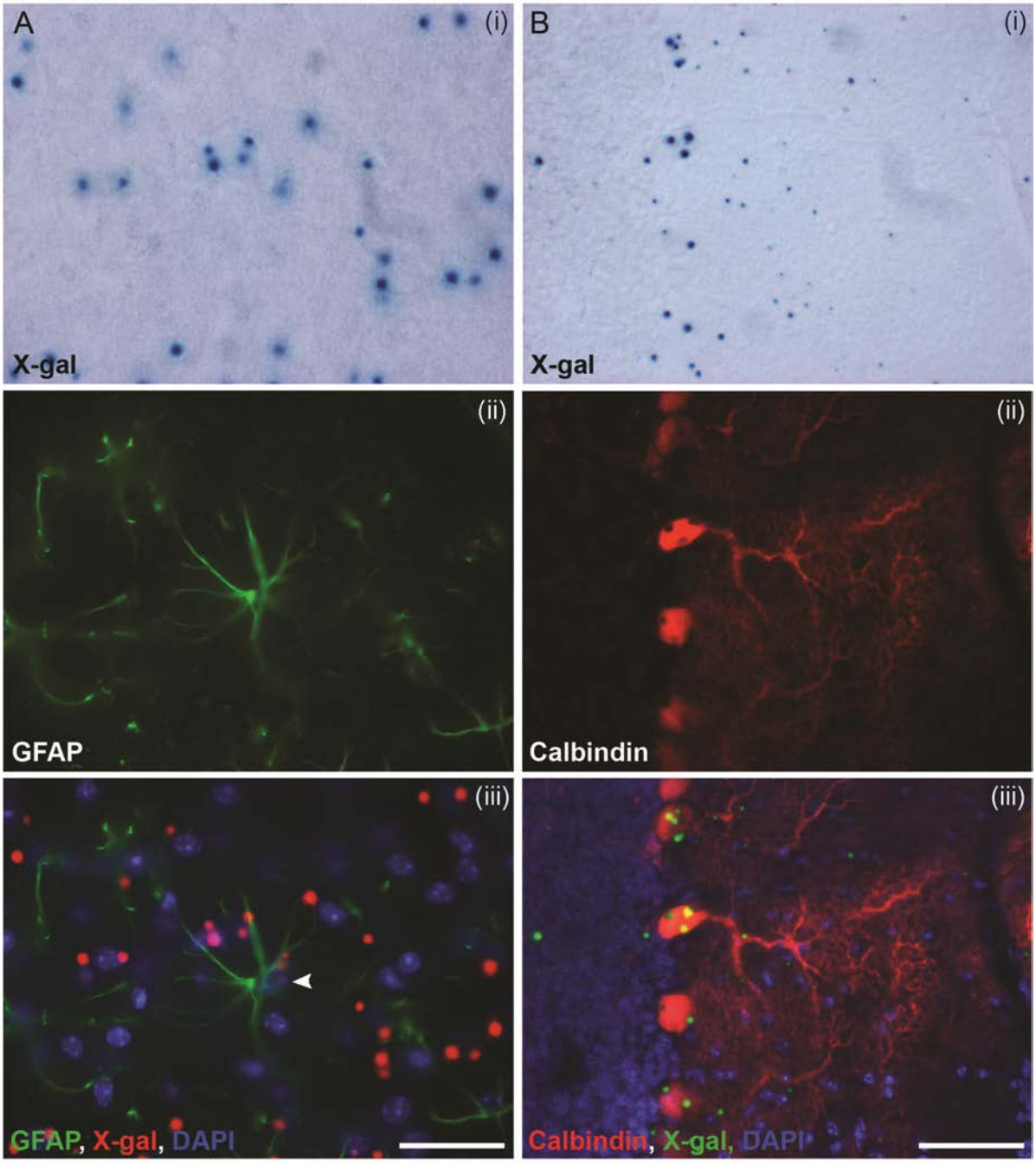

Figure 4.24: OMD is expressed in Purkinje cells and occasionally in astrocytes. (A) X-gal staining overlapped with anti-GFAP immunostaining (marking astrocytes), using an alexa-488 (green) as secondary and DAPI to stain the cell nuclei. As indicated by the arrowhead Lac-Z activity is occasionally seen in close vicinity of GFAP-positive cells, suggesting that it might be also expressed by these cells. (B) X-gal staining in the cerebellum overlapped with anti-Calbindin immunostaining (marking Purkinje cells), visualised with an alexa-546 (red) secondary antibody. In panel (iii) X-gal is coloured green and DAPI is used as nuclei stain. B-gal signal is localised within the soma of the Purkinje cells, while faint signal can be observed in either the Purkinje dendrites or in the adjacent basket cells. Scale bars, 50μm for all images.

4.2.5.4 OMD expression in the adult mouse bone

Evaluation of OMD expression in the adult bone was performed on the knee joint including part of the femur and the tibia. As mentioned before, X-gal activity was assessed through whole-mount staining of the tissue, followed by decalcification and cryo- or paraffin-sectioning. Sectioning and subsequent X-gal staining, that would give more accurate results, was not applicable in this case, as decalcification (which is necessary at this stage) would nullify the β-gal enzyme. Figure 4.25A is a representative image of an $OMD^{+/LacZ}$ knee joint, where X-gal staining can be generally seen in the periosteum, in articular cartilage of the femur and the patella, and in part of the meniscus. More specifically, in Figures 4.25 B&C we can observe strong OMD expression in the outermost layer of articular chondrocytes, while strong signal is also seen in the deposited osteoid matrix in the dorsal part of the femur as well as in the matrix/periosteum of the patella (arrows) and additionally in the tendon (arrowhead). Expression at the articular cartilage located at the centre of the joint is either not present or cannot be observed due to inadequate X-gal staining in deeper parts of the tissue, while another view of the positively stained cartilage including part of the femur and the meniscus is shown in panel E. Furthermore, intense staining is observed again in the cortical osteoid at the ventral side of the femur, suggesting OMD expression or deposition of the protein in the surrounding matrix by osteoblasts/osteocytes (Fig. 4.25D). In addition, in a magnified view of the cortical bone surrounding the bone marrow, clear OMD expression can be seen in the outer cortical layer (maybe the periosteum, arrow), but also within the matrix, where trapped osteoblasts (osteocytes) usually reside (arrowheads), further supporting expression of the protein by the latter cells. Interestingly, very faint "spotty" X-gal staining was also seen within the bone marrow (black arrowheads). Finally, in Figure 4.25G a section from an $OMD^{+/+}$ sample is presented, demonstrating minor background staining just below the chondrocytic growth plate (in detail in panel H), confirming the specificity of the β-gal signal under the OMD promoter in the current circumstances.

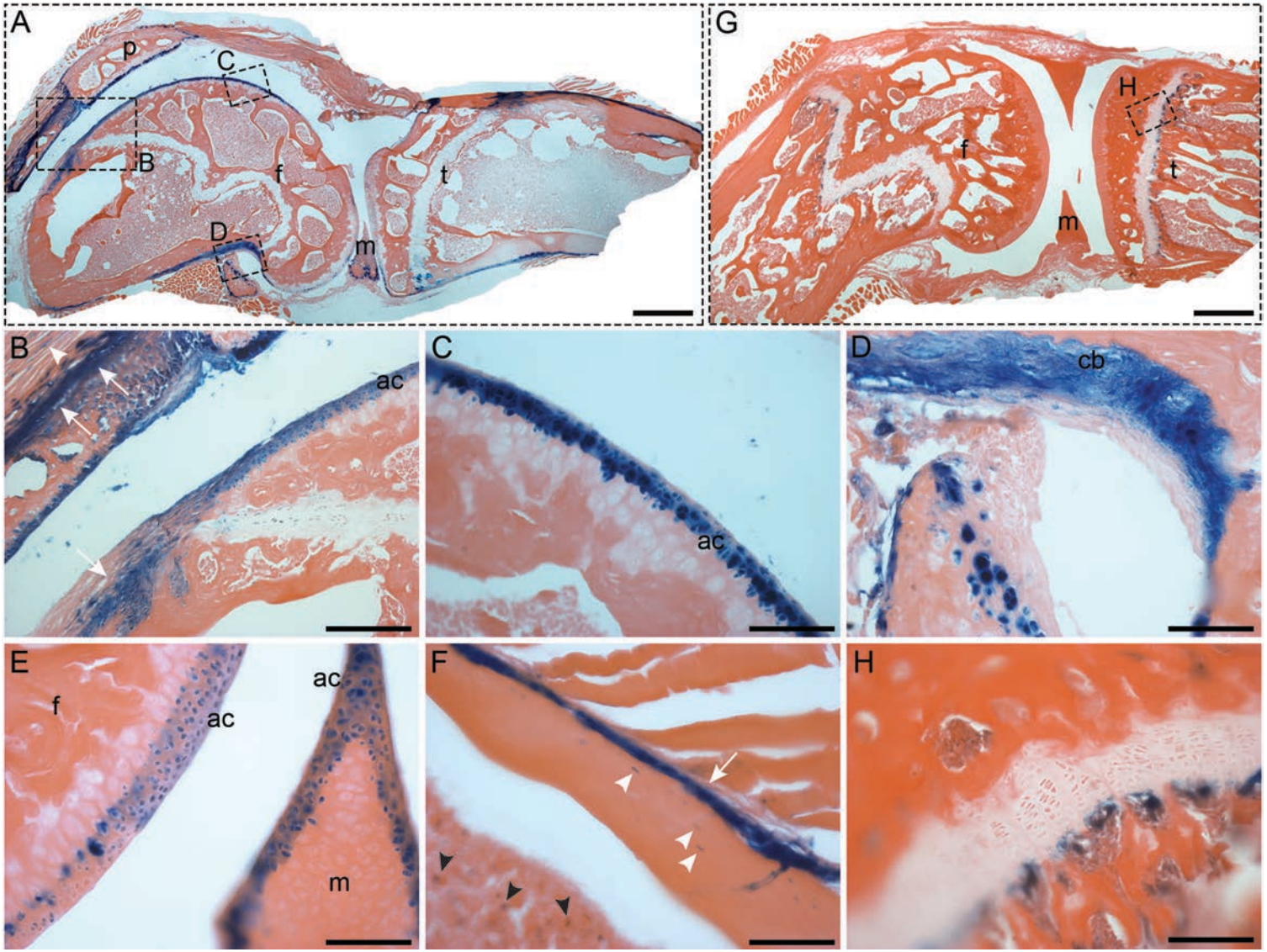

Figure 4.25: OMD expression in the adult bone. (A) X-gal stained knee joint from *OMD*$^{+/LacZ}$ animals demonstrating Lac-Z activity in the periosteum of the femur and tibia, and in articular cartilage. (B) B-gal signal can be seen in greater detail in the periosteum of the patella and within the osteoid matrix of the femur (arrows), but also in the patella tendon (arrowhead). Further signal in the articular cartilage is shown in (C) and (E), while OMD expression in the cortical bone (or periosteum) of the femur is also displayed in (D) and (F-arrow). Lac-Z activity is also seen in the trapped osteoblasts of the cortical bone (arrowheads), while faint signal can be observed in the bone marrow (black arrowheads), in (F). (G) & (H) Section of a wild type sample showing minor background staining just below the chondrocytic growth plate. Scale bars, 500µmfor (A), (G), 200µm for (B), 50µm for (F), 100µm for all the rest. f, femur; t, tibia; p, patella; m, meniscus; ac, articular cartilage; cb, cortical bone.

4.3 Discussion

In this part of the project the newly engineered OMD knock-out mice were used to characterise *OMD* expression during embryogenesis and in adult life. In this model, exons 2 and 3 (where the transcription domain is located) are replaced with a *Lac-Z* cassette, generating viable and fertile heterozygous ($OMD^{+/LacZ}$) and homozygous ($OMD^{LacZ/LacZ}$) mice, without any obvious congenital abnormalities during development or after birth. During development most of the Lac-Z activity was seen in craniofacial and skeletal tissues, in agreement with some of the previous studies showing OMD expression in bovine, rat and mouse bone (Petersson et al., 2003; Sommarin et al., 1998; Sugars et al., 2013). During adulthood Lac-Z activity remained present in the mature bone, but was also expanded to other tissues, such as bladder, eye and brain.

OMD expression during embryonic development is localised in the developing axial and appendicular skeleton

OMD expression was examined through whole-mount and whole-body section X-gal staining of embryos at stages E12.5, E15.5, E17.5 and new-borns (P0). Intensity of the staining was always higher in the $OMD^{LacZ/LacZ}$ than $OMD^{+/LacZ}$ animals, while no background staining was present in $OMD^{+/+}$ embryos, demonstrating the efficiency of the new mouse model. At the earliest stage (12.5 dpc) Lac-Z activity was limited in mesenchymal condensations of the developing mandible, while signal was also visible in the cartilage primordia of the front limbs in homozygote knock-out embryos (Fig. 4.2 & 4.3). The previous studies that have been published so far demonstrate OMD expression mainly in mature osteoblasts and do not include analysis at this early stage of mouse development. It is therefore noticeable that, OMD was found to be expressed in non-differentiated mesenchymal cells or pre-cartilage mesenchymal condensations, indicating a possible role the gene might play from the very early events of skeletogenesis.

In E15.5 embryos the development has progressed and osteogenesis has already initiated, with most of the long bones consisting of an avascular cartilage anlagen and pre-hypertrophic/hypertrophic chondrocytes in the diaphysis, while the perichondrium around that area becomes periosteum and cells start to differentiate

into osteoblasts (Gilbert SF, 2000). During this stage X-gal activity is seen in all the long bones, the digit tips, the ribs, the metacarpals/metatarsals and also the mandible/maxilla and the developing bones of the head (Fig. 4.4, 4.5, 4.7, 4.8). In sagittal sections of heterozygote embryos β-gal signal is specifically observed in the perichondrium/periosteum of long bones (such as radius, ulna, and femur, Fig. 4.8), suggesting expression of OMD in differentiating osteoblasts surrounding the primary ossification centre. These findings are in partial agreement with the recently published study on OMD expression during endochondral bone formation (Sugars et al., 2013). In this study, Sugars *et al*. focused on OMD expression in mouse metatarsal bones during stages E15, E18, P0, 5-days old and adult mice, where they showed expression within the primary ossification centre from stage E18 onwards, but not in E15 metatarsals. This can be attributed partly to the slightly earlier stage (E15 vs. E15.5), where the developing metatarsal is consisted still of only chondrocytes and mainly perichondrium and therefore, if no differentiating osteoblasts are present, OMD might not be expressed yet. In addition, in that study immunohistochemistry was performed using an anti-OMD antibody, which might not have been very efficient. During this project many anti-OMD antibodies were tested (Table 2.4) with either cell lysates of our over-expressing EJ28 cells or mouse tissues where we had confirmed expression through X-gal, and none of these antibodies showed a constant and specific signal. Finally, β-gal signal is also seen in some parts of the vertebral bodies, which at this stage are mostly consisting of chondrocytes (Fig. 4.8F), suggesting OMD expression in non-differentiated cartilage cells that are though probably committed to become osteoblasts.

Regarding expression in the cranio-facial tissues during this stage, X-gal activity was present in the forming intramembranous bones (frontal, parietal), the ossified regions of the mandible and maxilla, and also in chondrocytes of the nasal septum together with mesenchymal condensations of cells surrounding the latter area (Fig. 4.7). Again, there have been no studies describing OMD expression in the current context, with the exception of one paper by Nikdin *et al*. focusing in OMD expression during mouse tooth development and dentinogenesis during stages E15, 17, new-born and adult animals (Nikdin et al., 2012). In this study, OMD was detected by immunohistochemistry in the alveolar bone from E17 onwards, while no signal was seen in the tooth until dentinogenesis was well-established in P0 mice. In

agreement with these findings, we did not observe any β-gal signal at the early bell stage of the tooth in E15.5 mice, but we did see some expression in the surrounding bone, which again could be attributed to the slightly different stage and the method of detection.

X-gal staining persisted in the same pattern in E17.5 *OMD*$^{+/LacZ}$ embryos, where signal is seen again in all the long bones, the ribs, the vertebrae, the nasal septum and the alveolar bone in the head (Fig. 4.9 & 4.10). During this stage osteogenesis has advanced and the primary spongiosa is now properly formed, while osteoid matrix has been deposited in place of the hypertrophic chondrocytes. In the long bones, OMD expression is again evident in the periosteum, but with more specific localization now around the ossifying matrix (e.g. femur in Fig. 4.9 F-G), while smaller bones that have not advanced in the same stage yet (e.g. phalanges in Fig. 4.9 H-I-J) show strong staining in the perichondrium/periosteum surrounding the pre-apoptotic/apoptotic chondrocytes. It is noticeable that during this stage of development X-gal activity is observed in proliferating/mature chondrocytes of the vertebrae and occasionally in long bones (e.g. upper limb bone Fig. 4.9B and 4.9 D-E, J). While Sugars *et al*. also showed OMD expression in the endosteal surface and the deposited osteoid of the primary spongiosa in E18 metatarsals (Sugars et al., 2013), no localization of OMD was shown in any type of chondrocytes in previous studies.

Also, we can only assume the stage of chondrocytic maturation where β-gal signal is observed judging from the shape and size of the cells. It is known that during endochondral bone formation the epiphyseal growth plates are surrounded by chondrocytes divided into three distinct types/regions, including the proliferating/columnar cells (which are flattened and small), the mature/pre-hypertrophic (which are round and enlarged) and the hypertrophic/apoptotic (which become 5–12 times bigger and eventually die, triggering vascularisation and bone formation) (Kronenberg, 2003). Each chondrocyte, but also osteoblast, developmental stage is characterized by expression of specific genes, which include *Col2a1* (collagen 2) and *Acan* (aggrecan) for early chondrocytes; *Fgfr3* (fibroblast growth factor receptor 3) for columnar cells; *Ppr* (parathyroid hormone-related protein receptor), *Ihh* (Indian hedgehog), and *Col10a1* (collagen 10) for

prehypertrophic cells; *Mmp13* (matrix metalloproteinase 13) and *Bsp* (bone sialoprotein) for apoptotic chondrocytes and also mature osteoblasts, whereas early osteoblasts express *Osx* (Osterix) and *Col1a1* (collagen 1) (Dy et al., 2012; Lefebvre and Smits, 2005; Zuscik et al., 2008). Therefore, utilization of the above markers together with X-gal staining can define the exact cell types where OMD is expressed during endochondral bone formation as it progresses throughout the different developmental stages.

Lastly, β-gal expression remained through some chondrocytes of the nasal septum, while signal was also seen in the ossified regions of the mandible and maxilla, including the alveolar bone but not the developing teeth (Fig. 4.10) in line with previous findings (Nikdin et al., 2012). X-gal activity was not observed in any of the visceral organs (bladder, kidney, liver, etc.) or the eyes and brain during the three developmental stages that were examined, suggesting that OMD is not expressed in any pre-mature soft tissues, at least up to this developmental time point.

The expression pattern of five SLRPs (not including OMD or PRELP) was analysed by RNA *in situ* hybridisation at E14.5 mouse embryos by Wilda and colleagues (Wilda et al., 2000). At this stage (which is relatively close to E15.5), chondroadherin and fibromodulin are both expressed in the cartilaginous skeleton, lumican is lowly expressed in the nasal capsule and cartilaginous vertebrae, while decorin and biglycan show a more diffused expression pattern in connecting tissue derivatives, such as organ capsules, blood vessels walls, meninges and mesenchymal surroundings of skeletal structures (Wilda et al., 2000). Therefore, it is obvious that expression of SLPRs during development is quite variable, and although some proteins may share similar patters others are expressed in completely different tissues, indicating the multiple roles these molecules have even during early mouse development.

OMD expression in new-born mice persist mainly in the developing skeleton

In new-born $OMD^{+/LacZ}$ mice the X-gal activity was overall increased compared to the previous stages, indicating elevated OMD expression. In both the head and body β-gal signal is very strong in all the ossified regions, and specifically at the periosteum, but also within the deposited osteoid matrix (Fig. 4.11, 4.12, 4.13 and

4.14). This pattern suggests OMD expression in osteoblasts, in consonance with previous studies demonstrating osteoadherin expression in mouse tibia, bovine trabecular bone and in mouse osteoblast cell cultures (Rehn et al., 2008; Sommarin et al., 1998; Sugars et al., 2013; Wendel et al., 1998). Expression in chondrocytes can still be observed, but is now limited in the vertebrae, in some of the long bones depending on the cutting angle of the sample (e.g. Fig. 4.14D), in the nasal septum and also in the bones of the cranial base (hyoid, basisphenoid, exoccipital bones), which develop by endochondral ossification (Fig. 4.13). Similarly to before, X-gal activity seems to be present in the proliferating/mature chondrocytes, but staining with markers is needed to confirm this assumption. Overall, OMD expression seems to follow a specific pattern during endochondral osteogenesis, where expression starts in the perichondrium/periosteum surrounding the primary ossification centers, while at the same time expression is seen also in columnar chondrocytes surrounding the ossification groove. When ossification progresses, OMD is expressed additionally within the osteoid matrix.

Characteristic at this stage is also the strong X-gal activity observed in the developing teeth, including the top and bottom incisors, (Fig. 4.11 B & C respectively), as well as the top and bottom molars, which are currently at the bell stage (Fig. 4.12). Intense signal is seen in the dental pulp and also in the odontoblast layer, excluding though some polarized odontoblasts located under the secondary enamel knots and also the ameloblast cell layer (Fig. 4.12B). These findings are in opposition to previous studies showing OMD expression only in the pre-dentin/dentin phase and not in the pulp or the osteoblasts of P0 mice (Couble et al., 2004; Nikdin et al., 2012). These differences could be attributed to the different detection methods used. However, X-gal staining of $OMD^{+/LacZ}$ embryos was always consistent and very specific to the described areas and no activity was seen in any $OMD^{+/+}$ samples, indicating true and precise signal. In addition, the pre-dentin/dentin phase is still very thin in P0 mice and staining with H+E or specific markers is probably needed to differentiate between this area and the adjacent osteoblasts in our sections. Thus, we cannot exclude X-gal staining in the dentin layer under the current observations, but more focused study of the developing teeth is needed, including also later stages of development where the dentin gets thicker and enamel is also deposited. Another study by Lucchini *et al*. showed expression of

osteoadherin in human dental pulp and odontoblasts, while the same group had shown previously OMD expression in ameloblasts and odontoblasts of 19-day old rat embryos (Buchaille et al., 2000; Lucchini et al., 2004). Hence, OMD expression pattern in the developing tooth is quite variable, possibly owning to the efficacy of different antibodies or the detection of different forms of the protein, like the core protein versus different levels of glycosylated proteoglycan with added GAG chains.

Finally, no X-gal activity was observed in new-born heterozygote internal organs, although, as shown in Figure 4.14 A&B, it was technically difficult to study the viscera, as this part of the embryo body had the tendency to fall off the slide and was not stained properly. Thicker sections and increased fixation (which was avoided in order to keep the enzymatic activity of the β-galactosidase intact) might help solve this problem.

OMD is expressed in the adult mouse bladder, eye, brain and bone

Identifying OMD expression in the mouse bladder was of primary interest since this project was initially based on the lack of *OMD* and *PRELP* in human bladder cancer cells. Using our novel knock-out mice and through X-gal staining of $OMD^{+/LacZ}$ samples, OMD expression was defined in the adult mouse bladder. As discussed in the previous section, β-gal was not seen in any of the internal organs during mouse embryonic development, suggesting that OMD is mainly functioning in skeletogenesis in the course of embryonic growth. Interestingly, OMD expression expanded to several other organs during adulthood, including the bladder, the eye and the brain.

The mouse bladder is mainly composed of two distinct parts, the urothelium and the surrounding muscle layer; the urothelium in turn consists of three different cell layers, the basal, intermediate and the superficial umbrella cells (Birder and Andersson, 2013). X-gal activity of heterozygote $OMD^{+/LacZ}$ samples was observed in the surface of the umbrella cell layer (Fig. 4.15 C&D), while co-localisation of the β-gal signal with uroplakin and CK18, both specific markers for umbrella cells, confirmed this result (Fig. 4.16). Studies on SLRP expression in bladder are very limited, and mostly include decorin and biglycan. These two SLRPs were found to be expressed in the surface of umbrella cells in human bladders in a study conducted by

Hauser *et al*., while in another paper expression was seen in the interstitial area surrounding the muscle layer and not in the urothelium (Hauser et al., 2008; Maciejewski et al., 2012). Since the bladder urothelium is also densely coated with a layer of proteoglycans and glycoproteins referred to as the glycosaminoglycan (GAG) layer (Grist and Chakraborty, 1994), it is not surprising to find proteins that are characterised by chondroitin, keratan and dermatan sulphate side chains, like the SLRPs, in the umbrella cells. Furthermore, this GAG layer was proposed to play a major role in maintaining impermeability of the bladder urothelium and disruption of this layer is often seen in interstitial cystitis (IC) (Parsons et al., 2002), indicating a possible role that SLRPs and other proteoglycans might have in this environment. Lastly, a more recent study by Hurst *et al*. demonstrated a decrease of chondroitin sulphate in human IC bladders correlating with decreased ZO-1 staining (Hurst et al., 2007), showing a possible connection of proteoglycans and tight junction formation, which we already demonstrated in Chapter 3.

Expression of OMD in the mouse adult eye, through X-gal staining, was observed in the retinal ganglion cell layer (RGC), in part of the inner nuclear layer (INL) and in the non-pigmented epithelial cells of the ciliary body (CB) (Fig. 4.17). Immunostaining with specific retinal markers like Pax6, HuC/HuD, AP2-alpha and Islet-1 confirmed β-gal signal in the RGCs, in a sub-population of amacrines in the INL/displaced amacrines in the RGC layer, and in the epithelium of the CB (Fig. 4.18 & 4.19). Six other SLRPs have been found to be expressed in the mouse eye, including keratocan in mouse/chick cornea (Conrad and Conrad, 2003); fibromodulin and decorin in the mouse adult retina (Ali et al., 2011); opticin in the human and mouse eye, specifically in the vitreous and the non-pigmented CB (Ramesh et al., 2004; Takanosu et al., 2001), lumican in mouse corneal stroma (Ying et al., 1997) and tsukushi (TSK) in the lens epithelium and CB (Ohta et al., 2011). SLRPs that are localised in the cornea are considered to play key roles in modulating hydration of the corneal stroma and regulate corneal transparency, while for those localised in the retina it has been suggested that they can contribute to retinal cell differentiation and survival (Ali et al., 2011; Liu et al., 2003). In addition, TSK affects peripheral eye development through regulation of Wnt2b signaling in the CB area (Ohta et al., 2011). It is therefore obvious that SLRPs affect eye formation and function in

various ways. Expression of OMD in both the mouse retina and CB suggests it may have multiple roles in mouse eye biology.

X-gal staining of the heterozygote adult mouse brain revealed wide OMD expression in almost the whole brain with the exception of few areas like the olfactory bulbs, the corpus callosum and the optic nerves. All the other areas, including cortex, caudate putamen, hippocampus, choroid plexus, hypothalamic areas, cerebellum and pons were stained positively for Lac-Z activity, while there was no staining in the wild type samples indicating the specificity of the β-gal signal (Fig. 4.20 & 4.21). Moreover, double staining with X-gal and several different neuronal and glial markers showed widespread localisation of the β-gal signal in neurons, Purkinje cells and probably a sub-population of astrocytes (Fig. 4.22, 4.23 and 4.24). The above novel findings suggest that OMD must play a crucial role in neuronal cell functions or signaling. To date, involvement of SLRPs in brain biology is very narrow and few studies have been published on this subject. Two of these studies involve tsukushi, demonstrating TSK expression in the sub-ventricular zone of the adult mouse brain, while TSK null mice fail to form the anterior commissure (Hossain et al., 2013; Ito et al., 2010). Another two studies assessed the expression of SLRPs in the rat anterior pituitary gland and showed that decorin, biglycan, fibromodulin, lumican, PRELP and also OMD are all expressed in this area, where some of them are specifically localised in folliculostelate cells and pericytes (Horiguchi et al., 2013; Syaidah et al., 2013). Lastly, decorin was also found to be expressed in many areas of the brain in P21 young rats, including the neocortex, hippocampus, thalamus, choroid plexus and blood vessels (Kappler et al., 1998). Thus, many SLPRs are quite likely to have variable expression patterns in the murine brain and could play multiple roles in the neural environment, a field that is unfortunately highly under-studied so far.

Finally, OMD expression was assessed in the adult bone, in the area of the knee joint including part of the femur and tibia. Lac-Z activity was observed in the periosteum and the cortical bone, while osteoblasts trapped in the bone matrix were also positive (Fig. 4.25F). These findings are in agreement with previous studies showing consistent OMD expression in mouse and bovine bones and osteoblasts (Ninomiya et al., 2007; Sommarin et al., 1998; Sugars et al., 2013; Wendel et al.,

1998), indicating the role OMD has in bone matrix mineralisation. Lac-Z activity was also seen in the articular chondrocytes of the femur and also the meniscus, whereas no staining was seen in any of the chondrocytes in the epiphyseal plate (Fig. 4.25A, B, C & E). We therefore observe a shift of OMD expression from the proliferating chondrocytes in the developing embryo and new-born to only articular cartilage in the adult mouse. Also, this is the first time OMD expression has been reported in any kind of cartilage in the mouse. Finally, Lac-Z activity was not seen in the trabecular bone. However, the staining method has to be taken into consideration here, since whole-mount X-gal staining before sectioning may lead to partial and insufficient colouration of all parts of the tissue.

Summary

In summary, OMD is expressed in all the skeletal elements during mouse embryonic development and this expression is maintained in the adult bone. Expression appears to be localised in different cells, including chondrocytes and mesenchyme, but is mostly seen in osteoblasts, indicating its role in matrix mineralisation. OMD is also expressed in the mouse adult bladder, eye and brain, suggesting multiple and probably different roles in every organ.

Chapter 5

Expression patterns of the *PRELP* gene in mouse

5.1 Introduction

PRELP (proline, arginine-rich end leucine-rich repeat proteoglycan) is an extracellular matrix leucine-rich repeat protein, which belongs to class II of the SLRP family. PRELP is the only member of this family with a basic amino-terminal region that contains a high number of proline and arginine residues, while this domain has been shown to bind heparin and heparan sulfate (Bengtsson et al., 2000; Bengtsson et al., 1995). In addition, PRELP binds perlecan (a basement membrane heparin sulfate proteoglycan) and also collagen types I and II through its LRR domain (Bengtsson et al., 2002). Based on its extracellular localization and its interaction with the above factors, PRELP was proposed to function as a link between cells and ECM, but also as a molecule anchoring basement membranes to the underlying connective tissue (Bengtsson et al., 2000; Bengtsson et al., 2002).

PRELP was firstly isolated as a component of bovine articular cartilage with a molecular mass of 58 kDa, while radioimmunoassays demonstrated its presence in other bovine tissues as well, including kidney, sclera, liver, skeletal muscle, cornea, skin, and tendon (Heinegard et al., 1986). Grover et al. demonstrated PRELP expression in human adult, but not fetal, cartilage and meniscus (Grover et al., 1995). The same group found later, by immunohistochemistry and *in situ* hybridization, that PRELP is widely expressed in the mouse skeletal cartilage during development, whereas in adults the expression becomes more pronounced in the growth plates rather than the articular surface of the joints, in contrast to the human expression pattern (Grover and Roughley, 2001). Furthermore, Lui *et al*. demonstrated that PRELP is specifically expressed in proliferating chondrocytes of the adult rat tibia, while high PRELP expression was also found in human chondrocytes and intraarticular mesenchymal stem cells (Lui et al., 2010; Segawa et al., 2009). Lastly, apart from skeletal elements, PRELP was also found to be expressed in the human sclera, together with other SLRPs, where it was suggested as a possible candidate in regulating the biomechanical properties of scleral extracellular matrix (Johnson et al., 2006).

Although the exact biological functions of PRELP have not been elucidated yet, there are some studies showing involvement of this SLRP in pathological conditions. For instance, PRELP deficiency may account for Hutchinson-Gilford

progeria, which is characterized by the lack of collagen binding in basement membranes and cartilage (Lewis, 2003). Moreover, overexpression of PRELP in transgenic mice resulted in structural changes in the skin, accompanied by a decrease in collagen fiber bundles, and the hypodermal fat layer, suggesting interaction of PRELP with fibroblasts, adipocytes and the ECM components (Grover et al., 2007). On a different course, PRELP has been shown to inhibit the formation of the complement membrane attack complex (MAC), thereby limiting pathological complement activation in inflammatory diseases such as rheumatoid arthritis (RA) (Happonen et al., 2012; Happonen et al., 2009). Recently, PRELP-mediated inhibition of the MAC complex was successfully employed in adeno-associated virus gene therapy of an *in vivo* mouse model of wet age-related macular degeneration (AMD) (Birke et al., 2014). Complement inhibition has also been proposed as a new concept for cancer treatment, so this might constitute another possible mechanism through which PRELP could affect tumour growth (Pio et al., 2013). Finally, two studies by Rucci *et al*. demonstrated the ability of the heparan-binding domain of PRELP (^{hbd}PRELP) to impair osteoclastogenesis via cell type-specific NF-κB inhibition, resulting in the prevention and cure of both osteoporosis and breast cancer osteolytic metastases in a variety of preclinical *in vivo* models (Rucci et al., 2013; Rucci et al., 2009), highlighting the therapeutic potential of PRELP in various pathological conditions.

In *vivo* knock-out models are very important as they provide essential information on the functional roles of genes. However, no knock-out murine models for PRELP have been established to date. In collaboration with Takeda Pharmaceutical Company, we have generated the first PRELP KO mouse model, where, similarly to the OMD model, the coding sequence of the *PRELP* gene has been replaced with a Lac-Z reporter cassette so that transcription under the PRELP promoter leads to β-gal expression instead of PRELP. Since the expression patterns of PRELP have only been roughly studied in mice, the primary aim of this chapter is to examine in detail the temporal and spatial expression of PRELP during embryonic development and in adult life. Similarly to OMD, this is achieved through X-gal staining of heterozygote $PRELP^{+/LacZ}$ animals, while the effect of PRELP depletion is analysed in the next chapter.

5.2 Results

PRELP knock-out mice were constructed in Takeda with a similar strategy as the *OMD* knock-out model, where exons 2&3 (where the transcription domain is located) were replaced with a Lac-Z reporter gene. After receiving founders of the transgenic mice, our mouse colony was established through heterozygote-pair breeding as $PRELP^{+/lacZ}$ animals were fertile and produced litters containing all three genotypes. Heterozygote and knock-out animals grew normally into adulthood, while no apparent phenotypic differences could be seen during expansion of the colony. In Figure 5.1A a simple schematic of the *PRELP* gene locus and the position of the reporter gene are shown, while Figure 5.1B demonstrates the result of an example genotyping set.

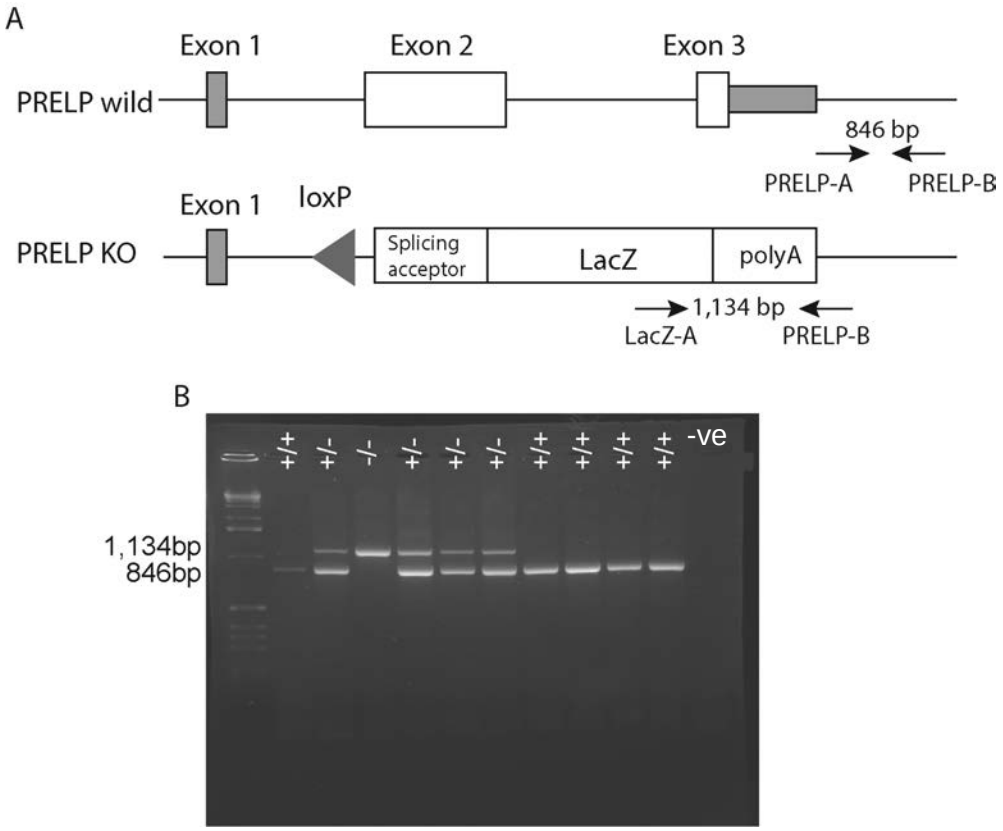

Figure 5.1: Knock-out strategy and genotyping of PRELP mice. (A) Schematic drawing of the *PRELP* gene locus and the Lac-Z insertion site together with the primer pairs used for genotyping. (B) An exemplar agarose gel from a genotyping set demonstrating the bands corresponding to the different genotypes.

PRELP protein expression – similarly to OMD – was examined through X-gal staining of mouse embryos during 3 developmental stages (12.5dpc, 15.5dpc and 17.5dpc), where expression was mostly seen in the developing cartilaginous skeleton and partly in the early developing brain, and also at day of birth (P0) where it was mainly localised in cartilaginous tissues. Interestingly, during adulthood (again similarly to *OMD*) this expression pattern appeared to be expanding to many internal organs, including specific areas of the brain, bladder and eye. Detailed analyses of the gene expression in every developmental stage and in several organs will be presented and discussed below.

5.2.1 PRELP expression in E12.5 embryos

Embryos were collected at 12.5dpc after arranged time-matings and litters were whole-mount stained for β-galactosidase. $PRELP^{+/+}$ embryos had no staining at all, while $PRELP^{+/LacZ}$ and $PRELP^{LacZ/LacZ}$ embryos showed staining in the forebrain, interestingly in a symmetrical pattern of two lines starting from the anterior part of the forebrain and extending towards the midbrain; the hindbrain, the developing somites and the chondrocytic condensations of the developing limbs (Fig. 5.2). In knock-out litter-mates expression pattern was exactly the same as seen in heterozygotes but with more intense staining, and long-bone cartilage primordia of the hindlimb were stained in addition to the frontlimb. After tissue-clearing the already X-gal stained embryos, all the stained areas can be seen more accurately (Fig. 5.3). In particular, we can see that the two lines of PRELP-positive cells in the head are indeed part of the forebrain; the neural tube and the notochord are both also stained, while in the hindbrain it appears that the 4th ventricle roofplate has the most intense signal. Looking closer at the hindbrain area we can see β-gal signal at the midbrain/hindbrain boundary, probably co-localised with the expression domains of *Wnt1* and *Fgf8* where, together with the floorplate, the isthmic organizer is located (Fig. 5.3C, arrows).

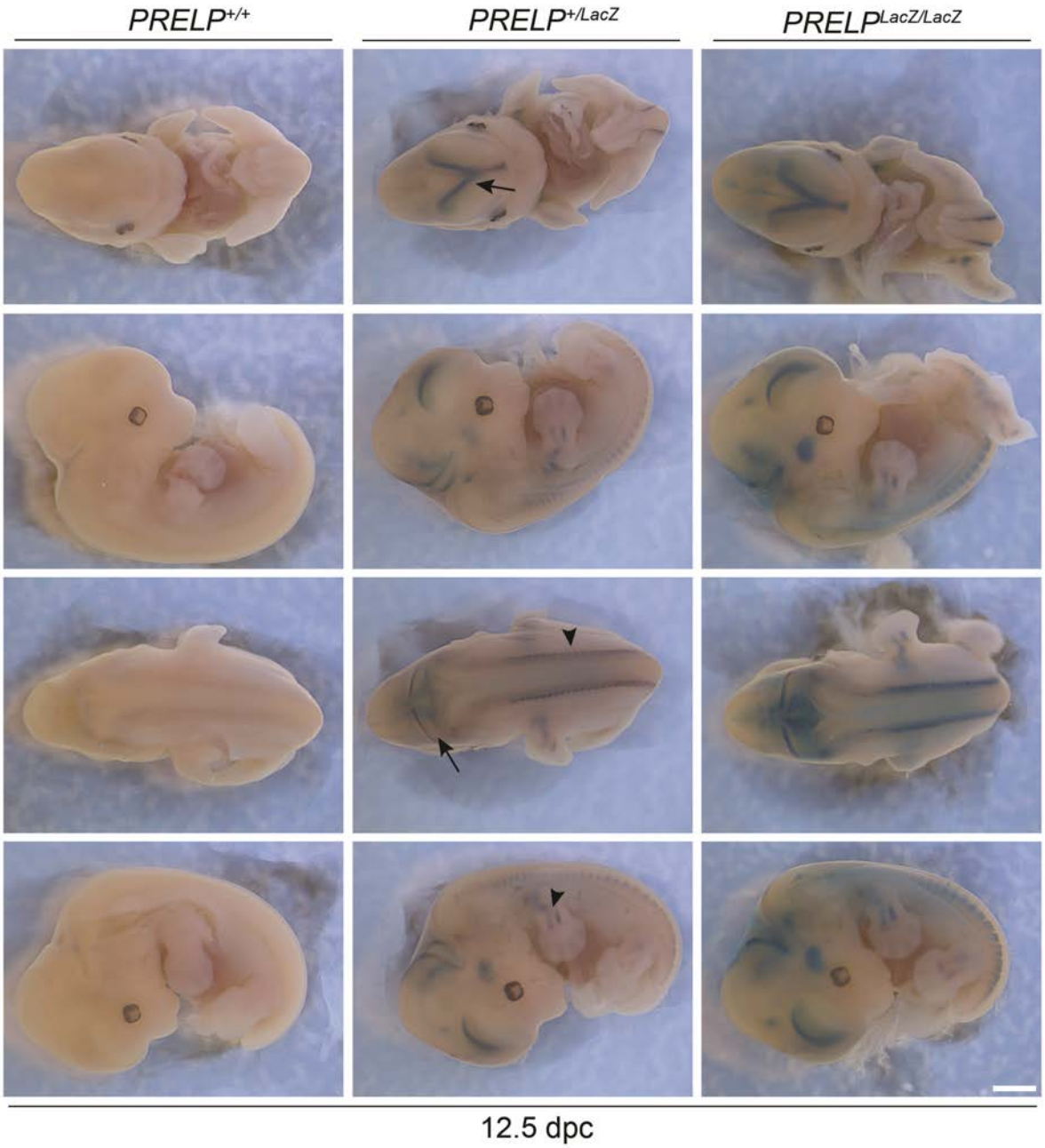

Figure 5.2: PRELP expression in E12.5 transgenic embryos. Whole-mount X-gal staining of PRELP 12.5 dpc litters. Lac-Z activity is seen in the *PRELP*$^{+/LacZ}$ and *PRELP*$^{LacZ/LacZ}$ embryos in two symmetrical lines starting from the anterior part of the brain and extending towards the midbrain, and also in the hindbrain around the 4th ventricle roofplate area (arrows). B-gal signal can be also observed in the developing limbs and in the somites (arrowheads). Scale bar, 1mm for all images.

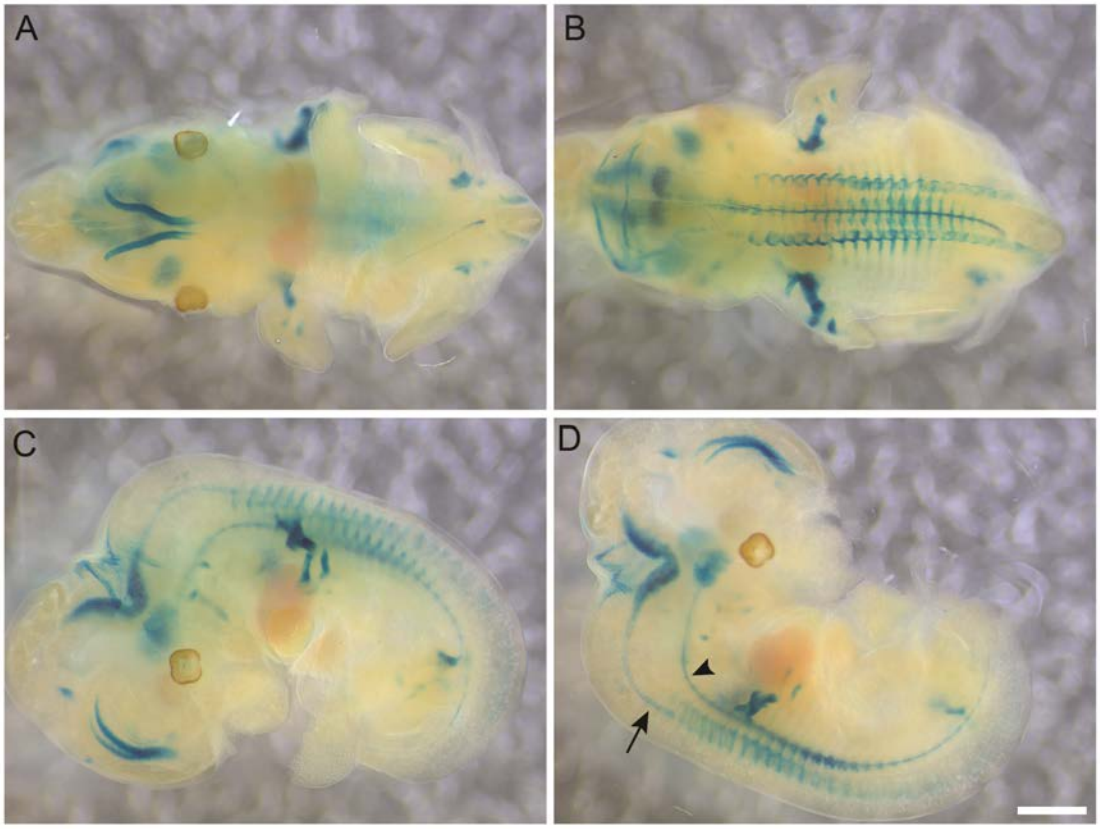

Figure 5.3: PRELP expression in cleared X-gal stained *PRELP*$^{+/LacZ}$ E12.5 embryos. Embryos were cleared after being whole-mount stained for X-gal. Lac-Z activity can be seen in the forebrain and hindbrain, the somites, the neural tube (Leatherbarrow et al.) and the notochord (arrowhead), and also in the developing limbs. Scale bar, 1mm for all images.

Sectioning of stained *PRELP*$^{+/LacZ}$ embryos was performed separately for head and body in the coronal direction and in whole embryos in sagittal direction (Fig. 5.4). In sections of the head the β-gal signal found in the forebrain appeared to be confined in the hippocampal allocortex and specifically in the cortical hem just above the developing choroid plexus (Fig. 5.4 A-C, arrowheads). However, the strong signal seen in the hindbrain of the whole-mount stained embryos is not that visible upon sectioning. As shown in Figure 5.4D, only faint signal is seen in the dorsal area of the 4th ventricle, maybe in the cerebellum ventricular zone (Fig 5.4D, arrow). In addition, in sagittal sections of the whole embryo faint staining is visible in the chondrocytic condensations of the forelimb (Fig. 5.4F), while we can also see signal in the notochord (Fig. 5.4G).

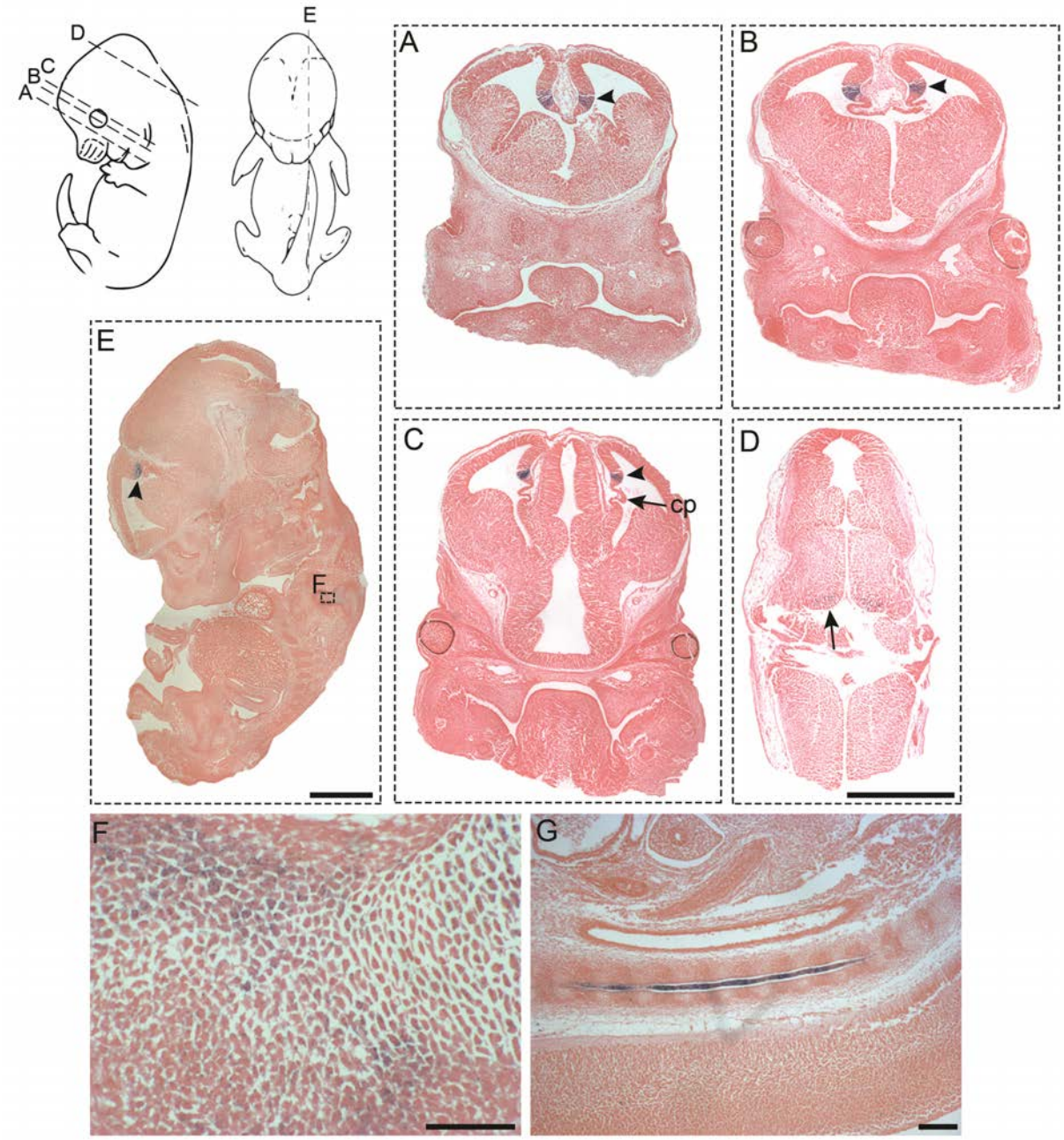

Figure 5.4: PRELP expression in sections of an X-gal stained *PRELP*$^{+/LacZ}$ E12.5 embryo. (A)-(D) Four different coronal planes of the embryonic head demonstrating Lac-Z activity in the area of the hippocampal allocortex and specifically in the cortical hem(arrowheads), just above the developing choroid plexus (marked with an arrow); cp, choroid plexus. The same area can be seen in a sagittal section of the whole embryo (E, arrowhead), while only faint signal is seen the hindbrain upon sectioning, which is localised in the dorsal area of the 4th ventricle (D, arrow). (F) Enlarged view of the developing forelimb showing β-gal signal in chondrocytic condensations. (G) Lac-Z activity can be seen in the notochord of sagittaly sectioned embryos. Scale bars, 1mm for (A)-(E), 100μm for (F), 140μm for (G).

5.2.2 PRELP expression in E15.5 embryos

Embryos were again collected at 15.5dpc after time-matings and the whole litter was stained for β-galactosidase overnight. Wild type embryos had no staining, while heterozygotes and knock-outs were both stained in some areas of the head but mostly in the developing skeleton (Fig. 5.5). Also, the intensity of the staining was much stronger in $PRELP^{LacZ/LacZ}$ compared to $PRELP^{+/LacZ}$ animals, as expected. As demonstrated in Figure 5.5, Lac-Z activity can be seen in the snout, in what probably is the nose cartilage, and in the back of the head in the whole area surrounding the future parietal and occipital bones, while in knock-out embryos (where the signal is stronger) faint staining can also been seen in the midbrain area. Furthermore, regarding the axial skeleton, β-gal activity can be seen in the developing vertebrae, the long bones of hands and legs, as well as in the cartilaginous formations of the digits including the metacarpals and phalanges of the forelimb and hindlimb. An enlarged view of the limbs showing the area in greater detail can be seen in Figure 5.6A. In addition, the ribs and the sternum are also positive for β-gal and thus PRELP (Fig. 5.5).

Similar to before, tissue clearing was performed in order to visualize the stained areas in greater detail. In Figure 5.6 B-D a cleared $PRELP^{LacZ/LacZ}$ embryo is presented, where it is visible that PRELP is expressed in the cartilaginous parts of the developing long bones, whereas it is absent from the center of the bones where the primary ossification center is localised. This is more obvious when looking at the forelimb, i.e. radius and ulna, together with the humerus and scapula (Fig 4.6D, arrows). Moreover, looking closer at the ribs we can see that the area adjacent to the vertebral column, where ossification firstly takes place, is not positive for PRELP, while the distant cartilaginous parts are expressing PRELP. In addition, apart from the nasal capsule some signal is also seen in the mandible area, probably in the forming lower jaw or in Meckel's cartilage (Fig 4.6B). Thus, it appears that PRELP expression is mostly confined to the cartilaginous elements of the growing axial and appendicular skeleton.

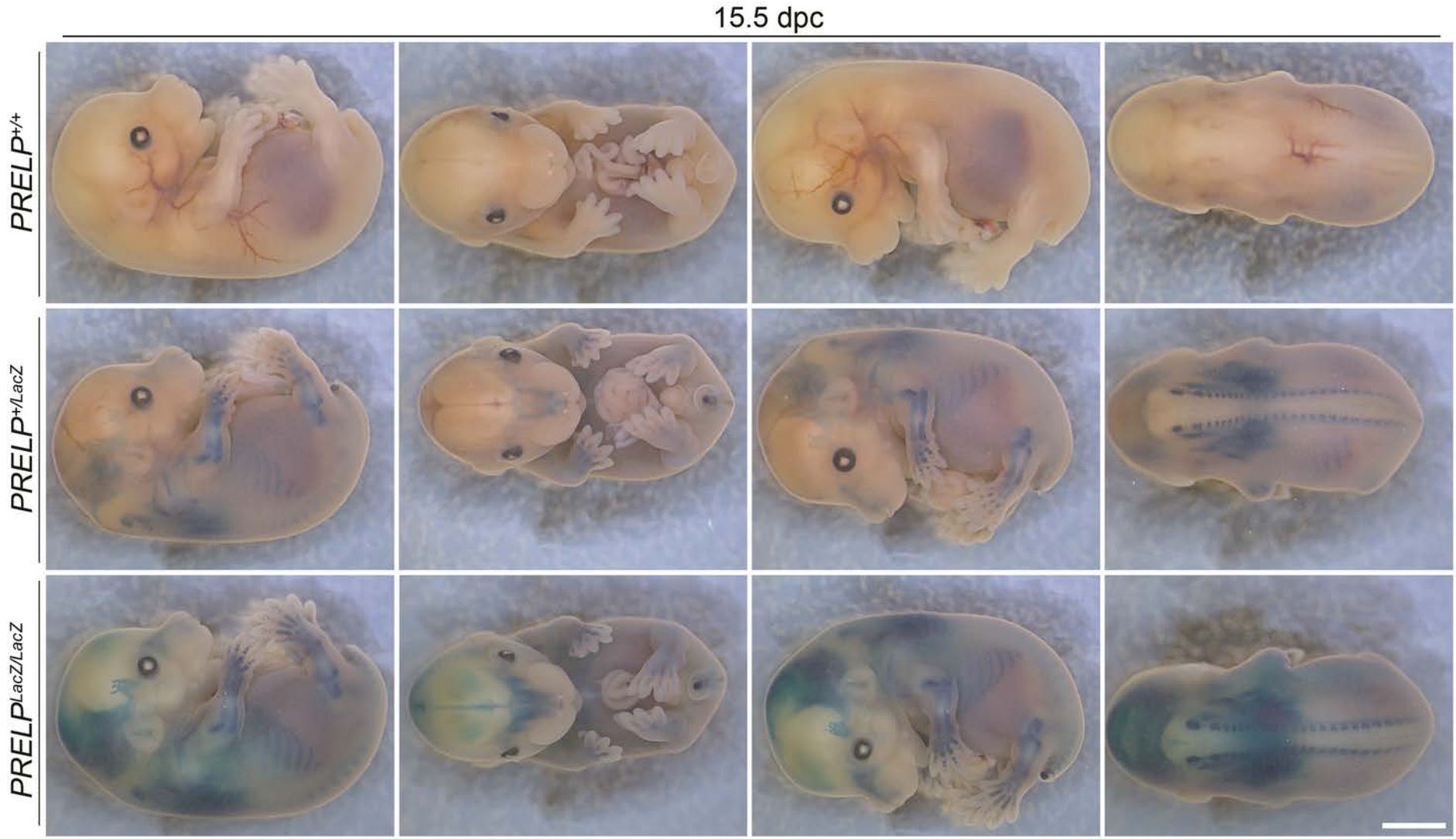

Figure 5.5: PRELP expression in E15.5 embryos. Whole mount X-gal staining of wild type, heterozygous and homozygous knock-out embryos demonstrating Lac-Z activity in the developing skeleton, and specifically in the ribs, the long bones of the limbs, the phalanges and metatarsals/metacarpals, and the vertebrae. In the head, staining can be seen in the nasal area and also in the back of the head. No background signal is seen in the wild type embryos. Scale bar, 2mm for all images.

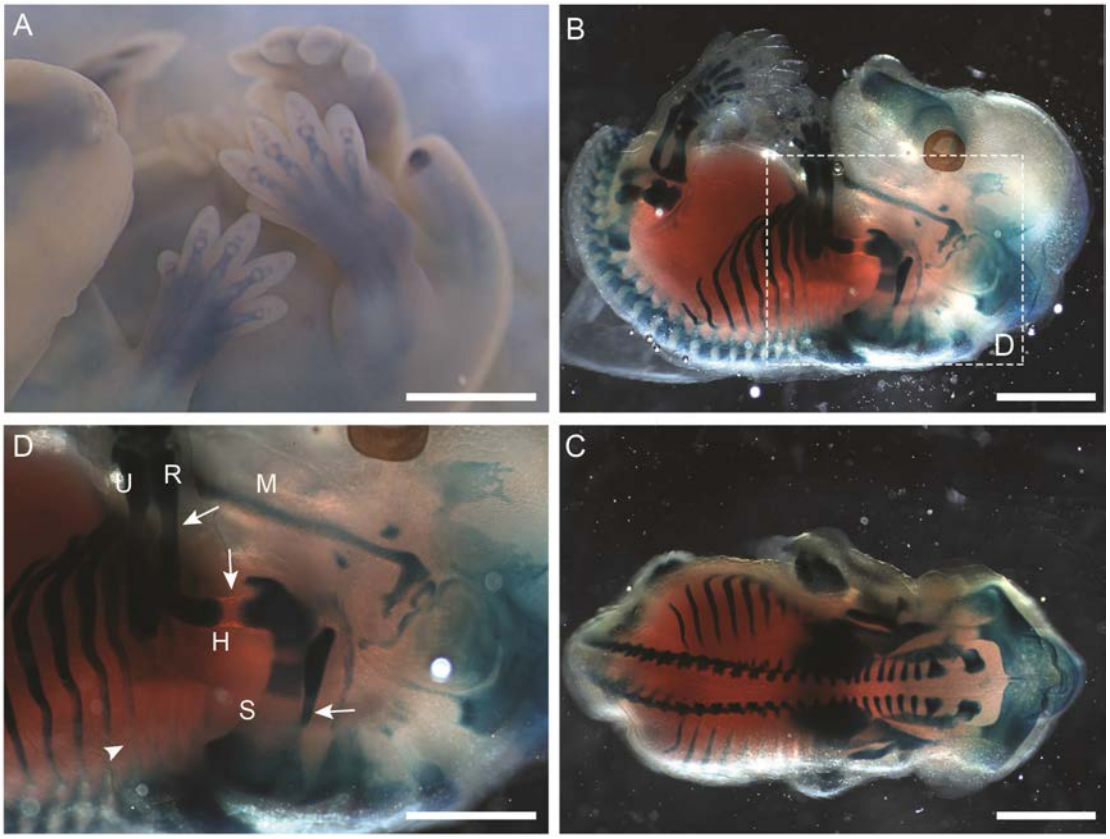

Figure 5.6: Cleared *PRELP*$^{LacZ/LacZ}$ embryo after X-gal staining. (A) An enlarged view of the limbs from a heterozygote embryo showing Lac-Z activity in the metatarsals/metacarpals and their connections. (B)-(C) Lateral and dorsal view of a homozygote knock-out embryo after X-gal staining and clearing, showing Lac-Z activity in the developing skeleton, in the nasal area, the ribs and vertebrae, and also in the back of the head probably in developing cranial bones. (D) Closer view of the upper limbs, where X-gal staining is observed in the cartilaginous parts of the growing long bones but not in the middle where the primary ossification centre is located (arrows). The same pattern can be seen in the ribs with the staining declining in the ossified areas closer to the vertebral column (arrowhead). Scale bars, 2mm for all images. M, mandible; R, radius; U, ulna; H, humerus; S, scapula.

Following the whole-mount LacZ staining, embryos were embedded in paraffin, sectioned and counterstained with eosin in order to further analyze the β-gal expression in detail. Some embryos were sectioned whole either sagittaly or coronaly, while in others head and body were separated for better angle positioning. Here, coronal sections of the head and sagittal sections of the body of a *PRELP*$^{+/LacZ}$ are presented, where the different elements expressing PRELP are clearer. Starting with the head, as demonstrated in Figure 5.7 A&C, β-gal signal is seen all around the nasal capsule and the cartilage primordium of the nasal septum. A little bit further into the snout (Fig. 5.7B) expression in the chondrocytes of the nasal capsule is decreased, while very faint signal can be seen the center of the tip of the tongue and in the cartilage of the vomeronasal organ (Fig. 5.7D). On the contrary, intense β-gal

staining is present at the chondrocytes of both left and right Meckel's cartilage as well as in the mesenchyme close to their fusion site (Fig. 5.7 E&F). While no staining is present at the primordia of incisors, moving towards the middle of the head very faint staining can be seen in the dental mesenchyme (dental papilla) of the upper and lower molars, which are at the dental cap stage (Fig. 5.8 A&D). In addition, moderate X-gal activity is seen in the cartilage primordia of all the cranial bones that develop by endochondral ossification, i.e. in the chondrocytes and the perichondrium of the basioccipital, sphenoid, exoccipital and temporal bones (Fig. 5.8 A-C & E). Finally, as shown in Figure 5.8F, there is some diffused β-gal signal at the roof plate of the future aqueduct.

Continuing with sagittal body sections of a *PRELP*$^{+/LacZ}$ embryo, LacZ activity is detected in all the cartilaginous tissues of the developing skeleton. In detail, β-gal signal is observed in the cartilage primordia of the tarsal and metatarsal bones, where it is visible that PRELP is expressed in almost all the different chondrocytic types apart from the hypertrophic ones, which are found around the middle of the bone where the primary ossification center will take place (Fig 5.9 A&H). Moreover, PRELP expression is seen in all the cartilaginous parts, which are not yet ossified, of the ribs, the sternum and the vertebral bodies (Fig 5.9 I&J). In all these elements expression is strong in the resting, proliferating, and pre-hypertrophic chondrocytes, while it decreases in the apoptotic hypertrophic chondrocytes until it is no longer present in the ossification groove (Fig. 5.9F). The same pattern of expression is observed as well in all the long bones of the frontlimb (i.e. radius, ulna, humerus) and the hindlimb (iliac bone, femur, tibia, fibula), where in addition signal is also visible in the perichondrium of the forming bones, and specifically around the proliferating and resting chondrocytes (Fig 5.9 D, E, G). No signal is observed in the ossification grove, where osteoid matrix is deposited, or the periosteum around the primary ossification center. Lastly, X-gal staining is noticed in the deposits of brown (multiocular) fat (Fig. 5.9B).

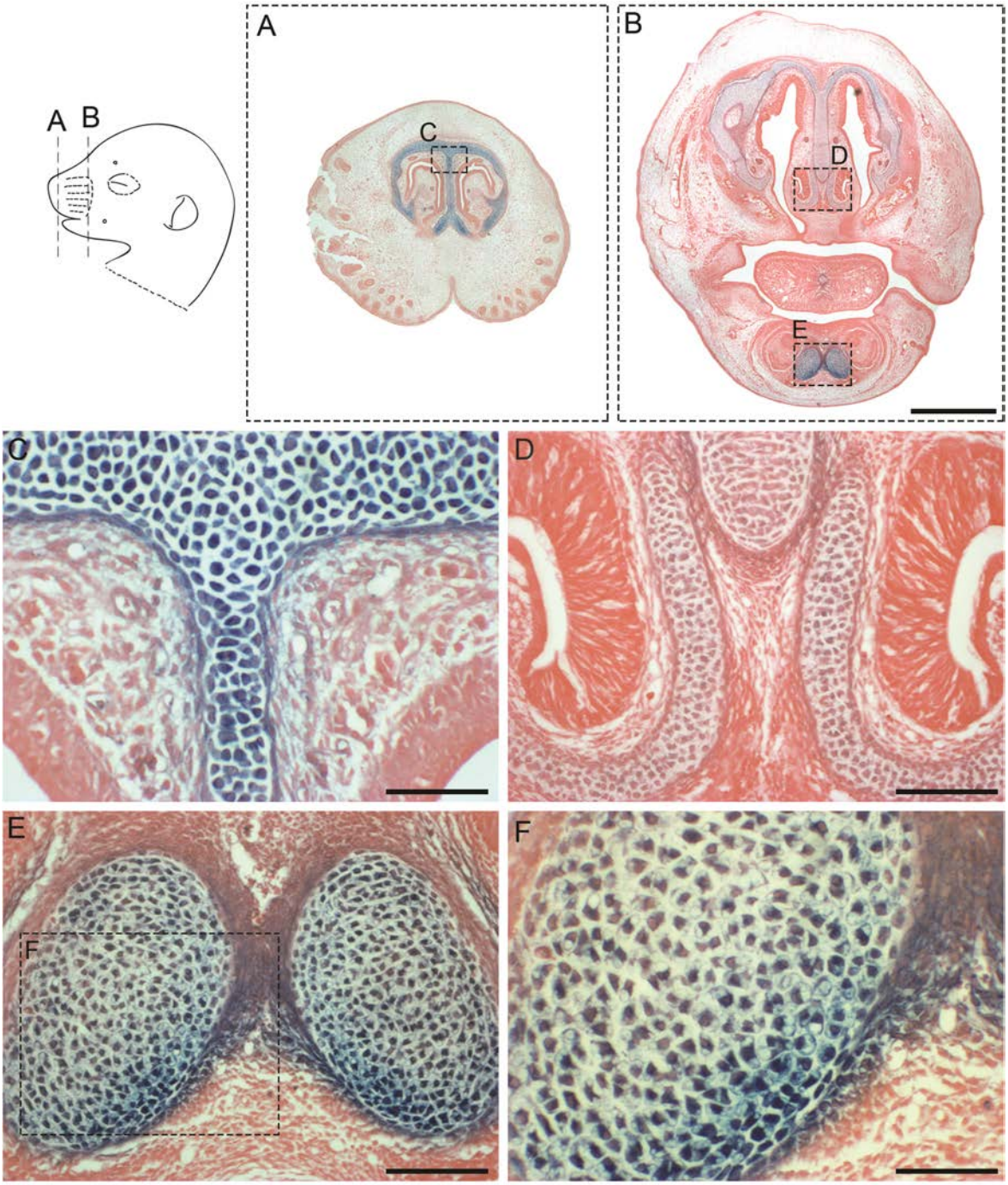

Figure 5.7: PRELP expression in the E15.5 embryonic head. (A)-(B) Two different coronal sections of an X-gal stained *PRELP*$^{+/LacZ}$ head demonstrating Lac-Z activity in the nasal septum and in Meckel's cartilage. (C) High magnification of the cartilaginous septum showing strong X-gal staining in the chondrocytes and the surrounding border. (D) Magnified view of the vomeronasal organ where faint β-gal signal can be seen only in the cartilaginous part. (E) & (F) Meckel's cartilages characterized by strong X-gal staining in the chondrocytes and in the mesenchyme close to their fusion site. Scale bars, 2mm for (A)-(B), 100μm for (D) and (E), 50μm for (C) and (F).

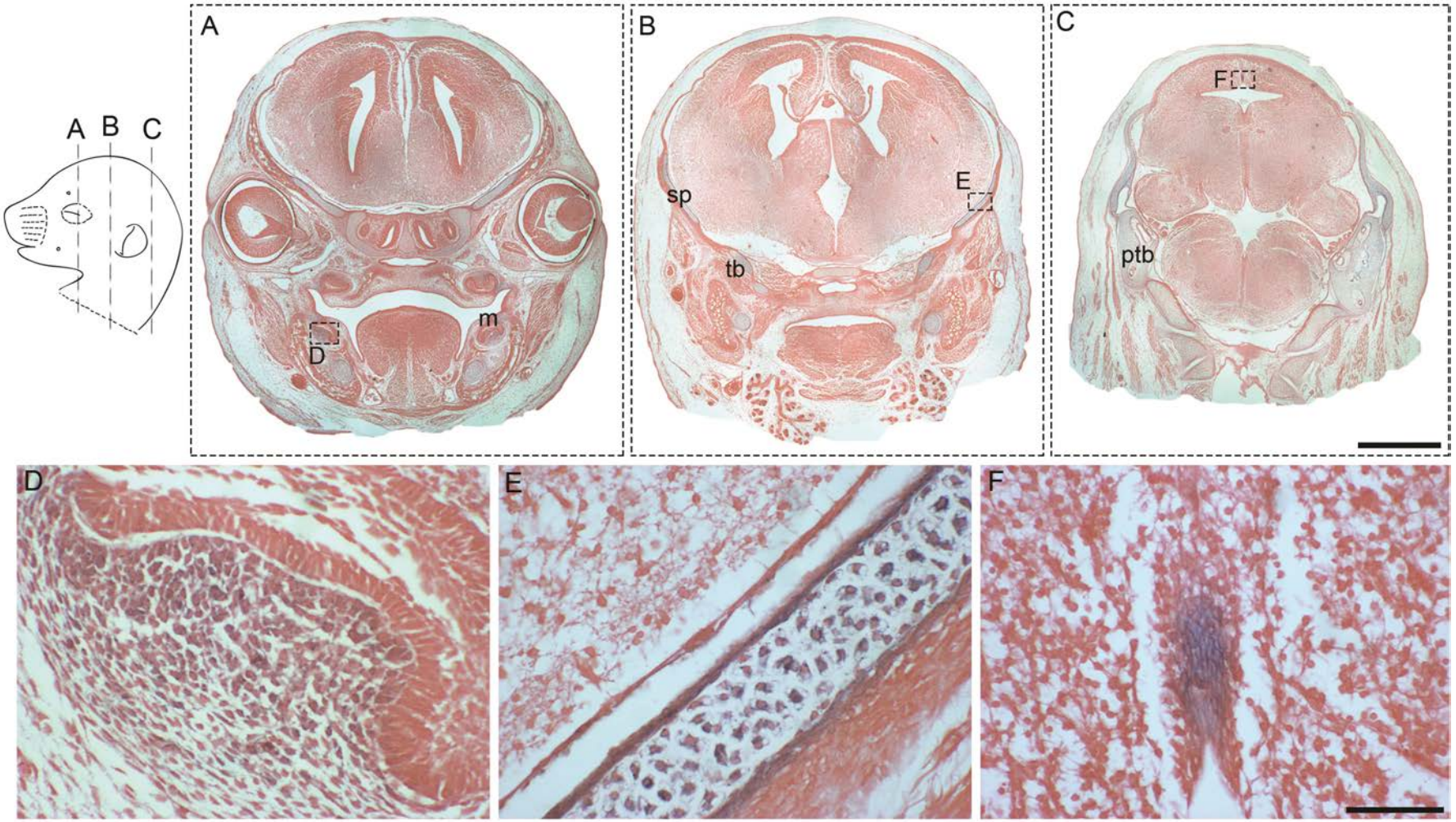

Figure 5.8: PRELP expression in the E15.5 embryonic head (continued). (A)-(C) Three different coronal sections of an X-gal stained *PRELP*$^{+/LacZ}$ head demonstrating Lac-Z activity mainly in the cartilage primordia of all the cranial bones that develop by endochondral ossification, i.e. the sphenoid bones (sp), the temporal bones (tb) and the petrous parts of the temporal bones (ptb). Faint signal can also be seen in the dental papilla of the molars (D). (E) Magnified view of the sphenoid bone showing X-gal staining in the chondrocytes and in the perichondrium. (F) Diffuse X-gal staining is observed at the roof plate of the future aqueduct. Scale bars, 2mm for (A)-(C), 50μm for (D)-(F).

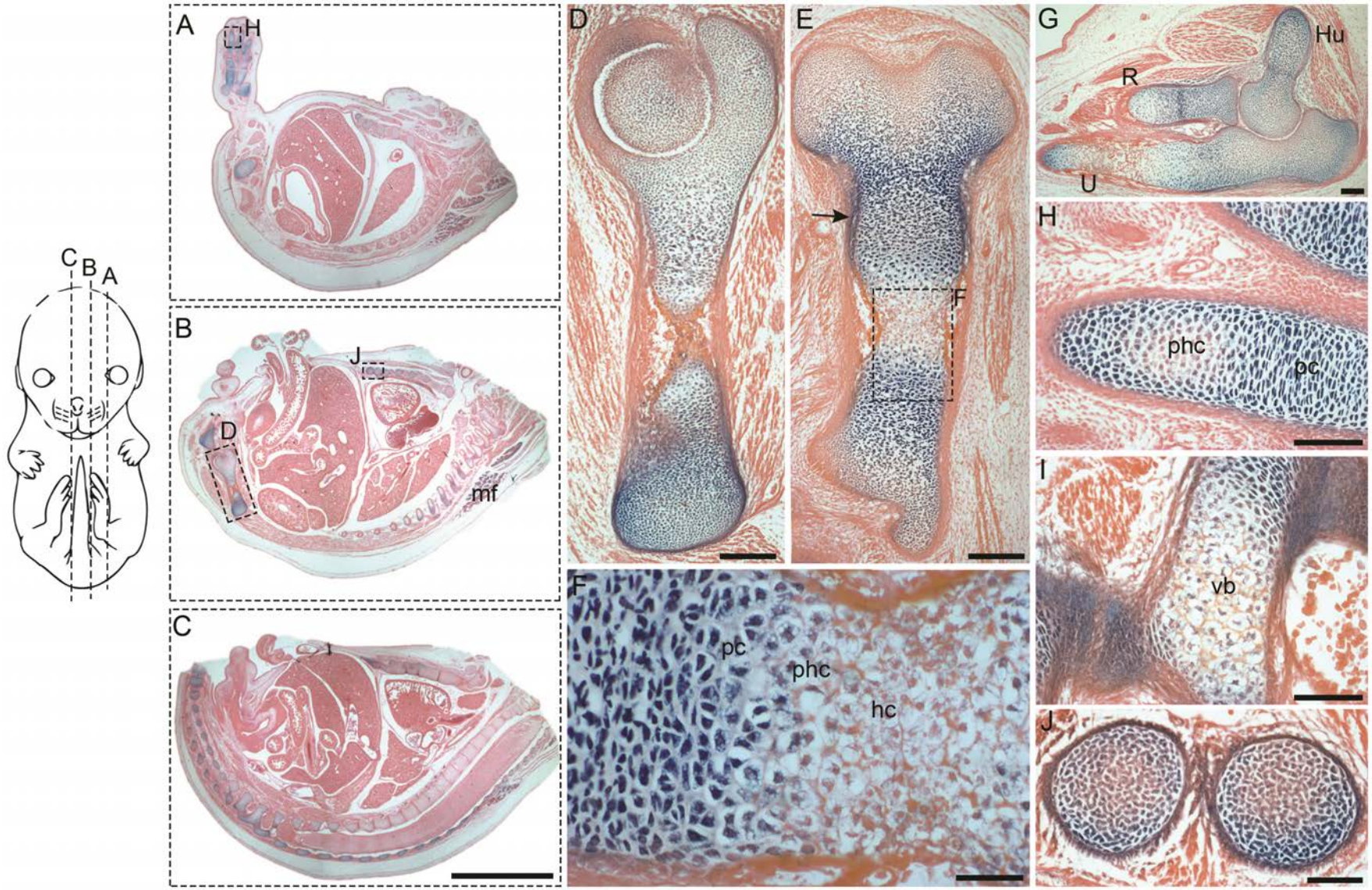

Figure 5.9: PRELP expression in sagittal sections of X-gal stained *PRELP*$^{+/LacZ}$ E15.5 embryos. (A)-(C) Three different sagittal planes demonstrating PRELP expression in the cartilaginous skeletal elements of all the developing bones. (D)-(E) Two femurs exhibiting X-gal staining in almost all the chondrocytic populations surrounding the primary ossification centre, while β-gal signal is also seen in the perichondrium (arrow). (F) Magnified view of the primary ossification groove of the femur in (E), showing strong Lac-Z activity in proliferating chondrocytes (pc), moderate activity in pre-hypertrophic (phc) and very faint signal in the hypertrophic chondrocytes (hc). Also there is no staining in the periosteum. The same pattern can be seen in the upper limb joint (G), and also in the digits and the vertebral bodies, where β-gal signal is decreased in the hypertrophic chondrocytes where ossification will take place (H) & (I). Finally, X-gal staining is observed in the chondrocytes of the sternum/ribs (J), while some staining is also seen in the deposits of multiocular fat (mf) just above the shoulders. Scale bars, 2mm for (A)-(C), 150μm for (D)-(E), 140μm for (G), 100μm for (H)-(I)-(J), 50μm for (F). R, radius; U, ulna; Hu, humerus.

5.2.3 PRELP expression in E17.5 embryos

Embryos at stage E17.5 were collected and whole mount-stained for X-gal overnight. Although the staining procedure worked, due to the big size and complete skin development of these embryos, penetration of the staining solutions in all internal tissues was unequal, resulting in variable coloration of the β-gal substrate, even between same genotypes within a litter. An example of a stained and cleared *PRELP*$^{+/LacZ}$ embryo is presented in Figure 5.10A, where it is visible that the enzymatic reaction took place only in the ventral part of the embryo. Thus, it was decided to freeze down E17.5 embryos and subsequently stain single cryo-sections for β-gal expression. In addition, head and body were separated in all embryos (for better penetration of fixative and cryopreservation solutions) and were sectioned individually.

Staining pattern in E17.5 embryos is very similar to E15.5 with most of the β-gal signal seen in the cartilaginous elements of the developing axial and appendicular skeleton. As observed initially, in the partially stained whole-mount embryo, β-gal signal is present in the forelimb and hindlimb, where all the small bones i.e. phalanges and metatarsals are strongly stained. In the long bones signal appears to be confined to the cartilaginous parts extending towards the edges, while it is absent from the primary ossification center in the middle of the bones (Fig. 5.10A, arrows). In addition, signal is seen in the ribs and sternum, whereas in the head, the nasal septum together with some of the cranial bones is positive for X-gal.

In X-gal stained sagittal cryo-sections of a *PRELP*$^{+/LacZ}$ embryo body all the areas described above can be seen in detail (Fig. 5.10 B&C). Firstly, PRELP signal in the metatarsals is present in all the chondrocytes apart from the apoptotic ones which will give space to the ossification groove (Fig 5.10D). Secondly, in the long bones of either hands or legs, PRELP is expressed only in the chondrocytes towards the edges of the bones (epiphyseal cartilage), while there is no expression at all in the diaphysis, including the primary ossification center and the periosteum. More specifically, in Figure 5.10 I&J magnified images of the left femur are presented, where we can see that the majority of mature/pre-hypertrophic, proliferating and resting chondrocytes are positive for b-gal, while very few apoptotic chondrocytes are stained. Additionally, another example of the shoulder joint is displayed in Figure

5.10 G&H, where the whole scapula and part of the humerus are included in the picture. Here we see the same pattern of expression, where signal is seen only in the mature, proliferating and resting chondrocytes but in addition we see that the articular cartilage – i.e. the chondrocytes that cover the ends of bones where they come together to form joints – is positive for β-gal, as well as some parts of the articular capsule and parts of the tendons surrounding the joint (Fig. 5.10H). Finally, in Figures 5.10 E&F two different cutting planes of the vertebral column are demonstrated showing Lac-Z activity in the proliferating/resting chondrocytes of the vertebral discs with few positive cells in the hypertrophic/apoptotic chondrocytes (ossifying vertebral bodies) accompanied by some positive cells in the annulus fibrosus (pf) and annuls pulposus (ap). Again, we see strong expression in the articular chondrocytes and the connecting tissue between each vertebral body, indicating PRELP as a component of the skeletal connecting-cartilage tissues (Fig. 5.10F).

In order to further analyse the expression of PRELP in the embryonic E17.5 head, frozen *PRELP*$^{+/LacZ}$ heads were sectioned coronally from front to back and subsequently stained with X-gal. In Figures 5.11 and 5.12 six different section planes are presented, where we can see that b-gal expression is overall similar to E15.5 heads, but has expanded to include some more areas. More specifically, PRELP is expressed in chondrocytes of the outer nasal capsule (Fig. 5.11A); in the inner nasal capsule the signal is lost (Fig. 5.11B), while chondrocytes of the nasal septum are again positive (Fig. 5.11C arrows). Few cells of the vomeronasal organ cartilage are b-gal positive, whereas both the right and left Meckel's cartilages, together with their fusion site, are also positive (Fig 5.11 D&E). Furthermore, some b-gal signal can be seen in the cartilaginous parts of the developing sphenoid bones that have not yet been ossified (Fig 5.11C arrowheads). On the contrary, no signal is present neither in the eyes or the olfactory bulbs, nor in the teeth primordia or any ossified mandible and maxilla regions.

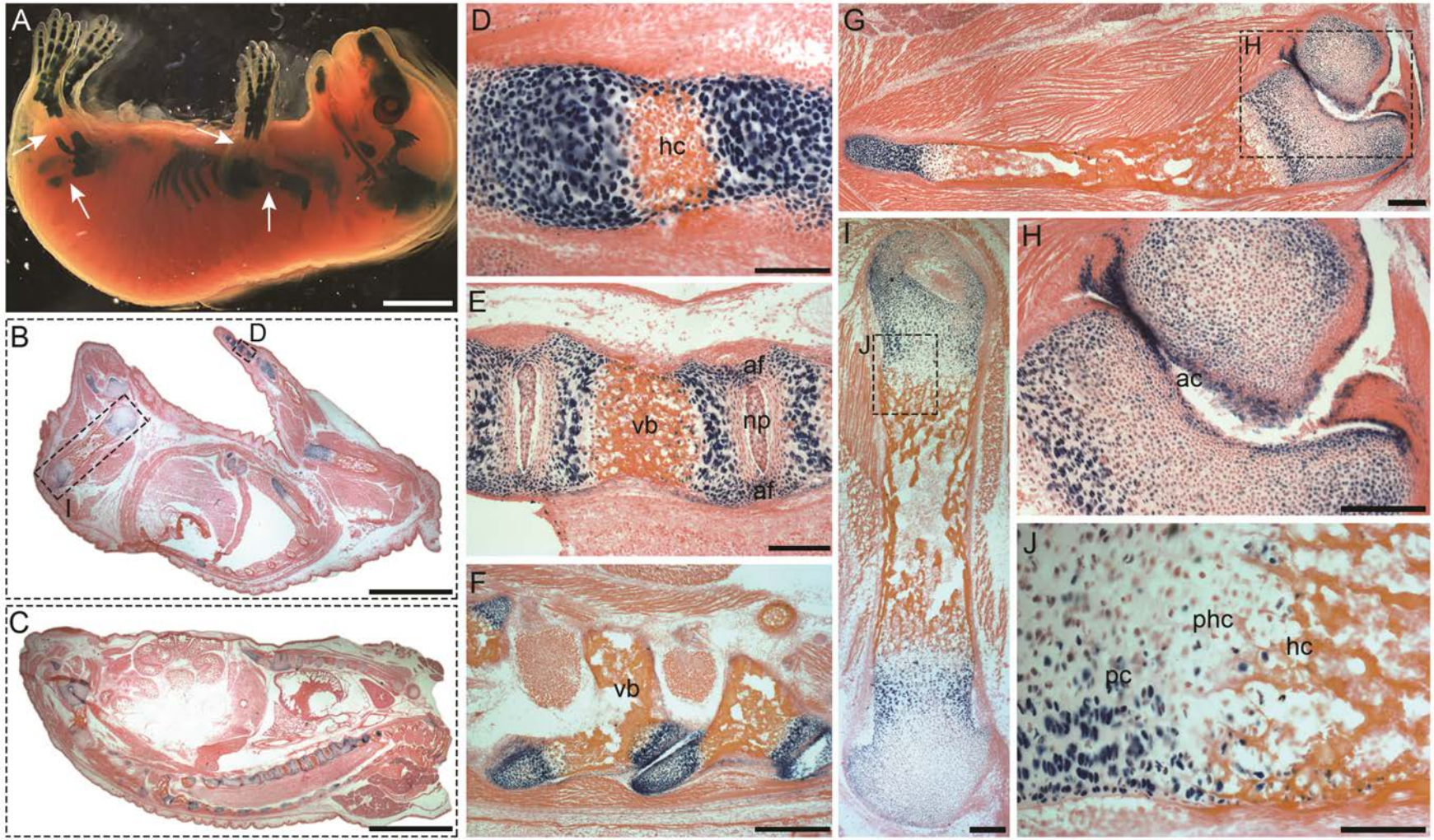

Figure 5.10: PRELP expression in sagittal sections of X-gal stained *PRELP*$^{+/LacZ}$ E17.5 embryos. (A) Whole-mount stained and cleared E17.5 heterozygote embryo demonstrating X-gal staining in all the cartilaginous skeletal elements. Arrows indicate primary ossification centres where staining is absent. (B)-(C) Two sagittal sections of the whole body showing X-gal staining in cartilage of long bones, ribs and vertebral bodies. (D) Magnified view of one metacarpal, where β-gal signal is seen in all the chondrocytes apart from the hypertrophic (hc) ones where ossification starts. (E)-(F) Vertebral bodies (vb) exhibiting Lac-Z activity in proliferating, resting and articular chondrocytes but not in the ossified areas. Signal is also seen in the nucleus pulposus (np) and annulus fibrosus (af). (G)-(H) Shoulder joint displaying X-gal staining additionally in the articular cartilage (ac), parts of the articular capsule and the tendons surrounding the joint. (I)-(J) Section of a femur where strong β-gal signal is observed in resting and proliferating (pc) chondrocytes, less signal is seen in pre-hypertrophic (phc) which declines even more in the hypertrophic chondrocytes (hc) until no staining is present at all in the ossified matrix. Scale bars, 3mm for (A)-(C), 200μm for (F), 140 μm for (I) and (J), 100μm for (D), (E), (H), 50μm for (J).

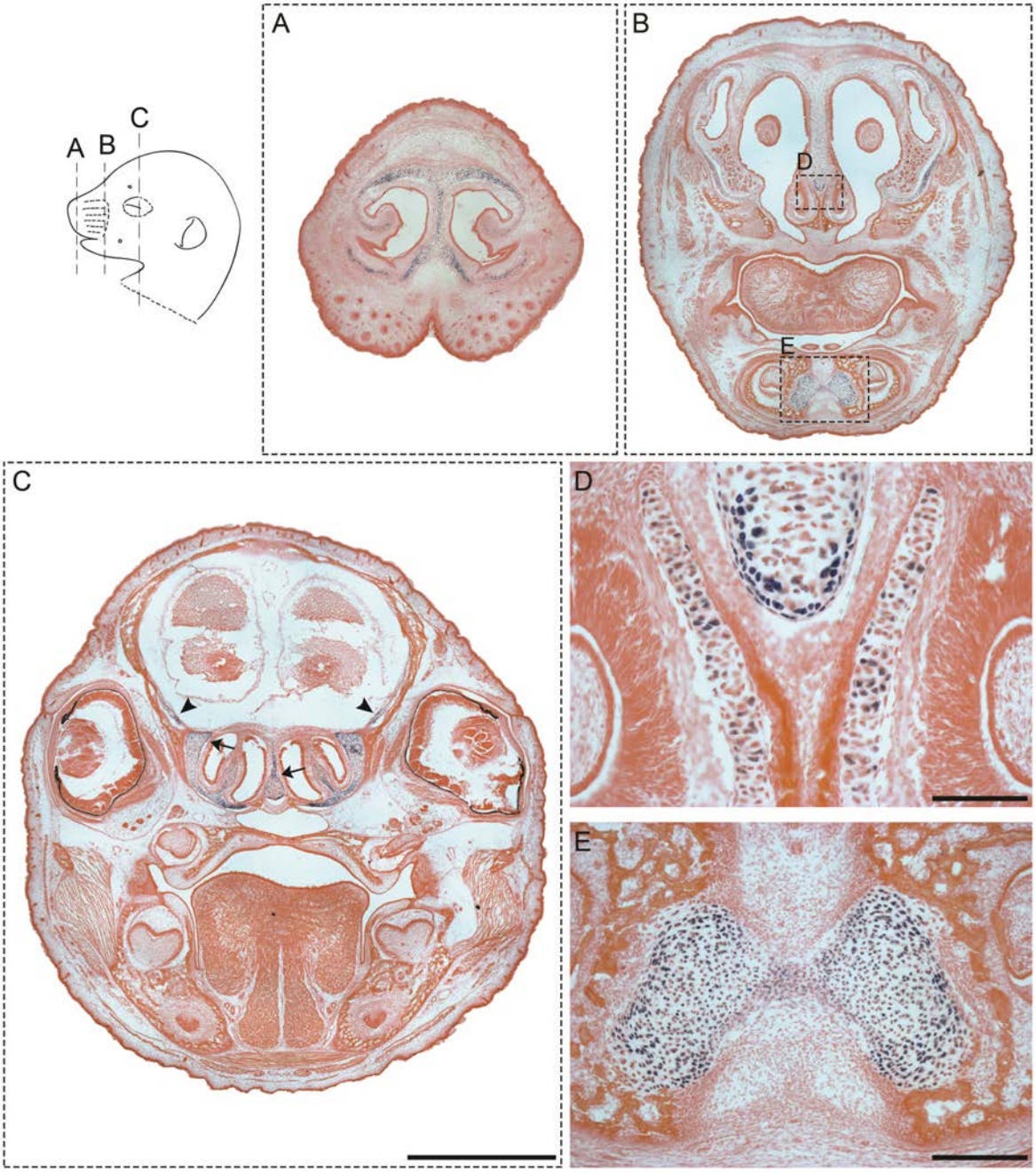

Figure 5.11: PRELP expression in coronal sections of X-gal stained *PRELP*$^{+/LacZ}$ E17.5 heads. (A)-(C) Three different coronal planes showing Lac-Z activity in the chondrocytes of the outer but not the inner nasal capsule, as well as in chondrocytes of the nasal septum (arrows) and in cartilage of the sphenoid bones (arrowheads). (D) Few cells of the vomeronasal cartilage are β-gal positive, while chondrocytes of the left and right Meckel's cartilages are exhibiting Lac-Z activity (E). No staining can be seen in other parts of the head like the developing teeth or eyes. Scale bars, 2mm for (A)-(C), 100µm for (E), 50µm for (D).

Moving further into the posterior half of the embryo head, Lac-Z activity can be seen in all the cartilaginous parts of the developing endochondral cranial bones and also in some areas of the brain (Fig. 5.12). In detail, β-gal signal is observed in the cartilage primordia of the sphenoid, the temporal, the petrous part of the temporal and the basioccipital bones, as well as in the thyroid cartilage and the chondrocytes of the greater horn of hyoid bone (Fig. 5.12 A&B). In addition, moderate PRELP expression is also seen in the brain, in the dorsal part of the 3rd ventricle wall closure and specifically in the future ependymal cells (Fig. 5.12D), as well as in the premature choroid plexus of the 4th ventricle (Fig 5.12E). Lastly, X-gal staining can be seen in the mature, proliferating and resting chondrocytes surrounding the ossified regions of the exoccipital bone (same expression pattern as seen in the long bones), accompanied by strong expression in the chondrocytes of the articular cartilage in the atlas and the other cervical vertebrae (Fig. 5.12C and in detail 5.12F).

In conclusion, during this developmental stage PRELP is expressed mainly in the developing skeletal elements, including mostly the mature, proliferating and resting chondrocytes, as well as in the articular cartilage between bone joints. Also, PRELP starts to be expressed in specific areas of the brain.

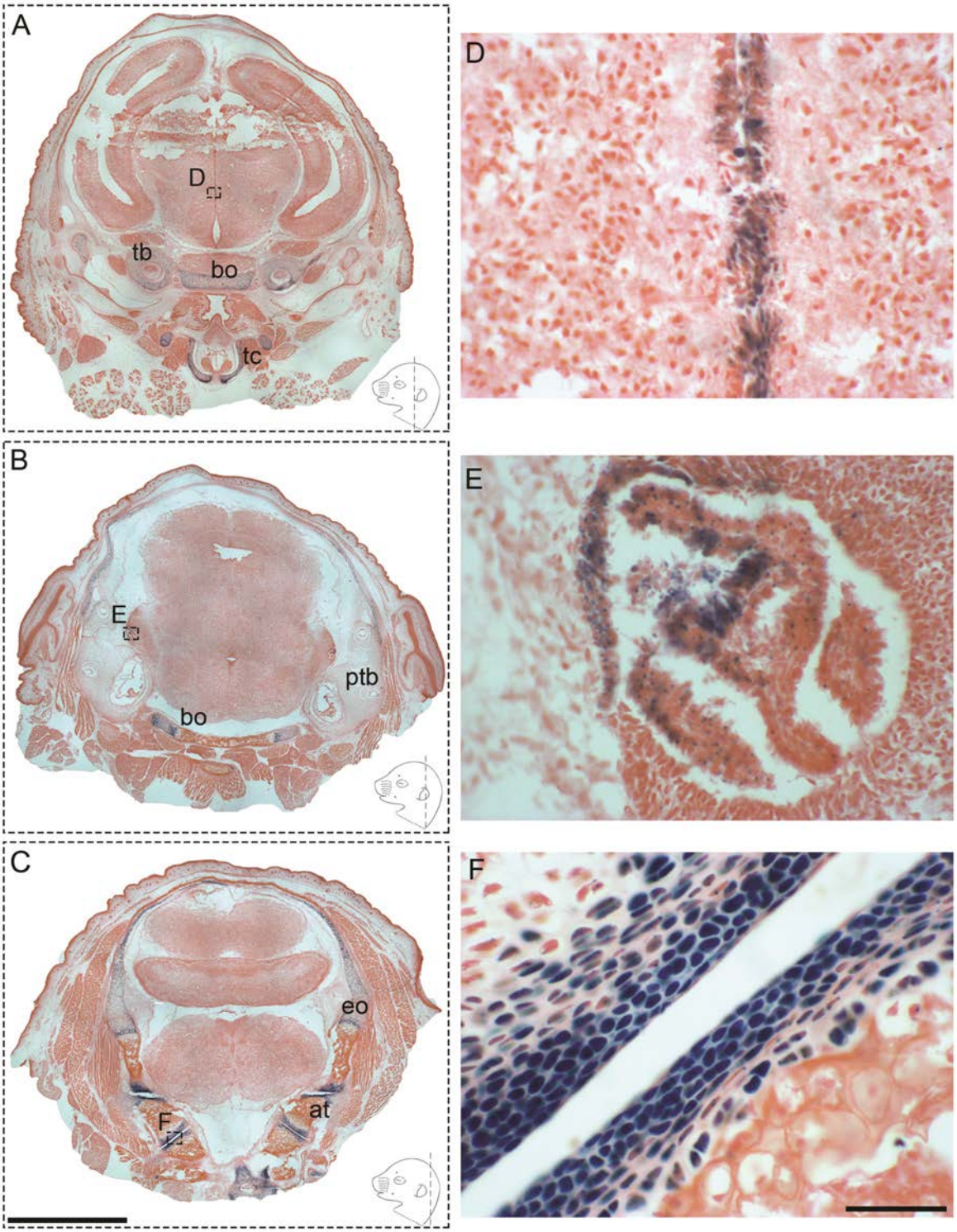

Figure 5.12: PRELP expression in coronal sections of X-gal stained *PRELP*$^{+/LacZ}$ E17.5 heads (continued). (A)-(C) Three different coronal planes showing Lac-Z activity in the cartilaginous parts of the developing endochondral cranial bones, i.e. the basioccipital (bo), temporal (tb), petrous parts of the temporal (ptb), and exoccipital (eo) bones, and also the thyroid cartilage (tc). B-gal signal is also seen in the resting, proliferating and articular chondrocytes of the atlas (at) and the other cervical vertebrae, as shown in higher magnification in (F). In addition, X-gal staining is observed in the dorsal 3rd ventricle wall of the brain (D) and also in the posterior developing choroid plexus (E). Scale bars, 2mm for (A)-(C), 50μm for (D)-(F).

5.2.4 PRELP expression in new-born (P0) mice

Similarly to the OMD analysis, new-born (P0) neonates were collected within 16 hours of their birth time from $PRELP^{+/LacZ}$ ♂ x $PRELP^{+/LacZ}$ ♀ crossings, so all the 3 genotypes would occur within the same litter. The size of the litters varied between 7-10 pups and the ratio of genotypes followed Mendelian inheritance, while no differences were observed in the size or gross anatomy between individual new-borns. Similarly to before, after euthanization heads and bodies were separated and processed for freezing, followed by subsequent sectioning and staining with X-gal. Due to the big size of the bodies and the restricted fixation time – in order to avoid reduction of the β-gal signal – intact sections were not always easy to achieve, but clear results of the staining pattern were obtained. Again, no staining was observed in any $PRELP^{+/+}$ sections, while β-gal signal was very specific in heterozygote samples.

Starting with the head, PRELP expression is confined to the cartilaginous tissues, similarly to what was seen previously, and is demonstrated in seven different coronal sections in Figures 5.13, 5.14 & 5.15. In detail, PRELP at this stage is expressed again at the snout, in chondrocytes of the nasal capsule (Fig. 5.13 A&C), of the nasal septum and the cartilaginous part of the vomeronasal organ, as well as in some of the chondrocytes at the fusion point of Meckel's cartilages (Fig. 5.13 B&D). Further ahead, the expression signal in the inner nasal septum is reduced (Fig. 5.14 A&C), while there is no staining at all in the olfactory bulbs or the developing eyes and teeth. However, signal is now present in the choroid plexus of the 3rd ventricle, as well as in the cells forming the adjacent epithelial lining of the ventricles (Fig. 5.14 B&D). In addition, faint signal can be seen in chondrocytes of the developing temporal bones, and the other cartilaginous formations (arrowheads). Moving towards the posterior end of the head, Lac-Z activity is present in the cartilage of the sphenoid and temporal bones, as well as in the chondrocytes encompassing the ossified region of the basioccipital bone (Fig. 5.15 A&B). Furthermore, β-gal signal is again observed in the differentiating ependymal cells of the 3rd ventricle wall, and also the 4th ventricle choroid plexus (Fig. 5.15 D&E). Finally, strong staining can be seen in the articular chondrocytes surrounding the ossified regions of the exoccipital

bones, the atlas and the other cervical vertebrae (very similar pattern to the E17.5 embryos) (Fig. 5.15 C&E).

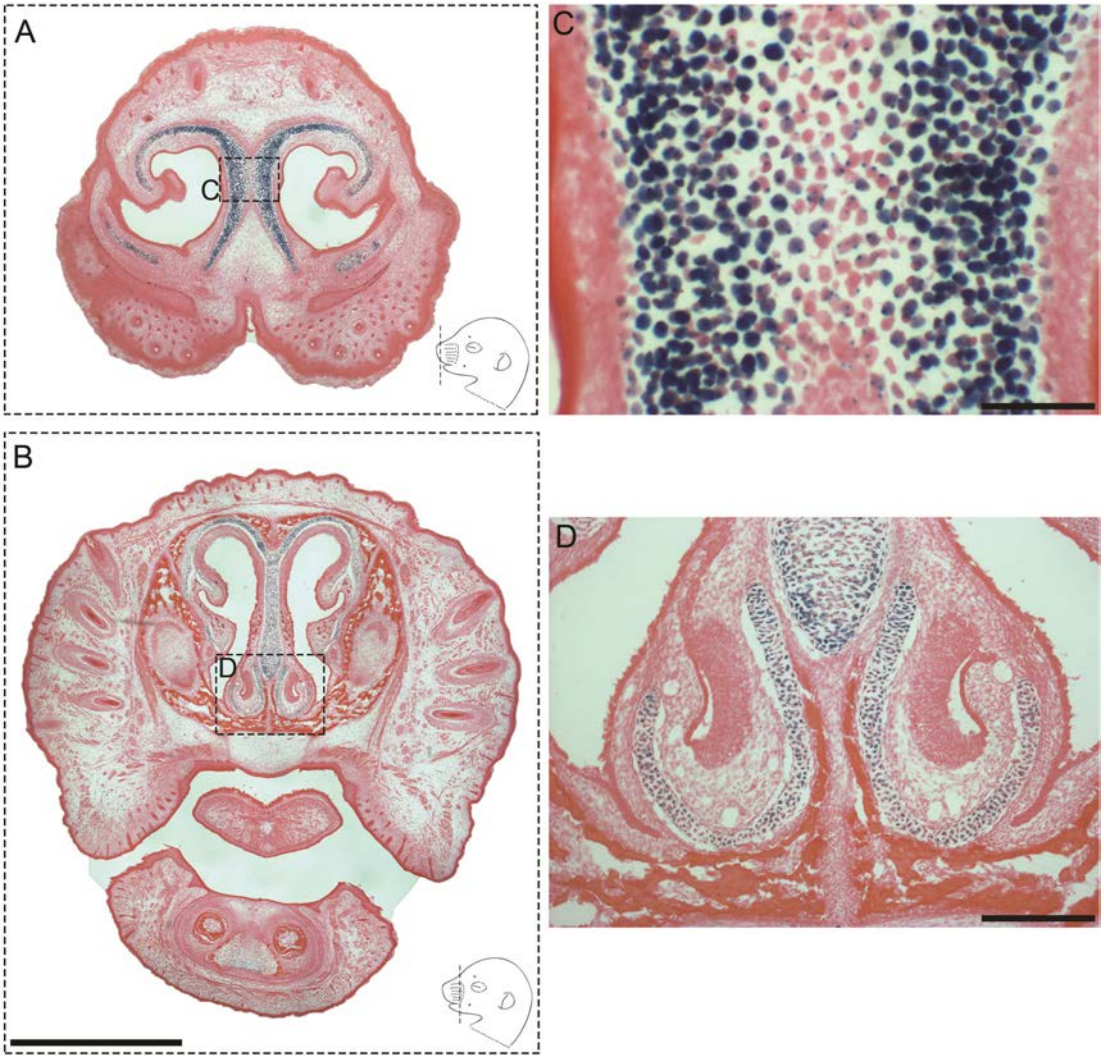

Figure 5.13: PRELP expression in coronal sections of X-gal stained *PRELP*$^{+/LacZ}$ P0 heads. Lac-Z activity is seen in chondrocytes of the nasal capsule (A) & (C), and in the nasal septum (B). (D) B-gal signal is also observed in the cartilaginous part of the vomeronasal organ, while fainter staining is present in some chondrocytes of Meckel's cartilage. No staining is seen in the developing incisors. Scale bars, 3mm for (A)-(B), 50μm for (C), 100μm for (D).

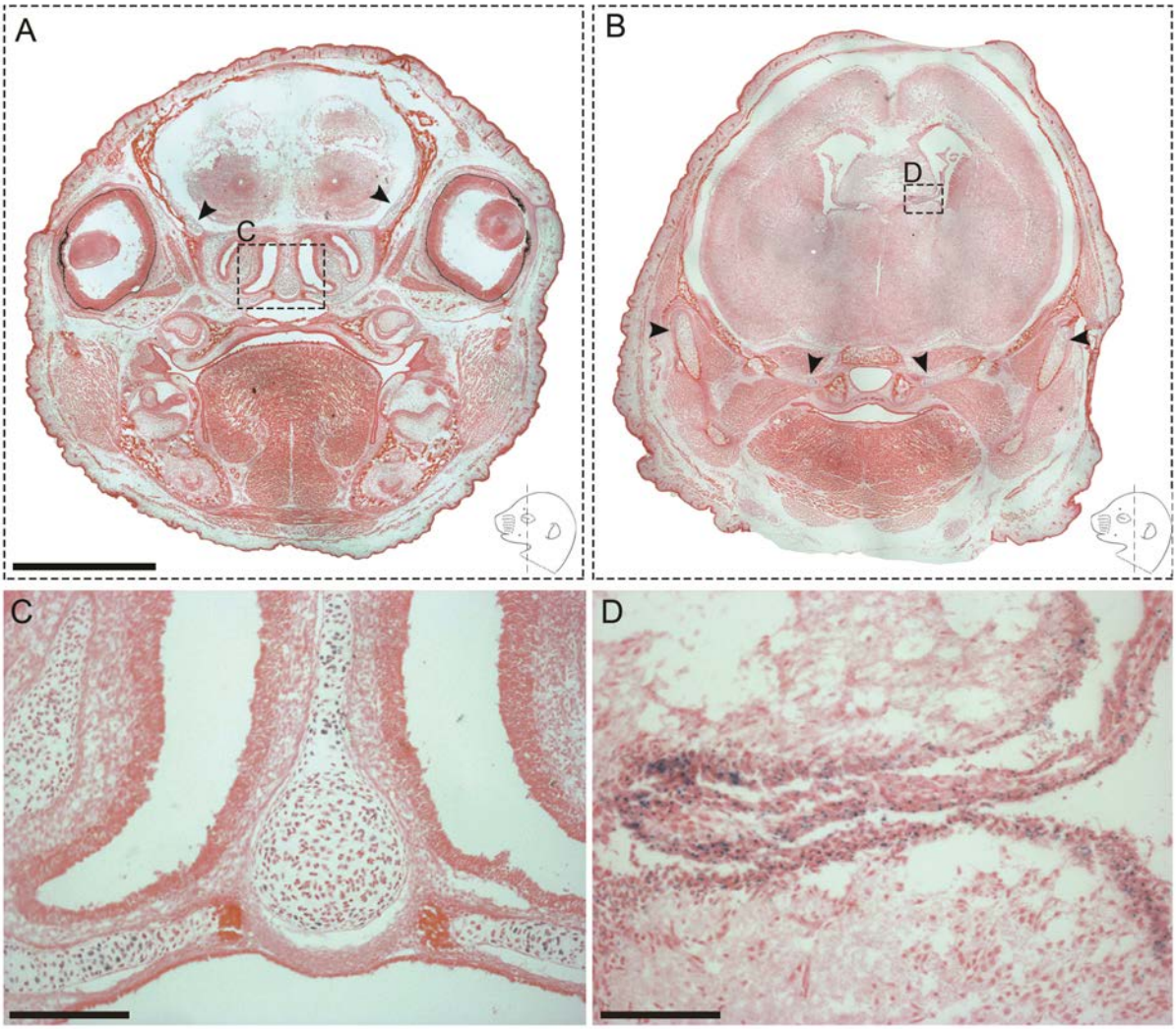

Figure 5.14: PRELP expression in coronal sections of X-gal stained *PRELP*$^{+/LacZ}$ P0 heads (continued). Lac-Z activity in the nasal septum is reduced, as shown in (A) and (C), while there is faint staining in the chondrocytes of the developing sphenoid bones (arrowheads), similarly to the previous stage examined. This expression pattern is seen in all the bones that develop by endochondral ossification in the head, also pointed by arrowheads in (B). B-gal signal is additionally seen the choroid plexus of the lateral ventricles and the cells that line the ventricle walls (D). Scale bars, 3mm for (A)-(B), 150μm for (C), 100μm for (D).

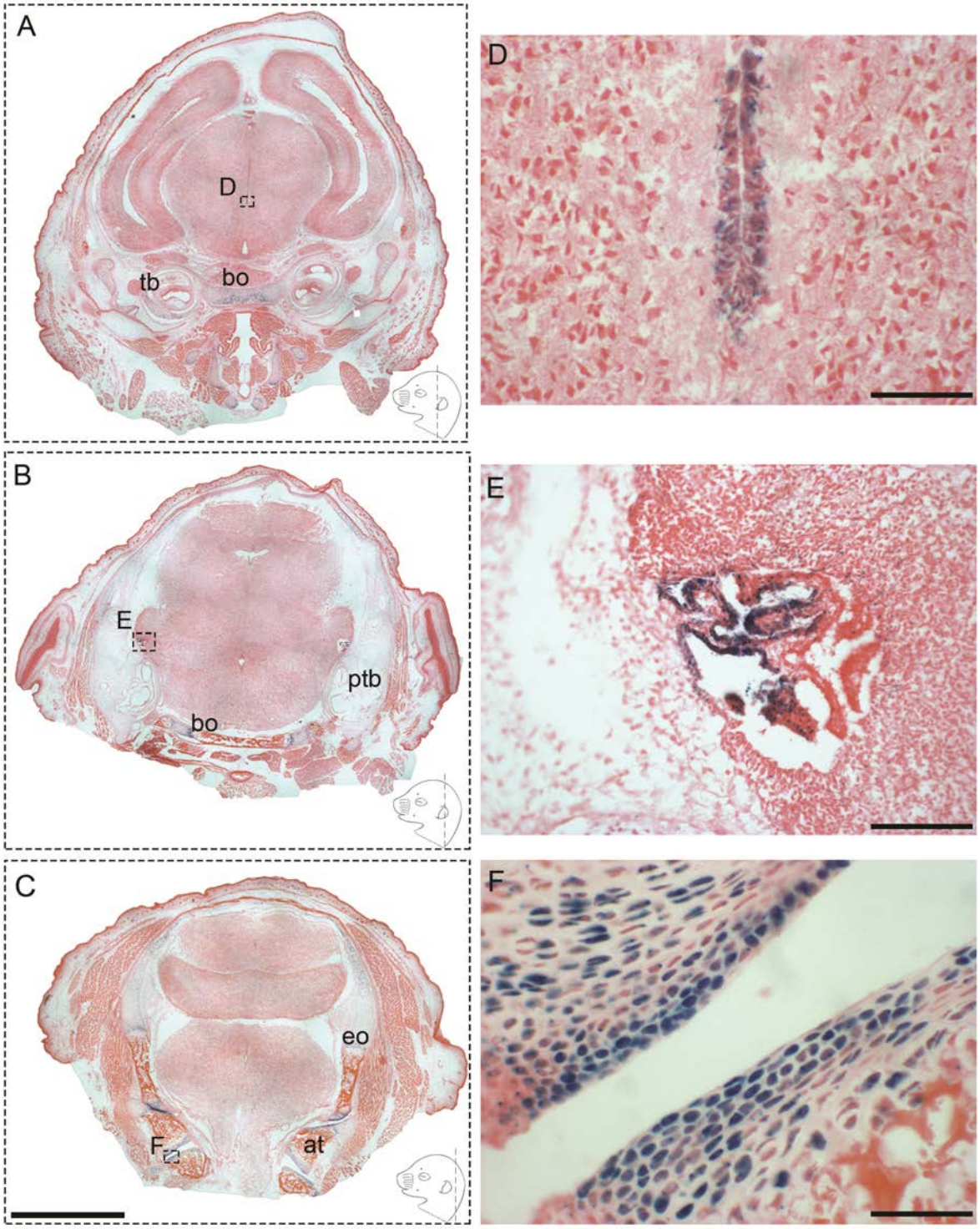

Figure 5.15: PRELP expression in coronal sections of X-gal stained *PRELP*$^{+/LacZ}$ P0 heads (last part). In the posterior part of the head X-gal staining is very similar to the E17.5 embryonic heads. Staining is seen in the cartilaginous parts of the developing bones, i.e. the basioccipital (bo), temporal (tb), pertrous parts of the temporal (ptb), and exoccipital (eo) bones (A)-(B). The signal is more intense in the proliferating and articular chondrocytes, while there is no staining in any ossified areas, as also seen in the atlas and the cervical vertebrae (C) & (F). Again, similarly to E17.5expression, β-gal signal is also observed in the 3rd ventricle wall (D) and the choired plexus of the 4th ventricle (E). Scale bars, 3mm for (A)-(C), 100μm for (E), 50μm for (D) & (F).

Regarding PRELP expression in the p0 body, sagittal sections of a *PRELP*$^{+/LacZ}$ embryo are displayed in Figure 5.16, where we can see that expression is confined in the cartilaginous parts of the long bones and the ribs (Fig 5.16 A&B). More specifically, Figure 5.16 C&D shows the ends of the scapula and humerus respectively, where β-gal signal is very strong in most chondrocytic populations excluding the hypertrophic/apoptotic ones near the ossification front. The different maturation stages can be clearly seen in Figure 5.16E, exhibiting intense PRELP expression in the proliferating chondrocytes, while the signal is reduced almost completely in the pre-hypertrophic and hypertrophic ones, and is non-existent in the ossified matrix. In addition, intense signal is also seen in the articular chondrocytes, especially in the joint areas (arrowheads). The same expression pattern is visible in the elbow joint, where we can see strong signal in the proliferating and some of the resting chondrocytes (Fig. 5.16F), while all the articular cells are positive for β-gal (Fig. 5.16G). Moreover, some diffuse X-gal staining is noticeable in muscle ligaments close to the joints (arrows). In agreement with the previous findings, Lac-Z activity in the cervical vertebrae is restricted to the non-ossified and articular cartilage (Fig. 5.16H, magnified image of the inset), whereas in the central vertebral discs positive are again the proliferating and some resting chondrocytes surrounding the ossified bodies, as are some cells in the inner annulus fibrosus and nucleus pulposus (Fig. 5.16I).

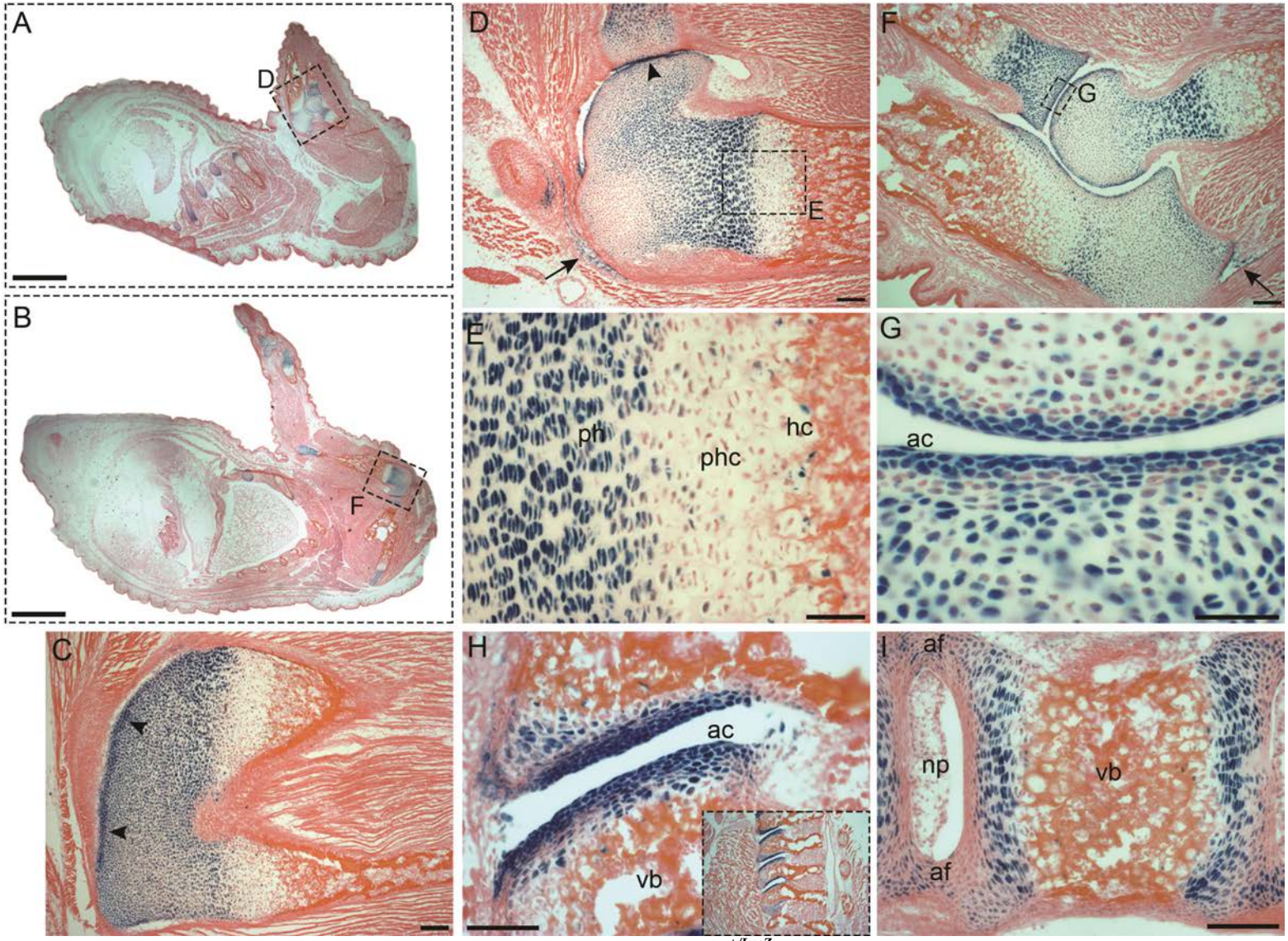

Figure 5.16: PRELP expression in sagittal sections of X-gal stained *PRELP*$^{+/LacZ}$ P0 bodies. (A)-(B) Sagittal sections of the whole body where Lac-Z activity is seen in all the cartilaginous elements of the developing skeleton, including the ribs and the long bones. (C) One end of the scapula exhibiting β-gal signal in all the chondrocytes apart from the ones close to the ossification front (pre-hypertrophic/hypertrophic). Also strong signal can be seen in the articular chondrocytes (ac) (arrowheads), as also seen in (G). The same expression pattern is seen in the humerus (D) and also in the elbow joint (F), where staining is additionally seen in adjacent muscle ligaments (arrows). (E) Enlarged view of the humerus ossification front where strong Lac-Z activity is seen in the proliferating chondrocytes (ph), declining in the pre-hypertrophic (phc) and hypertrophic chondrocytes (hc) until it is no longer present in the osteoid matrix. (H)-(I) Cervical and central vertebral bodies, where again β-gal signal is seen in the proliferating and articular chondrocytes , while less signal can be seen in the annulus fibrosus (af) and nucleus pulposus (np). Scale bars, 3mm for (A)-(C), 140μm for (C), (D), (F), 50μm for all the rest.

5.2.5 PRELP expression in adult mice

Heterozygous and homozygous transgenic mice grew into adulthood, were fertile and had a normal life span without any apparent abnormalities and with normal reproductive rate. In order to examine *PRELP* expression during adult life various internal organs were isolated from $PRELP^{+/LacZ}$ adult mice and subsequently stained for β-galactosidase. The organs that were analysed are brain, eye, bladder and bone, and all will be presented and discussed below, each in a separate sub-section. Due to the nature of the specimens, X-gal activity in the bone, and specifically in the knee joint, covering part of femur and part of tibia, was assessed by whole-mount staining, followed by decalcification and subsequent cryo-sectioning, while all the other organs where fixed, sectioned and afterwards stained for X-gal. In addition, kidney and spleen from heterozygote animals were also examined for β-gal activity, but X-gal staining here was non-specific with significant background signal even in the control $PRELP^{+/+}$ samples. Due to this endogenous β-galactosidase activity in these organs, *in situ* hybridization was attempted to explore the expression of mRNA *PRELP* gene transcripts in wild type samples. Unfortunately, this approach failed to work twice and no further study of these organs was done, focusing thereafter on the other organs analysed (bladder, eye and brain). Also, after confirming the expression patterns of PRELP in each of the above organs, immunofluorescence staining was performed to identify the specific cell types that were positive for β-gal, and thus PRELP.

5.2.5.1 PRELP expression in the adult mouse bladder

The structure of the mouse bladder has been previously described in Chapter 4 and in Figure 4.15 A&B H+E stained sections of a wild type bladder are presented, where the three different layers of the urothelium (basal, intermediate and umbrella cells) are visible. Similarly to before, in order to investigate if PRELP is expressed in the mouse bladder, whole bladders were isolated from adult $PRELP^{+/LacZ}$ and $PRELP^{+/+}$ littermates and after processing and sectioning were subsequently stained for Lac-Z activity. X-gal staining of heterozygote bladders revealed β-gal signal at the urothelium and particularly in the outer umbrella cell layer (Fig. 5.17 A&B), while no staining was seen in any of the wild type samples. Further immunofluorescence staining of heterozygote bladders with several markers against

the three different layers of the urothelium was performed, confirming expression of β-gal in the superficial umbrella cells. In detail, X-gal staining was co-localised with uroplakin-3 and CK18 (both are markers for umbrella cells) (Fig. 5.18 C-D), while it did not overlap with either CK5 (which is a marker for basal cells) or laminin (marker for the basement membrane between stromal and epithelial layers) (Fig. 5.18). Overall, we can conclude that PRELP is expressed in a sub-population of the umbrella epithelial cells, an expression pattern almost identical to OMD.

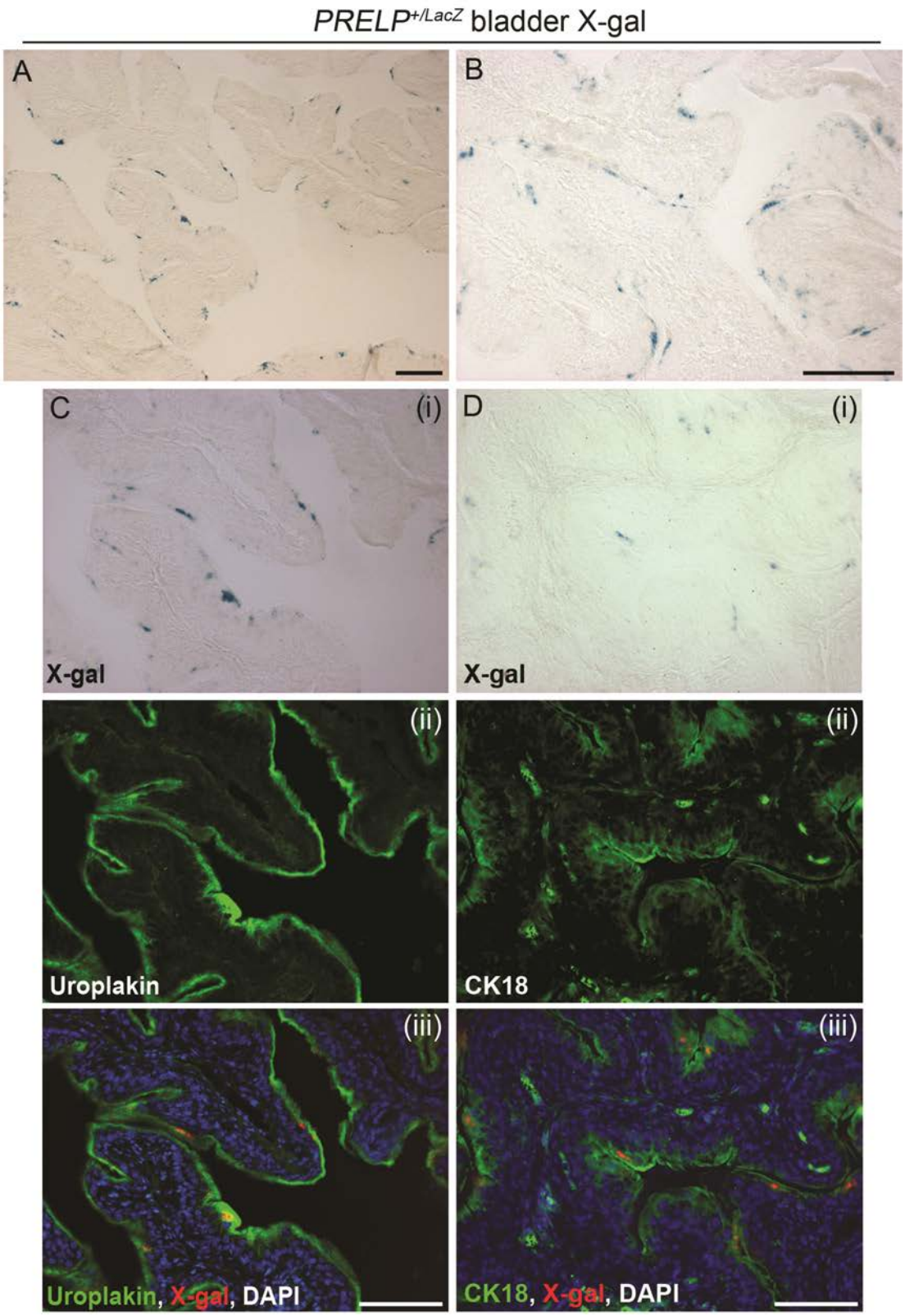

Figure 5.17: PRELP expression in adult mouse *PRELP*$^{+/Lac\text{-}Z}$ bladder is localised in the umbrella cell layer. (A)-(B) Two different images of a heterozygote X-gal stained bladder demonstrating signal in the outer layer of the urothelium. (C)-(D) X-gal staining followed by immunofluorescence revealed co-localisation of the β-gal signal with uroplakin- and CK18-positive areas, confirming PRELP expression in the umbrella cell layer. Panels (i) are X-gal staining, (ii) are specific immunostaining with the primary antibodies, visualized using alexa-488 (green) as secondary, while in panels (iii) are the merged images where X-gal is colored red and DAPI (blue) is used as a nuclei stain. Scale bars, 100μm for all images.

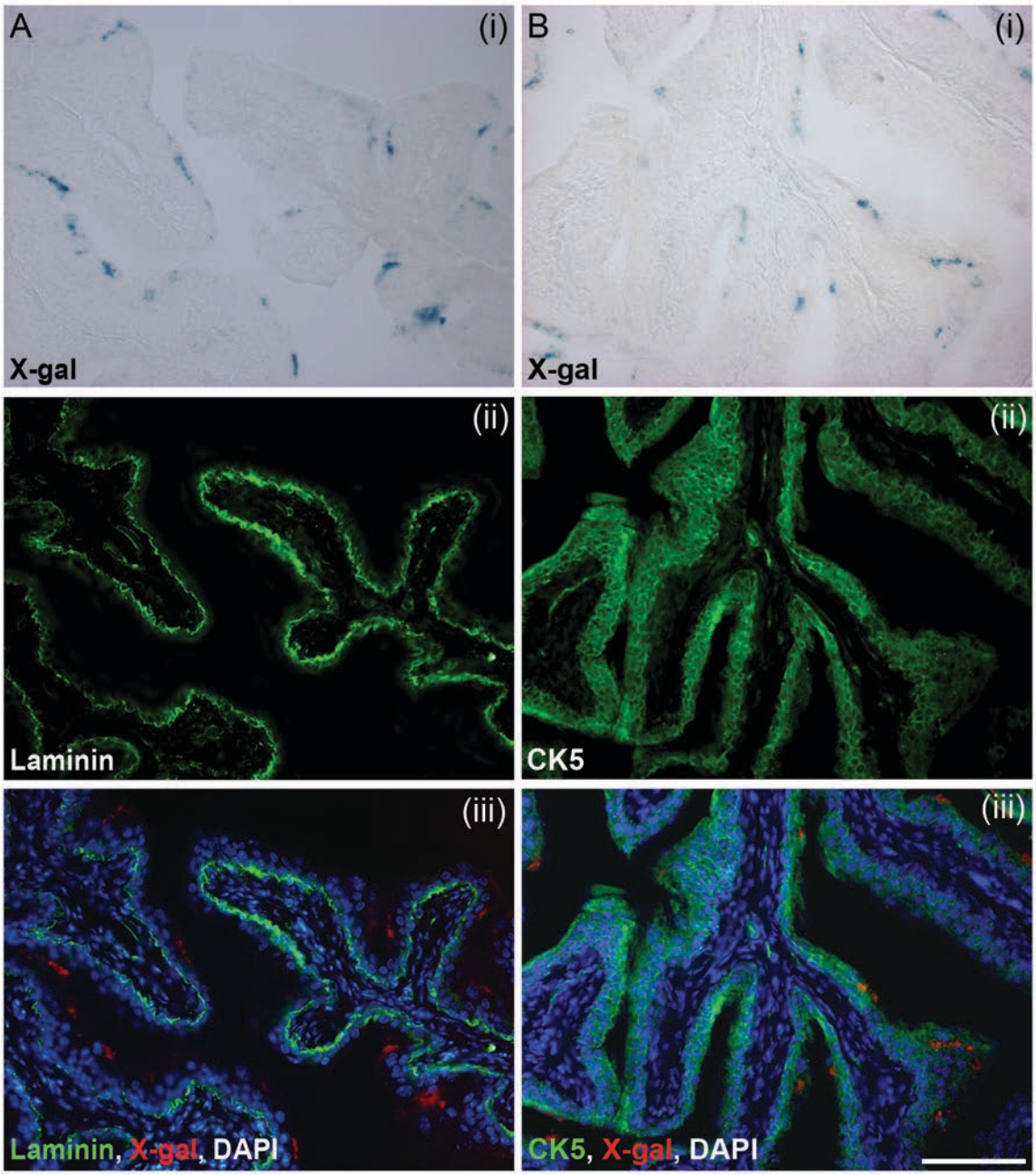

Figure 5.18: PRELP expression in the mouse bladder is confined to the outer layers of the urothelium. (A)-(B) X-gal and immunofluorescence staining of *PRELP*$^{+/LacZ}$ bladders using laminin and CK5 antibodies that mark the basement membrane of the lamina propria and the basal cells respectively. B-gal signal was not co-localised with any of these markers, confirming our previous result that PRELP is expressed within the umbrella cell layer. Panels (i) are X-gal staining, (ii) are specific immunostaining with the primary antibodies, visualized using alexa-488 (green) as secondary, while (iii) are the merged images where X-gal is colored red and DAPI (blue) is used as a nuclei stain. Scale bar, 100μm for all images.

5.2.5.2 PRELP expression in the adult mouse eye

The mouse eye structure, together with more detailed descriptions of the retina and ciliary body, is presented in Figure 4.17. After sagittaly cryo-sectioning whole eyes from *PRELP*$^{+/LacZ}$ mice, X-gal staining was always observed in the ciliary body, and more specifically in the non-pigmented epithelium, and occasionally in the trabecular meshwork (Fig. 5.19 A&C), while there was no staining in the retina or other areas of the eye (Fig. 5.19 B). Also, staining appeared "spotty" in some cells, while it was more diffuse in others. Sections from *PRELP*$^{+/+}$ littermates were always negative for X-gal staining, as expected. Moreover, X-gal staining followed by immunofluorescence with Pax6, a marker for the epithelial stem cells of the CB, revealed co-localization of the β-gal signal with Pax6-positive cells of the external epithelial layer of the CB, where in most cells the "spotty" signal appeared to be outside the cell nuclei (Fig. 5.19 C&D). Thus, we can conclude that PRELP is expressed in the majority of the non-pigmented CB epithelial cells.

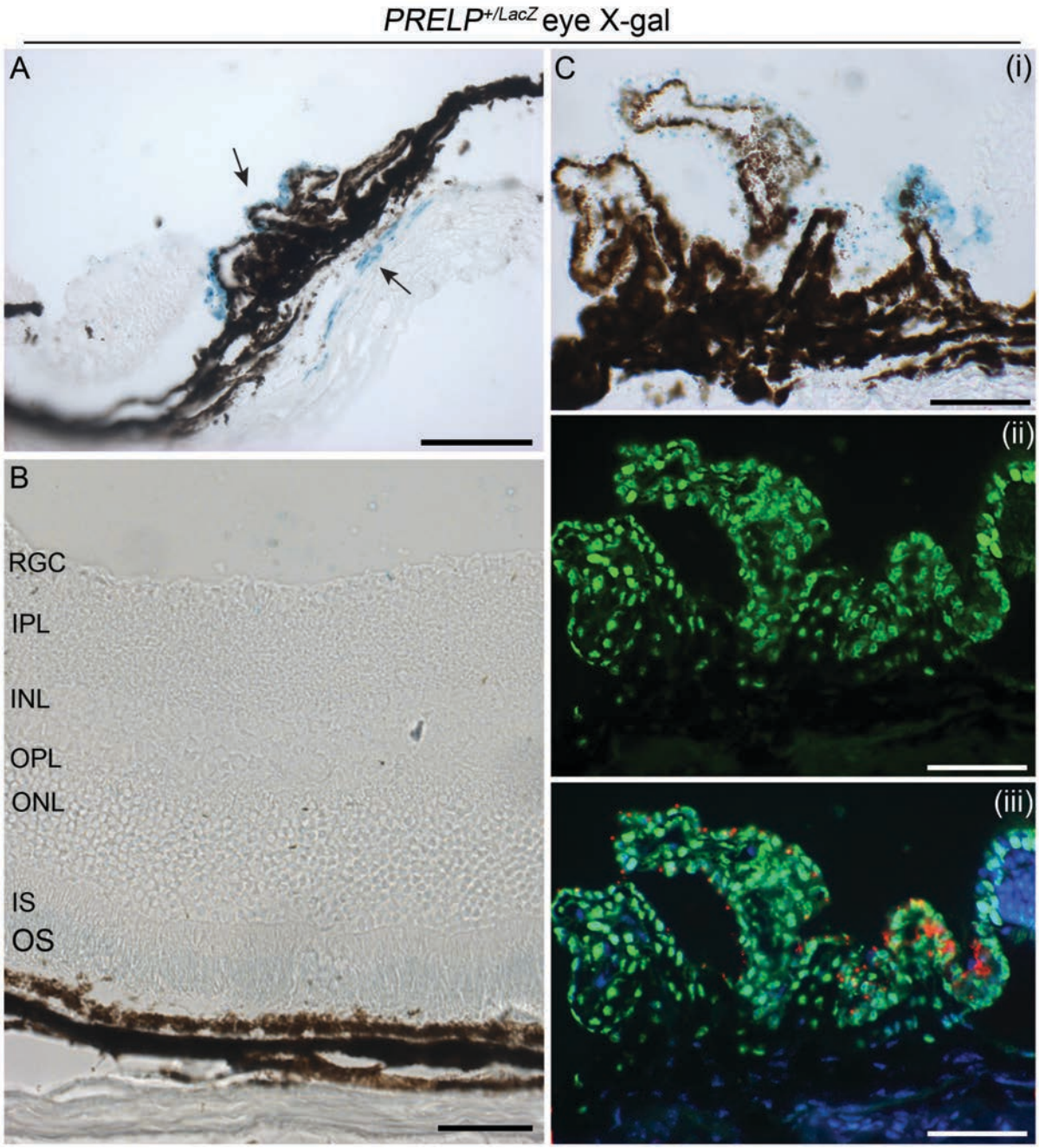

Figure 5.19: PRELP expression in the adult mouse eye is localised in the ciliary body and specifically in the non-pigmented epithelial cells. (A) X-gal staining of *PRELP*$^{+/LacZ}$ eye demonstrating Lac-Z activity in the epithelial cells of ciliary body and occasionally in the trabecular meshwork (arrows). (C) Higher magnification of an X-gal stained sample where the signal is visible in the non-pigmented cells. Immunofluorescence was performed using a Pax6 primary antibody and an alexa-488 (green) as secondary (ii). (C-iii) Merged images of (i) and (ii), where X-gal is coloured red and DAPI (blue) is added as nuclei stain. B-gal signal is co-localised with some of the Pax6-positive cells, while in others it appears to be located adjacent to the cell bodies. No X-gal staining is seen in any of the retinal cell layers (B). Scale bars, 200μm for (A), 50μm for all other images. RGC, retinal ganglion cells; IPL, inner plexiform layer; INL, inner nuclear layer; OPL, outer plexiform layer; ONL, outer nuclear layer; IS, inner segments; OS, outer segments.

5.2.5.3 PRELP expression in the adult mouse brain

Whole brains were isolated from adult *PRELP*$^{+/LacZ}$ and *PRELP*$^{+/+}$ littermates and were either whole-mount stained for X-gal, or processed for cryo-sectioning and subsequently stained. In the latter case, X-gal staining was performed in serial sections covering the whole brain from the olfactory lobes to the end of the cerebellum. Starting with Figure 5.20, where a heterozygote whole-mount stained brain is presented, strong β-galactosidase activity is observed in all the blood vessels covering both the dorsal and ventral part of the brain, as well as around the optic nerves, the space between the two hemispheres (superior sagittal sinus) and the central canal of the spinal cord (Fig. 5.20 A&B). In addition, there is some diffuse staining in the hypothalamic area, while no staining is present in the optic chiasm (Fig 5.20C arrow and arrowhead respectively). In figure 5.20D a magnified view of the middle cerebral artery is displayed, where it is clear that the X-gal staining is very specific to some cells surrounding the surface of the blood vessels, reminding pericyte-like cells whose cell bodies are encircling the capillaries. Upon dividing the brain into the two hemispheres (Fig. 5.20E), β-gal signal is present in the hypothalamic area, the dorsal 3rd ventricle (Fig. 5.20F), the aqueduct and the 4th ventricle together with the cerebellar vasculature (Fig. 5.20G). Furthermore, all the blood vessels of the cerebral cortex are also positive for X-gal (Fig. 5.20H), whereas in Figure 5.20I a closer view of the right olfactory bulb capillaries is shown, demonstrating b-gal and thus PRELP expression in the majority of the vessels.

In parallel, other *PRELP*$^{+/LacZ}$ brains were frozen, coronally sectioned and afterwards stained for X-gal. The results are demonstrated in Figure 5.21, where overall the b-gal signal is confined around the ventricle walls, the choroid plexus (CP) and the blood vessels (as was expected from the whole-mount staining). In detail, around 0.86 mm before the bregma, b-gal staining is seen in the cells surrounding the walls of the lateral ventricles (LV), indicating that PRELP is probably expressed by ependymal cells (thin epithelium-like cells lining the ventricular system of the brain and the spinal cord) (Fig. 5.21 A&D). Moving a little bit further after the bregma, very strong X-gal staining is observed in the choroid plexus of the dorsal 3rd ventricle (D3V), where some cells have more "spotty"-like staining, while others are fully stained (Fig 5.21 B&E). Reaching deeper into the

hippocampus area, signal is seen again in the walls of both the lateral ventricles, as well as the CP of the LV and D3V, together the lining of the 3rd ventricle (Fig. 5.21 C, F, G and H). Moreover, towards the posterior end of the brain, b-gal expression is seen in the walls of the 4th ventricle and the aqueduct (Aq) (Fig. 5.21I). Finally, the majority of the capillaries found in the coronal sections are also positive, as expected (Fig. 5.21 arrows), while no expression is seen in any possible neuronal cell types.

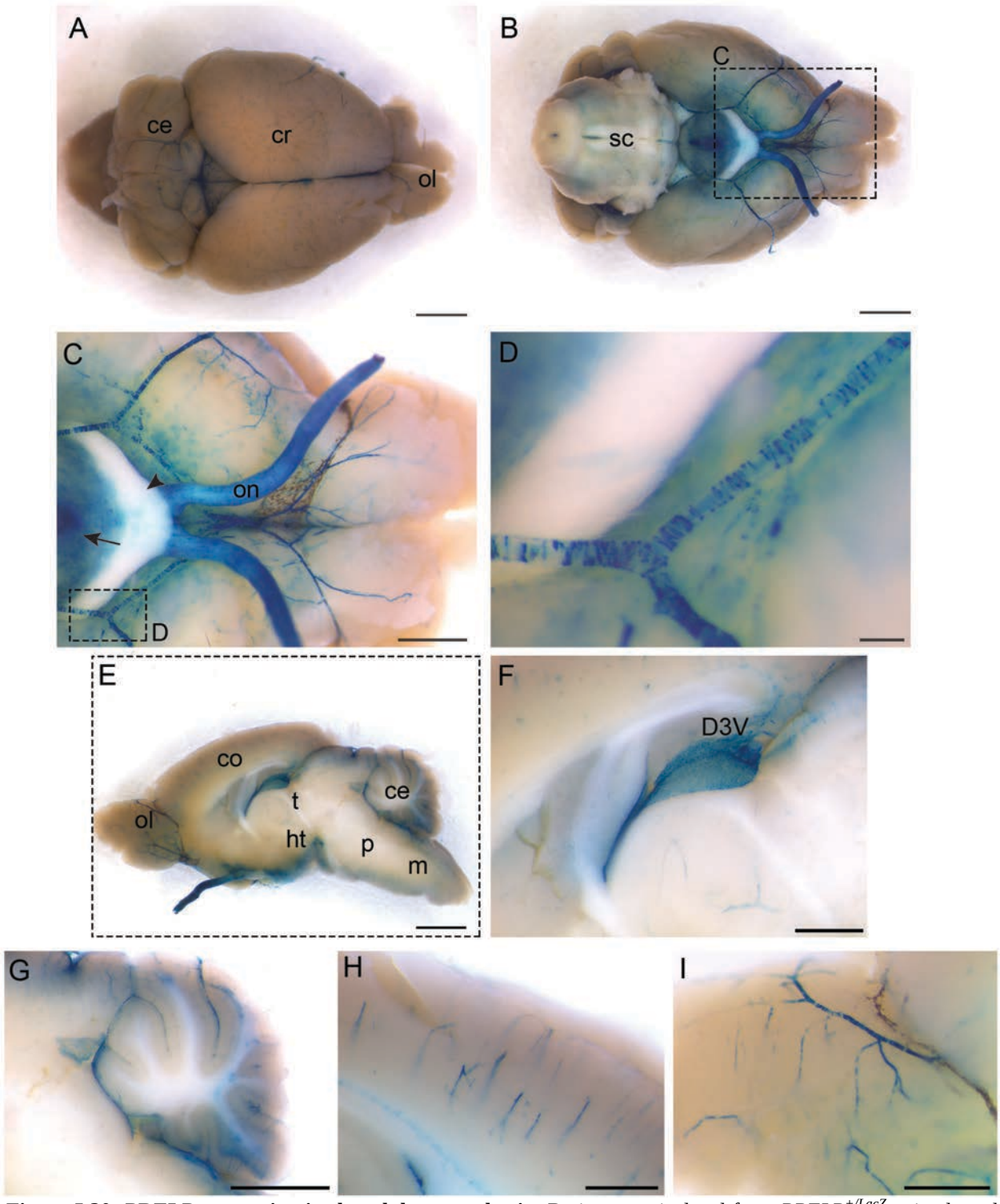

Figure 5.20: PRELP expression in the adult mouse brain. Brains were isolated from *PRELP*$^{+/LacZ}$ animals and were whole-mount stained for X-gal. (A)-(B) Dorsal and ventral sides of the brain demonstrating Lac-Z activity in the blood vessels, the optic nerves and the central canal of the spinal cord. (C) Magnified images showing additional X-gal staining in the hypothalamic area (arrow), but not the optic chiasm (arrowhead). (D) Enlarged view of the middle cerebral artery exhibiting specific β-gal signal around the capillaries. (E) Cutting the brain sagittaly revealed X-gal staining in the dorsal 3rd ventricle (F), the 4th ventricle and the aqueduct (G) and the cerebellar vasculature (H). In (I) a view of the olfactory bulb is shown, demonstrating again X-gal staining around the capillaries. Scale bars, 2mm for (A), (B) and (E), 1mm for (C), (G), 500μm for (F), (H), (I), 50μm for (D). cr, cerebrum; ce, cerebellum; ol, olfactory lobes; sc, spinal cord; co, cortex; t, thalamus; ht, hypothalamus; p, pons; m, medulla; D3V, dorsal 3rd ventricle.

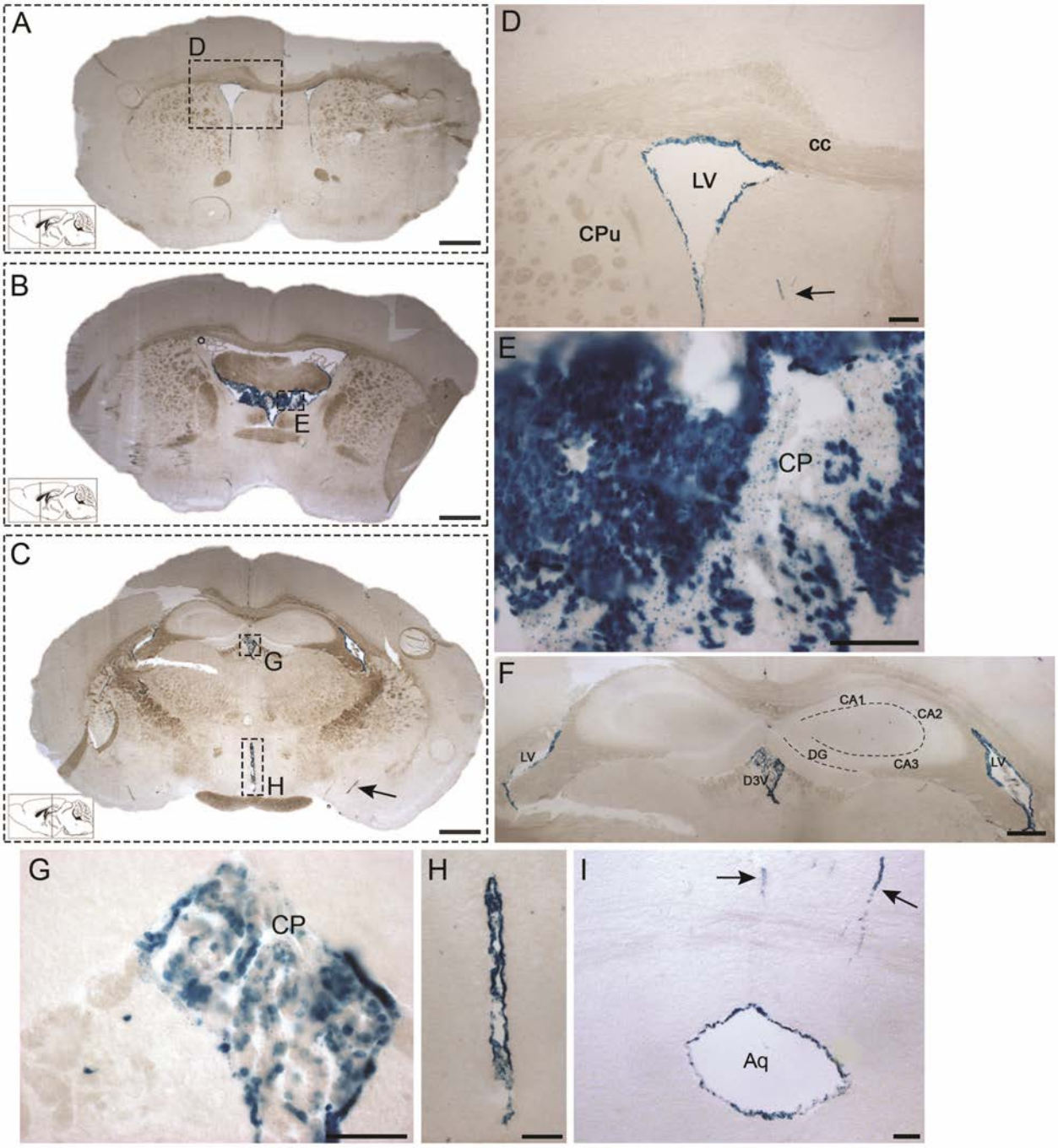

Figure 5.21: PRELP expression in sections of the adult mouse brain. Brains from PRELP heterozygous mice were cryo-sectioned and stained with X-gal. (A)-(C) Three different coronal planes demonstrating Lac-Z activity in the linings of ventricles, in choroid plexus and in blood vessels (arrows). (D) Enlarged view showing clear X-gal staining in the epithelial lining of the lateral ventricle, where ependymal cells reside. (E) Magnified view of the dorsal 3rd ventricle choroid plexus, where β-gal staining is very strong in some cells and faint in other. The same staining pattern is seen further inwards the brain (F) & (G), while the linings of the 3rd ventricle and the aqueduct are also positive for Lac-Z, as shown in (H) and (I). Arrows indicated X-gal stained blood vessels. Scale bars, 1mm for (A)-(C), 140μm for (D), (F), (I), 50μm for (E), (G) and (H). CPu, caudate putamen; cc corpus callosum; LV, lateral ventricle; CP, choroid plexus; D3V, dorsal 3rd ventricle; Aq, aqueduct; DG, dentate gyrus; CA1/2/3, pyramidal cell populations of the CA1/2/3 fields.

In order to identify the specific cell types where PRELP is expressed (through β-gal) fluorescence staining with several markers was performed on top of the X-gal reaction, and during image processing the X-gal signal was coloured either green or red. More specifically, β-gal staining was co-localised with vimentin, which is a marker for ependymal cells, in the epithelial-lining of the walls in all the ventricles. In Figure 5.22 A-C an image of the 3rd ventricle is shown, where most of the X-gal is localised around or inside the vimentin-positive ependymal cells. Furthermore, regarding PRELP expression around the brain capillaries, three different markers were used, namely NG2, PECAM-1 (or CD31) and anti-alpha smooth muscle actin (α-SMA) antibodies, which stain for pericytes, endothelial cells and smooth muscle cells respectively. In Figure 5.22 B-C two examples of stained blood vessels are presented, where the X-gal signal is expressed in a sub-population of NG2-positive pericytes. Particularly, in Figure 5.22 B-iii we can discern the main body of a pericyte, which is not positive for PRELP (arrow), whereas in Figure 5.22 C-iii, even though only one side of the branched vessel is positive for β-gal, the signal is co-localised with the pericytes found on that side (arrowheads). As pericytes are characterised by a large spherical shape around their nucleus (arrows in Fig. 5.22 B/C-iii) accompanied by thin extensions surrounding the vessels, it is possible that the β-gal signal (and thus PRELP) is localised, apart from the cytoplasm around the nucleus (like shown in Fig. 5.22 C), also in the thin extensions, which we cannot always pick up with this imaging resolution.

Continuing with the other markers, X-gal signal does not overlap with PECAM-1 positive endothelial cells, as shown in Figure 5.23A. In addition, when staining for vascular smooth muscle cells (VSMCs) using the α-SMA antibody, we observe that most of the signal does not co-localize with the X-gal staining, with the exception of few occasions (Fig. 5.23B, arrowheads). Thus, we can conclude that PRELP is expressed by a sub-population of pericytes and occasionally from VSMCs. However, complete characterization of PRELP expression in the brain vasculature still remains obscure, since all these different cells types are positioned in very close proximity with each other and higher resolution imaging technique is required to distinguish the exact localization of the X-gal signal. Finally, an area close to the 3rd ventricle was stained with X-gal and NeuN (a general neuronal marker), confirming that PRELP expression is absent from neurons (Fig. 5.23C).

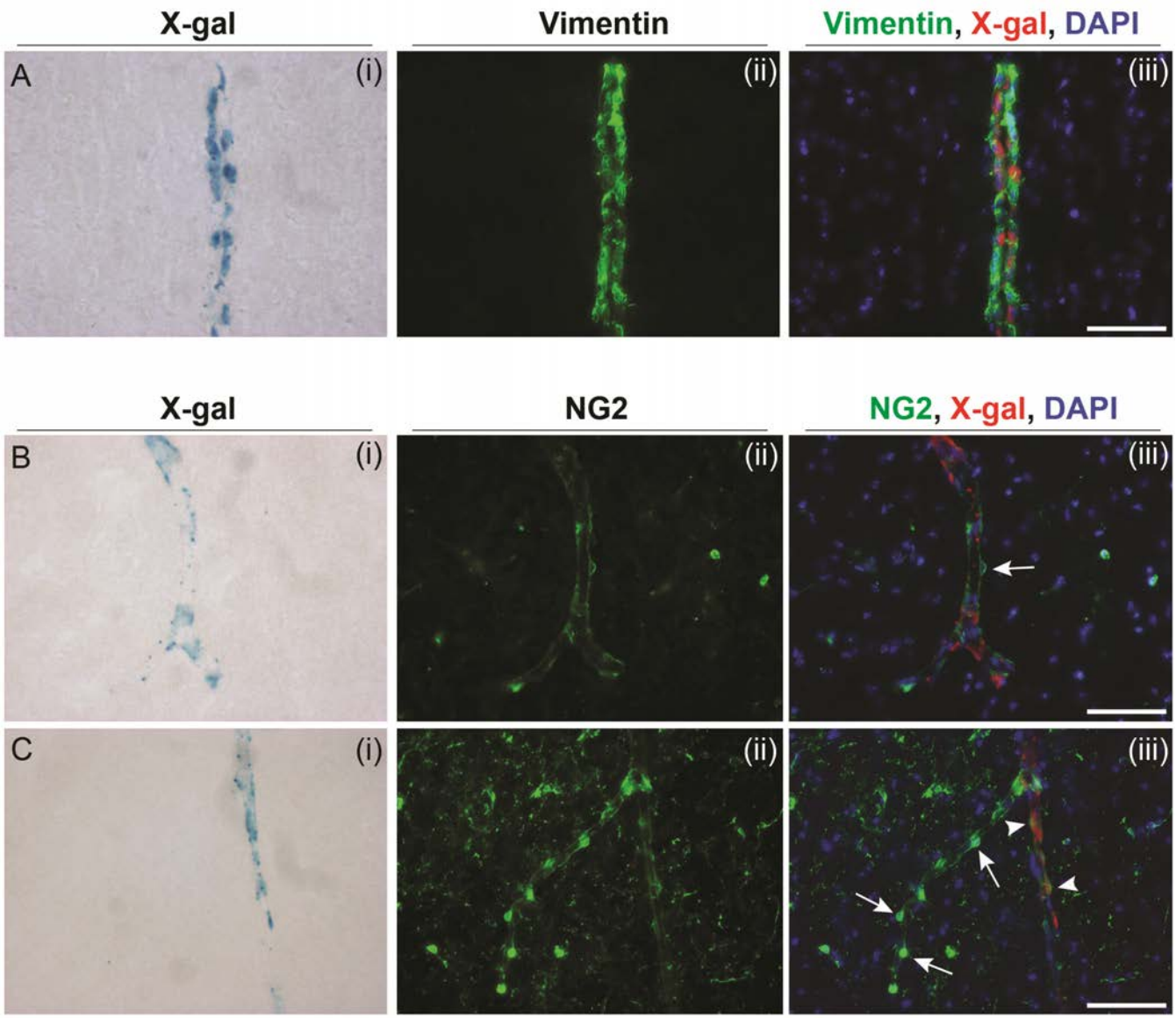

Figure 5.22: PRELP is expressed in ependymal cells and pericytes. (A) In the area of the 3rd ventricle X-gal overlaps with vimentin staining, suggesting PRELP expression in ependymal cells. (B)-(C) In the blood vessels β-gal signal occasionally overlaps with NG2-positive pericytes. Arrows indicate the main bodies of pericytes that do not express Lac-Z, while arrowheads show areas of co-localisation with X-gal, which can be seen either close to the pericyte main body or further away from it. Panels (i) are X-gal staining, panels (ii) are immunofluorescence using specific primary antibodies and alexa-488 (green) as secondary, and panels (iii) are merged images with DAPI (blue) as a nuclei stain. Scale bars, 50μm for all images.

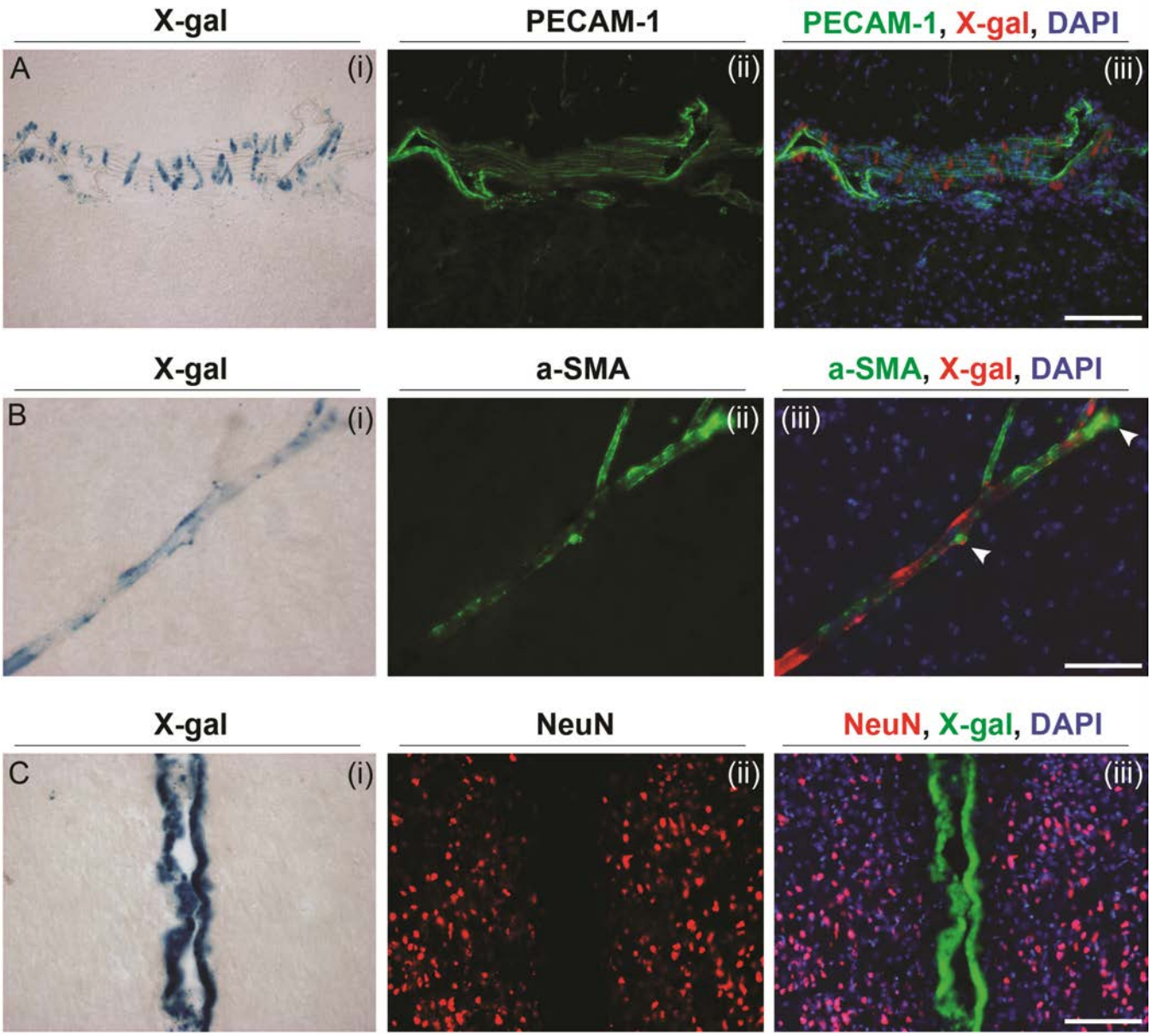

Figure 5.23: PRELP is occasionally expressed in vascular smooth muscle cells. (A) X-gal staining does not overlap with PECAM-1 positive endothelial cells around the blood vessels, while it occasionally overlaps with a-SMA positive vascular smooth muscle cells, as indicated by arrows in (B). (C) The area of the 3rd ventricle showing that the β-gal signal seen in the lining of the ventricle is not co-localised with any neuronal cells types (NeuN-positive cells). Panels (i) are X-gal staining, panels (ii) are immunofluorescence using specific primary antibodies and alexa-488 (green) as secondary for (A)&(B), alexa-546 (red) for (C), and panels (iii) are merged images with DAPI (blue) as a nuclei stain. Scale bars, 100μm for (A), 50μm for (B), (C).

5.2.5.4 PRELP expression in the adult mouse bone

Evaluation of PRELP expression in the adult bone was performed on the knee joint including part of the femur and the tibia. As mentioned before, X-gal activity was assessed through whole-mount staining of the tissue, followed by decalcification and cryo- or paraffin-sectioning. Sectioning and subsequent X-gal staining, that would give more accurate results, was not applicable in this case, as decalcification (which is necessary at this stage) would nullify the β-gal enzyme. In Figure 5.24 A&B two different sections of a *PRELP*$^{+/LacZ}$ knee joint are presented, where signal can be seen in the articular cartilage, the meniscus, the synovial tissue and occasionally in some areas around the cortical bone, between the calcified bone and the adjacent muscle (probably the periosteum). More specifically, strong staining is present in the outmost articular chondrocytes towards the ventral and dorsal sides of both femur and tibia, but not in the middle of the joint capsule. In addition, certain parts of the synovium are intensely stained, including the areas close to the articular cartilage and the meniscus (Fig. 5.24 C&D). Also, in Figure 5.24E a magnified view of the femur cortical bone is presented, where diffuse staining is visible in what probably is the periosteum. Furthermore, β-gal signal is present in the fat tissue surrounding the joint, while it is absent from the growth plate or the bone marrow. Finally, a section of a *PRELP*$^{+/+}$ sample is included in Figure 5.24 F&G, showing minimum background staining in the apoptotic/hypertrophic chondrocytes of the growth plate, indicating that the X-gal staining in the heterozygote knee joint is true and specific signal for PRELP.

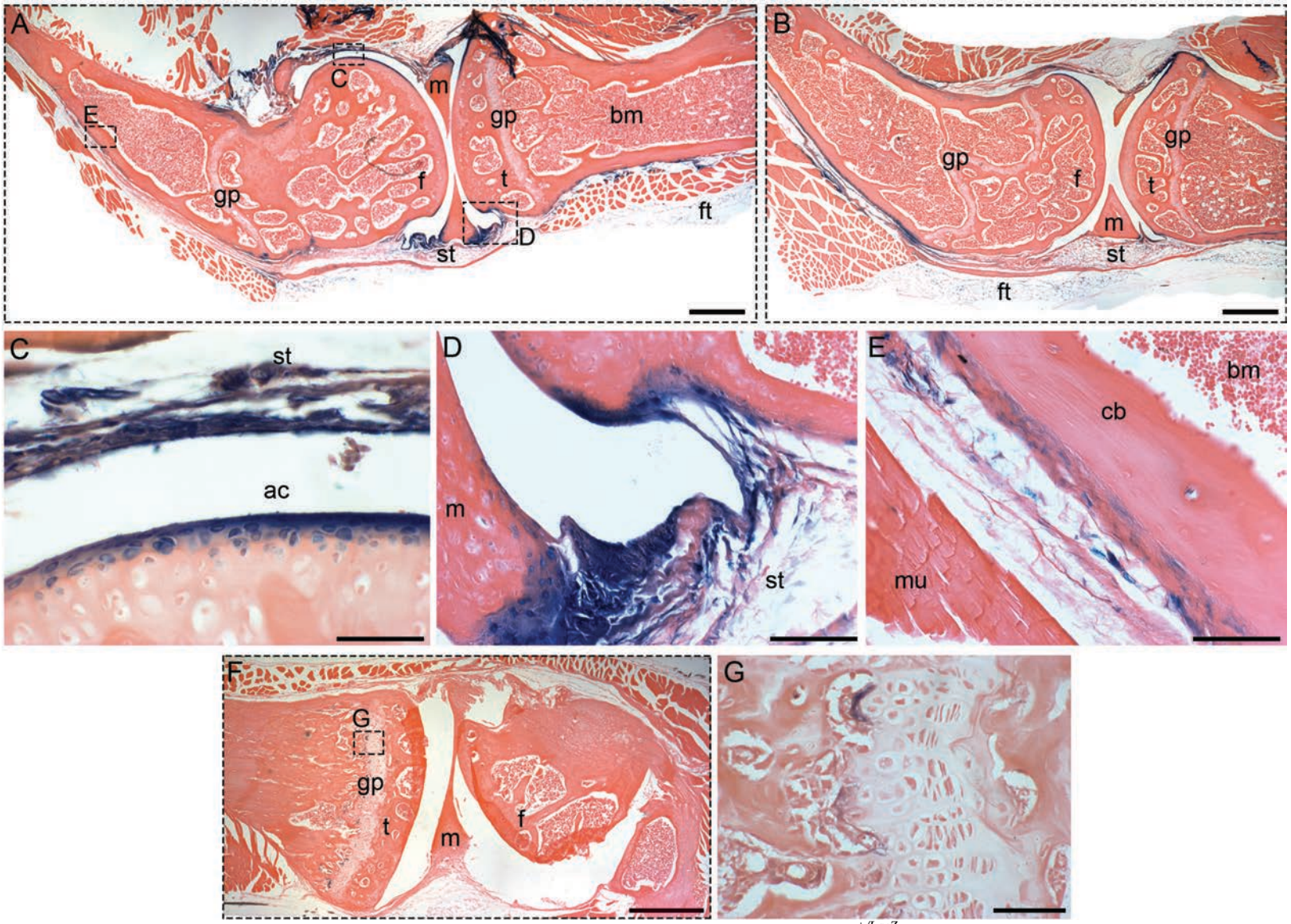

Figure 5.24: PRELP expression in the adult bone. (A)-(B) X-gal stained knee joints from *PRELP*$^{+/LacZ}$ animals demonstrating Lac-Z activity in the articular cartilage, the meniscus, the synovial tissue and occasionally around the cortical bone. (C) Magnified view showing strong β-gal signal in the articular chondrocytes of the femur and the adjacent synovial tissue. (D) Enlarged view of the meniscus area exhibiting again strong staining in the synovial tissue. (E) View of the femur cortical bone, were diffuse X-gal staining can be seen in the periosteum area. (F)-(G) X-gal staining of a wild type sample where minimum background staining can be seen in the apoptotic chondrocytes of the growth plate. Scale bars, 500μm for (A), (B), (F), 100μm for (D), 50μm for (C), (E) and (G). f, femur; t, tibia; m, meniscus; st, synovial tissue; ft, fat tissue; gp, growth plate; ac, articular cartilage; cb, cortical bone; bm, bone marrow; mu, muscle.

5.3 Discussion

Detailed analysis of the murine *PRELP* gene expression was performed using the newly established PRELP knock-out mouse model. In this model, the gene transcription domain, located in exons 2 & 3, is replaced with a Lac-Z cassette, generating viable and fertile heterozygous (*PRELP*$^{+/LacZ}$) and homozygous (*PRELP*$^{LacZ/LacZ}$) mice, without any obvious gross abnormalities during development or postnatal life. Expression of PRELP is widely detected in the cartilaginous skeleton during the embryonic stages, but also in the early and late fetal brain. This pattern expands to include other organs as well, like the eye and the bladder, in the adult animals.

PRELP expression in developing brain

Expression was examined in the E12.5, E15.5, and E17.5 embryonic stages, and in new-born P0 mice. Intensity of the β-gal signal after X-gal staining was always higher in the *PRELP*$^{LacZ/LacZ}$ than *PRELP*$^{+/LacZ}$ animals, while no background staining was present in wild type embryos, demonstrating specific expression of the Lac-Z cassette under the PRELP promoter. In E12.5 embryos expression is located in the developing somites and the brain, while signal is also visible in the cartilage primordia of the forelimb, the notochord, the neural tube and the 4th ventricle roofplate in the hindbrain (Fig. 5.2, 5.3 & 5.4). To our knowledge, this is the first time PRELP expression is seen in non-cartilaginous tissues during development. Grover and Roughley reported PRELP mRNA expression in 7.5dpc embryos, which declined afterwards, to be detected again at 14.5dpc following the onset of skeletogenesis (Grover and Roughley, 2001). However, this analysis included RNA extracted from whole embryos, so it is inconclusive of the areas of expression.

Interestingly, the symmetrical β-gal signal observed in the forebrain (Fig. 5.4 arrows), appears to be located in the cortical hem just above the developing choroid plexus (CP). The cortical hem was originally identified as an embryonic structure defined by Wnt expression that exhibits hippocampal organizer activity (Grove et al., 1998; Mangale et al., 2008). More specifically, Lac-Z staining is in the same area where *Wnt3a* and *Wnt2b* are expressed, marking the cortical neuroepithelium but not the CP (Grove et al., 1998; Himmelstein et al., 2010), indicating a possible role of

PRELP in early patterning of the telencephalon. In addition, the β-gal signal that is seen in the midbrain/hindbrain boundary could be co-localised with the expression domains of *Wnt1* and *Fgf8*, where, together with the floor plate, the isthmic organizer and the rhombic lip are located (Basson and Wingate, 2013). This could further suggest involvement of PRELP in the development of the vermis and cerebellum**.** Unfortunately, due to time restrictions, proper characterization of the Lac-Z positive cells could not be performed at this stage, and therefore we can only make speculations about PRELP activity in the early mouse brain patterning. Nevertheless, this spatiotemporal PRELP expression pattern is compelling, and detailed analysis of the expressing areas, as well as analysis of expression in earlier embryonic stages, would be very interesting.

Lac-Z activity in the fetal brain was reduced by stage E15.5, where β-gal signal was visible only at the roof plate of the future aqueduct and not in other structures like the cortical hem or the choroid plexus (Fig. 5.8). Lac-Z activity is seen again at 17.5dpc, specifically in the choroid plexus of the 4th ventricle and some cells on the lining of the dorsal 3rd ventricle wall closure (Fig. 5.12 D&E). The same staining pattern is observed in new-born mice with the additional staining of the 3rd ventricle choroid plexus and also the cells lining the ventricles (Fig. 5.14 D, 5.15 D&E). Although no staining with specific cell makers was performed, we can assume that the positive cells on the ventricle walls are ependymal cells due to their localization and epithelial-like shape.

Choroid plexuses are formed between E11 and E14 stages in the mouse embryo with the 4th ventricular CP differentiating first followed by the lateral ventricles and lastly the 3rd ventricle CP (Dziegielewska et al., 2001). The exact roles of the CP in brain development together with the factors that regulate CP development are still largely unknown. However, Notch and BMP signaling pathways regulated by the rhombic lip have been shown to be involved in choroid plexus development during the early embryonic stages (Hebert et al., 2002; Hunter and Dymecki, 2007). Also, CPs acquire their barrier and secretory functions shortly after formation, thus influencing cerebrospinal fluid (CSF) composition and the development of neural stem cells in the ventricle linings (Gotz and Huttner, 2005; Johansson et al., 2006; Johansson et al., 2005; Millgard et al., 1976). Therefore, expression of PRELP in the

CPs by day E17.5 indicates that PRELP probably does not affect choroid plexus formation, but becomes a component of the mature epithelial CP cells. Whether expression of PRELP in the rhombic lip at stage E12.5 could affect CP formation we do not know, but we cannot exclude such possibility.

These processes are also linked with ependymal cell differentiation. Most ependymal cells are generated between E14 and E16, while maturation and formation of the cilia occurs during the first postnatal week (Spassky et al., 2005). The ependymal progenitors are thought to be radial glial cells, while it appears that continuous contact with the CFS might also affect their differentiation (Spassky et al., 2005; Tramontin et al., 2003). Silva-Alvarez *et al*. showed that ependymal cell differentiation coincided with glucose transporter 1 (GLUT1) expression in the ventricular walls (Silva-Alvarez et al., 2005). Interestingly, Lac-Z activity in the P0 $PRELP^{+/LacZ}$ brain shows very similar staining to that of GLUT1, suggesting PRELP expression in the differentiating ependymal cells.

Embryonic brain morphogenesis and patterning is a very complex procedure involving many signaling molecules and regulators. Clearly PRELP is somehow involved in some stages of this process, but since this was not the primary subject of this project no more work was conducted on this field. However, it would be very interesting to unravel how PRELP acts during brain formation.

PRELP expression in the developing skeleton

At the earliest stage examined (E12.5) the developing skeleton is still very premature and X-gal activity was seen only faintly in the cartilage primordia of the forelimb (Fig. 5.4 F). However, by stage E15.5 skeletal development has progressed considerably and strong X-gal staining is present in all the cartilaginous elements of the developing axial and appendicular skeleton, including the forelimb and hindlimb, the ribs, the vertebrae, the nasal septum and Meckel's cartilage in the mandible (Fig. 5.5., 5.6 and 5.7). The main cell types expressing Lac-Z are chondrocytes, with some diffuse staining seen occasionally in mesenchymal cells, such as the borders of the nasal septum or Meckel's cartilage and the dental papilla of the developing molars (Fig. 5.7 and 5.8). Again, this mesenchymal-type expression has not been reported before and appears to be specific for this stage of development, as during the next

analysed stages (E17.5 & P0) β-gal is clearly expressed only in the chondrocytes of the respective tissues (Fig. 5.8 vs. 5.11/5.13).

Looking at the long bones of the forelimb or hindlimb at 15.5dpc (Fig. 5.9), it is visible that Lac-Z activity, and thus PRELP, follows a gradient of expression through the different chondrocytic populations. More specifically, signal is strong in the columnar/proliferating and the pre-hypertrophic chondrocytes, while it is decreased in the hypertrophic ones until it is no more present in the primary ossification groove. Signal is seen in some resting chondrocytes as well (localised in the opposite end of the ossification front) and also in the perichondrium. This pattern is slightly changed in E17.5 heterozygote embryos, where signal is still strong in the proliferating chondrocytes but has decreased in the pre-hypertrophic ones. Faint staining is still present in apoptotic/hypertrophic chondrocytes, marking the start of the mineralization front. In addition, staining is no longer present in the perichondrium but is now visible in the articular chondrocytes of the joints and in the early synovial tissues (Fig. 5.10). Furthermore, resting, proliferating and articular chondrocytes in the endochondral bones of the head are also β-gal positive (Fig.5.12 A, B, C, F) resembling the expression pattern seen in the long bones.

The same expression pattern is maintained in P0 new-born embryos. Briefly, X-gal staining can be seen the nasal septum, the cartilaginous part of the VNO, in part of Meckel's cartilage as well as the chondrocytic parts of the cranial bones that have not yet been ossified (Fig. 5.13, 5.14, 5.15). In the long bones β-gal signal is observed again in resting and proliferating chondrocytes, while the staining is also strong in the articular chondrocytes of the joints and the vertebral bodies (Fig. 5.16). All the above findings are in agreement with previous studies demonstrating PRELP expression in the skeletal cartilage of the developing mouse, in proliferating chondrocytes of rat tibia bones and in human cartilage (Grover et al., 1996; Grover and Roughley, 2001; Lui et al., 2010).

Overall, PRELP appears to be a cartilage-specific SLRP, following a specific chondrocytic expression pattern during endochondral osteogenesis. Although we have specified the main cell populations that are positive for X-gal activity, usage of markers to identify chondrocytic differentiation stages (as described in section 4.3) is necessary. Apart from the fetal brain, Lac-Z activity was not observed in any other

internal organs, indicating that PRELP mainly functions in the brain and skeletogenesis during development.

PRELP is expressed in the adult mouse bladder, eye, brain and bone

PRELP expression was examined in the adult bladder, eye, brain and knee joint through X-gal staining. In the bladder Lac-Z activity was seen in the umbrella cell layer, as demonstrated by co-localisation of the β-gal signal with uroplakin and CK18, but not laminin and CK5 (Fig. 5.17 & 5.18). This expression pattern is very similar to the OMD expression and since this was extensively discussed in the previous chapter it will not be reviewed again here.

In the adult eye β-gal signal is seen in the ciliary body and occasionally in the trabecular meshwork (Fig. 5.19A). Staining with Pax6 demonstrated Lac-Z expression in the non-pigmented epithelial cells of the CB, while no expression was seen in the retina or other areas of the eye. Also, we cannot exclude expression in the pigmented cells of the CB, but in order to test this other technical approaches, like removal of the pigment, have to be employed. The mammalian ciliary body contributes to lens accommodation and aqueous humor secretion. The epithelial layers of the CB are connected at their apical membranes through gap junctions, while tight junctions at the apical borders of the non-pigmented cells form the blood–aqueous barrier, which also affects and determines the intraocular pressure (IOP) (Ford et al., 2012; Freddo, 2013; Raviola and Raviola, 1978). Therefore, PRELP could have a potential role in IOP modulation through tight junction or gap junction regulation. Furthermore, the pigmented cells of the CB have been proposed to act as stem cells of the adult mammalian eye (Tropepe et al., 2000; Xu et al., 2007), although this has been a matter of controversy over the last decade. Hence, any possible involvement of PRELP in stem cell functions would also be an interesting proposition to examine.

In contrast to our findings, high mRNA and protein levels of PRELP, and also other SLRPs like decorin and lumican, were previously discovered in the human adult sclera (Johnson et al., 2006). Given the fact that sclera is a highly collagenous tissue, expression of ECM molecules like SLRPs would not be surprising. However, a different study demonstrated strong PRELP expression in the human neurosensory

retina and only moderate levels in the choroid and sclera (Keenan et al., 2012). We therefore see that findings are quite variable depending on the specificity and the efficacy of the method used, even within the same species examined. In the *PRELP*$^{+/LacZ}$ mouse eyes examined here the β-gal signal continuously appeared in the same areas, while no signal was seen in any *PRELP*$^{+/+}$ wild type mice, indicating the specificity of the staining. Thus, the different expression patterns seen in the above studies could probably be attributed to the species difference.

Amongst the other organs examined, PRELP expression is very intriguing in the adult brain as well. Lac-Z activity was observed all around the blood capillaries, the optic nerves, the lining of all the ventricles and in the choroid plexus (Fig. 5.20 & 5.21). Staining with vimentin confirmed β-gal signal in ependymal cells, while occasionally β-gal was co-localised with NG2 and a-SMA, demonstrating PRELP expression in pericytes and vascular smooth muscle cells (Fig. 5.22 & 5.23). Pericytes, ependymal cells and epithelial cells of the choroid plexus, all play important roles in forming barrier mechanisms within the brain. CP forms the blood-CSF barrier, pericytes together with smooth muscle and endothelial cells are part of the neurovascular unit (NVU) which forms the blood-brain barrier (BBB), while ependymal cells regulate the CSF flow as well as the uptake of molecules from the CSF to the brain parenchyma through gap junctions (Neuwelt et al., 2011; Winkler et al., 2011). PRELP expression was only mentioned in the adult brain in one study so far where it was localized in pericytes of the rat anterior pituitary (Horiguchi et al., 2013). Expression in other areas of the brain was not examined or at least was not mentioned in the above study. Therefore, PRELP might emerge as an important regulator of brain vessel permeability and could be involved in a variety of BBB-related pathological conditions such as Alzheimer's disease, Parkinson's disease or multiple sclerosis.

Finally, similarly to OMD, PRELP expression in the adult bone was assessed in the knee joint, where Lac-Z activity was observed mainly in the synovial tissue and in articular chondrocytes, and occasionally around the cortical bone (Fig. 5.24). These findings are in contrast with a previous study by Grover et al. demonstrating PRELP protein and mRNA expression in the growth plates rather than the articular cartilage of the joints in the adult mouse (Grover and Roughley, 2001). As our

method of detection involved whole-mount staining prior to sectioning we cannot exclude the possibility that staining solutions did not penetrate the sample equally or that the staining time was insufficient for the enzymatic reaction to take place in the whole tissue. Therefore, optimizing the current staining method but also testing alternative detection approaches, like *in situ* hybridisation, is necessary to determine if PRELP is indeed expressed in the growth plates of the adult bone. Also, our results indicate a shift of PRELP expression from the majority of chondrocytes (especially proliferating) in the developing embryo and new-born to only articular cartilage in the adult mouse, which is very similar to the OMD findings. In general agreement with our results, expression of PRELP in articular cartilage of adult human and bovine tissues has been shown before (Bengtsson et al., 1995; Grover et al., 1996; Grover and Roughley, 2001), confirming the role of PRELP in connecting tissues. Lastly, regarding the strong expression of PRELP in the knee synovial tissues, Segawa *et al*. also found high PRELP expression in mesenchymal stem cells isolated from human synovial tissues, suggesting a conserved role of PRELP in these cells (Segawa et al., 2009).

In conclusion, PRELP has a very dynamic expression pattern involving skeletal, connecting and also neural tissues, indicating the matricellular functions it may have throughout different biological systems.

Comparison of OMD and PRELP expression patterns

OMD and PRELP both belong to class II of the SLPR family based on their close homology, chromosomal organization and the spacing between their N-terminal Cys-rich clusters (Dellett et al., 2012). However, even though these two proteins are structurally similar, their expression patterns and functions may not always overlap, as is also seen with other SLRP members that belong to the same class. Utilising our novel knock-out mice models, OMD and PRELP expression patterns have now been extensively studied and thus we can assess their homology at the protein expression level.

During mouse embryonic development both proteins are strongly expressed in the growing skeletal elements. High levels of expression are seen already from E15.5 embryos, when skeletogenesis has slightly progressed and the first ossification

centres are starting to form. At this stage, OMD is exclusively localised in the periosteum/perichondrium and the primary ossification groove of the long bones, while very low levels of expression are occasionally seen in apoptotic chondrocytes. As skeletal development advances, OMD continues to be expressed in the periosteum but is additionally seen in proliferating chondrocytes, at 17.5 dpc. At the time of birth expression persists in the periosteum, but is also observed now in the osteoid matrix of the forming trabecular bone, while it is still present in the proliferating chondrocytes in some of the long bones.

On the contrary, at E15.5, PRELP expression is very strong in resting and proliferating chondrocytes, while it declines in the pre-hypertrophic and hypertrophic chondrocytes until it is no longer present in the ossification groove. This expression motif continues in E17.5 embryos and new-born mice, where PRELP is additionally seen in the articular chondrocytes of the joints. In contrast to OMD, PRELP expression is not seen at all in the ossification grooves or in the osteoid matrix.

We therefore see that during long bone development the two proteins are differentially expressed. OMD is mainly seen in areas where most cells will differentiate into osteoblasts, while PRELP is entirely seen in cartilage cells. These results are in agreement with previous findings on the two SLRPs. OMD binds to hydroxyapatite (which is found in mineralised tissues) and was initially isolated from the matrix of bovine bone (Sommarin et al., 1998; Wendel et al., 1998), while PRELP has been found in cartilaginous tissues of the developing mouse (Grover and Roughley, 2001), suggesting that the two proteins have different functions.

However, there are also some common areas of expression. For example, the proliferating chondrocytes of the growth plates, which are always positive for PRELP, are occasionally positive for OMD as well (Fig. 4.9J). This could indicate that both proteins share common roles in a specific stage of chondrocytic maturation. The rate of chondrocytic maturation in the growth plate cartilage is what regulates the endochondral bone development, and a complex network of interacting signalling pathways is employed to drive this process (reviewed by Kronenberg, 2003). Key players are the Indian hedgehog (Ihh) and parathyroid hormone-related peptide (PTHrP) protein. Briefly, Ihh is produced by pre-hypertrophic chondrocytes and induces the formation of proliferating chondrocytes while is also induces PTHrP

expression in the distant resting/periarticular chondrocytes. This secreted PTHrP antagonises then both the action of the Ihh and the maturation of the proliferative chondrocytes into pre-hypertrophic ones. With this negative-feedback loop the rate of chondrocytic maturation is regulated. Additionally to this mechanism, other factors likes Wnt5a and Wnt5b also regulate the transitions from resting to proliferative and proliferative to pre-hypertrophic chondrocytes, while bone morphogenic proteins (BMPs) and fibroblast growth factors (FGFs) also participate in this process (Kronenberg, 2003; Yang et al., 2003) (Fig. 5.25).

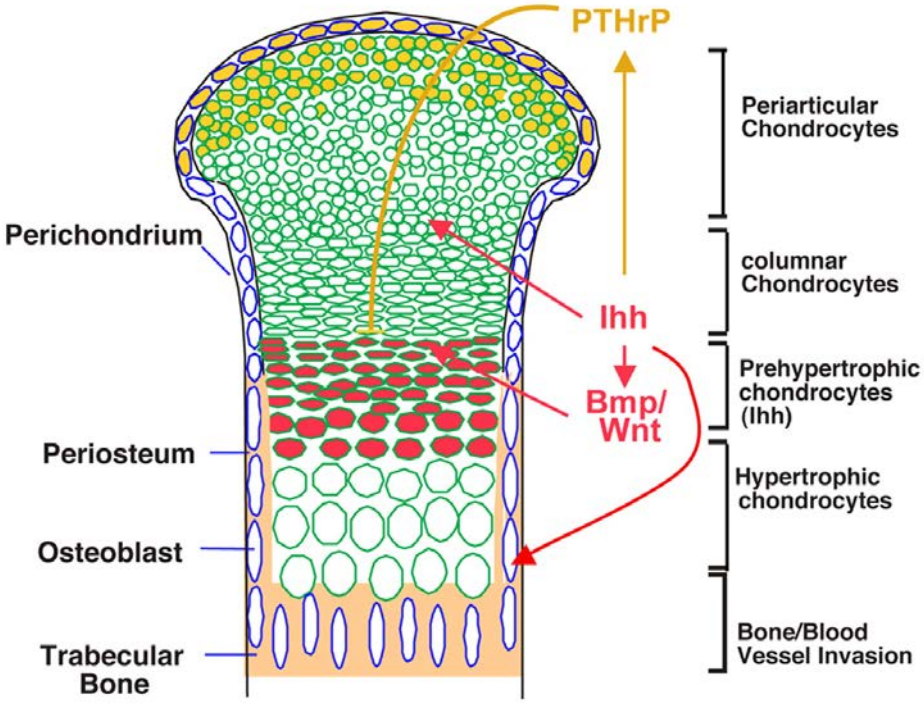

Figure 5.25: Model of the PTHrP and Ihh signaling in chondrocyte differentiation during long bone development. The morphology of a developing long bone is schematically shown, where chondrocytes proliferate and differentiate sequentially along the longitudinal axis. Ihh expression is shown in red and PTHrP expression is shown in yellow. Ihh acts through PTHrP to inhibit chondrocyte hypertrophy. Ihh acts independently of PTHrP to control chondrocyte proliferation, periarticular chondrocyte differentiation and osteoblast differentiation. Ihh also promotes chondrocyte hypertrophy independently of PTHrP and this function is likely to be mediated by Bmp and Wnt/β-catenin signalling. (Adopted by Mak et al., 2008).

Therefore, OMD and PRELP could both play potential roles in the regulation of the above signalling pathways and thus affect the rate of bone development. OMD has been found to interact with molecules of the Wnt pathway and with BMPs (Rehn et al., 2006) so it might somehow be involved in the proliferative to pre-hypertrophic/hypertrophic transition, while PRELP has already been used in a study

as a marker of proliferative chondrocytes during mouse endochondral development (Ahrens et al., 2009).

Apart from the periosteum and the osteoid matrix, OMD is also seen in the proliferating chondrocytes of the head endochondral bones, which develop similarly to the long bones. In the same area PRELP is also seen in the proliferating but also the articular chondrocytes (Fig. 4.13 vs. 5.15). Thus, this pattern of common expression in the developing growth plate is maintained even in all the endochondral bones, further supporting the notion that both proteins somehow affect the chondrocytic maturation process. In addition, chondrocytes of the outer nasal capsule and the inner nasal septum are positive for both OMD and PRELP, although OMD appears to have a more specific expression towards the marginal chondrocytes (and/or the perichondrium) found in these cartilaginous tissues (for example Fig. 4.11 vs. 5.13), suggesting potential functions in a particular chondrocyte maturation/differentiation stage. Finally, another common area of expression is the vertebral bodies and discs. In all the developmental stages examined both OMD and PRELP are expressed in the chondrocytes around the ossified vertebral bodies. Due to time limitations, in the current project specific staining was not performed in order to discriminate between the different chondrocytic types, but from cell morphology and shape we can hypothesize that these chondrocytes are again proliferating and/or resting. Thus, we can conclude that OMD and PRELP not only have their own specific roles during bone formation, but they additionally also share possible osteogenic functions and might have common signalling targets in the skeletal programming. The fact that in later life both proteins are expressed in the articular chondrocytes of the knee joint (and probably other joints as well) is quite intriguing, and additionally suggests specific roles of both OMD and PRELP for this type of chondrocytes.

Regarding expression in the adult mice, we have shown that OMD and PRELP are variably expressed in the different organs examined. Interestingly, both SLRPs are expressed in the bladder umbrella cells, indicating their potential common roles in these cell types. Taking into account our *in vitro* findings (Chapter 3) and Dr. Hamamoto's microarray data we can postulate that both OMD and PRELP could regulate junctional complexes in the umbrella cells. Since these cells play a critical

role as a permeability barrier to urine, proper regulation of their apical tight junctions is necessary for normal bladder homeostasis (Birder and Andersson, 2013). Moreover, a layer of polysaccharide GAGs and mucin usually covers the superficial urothelium and is thought to have variable functions, defending against microorganisms, toxic substances and carcinogens in the urine (Parsons et al., 2002; Parsons et al., 1990). Thus, SLRPs might constitute newly-discovered potential regulators of the bladder homeostasis.

As discussed in Chapter 4, several SLRPs are variably expressed throughout the different eye components and can affect eye formation and function in various ways. OMD and PRELP probably act in a similar manner and can potentially regulate functions of the mouse eye retina and ciliary body, which are yet to be discovered. The same applies to the mouse brain, where we have shown distinct expression patterns of the two SLRPs.

Summary

In conclusion, PRELP is expressed in specific areas of the early developing mouse brain but also in all the cartilaginous skeletal elements during embryonic growth. In adult life PRELP expression is confined to specific cell types in multiple organs, i.e. umbrella cells of the bladder, in pericytes and ependymal cells of the brain, in the epithelial ciliary body cells of the eye, and in articular and synovial tissues of the joints, demonstrating its multiple functions and roles in the living organism.

Chapter 6

Phenotyping of OMD and PRELP knock-out mice

6.1 Introduction

SLRPs are extra-cellular matrix components that can bind to many different molecules and receptors thereby regulating cell-matrix crosstalk and affecting various biological processes. Their spatial and temporal expression patterns are variable, and as structural and signaling molecules they play important roles during development but also in regulating the homeostasis of mature tissues. Utilizing animal models of SLPR deficiencies has revealed their importance in embryonic life and disease progression.

Several SLRP knock-out mice models have been established so far and the phenotypes arising are variable. To start with, decorin knock-out mice exhibit skin fragility phenotype with loosely packed collagen fibrils resembling the Ehlers-Danlos syndrome (Danielson et al., 1997), and are characterized by disrupted angiogenesis in the cornea (Schonherr et al., 2004) and altered mechanical lung morphology (Fust et al., 2005), emphasizing decorin's importance in regulating collagen fibrillogenesis. Most importantly, in the context of this project, one third of decorin-deficient mice develop intestinal tumours that further progress to adenocarcinomas (Bi et al., 2008), while double-KO mice of decorin and the tumour suppressor p53 showed accelerated lymphoma tumorigenesis which lead to earlier mortality (mice succumbed very early with a mean survival of ≈ 4 months versus 6 months for the p53 null mice alone) (Iozzo et al., 1999). As Iozzo and colleagues pointed out, these studies represent genetic evidence that lack of decorin is "permissive" for tumour development (Goldoni and Iozzo, 2008; Iozzo and Sanderson, 2011), strongly supporting the roles of SLRPs in cancer initiation and progression.

Other SLPR-KO models mainly involve biglycan, lumican and fibromodulin and again demonstrate several different phenotypes. Biglycan deficient mice have collagen fibril abnormalities, reduced bone mass and an osteoporosis-like phenotype (Chen et al., 2002; Corsi et al., 2002; Xu et al., 1998), while they also develop spontaneous aortic dissection and rupture (Heegaard et al., 2007). Fibromodulin-KO mice exhibit collagen fibril abnormalities in the cornea (Chen et al., 2010), impaired dental tissue and alveolar bone formation (Goldberg et al., 2009) and delayed wound closure (Zheng et al., 2011). Lumican deficient mice have skin fragility and reduced

corneal transparency (Chakravarti, 2002; Chakravarti et al., 1998), while keratocan-KO mice also display alterations in the cornea (Liu et al., 2003), but also decreased rates of bone formation and mineral apposition (Igwe et al., 2011).

SLRP double knock-out mice models have also been established and usually display stronger phenotypes that the single-KOs, indicating synergistic activity of the SLRPs. For example, biglycan and decorin deficient mice display severe osteopenia and increased skin fragility (Corsi et al., 2002; Young et al., 2002) and also severe fibril and stromal corneal phenotype (Zhang et al., 2009). Furthermore, biglycan and fibromodulin KO mice show severely impaired collagen fibrils in tendons and lead to gait differences, ectopic ossification and osteoarthritis (Ameye et al., 2002). In a similar context, epiphycan/biglycan deficient mice exhibited shorter femurs that the wild types and developed osteoarthritis, which had an earlier age onset compared to epiphycan single knock-outs (Nuka et al., 2010).

We therefore see that phenotypes arising from SLRP deficiencies vary from skin fragility to osteopenia, corneal opacity and cancer, further demonstrating the multiple functions of these proteins. In collaboration with Takeda Pharmaceutical Company we generated the first knock-out models of OMD and PRELP, where a Lac-Z cassette has been inserted in the two gene's coding regions. After defining the expression patterns of OMD and PRELP through X-gal staining (Chapters 4 & 5), our current aim is to investigate the phenotypes arising due to OMD/PRELP absence. Focus will be given mostly on the bladder as the initial *in vitro* data of this project were obtained from a bladder cancer cell line. Since we have already established a strong link of the *OMD* and *PRELP* genes with cancer in an *in vitro* experimental environment, cancer-related phenotypes constitute our primary interest, while preliminary analysis of other organs and other possible phenotypes will be also carried out.

6.2 Results

Construction of the OMD and PRELP knock-out mice was explained in Chapters 4 & 5, with no apparent severe defects in any of the heterozygote or knock-out mice, either during embryonic development or adulthood. This allowed us to study extensively not only the expression patterns of the two genes but also any latent phenotypic effects their deletion could generate. In adults, several organs were initially isolated in order to be studied, but due to time limitations primary attention was given to the analysis of the bladder, with less focus on the eye and bone. These organs were thoroughly investigated between wild types and knock-outs, while additional tests were occasionally performed in order to characterize any underlying phenotypes. Since both genes appear to be mostly expressed in skeletal development during gestation, examination of skeletal elements was performed in embryonic litters as well.

During the last months of the current project, and with the help of our lab technician Steven Bolsover, we managed to produce double knock-out animals where both the *OMD* and *PRELP* genes are disrupted by the Lac-Z cassette. $OMD^{LacZ/LacZ}PRELP^{LacZ/LacZ}$ double knockout mice were generated by interbreeding mice from the $OMD^{LacZ/LacZ}$ colony with mice from the $PRELP^{LacZ/LacZ}$ colony. Due to time restraints double KO samples were included only in the bladder analysis, while for the other organs single knock-out animals were used.

6.2.1 OMD/PRELP knock-out phenotypes in adult mice

6.2.1.1 Effect of *OMD* and *PRELP* targeted deletion in the mouse bladder

In order to analyze how depletion of *OMD* and *PRELP* could affect the normal function of the mouse bladder, three bladders from each $OMD^{+/+}$, $PRELP^{+/+}$, $OMD^{LacZ/LacZ}$, $PRELP^{LacZ/LacZ}$ and $OMD^{LacZ/LacZ}PRELP^{LacZ/LacZ}$ (named onwards as double KO) mice at 3 months of age, were isolated and studied. Since OMD and PRELP transgenic mice were generated using the same strategy and genetic background, $OMD^{+/+}$ and $PRELP^{+/+}$ mice should be phenotypically and genetically similar, and either of them would suffice as wild type. However, we chose to analyze both genotypes as WT controls in case any background alterations had occurred due to the extensive breeding and prolonged maintenance of the lines, at the

same time increasing our control numbers. As expected, no differences were found between *OMD*$^{+/+}$ and *PRELP*$^{+/+}$ WT bladders, and therefore samples from only one of the two genotypes will be presented as wild type in the following figures.

The first step in this analysis was the morphological and histological comparison of the bladders through H+E staining of paraffin sections. Shown in Figure 6.1 are panoramic views of all the bladders sectioned from each genotype. Interestingly, clot formations were found in three out of the nine knock-out samples tested. More specifically, clots were seen in the lumen of one out of the three *PRELP*$^{LacZ/LacZ}$ bladders, and in two out of the three double knock-outs (Fig. 6.1 C-ii & D-ii and more moderate in D-iii, arrows). In the PRELP-KO bladder the clot occupies the whole lumen, while in the double-KO (Fig. 6.1 D-ii) it covers almost half of the space in one case whereas it has slightly formed in the other (Fig. 6.1 D-iii). A more detailed analysis of these clots will be presented further below. Regarding the overall morphology of the bladders, all the samples appeared of similar size and the proportion of the mucosa (urothelium, basement membrane, lamina propria) and muscularis propria (surrounding muscle) remained analogous. In addition, the mucosal folds appeared to have the same density and length throughout the samples.

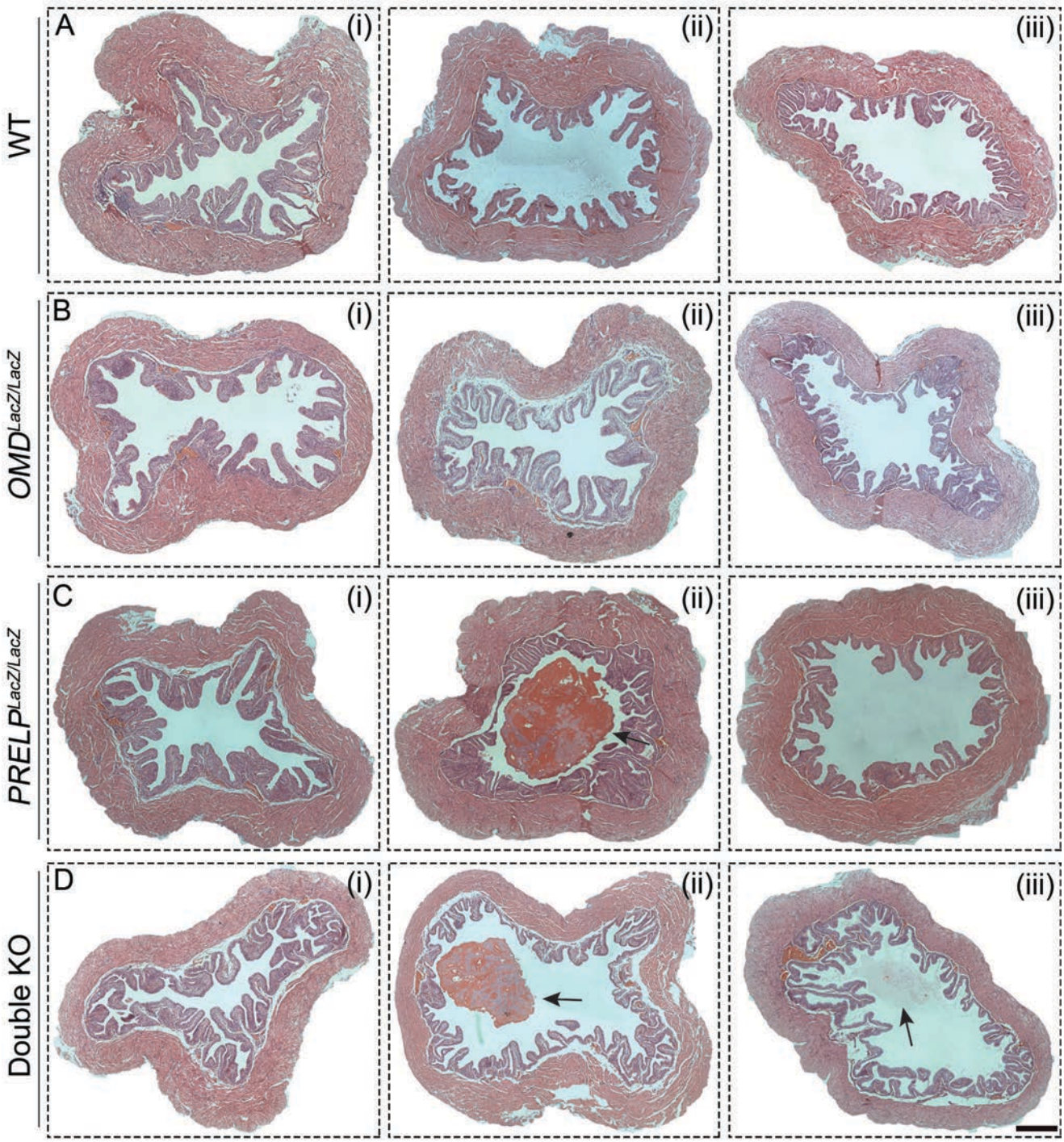

Figure 6.1: OMD and PRELP depletion leads to the formation of clots in the mouse bladder. Bladders were isolated from 3months-old mice, paraffin-sectioned and stained for H&E. Multiple mages were captured under the 10x magnification lens and were then stitched together to produce panoramic views of the whole organ. Clot formations were found in one PRELP KO and two double KO samples (arrows). In (C-ii) the clot is pretty big occupying the whole lumen, while in (D-ii) and (D-iii) the clots are smaller. Regarding the general morphology, wild type and knock-out samples appeared of similar size and the proportion of muscle and muscularis seems comparable. Scale bar, 500mm for all images.

In order to further analyse the tissue morphology, careful examination of the mucosal layer and specifically the urothelium was initially conducted. Figure 6.2

shows magnified images of the urothelium from all genotypes. When comparing the four different sample groups we found many sites with "disruption" or discontinuation of the urothelium apical surface in the knock-out bladders (Fig. 6.2 B-D, arrows). This disruption is characterized by a burst-like formation of the umbrella cell layer, and therefore we named these structures "epithelial bursts". Epithelial burst were seen in the wild type samples less frequently compared to the knock-outs. Quantification of the bursts was performed in five different sections of each sample, in all 15 bladders. The results are presented in Figure 6.3A, where interestingly, the mean number of epithelial bursts in all the knockout-samples is significantly higher than the wild type controls. In detail, the $OMD^{LacZ/LacZ}$ bladders have a mean number of 9.66 ± 2.9, n=3 (p=0.0031 against the control); the $PRELP^{LacZ/LacZ}$ bladders have 9.33 ± 1.45, n=3 (p<0.001 against the control); and the double KO have 10.67 ± 0.88, n=3 (p<0.001 against the control) versus the wild type samples with a mean value of 0.66 ± 0.49, n=6.

In addition, cells in the epithelial bursts were characterized by big and round nuclei, being histologically similar to the umbrella cells. Immunofluorescence staining using a uroplakin-III (marker for umbrella cells) antibody indeed confirmed that the spread cells of the epithelial bursts originated from umbrella cells. An example of an epithelial burst from an OMD KO bladder stained with uroplakin is shown in Figure 6.3 B-C.

These observations indicate that OMD and/or PRELP depletion results in occasional defects of the urothelium, leading to a possible epithelial dysplasia or early papilloma-like formations initiating from the umbrella cells.

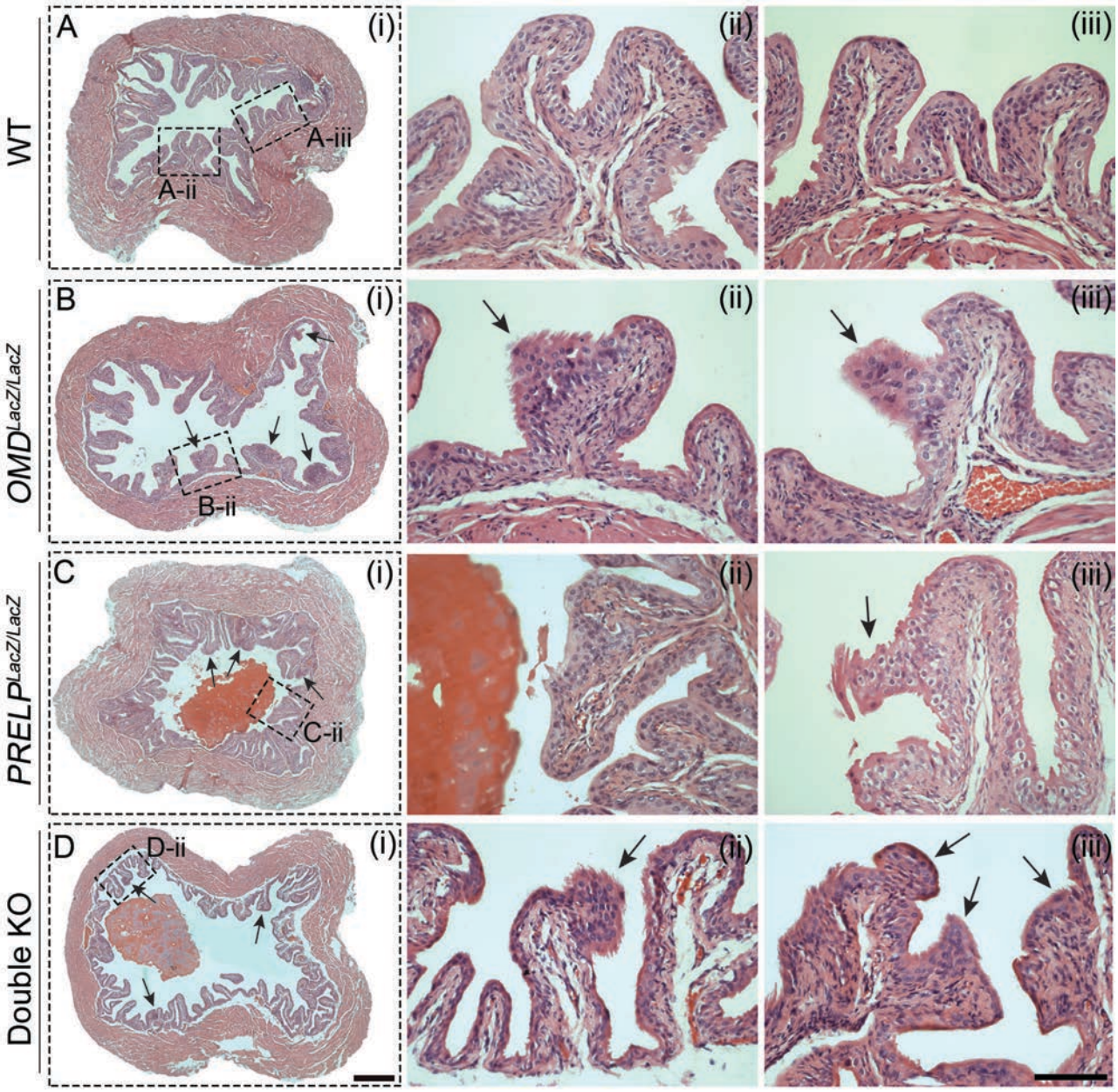

Figure 6.2: Knock-out bladders are characterised by disruptions in the urothelium. Panels (i) are panoramic views of the whole bladders, one of each genotype, while panels (ii) and (iii) are magnified areas of the urothelium seen in (i) but also from other samples. Arrows indicate the epithelial bursts seen in the knock-out samples, which are observed much less frequently in the wild type bladders. Scale bars, 500μm for panels (i), 100μm for (ii) & (iii).

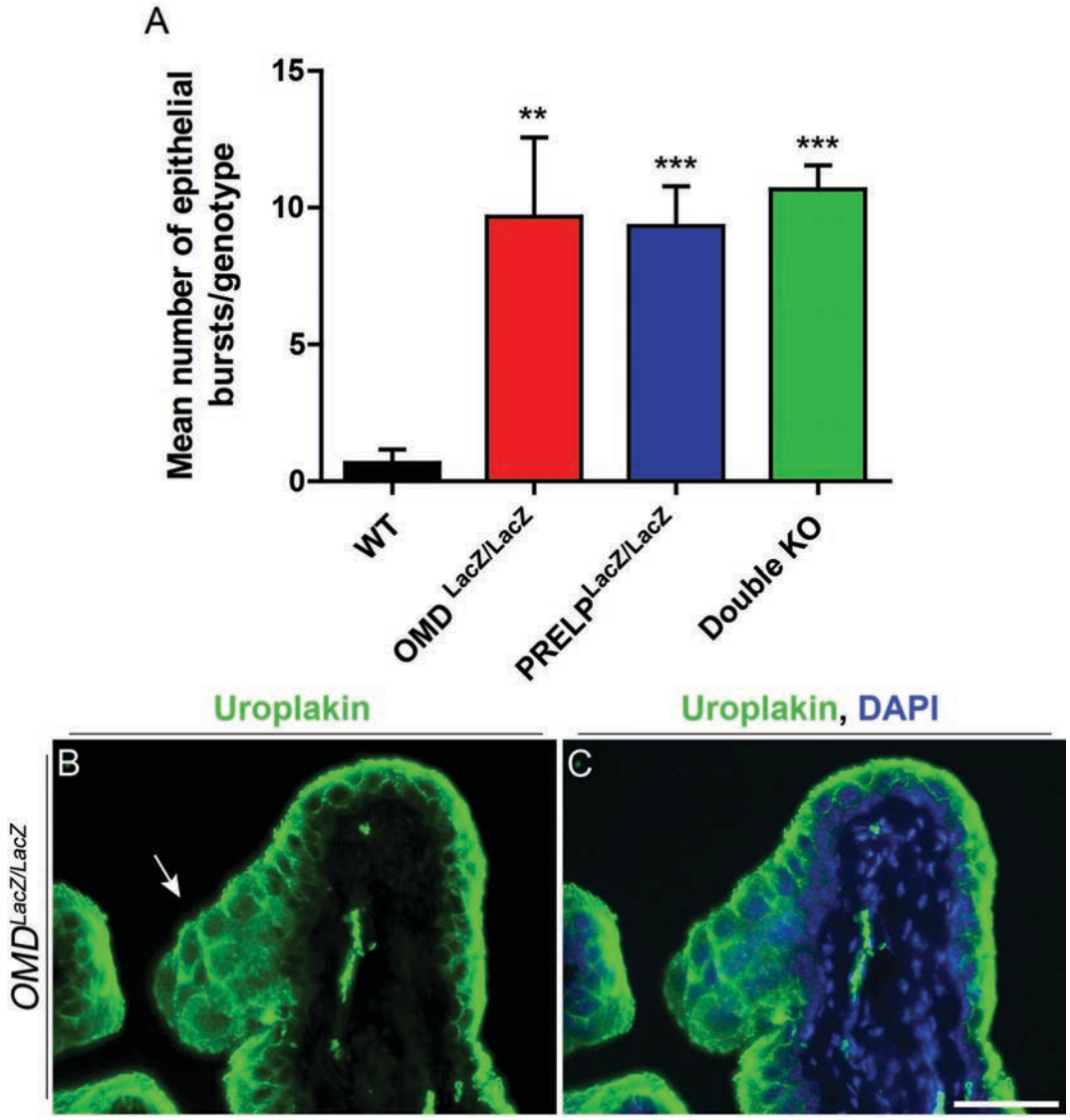

Figure 6.3: OMD and PRELP depletion results in occasional defects of the umbrella cell layer. (A) Number of epithelial bursts per genotype. Quantification was performed on 5 different sections from each bladder, where n=6 for the wild type, n=3 for each of the OMD, PRELP and double KOs. Data are presented as mean±SEM, multiple t-tests were carried out comparing means of the knock-outs to the WT control, **equals $p<0.01$, ***equals $p<0.001$, against the WT. (B) Immunofluorescence staining of an $OMD^{LacZ/LacZ}$ bladder using a uroplakin primary antibody and an alexa-488 (green) as secondary, demonstrating that cells of the epithelial bursts are umbrella cells. (C) Same as (B) with DAPI added as a nuclei stain. Arrow points to the epithelial burst. Scale bar, 50μm.

After studying the urothelium, a more detailed analysis of the clots was carried out. In Figure 6.4A three different H+E planes of the *PRELP*$^{LacZ/LacZ}$ bladder with the clot are shown in addition to the one presented at Fig. 6.1 C(ii), since this was the sample with the most abnormal morphology. We can see that around the middle of the bladder the clot takes up almost all the space of the lumen (Fig. 6.4 A-i), while further towards the anterior side it becomes smaller (A-ii) until it is not present anymore (A-iii). In parallel, the mucosa folds are abnormally increased, occupying the whole lumen, whereas a kind of "matrix" deposition is observed in the intermediate space. Magnified views of the clot are demonstrated in Figure 6.4 B, C & D, where it is visible that there are no cells in the main mass and only around the periphery some hematoxylin positive nucleuses are present (arrows). From their appearance and their close proximity to the urothelium we could speculate that these are umbrella cells, and as shown in panel B they either contribute somehow to the formation of the clot or they are damaged by it. Furthermore, under H+E staining 2 different colorations are visible within the clot mass, i.e. a red eosin color mixed with gray areas, suggesting different compositions within certain regions of the clot. The exact same pattern is seen in the fully formed clot mass found in the double knock-out sample (Fig. 6.1 D-ii & 6.4 G). On the contrary, the second double-KO affected bladder is characterized by a pale grey color with some eosin-positive depositions only towards the middle area, possibly suggesting that this clot is still at the first stages of formation and that the "hardening" and the progression to a fully formed hard mass starts from the center of the clot itself (Fig. 6.1 D-iii & 6.4 H-I). In addition, in panels E-F (Fig. 6.4) the abnormal mucosal folds are shown in greater detail, where we can observe an eosin-colored matrix in the lumen between the folds, which could either be deposited from the urothelial cells and in this way contribute to the formation of the clot, or oppositely it could be derived from the clot. Finally, in Figure 6.4J a possible point of abnormal cell invasion into the lamina propria/muscularis is shown, although examination of the sample by a specialized pathologist is needed to confirm such speculation.

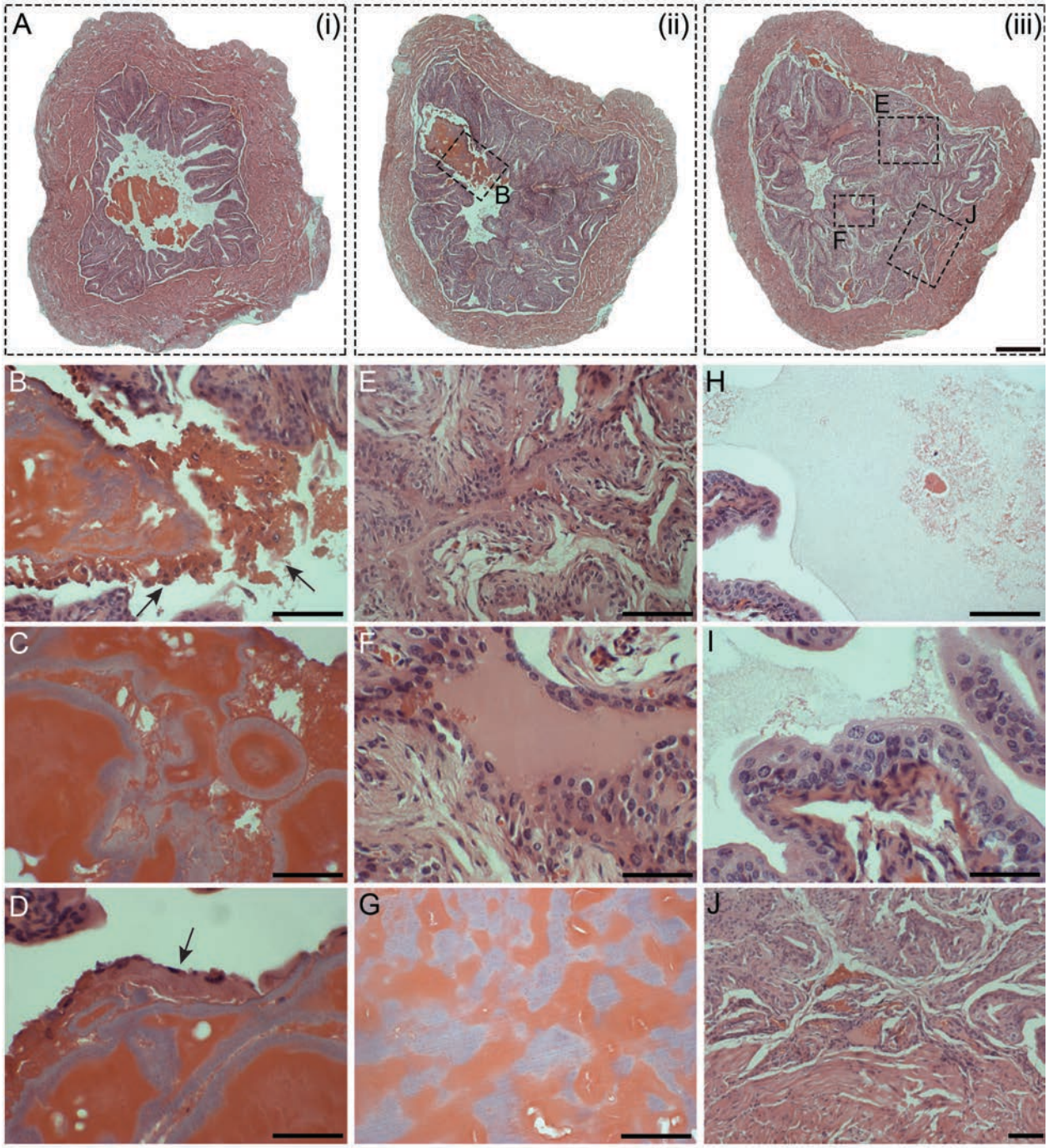

Figure 6.4: Abnormal mucosal and clot morphology in the PRELP and double KO mice. (A) Three different planes of the *PRELP*$^{LacZ/LacZ}$ bladder showing abnormally increased mucosal folds around the formed clot. (B)-(D) Enlarged images of the *PRELP*$^{LacZ/LacZ}$ clot displaying differential H+E colouration of the clot, while possible umbrella cells can be seen around the edges (arrows). (E)-(F) Magnified views of the mucosa folds and the matrix found between them. (G) The fully-formed clot of the double KO bladder, showing the same H+E colouration as the one found in the PRELP KO sample. (H)-(I) Half-formed clot from another double KO bladder, demonstrating a pale grey H+E staining. (J) Enlarged view of (A-iii) showing possible infiltration of abnormal urothelial cells into the muscle layer. Scale bars, 500μm for (A), 100μm for (B), (E), (H), (J), 50μm for all the rest.

In order to further identify the composition of these clots, a variety of tinctorial stains were utilised, which selectively stain different cellular components. As the clots had a really hard texture during paraffin sectioning, von Kossa staining was carried out firstly, aiming to identify any calcium deposits that would be in this case colored black. However, all the samples were negative for von Kossa, and therefore the possibility that these clots were urine or kidney stones was excluded. Next, congo red and alcian blue stains were performed, which identify amyloids and mucins respectively, and again none of the clots were positive for either stains.

Continuing, the trichrome MSB (Martius, Scarlet and Blue) stain was employed, which is a reliable technique for fibrin labeling, based on the property of the dyes to penetrate porous tissues depending on their molecular size. With this method, fibrin is stained red and fresh fibrin yellow, while collagen and connective tissue blue, red blood cells yellow, and muscle pale red. Surprisingly, the clots from all three affected bladders appeared positive for fibrin (Fig. 6.5A). The coloration of the clot mass can be seen in greater detail in Figure 6.5 B&C, where it is visible that it is a mix or fresh and older fibrin. Some areas are red (fibrin), while others are yellow to orange (fresh fibrin), probably explaining the differential staining of H+E as well. In addition, this deposited matrix that is seen in the lumen space between the mucosal folds is a mixture of mostly blue and red color, suggesting that it is comprised of extracellular matrix components which possibly undergo cleavage and then polymerise to form fibrin (Fig 6.5 D&E). The same can be seen in panels F+G (Fig. 6.5, high magnification images of A(iii)-*PRELP*$^{LacZ/LacZ}$ bladder) with a small part of fibrin clot surrounded by thick matrix (arrow). In conclusion, we can deduce that these clots found in three of the bladders analysed are composed of fibrin.

Further immunofluorescence staining with an anti-fibrinogen antibody additionally confirmed our result. Presented in Figure 6.5 H-I is a section of a double-KO bladder, showing positive staining for fibrinogen in certain areas of the clot with minimum background in the urothelium.

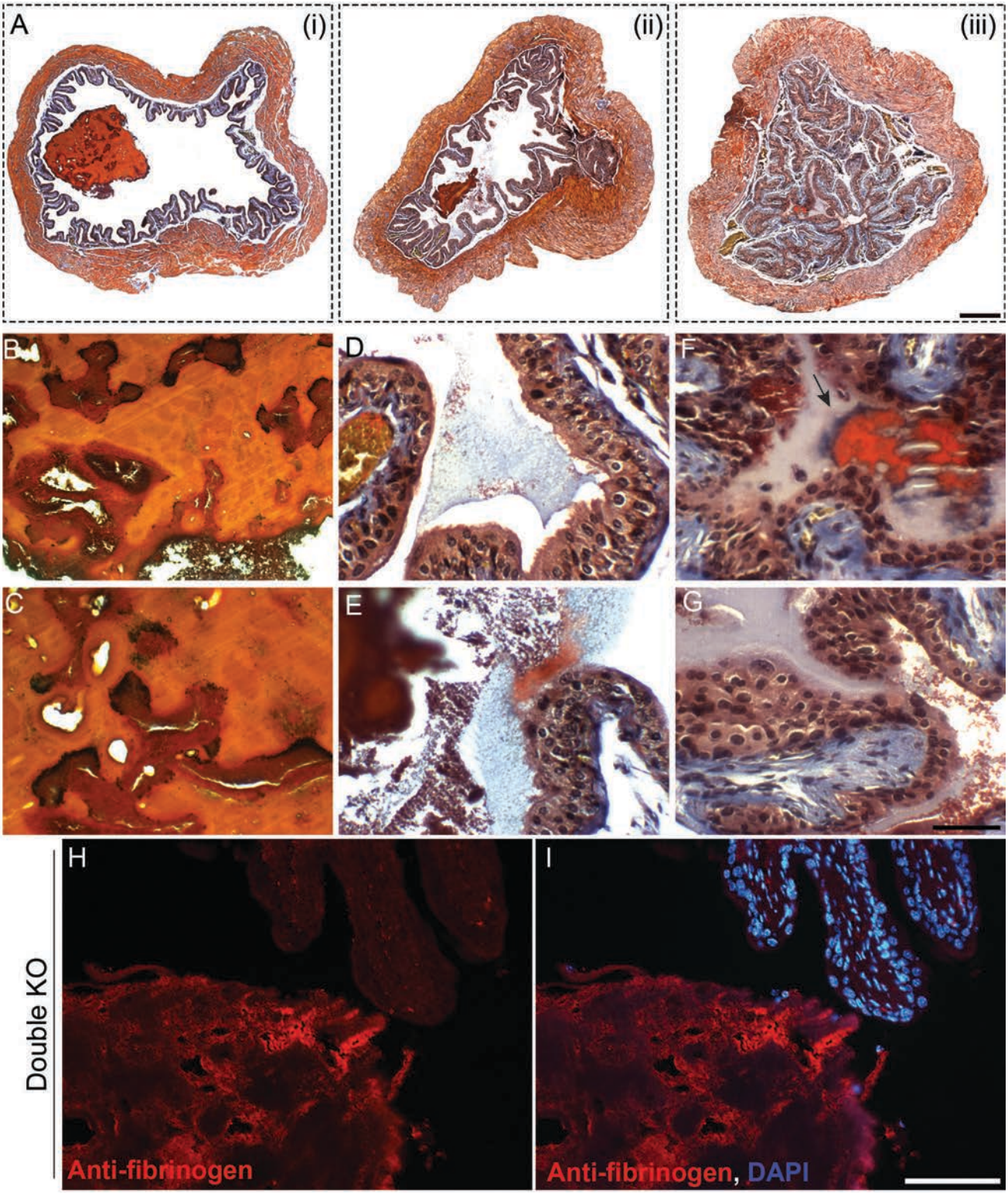

Figure 6.5: Clots found in the PRELP and double knock-out bladders are composed of fibrin. MSB (Martius, Scarlet and Blue) staining was performed and clots appeared positive for fibrin (red) and fresh fibrin (yellow). (A) Panoramic images of all three clot-containing bladders stained for MSB, where (i)-(ii) are double KO bladders and (iii) is the PRELP KO bladder. (B)-(C) Magnified images of the clot demonstrating a mixture of old and fresh fibrin. (D)-(E) The matrix seen in the lumen of these bladders is coloured blue and red under MSB staining, indicating the presence of extra-cellular matrix components that probably undergo cleavage and polymerisation to form fibrin. The same is also seen in panels (F) & (G) (images from the PRELP KO bladder), where the arrow indicates the thick blue matrix around the formed fibrin (red). (H)-(I) Immunofluorescence staining of a double KO bladder with an anti-fibrinogen primary antibody, visualised with alexa-546 (red) secondary and DAPI used as nuclei stain, further confirming that the clot is comprised of fibrinogen material. Scale bars, 500μm for (A), 50μm for (B)-(G), 100μm for (H)-(I).

Taking into account these findings we sought to find out if there is any hemorrhage or abnormalities in the composition of the urine in the transgenic mice. For this purpose, urine samples were collected from 11 wild types, 9 $OMD^{LacZ/LacZ}$, 10 $PRELP^{LacZ/LacZ}$ and 15 double-KO mice of variable ages and were subsequently tested with specific urine strips to detect blood or protein. No blood traces were detected in any of the samples tested, whereas the presence of protein varied slightly between the different genotypes (Fig. 6.6). In detail, no difference was seen between the wild types and OMD knock-outs with mean values of 0.2227 ± 0.02 and 0.2278 ± 0.09 g of protein/L respectively. In contrast, an increase of protein was observed in the PRELP knock-out mice, which although small was statistically significant (mean value 0.4650 ± 0.09, p=0.0410 against the WT), while the double-KOs were mostly ranged around the baseline values seen in the WT with a mean of 0.2500 ± 0.06. Overall, we can see a trend for increased protein content in the urine of the knock-out mice, and especially the PRELP-KOs, which probably is correlated with the matrix found in the lumen of some of the bladders and could further lead to the formation of the fibrin clots. Additionally, since urine is being produced from the kidneys, we cannot exclude the possibility of a defective filtration mechanism from the nephrons, resulting in high urine protein content. In order to unravel how the fibrin clots are formed and if they are related to the urine composition, further examination of the kidneys and the whole renal system is essential.

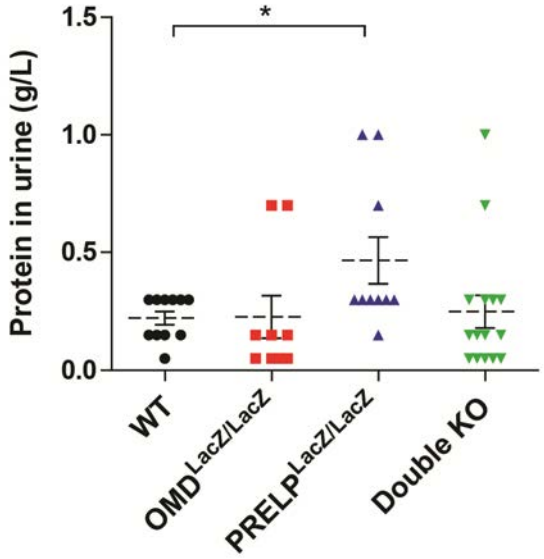

Figure 6.6: Protein levels in the urine are slightly elevated in the PRELP knock-out mice. Urine samples were collected from n=11 WT, n=9 $OMD^{LacZ/LacZ}$, n=10 $PRELP^{LacZ/LacZ}$ and n=15 double KO mice of variable ages (23-77 weeks old). Protein levels were assessed using specific urine strips, where concentration was measured according to the colouration of the strips. A trend for increased protein content can be seen in in the PRELP KO mice. Data are presented as mean±SEM, *equals p<0.05

Apart from the histological analysis described above, we wanted to further study the effect of OMD/PRELP depletion in the mouse urothelium, mostly since they appeared to be expressed in the umbrella cell layer (Sections 4.2.5.1 & 5.2.5.1). For this purpose, immunofluorescence staining was performed using various different markers against the mouse urothelium. Initially, uroplakin-III was used to stain the umbrella cells, and sections from every sample (15 sections in total) were compared between them. Representative images from every genotype are demonstrated in Figure 6.7, where we can see strong and specific staining of the outermost umbrella cell layer. No significant differences were found in the overall intensity of the staining and the thickness of the uroplakin-III positive cell layer between wild types and knock-outs (including the double-KOs).

Next, an anti-laminin antibody was used to stain the basal lamina, a component of the basement membrane which connects the urothelium with the lamina propria. Similarly to before, staining was conducted on all 15 samples and representative images from each genotype are shown in Figure 6.8. The basal lamina can be observed as a thin line surrounding the surface of the lamina propria just under the basal cells of the urothelium, while the staining seen towards the middle of the lamina propria represents blood vessels. Again, we could not detect any differences in the staining between WT and KO samples, suggesting that this layer of the basement membrane is not affected.

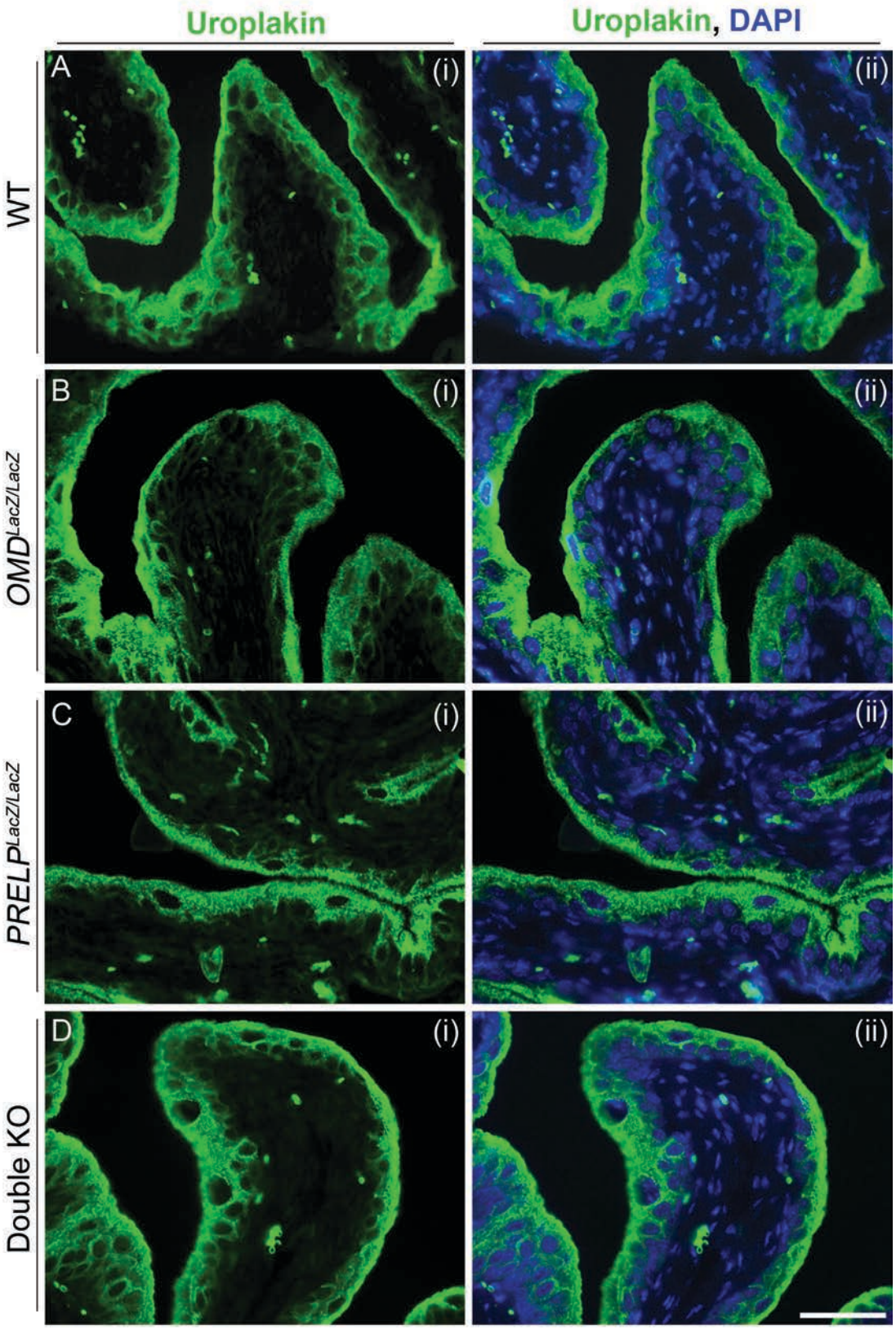

Figure 6.7: The umbrella cell layer appears to be normal in knock-out mice. Immunofluorescence staining was performed with a uroplakin primary antibody that marks the umbrella cells, visualised using alexa-488 (green) as secondary and DAPI as nuclei stain. Sections from all bladders (n=6 WT, n=3 for each single and double KOs) were stained and representative images are shown. No significant differences can be observed in the overall staining intensity or thickness of the umbrella cell layer between the different genotypes. Scale bar, 50μm for all images.

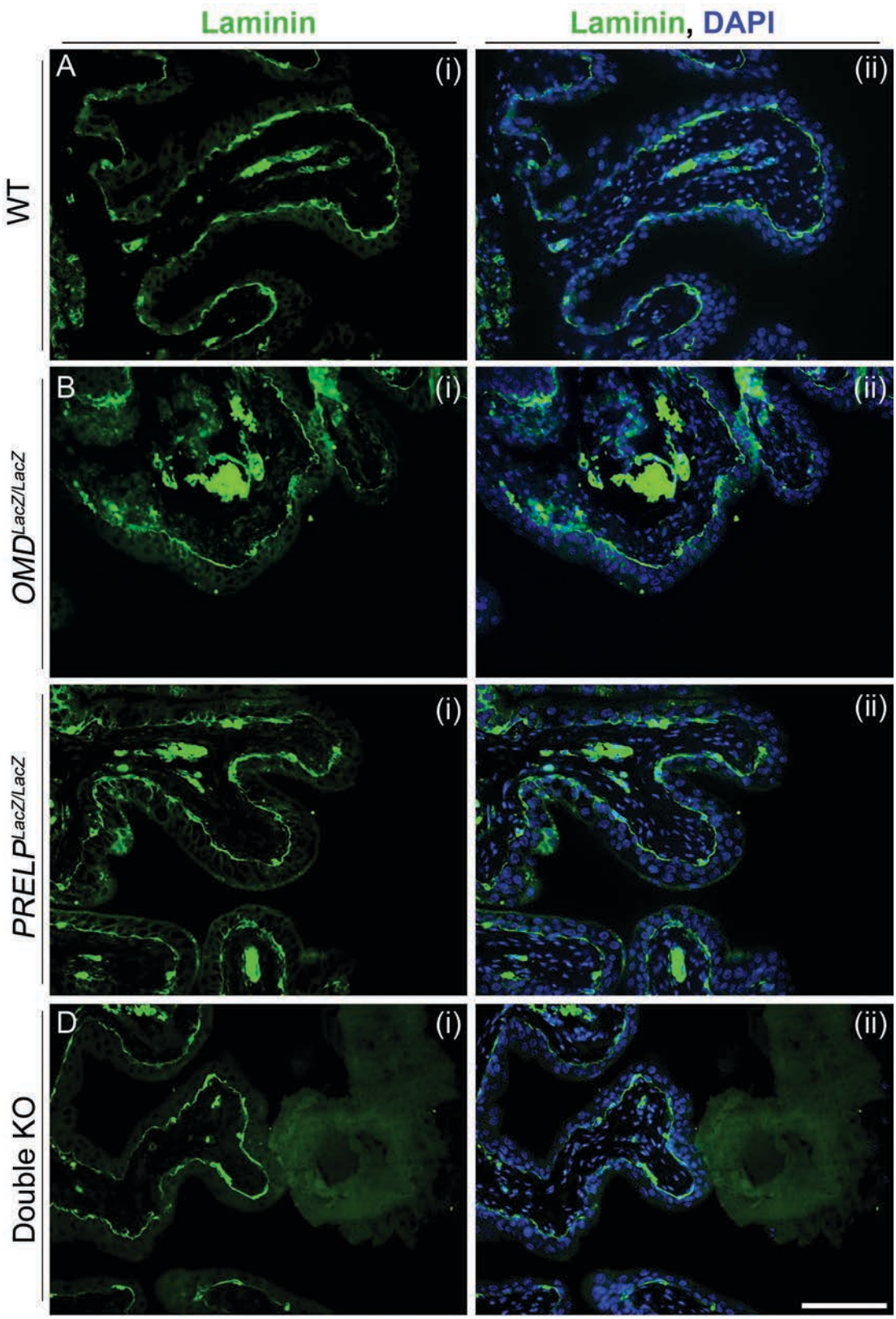

Figure 6.8: Laminin expression is similar between wild type and knock-out mice. Immunofluorescence staining was performed with a laminin primary antibody which marks the basal lamina, one layer of the basement membrane located between the lamina propria and the urothelium, visualised using alexa-488 (green) as secondary and DAPI as nuclei stain. Again, sections from all bladders (n=6 WT, n=3 for each single and double KOs) were stained and representative images are shown here. No significant differences can be observed between wild type and knock-out samples. Scale bar, 100μm for all images.

Continuing further with our analysis and in search of a cancer-related phenotype, we examined all the bladders for E-cadherin expression, since loss of function or expression of epithelial cadherin has been correlated with cancer progression and metastasis. In addition, adherens junction was also one of the affected pathways after altered expression of OMD and PRELP (Dr. Hamamoto's analysis, Appendix A). Again, immunofluorescence staining was carried out for all fifteen samples and exemplar images are presented in Figure 6.9. We can see that E-cadherin expression is strong in all the epithelial layers of the urothelium, i.e. basal, intermediate and umbrella cells. Moreover, it is specifically localised in cell-cell membranes and only a minimum cytoplasmic signal is present. Staining between the wild type and the OMD/PRELP or double-KO samples appeared similar, with comparable staining intensity and pattern. Occasionally a stronger signal was seen in the apical surface of the outermost umbrella cells in the knock-out samples, but under the current staining conditions we cannot make any definite conclusions about the adherens junction status of the knock-out bladders.

Zonula occludens 1 (ZO-1) is another adhesion protein, specific for tight junctions, which is associated with cancer at the point of epithelial-mesenchymal transition (EMT). During EMT both E-cadherin and ZO-1 are lost, resulting in transformation of the polarized epithelial cells into a more elongated, mesenchymal-like phenotype (Lamouille et al., 2014). In addition, ZO-1 and several claudins are key molecules in the bladder homeostasis, as they form tight junctions in the intersections of apical and lateral membranes of the umbrella cells, regulating in this way the paracellular transport of molecules (gate and fence functions) (Khandelwal et a., 2009). We have shown that OMD and PRELP are selectively expressed in a subpopulation of bladder umbrella cells (Chapters 4&5). Also, overexpression of OMD and PRELP in human bladder cancer cells led to an increase of TJ formation (Chapter 3), while microarray data acquired from Dr. Hamamoto showed that OMD/PRELP affect both tight junction and adherens junction pathways (see Appendix A). Thus, we wanted to evaluate the TJ status of the urothelium in the OMD/PRELP knock-out mice. For this purpose, immunofluorescence staining using a ZO-1 antibody was performed in all the mouse bladders (n=6 for WT, n=3 for each OMD/PRELP and double KOs). Additionally, ultrastructural analysis was also

performed by EM on one bladder from each WT, OMD/PRELP KO and double KO animals.

In Figure 6.10 A-D representative images of the ZO-1 stained bladders are shown, where strong staining is seen in the apicolateral borders of the umbrella cells in the wild type samples (arrowheads). This staining pattern appeared reduced in the single and double knock-outs and we therefore performed quantification of these apical ZO-1 positive junctions in relation to the outermost urothelial cell nuclei. Quantification was performed in three random viewing planes under the 40x magnification lens, where we counted how many times the intense positive ZO-1 signal was seen in the apicolateral borders of umbrella cells. In addition, the outermost DAPI cell nuclei were counted representing the umbrella cells, and the total tight junction number is presented as percentage of the apical ZO-1 positive junctions in relation to the umbrella cell number. Shown in Figure 6.10E, are the results of the quantification demonstrating reduction in the number of the ZO-1 positive tight junctions in all the knock-out samples compared to wild type. In detail, wild type samples had a mean value of 12.44 ± 1.34 (%) against 4.97 ± 0.69 for the $OMD^{LacZ/LacZ}$ (p=0.0004), 6.75 ± 0.68 for the $PRELP^{LacZ/LacZ}$ (p=0.0039) and 4.17 ± 0.72 for the double KO (p=0.0004) bladders. However, it must be noted that the staining pattern was quite variable between the different samples owning to the staining conditions (i.e. insufficient antigen retrieval of the paraffin sections and/or low specificity of the primary antibody under the current conditions), and therefore it is difficult to be sure of any definite conclusions.

In order to further investigate the TJ status of the bladder urothelium, electron microscopy analysis of wild type and knock-out bladders was performed and tight junction formation between adjacent umbrella cells was assessed. Shown in Figure 6.11A is a wide view of wild type bladder urothelium, which includes two umbrella cells and an intermediate cell. The apicolateral border of the two umbrella cells is strongly sealed by dense tight junctions (indicated by the black arrowheads), while another example of this strong connection is shown also in Figure 6.11B. In contrast, tight junction formation is much less intense, or junctions might not be properly formed, in the knock-out samples, especially in $PRELP^{LacZ/LacZ}$ and double KO samples (black arrowheads in D and E), and to a lesser extend in the $OMD^{LacZ/LacZ}$ (as

seen in panel C). Moreover, the cell membrane borders were not visible in the WT samples, whereas they are easily discernible in the knock-outs, indicating weaker connections or junctions. In the knock-out samples we can additionally see formations that probably are adherens junctions (white arrows) or desmosomes (white arrowheads), which are not visible in the wild type bladders. This may be due to the very strong TJ connections in the latter samples or can be an effect of the TJ disruption in the knock-outs.

Lastly, characteristic of the umbrella cells is the scalloped nature of their apical plasma membrane, which comprises plagues and intervening hinge regions, accompanied by the presence of discoidal or fusiform-shaped vesicles in their cytoplasm. No differences were seen in the above structures or the overall shapes of the umbrella cells between wild type and knock-out bladders under EM. We therefore see that OMD and PRELP depletion causes a decrease in tight junction formation between neighboring umbrella cells, agreeing also with our previous *in vitro* findings, and further suggesting that these two SLRPs can somehow regulate TJ formation.

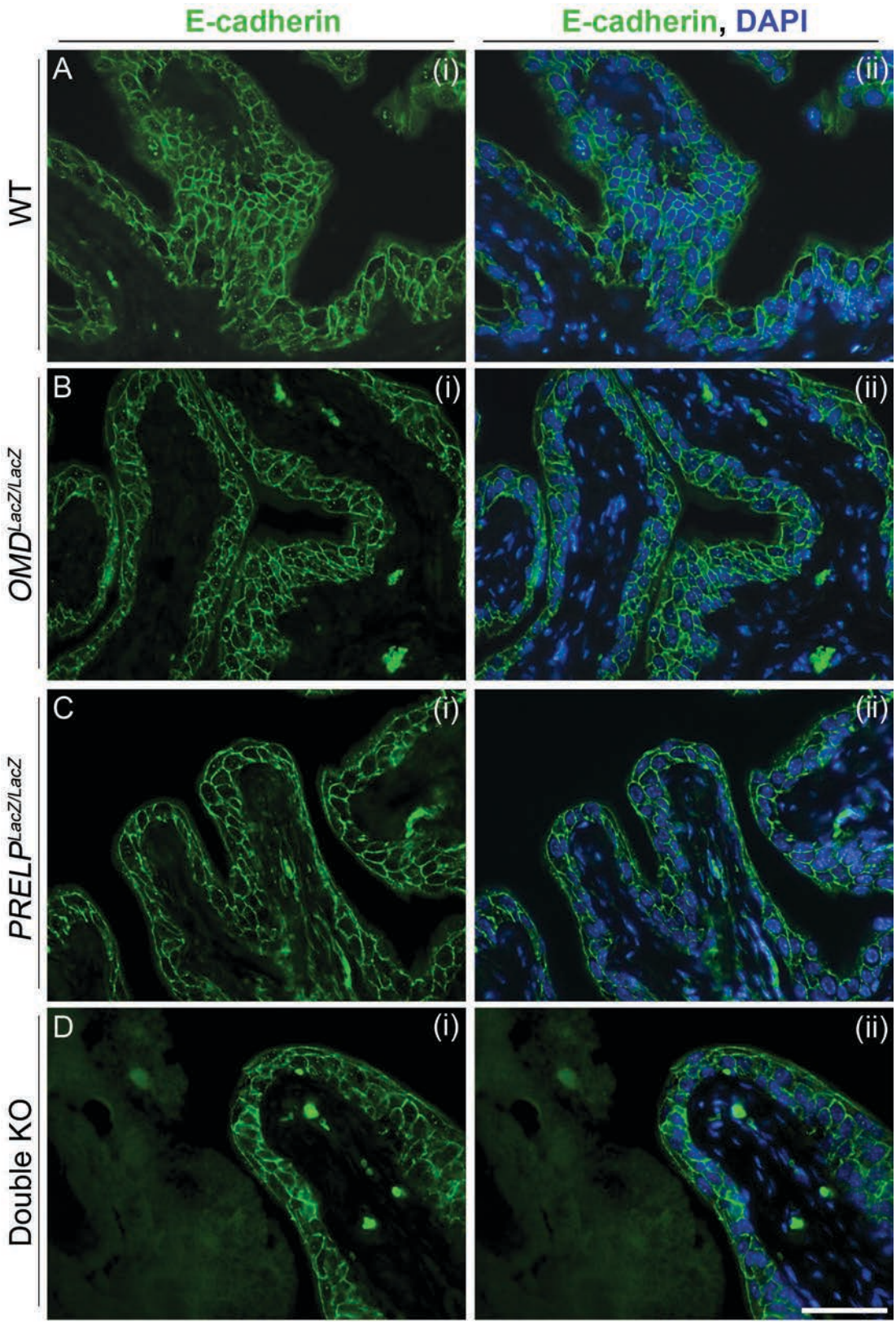

Figure 6.9: E-cadherin expression in the mouse urothelium of wild type and knock-out mice. Immunofluorescence staining was performed with an E-cadherin primary antibody, visualised using alexa-488 (green) as secondary and DAPI as nuclei stain. Staining can be seen in the cell membranes of the whole urothelium, with comparable staining intensity and pattern between wild type and knock-outs. Occasionally stronger signal could be observed in the apical surface of the outermost umbrella cells in the knock-out samples, but under the current staining circumstances we cannot make any definite conclusions about the adherens junction status of the knock-out bladders. Scale bar, 50μm for all images.

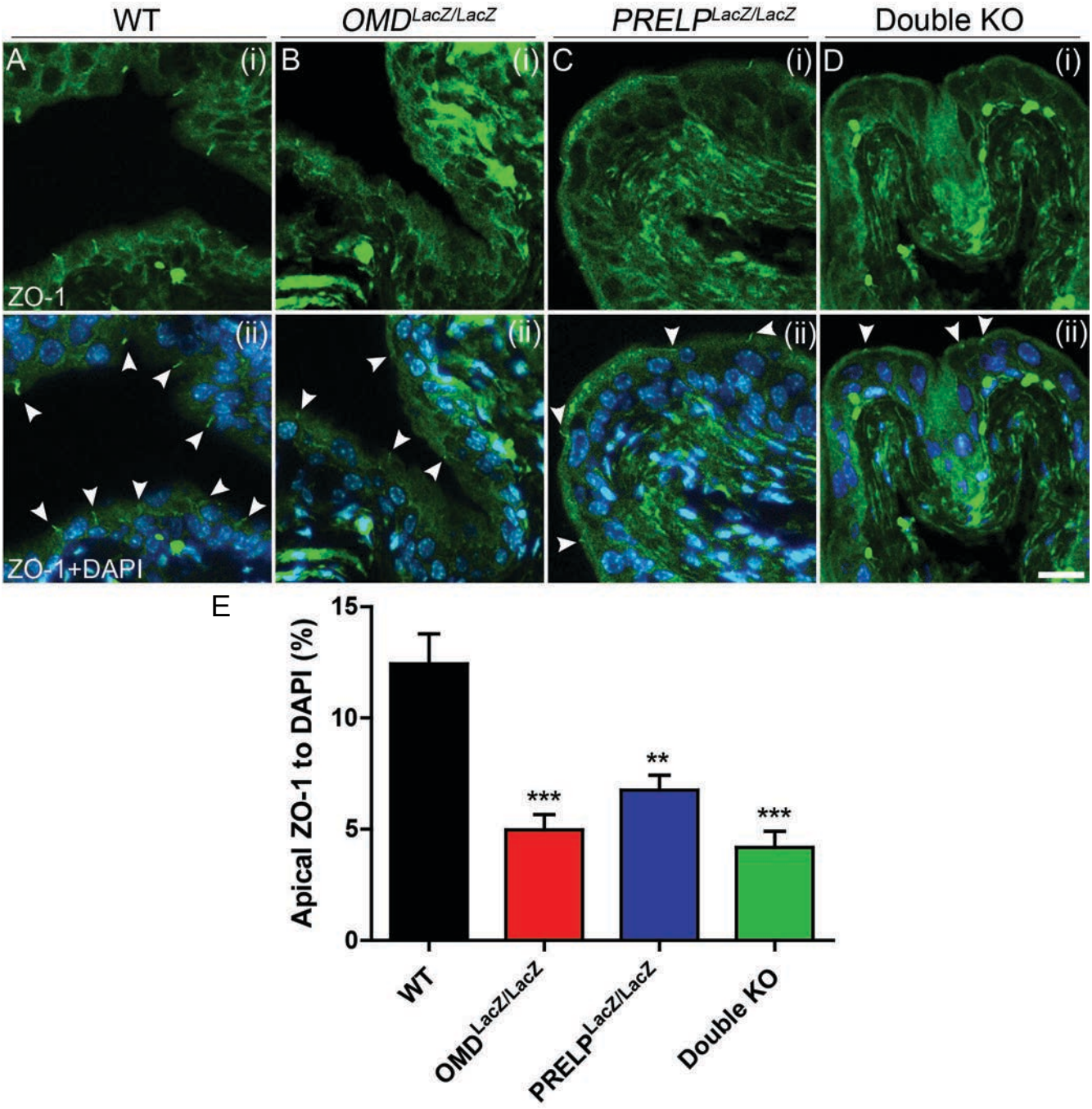

Figure 6.10: ZO-1 expression and tight junction formation in the urothelium of transgenic mice. (A)-(D) Immunofluorescence staining was performed with a ZO-1 primary antibody, visualised using alexa-488 (green) as secondary and DAPI was used as nuclei stain. Specific staining can be seen in the apical sides of the outermost umbrella cells, marked with arrowheads. This signal was reduced in the OMD/PRELP and double knock-outs. Scale bars, 20μm for all images. (E) Quantification was performed in 3 random viewing planes under the 40x magnification lens in every sample and the results are presented as percentage of the apical ZO-1 positive junctions in relation to the outermost urothelial cell nuclei. Data are presented as mean±SEM, $^{**}p<0.01$, $^{***}p<0.001$ against the WT.

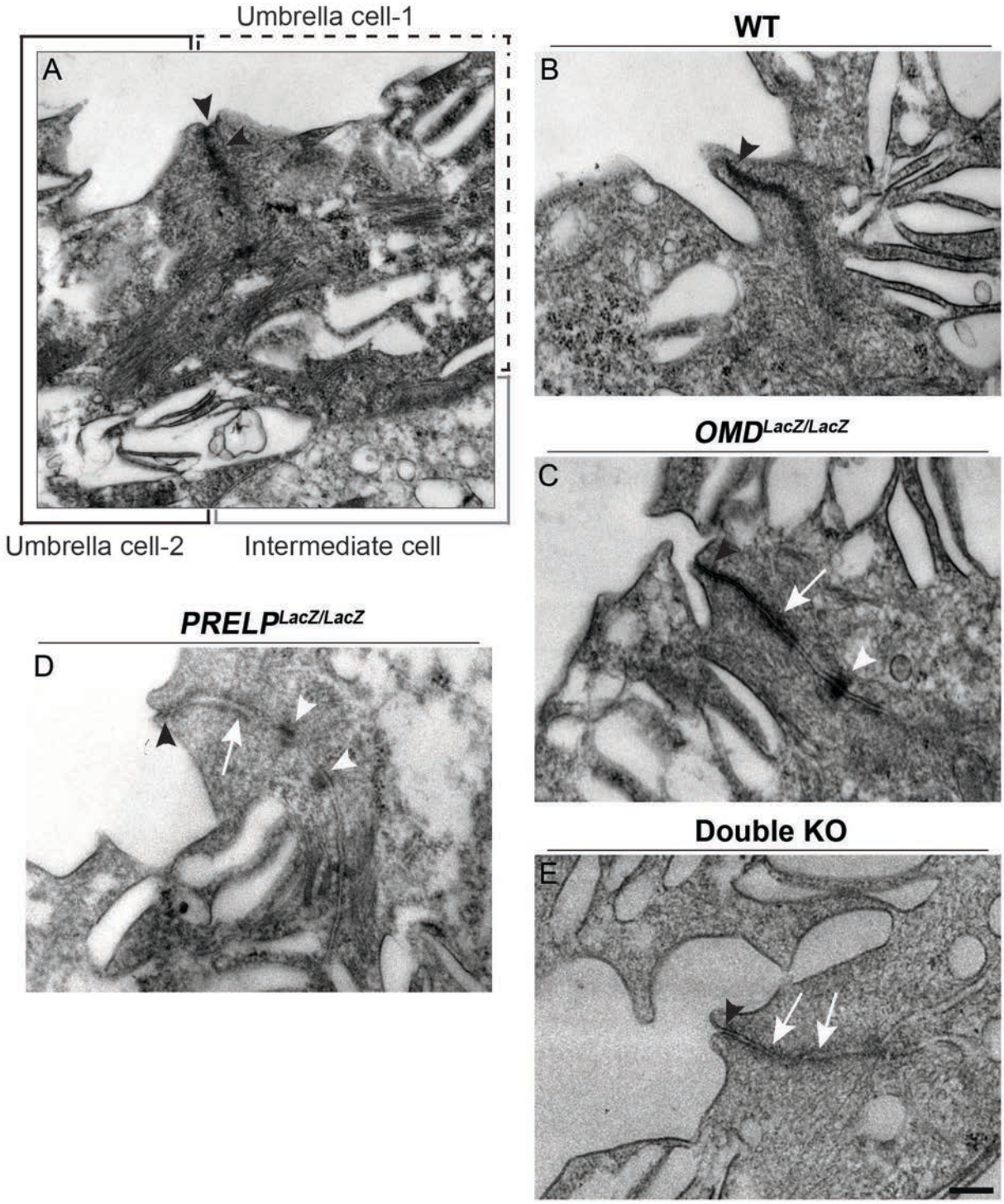

Figure 6.11: Ultrastructural analysis of the umbrella cells in wild type and knock-out bladders. One bladder of each WT, OMD/PRELP and double KO mice was processed and analysed under electron microscopy. In (A) a wide view of wild type bladder urothelium is shown, which includes two umbrella cells and an intermediate cell. The apicolateral border of the two umbrella cells is strongly sealed by dense tight junctions (black arrowheads). The same can be seen in (B), while tight junctions are much less intense or are not properly formed at all in the knock-out samples (black arrowheads in C, D and E). The effect is more pronounced in the PRELP and double KO bladders. Additionally, possible adherens junctions (white arrows) or desmosomes (white arrowheads) are visible in the knock-out samples. Also, cell plasma membranes are discernible in the knock-outs and not in the wild type, indicating weaker junctions in the former. Scale bar, 300nm for (A), 200nm for all other images.

Finally, since abnormal proliferation is one of the characteristics accompanying cancerous tissues and is involved in cancer progression, we sought to look for any irregular proliferation patterns in the knock-out bladders and specifically in the urothelium. To this end, immunostaining for the proliferation marker Ki-67 was conducted in all the different bladders and representative pictures are demonstrated in Figure 6.12A. As the proliferative index of the normal mouse bladder epithelium is quite low (without injuries, around 0.4-0.5% as previously reported)(Farsund, 1975) we did not expect to find many Ki-67 positive cells around the urothelium. Indeed, as shown in Figure 6.12, only few cells were Ki-67 positive, and these were observed to be umbrella, intermediate or basal cells (arrowheads). However, when comparing the wild type with the knock-outs we did notice a slight increase of Ki-67 positive cells in the latter samples, and this can be seen in panels (ii), (iii) & (iv), in which samples we often observed more than a single positive cell in the standard viewing plane in contrast with the WT (i). Counting all the Ki-67 stained cells in one section per bladder (a total of 4 sections for the WT samples and 3 sections for each single and double KO), revealed a two-fold increase of proliferative cells in the $OMD^{LacZ/LacZ}$ samples (mean value of 6.000 ± 3.0) and an approximate 3-fold increase in the double-KOs (mean of 10.33 ± 3.3) compared to the wild type mice (3.000 ± 1.4) (Fig. 6.12B). No difference was seen in the homozygous $PRELP^{LacZ/LacZ}$ bladders, where the total number of Ki-67 positive cells was almost identical to the WT with a mean value of 3.000 ± 2.0. Although these changes were not statistically significant, we can see that there is a trend, at least regarding the OMD and double knock-out mice, for an increased proliferation index in the urothelium, suggesting a potential role of OMD/PRELP in suppressing abnormal cell proliferation in the mouse bladder.

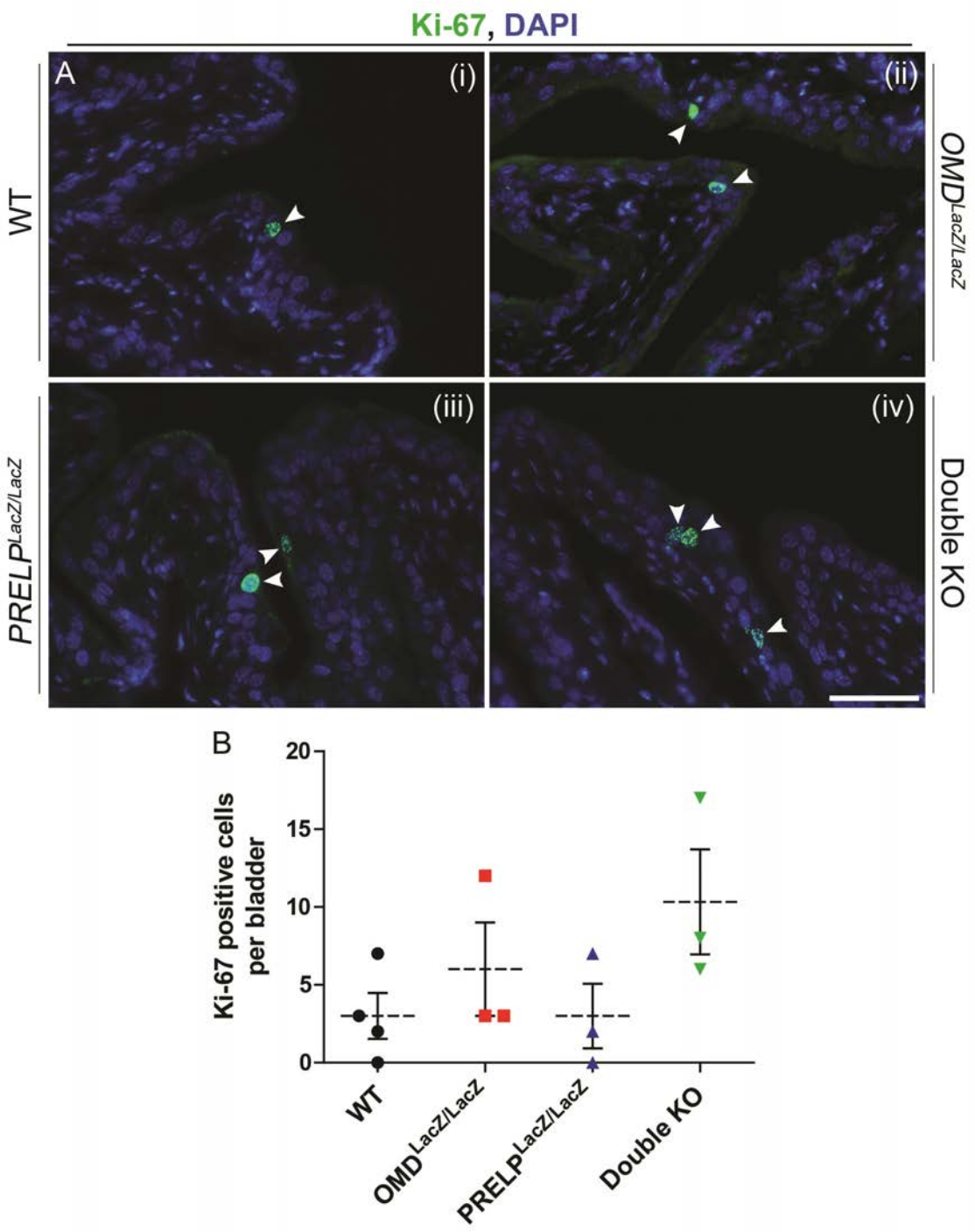

Figure 6.12: Proliferation of urothelial cells is slightly increased in OMD and double KO bladders. (A) Immunofluorescence staining was performed with a Ki-67 primary antibody which marks the proliferating cells, visualised using alexa-488 (green) as secondary and DAPI as nuclei stain. More Ki-67 positive urothelial cells were seen in the single and double knock-out samples, under the standard viewing plane, compared to the wild types (arrowheads). Scale bar, 50μm for all images. (B) Quantification of Ki-67 positive cells was performed in one section per bladder, with a total of n=4 bladder for the WT and n=3 bladders for each OMD, PRELP and double knock-outs. Data are presented as mean±SEM. No significant difference was seen between the different genotypes, but there is a trend for increased proliferation in the *OMD*$^{LacZ/LacZ}$ and double KO samples.

6.2.1.2 Effect of *OMD* and *PRELP* targeted deletion in the mouse eye

As explained earlier, during phenotyping of the knock-out mice primary attention was given to the bladder, while other organs, including the eye, were examined in less detail. As shown in Chapters 4 and 5, OMD and PRELP are both expressed in the adult mouse eye, and hence a preliminary analysis was conducted to evaluate any noticeable eye-related phenotypes that could arise from OMD & PRELP depletion. For this study eyes were collected from three of each WT, $OMD^{LacZ/LacZ}$ and $PRELP^{LacZ/LacZ}$ animals, at three months of age, and were subsequently processed.

Initially, H+E staining was performed and samples from wild type and knock-outs were compared in order to detect any gross histological differences. In Figure 6.13 A&B representative pictures of whole WT and $OMD^{LacZ/LacZ}$ eyes are displayed, where no noticeable differences can be observed regarding the size and the overall structure of the components of the eye (i.e. cornea, lens, retina, CB). Additionally, enlarged views of two ciliary bodies can be seen in panels C&D, demonstrating normal gross morphology of the pigmented and non-pigmented epithelial cells.

Further attention was given on the analysis of the retina, where close comparison between wild types and knock-outs was performed. Exemplar images of low and high magnification views of the central retina are shown in Figure 6.14, where we can observe a more "fractured" pattern in the retinal ganglion cell layer of the OMD KO samples, with more spaces between the cells and the inner limiting membrane (Fig. 6.14D, arrowheads). The retinal cell layers (RGC, IPL, INL, OPL, ONL, IS, OS) appeared to be of the same thickness and density between WT and KOs, indicating no abnormal decrease in cell numbers. However, since OMD is normally expressed in the RGCs, quantification of the ganglion cells was conducted in order to find any possible differences. Quantification was performed in four different areas of the retina, in 6 different sections from each sample. Those four areas include two parts of the central retina and two parts at the periphery, adjacent to the ciliary bodies, and they are noted with the red dotted boxes in Figure 6.13A. After quantification the two central retina counts were pooled together, as were the counts from the peripheral areas. Presented in Figure 6.14E are the results of the quantification, showing no significant differences between the wild type and the

OMD knock-out samples both in the central and the peripheral retina. In detail, central retina ganglion cells of wild types numbered a mean of 69 ± 4.7 versus 64.8 ± 3.0 for the knock-outs (p=0.4599), while the in the peripheral retina WTs had a mean of 35.7 ± 1.5 vs. 36.7 ± 1.5 for the KO respectively (p=0.6991). On the contrary, what we observed in all samples was that ganglion cells towards the periphery of the retina tend to decrease and therefore are considerably less than the central areas. Finally, since a more "fractured" pattern was seen in the space above the RGCs with H+E staining in the OMD knock-out eyes, it was decided to search for any disruptions at the inner limiting membrane through immunostaining with an anti-laminin antibody, and as shown in Figure 6.18 & 6.19, no breaks of the membrane were observed in the knock-outs, while their staining pattern was very similar to the wild types.

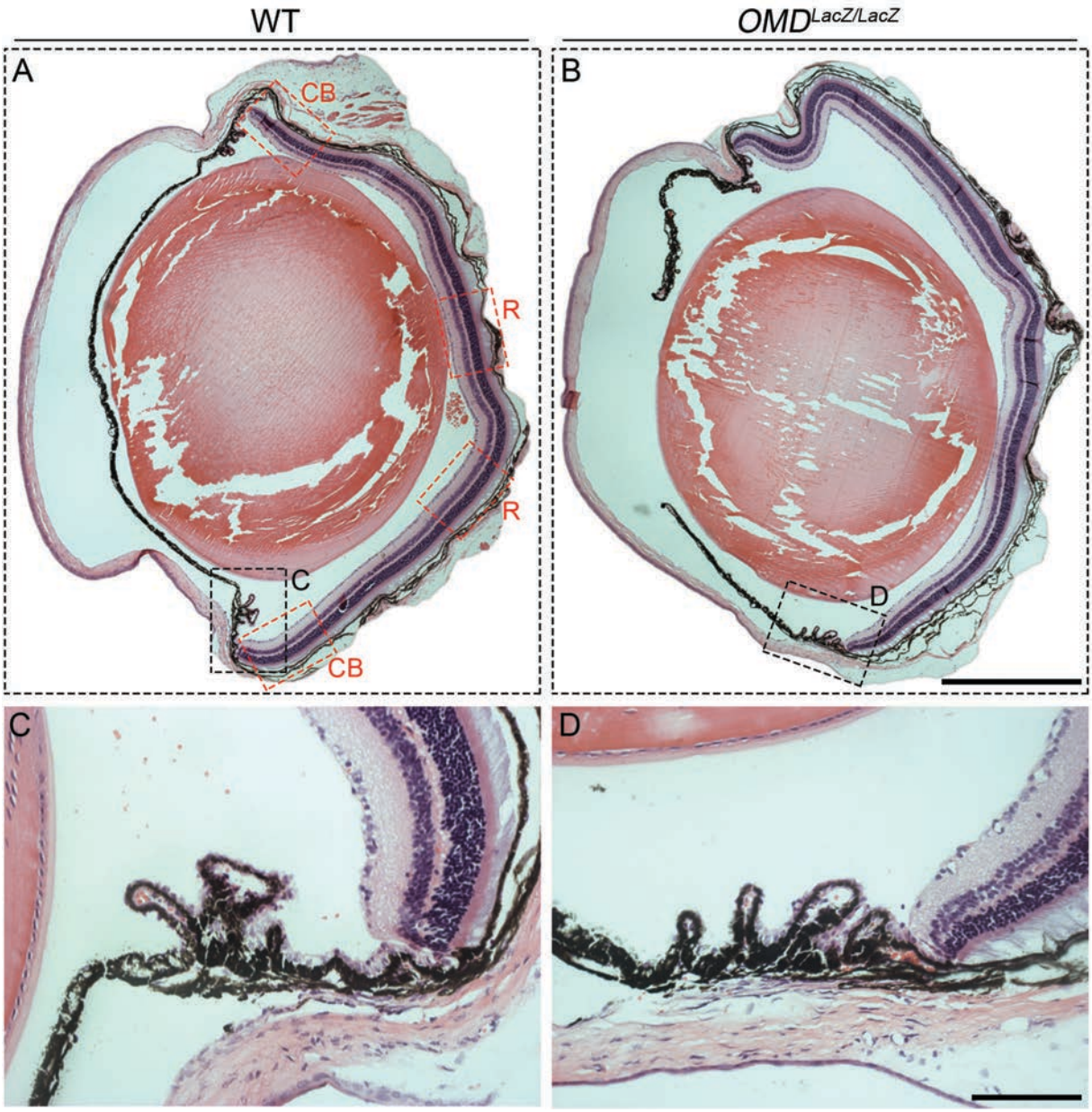

Figure 6.13: Comparison of eye morphology in wild type and OMD knock-out samples. (A)-(B) Panoramic views of the whole eyes from WT and OMD KO animals stained with H+E, showing no differences in the gross morphology or the size of the eyes. The red dotted boxes indicate the areas used for retinal ganglion cell counting, where R is central retina and CB the peripheral retina areas. (C)-(D) Magnified views of the ciliary bodies from each sample demonstrating normal cell structure in both genotypes. Scale bars, 1mm for (A)-(B), 100μm for (C)-(D)

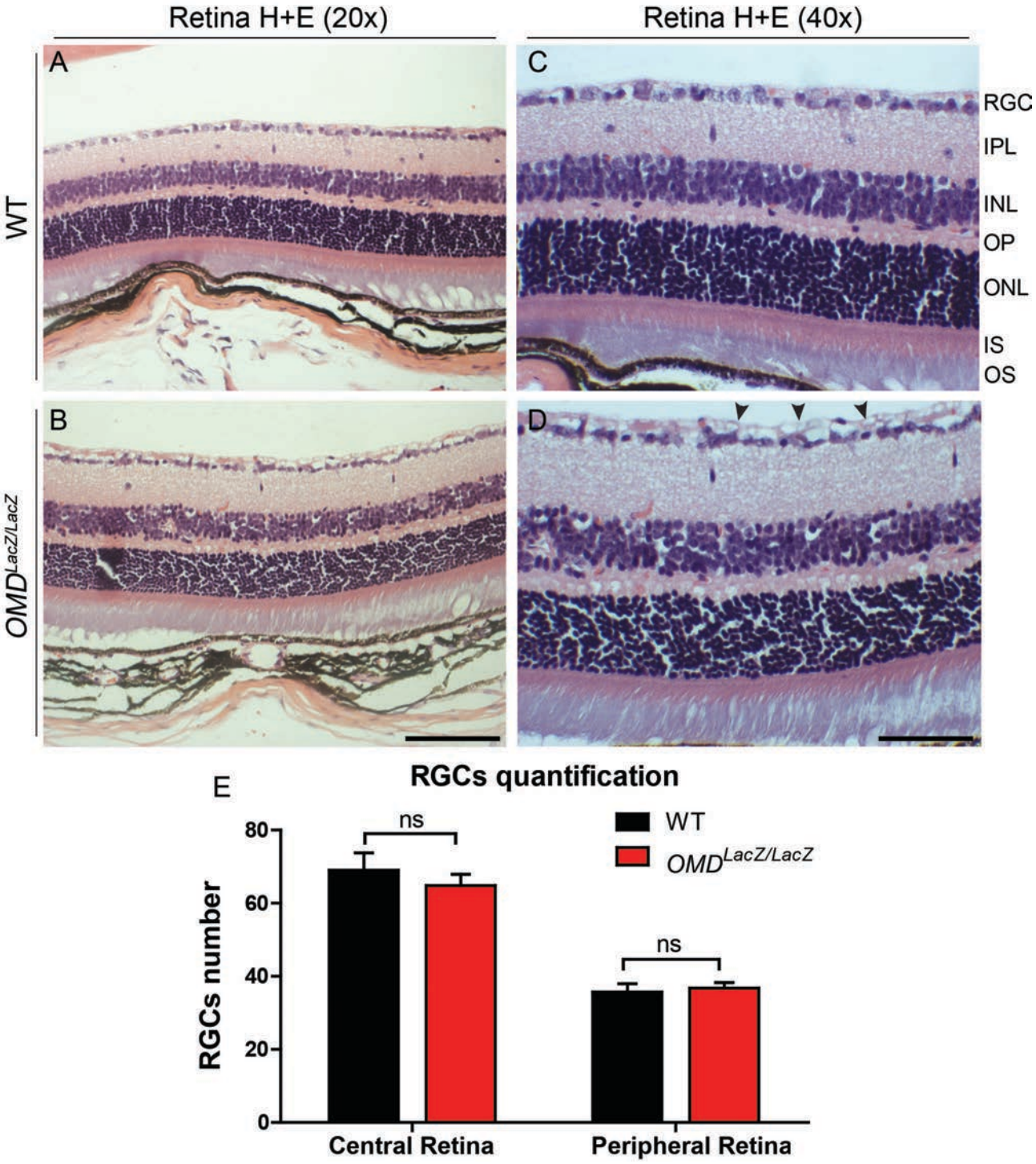

Figure 6.14: Analysis of the retina between wild type and OMD knock-out samples. (A)-(D) Two different magnifications of the central retina from WT and *OMD*$^{LacZ/LacZ}$ eyes. In the OMD KO samples a more "fractured" pattern of the RGC layer can be seen, with more spaces between the cells and the inner limiting membrane (arrowheads). All the other retinal layers appear to be of similar thickness and density as seen in the wild type retinas, indicating no abnormal decrease in cell number. Scale bars, 100μm for (A)-(B), 50μm for (C)-(D). RGC, retinal ganglion cells; IPL, inner plexiform layer; INL, inner nuclear layer; OPL, outer plexifrom layer; ONL, outer nuclear layer; IS, inner segments; OS, outer segments. (E) Quantification of RGC cells in the central and peripheral retina was performed in 6 different sections from each sample (n=3 eyes for WT, n=3 eyes for OMD KO), where no significant differences were seen between the control and the knock-out samples. Data are present as mean±SEM. ns, non-significant.

A similar analysis was performed on the PRELP knock-out eyes, where again the first step was to compare the gross histology between different samples with H+E staining. Demonstrated in Figure 6.15 A&B are two representative pictures of whole eyes from a wild type and a $PRELP^{LacZ/LacZ}$ sample, showing no major abnormalities in the overall structure and size of the eye. In addition, magnified views of the retina are displayed in panels C&D, showing similar retinal cell layers thickness and density. Since PRELP is normally expressed only at the ciliary bodies (Chapter 5), we would expect to find any phenotypic effects around the CB areas and therefore further attention was given in the analysis of the latter. Close histological examination of WT and KO ciliary bodies was performed, but no noticeable differences could be observed in the overall morphology or cell density of the ciliary body epithelium (Figure 6.16 A-D). Thus, we decided to then measure the area they occupy, as marked with the red dotted lines in Figure 6.16, panels C&D. The measurements were done on both dorsal and ventral CBs, in 6 different sections for each sample and for three samples/genotype, using the Image J analysis software. Interestingly, a modest but statistically significant reduction of the CB area was observed in the PRELP knock-out eyes compared to the wild types (Figure 6.16 E). More specifically, WT ciliary bodies occupied a mean area of 78220 ± 4140, measured in pixels, versus a value of 66570 ± 3172 for $PRELP^{LacZ/LacZ}$ samples (p=0.0301), suggesting a possible shrinkage of the CB epithelium due to PRELP deletion.

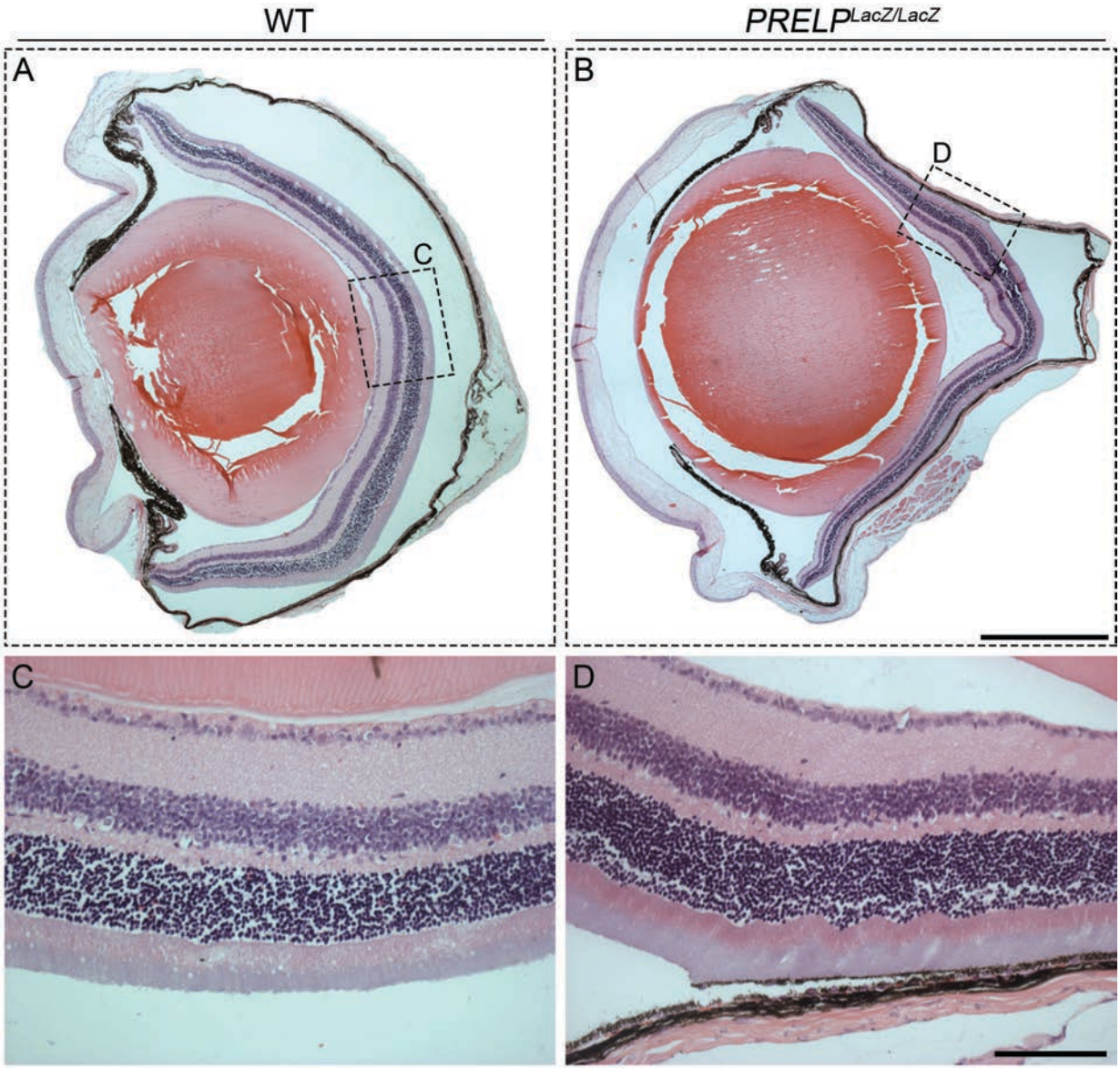

Figure 6.15: Comparison of eye morphology in wild type and PRELP knock-out samples. (A)-(B) Panoramic views of whole eyes from WT and PRELP KO animals stained with H+E, showing no differences in the gross morphology or the size of the eyes. (C)-(D) Magnified views of the retinas from each sample demonstrating similar thickness and density of the different cell layers. Scale bars, 1mm for (A)-(B), 100μm for (C)-(D).

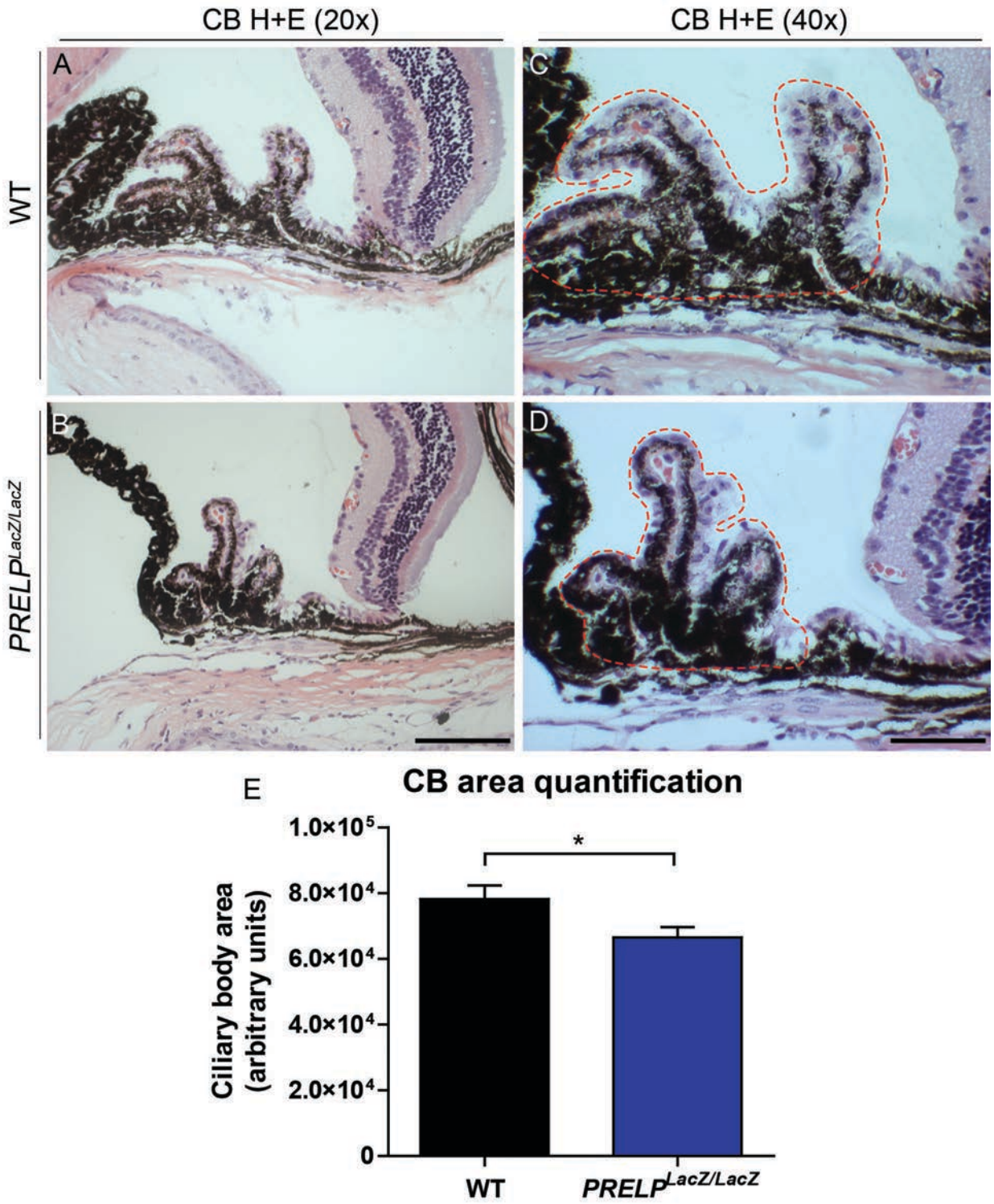

Figure 6.16: Analysis of the ciliary bodies between wild type and PRELP knock-out eyes. (A)-(D) Two different magnifications of H+E stained ciliary bodies from WT and *PRELP*$^{LacZ/LacZ}$ samples, demonstrating similar morphology and cell density of the CB epithelium. Red dotted lines demonstrate the chosen area to be measured. Scale bars, 100μm for (A)-(B), 50μm for (C)-(D). (E) Quantification of the CB area was performed in 6 different sections of each sample (n=3 eyes for WT, n=3 eyes for PRELP KO) using the Image J analysis software. PRELP KO animals had smaller ciliary bodies when compared to wild types. Data are presented as mean±SEM, *p<0.05.

Following this last finding, immunofluorescence staining was performed using an anti-Pax6 antibody, marking the pigmented and non-pigmented cells of the ciliary body epithelium. Presented in Figure 6.17 A&B are images of CBs from WT and *PRELP*$^{LacZ/LacZ}$ samples respectively, showing no difference in the intensity of the staining or the density of the Pax6 positive cells, indicating no apparent cell decrease in the epithelium. Lastly, staining with an anti-Laminin antibody was also carried out in all PRELP and OMD samples and representative images of both are exhibited together in Figures 6.18 and 6.19. More specifically, as already mentioned, laminin staining of the central retina marks the inner limiting membrane, which is localised above the ganglion cell layer (arrow), together with the blood capillary walls (arrowheads), as seen in Figure 6.18. Comparison of either the OMD or PRELP knock-outs with the WT revealed no difference the staining intensity or pattern. The same observation can be seen in the ciliary bodies staining, where laminin labels the basement membrane of the CB epithelial cells as well as the linings of the blood vessels (Fig. 6.19).

In conclusion, this preliminary analysis revealed a difference in the ciliary body size due to PRELP depletion. Other differences in cell viability or number were not found, although a more detailed analysis including more samples needs to be done in order to have a more conclusive result.

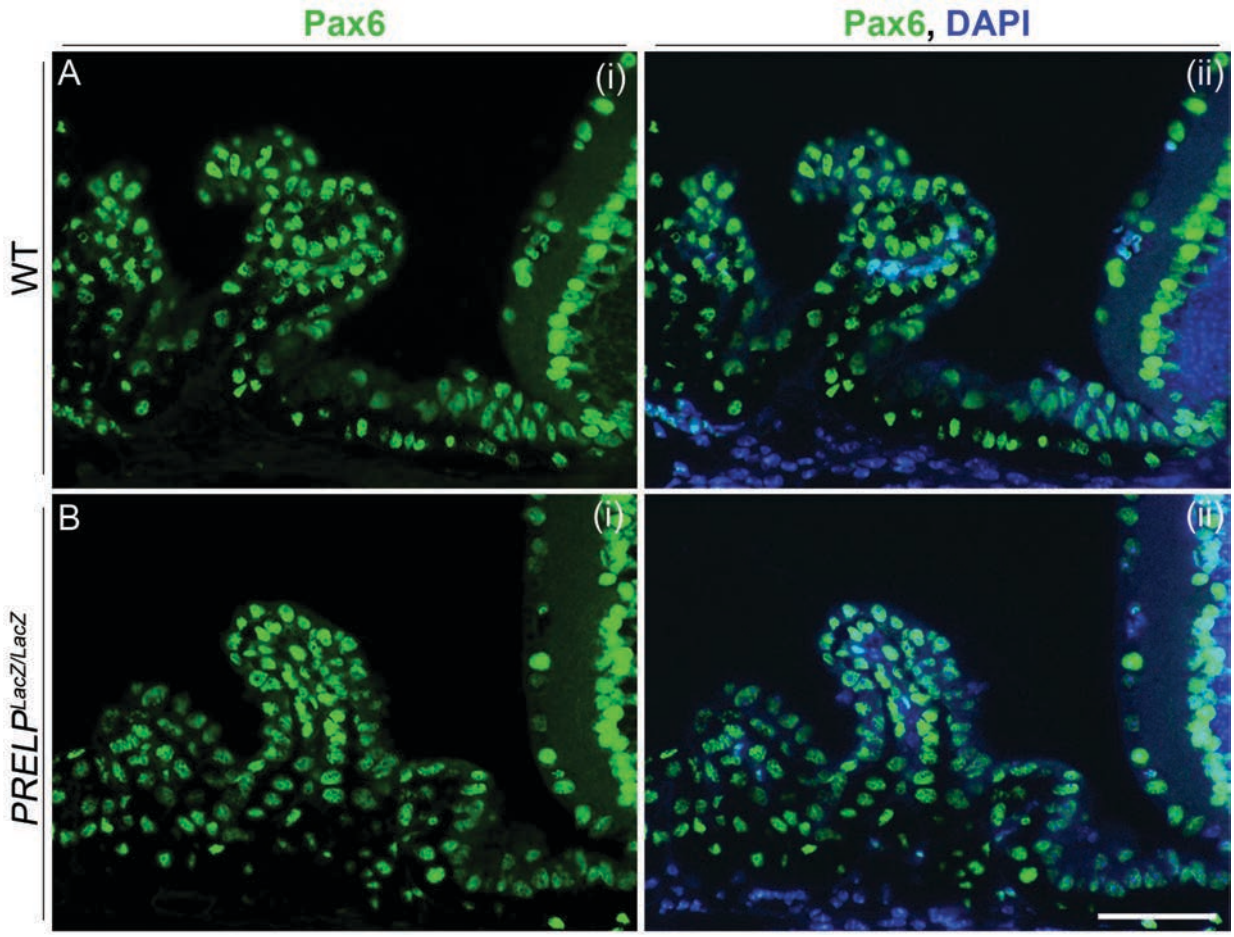

Figure 6.17: No decrease in the ciliary body epithelial cells is seen in the PRELP knock-out eyes. Immunofluorescence staining was performed with a Pax6 primary antibody and was visualised using alexa-488 (green) as secondary, and DAPI as nuclei stain. Comparison between wild type and PRELP knock-out samples did not reveal any differences in the staining intensity or cell density of the CB cells. Scale bar, 50μm for all images.

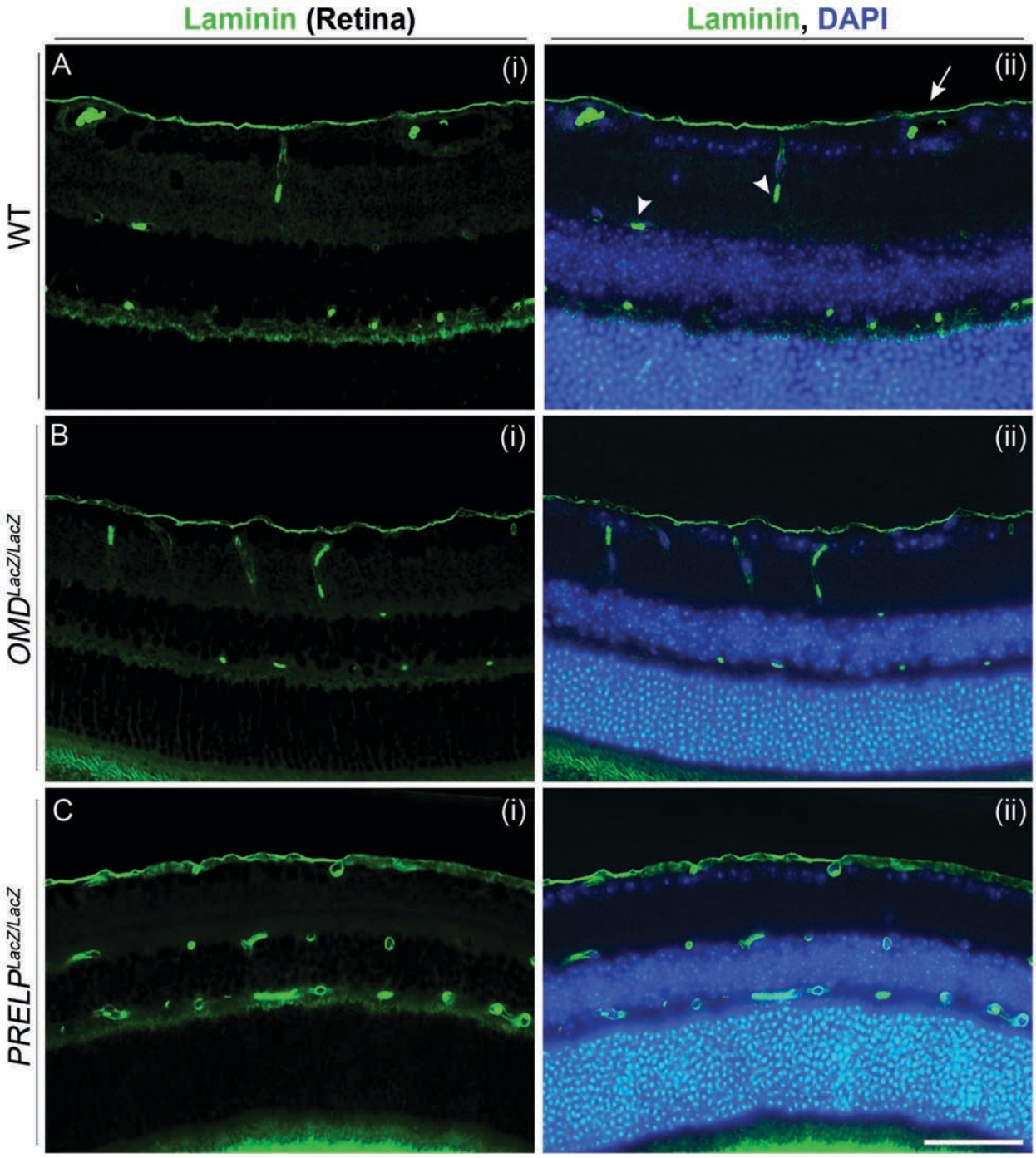

Figure 6.18: No differences were seen in the inner limiting membrane of wild type and knock-out retinas. Immunofluorescence staining was performed with a laminin primary antibody and was visualised using alexa-488 (green) as secondary, and DAPI as nuclei stain. Arrow indicates the inner limiting membrane which is positive for laminin, while arrowheads point to blood vessels walls which are also positive. Comparison between wild type and OMD/PRELP knock-out samples did not show any differences in the staining pattern or intensity. Scale bar, 50μm for all images.

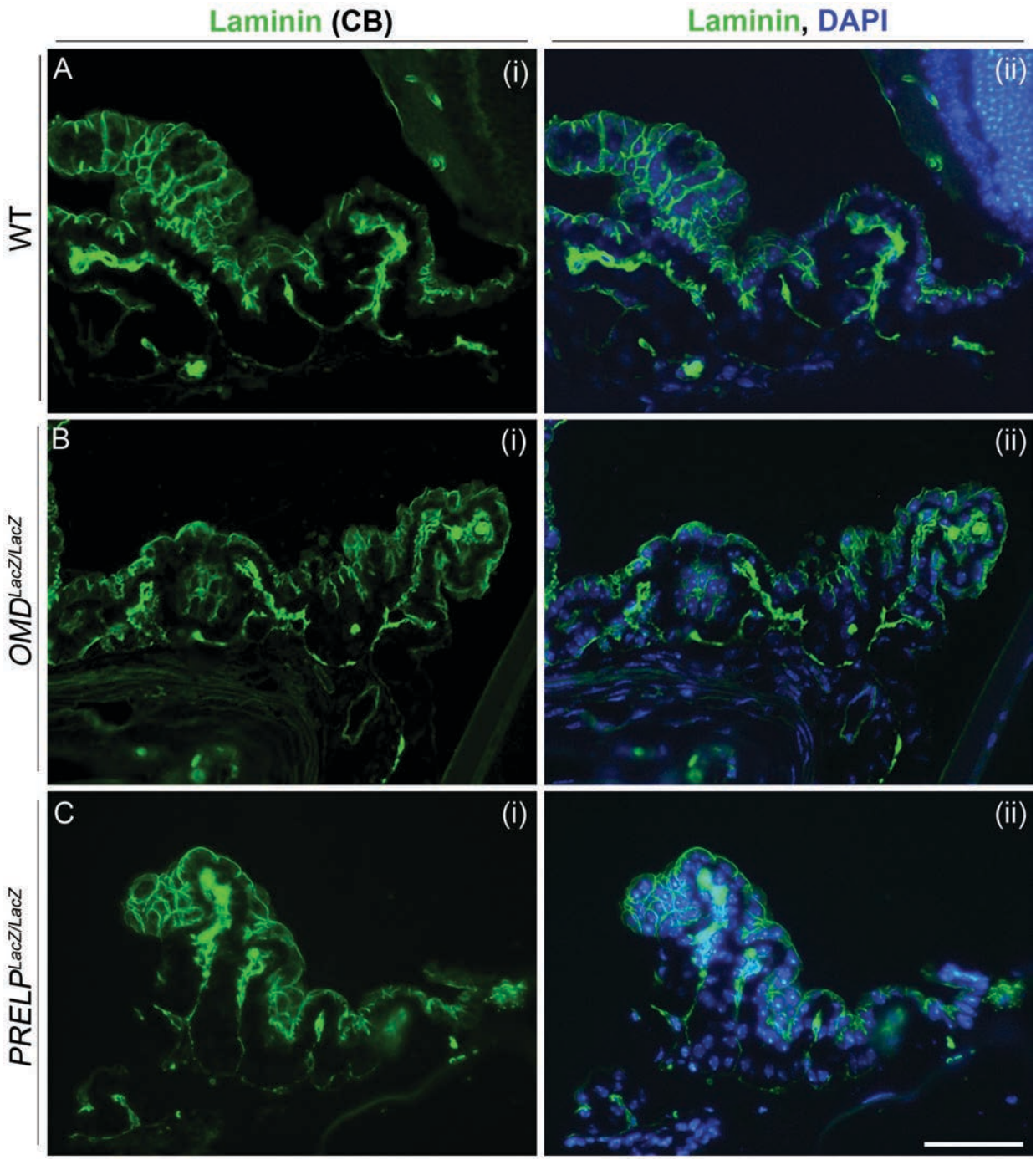

Figure 6.19: No differences were seen in the basement membrane of ciliary bodies between wild type and knock-out eyes. Immunofluorescence staining was performed with a laminin primary antibody and was visualised using alexa-488 (green) as secondary, and DAPI as nuclei stain. Laminin stains the basement membrane of the CB epithelial cells and the blood vessel walls. No obvious differences are seen in the staining pattern or intensity between the wild type and knock-out samples. Scale bar, 50μm for all images.

6.2.1.3 Effect of *OMD* and *PRELP* targeted deletion in the mouse gait locomotion and bone content

Since OMD and PRELP are expressed in both bone and brain, we wanted to assess any possible motor-related phenotypes. Gait analysis provides an easy way to evaluate neurological disorders as well as skeletal defects like arthritis or knee injuries. Therefore, we performed a preliminary gait study employing the footprint test, including only wild type and OMD knock-out mice at two months of age.

Five mice of each WT and $OMD^{LacZ/LacZ}$ genotypes were used in this study and representative images of the hindlimb ink-stained walking pattern are shown in Figure 6.20A. The parameters analysed are the stride length between the same feet, the sway distance and the stance, as indicated by the dotted lines. Each mouse was tested thrice and measurements were calculated using the Image J software. Histograms relative to the different elements are shown in Figure 6.20 B-D, demonstrating very small differences between the groups of mice. In detail, regarding the stride, WTs showed a mean length of 107.9 ± 1.63, measured in pixels, versus 109.4 ± 2.01 for the OMD-KO (p=0.5626). For the sway, WTs had a mean distance of 52.61 ± 0.69 whereas the knock-outs had 49.77 ± 1.09, a very small but significant difference (p=0.0315), while for the stance the values were at 77.43 ± 1.39 for controls against 80.09 ± 1.87 for transgenics (p=0.2562). Collectively, we can conclude that the gait between controls and OMD knock-out animals is similar with some minor differences, which however could indicate a possible role of OMD in affecting mouse mobility. In order to have a more convincing outcome we need to increase the number of the samples and also repeat the test in several different age points.

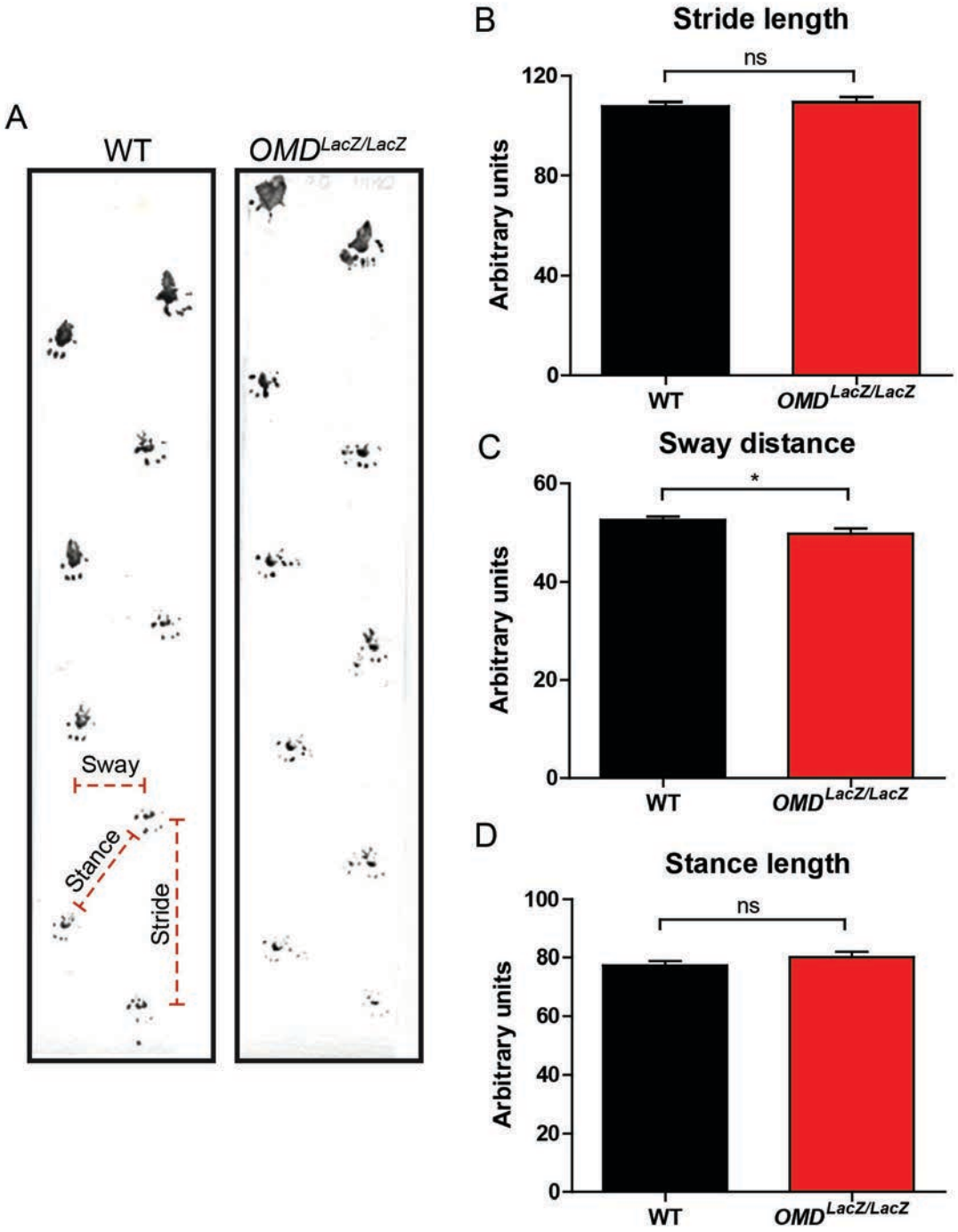

Figure 6.20: Gait analysis of OMD transgenic mice. Gait analysis was performed with the footprint test, where the front and hind paws are dipped in ink so that the mice leave a trail of footprints as they walk along a corridor. Measurements of stride, stance and sway length give an indication of gait. Five mice of each genotype were tested thrice. Measurements were calculated using the Image J analysis software. (A) Examples of the footprints seen in WT and OMD KO mice. (B)-(D) Measurements of stride length (B), sway distance (C) and stance length (D) between wild types and knock-outs. Data are presented as mean±SEM, *p<0.05. ns, non-significant.

Lastly, automated measurements were obtained for bone and soft-tissue composition of transgenic mice using the Lunar PIXImus Densitometer. The parameters tested are bone mineral density (BMD) and bone mineral composition (BMC), as well as the fat, lean and total fat+lean for the whole body. This study was performed on a preliminary basis as well, and thus, only a small number of mice were used. More specifically, two $OMD^{+/+}$ and four $OMD^{LacZ/LacZ}$ at four weeks of age were tested regarding the *OMD* gene, and five of each $PRELP^{+/+}$ and $PRELP^{LacZ/LacZ}$ for the *PRELP* gene at 8 weeks of age. The results are presented in Figure 6.21, where we can observe small differences between the controls and knock-outs, none of which are statistically significant though. The biggest differences can be seen in the lean and total measurements for the OMD group, but due to the small sample size tested no significant conclusions can be reached. Also, the differences observed between the $OMD^{+/+}$ and $PRELP^{+/+}$ mice can be attributed to the age difference between the two distinct groups. Therefore, under the current findings, we cannot make any significant conclusion concerning the effect of OMD or PRELP depletion on bone mineral or body composition of the transgenic mice.

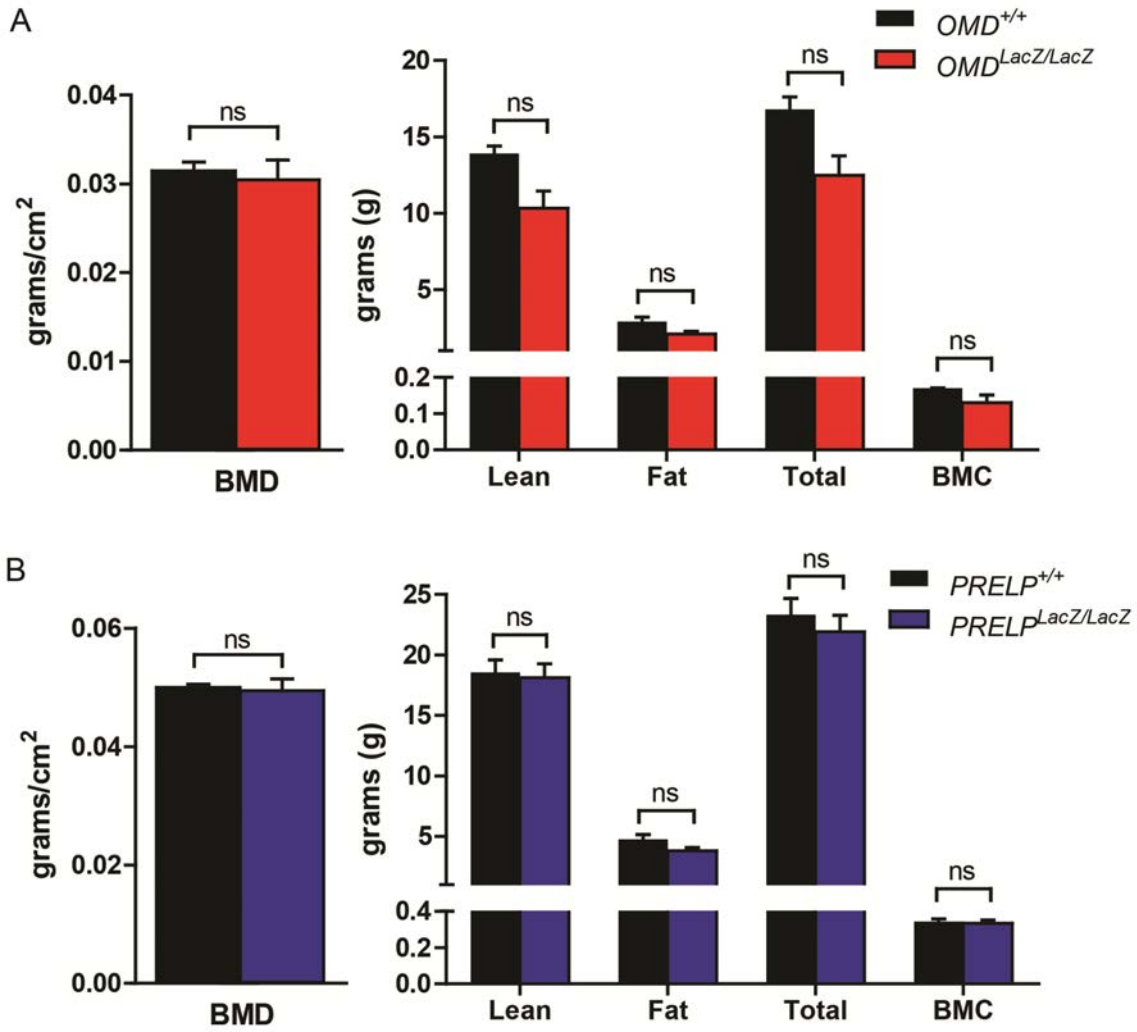

Figure 6.21: Piximus analysis of OMD and PRELP transgenic mice. Using the Lunar PIXImus Densitometer automated analysis of the bone mineral density (BMD), bone mineral composition (BMC), lean, fat and the total of lean+fat was performed. Two $OMD^{+/+}$ and four $OMD^{LacZ/LacZ}$ mice at four weeks of age (A), and five of each $PRELP^{+/+}$ and $PRELP^{LacZ/LacZ}$ mice at 8 weeks of age (B) were tested. No significant differences were seen between wild type and knock-out mice in the above parameters. Data are presented as mean±SEM. ns, non-significant.

6.2.2 Effect of OMD and PRELP depletion in mouse embryonic development

The initial step in most skeletal phenotype investigations is the analysis of whole-mount skeletal preparations. This specialized staining allows evaluation of different skeletal elements in their appropriate location and is the main technique used to detect changes in skeletal patterning. This method involves differential staining of cartilage and ossified bone, using alcian blue and alizarin red respectively, and can therefore also be used to assess the pace of skeletal maturation. Alcian blue/alizarin red whole-mount staining was performed in E15.5 and E17.5/E18.5 litters arising from $OMD^{+/LacZ}$ ♂ x $OMD^{+/LacZ}$ ♀ and $PRELP^{+/LacZ}$ ♂ x $PRELP^{+/LacZ}$ ♀ matings, and knock-out embryos were compared to wild types within the same litter.

Overall we could not detect any differences between wild type and knock-out embryos concerning skeletal preparations of E15.5 embryos. During this stage of development ossification has not progressed much and the areas that are stained with alizarin red are mostly the mandible, small parts of the vertebral discs and the ribs, together with the primary ossification centers of all the long bones, while all the other skeletal elements are cartilage and therefore stained blue. Starting with OMD transgenic E15.5 embryos, in Figure 6.22A representative images are shown of the lateral and dorsal sides of an $OMD^{+/+}$ and an $OMD^{LacZ/LacZ}$ embryo, where it is visible that there are no noticeable differences in the overall size of the embryos, the number of vertebrae or ribs, the length of the appendicular bones, or the shape of the head. In addition, magnified views of the forelimb and hindlimb long bones are presented in Figure 6.22B-C (i) and (ii) respectively. The primary ossification centers of radius (R), ulna (U) and humerus (H) are discernible, moderately stained with alizarin red, where we see no changes in the intensity of staining or the length of the epiphysis between wild type and knock-out embryos, suggesting that OMD depletion did not affect ossification or chondrocyte maturation rates even though it is expressed in the bone collar and in a sub-population of chondrocytes (Fig 6.22 B(i) vs. C(i)). The same pattern is seen in the leg bones femur (F), tibia (Ti) and fibula (Fi), where alizarin red staining is even less intense around the ossification grooves, and again there are no differences between the wild type and knock-outs (Fig. 6.22 B(ii) vs. C(ii)).

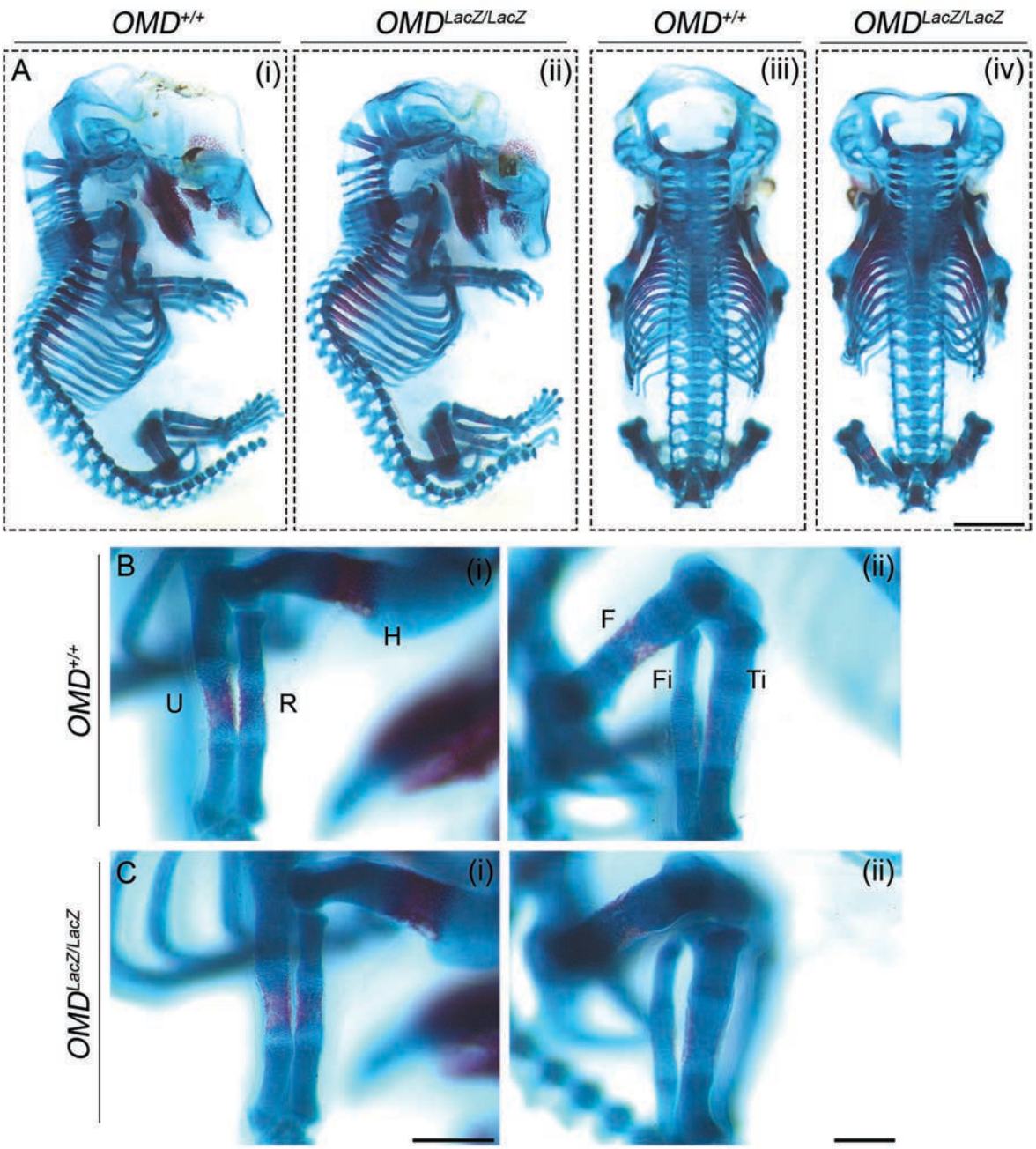

Figure 6.22: Skeletal preparations of E15.5 OMD transgenic embryos. Alizarin red and alcian blue staining of E15.5 wild type and OMD knock-out littermates was performed and representative images of the dorsal and lateral sides are shown in in (A). (B)-(C) Panels (i) and (ii) show magnified views of the frontlimb and hindlimb respectively. No differences were seen in the overall skeleton or in the long bones of the limbs between wild types and knock-outs, while ossification appears to be progressing in the same rate in both genotypes. Scale bars, 2mm for (A), 1mm for (B)-(C). H, humerus; R, radius; U, ulna; F, femur; Ti, tibia; Fi, fibula.

Moving on to older OMD transgenic embryos, the second target stage to be studied was E17.5, but due to technical difficulties E18.5 embryos were isolated instead and were prepared for skeletal staining. By this stage, skeletal development has progressed considerably and we can see that most of the osteoid elements of both the axial and appendicular skeleton have now been ossified. More specifically, all the cranial bones and the osseous parts of the vertebrae are stained with alizarin red, together with the dorsal segments of the ribs and most of the length of all the long bones in the limbs. In addition, the centers of metacarpals, metatarsals and phalanges are now ossified. Similarly to above, representative images of the lateral and dorsal sides of $OMD^{+/+}$ and $OMD^{LacZ/LacZ}$ embryos are presented in Figure 6.23A, where again there are no observable differences in the overall size of the embryos, the number of vertebrae or ribs, the length of the long bones, or the appearance of the head between the two genotypes. In Figure 6.23 B(i)&C(i) enlarged images of the forelimb are shown, where we can see that radius and ulna have both been ossified to the same extent in the wild type and knock-out embryos. Furthermore, when observing the hindlimb and specifically the femur, tibia and fibula, again we see no differences in the length of the bones or the ossification progression (Fig. 6.23 B(ii) vs. C(ii)). Also, when looking at the sternum the partly ossified sternebrae (St) can be identified, as well as the xiphoid bone and cartilage (Xi), both being at the same stage of endochondral ossification between $OMD^{+/+}$ and $OMD^{LacZ/LacZ}$ embryos (Fig. 6.3 B(iii) vs. C(iii)). Finally, no differences can be seen in the intramembranous ossification of the cranial bones when comparing the wild type with the OMD knock-out embryos. All the cranial elements, including the mandible (Man) and maxilla (Max), the frontal (F), parietal (P), intraparietal (I), supraoccipital (So) and exoccipital (Eo) bones, together with the first cervical vertebrae the atlas (At) and the hyoid bone (Hy) have the same alizarin red staining intensity and thus ossification progression (Fig. 6.3 D vs. E). In conclusion, OMD depletion does not have an apparent effect on skeletal development even at this more progressed stage of bone maturation.

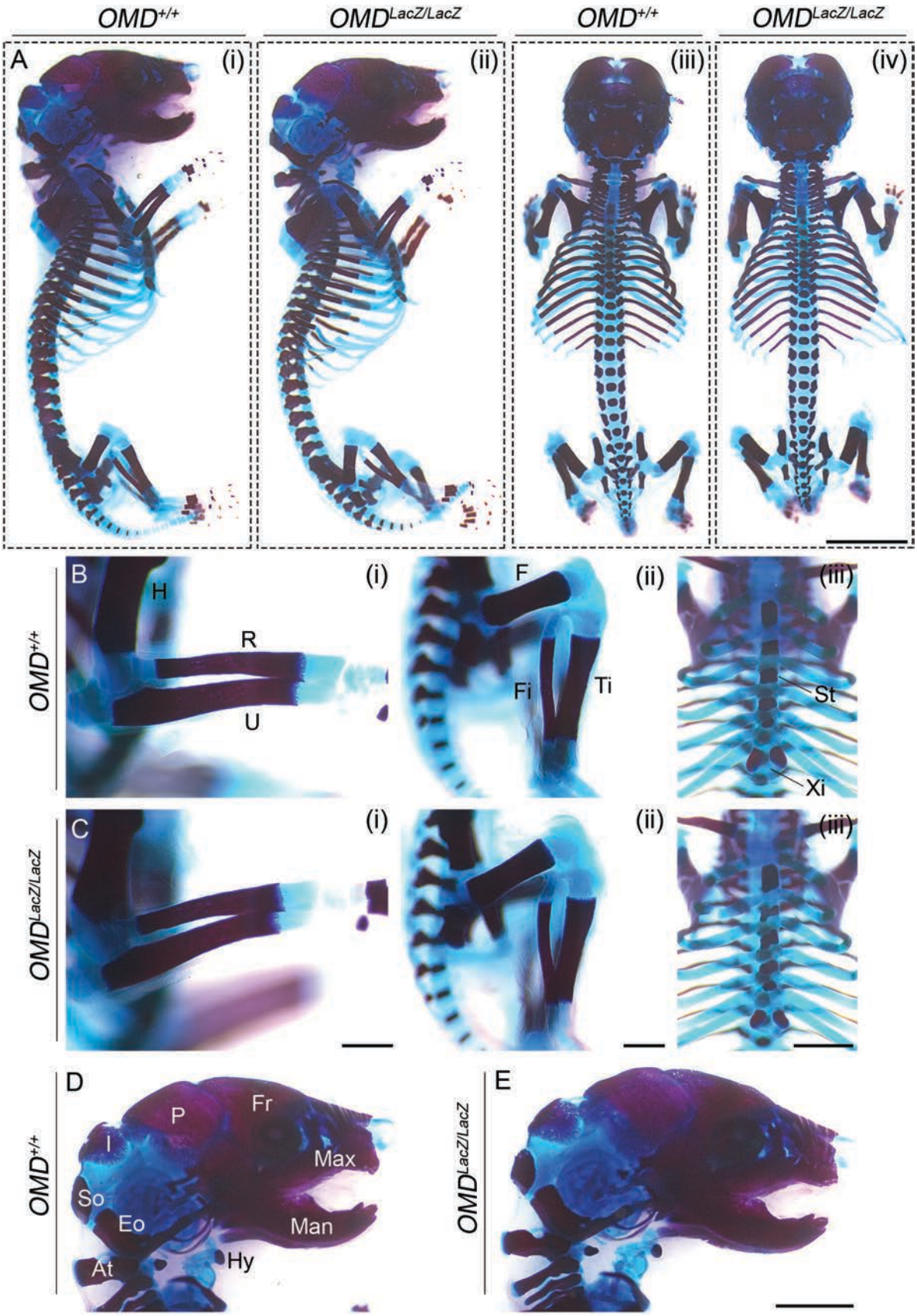

Figure 6.23: Skeletal preparations of E18.5 OMD transgenic embryos. Alizarin red and alcian blue staining was performed in E18.5 wild type and OMD knock-out littermate embryos and representative images of the dorsal and lateral sides are shown in (A). (B)-(C) Panels (i), (ii) and (iii) show magnified views of the frontlimb, hindlimb and sternum respectively. No differences can be seen in the length of the ossified bones or the alizarin red intensity between controls and KOs, demonstrating normal skeletal development in *OMD*$^{LacZ/LacZ}$ embryos. (D)-(E) Enlarged images of the head showing comparable pattern of ossification and similar head size/structure between wild type and transgenic embryos. Scale bars, 3mm for (A), 1mm for (B-i, B-ii) & (C-i, C-ii), 2mm for all the rest. H, humerus; R, radius; U, ulna; F, femur; Ti, tibia; Fi, fibula; St,sternum; Xi, xiphoid; Fr, frontal; P, parietal; I, intraparietal; So, supraoccipital; Eo, exoccipital; At, atlas; Hy, hyoid; Max, maxilla; Man, mandible.

The same analysis was performed in PRELP transgenic litters at stages E15.5 and E17.5 and again no differences were seen between $PRELP^{+/+}$ and $PRELP^{LacZ/LacZ}$ embryos. In Figure 6.24A E15.5 embryos are presented, where the ossification of the growing skeleton is still in early stages and most of the alizarin staining is seen in the mandible, in a small part of the vertebrae and ribs, and in the primary ossification centers of the long bones. More specifically, a magnified view of the humerus is shown with part of the radius and ulna, demonstrating the same level of endochondral maturation and ossification in the primary groove between wild type and knock-out (Fig. 6.24 B(i) vs. C(i)). The same applies for the long bones of the hindlimb, i.e. femur, tibia and fibula (Fig. 6.24 B(ii) vs. C(ii)).

Continuing with older PRELP embryos, stage E17.5 samples were stained for bone and cartilage, and in Figure 6.25A the lateral and dorsal views of two representative embryos are demonstrated, where we can see that skeletal development has progressed considerably, with no overall differences between $PRELP^{+/+}$ and $PRELP^{LacZ/LacZ}$ embryos in either the axial or appendicular skeleton. In detail, the biggest parts of the forelimb/hindlimb have now been ossified and alizarin red staining of the humerus, radius, ulna, femur, tibia and fibula has the same intensity and volume between wild types and knock-outs, suggesting similar chondrocytic maturation and ossification levels (Fig. 6.25 B(i-ii) vs. C(i-ii)). Moreover, ossification of the sternebrae has progressed at the same rate, while the xiphoid bones are still in a more cartilaginous stage (Fig. 6.25 B(iii) vs. C(iii)). Furthermore, close comparison between wild type and *PRELP* knock-out embryonic heads reveals no difference in the intramembranous or endochondral ossification of the cranial bones, where the mandible and maxilla, the frontal, parietal, intraparietal and exoccipital bones, along with the first cervical vertebrae and the hyoid bone have the same alizarin red staining intensity and thus ossification progression (Fig. 62.5 D vs. E). In comparison to E18.5 OMD embryos, it is visible that ossification has not advanced at the same level, which is expected since these PRELP embryos are one day younger, and for example, ossification of the supraoccipital bone has still not taken place in either $PRELP^{+/+}$ or $PRELP^{LacZ/LacZ}$ E17.5 embryos, whereas the bone is almost fully formed in the OMD E18.5 embryos.

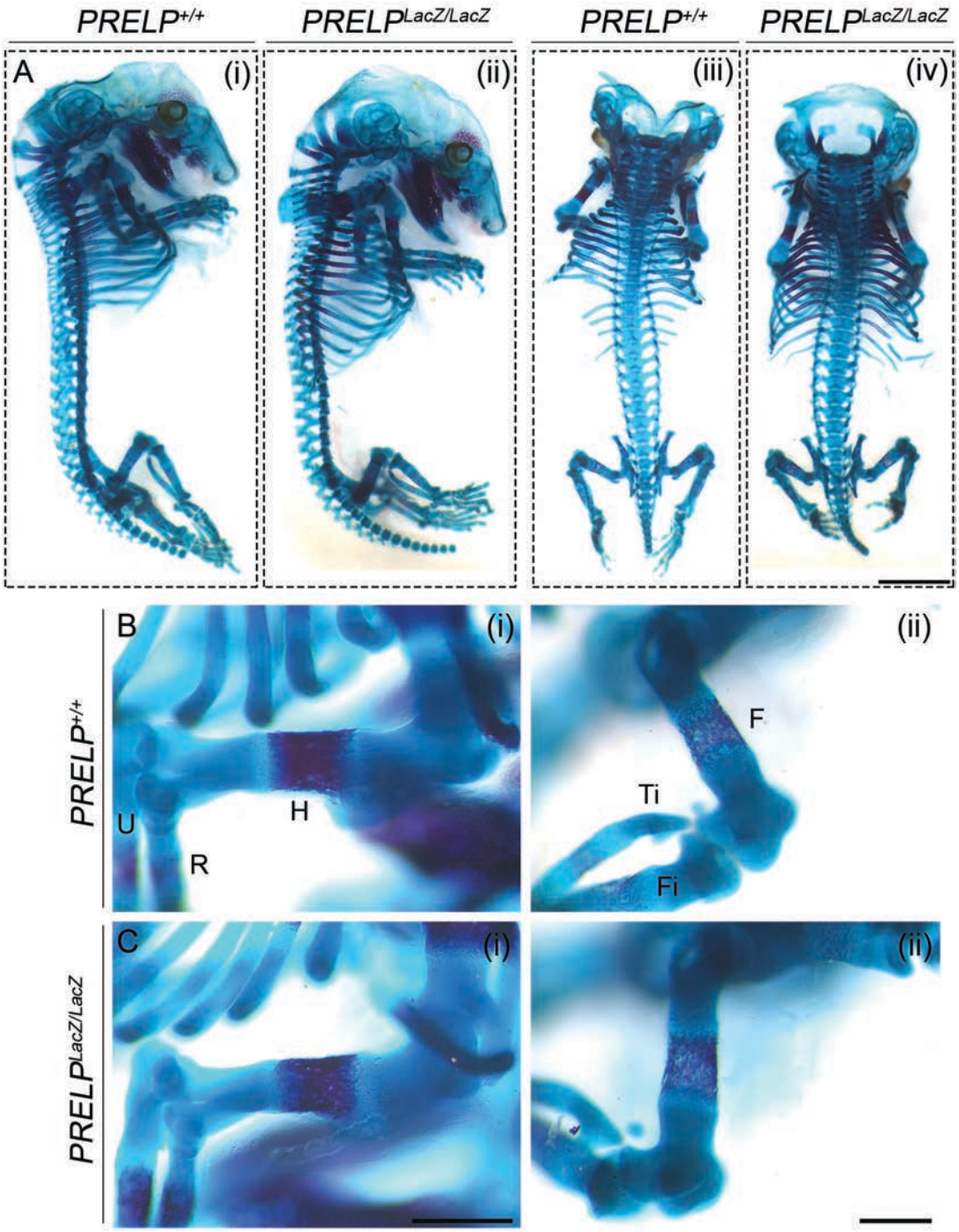

Figure 6.24: Skeletal preparations of E15.5 PRELP transgenic embryos. Alizarin red and alcian blue staining of E15.5 wild type and PRELP KO littermates was performed and representative images of the dorsal and lateral sides are shown in (A). Due to the prolonged period of handling the embryos during the skeletal staining, breaks at the ribs, as seen here, and other fragile parts of the embryo often occur. (B)-(C) Panels (i) and (ii) show magnified views of the frontlimb and hindlimb respectively. No differences were seen in the overall skeleton or in the staining and size of long bones in the limbs between wild types and knock-outs, while ossification appears to be progressing in the same rate in both genotypes. Scale bars, 2mm for (A), 1mm for (B)-(C). H, humerus; R, radius; U, ulna; F, femur; Ti, tibia; Fi, fibula.

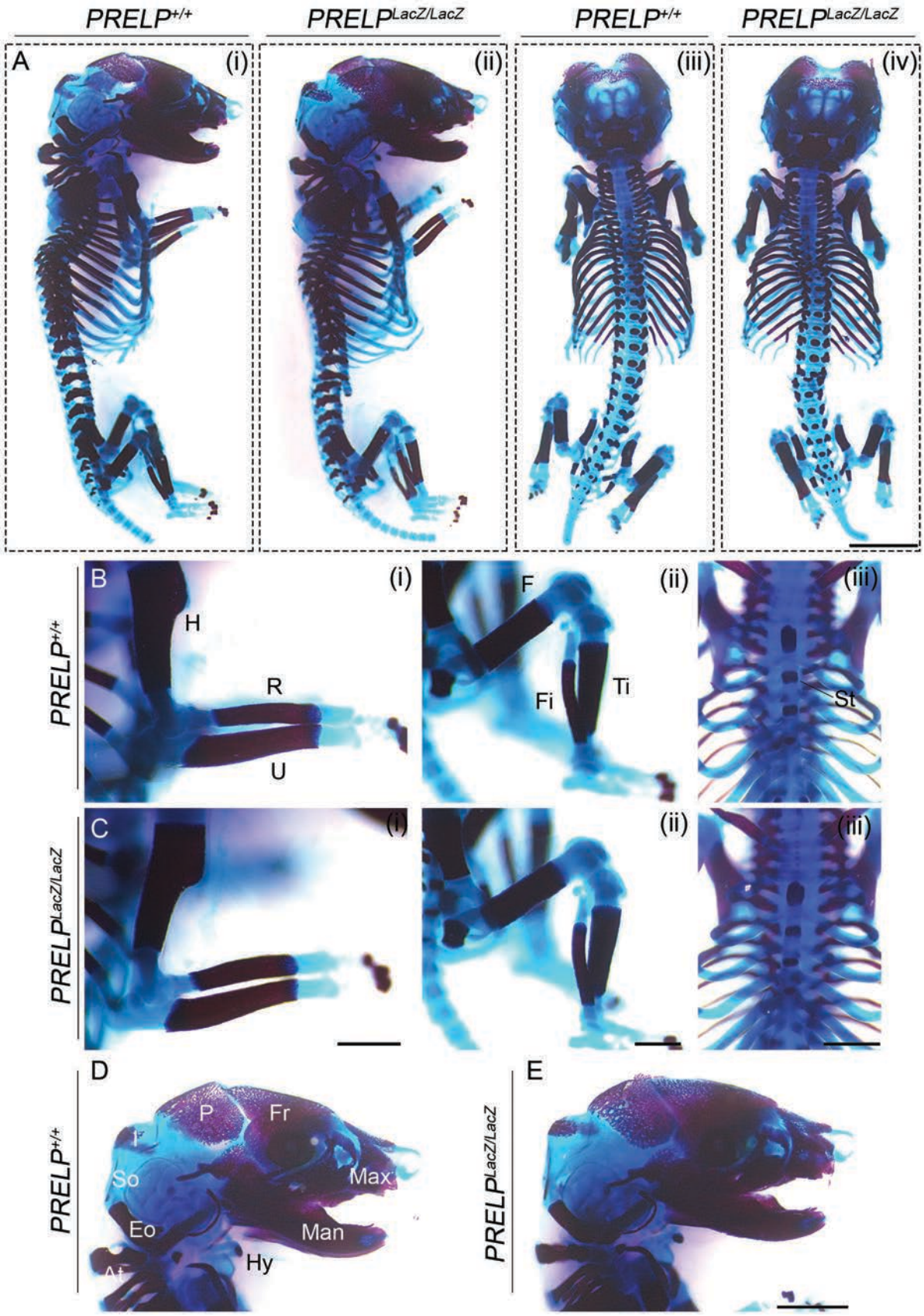

Figure 6.25: Skeletal preparations of E17.5 PRELP transgenic embryos. Similarly to before, lateral and dorsal sides of E17.5 wild type and PRELP KO littermate stained embryos are shown in (A), demonstrating no apparent differences in the size or the structure of the developing skeleton. (B)-(C) Panels (i), (ii) and (iii) show enlarged views of the frontlimb, hindlimb and sternum respectively. Again, no differences can be seen in the length of the ossified bones or the alizarin red intensity between controls and KOs, indicating normal skeletal development of KO embryos. (D)-(E) Enlarged images of the head showing similar alizarin red staining between wild type and transgenic embryos. Scale bars, 3mm for (A), 1mm for (B-i, B-ii) & (C-i, C-ii), 2mm for all the rest. H, humerus; R, radius; U, ulna; F, femur; Ti, tibia; Fi, fibula; St,sternum; Fr, frontal; P, parietal; I, intraparietal; So, supraoccipital; Eo, exoccipital; At, atlas; Hy, hyoid; Max, maxilla; Man, mandible.

In conclusion, OMD or PRELP depletion did not result in any discernible phenotypes during embryonic skeletal development. Even though both proteins are found to be largely expressed in skeletal elements (Chapters 4&5), alizarin red/alcian blue staining of embryos revealed no apparent differences in chondrocytic maturation or ossification rate.

6.2.3 Micro-CT of OMD E17.5 embryos

Since OMD and PRELP are strongly expressed during skeletal development it was decided to study more closely the embryonic bone formation. For this purpose micro computed tomography (micro-CT) was performed, which is X-ray imaging in 3D similar to the clinical "CAT" scans but on a smaller scale with very high resolution. This method basically represents 3D microscopy, where very fine scale internal structure of objects can be imaged by creating realistic visual models and in addition 3D bone morphometric parameters can be measured. However, due to the very high cost of the scanning equipment usage and the extensive time needed to complete the scans, this analysis was performed on OMD transgenic E17.5 embryos only, while PRELP embryos were not included in the present study.

Whole-embryo reconstructions were generated from ~3500 individual cross sections per sample, optimized for bone analysis, and were artificially colored to enhance the signal. Three wild type and five OMD knock-out embryos were included in this study. In Figure 6.26 A&B representative images of $OMD^{+/+}$ and $OMD^{LacZ/LacZ}$ embryos are shown respectively. In panels (i) the front/ventral sides of the embryos are shown, while in panels (ii) the back/dorsal and in (iii) the right/lateral views are displayed. Interestingly, small differences can be seen in the mineralization content of some skeletal elements. For example, ossification of the intraparietal bone is delayed in the OMD knock-out embryos compared to WT (Fig. 6.26 A(ii) vs. B(ii), arrows). In addition, the same effect can be observed for the metacarpal and metatarsal bones, where the signal in the $OMD^{LacZ/LacZ}$ samples is much less compared to $OMD^{+/+}$ (Fig 6.26 A(iii) vs. B(iii), arrows). All the other skeletal elements, including the ribs, frontlimb/hindlimb long bones and vertebrae appear to be of comparable ossification levels and size between wild types and knock-outs.

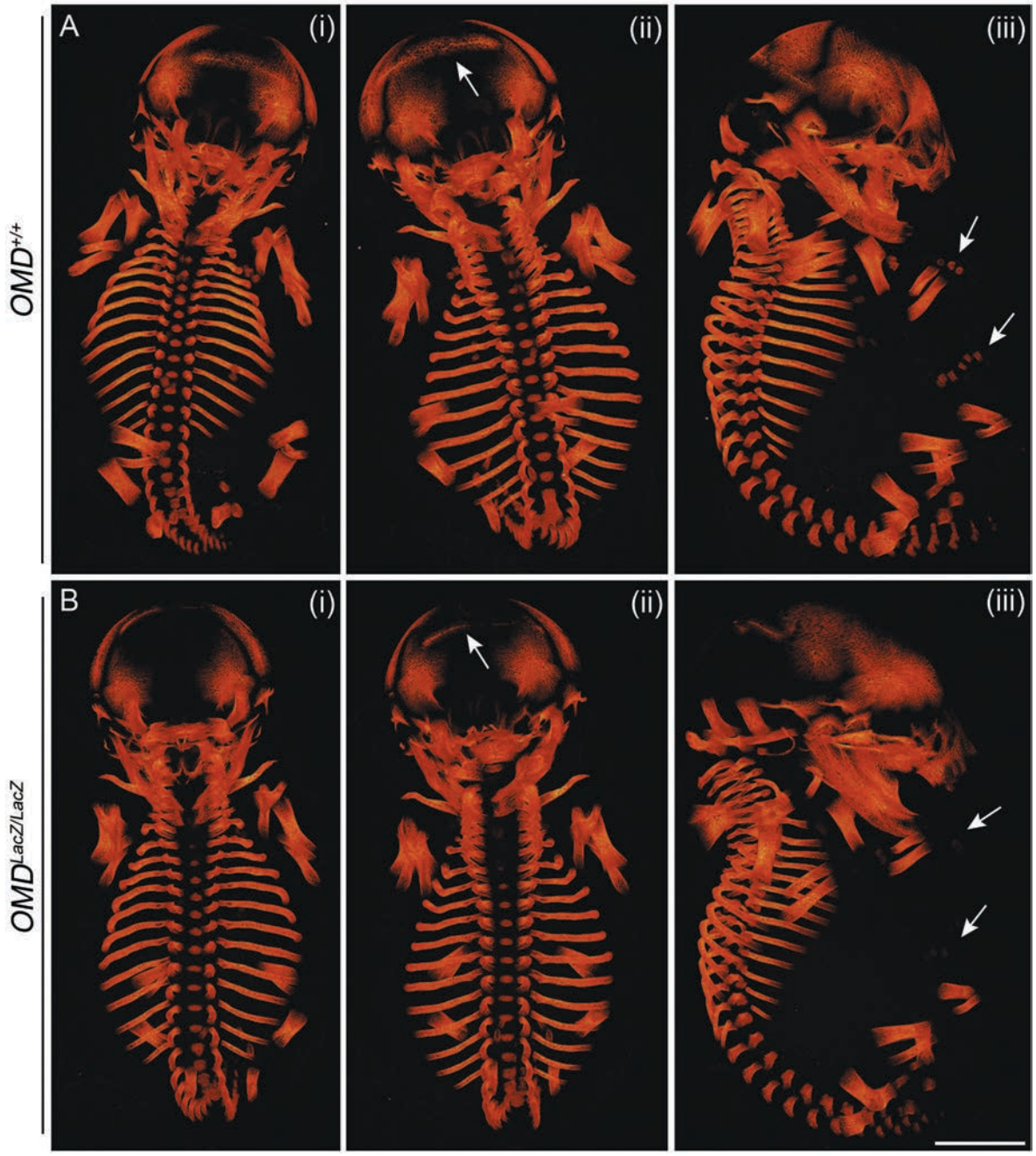

Figure 6.26: Micro-CT reconstructions of E17.5 OMD transgenic embryos. Three wild type and five OMD knock-out embryos were scanned for bone content. Reconstructions were generated with the CTvox software and colour was added to the images to enhance the signal. Therefore, orange colour represents ossified bone. Panels (i) show the front/ventral sides of the embryos while in panels (ii) the back/dorsal and in (iii) the right/lateral views are displayed. Arrows in panels (ii) indicate delayed intraparietal bone ossification in the knock-out embryos compared to the controls. Arrows in panels (iii) point to metatarsals and metacarpals, which are very faint in the OMD KO, demonstrating decreased ossification. All the other skeletal elements appear normal in both genotypes. Scale bar, 3mm for all images.

Quantitative bone morphometric analysis of the 3D reconstructed micro-CT models can be performed through the CTvol software, and can provide quantitative data about structural properties of cortical and trabecular bone. For instance, properties like tissue volume (TV), bone volume (BV), bone surface (BS), as well as bone volume density (BV/TV) and bone surface density (BS/TV) can all be measured and give us information about bone morphology. Three $OMD^{+/+}$ and five $OMD^{LacZ/LacZ}$ embryos were scanned and analysed for all the above parameters and the most important findings are presented in Figure 6.27. More specifically, the percent bone volume density (BV/TS) of the OMD knock-out embryos (0.16 ± 0.03, n=5) was lower compared to the wild type (0.21 ± 0.02, n=3), but not significantly different (p=0.2644) (Fig. 6.27A). The same was observed for the bone surface, where $OMD^{LacZ/LacZ}$ had a mean value of 580.3 ± 101.7 vs. 713.9 ± 54.06 for the $OMD^{+/+}$ (p=0.2983) (Fig. 6.27B), as well as for the bone surface density (BS/TV) with values of 0.34 ± 0.05 for OMD-KO against 0.43 ± 0.03 for WT (p=0.2358) (Fig. 6.27C). Finally, the bone surface/bone volume ratio, which gives information about cortical/trabecular proportion, was slightly but not significantly different between the two groups, with the knock-outs having a higher mean value of 218.7 ± 12.93 vs. 200.4 ± 7.2 for the WT (p=0.2734) (Fig. 6.27D). Since at this stage of development neither cortical nor trabecular bone has completely form, the latter measurements probably do not have any significant value for embryonic bone analysis.

In conclusion, although not statistically significant, the overall bone content of the knock-out embryos is lower compared to the wild types, as demonstrated from the bone volume density and bone surface density graphs. Thus, we can say that there is a trend towards a delayed or decreased skeletal mineralization rate caused by OMD depletion, at least during this stage of development. Since alizarin red/alcian blue staining of E18.5 embryos showed no differences between OMD-KOs and WTs, we cannot know if this effect is attenuated in later developmental stages, or whether it is not visible due to the lower sensitivity of the skeletal preparation against the micro-CT imaging.

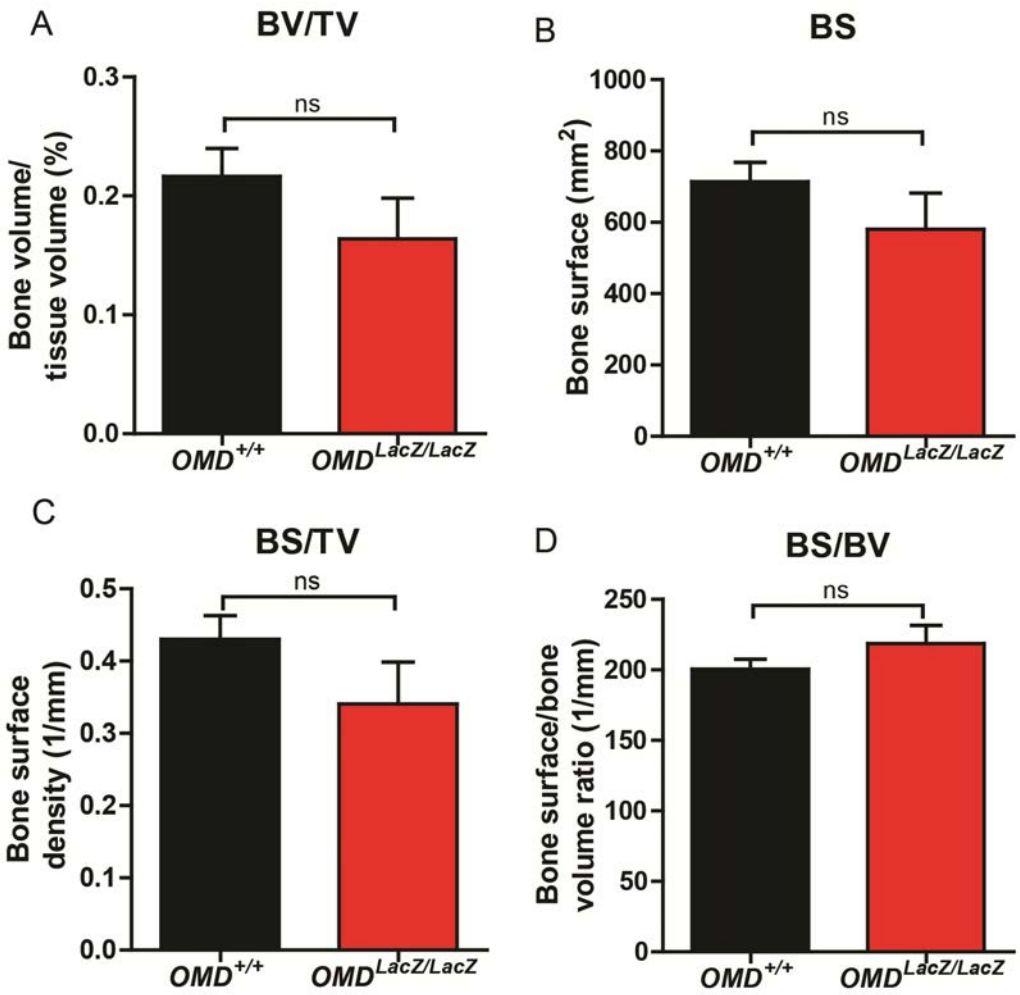

Figure 6.27: Bone morphometric analysis of E17.5 OMD transgenic embryos. Using the CTvol software structural properties of the developing bones were assessed, including: bone volume density (BV/TS), shown in (A); bone surface (BS), shown in (B); bone surface density (BS/TV), shown in (C); and bone surface/bone volume ratio, which gives information about cortical/trabecular proportion, shown in (D). In the first three parameters OMD KO embryos had lower, but not significantly different, values compared to the WT. Regarding the BS/BV ratio, OMD KO presented slightly higher values that the controls, but that was not significant as well. Data are presented as mean±SEM. ns, non-significant. BV, bone volume; BS, bone surface; TV, tissue volume.

6.3 Discussion

SLRPs have emerged as important regulators of multiple signaling pathways, thereby affecting various biological processes from development to tissue homeostasis. The development of knock-out transgenic mice has revealed their multiple roles in pathological conditions varying from cancer to osteoarthritis and eye abnormalities. Amongst the SLRP members studied extensively so far are decorin, lumican, biglycan and fibromodulin, but not OMD or PRELP. In the current study we used the novel OMD and PRELP knock-out mice to analyse any cancer-related but also other phenotypes that could arise from the targeted deletion of OMD and PRELP, with the aim of gaining insight into their functions.

OMD and PRELP depletion alter the bladder homeostasis and may contribute to cancer initiation

Extensive histological and immunohistochemical analysis of single and double OMD/PRELP knock-out bladders revealed three main findings, i.e. fibrin clots in the lumen, epithelial bursts formation in the urothelium and reduced tight junction formation between umbrella cells. The epithelial bursts have the appearance of disorganized masses of umbrella cells and are indeed composed of umbrella-originated cells, as shown by positive uroplakin staining (Fig. 6.2 & 6.3).

As we showed in the previous chapters, OMD and PRELP are expressed in a subpopulation of the outermost umbrella cells and not in the basal or intermediate cells. It has been previously shown that basal cells of the urothelium include multipotent stem cells that are capable of cell renewal and differentiation, which if triggered can lead to direct carcinoma *in situ* (CIS) formation, bypassing the non-invasive tumor stage (Ho et al., 2012; Shin et al., 2011). In contrast, bladder papillary non-invasive tumours might originate from umbrella cells, as shown in another study where selective overexpression of a mutant H-Ras under a uroplakin promoter resulted in low-grade papillary tumour (Castillo-Martin et al., 2010). Therefore, the epithelial bursts we observed in the OMD/PRELP knock-out mice might constitute very early stages of umbrella cell-papillary cancer formations. This is also supported by the slight increase in proliferating, Ki-67-positive cells in knock-out samples (Fig. 6.12).

Staining with specific cancer-related markers is necessary to confirm the true identity of the epithelial bursts cells. However, at the very early stages of tumor or papilloma formation cancer cells tend to grow slowly, are well differentiated and look quite similar to normal neighboring cells. Therefore, it is technically challenging to identify the exact nature of epithelial bursts.

Urothelial cell carcinomas can be generally separated into two molecular pathways: in one patients present with mutations in the *FGFR3, HRAS, PIK3CA* genes or deletions of candidate tumor suppressor genes mapping to chromosome 9q (where *OMD* is located as well), and they develop only superficial papillary tumours with good prognosis; the other tumour subtype have *TP53*, *RB* or *PTEN* gene mutations, leading to CIS and invasive cancer (Ahmad et al., 2011; Castillo-Martin et al., 2010; Luis et al., 2007; Wu, 2005). Therefore, if epithelial bursts are initiators of papilloma formations they would probably belong to the first genetic type and further research on the status of the aforementioned genes in the knock-out bladders is desirable. Taking into account our findings so far, it might be highly possible that *OMD* is one of the tumor suppressor genes mapped in the 9q locus that contribute to bladder cancer initiation.

Umbrella cells line the mucosal surface of the bladder and are characterised by junctional complexes in the intersections of their apical and lateral membranes. These complexes include tight junction and adherens junction (both of which form continuous belts) and desmosomes. Similarly to other epithelia, umbrella cell TJs modulate the paracellular transport of molecules (gate function), while they also restrict the movement of lipids and membrane proteins in the exofacial leaflet of the apical and basolateral plasma membrane domains (fence function) (Khandelwal et al., 2009; Matter and Balda, 2003). Therefore, proper regulation of tight junction components and formation is necessary for maintenance of the bladder homeostasis. ZO-1 staining and ultrastructural analysis of OMD KO, PRELP KO and double knock-out bladders revealed decreased and/or incomplete TJ formation in the apicolateral borders of the umbrella cells (Fig. 6.10 and 6.11), indicating regulation of tight junction by OMD and PRELP. These findings are in agreement with our *in vitro* data, where tight junction formation was increased in a bladder cancer cell line after overexpression of OMD/PRELP.

As was discussed in Chapter 3, altered expression of many TJ components has been related with cancer cells transformation and metastasis (Runkle and Mu, 2013). In addition, during EMT epithelial cells lose their junctions and polarity, and reorganize their cytoskeleton. This reorganization is accompanied by changes in gene expression of junctional proteins, i.e. downregulation of claudins, occludin, ZO-1 and E-cadherin, and activation of N-cadherin and vimentin (Lamouille et al., 2014). We did not observe any significant changes in E-cadherin expression in knock-out bladders under our current staining conditions (Fig 6.9), while staining for vimentin was attempted but unfortunately did not work. Thus, at this point we cannot conclude that the urothelium undergoes EMT due to OMD/PRELP depletion. But we did observe a considerable decrease in tight junction formation, suggesting that knock-out umbrella cells might be in the initial stages of epithelial cytoskeleton reorganization.

Other components of the tight junction complex, such as occludin, claudin-4 and ZO-2/ZO-3, were also examined but specific signal could not be seen in any of the wild type or knock-out samples, which can probably be attributed to inefficient staining conditions. In a previous study, ZO-1 was localised in punctate structures at the apicolateral borders of adjacent mouse umbrella cells, while it had a more diffuse cytoplasmic distribution in the underlying cell layers, a similar pattern to our staining (Acharya et al., 2004). In the same study, occludin also showed an apicolateral distribution at the umbrella cells but was additionally expressed in the basolateral surface and on the plasma membranes of the underlying cells layers, while claudin-4 was localised as well in the apicolateral junction of umbrella cells where TJ are formed (Acharya et al., 2004). Claudins-4,-8, and -12 are associated with high resistance TJ and expression of these claudins in the junctions of umbrella cells is consistent with the high-resistance, low-permeability barrier function of latter cells (Lewis, 2000). Therefore, further examination of these proteins in the knock-out bladders will definitely contribute to our understanding of how OMD and PRELP can regulate such complexes.

In addition, other components of the adherens junction, such as β-catenin, α-catenin and p120-catenin should also be investigated, especially since adherens junctions became more apparent in knock-out samples under EM examination. Some tight

junction components can also interact with proteins that are concentrated at adherens junction, for instance ZO-1 can form complexes with α-catenin, coupling the assembly of tight junctions to adherens junctions (Maiers et al., 2013; Rajasekaran et al., 1996), further demonstrating the importance of investigating both complexes. Overall, tight junctions have central roles in processes that regulate epithelial proliferation and differentiation and their functions are modulated by multiple signalling pathways and mediators including GTP-binding proteins, GTPases, and multiple kinases and phosphatases (Matter and Balda, 2003; Matter and Balda, 2014). Although we have already discovered some of the signalling mediators that are affected by OMD and PRELP, further investigation of TJ and AJ-related pathways is crucial in order to unravel how these two SLRPs can regulate junction assembly.

Interestingly, fibrin clots were found in the lumen of $PRELP^{LacZ/LacZ}$ and double KO bladders, which are the samples that also showed the strongest decrease in umbrella TJs under EM examination. Fibrin is a protein involved in blood clotting and is produced in response to bleeding. It is formed through fibrinogen polymerization by the action of thrombin, which forms a spongy mass that gradually hardens to form the clot. We cannot know exactly how or why these fibrin clots were formed in the lumen of the bladders. However, it is possible that fibrinogen could leak from vasculature if the blood-urine barrier is malfunctioning, or vice versa if the blood-urine barrier is not working properly pathogens and other urine substances could infiltrate the urothelium and cause scarring (as is the case with intersticial cystitis), which could lead to fibrin production. Tight junction formation is one of the earliest cellular events during urothelial differentiation, highlighting its importance in the blood-urine barrier (Jezernik and Pipan, 1993). In addition, during superficial and full-thickness urothelial wound healing restoration of tight junctions is also a primary event (Kreft et al., 2010). Therefore, decreased TJs in the knock-out samples due to PRELP/OMD depletion could be also involved with the fibrin clots found in the bladder lumen of these mice.

Finally, the presence of fibrin/fibrinogen degradation products has been used as a bladder cancer marker in human urine samples (Bassi et al., 2005; Jeong et al., 2012; Tsihlias and Grossman, 2000), demonstrating another probable link of PRELP

and/or combined OMD/PRELP depletion with bladder cancer. In a small preliminary analysis we conducted, detection of protein in urine samples was slightly higher in the PRELP and double KO mice compared to wild types (Fig. 6.6), and therefore further analysis of mouse urine for possible fibrinogen degradation products is very compelling.

Overall, we have shown that OMD and PRELP depletion may potentiate the formation of superficial, low-grade papillary formations in the bladder urothelium and, consistent with our previous observations, OMD and PRELP can regulate tight junction formation in the umbrella cells, where they are expressed.

Non-cancer related OMD and PRELP knock-out phenotypes

A preliminary analysis was performed in the eyes of OMD and PRELP knock-out mice, where no gross abnormalities in morphology or histology were detected. $OMD^{LacZ/LacZ}$ samples occasionally presented with slightly fractured tissue between the RGCs and the inner limiting membrane (Fig. 6.14). However, retinal ganglion cells quantification (Fig. 6.14) and laminin staining (Fig. 6.18) did not show any differences in the RGC number or in the inner limiting membrane structure between wild types and knock-outs. Interestingly, $PRELP^{LacZ/LacZ}$ eyes had smaller ciliary body area compared to WTs (Fig. 6.16), although CB epithelial cell viability or basement membrane structure was not affected, as shown by Pax6 and laminin staining (Fig. 6.17 & 6.19.). Tsukushi was also found to be expressed in the epithelial cells of the ciliary body mouse eyes and a similar histological analysis showed that TSK null animals had expanded dorsal and ventral CB areas (Ohta et al., 2011). In addition, depletion of other SLRPs, such as lumican and keratocan, resulted in eye abnormalities, mostly in the cornea (Chakravarti et al., 2000; Liu et al., 2003), demonstrating the multiple roles of SLRPs in eye homeostasis. Therefore, since we have confirmed OMD and PRELP expression in the mouse retina and CB, a more thorough analysis of PRELP and OMD knock-out eyes would possibly unravel their functions in eye biology.

Since OMD and PRELP are expressed in the developing skeleton and the adult bone and brain, a small-scale analysis was also conducted in search of any bone-related or motor-related phenotypes. OMD knock-out mice were tested with the gait ink test,

where they had a marginally lower sway distance whereas no differences were seen in the stride or stance length compared to wild types (Fig. 6.20). Bone mineral density and bone mineral content were also assessed, and although not statistically significant, they had lower values in the OMD knock-out mice compared to wild type (Fig. 6.21), which might be indicative of potential bone defects or possible delay in bone mineralisation. It must be noted that the number of mice included in the aforementioned analyses was quite small and more importantly all the mice that were tested were very young (4-8 weeks of age). Increasing the sample size and also assessing mice at different ages is important to unravel potential phenotypic effects related to the above functions.

SLRPs are involved in all phases of bone formation including cell proliferation, matrix deposition, remodelling and mineral deposition and their roles in bone pathophysiology are now firmly established (reviewed by Nikitovic et al., 2012). Knock-out models of biglycan, keratocan and fibromodulin all display abnormalities in bone morphology and mineral matrix content (Gill et al., 2002; Igwe et al., 2011; Xu et al., 1998). Furthermore, many SLRP double knock-out mice exhibit osteoarthritis (OA)-related phenotypes, demonstrating their importance in joints and bony tissues maintenance (reviewed by Ni et al., 2014). Briefly, biglycan/fibromodulin, epihycan/biglycan and lumican/fibromodulin double KOs present with alterations in joint laxity and integrity, in tendon mechanics, in the gait pattern, in bone content, in chondrocyte proliferation and in cartilage maintenance, resulting in OA- like phenotypes (Ameye et al., 2002; Jepsen et al., 2002; Kilts et al., 2009; Nuka et al., 2010). In all the above studies phenotypes were observed in mice at 3,6 and 9 months of age and above, while the older the mice the stronger the phenotypes they had. Thus, it is crucial to assess bone and joint-related phenotypes in OMD/PRELP knock-out mice that are at least 3 months or older.

Moreover, double SLRP-deficient mice usually display more severe phenotypes compared to their single knock-out counterparts, demonstrating that they have either overlapping functions, or that they have independent functions and when both are deleted result in a stronger phenotype. Therefore, assessment of bone and OA-related abnormalities in old OMD/PRELP double-KO animals will be very interesting and is highly likely that strong phenotypes can be observed under these circumstances.

Finally, in the aforementioned studies it was shown that some SLPRs compensate for the loss of others. Hence, it may be possible that the effects of OMD/PRELP depletion are attenuated by increased expression of other family members. Examining the levels of other SLRPs in our knock-out mice will further contribute to our understanding of their functions.

OMD and PRELP depletion might affect embryonic skeletal development

Since OMD and PRELP are strongly expressed in bone and cartilage during embryonic development, we wanted to assess any possible defects in skeletal development arising from OMD and PRELP depletion. For this purpose skeletal preparations of alizarin red/alcian blue staining were performed in two different embryonic stages of transgenic littermates.

No differences were seen between wild type and OMD KO embryos regarding their overall size, the size of the long bones or the ossification progression in the axial and appendicular skeleton during E15.5 and E18.5 stages (Fig. 6.22 & 6.23). The same result was observed for wild type and PRELP KO littermate embryos at stages 15.5 and 17.5 dpc (Fig. 6.24 & 6.25). It should be noted that occasional defects seen in E15.5 embryos, for example the "squashed" dorsal part of the cranium in OMD and PRELP embryos in Fig. 6.22A and 6.24A or the broken ribs seen in the latter samples, can be attributed to the handling of the embryos during the staining. Since at this embryonic stage most of the skeleton is still cartilage and the embryos are very fragile, it was very difficult to keep embryonic structures completely intact during the very long protocol of alizarin red/alcian blue staining.

Interestingly, small-scale differences were seen when micro-CT was performed in E17.5 OMD WT and KO littermate embryos. These included delayed ossification of the metatarsals/metacarpals and the intraparietal bone in the knock-out embryos (Fig. 6.26). However, quantification of bone volume/density or bone surface/density of the whole embryos did not reveal any significant differences, although OMD knock-out embryos had overall lower values in most of the examined parameters (Fig. 6.27). Analysis of these parameters in single bones might reveal a possible effect of OMD depletion in the ossification rate of different skeletal elements. These

differences were not observed with alizarin red/alcian blue staining, probably due to the lower sensitivity of the skeletal staining compared to micro-CT scanning.

The ultimate sizes, structures and growth rates of the endochondral bones depend on the coordinated regulation of chondrocyte proliferation, maturation and hypertrophy in response to multiple extracellular signals, and the major regulators of these processes were mentioned in Chapter 5. Considering that OMD and PRELP knock-out embryos grow normally into adulthood and no gross abnormalities are seen in skeletal development, in order to observe possible small-scale defects it is essential to assess chondrocyte maturation rates in a more detailed level. Transcription factors such as hypoxia inducible factor-2 (HIF-2α), runt-related transcription factor-2/3 (RUNX2/RUNX3), myocyte enhancer factor-2C (MEF2C) and specificity protein-3 (SP3) all regulate chondrocyte maturation and affect bone development (Arnold et al., 2007; Komori, 2005; Magee et al., 2005; Saito et al., 2010). Examining the status of the above factors but also of other genes that are differentially expressed in every chondrocyte and osteoblast maturation stage (such *Col2a1*, *Col10a1*, *Bsp*, *Ihh*, *Fgfr3* and others-explained in detail in Chapter 4) will definitely provide insight on how OMD and PRELP deficiencies can affect bone development. Finally, examination of skeletal development in double-KO embryos, which was not performed in this project due to time restraints and the late generation of the double knock-out mice, is also necessary and will certainly contribute in understanding how these two genes function.

Summary

To conclude, OMD and PRELP deficiency resulted in epithelial bursts/early papilloma formations in the mouse bladder urothelium, fibrin clot formation in the lumen of PRELP and double KO bladders, and reduced tight junction formation in the umbrella cell layer of the knock-out bladders. All these demonstrate how OMD and PRELP, through regulation of TJ formation, can affect bladder homeostasis and cancer initiation. In addition, OMD and PRELP depletion appeared to slightly affect eye and bone functions, while no definite conclusions could be made about their roles in skeletal development.

Chapter 7

General discussion

The aims of this study were 1) to determine the roles of OMD and PRELP in cellular functions involved in carcinogenesis and specifically in bladder cancer, and elucidate their mechanisms of action; 2) to establish the spatial-temporal pattern of *OMD* and *PRELP* expression in the mouse; and 3) to characterise any cancer-related phenotypes, mainly in the bladder, of the OMD and PRELP knock-out mice. Since these knock-out mice are novel, preliminary assessment of other, non-cancer phenotypes was also conducted.

OMD and PRELP belong to the SLRP family of proteins, which serve as as structural components modulating synthesis, assembly and degradation of collagen fibrils (Chen and Birk, 2013). Apart from their regulatory roles in extra-cellular matrix assembly, SLRPs can act as modulators of many signalling pathways, thereby affecting various biological processes from development to tissue homeostasis (Merline et al., 2009). Mutations or aberrant expression of SLRPs can cause a variety of diseases ranging from skin fragility to osteoarthritis, corneal opacity and cancer (an overview of human disorders caused by SLRP defects is presented in our review, by Dellett et al., 2012), highlighting their importance in biological systems.

Our main interest is the cancer-related functions of SLRPs, and specifically how OMD and PRELP are involved in bladder cancer. There is an emerging body of evidence demonstrating the roles of multiple other SLRPs in carcinogenesis, including mainly decorin, biglycan and lumican. Altered expression patterns of these proteins have been found in resected tumours compared to normal tissue, decorin and lumican have been used as predictive biomarkers in breast cancer, decorin knock-out mice exhibit enhanced susceptibility to cancer, while there many other lines of functional evidence from *in vitro* and *in vivo* studies (Iozzo and Sanderson, 2011; Iozzo and Schaefer, 2010; Schaefer and Iozzo, 2012; Theocharis et al., 2010). Regarding OMD and PRELP, there have been some studies mostly demonstrating their roles in cartilage, connecting tissues, and differentiating osteoblasts (Heinegard et al., 1986; Rehn et al., 2006; Stanford et al., 1995), while there has been almost no evidence so far of their involvement in cancer. PRELP was mentioned only once as one of a four-gene signature that could be used to discriminate different types of brain cancer (Castells et al, 2009).

7.1 OMD and PRELP affect cancer-related properties of the EJ28 bladder cancer cell line

The first evidence associating OMD and PRELP with cancer was obtained by previous lab members in collaboration with Dr. Ryuji Hamamoto, who performed a gene expression analysis in 31 normal and 126 transformed kidney samples, and 16 normal and 79 bladder cancer samples. Interestingly, he found that expression of *OMD* and *PRELP* was markedly reduced in urothelial cell carcinoma and renal cell carcinoma, compared to normal bladder and kidney tissue respectively (Fig. 1.5 and Appendix A). Furthermore, this reduction in expression was an early event in carcinogenesis, and it was possible to differentiate between normal and cancer tissue with high sensitivity and specificity (Appendix A). Thus, we obtained very strong indications that OMD and PRELP are involved in cancer, and that they may represent potential tumour-suppressor genes, functioning in a similar way to other SLRPs that were discussed previously. A previous lab member, Dr. Julie Watson, conducted the initial analysis to prove the above hypothesis, and indeed found that they regulate numerous cellular processes important in carcinogenesis, such as cell cycle progression and proliferation, migration, apoptosis and drug-mediated apoptosis, and cellular morphology.

I continued this project and together with Dr. Toshiya Tamura we managed to further support the hypothesis that *OMD* and *PRELP* can act as tumour-suppressor genes. Through a series of *in vitro* experiments we demonstrated that over-expression of OMD and PRELP in the EJ28 bladder cancer cell line lead to inhibition of anchorage independent growth and cell invasion, and also altered the morphology of cells in an ECM-mimicking microenvironment (Chapter 3). All these processes constitute "hallmark" characteristics of cancer cells (Hanahan and Weinberg, 2011), and exhibit that OMD and PRELP can modulate cancer-related functions. Most importantly, overexpression of OMD and PRELP resulted in inhibition of tumour growth *in vivo* using mouse xenograft models, strongly demonstrating their anti-tumour properties. Similar *in vivo* findings with other SLRPs are not that many and mainly involve decorin, where it was shown that overexpression or injection of recombinant decorin protein into mouse xenograft models slows the growth of lung, squamous, mammary and colon carcinoma cells

(Buraschi et al., 2010; Goldoni et al., 2008; Reed et al., 2002; Reed et al., 2005; Tralhao et al., 2003).

Apart from OMD and PRELP, few other SLRPs have been implicated in the development of urological cancers. Overexpression of biglycan resulted in inhibition of bladder tumour growth both *in vitro* and *in vivo*, whilst high biglycan expression in human tumour biopsies was associated with favourable prognosis (Niedworok et al., 2013); also decorin was shown to negatively regulate IGF-IR signalling in urothelial carcinoma-derived cells, inhibiting their migration and invasion (Iozzo et al., 2011). It is also interesting that the pattern we observed is one of down- rather than up-regulation, as of the seven SLRPs that have thus far been described as differentially expressed in cancer, only two (decorin and opticin) have been downregulated in certain types of cancer.

In addition, together with Dr. Tamura we discovered that OMD and PRELP regulate tight junction formation in the EJ28 cells. Dr. Hamamoto had previously found that altered expression of *OMD* and *PRELP* could affect tight junction and adheren's junction pathways, but no studies were performed towards this direction so far. This finding is very compelling as tight junctions have not been mentioned in any other SLRP action mechanisms. Modulation of the EFG and TGF-β pathways by OMD and PRELP were also confirmed, in agreement with other findings where SLRPs can affect the above signaling pathways (Morris et al., 2007; Nikitovic et al., 2011). Therefore, we have now completed a mainly *in-vitro* analysis showing for the first time that OMD and PRELP can affect cell cancer-related properties and we have identified their possible mechanisms of action.

Limitations of our analysis and potential future extensions

For this *in vitro* analysis Dr. Watson's stably-transfected EJ28 cells were used and the overexpression of OMD and PRELP was confirmed at the RNA level. However, expression at the RNA level may not always correlate with expression at the protein level, because there are numerous mechanisms of post-transcriptional and post-translational regulation that can alter the steady state level of protein. Ideally, we would like to assess the expression of OMD and PRELP at the protein level by immunohistochemistry or western blot. Unfortunately, although we tried various

commercially available antibodies for OMD/PRELP, we could not obtain consistent and specific detection. Using tagged versions of the proteins was an alternative method, which we tried to employ in some of our experimental approaches. Occasionally though, we observed slightly different responses from tagged and non-tagged cells (for example in the anchorage independent growth experiment, section 3.2.1), which might imply that the tag could affect the functionality of the protein.

Additionally, as was explained in chapter 3, Dr. Watson had initially isolated and tested two different clones of all the transfected cell lines, in order to confirm that the obtained results were due to OMD/PRELP overexpression and not because of any functional cell changes arising from the insertion site of the plasmids. We also tried to use both clones of each transfectant in our *in vitro* experiments, but unfortunately due to time and material limitations, this was not applied in all the assays tested. However, when both clones were used they always gave comparable results, indicating the validity of our results. Another weak point of this analysis was the lack of vector-only transfected cells in some of the performed assays (i.e. Fig. 3.4; 3.5; 3.6 & 3.11), where EJ28 wild type cells were used instead. However, during our whole *in vitro* experimentation vector only-transfected cells (expressing only GFP without OMD or PRELP cDNA) always behaved similarly to the wild type cells and therefore we can make valid comparisons of our results. This certainly does not ablate the need to have both wild type and mock-transfected cells in the system we studied, and both cell types should be certainly included in future experiments. Furthermore, some of the *in vitro* experiments we conducted together with Dr. Tamura were only performed twice or included only the OMD and not the other transfected cell lines (mtOMD, PRELP and mtPRELP), usually due to time and technical restraints, and therefore further repetition of these experiments using all our cell lines would be desirable.

Another possible route would be to apply recombinant or core OMD and PRELP proteins directly in the cell media and assess their effects. We have shown that secretion of OMD and PRELP in a co-culture assay caused cell death of EJ28 cells (section 3.2.4), which implies that they can be distant-mediators of their effects. In a similar context, systemic injection of decorin protein core into A431 squamous carcinoma tumours induced apoptosis of the tumour cells by antagonizing EFGR

activity (Seidler et al., 2006). This was one of the first studies demonstrating that decorin can be administered as a therapeutic agent against cancer. The same concept could therefore be applied to OMD and PRELP. Also, the application of molecules such as OMD and PRELP as anticancer therapeutics is feasible in early-stage bladder cancer patients, as chemotherapy during that stage involves perfusing the bladder with drugs on a one-off basis, a situation in which OMD or PRELP could easily be introduced. In addition, since OMD and PRELP are thought to mediate their effects from the surrounding environment/ECM, internalization into the cell would not necessarily be required.

Additionally, overexpression of OMD and PRELP in other cell lines and assessment of their effects in different cancer types is also very compelling. In Dr. Hamamoto's analysis, these two SLRPs were reduced in renal cell carcinoma, so a similar approach to our experimental setup using cell lines derived from renal cancer would be useful to see if OMD and PRELP can mediate their anti-cancer effects in these cells. Additionally since other SLRPs are involved in a variety of cancers likes breast, ovarian and lung, it would be interesting to examine if OMD and PRELP can negatively affect these cell types as well.

Finally, one important issue that is not addressed at all during this project is the mechanism by which OMD and PRELP expression is reduced in cancer. One possible mechanism could be deletion, since *OMD*'s locus is frequently deleted in bladder cancer. Loss of heterozygosity on chromosome 9 is the most frequent genetic alteration identified in bladder tumours, with around 60-70% of the tumours showing LOH of at least one locus on either arm of the chromosome (Keen and Knowles, 1994; Simoneau et al., 1996; Stadler et al., 1994). Another common mechanism of gene silencing in cancer is methylation (Baylin and Ohm, 2006). Methylation has previously been shown to play a role in SLRP expression, where hypomethylation of the decorin promoter in colorectal cancer led to its increased expression (Adany et al, 1991). We suspect that they converse might be true for *OMD* and *PRELP* in bladder and kidney cancer, where their promoters could lead to downregulation of expression due to hypermethylation. Analysis of the *OMD* and *PRELP* loci on a genetic level may be necessary to determine the mechanisms of downregulation.

7.2 Development of OMD and PRELP knock-out mouse models – analysis of expression patterns

Having collected all these exciting data we wanted to further advance the current project towards a more *in vivo* direction. For this purpose, we aimed to perform functional analysis of OMD and PRELP anti-cancer activities in mouse models. Based on Dr. Hamamoto's microarray study, which showed that OMD and PRELP were differentially expressed in several different types of cancer (Appendix A), it was suspected that OMD and PRELP are involved in many types of epithelial cancer. For this reason, it was decided to construct a whole animal knock-out, rather than just a urothelium-specific one. Our novel knock-out mice were produced in collaboration with Takeda and the strategy utilised involved the insertion of a Lac-Z cassette in the transcription domains of the *OMD* and *PRELP* genes. This would also allow us to follow and identify the expression of the genes by simple X-gal staining.

Since this was the first time OMD and PRELP knock-out mice were generated and the effects of the gene knock-down were unknown, we established our mouse colony through heterozygote pairings. It soon became obvious that both heterozygote and homozygote knock-out animals were fertile and grew normally into adulthood. Although there were some studies in the literature describing expression of OMD and PRELP mainly in osteoblasts and cartilage respectively (Heinegard et al., 1986; Rehn et al., 2006; Stanford et al., 1995), these were focused on specific adult organs or in other organisms rather than mouse. Therefore, before assessing the effects of OMD and PRELP depletion, we decided to examine in detail the expression patterns of the two genes during embryonic mouse development and in certain adult organs.

We demonstrated that OMD and PRELP are mostly expressed in the developing skeleton during embryonic growth. PRELP is additionally expressed in the early developing brain, while during adult life both genes appear to be expressed in various organs (Chapters 4 & 5). It is noticeable that expression was not seen in any internal organs during gestation, but was present in later life in the bladder, brain and eye, demonstrating that SLRP production, turnover and ultimate localisation are dynamic processes.

Furthermore, we identified for the first time the specific cell types that express OMD and PRELP in the adult bladder, eye and brain. Many SLRPs have been previously described to be expressed in the eye and some in the brain, but none in the mouse bladder (Conrad & Conrad, 2003; Kappler et al., 1998; Ali et al, 2011). Thus, we have greatly improved the current knowledge of OMD and PRELP expression and localisation in the mouse model organism, demonstrating that SLRPs are indeed matricellular molecules which have the potential to affect various biological processes. A detailed spatio-temporal analysis of expression constitutes an initial and important step to understand how molecules work and can help to identify novel functional roles of the proteins we are investigating.

Technical considerations and further explorations

Defining the expression patterns of OMD and PRELP through X-gal staining was quite efficient and specific for heterozygote embryos and most of the adult organs examined. However, in several cases, such as kidney and spleen (not shown in the current thesis), specific OMD and PRELP expression could not be defined due to endogenous β-galactosidase activity in the wild type samples. Mammalian beta galactosidase (β-D-galactosidase) is localised in the lysosomes of mammalian cells. Consistent with is localization in this acidic organelle, this lysosomal β-galactosidase displays maximum activity between pH 4.0 and 4.5 but markedly lower activity at pH 6.0 (Zhang et al., 1994). In addition, another type of the β-gal enzyme named SA-β-gal (senescence associated β-gal) is a β-galactosidase activity detectable at pH 6.0 in cultured cells undergoing replicative or induced senescence, and is considered as marker for senescent cells (Dimri et al., 1995). Our detection method for the bacterial β-galactosidase of the LacZ-inserted cassette involved X-gal reaction in pH 7.0, so theoretically none of the SA-β-gal or β-D-gal should be detected. We cannot know if the background signal seen in kidney and spleen represents lysosomal or senescent β-gal, but performing the reaction at higher pH of 8.0-9.0 might help to increase the signal specificity, as also shown by Weiss et al. (Weiss et al., 1999).

Additionally to our β-gal mediated detection of OMD and PRELP expression, *in situ* hybridization is an alternative method of detection which should be performed. *In situ* hybridization detects expression at the RNA level, and could therefore present a slightly different pattern that the one we observed. Nevertheless,

it is a necessary approach to further confirm our current findings, especially since there are no efficient antibodies for immunohistochemistry so far. Previous lab member Dr. Margaret Dellett managed to successfully detect *OMD* and *PRELP* expression by *in situ* hybridization in the bladder urothelium, in agreement with our results (Appendix A). During this project *in situ* hybridization for *OMD* and *PRELP* was carried out in spleen and kidney sections of wild type mice but unfortunately we could not obtain any conclusive results.

Another point that perhaps should be considered in future work is the cellular localisation of the β-gal enzyme. The Lac-Z cassette is transcribed under the OMD and PRELP promoters and therefore β-gal is present in the cell types where these promoters are active. However, SLRPs are proteoglycans and as such undergo high levels of post-translational modifications. After synthesis, PGs are transported from the Golgi (where glycosylation takes place) to their specific destinations, which can be the ECM, the cell surface or intracellular organelles. Many of the responsible mechanisms for this kind of sorting and delivery require determinants that are present in the GAG chains and/or in the PG protein cores (Prydz and Dalen, 2000). Thus, localisation of the β-gal might be slightly different that the actual OMD or PRELP protein localization. Nonetheless, even if such small differences exist, our system provided a very efficient method of detection, where identification of the specific cell types where the two genes are expressed could be performed.

Finally, due to time restraints, specific analysis of the Lac-Z-expressing cell types was not performed in the embryonic stages. As discussed also in Chapters 4 & 5, usage of specific markers to identify the particular chondrocyte and osteoblast maturation stages where OMD and PRELP are expressed is desirable, and will definitely help to understand how these molecules operate during skeletal development.

7.3 Effects of OMD and PRELP depletion in knock-out mice

Once the expression analysis was completed we sought to find any cancer-related phenotypes emerging from OMD and PRELP depletion and primary attention was given to the bladder. Interestingly, knock-out mice presented with the initial symptoms of bladder papillary cancer initiation, where spontaneous formations that

we called "epithelial bursts" could be observed in the umbrella cell layer. These bursts had the appearance of disorganized masses of umbrella cells (Chapter 6). This is the second time that SLPRs are involved in spontaneous tumour growth. Similar findings were shown before in a decorin knock-out mouse model, where 30% of decorin-deficient mice spontaneously developed intestinal tumours (Bi et al, 2008). Tumourigenesis in these mice was associated with disruption of intestinal maturation and was also characterised by decreased cell differentiation and increased proliferation. In the same context, we did not observe any decrease in the outer umbrella cells maturation but we did notice a small increase of proliferating cells in the urothelium. Moreover, in decorin knock-out tumours E-cadherin was downregulated while β-catenin was upregulated, indicating an EMT-like behavior. In turn, we did not observe any E-cadherin changes but we found possible decreased tight junction formation, which potentially could be associated with an EMT-like condition.

Other SLRP deficient models, including biglycan, fibromodulin, keratocan, epiphycan, osteoglycin and tsukushi knock-out mice have not been described as having specific susceptibilities to cancer, although this may be because the scientists who generated them were more interested in other aspects of their phenotype.

Fibrin clots were also found in the PRELP and double-KO mice, which might be potentially linked with the papillary formations or with damaged blood-urine barrier due to reduced tight junction formation in the umbrella cells. We have shown that OMD and PRELP are selectively expressed in the ciliary body of the eye and in ependymal cells of the brain, epithelia that have strong tight junctions and help form the blood–aqueous barrier and blood-brain barrier respectively. Therefore, our overall findings so far indicate that OMD and PRELP have potentially fundamental roles in tight junction regulation.

Regarding other possible phenotypes, preliminary experiments were performed including eye histology, gait and bone content assessment, and also examination of embryonic skeletal development, demonstrating potential functional roles of OMD and PRELP in those systems. Due to time limitations more extensive analyses could not be conducted in the above structures. However, we have shown strong expression of OMD and PRELP in these systems and taking into account our preliminary

findings as well, we are confident that potential abnormal phenotypes might arise from OMD/PRELP/double-deficiencies. A more detailed examination of the above organs, including brain as well, is already ongoing.

Technical considerations and future perspectives

Our analysis so far has been successful in identifying *OMD* and *PRELP* as potential tumour-suppressor genes, as their absence leads to spontaneous urothelial papillary formations. It has to be noted that these findings were obtained from OMD/PRELP knock-out mice at 3 months of age, which can be considered a very young age for the occurrence of such malignancies. P53 null mice have an average time of tumour development at 4.5 months of age, while half of the heterozygous ($p53^{+/-}$) mice develop tumours by 18 months (Donehower, 1996). Also, the decorin knock-out mice were found to have intestinal tumours at 9 months of age (Bi et al, 2008). Therefore it is essential to study OMD and PRELP knock-out mice at later ages, maybe in specified time points, for example at 6, 9, 12 and 15 months. Assessment of spontaneous tumorigenesis over a certain time-course will help us observe if the epithelial bursts remain as low-grade non-invasive papilloma formations or whether they can develop into a more invasive tumour type. Some of our mice have already been set under this kind of time-course setup and will be examined in the forthcoming months.

Our understanding so far is that although OMD and PRELP knock-out mice initiated bladder papillary-like formations these are unlikely to develop to late stage bladder cancer. This is because the majority of urothelial cell carcinomas, which have mutations in the *FGFR3*, *HRAS*, *PIK3CA* genes or deletions of candidate tumor suppressor genes mapping to chromosome 9q (where *OMD* is located as well), develop only superficial papillary tumours with good prognosis. Subsequent mutations of other cancer genes such as *TP53* and *RB1* are required for progression into malignant cancer (Castillo-Martin et al., 2010).

Furthermore, it was previously found that decorin/p53 double knock-out mice develop spontaneous thymic lymphoma, which lead to earlier mortality compared to single p53 null mice (Iozzo et al., 1999). Accordingly, it would be very interesting to cross our knock-out mice with p53 null mice and study if susceptibility to tumour

initiation and progression is affected. To this end, we have already purchased p53-mutant mice that carry a R270H missense mutation in exon 8 of the *Trp53* mouse gene. Heterozygous mice develop a broad spectrum of tumours with a mean survival time of 16 months, while homozygotes have a mean survival time of 4.5 months. We are now in the process of mouse cross-breeding to generate OMD/p53, PRELP/p53, but also OMD/PRELP/p53 triple knock-out mice in order to assess if susceptibility to tumour initiation and progression is further affected from OMD/PRELP deficiency.

Another interesting objective would be to examine if OMD and PRELP knock-out mice have increased susceptibility to chemically-induced cancer formation. The use or inorganic arsenic is a possible candidate, as oral administration of this substance to rats and mice has already been shown to cause urothelial hyperplasia (Arnold et al., 2013). Also, another point to be considered for all the above future experiments is the sample size. In the present analysis our sample size was relatively small; comprising only 3 knock-out samples of each genotype and 6 wild type samples. It would be preferable to increase this number to at least 10 mice/genotype, considering that the study with the decorin knock-out mice examined 12 homozygous mice (Bi et al, 2008), while the earlier study with the decorin/p53 null mice examined 58 double and 68 single knock-out mice (Iozzo et al., 1999), numbers substantially larger.

Regarding the mechanisms of action, we have established so far some of the possible pathways affected by OMD and PRELP altered expression. Combining the microarray and functional data gathered from previous lab members together with our *in vitro* and *in vivo* analysis we can conclude that: OMD and PRELP could potentially regulate tight junction formation; can affect Akt and ERK1/2 phosphorylation; and can affect the EGF/TGF-β/Wnt pathways, but not the IGF pathway. Certainly the data we have gathered so far are not completely conclusive and include various limitations that should be addressed. For example, differences seen in tight junction formation between wild type and knock-out mice are not very clear, judging only from the ZO-1 staining of the different samples (Fig. 6.10), and further staining with other TJ markers is also necessary. In addition, when performing ultrastructural analysis of the junctions between the umbrella cells only one sample of each WT and OMD/PRELP/double KO animals was used, which

unfortunately cannot lead to conclusive results. Electron microscopy analysis combined with immuno-gold labeling of TJ and also AJ components would certainly give us more clear results on how this complexes are affected by OMD and PRELP depletion. Moreover, performing freeze-fructure EM would allow us to examine in detail the tight junction structures and functionality, increasing importantly the validity of our data.

Moreover, now that our mouse colony has been established and we have identified some of the possible abnormal phenotypes, a more detailed functional analysis can be conducted. To this end, we have already collected RNA from several tissues, including the bladder urothelium, the eye ciliary body and the brain capillaries from OMD/PRELP knock-out and wild type mice, and we are planning to conduct microarray analysis in order to identify affected target genes. Additionally, in all the above tissues (where tight junctions have important functions and OMD/PRELP as also expressed-the brain choroid plexus can also be added here), a more detailed examination of tight junction components and TJ-related signaling pathways is necessary in order to unravel how OMD and PRELP can specifically regulate TJ formation.

Apart from the bladder, examination of other organs, such as brain and kidneys, for spontaneous tumour formation is a desirable objective. Also, it will be very intriguing to examine other, non-cancer related abnormalities, arising from OMD and PRELP depletion. During this project we performed some preliminary experiments on eye and bone functions, which showed that OMD/PRELP have potential roles in these systems as well. Given the fact that our OMD and PRELP knock-out mice are novel model systems of these genes, it is compelling to perform a full phenotypic analysis. This entails a series of assessments including embryologic evaluation; specialised pathologic evaluation; specialised biochemical and genetic analyses; physiologic and behavioural assessments; and other possible pathologic effects like environmental and housing conditions (Wood, 2000).

Finally, one missing point of the current study is the examination of expression levels of other SLRPs upon deletion of OMD or PRELP. As was already discussed in Chapter 6, knock-out models of combined SLRPs often exhibited more severe phenotypes that single knock-outs, demonstrating that some SLRPs may be

functionally redundant. Also, it has been shown that some SLRPs compensate for the loss of others; for example in the epiphycan/biglycan double-deficient mice the mRNA levels of asporin, fibromodulin and lumican were increased compared to wild type mice (Nuka et al., 2010). Hence, it will be worthwhile to analyse expression levels of other SLRPs in our knock-out mice, especially since these alterations might also be a potential reason for the lack of aberrant phenotypes.

7.4 Summary

We have identified OMD and PRELP as potent regulators of cancer-related cell properties, whereby OMD and PRELP overexpression inhibits anchorage independent growth and migration of bladder cancer cells *in vitro*, while it also inhibits tumour growth *in vivo* in EJ28 xenograft mouse models. Similar results were previously obtained by overexpressing other SLRPs, such as decorin, biglycan and lumican in other cell systems, demonstrating the potential that these extracellular molecules have in affecting or regulating the cancer microenvironment and tumour growth. Although we have not elucidated the exact mechanisms of action, we have concluded that these two molecules mediate their effects by cross-regulating different signalling molecules, including Akt and ERK1/2 but also the EGF, TGF-β and Wnt pathways. Since these signaling pathways are also affected by other SLRPs, they are likely to be key molecules for the actions of this protein family and a more detailed examination of OMD/PRELP signaling cascade will certainly help us unravel exactly how they work. Furthermore, we have made a correlation of OMD and PRELP overexpression with tight junction formation in the EJ28 cells, where we noticed that TJ components such as occludin, ZO-1 and cingulin are found increased in the cell membrane compartments when these two SLRPs are overexpressed. Although these data are preliminary and do not yet demonstrate a complete link, we believe that there is a potential, probably indirect, connection between the two SLRPs and the junctional complexes of epithelial cells. As extra-cellular proteins are recognised as important regulators of cell-matrix crosstalk and can influence a variety of biological processes such as cell proliferation, differentiation, adhesion, etc., it would not be surprising if SLRPs could somehow modulate cell junctions amongst many other components.

In addition, we generated novel OMD and PRELP knock-out mouse models, which, amidst other findings, presented with spontaneous urothelial papillary-like formations, suggesting that lack of OMD and/or PRELP might be permissive for cancer initiation. Similar findings were also seen in decorin knock-out mice, indicating again the possible roles of these ECM molecules in cancer initiation and progression. OMD and PRELP depletion also had small-scale effects in the eye ciliary body, the gait, and the skeletal development of the mice, further confirming their multiple roles in biological systems and how they can indeed act also as matricellular proteins.

Overall, with our current findings we hope to improve the understanding of SLRP biology in carcinogenesis, and we would like to propose OMD and PRELP, or OMD/PRELP-regulated pathways, as potential targets for the development of cancer therapies. Lastly, we have performed a detailed analysis of the spatial and temporal expression patters of OMD and PRELP in the mouse, significantly contributing to the current knowledge of SLRP biology. Our results further demonstrate that SLRPs are dynamically-synthesized proteins with multiple functions, which have the potential to affect many biological processes.

Appendix A: OMD and PRELP in cancer

All the data presented in this section are acquired by former lab members Dr. Hamamoto, Dr. Julie, Dr. Tamura and Dr. Dellett

Former lab members Dr. R. Hamamoto and Dr. T. Tamura, previously discovered that expression of *OMD* and *PRELP* is reduced in a number of cancers through microarray data comparing expression in tumours and normal tissue for many different types of cancer. *OMD* expression was reduced in bladder cancer and non-small cell lung cancer to less than a tenth of its normal level, and in small cell lung cancer to less than half of its normal level (Table A.1). *PRELP* expression was reduced in bladder cancer and small cell lung cancer to less than a tenth of its normal level, and in breast cancer, cervical cancer, cholangiocellular carcinoma, lymphoma, oesophageal cancer, non-small cell lung cancer, prostate cancer and renal cell carcinoma to a lesser extent (Table A.2).

Table A.1: Cancers in which OMD is differentially expressed

Type of cancer	Number of cases	Ratio (tumour/normal)			
		Below 1/2	Below 1/3	Below 1/5	Below 1/10
Bladder cancer	31	31 (100%)	31 (100%)	31 (100%)	31 (100%)
Non small-cell lung cancer	2	2 (100%)	2 (100%)	2 (100%)	2 (100%)
Small cell lung cancer	6	6 (100%)	4 (66.7%)	3 (50.0%)	1 (16.7%)

Table A.2: Cancers in which PRELP is differentially expressed

Type of cancer	Number of cases	Ratio (tumour/normal)			
		Below 1/2	Below 1/3	Below 1/5	Below 1/10
Bladder cancer	34	34 (100%)	34 (100%)	34 (100%)	34 (100%)
Breast cancer	73	70 (96%)	69 (94.5%)	67 (91.8%)	61 (83.6%)
Cervical cancer	19	15 (78.9%)	13 (68.4%)	7 (36.8%)	2 (10.5%)
Cholangiocellular carcinoma	25	23 (92.0%)	20 (80.0%)	15 (60.0%)	13 (52.0%)
Oesophageal cancer	52	39 (75.0%)	37 (71.2%)	28 (53.8%)	17 (32.7%)
Gastric cancer	16	11 (68.8%)	9 (56.3%)	7 (43.8%)	6 (37.5%)
Non-small cell lung cancer	37	36 (97.3%)	36 (97.3%)	33 (89.2%)	26 (70.2%)
Lymphoma	21	18 (85.7%)	15 (71.4%)	12 (66.7%)	9 (42.9%)
Prostate cancer	40	32 (80.0%)	28 (70.0%)	23 (57.5%	12 (20%)
Renal cell carcinoma	23	16 (70%)	15 (65.2%)	13 (56.5%)	13 (56.5%)
Small cell lung cancer	15	15 (100%)	15 (100%)	15 (100%)	15 (100%)

Since the largest differences in expression were seen in bladder cancer, it decided to reconfirm the downregulation of *OMD* and *PRELP* in urological cancers by RT-PCR (performed by Dr. Hamamoto and Dr. Watson). To this end, 126 bladder tumours and 31 normal bladder samples were studied, and on average OMD and PRELP expression were reduced by 90%. 76 kidney tumours and 16 normal kidney tissues were also studied, and on average OMD and PRELP expression were reduced by 90% and 80%, respectively (also shown in Fig. 1.5). Furthermore, expression of both *OMD* and *PRELP* was greatly reduced even in early stage bladder tumours, but was significantly reduced even further between stages pT2 and pT3/4 (i.e. as the tumour invaded into muscle tissue and metastasized) (Fig. A.1 and Table A.3). Expression of *OMD* and *PRELP* in bladder cancer also correlated with grade and metastatic potential. In kidney cancer, expression of both *OMD* and *PRELP* was greatly reduced even in early stage tumours, but no correlations were seen between *OMD* and *PRELP* expression and stage, grade or metastatic potential (Fig. A.2 and Table A.4). In addition, *OMD* and *PRELP* expression could be used to differentiate cancerous bladder or kidney tissue from normal tissue with high sensitivity and specificity. Looking at both gene's expression, it was possible to identify normal tissue with 100% specificity and bladder tumours 84.1% specificity (Fig. A.1 and Table A.5), and normal tissue with 100% specificity and kidney tumours with 78.4% sensitivity (Fig. A.2 and Table A.6).

Table A.3: The expression of *OMD* and *PRELP* in urothelial cell carcinoma

Characteristic	OMD			PRELP		
	n	Mean	95% CI	n	Mean	95% CI
Normal	31	4.40	3.08 - 5.72	31	1.67	0.32 - 2.03
Tumour (total)	126	0.42	0.19 - 0.65	126	0.22	0.13 - 0.41
Tumour stage						
pTa, pT1	90	0.45	0.15 - 0.76	90	0.26	0.12 - 0.40
pT2	26	0.43	0.12 - 0.75	26	0.12	0.05 - 0.20
pT3/4	7	0.01	-0.01 - 0.028	7	0.02	-0.01 - 0.05
Tumour grade						
G1	12	1.13	-0.95 - 3.20	10	0.50	0.06 - 1.05
G2	63	0.28	0.09 - 0.47	63	0.21	0.05 - 0.37
G3	50	0.44	0.16 - 0.72	50	0.16	0.07 - 0.24
Metastasis						
Negative	99	0.48	0.20 - 0.77	99	0.25	0.13 - 0.38
Positive	27	0.19	0.06 - 0.33	27	0.08	0.01 - 0.14

Table A.4: The expression of *OMD* and *PRELP* in renal cell carcinoma

Characteristic	OMD			PRELP		
	n	Mean	95% CI	n	Mean	95% CI
Normal	16	1.76	1.05 - 2.47	16	0.36	0.24 - 0.47
Tumour (total)	79	0.22	0.14 - 0.30	79	0.07	0.05 - 0.09
Tumour stage						
pT1	25	0.20	0.10 - 0.30	25	0.09	0.04 - 0.14
pT2	20	0.17	0.02 - 0.32	20	0.06	0.02 - 0.10
pT3/4	19	0.15	0.04 - 0.25	19	0.06	0.01 - 0.12
Tumour grade						
G1, G2	42	0.24	0.12 - 0.36	42	0.07	0.04 - 0.10
G3, G4	27	0.18	0.09 - 0.27	27	0.08	0.03 - 0.13
Metastasis						
Negative	58	0.29	0.12 - 0.27	58	0.08	0.05 - 0.11
Positive	8	0.23	-0.03 - 0.43	8	0.02	0 - 0.05

Table A.5: The sensitivity and specificity of diagnosing urothelial cell carcinoma solely by *OMD* and *PRELP* expression

Characteristic	Normal		Tumour		Tumour (early stage: Ta & T1)		Tumour (late stage: T2, T3 & T4)	
	n	Specificity (%)	n	Sensitivity (%)	n	Sensitivity (%)	n	Sensitivity (%)
OMD (cutoff: 0.897)								
Below cutoff:	26	83.9	14	88.9	10	88.9	4	88.9
Above cutoff:	5		112		80		32	
PRELP (cutoff: 0.415)								
Below cutoff:	28	90.3	12	90.5	10	88.9	2	94.4
Above cutoff:	3		114		80		34	
Combined OMD & PRELP								
Both above cutoff:	26	83.9	6	95.2	5	94.4	1	97.2
At least 1 below cutoff:	5		120		85		35	
At least 1 above cutoff:	31	100	20	84.1	15	83.3	5	86.1
Both below cutoff:	0		106		75		75	

Table A.6: The sensitivity and specificity of diagnosing renal cell carcinoma solely by *OMD* and *PRELP* expression

Characteristic	Normal		Tumour		Tumour (early stage: Ta & T1)		Tumour (late stage: T2, T3 & T4)	
	n	Specificity (%)	n	Sensitivity (%)	n	Sensitivity (%)	n	Sensitivity (%)
OMD (cutoff: 0.489)								
Below cutoff:	14	87.5	12	84.8	10	80.0	4	87.0
Above cutoff:	2		67		80		32	
PRELP (cutoff: 0.170)								
Below cutoff:	12	75.0	10	87.3	10	80.0	2	90.7
Above cutoff:	4		69		80		34	
Combined OMD & PRELP								
Both above cutoff:	10	62.5	5	93.6	2	92.0	3	94.4
At least 1 below cutoff:	6		74		23		51	
At least 1 above cutoff:	16	100	17	78.4	8	68.0	9	83.3
Both below cutoff:	0		62		17		45	

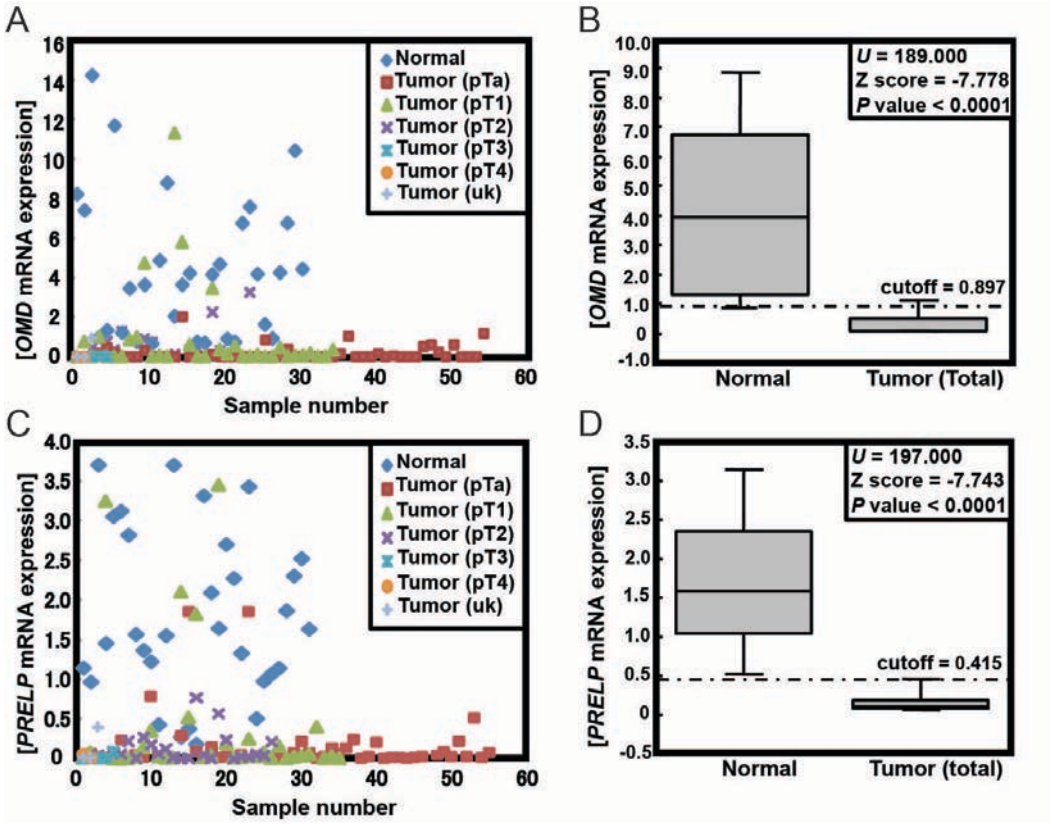

Figure A.1: Expression of *OMD* and *PRELP* in urothelial cell carcinoma. (A) Quantitative analysis of *OMD* expression in different stages of bladder cancer. (B) Box-whisker plot of (A). (C) Quantitative analysis of *PRELP* expression in different stages of bladder cancer. (D) Box-whisker plot of (C). Graphs are kindly provided by Dr. Hamamoto.

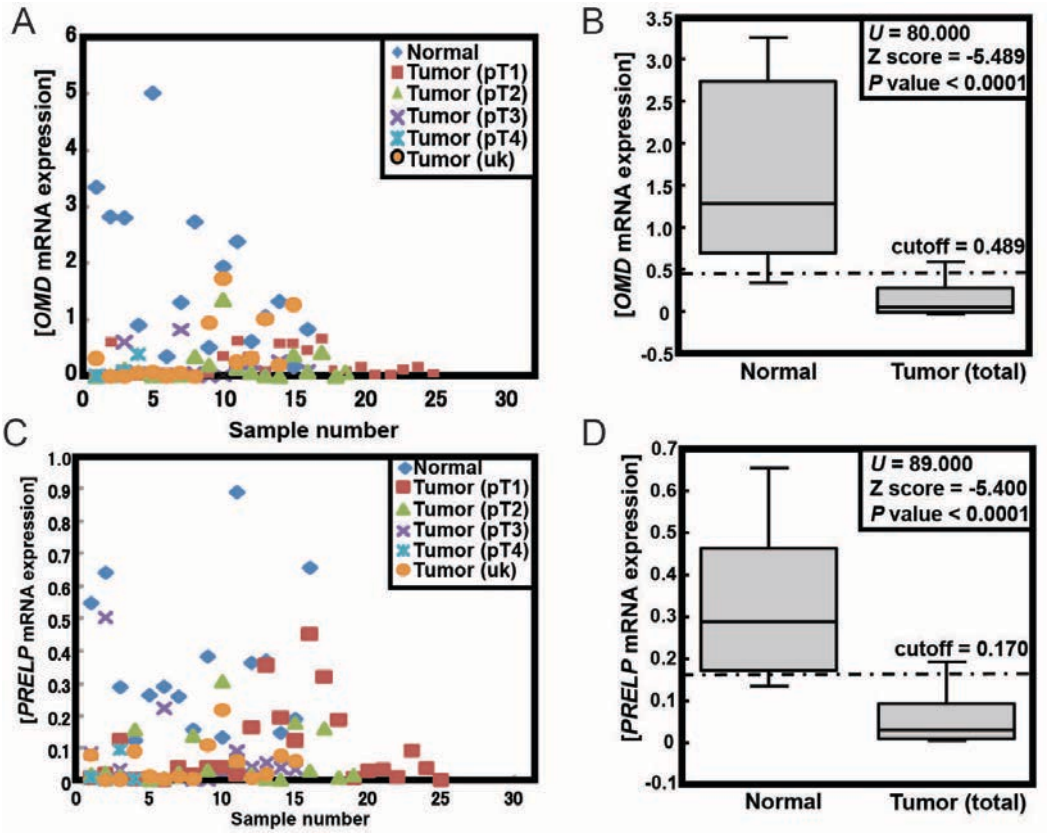

Figure A.2: Expression of *OMD* and *PRELP* in renal cell carcinoma. (A) Quantitative analysis of *OMD* expression in different stages of kidney cancer. (B) Box-whisker plot of (A). (C) Quantitative analysis of *PRELP* expression in different stages of kidney cancer. (D) Box-whisker plot of (C). Graphs are kindly provided by Dr. Hamamoto.

Finally, Dr. Hamamoto further performed KEGG pathway analysis of OMD and PRELP based on the Affymetrix's microarray data and identified the major pathways affected from altered expression of the two genes (Table A.7)

Table A.7: The KEGG pathway analysis of OMD and PRELP based on the Affymetrix's microarray data

	Entry ID	Name	*P*
OMD	**hsa04115**	**p53 signalling pathway**	**0.012294**
	hsa04530	Tight junction	0.014608
	hsa04520	Adherens junction	0.0160148
	hsa04310	Wnt signalling pathway	0.0194646
	hsa04210	Apoptosis	0.0194646
	hsa05222	Small cell lung cancer	0.0237281
PRELP	**hsa04115**	**p53 signalling pathway**	**4.32×10^{-5}**
	hsa04210	Apoptosis	0.0088029
	hsa04530	Tight junction	0.04122528

Expression of OMD and PRELP by *in situ* hybridisation in the mouse bladder (performed by Dr. Dellett)

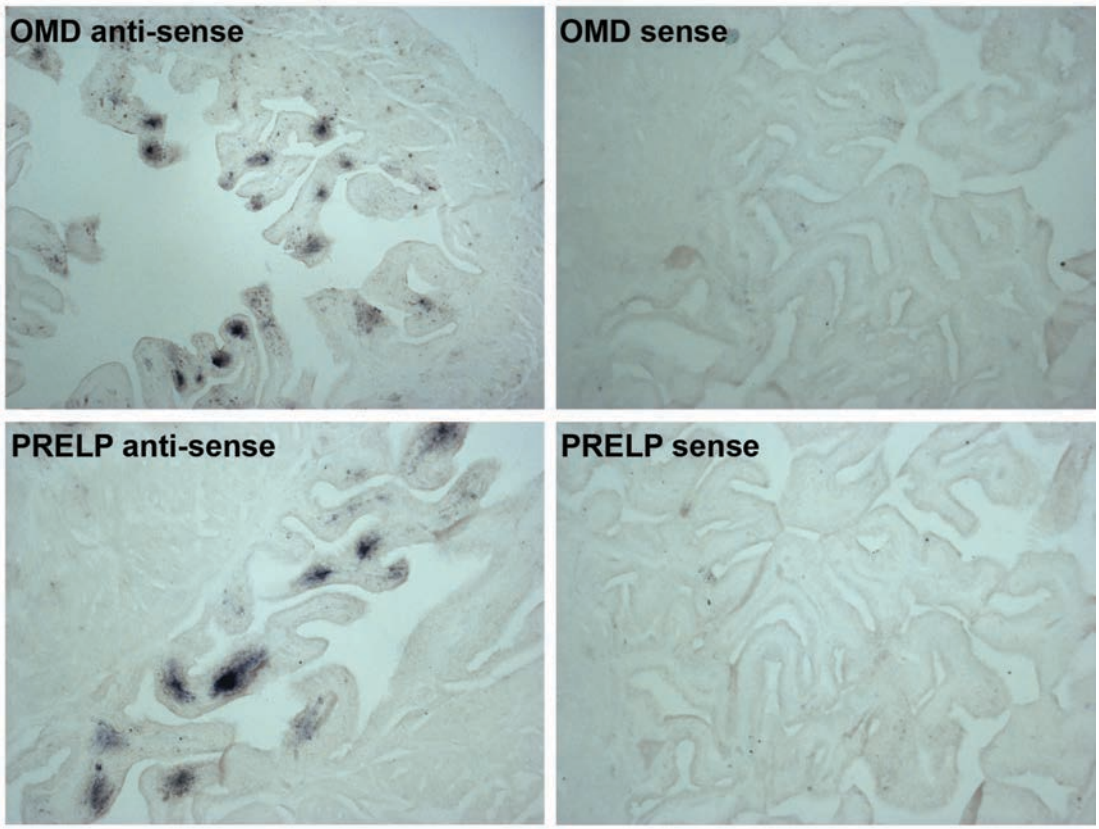

Figure A.3: *OMD* and *PRELP* expression by *in situ* hybridisation in the mouse bladder. Specific signal is seen with both the OMD and PRELP anti-sense probes in the mouse urothelium, while no background signal is seen using the sense probes. Magnification is 10x for all panels. Images are kindly provided by Dr. Dellett.

Bibliography

Acharya, P., Beckel, J., Ruiz, W.G., Wang, E., Rojas, R., Birder, L. & Apodaca, G. (2004) Distribution of the tight junction proteins ZO-1, occludin, and claudin-4, -8, and -12 in bladder epithelium. American journal of physiology. Renal physiology, 287, F305-318.

Adany, R. & Iozzo, R.V. (1991) Hypomethylation of the decorin proteoglycan gene in human colon cancer. Biochem J, 276 (Pt 2), 301-306.

Ahmad, I., Morton, J.P., Singh, L.B., Radulescu, S.M., Ridgway, R.A., Patel, S., Woodgett, J., Winton, D.J., Taketo, M.M., Wu, X.R., Leung, H.Y. & Sansom, O.J. (2011) beta-Catenin activation synergizes with PTEN loss to cause bladder cancer formation. Oncogene, 30, 178-189.

Ahrens, M.J., Li, Y., Jiang, H. & Dudley, A.T. (2009) Convergent extension movements in growth plate chondrocytes require gpi-anchored cell surface proteins. Development, 136, 3463-3474.

Ali, S.A., Hosaka, Y.Z. & Uehara, M. (2011) Expression of small leucine-rich proteoglycans in the developing retina and kainic acid-induced retinopathy in ICR mice. The Journal of veterinary medical science / the Japanese Society of Veterinary Science, 73, 439-445.

Ameye, L., Aria, D., Jepsen, K., Oldberg, A., Xu, T. & Young, M.F. (2002) Abnormal collagen fibrils in tendons of biglycan/fibromodulin-deficient mice lead to gait impairment, ectopic ossification, and osteoarthritis. FASEB journal : official publication of the Federation of American Societies for Experimental Biology, 16, 673-680.

Anand, P., Kunnumakkara, A.B., Sundaram, C., Harikumar, K.B., Tharakan, S.T., Lai, O.S., Sung, B. & Aggarwal, B.B. (2008) Cancer is a preventable disease that requires major lifestyle changes. Pharm Res, 25, 2097-2116.

Arnaldi, L.A., Borra, R.C., Maciel, R.M. & Cerutti, J.M. (2005) Gene expression profiles reveal that DCN, DIO1, and DIO2 are underexpressed in benign and malignant thyroid tumors. Thyroid : official journal of the American Thyroid Association, 15, 210-221.

Arnold, L.L., Suzuki, S., Yokohira, M., Kakiuchi-Kiyota, S., Pennington, K.L. & Cohen, S.M. (2013) Time Course of Urothelial Changes in Rats and Mice Orally Administered Arsenite. Toxicologic pathology, 42, 855-862.

Arnold, M.A., Kim, Y., Czubryt, M.P., Phan, D., McAnally, J., Qi, X., Shelton, J.M., Richardson, J.A., Bassel-Duby, R. & Olson, E.N. (2007) MEF2C transcription factor controls chondrocyte hypertrophy and bone development. Dev Cell, 12, 377-389.

Aumailley, M. & Gayraud, B. (1998) Structure and biological activity of the extracellular matrix. Journal of molecular medicine, 76, 253-265.

Barde, I., Zanta-Boussif, M.A., Paisant, S., Leboeuf, M., Rameau, P., Delenda, C. & Danos, O. (2006) Efficient control of gene expression in the hematopoietic system using a single Tet-on inducible lentiviral vector. Molecular therapy : the journal of the American Society of Gene Therapy, 13, 382-390.

Barrios-Rodiles, M., Brown, K.R., Ozdamar, B., Bose, R., Liu, Z., Donovan, R.S., Shinjo, F., Liu, Y., Dembowy, J., Taylor, I.W., Luga, V., Przulj, N., Robinson, M., Suzuki, H.,

Hayashizaki, Y., Jurisica, I. & Wrana, J.L. (2005) High-throughput mapping of a dynamic signaling network in mammalian cells. Science, 307, 1621-1625.

Bassi, P., De Marco, V., De Lisa, A., Mancini, M., Pinto, F., Bertoloni, R. & Longo, F. (2005) Non-invasive diagnostic tests for bladder cancer: a review of the literature. Urologia internationalis, 75, 193-200.

Basson, M.A. & Wingate, R.J. (2013) Congenital hypoplasia of the cerebellum: developmental causes and behavioral consequences. Frontiers in neuroanatomy, 7, 29.

Baylin, S.B. & Ohm, J.E. (2006) Epigenetic gene silencing in cancer - a mechanism for early oncogenic pathway addiction? Nat Rev Cancer, 6, 107-116.

Bengtsson, E., Aspberg, A., Heinegard, D., Sommarin, Y. & Spillmann, D. (2000) The amino-terminal part of PRELP binds to heparin and heparan sulfate. J Biol Chem, 275, 40695-40702.

Bengtsson, E., Morgelin, M., Sasaki, T., Timpl, R., Heinegard, D. & Aspberg, A. (2002) The leucine-rich repeat protein PRELP binds perlecan and collagens and may function as a basement membrane anchor. J Biol Chem, 277, 15061-15068.

Bengtsson, E., Neame, P.J., Heinegard, D. & Sommarin, Y. (1995) The primary structure of a basic leucine-rich repeat protein, PRELP, found in connective tissues. J Biol Chem, 270, 25639-25644.

Berendsen, A.D., Fisher, L.W., Kilts, T.M., Owens, R.T., Robey, P.G., Gutkind, J.S. & Young, M.F. (2011) Modulation of canonical Wnt signaling by the extracellular matrix component biglycan. Proc Natl Acad Sci U S A, 108, 17022-17027.

Bergers, G., Brekken, R., McMahon, G., Vu, T.H., Itoh, T., Tamaki, K., Tanzawa, K., Thorpe, P., Itohara, S., Werb, Z. & Hanahan, D. (2000) Matrix metalloproteinase-9 triggers the angiogenic switch during carcinogenesis. Nature cell biology, 2, 737-744.

Bi, X., Tong, C., Dockendorff, A., Bancroft, L., Gallagher, L., Guzman, G., Iozzo, R.V., Augenlicht, L.H. & Yang, W. (2008) Genetic deficiency of decorin causes intestinal tumor formation through disruption of intestinal cell maturation. Carcinogenesis, 29, 1435-1440.

Bidanset, D.J., Guidry, C., Rosenberg, L.C., Choi, H.U., Timpl, R. & Hook, M. (1992) Binding of the proteoglycan decorin to collagen type VI. J Biol Chem, 267, 5250-5256.

Biglari, A., Bataille, D., Naumann, U., Weller, M., Zirger, J., Castro, M.G. & Lowenstein, P.R. (2004) Effects of ectopic decorin in modulating intracranial glioma progression in vivo, in a rat syngeneic model. Cancer Gene Ther, 11, 721-732.

Birder, L. & Andersson, K.E. (2013) Urothelial signaling. Physiological reviews, 93, 653-680.

Birke, M.T., Lipo, E., Adhi, M., Birke, K. & Kumar-Singh, R. (2014) AAV-mediated expression of human PRELP inhibits complement activation, choroidal neovascularization and deposition of membrane attack complex in mice. Gene therapy, 21, 507-513.

Bissell, M.J. & Hines, W.C. (2011) Why don't we get more cancer? A proposed role of the microenvironment in restraining cancer progression. Nature medicine, 17, 320-329.

Blansfield, J.A., Caragacianu, D., Alexander, H.R., 3rd, Tangrea, M.A., Morita, S.Y., Lorang, D., Schafer, P., Muller, G., Stirling, D., Royal, R.E. & Libutti, S.K. (2008) Combining agents that target the tumor microenvironment improves the efficacy of anticancer therapy. Clin Cancer Res, 14, 270-280.

Blavier, L., Lazaryev, A., Dorey, F., Shackleford, G.M. & DeClerck, Y.A. (2006) Matrix metalloproteinases play an active role in Wnt1-induced mammary tumorigenesis. Cancer Res, 66, 2691-2699.

Blochberger, T.C., Cornuet, P.K. & Hassell, J.R. (1992) Isolation and partial characterization of lumican and decorin from adult chicken corneas. A keratan sulfate-containing isoform of decorin is developmentally regulated. J Biol Chem, 267, 20613-20619.

Boire, A., Covic, L., Agarwal, A., Jacques, S., Sherifi, S. & Kuliopulos, A. (2005) PAR1 is a matrix metalloprotease-1 receptor that promotes invasion and tumorigenesis of breast cancer cells. Cell, 120, 303-313.

Brandan, E., Retamal, C., Cabello-Verrugio, C. & Marzolo, M.P. (2006) The low density lipoprotein receptor-related protein functions as an endocytic receptor for decorin. J Biol Chem, 281, 31562-31571.

Brezillon, S., Radwanska, A., Zeltz, C., Malkowski, A., Ploton, D., Bobichon, H., Perreau, C., Malicka-Blaszkiewicz, M., Maquart, F.X. & Wegrowski, Y. (2009) Lumican core protein inhibits melanoma cell migration via alterations of focal adhesion complexes. Cancer Lett, 283, 92-100.

Brezillon, S., Venteo, L., Ramont, L., D'Onofrio, M.F., Perreau, C., Pluot, M., Maquart, F.X. & Wegrowski, Y. (2007) Expression of lumican, a small leucine-rich proteoglycan with antitumour activity, in human malignant melanoma. Clinical and experimental dermatology, 32, 405-416.

Brezillon, S., Zeltz, C., Schneider, L., Terryn, C., Vuillermoz, B., Ramont, L., Perrau, C., Pluot, M., Diebold, M.D., Radwanska, A., Malicka-Blaszkiewicz, M., Maquart, F.X. & Wegrowski, Y. (2009) Lumican inhibits B16F1 melanoma cell lung metastasis. Journal of physiology and pharmacology : an official journal of the Polish Physiological Society, 60 Suppl 4, 15-22.

Buchaille, R., Couble, M.L., Magloire, H. & Bleicher, F. (2000) Expression of the small leucine-rich proteoglycan osteoadherin/osteomodulin in human dental pulp and developing rat teeth. Bone, 27, 265-270.

Buraschi, S., Neill, T., Goyal, A., Poluzzi, C., Smythies, J., Owens, R.T., Schaefer, L., Torres, A. & Iozzo, R.V. (2013) Decorin causes autophagy in endothelial cells via Peg3. Proc Natl Acad Sci U S A, 110, E2582-2591.

Buraschi, S., Pal, N., Tyler-Rubinstein, N., Owens, R.T., Neill, T. & Iozzo, R.V. (2010) Decorin antagonizes Met receptor activity and down-regulates {beta}-catenin and Myc levels. J Biol Chem, 285, 42075-42085.

Burkhart, D.L. & Sage, J. (2008) Cellular mechanisms of tumour suppression by the retinoblastoma gene. Nat Rev Cancer, 8, 671-682.

Cabello-Verrugio, C. & Brandan, E. (2007) A novel modulatory mechanism of transforming growth factor-beta signaling through decorin and LRP-1. J Biol Chem, 282, 18842-18850.

Cairns, P., Tokino, K., Eby, Y. & Sidransky, D. (1994) Homozygous deletions of 9p21 in primary human bladder tumors detected by comparative multiplex polymerase chain reaction. Cancer Res, 54, 1422-1424.

Cam, Y., Lesot, H., Colosetti, P. & Ruch, J.V. (1997) Distribution of transforming growth factor beta1-binding proteins and low-affinity receptors during odontoblast differentiation in the mouse. Archives of oral biology, 42, 385-391.

Campo, S., Campo, G.M., Avenoso, A., D'Ascola, A., Musolino, C., Calabro, L., Bellomo, G., Quartarone, E. & Calatroni, A. (2006) Lymphocytes from patients with early stage of B-cell chronic lymphocytic leukaemia and long survival synthesize decorin. Biochimie, 88, 1933-1939.

Castells, X., Garcia-Gomez, J.M., Navarro, A., Acebes, J.J., Godino, O., Boluda, S., Barcelo, A., Robles, M., Arino, J. & Arus, C. (2009) Automated brain tumor biopsy prediction using single-labeling cDNA microarrays-based gene expression profiling. Diagnostic molecular pathology : the American journal of surgical pathology, part B, 18, 206-218.

Castillo-Martin, M., Domingo-Domenech, J., Karni-Schmidt, O., Matos, T. & Cordon-Cardo, C. (2010) Molecular pathways of urothelial development and bladder tumorigenesis. Urol Oncol, 28, 401-408.

Chakravarti, S. (2002) Functions of lumican and fibromodulin: lessons from knockout mice. Glycoconjugate journal, 19, 287-293.

Chakravarti, S., Magnuson, T., Lass, J.H., Jepsen, K.J., LaMantia, C. & Carroll, H. (1998) Lumican regulates collagen fibril assembly: skin fragility and corneal opacity in the absence of lumican. J Cell Biol, 141, 1277-1286.

Chakravarti, S., Petroll, W.M., Hassell, J.R., Jester, J.V., Lass, J.H., Paul, J. & Birk, D.E. (2000) Corneal opacity in lumican-null mice: defects in collagen fibril structure and packing in the posterior stroma. Investigative ophthalmology & visual science, 41, 3365-3373.

Chen, Q., Johnson, D.M., Haudenschild, D.R. & Goetinck, P.F. (1995) Progression and recapitulation of the chondrocyte differentiation program: cartilage matrix protein is a marker for cartilage maturation. Developmental biology, 172, 293-306.

Chen, S. & Birk, D.E. (2013) The regulatory roles of small leucine-rich proteoglycans in extracellular matrix assembly. The FEBS journal, 280, 2120-2137.

Chen, S., Oldberg, A., Chakravarti, S. & Birk, D.E. (2010) Fibromodulin regulates collagen fibrillogenesis during peripheral corneal development. Developmental dynamics : an official publication of the American Association of Anatomists, 239, 844-854.

Chen, S., Oldberg, A., Chakravarti, S. & Birk, D.E. (2010) Fibromodulin regulates collagen fibrillogenesis during peripheral corneal development. Developmental dynamics : an official publication of the American Association of Anatomists, 239, 844-854.

Chen, W.B., Lenschow, W., Tiede, K., Fischer, J.W., Kalthoff, H. & Ungefroren, H. (2002) Smad4/DPC4-dependent regulation of biglycan gene expression by transforming growth factor-beta in pancreatic tumor cells. J Biol Chem, 277, 36118-36128.

Chen, X.D., Fisher, L.W., Robey, P.G. & Young, M.F. (2004) The small leucine-rich proteoglycan biglycan modulates BMP-4-induced osteoblast differentiation. FASEB journal

: official publication of the Federation of American Societies for Experimental Biology, 18, 948-958.

Chen, X.D., Shi, S., Xu, T., Robey, P.G. & Young, M.F. (2002) Age-related osteoporosis in biglycan-deficient mice is related to defects in bone marrow stromal cells. Journal of bone and mineral research : the official journal of the American Society for Bone and Mineral Research, 17, 331-340.

Clarijs, R., Ruiter, D.J. & De Waal, R.M. (2003) Pathophysiological implications of stroma pattern formation in uveal melanoma. Journal of cellular physiology, 194, 267-271.

Conrad, A.H. & Conrad, G.W. (2003) The keratocan gene is expressed in both ocular and non-ocular tissues during early chick development. Matrix biology : journal of the International Society for Matrix Biology, 22, 323-337.

Cordon-Cardo, C. (2008) Molecular alterations associated with bladder cancer initiation and progression. Scandinavian journal of urology and nephrology. Supplementum, 154-165.

Corpuz, L.M., Funderburgh, J.L., Funderburgh, M.L., Bottomley, G.S., Prakash, S. & Conrad, G.W. (1996) Molecular cloning and tissue distribution of keratocan. Bovine corneal keratan sulfate proteoglycan 37A. J Biol Chem, 271, 9759-9763.

Corsi, A., Xu, T., Chen, X.D., Boyde, A., Liang, J., Mankani, M., Sommer, B., Iozzo, R.V., Eichstetter, I., Robey, P.G., Bianco, P. & Young, M.F. (2002) Phenotypic effects of biglycan deficiency are linked to collagen fibril abnormalities, are synergized by decorin deficiency, and mimic Ehlers-Danlos-like changes in bone and other connective tissues. Journal of bone and mineral research : the official journal of the American Society for Bone and Mineral Research, 17, 1180-1189.

Couble, M.L., Bleicher, F., Farges, J.C., Peyrol, S., Lucchini, M., Magloire, H. & Staquet, M.J. (2004) Immunodetection of osteoadherin in murine tooth extracellular matrices. Histochemistry and cell biology, 121, 47-53.

Crnogorac-Jurcevic, T., Efthimiou, E., Capelli, P., Blaveri, E., Baron, A., Terris, B., Jones, M., Tyson, K., Bassi, C., Scarpa, A. & Lemoine, N.R. (2001) Gene expression profiles of pancreatic cancer and stromal desmoplasia. Oncogene, 20, 7437-7446.

Croce, C.M. (2008) Oncogenes and cancer. N Engl J Med, 358, 502-511.

Csordas, G., Santra, M., Reed, C.C., Eichstetter, I., McQuillan, D.J., Gross, D., Nugent, M.A., Hajnoczky, G. & Iozzo, R.V. (2000) Sustained down-regulation of the epidermal growth factor receptor by decorin. A mechanism for controlling tumor growth in vivo. J Biol Chem, 275, 32879-32887.

Cui, X., Song, B., Hou, L., Wei, Z. & Tang, J. (2008) High expression of osteoglycin decreases the metastatic capability of mouse hepatocarcinoma Hca-F cells to lymph nodes. Acta biochimica et biophysica Sinica, 40, 349-355.

Czerniak, B., Chaturvedi, V., Li, L., Hodges, S., Johnston, D., Roy, J.Y., Luthra, R., Logothetis, C., Von Eschenbach, A.C., Grossman, H.B., Benedict, W.F. & Batsakis, J.G. (1999) Superimposed histologic and genetic mapping of chromosome 9 in progression of human urinary bladder neoplasia: implications for a genetic model of multistep urothelial carcinogenesis and early detection of urinary bladder cancer. Oncogene, 18, 1185-1196.

Dammer, U., Popescu, O., Wagner, P., Anselmetti, D., Guntherodt, H.J. & Misevic, G.N. (1995) Binding strength between cell adhesion proteoglycans measured by atomic force microscopy. Science, 267, 1173-1175.

Danielson, K.G., Baribault, H., Holmes, D.F., Graham, H., Kadler, K.E. & Iozzo, R.V. (1997) Targeted disruption of decorin leads to abnormal collagen fibril morphology and skin fragility. J Cell Biol, 136, 729-743.

Dellett, M., Hu, W., Papadaki, V. & Ohnuma, S. (2012) Small leucine rich proteoglycan family regulates multiple signalling pathways in neural development and maintenance. Development, growth & differentiation, 54, 327-340.

Derynck, R., Akhurst, R.J. & Balmain, A. (2001) TGF-beta signaling in tumor suppression and cancer progression. Nature genetics, 29, 117-129.

Desnoyers, L., Arnott, D. & Pennica, D. (2001) WISP-1 binds to decorin and biglycan. J Biol Chem, 276, 47599-47607.

Devy, L., Huang, L., Naa, L., Yanamandra, N., Pieters, H., Frans, N., Chang, E., Tao, Q., Vanhove, M., Lejeune, A., van Gool, R., Sexton, D.J., Kuang, G., Rank, D., Hogan, S., Pazmany, C., Ma, Y.L., Schoonbroodt, S., Nixon, A.E., Ladner, R.C., Hoet, R., Henderikx, P., Tenhoor, C., Rabbani, S.A., Valentino, M.L., Wood, C.R. & Dransfield, D.T. (2009) Selective inhibition of matrix metalloproteinase-14 blocks tumor growth, invasion, and angiogenesis. Cancer Res, 69, 1517-1526.

Dimri, G.P., Lee, X., Basile, G., Acosta, M., Scott, G., Roskelley, C., Medrano, E.E., Linskens, M., Rubelj, I., Pereira-Smith, O. & et al. (1995) A biomarker that identifies senescent human cells in culture and in aging skin in vivo. Proc Natl Acad Sci U S A, 92, 9363-9367.

Donehower, L.A. (1996) The p53-deficient mouse: a model for basic and applied cancer studies. Semin Cancer Biol, 7, 269-278.

D'Onofrio, M.F., Brezillon, S., Baranek, T., Perreau, C., Roughley, P.J., Maquart, F.X. & Wegrowski, Y. (2008) Identification of beta1 integrin as mediator of melanoma cell adhesion to lumican. Biochem Biophys Res Commun, 365, 266-272.

Douglas, T., Heinemann, S., Bierbaum, S., Scharnweber, D. & Worch, H. (2006) Fibrillogenesis of collagen types I, II, and III with small leucine-rich proteoglycans decorin and biglycan. Biomacromolecules, 7, 2388-2393.

Duan, L., Raja, S.M., Chen, G., Virmani, S., Williams, S.H., Clubb, R.J., Mukhopadhyay, C., Rainey, M.A., Ying, G., Dimri, M., Chen, J., Reddi, A.L., Naramura, M., Band, V. & Band, H. (2011) Negative regulation of EGFR-Vav2 signaling axis by Cbl ubiquitin ligase controls EGF receptor-mediated epithelial cell adherens junction dynamics and cell migration. J Biol Chem, 286, 620-633.

Dutta, A., Li, J., Lu, H., Akech, J., Pratap, J., Wang, T., Zerlanko, B.J., FitzGerald, T.J., Jiang, Z., Birbe, R., Wixted, J., Violette, S.M., Stein, J.L., Stein, G.S., Lian, J.B. & Languino, L.R. (2014) Integrin alphavbeta6 promotes an osteolytic program in cancer cells by upregulating MMP2. Cancer Res, 74, 1598-1608.

Dy, P., Wang, W., Bhattaram, P., Wang, Q., Wang, L., Ballock, R.T. & Lefebvre, V. (2012) Sox9 directs hypertrophic maturation and blocks osteoblast differentiation of growth plate chondrocytes. Dev Cell, 22, 597-609.

Dyrskjot, L., Kruhoffer, M., Thykjaer, T., Marcussen, N., Jensen, J.L., Moller, K. & Orntoft, T.F. (2004) Gene expression in the urinary bladder: a common carcinoma in situ gene expression signature exists disregarding histopathological classification. Cancer Res, 64, 4040-4048.

Dziegielewska, K.M., Ek, J., Habgood, M.D. & Saunders, N.R. (2001) Development of the choroid plexus. Microscopy research and technique, 52, 5-20.

Ehnis, T., Dieterich, W., Bauer, M., Kresse, H. & Schuppan, D. (1997) Localization of a binding site for the proteoglycan decorin on collagen XIV (undulin). J Biol Chem, 272, 20414-20419.

El Behi, M., Krumeich, S., Lodillinsky, C., Kamoun, A., Tibaldi, L., Sugano, G., De Reynies, A., Chapeaublanc, E., Laplanche, A., Lebret, T., Allory, Y., Radvanyi, F., Lantz, O., Eijan, A.M., Bernard-Pierrot, I. & Thery, C. (2013) An essential role for decorin in bladder cancer invasiveness. EMBO molecular medicine, 5, 1835-1851.

Elefteriou, F., Exposito, J.Y., Garrone, R. & Lethias, C. (2001) Binding of tenascin-X to decorin. FEBS letters, 495, 44-47.

Ezura, Y., Chakravarti, S., Oldberg, A., Chervoneva, I. & Birk, D.E. (2000) Differential expression of lumican and fibromodulin regulate collagen fibrillogenesis in developing mouse tendons. J Cell Biol, 151, 779-788.

Fang, H. & Declerck, Y.A. (2013) Targeting the tumor microenvironment: from understanding pathways to effective clinical trials. Cancer Res, 73, 4965-4977.

Farsund, T. (1975) Cell kinetics of mouse urinary bladder epithelium. I. Circadian and age variations in cell proliferation and nuclear DNA content. Virchows Archiv. B: Cell pathology, 18, 35-49.

Font, B., Eichenberger, D., Rosenberg, L.M. & van der Rest, M. (1996) Characterization of the interactions of type XII collagen with two small proteoglycans from fetal bovine tendon, decorin and fibromodulin. Matrix biology : journal of the International Society for Matrix Biology, 15, 341-348.

Ford, K.M., Saint-Geniez, M., Walshe, T.E. & D'Amore, P.A. (2012) Expression and role of VEGF--a in the ciliary body. Investigative ophthalmology & visual science, 53, 7520-7527.

Frantz, C., Stewart, K.M. & Weaver, V.M. (2010) The extracellular matrix at a glance. Journal of cell science, 123, 4195-4200.

Freddo, T.F. (2013) A contemporary concept of the blood-aqueous barrier. Progress in retinal and eye research, 32, 181-195.

Friedl, P. & Wolf, K. (2008) Tube travel: the role of proteases in individual and collective cancer cell invasion. Cancer Res, 68, 7247-7249.

Funderburgh, J.L., Corpuz, L.M., Roth, M.R., Funderburgh, M.L., Tasheva, E.S. & Conrad, G.W. (1997) Mimecan, the 25-kDa corneal keratan sulfate proteoglycan, is a product of the gene producing osteoglycin. J Biol Chem, 272, 28089-28095.

Fust, A., LeBellego, F., Iozzo, R.V., Roughley, P.J. & Ludwig, M.S. (2005) Alterations in lung mechanics in decorin-deficient mice. American journal of physiology. Lung cellular and molecular physiology, 288, L159-166.

Galamb, O., Sipos, F., Spisak, S., Galamb, B., Krenacs, T., Valcz, G., Tulassay, Z. & Molnar, B. (2009) Potential biomarkers of colorectal adenoma-dysplasia-carcinoma progression: mRNA expression profiling and in situ protein detection on TMAs reveal 15 sequentially upregulated and 2 downregulated genes. Cellular oncology : the official journal of the International Society for Cellular Oncology, 31, 19-29.

Gilbert SF, 2000. Developmental Biology, 6th edition. Sunderland (MA): Sinauer Associates

Giles, R.H., van Es, J.H. & Clevers, H. (2003) Caught up in a Wnt storm: Wnt signaling in cancer. Biochim Biophys Acta, 1653, 1-24.

Gilkes, D.M., Semenza, G.L. & Wirtz, D. (2014) Hypoxia and the extracellular matrix: drivers of tumour metastasis. Nat Rev Cancer.

Gill, M.R., Oldberg, A. & Reinholt, F.P. (2002) Fibromodulin-null murine knee joints display increased incidences of osteoarthritis and alterations in tissue biochemistry. Osteoarthritis and cartilage / OARS, Osteoarthritis Research Society, 10, 751-757.

Girirajan, S., Patel, N., Slager, R.E., Tokarz, M.E., Bucan, M., Wiley, J.L. & Elsea, S.H. (2008) How much is too much? Phenotypic consequences of Rai1 overexpression in mice. European journal of human genetics : EJHG, 16, 941-954.

Goldberg, M., Ono, M., Septier, D., Bonnefoix, M., Kilts, T.M., Bi, Y., Embree, M., Ameye, L. & Young, M.F. (2009) Fibromodulin-deficient mice reveal dual functions for fibromodulin in regulating dental tissue and alveolar bone formation. Cells, tissues, organs, 189, 198-202.

Goldoni, S., Humphries, A., Nystrom, A., Sattar, S., Owens, R.T., McQuillan, D.J., Ireton, K. & Iozzo, R.V. (2009) Decorin is a novel antagonistic ligand of the Met receptor. J Cell Biol, 185, 743-754.

Goldoni, S. & Iozzo, R.V. (2008) Tumor microenvironment: Modulation by decorin and related molecules harboring leucine-rich tandem motifs. Int J Cancer, 123, 2473-2479.

Goldoni, S., Seidler, D.G., Heath, J., Fassan, M., Baffa, R., Thakur, M.L., Owens, R.T., McQuillan, D.J. & Iozzo, R.V. (2008) An antimetastatic role for decorin in breast cancer. The American journal of pathology, 173, 844-855.

Goodsell, D.S. (1999) The molecular perspective: the ras oncogene. Stem cells, 17, 235-236.

Gori, F., Schipani, E. & Demay, M.B. (2001) Fibromodulin is expressed by both chondrocytes and osteoblasts during fetal bone development. Journal of cellular biochemistry, 82, 46-57.

Gotz, M. & Huttner, W.B. (2005) The cell biology of neurogenesis. Nature reviews. Molecular cell biology, 6, 777-788.

Goyal, A., Neill, T., Owens, R.T., Schaefer, L. & Iozzo, R.V. (2014) Decorin activates AMPK, an energy sensor kinase, to induce autophagy in endothelial cells. Matrix biology : journal of the International Society for Matrix Biology, 34, 46-54.

Grist, M. & Chakraborty, J. (1994) Identification of a mucin layer in the urinary bladder. Urology, 44, 26-33.

Grove, E.A., Tole, S., Limon, J., Yip, L. & Ragsdale, C.W. (1998) The hem of the embryonic cerebral cortex is defined by the expression of multiple Wnt genes and is compromised in Gli3-deficient mice. Development, 125, 2315-2325.

Grover, J., Chen, X.N., Korenberg, J.R., Recklies, A.D. & Roughley, P.J. (1996) The gene organization, chromosome location, and expression of a 55-kDa matrix protein (PRELP) of human articular cartilage. Genomics, 38, 109-117.

Grover, J., Chen, X.N., Korenberg, J.R. & Roughley, P.J. (1995) The human lumican gene. Organization, chromosomal location, and expression in articular cartilage. J Biol Chem, 270, 21942-21949.

Grover, J., Lee, E.R., Mounkes, L.C., Stewart, C.L. & Roughley, P.J. (2007) The consequence of PRELP overexpression on skin. Matrix biology : journal of the International Society for Matrix Biology, 26, 140-143.

Grover, J. & Roughley, P.J. (2001) Characterization and expression of murine PRELP. Matrix biology : journal of the International Society for Matrix Biology, 20, 555-564.

Habuchi, T., Devlin, J., Elder, P.A. & Knowles, M.A. (1995) Detailed deletion mapping of chromosome 9q in bladder cancer: evidence for two tumour suppressor loci. Oncogene, 11, 1671-1674.

Hanahan, D. & Weinberg, R.A. (2011) Hallmarks of cancer: the next generation. Cell, 144, 646-674.

Hanna, E., Quick, J. & Libutti, S.K. (2009) The tumour microenvironment: a novel target for cancer therapy. Oral diseases, 15, 8-17.

Happonen, K.E., Furst, C.M., Saxne, T., Heinegard, D. & Blom, A.M. (2012) PRELP protein inhibits the formation of the complement membrane attack complex. J Biol Chem, 287, 8092-8100.

Happonen, K.E., Sjoberg, A.P., Morgelin, M., Heinegard, D. & Blom, A.M. (2009) Complement inhibitor C4b-binding protein interacts directly with small glycoproteins of the extracellular matrix. Journal of immunology, 182, 1518-1525.

Harten, S.K., Shukla, D., Barod, R., Hergovich, A., Balda, M.S., Matter, K., Esteban, M.A. & Maxwell, P.H. (2009) Regulation of renal epithelial tight junctions by the von Hippel-Lindau tumor suppressor gene involves occludin and claudin 1 and is independent of E-cadherin. Molecular biology of the cell, 20, 1089-1101.

Hauser, P.J., Dozmorov, M.G., Bane, B.L., Slobodov, G., Culkin, D.J. & Hurst, R.E. (2008) Abnormal expression of differentiation related proteins and proteoglycan core proteins in the urothelium of patients with interstitial cystitis. The Journal of urology, 179, 764-769.

He, X.L., Bazan, J.F., McDermott, G., Park, J.B., Wang, K., Tessier-Lavigne, M., He, Z. & Garcia, K.C. (2003) Structure of the Nogo receptor ectodomain: a recognition module implicated in myelin inhibition. Neuron, 38, 177-185.

Hebert, J.M., Mishina, Y. & McConnell, S.K. (2002) BMP signaling is required locally to pattern the dorsal telencephalic midline. Neuron, 35, 1029-1041.

Heegaard, A.M., Corsi, A., Danielsen, C.C., Nielsen, K.L., Jorgensen, H.L., Riminucci, M., Young, M.F. & Bianco, P. (2007) Biglycan deficiency causes spontaneous aortic dissection and rupture in mice. Circulation, 115, 2731-2738.

Heinegard, D., Larsson, T., Sommarin, Y., Franzen, A., Paulsson, M. & Hedbom, E. (1986) Two novel matrix proteins isolated from articular cartilage show wide distributions among connective tissues. J Biol Chem, 261, 13866-13872.

Henry, S.P., Takanosu, M., Boyd, T.C., Mayne, P.M., Eberspaecher, H., Zhou, W., de Crombrugghe, B., Hook, M. & Mayne, R. (2001) Expression pattern and gene characterization of asporin. a newly discovered member of the leucine-rich repeat protein family. J Biol Chem, 276, 12212-12221.

Himmelstein, D.S., Bi, C., Clark, B.S., Bai, B. & Kohtz, J.D. (2010) Balanced Shh signaling is required for proper formation and maintenance of dorsal telencephalic midline structures. BMC developmental biology, 10, 118.

Hirao, S., Hirao, T., Marsit, C.J., Hirao, Y., Schned, A., Devi-Ashok, T., Nelson, H.H., Andrew, A., Karagas, M.R. & Kelsey, K.T. (2005) Loss of heterozygosity on chromosome 9q and p53 alterations in human bladder cancer. Cancer, 104, 1918-1923.

Ho, P.L., Lay, E.J., Jian, W., Parra, D. & Chan, K.S. (2012) Stat3 activation in urothelial stem cells leads to direct progression to invasive bladder cancer. Cancer Res, 72, 3135-3142.

Hocking, A.M., Shinomura, T. & McQuillan, D.J. (1998) Leucine-rich repeat glycoproteins of the extracellular matrix. Matrix biology : journal of the International Society for Matrix Biology, 17, 1-19.

Horiguchi, K., Syaidah, R., Fujiwara, K., Tsukada, T., Ramadhani, D., Jindatip, D., Kikuchi, M. & Yashiro, T. (2013) Expression of small leucine-rich proteoglycans in rat anterior pituitary gland. Cell Tissue Res, 351, 207-212.

Hossain, M., Ahmed, G., Naser, I.B., Shinmyo, Y., Ito, A., Riyadh, M.A., Felemban, A., Song, X., Ohta, K. & Tanaka, H. (2013) The combinatorial guidance activities of draxin and Tsukushi are essential for forebrain commissure formation. Developmental biology, 374, 58-70.

Hu, Y., Sun, H., Owens, R.T., Wu, J., Chen, Y.Q., Berquin, I.M., Perry, D., O'Flaherty, J.T. & Edwards, I.J. (2009) Decorin suppresses prostate tumor growth through inhibition of epidermal growth factor and androgen receptor pathways. Neoplasia, 11, 1042-1053.

Huizinga, E.G., Tsuji, S., Romijn, R.A., Schiphorst, M.E., de Groot, P.G., Sixma, J.J. & Gros, P. (2002) Structures of glycoprotein Ibalpha and its complex with von Willebrand factor A1 domain. Science, 297, 1176-1179.

Hunter, N.L. & Dymecki, S.M. (2007) Molecularly and temporally separable lineages form the hindbrain roof plate and contribute differentially to the choroid plexus. Development, 134, 3449-3460.

Hunzelmann, N., Schonherr, E., Bonnekoh, B., Hartmann, C., Kresse, H. & Krieg, T. (1995) Altered immunohistochemical expression of small proteoglycans in the tumor tissue and stroma of basal cell carcinoma. The Journal of investigative dermatology, 104, 509-513.

Hynes, R.O. (2009) The extracellular matrix: not just pretty fibrils. Science, 326, 1216-1219.

Iden, S. & Collard, J.G. (2008) Crosstalk between small GTPases and polarity proteins in cell polarization. Nature reviews. Molecular cell biology, 9, 846-859.

Igwe, J.C., Gao, Q., Kizivat, T., Kao, W.W. & Kalajzic, I. (2011) Keratocan is expressed by osteoblasts and can modulate osteogenic differentiation. Connective tissue research, 52, 401-407.

Inkson, C.A., Ono, M., Bi, Y., Kuznetsov, S.A., Fisher, L.W. & Young, M.F. (2009) The potential functional interaction of biglycan and WISP-1 in controlling differentiation and proliferation of osteogenic cells. Cells, tissues, organs, 189, 153-157.

Iozzo, R.V. (1997) The family of the small leucine-rich proteoglycans: key regulators of matrix assembly and cellular growth. Crit Rev Biochem Mol Biol, 32, 141-174.

Iozzo, R.V. (1998) Matrix proteoglycans: from molecular design to cellular function. Annual review of biochemistry, 67, 609-652.

Iozzo, R.V. (1999) The biology of the small leucine-rich proteoglycans. Functional network of interactive proteins. J Biol Chem, 274, 18843-18846.

Iozzo, R.V., Buraschi, S., Genua, M., Xu, S.Q., Solomides, C.C., Peiper, S.C., Gomella, L.G., Owens, R.C. & Morrione, A. (2011) Decorin antagonizes IGF receptor I (IGF-IR) function by interfering with IGF-IR activity and attenuating downstream signaling. J Biol Chem, 286, 34712-34721.

Iozzo, R.V., Chakrani, F., Perrotti, D., McQuillan, D.J., Skorski, T., Calabretta, B. & Eichstetter, I. (1999) Cooperative action of germ-line mutations in decorin and p53 accelerates lymphoma tumorigenesis. Proc Natl Acad Sci U S A, 96, 3092-3097.

Iozzo, R.V., Moscatello, D.K., McQuillan, D.J. & Eichstetter, I. (1999) Decorin is a biological ligand for the epidermal growth factor receptor. J Biol Chem, 274, 4489-4492.

Iozzo, R.V. & Sanderson, R.D. (2011) Proteoglycans in cancer biology, tumour microenvironment and angiogenesis. Journal of cellular and molecular medicine, 15, 1013-1031.

Iozzo, R.V. & Schaefer, L. (2010) Proteoglycans in health and disease: novel regulatory signaling mechanisms evoked by the small leucine-rich proteoglycans. The FEBS journal, 277, 3864-3875.

Ishiwata, T., Cho, K., Kawahara, K., Yamamoto, T., Fujiwara, Y., Uchida, E., Tajiri, T. & Naito, Z. (2007) Role of lumican in cancer cells and adjacent stromal tissues in human pancreatic cancer. Oncol Rep, 18, 537-543.

Ishiwata, T., Fujii, T., Ishiwata, S., Ikegawa, S. & Naito, Z. (2004) Effect of morpholino antisense oligonucleotide against lumican mRNA in human embryonic kidney (HEK) 293 cells. Pathology international, 54, 77-81.

Ito, A., Shinmyo, Y., Abe, T., Oshima, N., Tanaka, H. & Ohta, K. (2010) Tsukushi is required for anterior commissure formation in mouse brain. Biochem Biophys Res Commun, 402, 813-818.

Itoh, Y. & Seiki, M. (2006) MT1-MMP: a potent modifier of pericellular microenvironment. Journal of cellular physiology, 206, 1-8.

Jeong, S., Park, Y., Cho, Y., Kim, Y.R. & Kim, H.S. (2012) Diagnostic values of urine CYFRA21-1, NMP22, UBC, and FDP for the detection of bladder cancer. Clin Chim Acta, 414, 93-100.

Jepsen, K.J., Wu, F., Peragallo, J.H., Paul, J., Roberts, L., Ezura, Y., Oldberg, A., Birk, D.E. & Chakravarti, S. (2002) A syndrome of joint laxity and impaired tendon integrity in lumican- and fibromodulin-deficient mice. J Biol Chem, 277, 35532-35540.

Jezernik, K. & Pipan, N. (1993) Blood-urine barrier formation in mouse urinary bladder development. The Anatomical record, 235, 533-538.

Johansson, P.A., Dziegielewska, K.M., Ek, C.J., Habgood, M.D., Liddelow, S.A., Potter, A.M., Stolp, H.B. & Saunders, N.R. (2006) Blood-CSF barrier function in the rat embryo. The European journal of neuroscience, 24, 65-76.

Johansson, P.A., Dziegielewska, K.M., Ek, C.J., Habgood, M.D., Mollgard, K., Potter, A., Schuliga, M. & Saunders, N.R. (2005) Aquaporin-1 in the choroid plexuses of developing mammalian brain. Cell Tissue Res, 322, 353-364.

Johnson, G.L. & Lapadat, R. (2002) Mitogen-activated protein kinase pathways mediated by ERK, JNK, and p38 protein kinases. Science, 298, 1911-1912.

Johnson, H.J., Rosenberg, L., Choi, H.U., Garza, S., Hook, M. & Neame, P.J. (1997) Characterization of epiphycan, a small proteoglycan with a leucine-rich repeat core protein. J Biol Chem, 272, 18709-18717.

Johnson, J.M., Young, T.L. & Rada, J.A. (2006) Small leucine rich repeat proteoglycans (SLRPs) in the human sclera: identification of abundant levels of PRELP. Molecular vision, 12, 1057-1066.

Kalamajski, S. & Oldberg, A. (2009) Homologous sequence in lumican and fibromodulin leucine-rich repeat 5-7 competes for collagen binding. J Biol Chem, 284, 534-539.

Kandoth, C., McLellan, M.D., Vandin, F., Ye, K., Niu, B., Lu, C., Xie, M., Zhang, Q., McMichael, J.F., Wyczalkowski, M.A., Leiserson, M.D., Miller, C.A., Welch, J.S., Walter, M.J., Wendl, M.C., Ley, T.J., Wilson, R.K., Raphael, B.J. & Ding, L. (2013) Mutational landscape and significance across 12 major cancer types. Nature, 502, 333-339.

Kaplan, R.N., Riba, R.D., Zacharoulis, S., Bramley, A.H., Vincent, L., Costa, C., MacDonald, D.D., Jin, D.K., Shido, K., Kerns, S.A., Zhu, Z., Hicklin, D., Wu, Y., Port, J.L., Altorki, N., Port, E.R., Ruggero, D., Shmelkov, S.V., Jensen, K.K., Rafii, S. & Lyden, D. (2005) VEGFR1-positive haematopoietic bone marrow progenitors initiate the pre-metastatic niche. Nature, 438, 820-827.

Kappler, J., Stichel, C.C., Gleichmann, M., Gillen, C., Junghans, U., Kresse, H. & Muller, H.W. (1998) Developmental regulation of decorin expression in postnatal rat brain. Brain research, 793, 328-332.

Keen, A.J. & Knowles, M.A. (1994) Definition of two regions of deletion on chromosome 9 in carcinoma of the bladder. Oncogene, 9, 2083-2088.

Keenan, T.D., Clark, S.J., Unwin, R.D., Ridge, L.A., Day, A.J. & Bishop, P.N. (2012) Mapping the differential distribution of proteoglycan core proteins in the adult human retina, choroid, and sclera. Investigative ophthalmology & visual science, 53, 7528-7538.

Kessenbrock, K., Plaks, V. & Werb, Z. (2010) Matrix metalloproteinases: regulators of the tumor microenvironment. Cell, 141, 52-67.

Khandelwal, P., Abraham, S.N. & Apodaca, G. (2009) Cell biology and physiology of the uroepithelium. American journal of physiology. Renal physiology, 297, F1477-1501.

Kilts, T., Ameye, L., Syed-Picard, F., Ono, M., Berendsen, A.D., Oldberg, A., Heegaard, A.M., Bi, Y. & Young, M.F. (2009) Potential roles for the small leucine-rich proteoglycans biglycan and fibromodulin in ectopic ossification of tendon induced by exercise and in modulating rotarod performance. Scandinavian journal of medicine & science in sports, 19, 536-546.

Kizawa, H., Kou, I., Iida, A., Sudo, A., Miyamoto, Y., Fukuda, A., Mabuchi, A., Kotani, A., Kawakami, A., Yamamoto, S., Uchida, A., Nakamura, K., Notoya, K., Nakamura, Y. & Ikegawa, S. (2005) An aspartic acid repeat polymorphism in asporin inhibits chondrogenesis and increases susceptibility to osteoarthritis. Nature genetics, 37, 138-144.

Knudson, A.G., Jr. (1971) Mutation and cancer: statistical study of retinoblastoma. Proc Natl Acad Sci U S A, 68, 820-823.

Kojima, T., Takano, K., Yamamoto, T., Murata, M., Son, S., Imamura, M., Yamaguchi, H., Osanai, M., Chiba, H., Himi, T. & Sawada, N. (2008) Transforming growth factor-beta induces epithelial to mesenchymal transition by down-regulation of claudin-1 expression and the fence function in adult rat hepatocytes. Liver international : official journal of the International Association for the Study of the Liver, 28, 534-545.

Komori, T. (2005) Regulation of skeletal development by the Runx family of transcription factors. Journal of cellular biochemistry, 95, 445-453.

Koninger, J., Giese, T., di Mola, F.F., Wente, M.N., Esposito, I., Bachem, M.G., Giese, N.A., Buchler, M.W. & Friess, H. (2004) Pancreatic tumor cells influence the composition of the extracellular matrix. Biochem Biophys Res Commun, 322, 943-949.

Kreft, M.E., Hudoklin, S., Jezernik, K. & Romih, R. (2010) Formation and maintenance of blood-urine barrier in urothelium. Protoplasma, 246, 3-14.

Kronenberg, H.M. (2003) Developmental regulation of the growth plate. Nature, 423, 332-336.

Kronenberg, H.M. (2003) Developmental regulation of the growth plate. Nature, 423, 332-336.

Kuriyama, S., Lupo, G., Ohta, K., Ohnuma, S., Harris, W.A. & Tanaka, H. (2006) Tsukushi controls ectodermal patterning and neural crest specification in Xenopus by direct regulation of BMP4 and X-delta-1 activity. Development, 133, 75-88.

Lamouille, S., Xu, J. & Derynck, R. (2014) Molecular mechanisms of epithelial-mesenchymal transition. Nature reviews. Molecular cell biology, 15, 178-196.

Lefebvre, V. & Smits, P. (2005) Transcriptional control of chondrocyte fate and differentiation. Birth defects research. Part C, Embryo today : reviews, 75, 200-212.

Leivo, I., Jee, K.J., Heikinheimo, K., Laine, M., Ollila, J., Nagy, B. & Knuutila, S. (2005) Characterization of gene expression in major types of salivary gland carcinomas with epithelial differentiation. Cancer Genet Cytogenet, 156, 104-113.

Levens, E., Luo, X., Ding, L., Williams, R.S. & Chegini, N. (2005) Fibromodulin is expressed in leiomyoma and myometrium and regulated by gonadotropin-releasing hormone analogue therapy and TGF-beta through Smad and MAPK-mediated signalling. Molecular human reproduction, 11, 489-494.

Lewis, M. (2003) PRELP, collagen, and a theory of Hutchinson-Gilford progeria. Ageing research reviews, 2, 95-105.

Lewis, S.A. (2000) Everything you wanted to know about the bladder epithelium but were afraid to ask. American journal of physiology. Renal physiology, 278, F867-874.

Leygue, E., Snell, L., Dotzlaw, H., Hole, K., Hiller-Hitchcock, T., Roughley, P.J., Watson, P.H. & Murphy, L.C. (1998) Expression of lumican in human breast carcinoma. Cancer Res, 58, 1348-1352.

Leygue, E., Snell, L., Dotzlaw, H., Troup, S., Hiller-Hitchcock, T., Murphy, L.C., Roughley, P.J. & Watson, P.H. (2000) Lumican and decorin are differentially expressed in human breast carcinoma. J Pathol, 192, 313-320.

Li, X., McFarland, D.C. & Velleman, S.G. (2008) Extracellular matrix proteoglycan decorin-mediated myogenic satellite cell responsiveness to transforming growth factor-beta1 during cell proliferation and differentiation Decorin and transforming growth factor-beta1 in satellite cells. Domestic animal endocrinology, 35, 263-273.

Li, Y., Aoki, T., Mori, Y., Ahmad, M., Miyamori, H., Takino, T. & Sato, H. (2004) Cleavage of lumican by membrane-type matrix metalloproteinase-1 abrogates this proteoglycan-mediated suppression of tumor cell colony formation in soft agar. Cancer Res, 64, 7058-7064.

Lin, D., Edwards, A.S., Fawcett, J.P., Mbamalu, G., Scott, J.D. & Pawson, T. (2000) A mammalian PAR-3-PAR-6 complex implicated in Cdc42/Rac1 and aPKC signalling and cell polarity. Nature cell biology, 2, 540-547.

Linnenbach, A.J., Pressler, L.B., Seng, B.A., Kimmel, B.S., Tomaszewski, J.E. & Malkowicz, S.B. (1993) Characterization of chromosome 9 deletions in transitional cell carcinoma by microsatellite assay. Hum Mol Genet, 2, 1407-1411.

Littlepage, L.E., Sternlicht, M.D., Rougier, N., Phillips, J., Gallo, E., Yu, Y., Williams, K., Brenot, A., Gordon, J.I. & Werb, Z. (2010) Matrix metalloproteinases contribute distinct roles in neuroendocrine prostate carcinogenesis, metastasis, and angiogenesis progression. Cancer Res, 70, 2224-2234.

Liu, C.Y., Birk, D.E., Hassell, J.R., Kane, B. & Kao, W.W. (2003) Keratocan-deficient mice display alterations in corneal structure. J Biol Chem, 278, 21672-21677.

Lorenzo, P., Aspberg, A., Onnerfjord, P., Bayliss, M.T., Neame, P.J. & Heinegard, D. (2001) Identification and characterization of asporin. a novel member of the leucine-rich repeat protein family closely related to decorin and biglycan. J Biol Chem, 276, 12201-12211.

Lu, J., Xu, Z., Jiang, F., Wang, Y., Hou, Y., Wang, C. & Chen, Q. (2012) Primary clear cell adenocarcinoma of the bladder with recurrence: a case report and literature review. World journal of surgical oncology, 10, 33.

Lu, P., Weaver, V.M. & Werb, Z. (2012) The extracellular matrix: a dynamic niche in cancer progression. J Cell Biol, 196, 395-406.

Lu, Y.P., Ishiwata, T., Kawahara, K., Watanabe, M., Naito, Z., Moriyama, Y., Sugisaki, Y. & Asano, G. (2002) Expression of lumican in human colorectal cancer cells. Pathology international, 52, 519-526.

Lucchini, M., Couble, M.L., Romeas, A., Staquet, M.J., Bleicher, F., Magloire, H. & Farges, J.C. (2004) Alpha v beta 3 integrin expression in human odontoblasts and co-localization with osteoadherin. Journal of dental research, 83, 552-556.

Lucchini, M., Couble, M.L., Romeas, A., Staquet, M.J., Bleicher, F., Magloire, H. & Farges, J.C. (2004) Alpha v beta 3 integrin expression in human odontoblasts and co-localization with osteoadherin. Journal of dental research, 83, 552-556.

Lui, J.C., Andrade, A.C., Forcinito, P., Hegde, A., Chen, W., Baron, J. & Nilsson, O. (2010) Spatial and temporal regulation of gene expression in the mammalian growth plate. Bone, 46, 1380-1390.

Lui, W.Y., Lee, W.M. & Cheng, C.Y. (2003) TGF-betas: their role in testicular function and Sertoli cell tight junction dynamics. International journal of andrology, 26, 147-160.

Luis, N.M., Lopez-Knowles, E. & Real, F.X. (2007) Molecular biology of bladder cancer. Clinical & translational oncology : official publication of the Federation of Spanish Oncology Societies and of the National Cancer Institute of Mexico, 9, 5-12.

Luis, N.M., Lopez-Knowles, E. & Real, F.X. (2007) Molecular biology of bladder cancer. Clinical & translational oncology : official publication of the Federation of Spanish Oncology Societies and of the National Cancer Institute of Mexico, 9, 5-12.

Macconaill, L.E. & Garraway, L.A. (2010) Clinical implications of the cancer genome. J Clin Oncol, 28, 5219-5228.

Maciejewski, C.C., Honardoust, D., Tredget, E.E. & Metcalfe, P.D. (2012) Differential expression of class I small leucine-rich proteoglycans in an animal model of partial bladder outlet obstruction. The Journal of urology, 188, 1543-1548.

Magee, C., Nurminskaya, M., Faverman, L., Galera, P. & Linsenmayer, T.F. (2005) SP3/SP1 transcription activity regulates specific expression of collagen type X in hypertrophic chondrocytes. J Biol Chem, 280, 25331-25338.

Maiers, J.L., Peng, X., Fanning, A.S. & DeMali, K.A. (2013) ZO-1 recruitment to alpha-catenin--a novel mechanism for coupling the assembly of tight junctions to adherens junctions. Journal of cell science, 126, 3904-3915.

Mak, K.K., Kronenberg, H.M., Chuang, P.T., Mackem, S. & Yang, Y. (2008) Indian hedgehog signals independently of PTHrP to promote chondrocyte hypertrophy. Development, 135, 1947-1956.

Malinowski, M., Pietraszek, K., Perreau, C., Boguslawski, M., Decot, V., Stoltz, J.F., Vallar, L., Niewiarowska, J., Cierniewski, C., Maquart, F.X., Wegrowski, Y. & Brezillon, S. (2012)

Effect of lumican on the migration of human mesenchymal stem cells and endothelial progenitor cells: involvement of matrix metalloproteinase-14. PLoS One, 7, e50709.

Mangale, V.S., Hirokawa, K.E., Satyaki, P.R., Gokulchandran, N., Chikbire, S., Subramanian, L., Shetty, A.S., Martynoga, B., Paul, J., Mai, M.V., Li, Y., Flanagan, L.A., Tole, S. & Monuki, E.S. (2008) Lhx2 selector activity specifies cortical identity and suppresses hippocampal organizer fate. Science, 319, 304-309.

Mangiameli, D.P., Blansfield, J.A., Kachala, S., Lorang, D., Schafer, P.H., Muller, G.W., Stirling, D.I. & Libutti, S.K. (2007) Combination therapy targeting the tumor microenvironment is effective in a model of human ocular melanoma. Journal of translational medicine, 5, 38.

Matsuda, Y., Yamamoto, T., Kudo, M., Kawahara, K., Kawamoto, M., Nakajima, Y., Koizumi, K., Nakazawa, N., Ishiwata, T. & Naito, Z. (2008) Expression and roles of lumican in lung adenocarcinoma and squamous cell carcinoma. Int J Oncol, 33, 1177-1185.

Matsumine, A., Shintani, K., Kusuzaki, K., Matsubara, T., Satonaka, H., Wakabayashi, T., Iino, T. & Uchida, A. (2007) Expression of decorin, a small leucine-rich proteoglycan, as a prognostic factor in soft tissue tumors. Journal of surgical oncology, 96, 411-418.

Matsushima, N., Ohyanagi, T., Tanaka, T. & Kretsinger, R.H. (2000) Super-motifs and evolution of tandem leucine-rich repeats within the small proteoglycans--biglycan, decorin, lumican, fibromodulin, PRELP, keratocan, osteoadherin, epiphycan, and osteoglycin. Proteins, 38, 210-225.

Matter, K. & Balda, M.S. (2003) Signalling to and from tight junctions. Nature reviews. Molecular cell biology, 4, 225-236.

Matter, K. & Balda, M.S. (2014) SnapShot: Epithelial tight junctions. Cell, 157, 992-992 e991.

Mayr, C., Bund, D., Schlee, M., Moosmann, A., Kofler, D.M., Hallek, M. & Wendtner, C.M. (2005) Fibromodulin as a novel tumor-associated antigen (TAA) in chronic lymphocytic leukemia (CLL), which allows expansion of specific CD8+ autologous T lymphocytes. Blood, 105, 1566-1573.

McDoniels-Silvers, A.L., Nimri, C.F., Stoner, G.D., Lubet, R.A. & You, M. (2002) Differential gene expression in human lung adenocarcinomas and squamous cell carcinomas. Clin Cancer Res, 8, 1127-1138.

McEwan, P.A., Scott, P.G., Bishop, P.N. & Bella, J. (2006) Structural correlations in the family of small leucine-rich repeat proteins and proteoglycans. Journal of structural biology, 155, 294-305.

Merle, B., Durussel, L., Delmas, P.D. & Clezardin, P. (1999) Decorin inhibits cell migration through a process requiring its glycosaminoglycan side chain. Journal of cellular biochemistry, 75, 538-546.

Merline, R., Moreth, K., Beckmann, J., Nastase, M.V., Zeng-Brouwers, J., Tralhao, J.G., Lemarchand, P., Pfeilschifter, J., Schaefer, R.M., Iozzo, R.V. & Schaefer, L. (2011) Signaling by the matrix proteoglycan decorin controls inflammation and cancer through PDCD4 and MicroRNA-21. Science signaling, 4, ra75.

Merline, R., Schaefer, R.M. & Schaefer, L. (2009) The matricellular functions of small leucine-rich proteoglycans (SLRPs). Journal of cell communication and signaling, 3, 323-335.

Mikaelsson, E., Danesh-Manesh, A.H., Luppert, A., Jeddi-Tehrani, M., Rezvany, M.R., Sharifian, R.A., Safaie, R., Roohi, A., Osterborg, A., Shokri, F., Mellstedt, H. & Rabbani, H. (2005) Fibromodulin, an extracellular matrix protein: characterization of its unique gene and protein expression in B-cell chronic lymphocytic leukemia and mantle cell lymphoma. Blood, 105, 4828-4835.

Millgard, K., Milinowska, D.H. & Saunders, N.R. (1976) Lack of correlation between tight junction morphology and permeability properties in developing choroid plexus. Nature, 264, 293-294.

Mimura, T., Chang, J.H., Kim, T.I., Onguchi, T., Kojima, T., Sakimoto, T. & Azar, D.T. (2011) MT1-MMP cleavage of the antiangiogenic proteoglycan decorin: role in corneal angiogenesis. Cornea, 30 Suppl 1, S45-49.

Mlakar, V., Berginc, G., Volavsek, M., Stor, Z., Rems, M. & Glavac, D. (2009) Presence of activating KRAS mutations correlates significantly with expression of tumour suppressor genes DCN and TPM1 in colorectal cancer. BMC cancer, 9, 282.

Mochida, Y., Kaku, M., Yoshida, K., Katafuchi, M., Atsawasuwan, P. & Yamauchi, M. (2011) Podocan-like protein: a novel small leucine-rich repeat matrix protein in bone. Biochem Biophys Res Commun, 410, 333-338.

Monfort, J., Tardif, G., Reboul, P., Mineau, F., Roughley, P., Pelletier, J.P. & Martel-Pelletier, J. (2006) Degradation of small leucine-rich repeat proteoglycans by matrix metalloprotease-13: identification of a new biglycan cleavage site. Arthritis research & therapy, 8, R26.

Moreno, M., Munoz, R., Aroca, F., Labarca, M., Brandan, E. & Larrain, J. (2005) Biglycan is a new extracellular component of the Chordin-BMP4 signaling pathway. Embo J, 24, 1397-1405.

Moreth, K., Iozzo, R.V. & Schaefer, L. (2012) Small leucine-rich proteoglycans orchestrate receptor crosstalk during inflammation. Cell Cycle, 11, 2084-2091.

Morin, P.J., Sparks, A.B., Korinek, V., Barker, N., Clevers, H., Vogelstein, B. & Kinzler, K.W. (1997) Activation of beta-catenin-Tcf signaling in colon cancer by mutations in beta-catenin or APC. Science, 275, 1787-1790.

Morrione, A., Neill, T. & Iozzo, R.V. (2013) Dichotomy of decorin activity on the insulin-like growth factor-I system. The FEBS journal, 280, 2138-2149.

Morris, S.A., Almeida, A.D., Tanaka, H., Ohta, K. & Ohnuma, S. (2007) Tsukushi modulates Xnr2, FGF and BMP signaling: regulation of Xenopus germ layer formation. PLoS One, 2, e1004.

Morton, C.L. & Houghton, P.J. (2007) Establishment of human tumor xenografts in immunodeficient mice. Nature protocols, 2, 247-250.

Moscatello, D.K., Santra, M., Mann, D.M., McQuillan, D.J., Wong, A.J. & Iozzo, R.V. (1998) Decorin suppresses tumor cell growth by activating the epidermal growth factor receptor. J Clin Invest, 101, 406-412.

Nash, M.A., Deavers, M.T. & Freedman, R.S. (2002) The expression of decorin in human ovarian tumors. Clin Cancer Res, 8, 1754-1760.

Nastase, M.V., Iozzo, R.V. & Schaefer, L. (2014) Key roles for the small leucine-rich proteoglycans in renal and pulmonary pathophysiology. Biochim Biophys Acta.

Nastase, M.V., Iozzo, R.V. & Schaefer, L. (2014) Key roles for the small leucine-rich proteoglycans in renal and pulmonary pathophysiology. Biochim Biophys Acta.

Neame, P.J., Sommarin, Y., Boynton, R.E. & Heinegard, D. (1994) The structure of a 38-kDa leucine-rich protein (chondroadherin) isolated from bovine cartilage. J Biol Chem, 269, 21547-21554.

Neill, T., Painter, H., Buraschi, S., Owens, R.T., Lisanti, M.P., Schaefer, L. & Iozzo, R.V. (2012) Decorin antagonizes the angiogenic network: concurrent inhibition of Met, hypoxia inducible factor 1alpha, vascular endothelial growth factor A, and induction of thrombospondin-1 and TIMP3. J Biol Chem, 287, 5492-5506.

Newton, T.R., Parsons, P.G., Lincoln, D.J., Cummings, M.C., Wyld, D.K., Webb, P.M., Green, A.C. & Boyle, G.M. (2006) Expression profiling correlates with treatment response in women with advanced serous epithelial ovarian cancer. Int J Cancer, 119, 875-883.

Ni, G.X., Li, Z. & Zhou, Y.Z. (2014) The role of small leucine-rich proteoglycans in osteoarthritis pathogenesis. Osteoarthritis and cartilage / OARS, Osteoarthritis Research Society, 22, 896-903.

Niedworok, C., Rock, K., Kretschmer, I., Freudenberger, T., Nagy, N., Szarvas, T., Vom Dorp, F., Reis, H., Rubben, H. & Fischer, J.W. (2013) Inhibitory role of the small leucine-rich proteoglycan biglycan in bladder cancer. PLoS One, 8, e80084.

Niewiarowska, J., Brezillon, S., Sacewicz-Hofman, I., Bednarek, R., Maquart, F.X., Malinowski, M., Wiktorska, M., Wegrowski, Y. & Cierniewski, C.S. (2011) Lumican inhibits angiogenesis by interfering with alpha2beta1 receptor activity and downregulating MMP-14 expression. Thrombosis research, 128, 452-457.

Nikdin, H., Olsson, M.L., Hultenby, K. & Sugars, R.V. (2012) Osteoadherin accumulates in the predentin towards the mineralization front in the developing tooth. PLoS One, 7, e31525.

Nikitovic, D., Aggelidakis, J., Young, M.F., Iozzo, R.V., Karamanos, N.K. & Tzanakakis, G.N. (2012) The biology of small leucine-rich proteoglycans in bone pathophysiology. J Biol Chem, 287, 33926-33933.

Nikitovic, D., Aggelidakis, J., Young, M.F., Iozzo, R.V., Karamanos, N.K. & Tzanakakis, G.N. (2012) The biology of small leucine-rich proteoglycans in bone pathophysiology. J Biol Chem, 287, 33926-33933.

Nikitovic, D., Berdiaki, A., Zafiropoulos, A., Katonis, P., Tsatsakis, A., Karamanos, N.K. & Tzanakakis, G.N. (2008) Lumican expression is positively correlated with the differentiation and negatively with the growth of human osteosarcoma cells. The FEBS journal, 275, 350-361.

Nikitovic, D., Chalkiadaki, G., Berdiaki, A., Aggelidakis, J., Katonis, P., Karamanos, N.K. & Tzanakakis, G.N. (2011) Lumican regulates osteosarcoma cell adhesion by modulating TGFbeta2 activity. The international journal of biochemistry & cell biology, 43, 928-935.

Ninomiya, K., Miyamoto, T., Imai, J., Fujita, N., Suzuki, T., Iwasaki, R., Yagi, M., Watanabe, S., Toyama, Y. & Suda, T. (2007) Osteoclastic activity induces osteomodulin expression in osteoblasts. Biochem Biophys Res Commun, 362, 460-466.

Nishino, R., Honda, M., Yamashita, T., Takatori, H., Minato, H., Zen, Y., Sasaki, M., Takamura, H., Horimoto, K., Ohta, T., Nakanuma, Y. & Kaneko, S. (2008) Identification of novel candidate tumour marker genes for intrahepatic cholangiocarcinoma. Journal of hepatology, 49, 207-216.

Nuka, S., Zhou, W., Henry, S.P., Gendron, C.M., Schultz, J.B., Shinomura, T., Johnson, J., Wang, Y., Keene, D.R., Ramirez-Solis, R., Behringer, R.R., Young, M.F. & Hook, M. (2010) Phenotypic characterization of epiphycan-deficient and epiphycan/biglycan double-deficient mice. Osteoarthritis and cartilage / OARS, Osteoarthritis Research Society, 18, 88-96.

Ohta, K., Ito, A., Kuriyama, S., Lupo, G., Kosaka, M., Ohnuma, S., Nakagawa, S. & Tanaka, H. (2011) Tsukushi functions as a Wnt signaling inhibitor by competing with Wnt2b for binding to transmembrane protein Frizzled4. Proc Natl Acad Sci U S A, 108, 14962-14967.

Ohta, K., Kuriyama, S., Okafuji, T., Gejima, R., Ohnuma, S. & Tanaka, H. (2006) Tsukushi cooperates with VG1 to induce primitive streak and Hensen's node formation in the chick embryo. Development, 133, 3777-3786.

Ohta, K., Lupo, G., Kuriyama, S., Keynes, R., Holt, C.E., Harris, W.A., Tanaka, H. & Ohnuma, S. (2004) Tsukushi functions as an organizer inducer by inhibition of BMP activity in cooperation with chordin. Dev Cell, 7, 347-358.

Oster, S.K., Ho, C.S., Soucie, E.L. & Penn, L.Z. (2002) The myc oncogene: MarvelouslY Complex. Advances in cancer research, 84, 81-154.

Ozdamar, B., Bose, R., Barrios-Rodiles, M., Wang, H.R., Zhang, Y. & Wrana, J.L. (2005) Regulation of the polarity protein Par6 by TGFbeta receptors controls epithelial cell plasticity. Science, 307, 1603-1609.

Paez, J.G., Janne, P.A., Lee, J.C., Tracy, S., Greulich, H., Gabriel, S., Herman, P., Kaye, F.J., Lindeman, N., Boggon, T.J., Naoki, K., Sasaki, H., Fujii, Y., Eck, M.J., Sellers, W.R., Johnson, B.E. & Meyerson, M. (2004) EGFR mutations in lung cancer: correlation with clinical response to gefitinib therapy. Science, 304, 1497-1500.

Parsons, C.L., Boychuk, D., Jones, S., Hurst, R. & Callahan, H. (1990) Bladder surface glycosaminoglycans: an epithelial permeability barrier. The Journal of urology, 143, 139-142.

Parsons, C.L., Forrest, J., Nickel, J.C., Evans, R., Lloyd, L.K., Barkin, J., Mosbaugh, P.G., Kaufman, D.M., Hernandez-Graulau, J.M., Atkinson, L., Albrecht, D. & Elmiron Study, G. (2002) Effect of pentosan polysulfate therapy on intravesical potassium sensitivity. Urology, 59, 329-333.

Petersson, U., Hultenby, K. & Wendel, M. (2003) Identification, distribution and expression of osteoadherin during tooth formation. European journal of oral sciences, 111, 128-136.

Pfaffl, M.W. (2001) A new mathematical model for relative quantification in real-time RT-PCR. Nucleic acids research, 29, e45.

Pio, R., Ajona, D. & Lambris, J.D. (2013) Complement inhibition in cancer therapy. Seminars in immunology, 25, 54-64.

Plaas, A.H. & Wong-Palms, S. (1993) Biosynthetic mechanisms for the addition of polylactosamine to chondrocyte fibromodulin. J Biol Chem, 268, 26634-26644.

Pogany, G. & Vogel, K.G. (1992) The interaction of decorin core protein fragments with type I collagen. Biochem Biophys Res Commun, 189, 165-172.

Pollak, M. (2012) The insulin and insulin-like growth factor receptor family in neoplasia: an update. Nat Rev Cancer, 12, 159-169.

Polyak, K. & Weinberg, R.A. (2009) Transitions between epithelial and mesenchymal states: acquisition of malignant and stem cell traits. Nat Rev Cancer, 9, 265-273.

Prydz, K. & Dalen, K.T. (2000) Synthesis and sorting of proteoglycans. Journal of cell science, 113 Pt 2, 193-205.

Radisky, D.C. & Bissell, M.J. (2004) Cancer. Respect thy neighbor! Science, 303, 775-777.

Rajan, R., Poniecka, A., Smith, T.L., Yang, Y., Frye, D., Pusztai, L., Fiterman, D.J., Gal-Gombos, E., Whitman, G., Rouzier, R., Green, M., Kuerer, H., Buzdar, A.U., Hortobagyi, G.N. & Symmans, W.F. (2004) Change in tumor cellularity of breast carcinoma after neoadjuvant chemotherapy as a variable in the pathologic assessment of response. Cancer, 100, 1365-1373.

Rajasekaran, A.K., Hojo, M., Huima, T. & Rodriguez-Boulan, E. (1996) Catenins and zonula occludens-1 form a complex during early stages in the assembly of tight junctions. J Cell Biol, 132, 451-463.

Ramesh, S., Bonshek, R.E. & Bishop, P.N. (2004) Immunolocalisation of opticin in the human eye. The British journal of ophthalmology, 88, 697-702.

Ramstad, V.E., Franzen, A., Heinegard, D., Wendel, M. & Reinholt, F.P. (2003) Ultrastructural distribution of osteoadherin in rat bone shows a pattern similar to that of bone sialoprotein. Calcified tissue international, 72, 57-64.

Raouf, A., Ganss, B., McMahon, C., Vary, C., Roughley, P.J. & Seth, A. (2002) Lumican is a major proteoglycan component of the bone matrix. Matrix biology : journal of the International Society for Matrix Biology, 21, 361-367.

Raviola, G. & Raviola, E. (1978) Intercellular junctions in the ciliary epithelium. Investigative ophthalmology & visual science, 17, 958-981.

Reardon, A.J., Le Goff, M., Briggs, M.D., McLeod, D., Sheehan, J.K., Thornton, D.J. & Bishop, P.N. (2000) Identification in vitreous and molecular cloning of opticin, a novel member of the family of leucine-rich repeat proteins of the extracellular matrix. J Biol Chem, 275, 2123-2129.

Recktenwald, C.V., Leisz, S., Steven, A., Mimura, K., Muller, A., Wulfanger, J., Kiessling, R. & Seliger, B. (2012) HER-2/neu-mediated down-regulation of biglycan associated with altered growth properties. J Biol Chem, 287, 24320-24329.

Reed, C.C., Gauldie, J. & Iozzo, R.V. (2002) Suppression of tumorigenicity by adenovirus-mediated gene transfer of decorin. Oncogene, 21, 3688-3695.

Reed, C.C. & Iozzo, R.V. (2002) The role of decorin in collagen fibrillogenesis and skin homeostasis. Glycoconjugate journal, 19, 249-255.

Reed, C.C., Waterhouse, A., Kirby, S., Kay, P., Owens, R.T., McQuillan, D.J. & Iozzo, R.V. (2005) Decorin prevents metastatic spreading of breast cancer. Oncogene, 24, 1104-1110.

Rehn, A.P., Cerny, R., Sugars, R.V., Kaukua, N. & Wendel, M. (2008) Osteoadherin is upregulated by mature osteoblasts and enhances their in vitro differentiation and mineralization. Calcified tissue international, 82, 454-464.

Rehn, A.P., Chalk, A.M. & Wendel, M. (2006) Differential regulation of osteoadherin (OSAD) by TGF-beta1 and BMP-2. Biochem Biophys Res Commun, 349, 1057-1064.

Ross, M.D., Bruggeman, L.A., Hanss, B., Sunamoto, M., Marras, D., Klotman, M.E. & Klotman, P.E. (2003) Podocan, a novel small leucine-rich repeat protein expressed in the sclerotic glomerular lesion of experimental HIV-associated nephropathy. J Biol Chem, 278, 33248-33255.

Roukos, D.H. (2009) Genome-wide association studies: how predictable is a person's cancer risk? Expert Rev Anticancer Ther, 9, 389-392.

Rubinfeld, B., Souza, B., Albert, I., Muller, O., Chamberlain, S.H., Masiarz, F.R., Munemitsu, S. & Polakis, P. (1993) Association of the APC gene product with beta-catenin. Science, 262, 1731-1734.

Rucci, N., Capulli, M., Ventura, L., Angelucci, A., Peruzzi, B., Tillgren, V., Muraca, M., Heinegard, D. & Teti, A. (2013) Proline/arginine-rich end leucine-rich repeat protein N-terminus is a novel osteoclast antagonist that counteracts bone loss. Journal of bone and mineral research : the official journal of the American Society for Bone and Mineral Research, 28, 1912-1924.

Rucci, N., Rufo, A., Alamanou, M., Capulli, M., Del Fattore, A., Ahrman, E., Capece, D., Iansante, V., Zazzeroni, F., Alesse, E., Heinegard, D. & Teti, A. (2009) The glycosaminoglycan-binding domain of PRELP acts as a cell type-specific NF-kappaB inhibitor that impairs osteoclastogenesis. J Cell Biol, 187, 669-683.

Ruiter, D., Bogenrieder, T., Elder, D. & Herlyn, M. (2002) Melanoma-stroma interactions: structural and functional aspects. Lancet Oncol, 3, 35-43.

Runkle, E.A. & Mu, D. (2013) Tight junction proteins: from barrier to tumorigenesis. Cancer Lett, 337, 41-48.

Sabeh, F., Li, X.Y., Saunders, T.L., Rowe, R.G. & Weiss, S.J. (2009) Secreted versus membrane-anchored collagenases: relative roles in fibroblast-dependent collagenolysis and invasion. J Biol Chem, 284, 23001-23011.

Sabeh, F., Ota, I., Holmbeck, K., Birkedal-Hansen, H., Soloway, P., Balbin, M., Lopez-Otin, C., Shapiro, S., Inada, M., Krane, S., Allen, E., Chung, D. & Weiss, S.J. (2004) Tumor cell traffic through the extracellular matrix is controlled by the membrane-anchored collagenase MT1-MMP. J Cell Biol, 167, 769-781.

Sainio, A., Nyman, M., Lund, R., Vuorikoski, S., Bostrom, P., Laato, M., Bostrom, P.J. & Jarvelainen, H. (2013) Lack of decorin expression by human bladder cancer cells offers new tools in the therapy of urothelial malignancies. PLoS One, 8, e76190.

Sainio, A.a.J., H (2014) Extracellular matrix macromolecules: potential tools and targets in cancer gene therapy Molecular and Cellular Therapies.

Saito, T., Fukai, A., Mabuchi, A., Ikeda, T., Yano, F., Ohba, S., Nishida, N., Akune, T., Yoshimura, N., Nakagawa, T., Nakamura, K., Tokunaga, K., Chung, U.I. & Kawaguchi, H. (2010) Transcriptional regulation of endochondral ossification by HIF-2alpha during skeletal growth and osteoarthritis development. Nature medicine, 16, 678-686.

Sanchez-Carbayo, M., Socci, N.D., Lozano, J., Saint, F. & Cordon-Cardo, C. (2006) Defining molecular profiles of poor outcome in patients with invasive bladder cancer using oligonucleotide microarrays. J Clin Oncol, 24, 778-789.

Santra, M., Eichstetter, I. & Iozzo, R.V. (2000) An anti-oncogenic role for decorin. Down-regulation of ErbB2 leads to growth suppression and cytodifferentiation of mammary carcinoma cells. J Biol Chem, 275, 35153-35161.

Santra, M., Katakowski, M., Zhang, R.L., Zhang, Z.G., Meng, H., Jiang, F. & Chopp, M. (2006) Protection of adult mouse progenitor cells and human glioma cells by de novo decorin expression in an oxygen- and glucose-deprived cell culture model system. Journal of cerebral blood flow and metabolism : official journal of the International Society of Cerebral Blood Flow and Metabolism, 26, 1311-1322.

Santra, M., Mann, D.M., Mercer, E.W., Skorski, T., Calabretta, B. & Iozzo, R.V. (1997) Ectopic expression of decorin protein core causes a generalized growth suppression in neoplastic cells of various histogenetic origin and requires endogenous p21, an inhibitor of cyclin-dependent kinases. J Clin Invest, 100, 149-157.

Santra, M., Reed, C.C. & Iozzo, R.V. (2002) Decorin binds to a narrow region of the epidermal growth factor (EGF) receptor, partially overlapping but distinct from the EGF-binding epitope. J Biol Chem, 277, 35671-35681.

Santra, M., Skorski, T., Calabretta, B., Lattime, E.C. & Iozzo, R.V. (1995) De novo decorin gene expression suppresses the malignant phenotype in human colon cancer cells. Proc Natl Acad Sci U S A, 92, 7016-7020.

Schaefer, L., Babelova, A., Kiss, E., Hausser, H.J., Baliova, M., Krzyzankova, M., Marsche, G., Young, M.F., Mihalik, D., Gotte, M., Malle, E., Schaefer, R.M. & Grone, H.J. (2005) The matrix component biglycan is proinflammatory and signals through Toll-like receptors 4 and 2 in macrophages. J Clin Invest, 115, 2223-2233.

Schaefer, L., Beck, K.F., Raslik, I., Walpen, S., Mihalik, D., Micegova, M., Macakova, K., Schonherr, E., Seidler, D.G., Varga, G., Schaefer, R.M., Kresse, H. & Pfeilschifter, J. (2003) Biglycan, a nitric oxide-regulated gene, affects adhesion, growth, and survival of mesangial cells. J Biol Chem, 278, 26227-26237.

Schaefer, L. & Iozzo, R.V. (2008) Biological functions of the small leucine-rich proteoglycans: from genetics to signal transduction. J Biol Chem, 283, 21305-21309.

Schaefer, L. & Iozzo, R.V. (2012) Small leucine-rich proteoglycans, at the crossroad of cancer growth and inflammation. Curr Opin Genet Dev, 22, 56-57.

Schaefer, L. & Schaefer, R.M. (2010) Proteoglycans: from structural compounds to signaling molecules. Cell Tissue Res, 339, 237-246.

Schaefer, L., Tsalastra, W., Babelova, A., Baliova, M., Minnerup, J., Sorokin, L., Grone, H.J., Reinhardt, D.P., Pfeilschifter, J., Iozzo, R.V. & Schaefer, R.M. (2007) Decorin-mediated regulation of fibrillin-1 in the kidney involves the insulin-like growth factor-I receptor and Mammalian target of rapamycin. The American journal of pathology, 170, 301-315.

Scholzen, T., Solursh, M., Suzuki, S., Reiter, R., Morgan, J.L., Buchberg, A.M., Siracusa, L.D. & Iozzo, R.V. (1994) The murine decorin. Complete cDNA cloning, genomic organization, chromosomal assignment, and expression during organogenesis and tissue differentiation. J Biol Chem, 269, 28270-28281.

Schonherr, E., Sunderkotter, C., Iozzo, R.V. & Schaefer, L. (2005) Decorin, a novel player in the insulin-like growth factor system. J Biol Chem, 280, 15767-15772.

Schonherr, E., Sunderkotter, C., Schaefer, L., Thanos, S., Grassel, S., Oldberg, A., Iozzo, R.V., Young, M.F. & Kresse, H. (2004) Decorin deficiency leads to impaired angiogenesis in injured mouse cornea. Journal of vascular research, 41, 499-508.

Schonherr, E., Witsch-Prehm, P., Harrach, B., Robenek, H., Rauterberg, J. & Kresse, H. (1995) Interaction of biglycan with type I collagen. J Biol Chem, 270, 2776-2783.

Scott, P.G., McEwan, P.A., Dodd, C.M., Bergmann, E.M., Bishop, P.N. & Bella, J. (2004) Crystal structure of the dimeric protein core of decorin, the archetypal small leucine-rich repeat proteoglycan. Proc Natl Acad Sci U S A, 101, 15633-15638.

Segawa, Y., Muneta, T., Makino, H., Nimura, A., Mochizuki, T., Ju, Y.J., Ezura, Y., Umezawa, A. & Sekiya, I. (2009) Mesenchymal stem cells derived from synovium, meniscus, anterior cruciate ligament, and articular chondrocytes share similar gene expression profiles. Journal of orthopaedic research : official publication of the Orthopaedic Research Society, 27, 435-441.

Seidler, D.G., Goldoni, S., Agnew, C., Cardi, C., Thakur, M.L., Owens, R.T., McQuillan, D.J. & Iozzo, R.V. (2006) Decorin protein core inhibits in vivo cancer growth and metabolism by hindering epidermal growth factor receptor function and triggering apoptosis via caspase-3 activation. J Biol Chem, 281, 26408-26418.

Seomun, Y. & Joo, C.K. (2008) Lumican induces human corneal epithelial cell migration and integrin expression via ERK 1/2 signaling. Biochem Biophys Res Commun, 372, 221-225.

Sharpless, N.E. & DePinho, R.A. (1999) The INK4A/ARF locus and its two gene products. Curr Opin Genet Dev, 9, 22-30.

Shaulian, E. & Karin, M. (2001) AP-1 in cell proliferation and survival. Oncogene, 20, 2390-2400.

Shekhar, M.P., Werdell, J., Santner, S.J., Pauley, R.J. & Tait, L. (2001) Breast stroma plays a dominant regulatory role in breast epithelial growth and differentiation: implications for tumor development and progression. Cancer Res, 61, 1320-1326.

Shen, Z., Gantcheva, S., Sommarin, Y. & Heinegard, D. (1999) Tissue distribution of a novel cell binding protein, osteoadherin, in the rat. Matrix biology : journal of the International Society for Matrix Biology, 18, 533-542.

Sherr, C.J. (2001) The INK4a/ARF network in tumour suppression. Nature reviews. Molecular cell biology, 2, 731-737.

Sherr, C.J. (2004) Principles of tumor suppression. Cell, 116, 235-246.

Shin, K., Lee, J., Guo, N., Kim, J., Lim, A., Qu, L., Mysorekar, I.U. & Beachy, P.A. (2011) Hedgehog/Wnt feedback supports regenerative proliferation of epithelial stem cells in bladder. Nature, 472, 110-114.

Shintani, K., Matsumine, A., Kusuzaki, K., Morikawa, J., Matsubara, T., Wakabayashi, T., Araki, K., Satonaka, H., Wakabayashi, H., Iino, T. & Uchida, A. (2008) Decorin suppresses lung metastases of murine osteosarcoma. Oncol Rep, 19, 1533-1539.

Siegel, R., Ma, J., Zou, Z. & Jemal, A. (2014) Cancer statistics, 2014. CA Cancer J Clin, 64, 9-29.

Sifaki, M., Assouti, M., Nikitovic, D., Krasagakis, K., Karamanos, N.K. & Tzanakakis, G.N. (2006) Lumican, a small leucine-rich proteoglycan substituted with keratan sulfate chains is expressed and secreted by human melanoma cells and not normal melanocytes. IUBMB life, 58, 606-610.

Silva-Alvarez, C., Carrasco, M., Balmaceda-Aguilera, C., Pastor, P., Garcia Mde, L., Reinicke, K., Aguayo, L., Molina, B., Cifuentes, M., Medina, R. & Nualart, F. (2005) Ependymal cell differentiation and GLUT1 expression is a synchronous process in the ventricular wall. Neurochemical research, 30, 1227-1236.

Simoneau, A.R., Spruck, C.H., 3rd, Gonzalez-Zulueta, M., Gonzalgo, M.L., Chan, M.F., Tsai, Y.C., Dean, M., Steven, K., Horn, T. & Jones, P.A. (1996) Evidence for two tumor suppressor loci associated with proximal chromosome 9p to q and distal chromosome 9q in bladder cancer and the initial screening for GAS1 and PTC mutations. Cancer Res, 56, 5039-5043.

Simoneau, M., Aboulkassim, T.O., LaRue, H., Rousseau, F. & Fradet, Y. (1999) Four tumor suppressor loci on chromosome 9q in bladder cancer: evidence for two novel candidate regions at 9q22.3 and 9q31. Oncogene, 18, 157-163.

Singh, A.B. & Harris, R.C. (2004) Epidermal growth factor receptor activation differentially regulates claudin expression and enhances transepithelial resistance in Madin-Darby canine kidney cells. J Biol Chem, 279, 3543-3552.

Skandalis, S.S., Kletsas, D., Kyriakopoulou, D., Stavropoulos, M. & Theocharis, D.A. (2006) The greatly increased amounts of accumulated versican and decorin with specific post-translational modifications may be closely associated with the malignant phenotype of pancreatic cancer. Biochim Biophys Acta, 1760, 1217-1225.

Skandalis, S.S., Theocharis, D.A., Papageorgakopoulou, N. & Vynios, D.H. (2005) The extractability of extracellular matrix components as a marker of cartilage remodeling in laryngeal squamous cell carcinoma. Biochim Biophys Acta, 1721, 81-88.

Soderstrom, M., Bohling, T., Ekfors, T., Nelimarkka, L., Aro, H.T. & Vuorio, E. (2002) Molecular profiling of human chondrosarcomas for matrix production and cancer markers. Int J Cancer, 100, 144-151.

Sommarin, Y., Wendel, M., Shen, Z., Hellman, U. & Heinegard, D. (1998) Osteoadherin, a cell-binding keratan sulfate proteoglycan in bone, belongs to the family of leucine-rich repeat proteins of the extracellular matrix. J Biol Chem, 273, 16723-16729.

Soria-Valles, C., Gutierrez-Fernandez, A., Guiu, M., Mari, B., Fueyo, A., Gomis, R.R. & Lopez-Otin, C. (2013) The anti-metastatic activity of collagenase-2 in breast cancer cells is mediated by a signaling pathway involving decorin and miR-21. Oncogene.

Spassky, N., Merkle, F.T., Flames, N., Tramontin, A.D., Garcia-Verdugo, J.M. & Alvarez-Buylla, A. (2005) Adult ependymal cells are postmitotic and are derived from radial glial cells during embryogenesis. The Journal of neuroscience : the official journal of the Society for Neuroscience, 25, 10-18.

Stadler, W.M., Sherman, J., Bohlander, S.K., Roulston, D., Dreyling, M., Rukstalis, D. & Olopade, O.I. (1994) Homozygous deletions within chromosomal bands 9p21-22 in bladder cancer. Cancer Res, 54, 2060-2063.

Stephens, P., Hunter, C., Bignell, G., Edkins, S., Davies, H., Teague, J., Stevens, C., O'Meara, S., Smith, R., Parker, A., Barthorpe, A., Blow, M., Brackenbury, L., Butler, A., Clarke, O., Cole, J., Dicks, E., Dike, A., Drozd, A., Edwards, K., Forbes, S., Foster, R., Gray, K., Greenman, C., Halliday, K., Hills, K., Kosmidou, V., Lugg, R., Menzies, A., Perry, J., Petty, R., Raine, K., Ratford, L., Shepherd, R., Small, A., Stephens, Y., Tofts, C., Varian, J., West, S., Widaa, S., Yates, A., Brasseur, F., Cooper, C.S., Flanagan, A.M., Knowles, M., Leung, S.Y., Louis, D.N., Looijenga, L.H., Malkowicz, B., Pierotti, M.A., Teh, B., Chenevix-Trench, G., Weber, B.L., Yuen, S.T., Harris, G., Goldstraw, P., Nicholson, A.G., Futreal, P.A., Wooster, R. & Stratton, M.R. (2004) Lung cancer: intragenic ERBB2 kinase mutations in tumours. Nature, 431, 525-526.

Sternlicht, M.D. & Werb, Z. (2001) How matrix metalloproteinases regulate cell behavior. Annual review of cell and developmental biology, 17, 463-516.

Stoker, M., O'Neill, C., Berryman, S. & Waxman, V. (1968) Anchorage and growth regulation in normal and virus-transformed cells. Int J Cancer, 3, 683-693.

Stratton, M.R., Campbell, P.J. & Futreal, P.A. (2009) The cancer genome. Nature, 458, 719-724.

Strongin, A.Y. (2006) Mislocalization and unconventional functions of cellular MMPs in cancer. Cancer Metastasis Rev, 25, 87-98.

Stylianou, M., Skandalis, S.S., Papadas, T.A., Mastronikolis, N.S., Theocharis, D.A., Papageorgakopoulou, N. & Vynios, D.H. (2008) Stage-related decorin and versican expression in human laryngeal cancer. Anticancer Res, 28, 245-251.

Sugars, R.V., Olsson, M.L., Marchner, S., Hultenby, K. & Wendel, M. (2013) The glycosylation profile of osteoadherin alters during endochondral bone formation. Bone, 53, 459-467.

Sulis, M.L. & Parsons, R. (2003) PTEN: from pathology to biology. Trends in cell biology, 13, 478-483.

Svensson, L., Aszodi, A., Reinholt, F.P., Fassler, R., Heinegard, D. & Oldberg, A. (1999) Fibromodulin-null mice have abnormal collagen fibrils, tissue organization, and altered lumican deposition in tendon. J Biol Chem, 274, 9636-9647.

Syaidah, R., Horiguchi, K., Fujiwara, K., Tsukada, T., Kikuchi, M. & Yashiro, T. (2013) Laminin and collagen modulate expression of the small leucine-rich proteoglycan fibromodulin in rat anterior pituitary gland. Cell Tissue Res, 354, 633-638.

Takanosu, M., Boyd, T.C., Le Goff, M., Henry, S.P., Zhang, Y., Bishop, P.N. & Mayne, R. (2001) Structure, chromosomal location, and tissue-specific expression of the mouse opticin gene. Investigative ophthalmology & visual science, 42, 2202-2210.

Takeuchi, K. & Ito, F. (2010) EGF receptor in relation to tumor development: molecular basis of responsiveness of cancer cells to EGFR-targeting tyrosine kinase inhibitors. The FEBS journal, 277, 316-326.

Tasheva, E.S., Klocke, B. & Conrad, G.W. (2004) Analysis of transcriptional regulation of the small leucine rich proteoglycans. Molecular vision, 10, 758-772.

Theocharis, A.D. (2002) Human colon adenocarcinoma is associated with specific post-translational modifications of versican and decorin. Biochim Biophys Acta, 1588, 165-172.

Theocharis, A.D., Skandalis, S.S., Tzanakakis, G.N. & Karamanos, N.K. (2010) Proteoglycans in health and disease: novel roles for proteoglycans in malignancy and their pharmacological targeting. The FEBS journal, 277, 3904-3923.

Tillgren, V., Onnerfjord, P., Haglund, L. & Heinegard, D. (2009) The tyrosine sulfate-rich domains of the LRR proteins fibromodulin and osteoadherin bind motifs of basic clusters in a variety of heparin-binding proteins, including bioactive factors. J Biol Chem, 284, 28543-28553.

Todd, R. & Wong, D.T. (1999) Oncogenes. Anticancer Res, 19, 4729-4746.

Tomlins, S.A., Rhodes, D.R., Perner, S., Dhanasekaran, S.M., Mehra, R., Sun, X.W., Varambally, S., Cao, X., Tchinda, J., Kuefer, R., Lee, C., Montie, J.E., Shah, R.B., Pienta, K.J., Rubin, M.A. & Chinnaiyan, A.M. (2005) Recurrent fusion of TMPRSS2 and ETS transcription factor genes in prostate cancer. Science, 310, 644-648.

Tralhao, J.G., Schaefer, L., Micegova, M., Evaristo, C., Schonherr, E., Kayal, S., Veiga-Fernandes, H., Danel, C., Iozzo, R.V., Kresse, H. & Lemarchand, P. (2003) In vivo selective and distant killing of cancer cells using adenovirus-mediated decorin gene transfer. FASEB journal : official publication of the Federation of American Societies for Experimental Biology, 17, 464-466.

Tramontin, A.D., Garcia-Verdugo, J.M., Lim, D.A. & Alvarez-Buylla, A. (2003) Postnatal development of radial glia and the ventricular zone (VZ): a continuum of the neural stem cell compartment. Cerebral cortex, 13, 580-587.

Tropepe, V., Coles, B.L., Chiasson, B.J., Horsford, D.J., Elia, A.J., McInnes, R.R. & van der Kooy, D. (2000) Retinal stem cells in the adult mammalian eye. Science, 287, 2032-2036.

Troup, S., Njue, C., Kliewer, E.V., Parisien, M., Roskelley, C., Chakravarti, S., Roughley, P.J., Murphy, L.C. & Watson, P.H. (2003) Reduced expression of the small leucine-rich proteoglycans, lumican, and decorin is associated with poor outcome in node-negative invasive breast cancer. Clin Cancer Res, 9, 207-214.

Tsihlias, J. & Grossman, H.B. (2000) The utility of fibrin/fibrinogen degradation products in superficial bladder cancer. Urol Clin North Am, 27, 39-46.

Tsukita, S., Yamazaki, Y., Katsuno, T., Tamura, A. & Tsukita, S. (2008) Tight junction-based epithelial microenvironment and cell proliferation. Oncogene, 27, 6930-6938.

Tufvesson, E. & Westergren-Thorsson, G. (2002) Tumour necrosis factor-alpha interacts with biglycan and decorin. FEBS letters, 530, 124-128.

Turashvili, G., Bouchal, J., Baumforth, K., Wei, W., Dziechciarkova, M., Ehrmann, J., Klein, J., Fridman, E., Skarda, J., Srovnal, J., Hajduch, M., Murray, P. & Kolar, Z. (2007) Novel markers for differentiation of lobular and ductal invasive breast carcinomas by laser microdissection and microarray analysis. BMC cancer, 7, 55.

Uff, S., Clemetson, J.M., Harrison, T., Clemetson, K.J. & Emsley, J. (2002) Crystal structure of the platelet glycoprotein Ib(alpha) N-terminal domain reveals an unmasking mechanism for receptor activation. J Biol Chem, 277, 35657-35663.

van Tilborg, A.A., de Vries, A., de Bont, M., Groenfeld, L.E. & Zwarthoff, E.C. (2002) The random development of LOH on chromosome 9q in superficial bladder cancers. J Pathol, 198, 352-358.

Vij, N., Roberts, L., Joyce, S. & Chakravarti, S. (2004) Lumican suppresses cell proliferation and aids Fas-Fas ligand mediated apoptosis: implications in the cornea. Experimental eye research, 78, 957-971.

Vij, N., Roberts, L., Joyce, S. & Chakravarti, S. (2005) Lumican regulates corneal inflammatory responses by modulating Fas-Fas ligand signaling. Investigative ophthalmology & visual science, 46, 88-95.

Viola, M., Bartolini, B., Sonaggere, M., Giudici, C., Tenni, R. & Tira, M.E. (2007) Fibromodulin interactions with type I and II collagens. Connective tissue research, 48, 141-148.

Vogel, K.G. (1994) Glycosaminoglycans and Proteoglycans Academic Press, New York. Academic Press, New York.

Vuillermoz, B., Khoruzhenko, A., D'Onofrio, M.F., Ramont, L., Venteo, L., Perreau, C., Antonicelli, F., Maquart, F.X. & Wegrowski, Y. (2004) The small leucine-rich proteoglycan lumican inhibits melanoma progression. Exp Cell Res, 296, 294-306.

Watanabe, T., Komuro, Y., Kiyomatsu, T., Kanazawa, T., Kazama, Y., Tanaka, J., Tanaka, T., Yamamoto, Y., Shirane, M., Muto, T. & Nagawa, H. (2006) Prediction of sensitivity of rectal cancer cells in response to preoperative radiotherapy by DNA microarray analysis of gene expression profiles. Cancer Res, 66, 3370-3374.

Weber, C.K., Sommer, G., Michl, P., Fensterer, H., Weimer, M., Gansauge, F., Leder, G., Adler, G. & Gress, T.M. (2001) Biglycan is overexpressed in pancreatic cancer and induces G1-arrest in pancreatic cancer cell lines. Gastroenterology, 121, 657-667.

Wegrowski, Y., Pillarisetti, J., Danielson, K.G., Suzuki, S. & Iozzo, R.V. (1995) The murine biglycan: complete cDNA cloning, genomic organization, promoter function, and expression. Genomics, 30, 8-17.

Weinstein, I.B. (2000) Disorders in cell circuitry during multistage carcinogenesis: the role of homeostasis. Carcinogenesis, 21, 857-864.

Weinstein, I.B. (2002) Cancer. Addiction to oncogenes--the Achilles heal of cancer. Science, 297, 63-64.

Weinstein, I.B. & Joe, A.K. (2006) Mechanisms of disease: Oncogene addiction--a rationale for molecular targeting in cancer therapy. Nature clinical practice. Oncology, 3, 448-457.

Weiss, D.J., Liggitt, D. & Clark, J.G. (1999) Histochemical discrimination of endogenous mammalian beta-galactosidase activity from that resulting from lac-Z gene expression. The Histochemical journal, 31, 231-236.

Wendel, M., Sommarin, Y. & Heinegard, D. (1998) Bone matrix proteins: isolation and characterization of a novel cell-binding keratan sulfate proteoglycan (osteoadherin) from bovine bone. J Cell Biol, 141, 839-847.

Whinna, H.C., Choi, H.U., Rosenberg, L.C. & Church, F.C. (1993) Interaction of heparin cofactor II with biglycan and decorin. J Biol Chem, 268, 3920-3924.

Wiberg, C., Heinegard, D., Wenglen, C., Timpl, R. & Morgelin, M. (2002) Biglycan organizes collagen VI into hexagonal-like networks resembling tissue structures. J Biol Chem, 277, 49120-49126.

Wilda, M., Bachner, D., Just, W., Geerkens, C., Kraus, P., Vogel, W. & Hameister, H. (2000) A comparison of the expression pattern of five genes of the family of small leucine-rich proteoglycans during mouse development. Journal of bone and mineral research : the official journal of the American Society for Bone and Mineral Research, 15, 2187-2196.

Wood, P.A. (2000) Phenotype assessment: are you missing something? Comparative medicine, 50, 12-15.

Wu, X.R. (2005) Urothelial tumorigenesis: a tale of divergent pathways. Nat Rev Cancer, 5, 713-725.

Xu, H., Sta Iglesia, D.D., Kielczewski, J.L., Valenta, D.F., Pease, M.E., Zack, D.J. & Quigley, H.A. (2007) Characteristics of progenitor cells derived from adult ciliary body in mouse, rat, and human eyes. Investigative ophthalmology & visual science, 48, 1674-1682.

Xu, T., Bianco, P., Fisher, L.W., Longenecker, G., Smith, E., Goldstein, S., Bonadio, J., Boskey, A., Heegaard, A.M., Sommer, B., Satomura, K., Dominguez, P., Zhao, C., Kulkarni, A.B., Robey, P.G. & Young, M.F. (1998) Targeted disruption of the biglycan gene leads to an osteoporosis-like phenotype in mice. Nature genetics, 20, 78-82.

Yamaguchi, Y., Mann, D.M. & Ruoslahti, E. (1990) Negative regulation of transforming growth factor-beta by the proteoglycan decorin. Nature, 346, 281-284.

Yamamoto, K., Ohga, N., Hida, Y., Maishi, N., Kawamoto, T., Kitayama, K., Akiyama, K., Osawa, T., Kondoh, M., Matsuda, K., Onodera, Y., Fujie, M., Kaga, K., Hirano, S., Shinohara, N., Shindoh, M. & Hida, K. (2012) Biglycan is a specific marker and an autocrine angiogenic factor of tumour endothelial cells. Br J Cancer, 106, 1214-1223.

Yang, Y., Topol, L., Lee, H. & Wu, J. (2003) Wnt5a and Wnt5b exhibit distinct activities in coordinating chondrocyte proliferation and differentiation. Development, 130, 1003-1015.

Ying, S., Shiraishi, A., Kao, C.W., Converse, R.L., Funderburgh, J.L., Swiergiel, J., Roth, M.R., Conrad, G.W. & Kao, W.W. (1997) Characterization and expression of the mouse lumican gene. J Biol Chem, 272, 30306-30313.

Yoshioka, N., Inoue, H., Nakanishi, K., Oka, K., Yutsudo, M., Yamashita, A., Hakura, A. & Nojima, H. (2000) Isolation of transformation suppressor genes by cDNA subtraction: lumican suppresses transformation induced by v-src and v-K-ras. J Virol, 74, 1008-1013.

Young, M.F., Bi, Y., Ameye, L. & Chen, X.D. (2002) Biglycan knockout mice: new models for musculoskeletal diseases. Glycoconjugate journal, 19, 257-262.

Zarrabi, K., Dufour, A., Li, J., Kuscu, C., Pulkoski-Gross, A., Zhi, J., Hu, Y., Sampson, N.S., Zucker, S. & Cao, J. (2011) Inhibition of matrix metalloproteinase 14 (MMP-14)-mediated cancer cell migration. J Biol Chem, 286, 33167-33177.

Zeltz, C., Brezillon, S., Perreau, C., Ramont, L., Maquart, F.X. & Wegrowski, Y. (2009) Lumcorin: a leucine-rich repeat 9-derived peptide from human lumican inhibiting melanoma cell migration. FEBS letters, 583, 3027-3032.

Zhang, G., Chen, S., Goldoni, S., Calder, B.W., Simpson, H.C., Owens, R.T., McQuillan, D.J., Young, M.F., Iozzo, R.V. & Birk, D.E. (2009) Genetic evidence for the coordinated regulation of collagen fibrillogenesis in the cornea by decorin and biglycan. J Biol Chem, 284, 8888-8897.

Zhang, S., McCarter, J.D., Okamura-Oho, Y., Yaghi, F., Hinek, A., Withers, S.G. & Callahan, J.W. (1994) Kinetic mechanism and characterization of human beta-galactosidase precursor secreted by permanently transfected Chinese hamster ovary cells. Biochem J, 304 (Pt 1), 281-288.

Zheng, Z., Nguyen, C., Zhang, X., Khorasani, H., Wang, J.Z., Zara, J.N., Chu, F., Yin, W., Pang, S., Le, A., Ting, K. & Soo, C. (2011) Delayed wound closure in fibromodulin-deficient mice is associated with increased TGF-beta3 signaling. The Journal of investigative dermatology, 131, 769-778.

Zhu, J.X., Goldoni, S., Bix, G., Owens, R.T., McQuillan, D.J., Reed, C.C. & Iozzo, R.V. (2005) Decorin evokes protracted internalization and degradation of the epidermal growth factor receptor via caveolar endocytosis. J Biol Chem, 280, 32468-32479.

Zuscik, M.J., Hilton, M.J., Zhang, X., Chen, D. & O'Keefe, R.J. (2008) Regulation of chondrogenesis and chondrocyte differentiation by stress. J Clin Invest, 118, 429-438.